Terahertz time-domain ellipsometry based on spintronic phenomena

Dissertation by

Pierre Koleják

UNIVERSITY OF LILLE
Institute of Electronics, Microelectronics and Nanotechnology

&

VSB – TECHNICAL UNIVERSITY OF OSTRAVA
Faculty of Materials Science and Technology

December 10, 2024

Committee members:

HENRI JAFFRES Directeur de recherche, Laboratoire Albert Fert, CNRS, France	President
MATHIAS VANWOLLEGHEM Chargé de recherche, IEMN CNRS, Université de Lille, France	Supervisor
KAMIL POSTAVA Associate professor, VSB-Technical University of Ostrava, Czech Republic	Supervisor
PETR KUŽEL Associate professor, Czech Academy of Sciences, Czech Republic	Reviewer
ILEANA-CRISTINA BENEA-CHELMUS Assistant professor, École Polytechnique Fédérale de Lausanne, Switzerland	Reviewer
DMITRY TURCHINOVICH Professor, Fakultät für Physik, Universität Bielefeld, Germany	Reviewer
NICOLAS TIERCELIN Directeur de recherche, IEMN CNRS, Université de Lille, France	Invited

Ellipsométrie temporelle térahertz basée sur des phénomènes spintroniques

Thèse de doctorat par

Pierre Koleják

UNIVERSITÉ DE LILLE
Institut d'Électronique, de Microélectronique et de Nanotechnologie

&

VSB – UNIVERSITÉ TECHNIQUE D'OSTRAVA
Faculté des Sciences et Technologies des Matériaux

10 décembre 2024

Membres du jury:

HENRI JAFFRES Directeur de recherche, Laboratoire Albert Fert, CNRS, France	Président
MATHIAS VANWOLLEGHEM Chargé de recherche, IEMN CNRS, Université de Lille, France	Directeur
KAMIL POSTAVA Professeur associé, VSB-Université Technique d'Ostrava, République tchèque	Directeur
PETR KUŽEL Professeur associé, Académie tchèque des sciences, République tchèque	Rapporteur
ILEANA-CRISTINA BENEA-CHELMUS Professeur assistant, École Polytechnique Fédérale de Lausanne, Suisse	Rapporteur
DMITRY TURCHINOVICH Professeur, Faculté de Physique, Université de Bielefeld, Allemagne	Rapporteur
NICOLAS TIERCELIN Directeur de recherche, IEMN CNRS, Université de Lille, France	Invité

I have never let my schooling interfere with my education.

Mark Twain

Acknowledgement

I would like to thank my family, friends, and everyone who has supported me and wished me success throughout my academic journey. First and foremost, I would like to thank my parents for all the good they have done for me. To my mother, who has been a true example of kindness and selflessness, and to my father, whose knowledge and skills I have admired since childhood. Special thanks also go to my siblings, Charlotte and Daniel, who have always stood by my side. Among my long-time friends, I am especially grateful to Eva, Filip, Michal and Niky for their support, which has always meant a lot to me.

None of this would have been possible without the guidance of my supervisors, Mathias Vanwolleghem and Kamil Postava. I thank them for all the opportunities, experiences, patience, and sometimes even exhausting meticulousness that have led to my personal growth. I greatly appreciate their willingness to undertake the challenging form of joint supervision, which provided me with two perspectives throughout my studies. I believe it broadened my perspective and made me a better scientist. I also thank Kamil for the nine years I spent as his student and his progressive approach, even in places full of outdated practices. I want to extend special thanks to Mathias for the revolution he introduced into my studies with his thoughtful and demanding nature. I admit that even until my PhD ended, I felt there was still much I could learn from him.

A huge thanks goes to my long-time colleague, classmate, and close friend Daniel Vala, with whom I shared the joys and hardships that university life brings. Especially during the PhD, he was a kindred spirit with whom I could communicate even without words. It was an honor to face all the challenges and crises alongside someone with both heart and mind in the right place.

I would also like to thank Martin Mičica, who was an inspiring figure for me in experimental work and who was never *a chachar*. I could always turn to him, and he never turned his back on me.

Special thanks go to Tomáš, to whom I owe many battles we fought together over board games. Also, to Mariusz, Iva, Vlaďka, Lenka, Adam, Martin T., Roman, Kuba Ch., Michal, Kuba T., Eva, Zuzka, Pavlína, and many others for countless great moments and experiences. Among my colleagues, I would like to thank Robin, Lukáš, Jiamig, and Michal Lesňák for creating a pleasant working environment. My thanks also extend to Tibor, whose unique approach to problem-solving never seemed to avoid offering a fresh perspective.

I thank Felix Paries for the fantastic collaboration, discussions, and friendship. His enthusiasm, motivation, and managerial skills have been an example for me.

Among my French colleagues, I would like to thank Jean-Francois Lampin, whose abilities and knowledge I deeply admired and from whom I learned a great deal. I am also grateful to Nicolas Tiercelin and Geoffrey Lezier, with whom I have collaborated closely and gladly throughout my PhD studies. Additionally, I would like to thank Emilien, Cristianne, Victor, Alex, Charbel, Quintin, Alexandra, and Romain.

In conclusion, I would like to thank all the paper co-authors for their excellent collaboration, insightful discussions, and valuable advice, which, through our collective efforts, led to several scientific achievements.

Poděkování

Chtěl bych poděkovat své rodině, přátelům a všem, kteří mě od počátků mého studia podporovali a přáli mi mnoho úspěchů. Na prvním místě bych chtěl poděkovat svým rodičům za všechno dobré, co pro mě v životě udělali. Mamince, která mi byla vzorem laskavého a obětavého člověka, a otci, jehož znalosti a zručnost jsem od malička obdivoval. Zvláštní poděkování patří i mým sourozencům, Charlotte a Danielovi, kteří vždy stáli po mém boku. Z mých dlouholetých přátel pak Evě, Filipovi, Michalovi a Niky za podporu, která pro mě vždy hodně znamenala.

Nic z toho by se nepodařilo bez vedení mých školitelů Mathiase Vanwolleghema a Kamila Postavy. Děkuji jim za všechny příležitosti, zkušenosti, trpělivost a někdy až vyčerpávající pedantství, které mi přinesly velký osobní růst. Cením si, že přistoupili na tak náročnou formu vedení, jako je cotutelle, který mi poskytl dvojitý pohled napříč celým studiem. Věřím, že mě to obohatilo o nadhled a udělalo ze mě lepšího vědce. Kamilovi navíc děkuji za všech devět let, které jsem byl jeho studentem. I za to, jak pokrokový byl i na místech plných přežitků. Mathiasovi bych chtěl speciálně poděkovat za to, jakou revoluci pro mě znamenal vstup tak přemýšlivého a náročného člověka do mého studia. A přiznávám, že až do konce svého doktorského studia jsem cítil, že mě má mnoho co naučit.

Velké díky bych chtěl věnovat svému dlouholetému kolegovi, spolužákovi a blízkému příteli Danielu Valovi, s nímž jsem sdílel radosti i útrapy, které vysokoškolské studium přináší. Zvláště v doktorském studiu mi byl spřízněnou duší, se kterou jsem si rozuměl i beze slov. Bylo mi ctí čelit všem výzvám i krizím s tímto člověkem se srdcem a hlavou na správném místě.

Dále bych chtěl poděkovat Martinu Mičicovi, který mi byl velkým vzorem v experimentální práci, a který nikdy nebyl *chachar*, vždy jsem se na něj mohl obrátit a nikdy se ke mně neotočil zády.

Speciální díky patří také Tomášovi, kterému děkuji za mnoho bitev, které jsme spolu svedli na hracím plátně. Dále pak Mariuszovi, Ivě, Vlaďce, Lence, Adamovi, Martinu T., Romanovi, Kubovi Ch., Michalovi, Kubovi T., Evě, Zuzce, Pavlíně a dalším za mnoho skvělých chvil a zážitků. Z kolegů pak samozřejmě Robinovi, Lukášovi, Jiamigovi a Michalu Lesňákovi za příjemné pracovní prostředí. Mému poděkování se nevyhne ani Tibor, jehož originální přístup k řešení problémů mi poskytl nevídaný rozhled.

Chtěl bych také poděkovat Felixu Pariesovi za úžasnou spolupráci, diskuze a hlavně přátelství. Jeho nadšení, motivace a manažerské schopnosti pro mě byly příkladem.

Z mých francouzských kolegů bych chtěl poděkovat zcela určitě Jean-Francoisi Lampinovi, jehož schopností jsem si hluboce vážil a který mě mnohému naučil. Dále Nicolasovi Tiercelinovi a Geoffreymu Lezierovi, se kterými jsem velmi úzce a rád spolupracoval napříč celým mým doktorským studiem. Dále pak také Emilienovi, Cristianne, Victorovi, Alexovi, Charbelovi, Quintinovi, Alexandře a Romainovi.

Na závěr bych rád poděkoval všem spoluautorům článků za vynikající spolupráci, odborné diskuze a cenné rady, které společným úsilím vedly k dosažení několika vědeckých výsledků.

Abstract

Ellipsometry is a foundational technique in materials science, enabling precise characterization of optical properties, thickness, and composition. Extending ellipsometry into the terahertz (THz) range unlocks new opportunities to probe fundamental material characteristics such as conductivity and carrier dynamics—key for advancements in semiconductors, energy storage, and ultra-fast telecommunications. However, existing THz ellipsometry methods often adapt traditional optical ellipsometry without fully exploiting the unique capabilities of time-domain spectroscopy. These systems result in incomplete polarization descriptions and face challenges in achieving high-quality polarization control due to the limitations of THz components. Consequently, they are insufficient for analyzing general anisotropic materials, lacking complete amplitude and phase information essential for comprehensive characterization.

This dissertation overcomes these limitations by developing a novel terahertz complete time-domain spectroscopic ellipsometry (THz-cTDSE). Our system captures both amplitude and phase information, determining the full Jones and Mueller matrices of anisotropic samples. Ellipsometry often requires advanced expertise in interpreting complex matrix data; therefore, we introduced Pauli exponential coefficients, which intuitively represent polarization responses such as retardation and diattenuation across all linear, diagonal, and circular polarizations—until now experimentally unattainable due to the absence of complete coherent ellipsometry. Furthermore, we developed a robust calibration technique compensating for misalignments and eliminating the need for precise component alignment, enhancing measurement accuracy and reliability applicable to many ellipsometric systems.

To address the requirement for refined polarization, we employ spintronic terahertz emitters (STEs), which provide broadband, gapless emission of linear polarization that is easily controllable via a magnetic field and offers high extinction ratios. We present the first experimental application of STEs for polarization control in ellipsometry. To fully leverage the potential of STEs, we developed emitters capable of generating robust signals with advanced methods for polarization control: (i) By integrating STEs with photonic cavities, we maximized pump absorption within the STE layers, achieving an 8dB increase—one of the highest reported enhancements—facilitating faster measurements and improved data quality. Additionally, we incorporated THz resonant cavities, enabling constructive interference that doubles the THz extraction, leading to an overall estimated improvement of 15dB. (ii) We engineered uniaxial magnetic anisotropy in STEs using a ferromagnetic trilayer for advanced polarization control, enabling precise 360° polarization rotation essential for accurate ellipsometry. Additionally, we developed voltage-controlled polarization mechanisms using magnetostrictive emitters, marking a crucial step toward fully integrable STE systems.

Recognizing the potential of STEs' ultrafast and uniform spectral response for frequency-domain applications, we extended our work beyond the time domain. We demonstrated a proof-of-concept for highly tunable spintronic photomixers with frequency-stable efficiency, overcoming limitations of conventional photomixers that suffer efficiency loss at higher frequencies. By generating sustained frequency combs up to 1.05 THz, we showcased the versatility of STEs and unlocked new possibilities for high-resolution, tunable THz applications.

This work establishes a robust platform for precise THz material characterization, significantly advancing materials science and technologies. By leveraging polarization sensitivity, our THz-cTDSE system offers deeper insights into material properties, driving innovations in non-invasive diagnostics, heterostructure fabrication, quality control, and the development of novel materials.

Abstrakt

Ellipsometrie je klíčová technika v materiálových vědách, která umožňuje precizní měření optických vlastností, tloušťky a složení materiálů. Její rozšíření do terahertzové (THz) oblasti přináší zcela nové možnosti, jak zkoumat základní charakteristiky materiálů, jako je vodivost a dynamika nosičů náboje – což je zásadní pro průlomové inovace v oblasti polovodičů, ukládání energie a ultrarychlých telekomunikací. Současné metody THz ellipsometrie však často vycházejí z tradiční optické ellipsometrie, aniž by plně využívaly potenciál časově-rozlišovací spektroskopie. Výsledkem jsou neúplné popisy polarizace a potíže s dosažením vysoké kvality kontroly polarizace kvůli omezením THz komponent. Tyto systémy tedy nejsou vhodné pro analýzu obecně anizotropních materiálů, protože chybí komplexní informace o amplitudě a fázi – klíčové pro plnohodnotnou charakterizaci.

Tato disertační práce řeší uvedené nedostatky vývojem nové techniky – kompletní časově-rozlišovací spektroskopické THz ellipsometrie (THz-cTDSE). Náš systém je schopný zachytit jak amplitudu, tak fázovou informaci a umožňuje určovat plné Jonesovy a Muellerovy matice anizotropních vzorků. Ellipsometrie je často složitá na interpretaci, protože vyžaduje pokročilé znalosti pro analýzu maticových dat. Proto jsme zavedli koeficienty Pauliho exponenciální reprezentace, které intuitivně vyjadřují polarizační odezvy, jako je retardace a diattenuace, pro všechny druhy polarizací – lineární, diagonální i kruhové. Tyto koeficienty nebyly doposud experimentálně dostupné kvůli absenci kompletní koherentní ellipsometrie. Vyvinuli jsme také robustní kalibrační techniku, která kompenzuje chyby vyplývající z nesprávného nastavení komponent a odstraňuje nutnost precizního nastavení, čímž zvyšuje přesnost a spolehlivost měření pro širokou škálu ellipsometrických systémů.

Pro dosažení pokročilé kontroly polarizace jsme využili spintronické terahertzové emitory (STE), které poskytují širokopásmové, spojité záření s lineární polarizací, snadno ovladatelné pomocí magnetického pole, s vysokými hodnotami extinkčního poměru. Představujeme vůbec první experimentální využití STE k řízení polarizace v ellipsometrii. Abychom naplno využili potenciál těchto STE, vyvinuli jsme emitory schopné generovat silné signály a implementovali pokročilé metody kontroly polarizace: (i) Integrací STE s fotonickými dutinami jsme maximalizovali absorpci čerpacího záření ve vrstvách STE, čímž jsme dosáhli 8dB zvýšení výkonu – což je jedno z nejvyšších dosud zaznamenaných vylepšení – umožňující rychlejší měření a vyšší kvalitu dat. Kromě toho jsme implementovali THz rezonanční kavity, které umožňují konstruktivní interferenci, což vedlo k dvojnásobnému zvýšení THz extrakce a při kombinaci vedoucí k celkovému zlepšení o přibližně 15dB. (ii) Vytvořili jsme jednoosou magnetickou anizotropii v STE pomocí feromagnetické trojvrstvy, což umožnilo pokročilou kontrolu polarizace s možností 360° rotace, která je klíčová pro přesnou ellipsometrii. Dále jsme vyvinuli mechanismy kontroly polarizace pomocí napětí, založené na magnetostrikčních emitorech, čímž jsme učinili zásadní krok směrem k plně integrovatelným STE systémům.

Vzhledem k tomu, že STE mají ultrarychlou a uniformní spektrální odezvu, jsme naši práci rozšířili i na aplikace ve frekvenční oblasti. Představili jsme proof-of-concept vysoce laditelných spintronických fotomixérů s frekvenčně stabilní účinností, což překonává omezení konvenčních fotomixérů, které ztrácejí účinnost při vyšších frekvencích. Generováním stabilních frekvenčních čar až do 1.05 THz jsme ukázali univerzálnost STE a otevřeli nové možnosti pro vysokorozlišovací a laditelné THz aplikace.

Tato práce představuje robustní platformu pro precizní THz charakterizaci materiálů a významně přispívá k rozvoji materiálových věd a technologií. Využitím citlivosti na polarizaci náš systém THz-cTDSE přináší hlubší vhled do vlastností materiálů, což podpoří inovace v oblastech neinvazivní diagnostiky, výroby heterostruktur, kontroly kvality a vývoje nových materiálů.

Résumé

L'ellipsométrie est une technique fondamentale dans les sciences des matériaux, permettant une caractérisation précise des propriétés optiques, de l'épaisseur et de la composition. L'extension de l'ellipsométrie au domaine des térahertz (THz) ouvre de nouvelles perspectives pour explorer des caractéristiques essentielles des matériaux, telles que la conductivité et la dynamique des porteurs de charge, des éléments cruciaux pour les avancées dans les semi-conducteurs, le stockage d'énergie et les télécommunications ultra-rapides. Cependant, les méthodes actuelles d'ellipsométrie THz se contentent souvent d'adapter l'ellipsométrie optique traditionnelle, sans exploiter pleinement les capacités uniques de la spectroscopie dans le domaine temporel. Ces systèmes aboutissent à des descriptions incomplètes de la polarisation et rencontrent des difficultés à contrôler la polarisation avec une qualité suffisante en raison des limitations des composants THz. Par conséquent, ils s'avèrent insuffisants pour analyser les matériaux anisotropes, manquant d'informations complètes sur l'amplitude et la phase, qui sont essentielles pour une caractérisation exhaustive.

Cette thèse surmonte ces limitations en développant une nouvelle ellipsométrie spectroscopique complète dans le domaine temporel des térahertz (THz-cTDSE). Notre système capte à la fois les informations d'amplitude et de phase, permettant de déterminer les matrices complètes de Jones et de Mueller pour les échantillons anisotropes. L'ellipsométrie nécessite souvent une expertise avancée pour interpréter des données matricielles complexes. C'est pourquoi nous avons introduit des coefficients exponentiels de Pauli, qui représentent intuitivement les réponses de polarisation telles que le retard de phase et la diatténuation pour toutes les polarisations linéaires, diagonales et circulaires — jusqu'à présent impossibles à obtenir expérimentalement en raison de l'absence d'une ellipsométrie cohérente complète. De plus, nous avons développé une technique de calibration robuste qui compense les désalignements et élimine le besoin d'un alignement précis des composants, améliorant ainsi la précision et la fiabilité des mesures, applicables à de nombreux systèmes ellipsométriques.

Pour répondre aux exigences de contrôle avancé de la polarisation, nous utilisons des émetteurs térahertz spintroniques (STE), qui offrent une émission large bande et sans lacunes de polarisation linéaire, facilement contrôlable par un champ magnétique, avec des rapports d'extinction élevés. Nous présentons la première application expérimentale des STE pour le contrôle de la polarisation en ellipsométrie. Afin de tirer pleinement parti du potentiel des STE, nous avons développé des émetteurs capables de générer des signaux puissants avec des méthodes avancées de contrôle de la polarisation : (i) En intégrant les STE avec des cavités photoniques, nous avons maximisé l'absorption de la pompe dans les couches STE, atteignant une augmentation de 8 dB — l'une des améliorations les plus élevées jamais rapportées — facilitant des mesures plus rapides et une qualité de données améliorée. De plus, nous avons incorporé des cavités résonantes THz permettant une interférence constructive qui double l'extraction des signaux THz, conduisant à une amélioration globale estimée à 15 dB. (ii) Nous avons conçu une anisotropie magnétique uniaxiale dans les STE à l'aide d'une trilame ferromagnétique pour un contrôle avancé de la polarisation, permettant une rotation précise de 360° de la polarisation, indispensable pour une ellipsométrie précise. De plus, nous avons développé des mécanismes de polarisation contrôlés par tension utilisant des émetteurs magnétostrictifs, marquant une étape cruciale vers des systèmes STE entièrement intégrés.

Reconnaissant le potentiel des STE avec leur réponse spectrale ultrarapide et uniforme pour des applications dans le domaine fréquentiel, nous avons étendu notre travail au-delà du domaine temporel. Nous avons démontré une preuve de concept pour des photomélangeurs spintroniques

hautement réglables avec une efficacité stable en fréquence, surmontant les limitations des photomélangeurs conventionnels qui perdent en efficacité à des fréquences plus élevées. En générant des peignes de fréquence continus allant jusqu'à 1,05 THz, nous avons montré la polyvalence des STE et ouvert de nouvelles perspectives pour des applications THz à haute résolution et réglables.

Ce travail établit une plateforme solide pour la caractérisation précise des matériaux dans le domaine THz, faisant progresser de manière significative les sciences et technologies des matériaux. En exploitant la sensibilité à la polarisation, notre système THz-cTDSE offre une compréhension plus approfondie des propriétés des matériaux, favorisant des innovations dans le diagnostic non invasif, la fabrication d'hétérostructures, le contrôle de la qualité et le développement de nouveaux matériaux.

Contents

1 Introduction **1**
1.1 Context of the research . . . 1
1.1.1 Terahertz radiation and its importance . . . 1
1.1.2 Why is the terahertz gap challenging? . . . 2
1.1.3 Need for terahertz time-domain ellipsometry . . . 4
1.2 Challenges in terahertz time-domain ellipsometry . . . 6
1.3 Proposed solution: terahertz complete time-domain ellipsometry based on spintronic emitters . . . 8
1.4 Principles of spintronic terahertz emitters . . . 9
1.5 Potential of spintronic terahertz emitters . . . 10
1.5.1 Broadband and gapless THz emission . . . 10
1.5.2 Intrinsic polarization control . . . 11
1.5.3 Peak-power and optical-to-THz conversion efficiency . . . 12
1.6 Development of spintronic emitters for ellipsometry: objectives and methodology . . . 14
1.6.1 Research objectives . . . 14
1.7 Structure of the thesis . . . 16

2 Introduction to polarized light and ellipsometry **17**
2.1 Polarization of light . . . 17
2.1.1 Mueller and Jones calculus . . . 19
2.1.2 Interpreting Jones and Mueller Matrices . . . 22

3 Development of terahertz laboratory **32**
3.1 Motivation behind constructing the laser infrastructure . . . 32
3.2 Development of STE-based THz-TDS ellipsometer . . . 32
3.3 Principle of acquisition with the amplifier . . . 34
3.4 Expansion of THz-TDS experimental capabilities . . . 35
3.5 Concluding remarks on experimental design . . . 37

4 Overview of publications and their relevance to the thesis **39**
4.1 Enhancement of efficiency and performance of terahertz spintronic emitters . . . 39
4.1.1 Maximizing the electromagnetic efficiency of spintronic terahertz emitters . . . 42
4.1.2 Spintronic terahertz emitters with integrated metallic terahertz cavities . . . 45
4.1.3 Optical damage thresholds of single-mode fiber-tip spintronic terahertz emitters 51
4.2 Polarization control of spintronic emitters . . . 55

4.2.1 360° polarization control of terahertz spintronic emitters using uniaxial FeCo/$TbCo_2$/FeCo trilayers . . . 58
4.2.2 Fully reversible magnetoelectric voltage controlled THz polarization rotation in magnetostrictive spintronic emitters on PMN-PT . . . 61
4.3 Complete time-domain ellipsometry . . . 65
4.3.1 Terahertz time-domain ellipsometry with spintronic emitters: Pauli coefficients as a superior alternative to Jones and Mueller matrices . . . 67
4.3.2 Effects of optical activity to Mueller matrix ellipsometry of composed waveplates . . . 72
4.4 Ultra-broadband spin-driven photomixing . . . 77
4.4.1 Spintronic inverse spin hall photomixing beyond 1 THz . . . 78

5 Publications **83**
Paper I
Koleják, Pierre, *et al.* "Maximizing the electromagnetic efficiency of spintronic terahertz emitters." *Advanced Photonics Research* (2024): 2400064 . . . 83
Paper II
Mičica, Martin, *et al.* "Spintronic terahertz emitters with integrated metallic terahertz cavities." *Nanophotonics* 13.10 (2024): 1899-1907 . . . 111
Paper III
Paries, Felix, *et al.* "Optical damage thresholds of single-mode fiber-tip spintronic terahertz emitters." *Optics Express* 32.14 (2024): 24826-24838 . . . 121
Paper IV
Koleják, Pierre, *et al.* "360° polarization control of terahertz spintronic emitters using uniaxial FeCo/$TbCo_2$/FeCo trilayers." *ACS photonics* 9.4 (2022): 1274-1285 . . . 135
Paper V
Lezier, Geoffrey, *et al.* "Fully reversible magnetoelectric voltage controlled THz polarization rotation in magnetostrictive spintronic emitters on PMN-PT." *Applied Physics Letters* 120.15 (2022) . . . 157
Paper VI
Koleják, Pierre, *et al.* "Terahertz time-domain ellipsometry with spintronic emitters: Pauli coefficients as a superior alternative to Jones and Mueller matrices." (2024): submitted . . . 164
Paper VII
Vala, Daniel, *et al.* "Effects of optical activity to Mueller matrix ellipsometry of composed waveplates." *Optics Express* 29.7 (2021): 10434-10450 . . . 188
Paper VIII
Kolejak, Pierre, *et al.* "Spintronic inverse spin hall photomixing beyond 1THz." *48th IRMMW-THz. IEEE*, 2023: 17–22 . . . 206

6 Conclusion **209**

List of Figures

1.1 Transparency of Earth's atmosphere across the electromagnetic spectrum 3
1.2 Time-Frequency demonstration of a THz field 4
1.3 Illustration of the terahertz time-domain ellipsometry setup 5
1.4 Operational principles of a spintronic terahertz emitter 10
1.5 Frequency and time domain comparison of terahertz sources 11
2.1 Graphical representation of the polarization ellipse formed by an oscillating electromagnetic field 18
2.2 Schematic representation of polarization states in the infinite complex plane $\tilde{\chi}$ 19
2.3 Creation of Poincaré sphere 20
2.4 Poincaré sphere and Stokes vectors 20
2.5 Illustration of depolarization 28
2.6 Graphical interpretation of Jones and Mueller matrices 29
3.1 Developed ultrashort and high-power laser infrastructure 33
3.2 Photograph of the constructed terahertz time-domain ellipsometer 34
3.3 Comparison of repetition rate regimes of pulsed lasers 35
3.4 Constructed arrangement with tunable source pumping 36
3.5 Constructed arrangement with tunable sample pumping 37
3.6 Alternative configuration in focused mode 38
4.1 Comparison of terahertz sources based on different generation mechanisms, including optical rectification (OR), difference frequency generation (DFG), plasma sources, photoconductive antennas, and spintronic emitters 40
4.2 Process flow of our simulation framework 41
4.3 Simulation of THz emitter configurations 43
4.4 Comparison of terahertz waveform and absorption profiles for the enhanced spintronic emitter 44
4.5 Scheme of spintronic terahertz emitter (STE) integrated with a terahertz cavity . . . 46
4.6 Simulated terahertz emission from a spintronic emitter integrated with a terahertz cavity 47
4.7 The simulated nonstationary absorption of a spintronic emitter integrated with the terahertz cavity 47
4.8 Simulated terahertz spectra of a spintronic emitter integrated with a terahertz cavity 48
4.9 Comparison of experimental and simulated terahertz waveforms for a spintronic emitter integrated with a terahertz cavity 49
4.10 Demonstration of terahertz emitter integrated with an anisotropic A-cut sapphire substrate 50
4.11 Simulated terahertz signal for a spintronic emitter integrated with an optimized photonic cavity and a terahertz cavity of varying thickness 51

4.12 Fluent thresholds of the free-standing spintronic emitter at high power regime 52
4.13 Close-up image of a fiber-tip spintronic terahertz emitter 53
4.14 The optical damage threshold for a fiber-tip spintronic terahertz emitter 54
4.15 Simulated magnetic and terahertz polarization field distributions for spintronic emitter 55
4.16 Comparison of magnetic hysteresis loops measured by terahertz time-domain spectroscopy and vibrating sample magnetometry 56
4.17 Comparison of standard and anisotropic spintronic terahertz emitter designs 57
4.18 Magnetic properties of FeCo, $TbCo_2$, and FeCo/$TbCo_2$/FeCo Structures 58
4.19 Magnetization control in spintronic terahertz emitters using the Stoner-Wohlfarth model 59
4.20 Stoner-Wohlfarth control of the polarization of uniaxial spintronic terahertz emitter . 60
4.21 Experimental demonstration of time-resolved terahertz polarization control 61
4.22 Demonstration of magnetostriction in a Tb^{3+} $4f^8$ system 62
4.23 Control of terahertz polarization via the magnetoelastic effect 63
4.24 Experimental demonstration of polarization control via magnetostriction 63
4.25 Comparison of complete time-domain versus frequency-domain ellipsometry 66
4.26 Schematic of the time-domain ellipsometry 68
4.27 Demonstration of experimental Jones matrix 69
4.28 Demonstration of experimental Mueller matrix 69
4.29 Experimental Pauli exponential coefficients for quartz 71
4.30 Comparison of experimental and theoretical Mueller Matrix elements of a quartz waveplate 73
4.31 Quartz crystal faces and tetrahedral arrangement 74
4.32 Comparison of retardation matrix elements and circular birefringence 75
4.33 Comparison of experimental and theoretical Mueller matrix elements of quartz biplate 76
4.34 Generation of terahertz continuous wave using a photomixing 77
4.35 Schematic of terahertz frequency comb generation using a mode-locked laser 79
4.36 Evolution of frequency comb spectroscopy using spintronic terahertz emitters 80
4.37 Scheme of a feedback loop to stabilize mode-locked repetition frequency 81

Publication list

Peer-review articles

[Article1] P. Koleják, J. Liu, R. Silber, M. Mičica, O. Ballada, Čestmír Barta, R. Lebrun, N. Tiercelin, M. Vanwolleghem, and K. Postava, "Terahertz time-domain ellipsometry with spintronic emitters: Pauli coefficients as a superior alternative to Jones and Mueller matrices," 2024. (under submission).

[Article2] P. Koleják, G. Lezier, D. Vala, B. Mathmann, L. Halagačka, Z. Gelnárová, Y. Dusch, J.-F. Lampin, N. Tiercelin, K. Postava, *et al.*, "Maximizing the electromagnetic efficiency of spintronic terahertz emitters," *Adv. Photonics Res.*, vol. 5, no. 11, p. 2400064, 2024.

[Article3] M. Mičica, A. Wright, P. Koleják, G. Lezier, K. Postava, J. Hawecker, A. De Vetter, J. Tignon, J. Mangeney, H. Jaffres, R. Lebrun, N. Tiercelin, M. Vanwolleghem, and S. Dhillon, "Spintronic terahertz emitters with integrated metallic terahertz cavities," *Nanophotonics*, vol. 13, no. 10, pp. 1899–1907, 2024.

[Article4] F. Paries, F. Selz, C. N. Santos, J.-F. Lampin, P. Koleják, G. Lezier, D. Troadec, N. Tiercelin, M. Vanwolleghem, A. Addda, *et al.*, "Optical damage thresholds of single-mode fiber-tip spintronic terahertz emitters," *Opt. Express*, vol. 32, no. 14, pp. 24826–24838, 2024.

[Article5] P. Koleják, G. Lezier, K. Postava, J.-F. Lampin, N. Tiercelin, and M. Vanwolleghem, "360° polarization control of terahertz spintronic emitters using uniaxial FeCo/TbCo2/FeCo trilayers," *ACS Photonics*, vol. 9, no. 4, pp. 1274–1285, 2022.

[Article6] G. Lezier, P. Koleják, J.-F. Lampin, K. Postava, M. Vanwolleghem, and N. Tiercelin, "Fully reversible magnetoelectric voltage controlled thz polarization rotation in magnetostrictive spintronic emitters on PMN-PT," *Appl. Phys. Lett.*, vol. 120, no. 15, p. 152404, 2022.

[Article7] D. Vala, P. Koleják, K. Postava, M. Kildemo, P. Provazníková, and J. Pištora, "Effects of optical activity to mueller matrix ellipsometry of composed waveplates," *Opt. Express*, vol. 29, pp. 10434–10450, 2021.

[Article8] P. Koleják, D. Vala, K. Postava, P. Provazníková, and J. Pištora, "Mueller matrix ellipsometry of waveplates for control of their properties and alignment," *J. Vac. Sci. Technol. B*, vol. 38, p. 014006, 2020.

[Article9] M. Gryga, D. Vala, P. Kolejak, L. Gembalova, D. Ciprian, and P. Hlubina, "One-dimensional photonic crystal for bloch surface waves and radiation modes based sensing," *Opt. Mater. Express*, vol. 9, pp. 4009–4022, 2019.

[Article10] P. Koleják, K. Postava, M. Mičica, P. Kužel, F. Kadlec, and J. Pištora, "Experimental gouy phase shift compensation in terahertz time-domain spectroscopy," *J. Phot. Nanostr.*, vol. 31, pp. 129–133, 2018.

International conference proceedings

[Proceeding1] P. Koleják, G. Lezier, L. Halagačka, B. Mathmann, D. Vala, Z. Gelnárová, Y. Dusch, J.-F. Lampin, N. Tiercelin, K. Postava, and M. Vanwolleghem, "Adapting terahertz spintronic emitters towards maximum performance," in *2023 48th International Conference on Infrared, Millimeter, and Terahertz Waves (IRMMW-THz)*, pp. 17–22, IEEE.

[Proceeding2] P. Kolejak, G. Lezier, G. Ducournau, J.-F. Lampin, N. Tiercelin, and M. Vanwolleghem, "Spintronic inverse spin hall photomixing beyond 1THz," in *2023 48th International Conference on Infrared, Millimeter, and Terahertz Waves (IRMMW-THz)*, pp. 17–22, IEEE.

[Proceeding3] G. Lezier, P. Koleják, P. Koleják, J.-F. Lampin, K. Postava, M. Vanwolleghem, and N. Tiercelin, "Ultrafast Modulation of Polarization in Spintronic THz Emitters Enhanced by Field Induced Spin Reorientation Transition," p. SF2I.4, Optica Publishing Group, May 2023.

[Proceeding4] P. Koleják, G. Lezier, K. Postava, J.-F. Lampin, N. Tiercelin, and M. Vanwolleghem, "Magnetization rotation-based polarization control of spintronic terahertz emitter," in *22nd Polish-Slovak-Czech Optical Conference on Wave and Quantum Aspects of Contemporary Optics*, vol. 12502, pp. 50–54, SPIE, Dec. 2022.

[Proceeding5] I. Hlobílková, P. Koleják, M. Mičica, and K. Postava, "Polarization controlled terahertz time domain spectroscopy using dual-color plasma," in *22nd Polish-Slovak-Czech Optical Conference on Wave and Quantum Aspects of Contemporary Optics*, vol. 12502, pp. 44–49, SPIE, Dec. 2022.

[Proceeding6] P. Kolejak, G. Lezier, S. Kassi, L. Djevahirdjian, M.-A. Martin, O. Pirali, G. Ducournau, J.-F. Lampin, N. Tiercelin, and M. Vanwolleghem, "Spintronic inverse spin hall photomixing: demonstration of THz CW and frequency comb generation," in *2022 47th International Conference on Infrared, Millimeter and Terahertz Waves (IRMMW-THz)*, pp. 2022–02, IEEE.

[Proceeding7] P. Koleják, G. Lezier, L. Halagačka, Z. Gelnárová, J.-F. Lampin, N. Tiercelin, M. Vanwolleghem, and K. Postava, "Highly Efficient Terahertz Spintronic Emitter Integrated with Optimized Photonic Crystal," in *2022 47th International Conference on Infrared, Millimeter and Terahertz Waves (IRMMW-THz)*, pp. 2022–02, IEEE.

[Proceeding8] G. Lezier, P. Koleják, P. Koleják, J.-F. Lampin, K. Postava, M. Vanwolleghem, and N. Tiercelin, "Reversible Magnetoelectric Control of THz Polarization Rotation in Magnetostrictive Spintronic Emitters on PMN-PT," p. STh4O.5, Optica Publishing Group, May 2022.

[Proceeding9] P. Koleják, G. Lezier, K. Postava, J.-F. Lampin, N. Tiercelin, and M. Vanwolleghem, "Optimized optical cavity for maximal enhancement of terahertz spintronic emission," in *2021 46th International Conference on Infrared, Millimeter and Terahertz Waves (IRMMW-THz)*, pp. 2021–03, IEEE.

[Proceeding10] G. Lezier, P. Koleják, J.-F. Lampin, K. Postava, M. Vanwolleghem, and N. Tiercelin, "Polarization control of emitted THz waves using spintronic emitters with anisotropic magnetic layers & birefringence characterization of Quartz," in *2021 46th International Conference on Infrared, Millimeter and Terahertz Waves (IRMMW-THz)*, pp. 2021–03, IEEE.

[Proceeding11] N. Tiercelin, G. Lezier, P. Koleják, J.-F. Lampin, Y. Dusch, K. Postava, and M. Vanwolleghem, "Magneto-electric control of polarization in spintronic terahertz emitters," in *2021 46th International Conference on Infrared, Millimeter and Terahertz Waves (IRMMW-THz)*, pp. 2021–03, IEEE.

[Proceeding12] G. Lezier, P. Koleják, P. Koleják, J.-F. Lampin, K. Postava, M. Vanwolleghem, and N. Tiercelin, "Coherent polarization rotation of TeraHertz spintronic emitters with in-plane uni-axial magnetic anisotropy," p. JM3G.2, Optica Publishing Group, May 2021.

[Proceeding13] N. Tiercelin, G. Lezier, P. Koleják, J.-F. Lampin, K. Postava, and M. Vanwolleghem, "THz spintronic emitters with magnetoelectric control of the polarization and applications to polarimetry.," in *Spintronics XIV*, vol. 11805, p. 118050O, SPIE, Aug. 2021.

[Proceeding14] P. Koleják, K. Postava, L. Jean-François, N. Tiercelin, and M. Vanwolleghem, "Terahertz Spintronic Emitter with Arbitrarily Controllable Linear Polarization Properties not Needing a Rotating Magnetic Bias," in *2020 45th International Conference on Infrared, Millimeter, and Terahertz Waves (IRMMW-THz)*, pp. 08–13, IEEE.

[Proceeding15] P. Koleják, K. Postava, M. Mičica, M. Vanwolleghem, and J. Pištora, "The Gouy phase shift in terahertz time-domain spectroscopy and its experimental estimation, modelling and compensation," in *2019 44th International Conference on Infrared, Millimeter, and Terahertz Waves (IRMMW-THz)*, pp. 01–06, IEEE.

[Proceeding16] P. Koleják, K. Postava, M. Mičica, and J. Pištora, "Analytical model of Gouy phase influence in terahertz time-domain spectroscopy," in *21st Czech-Polish-Slovak Optical Conference on Wave and Quantum Aspects of Contemporary Optics*, vol. 10976, pp. 218–222, SPIE, Dec. 2018.

[Proceeding17] K. Postava, J. Chochol, M. Mičica, M. Vanwolleghem, P. Kolejak, L. Halagačka, M. Cada, J. Pištora, and J.-F. Lampin, "Spectroscopy of materials for terahertz photonics," in *20th Slovak-Czech-Polish Optical Conference on Wave and Quantum Aspects of Contemporary Optics*, vol. 10142, pp. 45–51, SPIE, Dec. 2016.

[Proceeding18] T. Horák, M. Vanwolleghem, G. Ducournau, K. Postava, P. Koleják, and J.-F. Lampin, "Magneto-optical hexaferrites for terahertz isolating applications," in *2016 41st International Conference on Infrared, Millimeter, and Terahertz waves (IRMMW-THz)*, pp. 25–30, IEEE.

1

INTRODUCTION

1.1 Context of the research

1.1.1 Terahertz radiation and its importance

The terahertz (THz) frequency range, spanning from 0.1 THz to 10 THz (wavelengths from 3 mm to 30 μm), bridges the gap between the microwave and infrared regions of the electromagnetic spectrum [1–4]. This region is particularly significant due to its transitional nature between electronics and photonics. THz waves can be manipulated similarly to microwaves at lower frequencies, utilizing waveguides and antennas for guided transmission, reflection, and beam steering. This includes using resonators, filters, and couplers to control signal propagation, much like in microwave technology, allowing for efficient routing and modulation of THz waves over short to medium distances. However, it interacts with optical phenomena at higher frequencies. Such positioning allows THz radiation to uniquely probe a range of material excitations, including phonons, plasmons, and molecular rotations, which are not as easily accessible at other frequencies. Furthermore, THz waves offer a compromise between the high spatial resolution of infrared radiation and the greater penetration depth of microwaves, making them well-suited for investigating materials at different scales.

One of the critical features of terahertz waves is their ability to penetrate various non-conductive materials, such as plastics, fabrics, paper, and ceramics [5, 6]. This property makes THz radiation highly suitable for non-destructive testing and quality control in industries such as aerospace, semiconductor manufacturing, automotive, and material science. Furthermore, terahertz radiation is non-ionizing, as its photon energies (approximately 4–40 meV) are several magnitudes lower than those of ultraviolet or X-ray radiation. The power of THz waves is insufficient to ionize atoms or molecules, making them harmless to biological tissues [7–9]. Consequently, THz imaging is a promising tool for medical diagnostics, offering detailed, non-invasive scans that could potentially aid in early disease detection, such as skin cancer or dental caries.

In addition to imaging applications, terahertz radiation is sensitive to vibrational and rotational transitions in molecules, especially in complex organic and biological molecules [10–13]. Due to these molecular motions, many chemical and biological substances have characteristic absorption spectra in the THz range. The sensitivity of THz waves to molecular motions makes THz spectroscopy a powerful tool for chemical identification and analysis, with applications in security screening for detecting explosives and illicit drugs, environmental monitoring, and pharmaceutical quality control.

Overall, the unique interaction of THz radiation with matter opens up many applications in fields

such as material science, medicine, biology, security, and communications.

1.1.2 Why is the terahertz gap challenging?

Despite the promising applications, the practical utilization of terahertz radiation has been historically tricky—a situation often referred to as the *terahertz gap* [14, 15]. This gap stems from significant technical issues in generating, detecting, and manipulating THz radiation, as it lies in a frequency range where neither conventional electronic nor photonic technologies perform efficiently [16–18]. The main challenges in terahertz technology included:

- **Lack of efficient sources and detectors**: Traditional electronic devices, such as transistors and conventional diodes, are designed to operate effectively only at frequencies up to a few hundred gigahertz. At THz frequencies, the transit time of charge carriers and parasitic capacitance severely limit their performance [19, 20]. Additionally, antennas for THz radiation must be fabricated at sub-millimeter scales, which presents significant manufacturing challenges. On the photonic side, devices such as lasers and photodetectors are optimized for much higher frequencies in the infrared and visible ranges. The photon energy at THz frequencies ($<$40 meV) is insufficient to overcome the bandgaps of conventional semiconductor materials, making efficient THz generation and detection difficult [21, 22]. As a result, there was a technological gap in efficient THz sources and detectors.

- **Strong atmospheric absorption**: Terahertz waves are significantly absorbed by atmospheric water vapor, greatly limiting their propagation range. Figure 1.1 shows the atmospheric absorption and transmission windows across the electromagnetic spectrum [23]. The terahertz range creates the boundary between the microwave and infrared regions, characterized by significant water vapor absorption. Vibrational transitions are predominant in the infrared spectrum, where molecules transition between different vibrational energy levels [21, 24]. In the microwave spectrum, rotational transitions are dominant, with molecules transitioning between distinct rotational energy states [25, 26]. The combination of these transitions results in dense absorption bands at the junction of these two regions [27].

- **Thermal background noise**: At room temperature, objects emit significant thermal radiation in the THz frequency range according to Planck's law [21, 22]. This thermal background can mask weak THz signals, reducing the signal-to-noise ratio in detection systems. The development of terahertz pulsed technologies was highly anticipated as a solution. By using terahertz pulses as concentrated electromagnetic bursts, these technologies significantly improve the distinction between signal and noise compared to continuous waves, enhancing signal by several orders of magnitude.

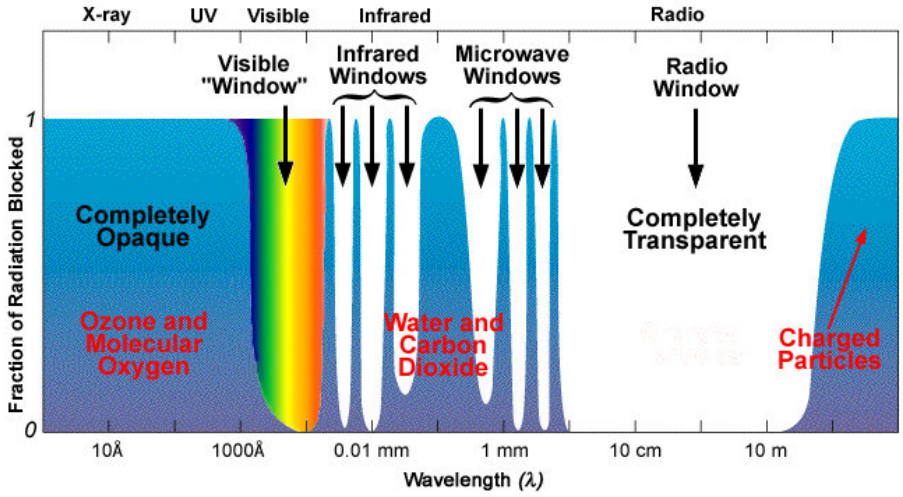


Figure 1.1: Transparency of Earth's atmosphere across the electromagnetic spectrum: This graph illustrates the fraction of radiation blocked by Earth's atmosphere across different wavelengths, ranging from X-ray to radio waves. The atmosphere is completely opaque at X-ray and UV wavelengths due to ozone and molecular oxygen absorption. The visible light spectrum shows a transparent window through which most radiation passes. In contrast, the infrared and microwave spectra have several windows containing absorption bands primarily due to water vapor and carbon dioxide. The atmosphere is completely transparent in the radio window, except for attenuation by charged particles at longer wavelengths. Adapted from [23].

These challenges have hindered the widespread adoption of THz technologies and have motivated extensive research efforts to develop novel sources, detectors, and components that can operate efficiently in the THz frequency range. In the last three decades, significant progress has been made in bridging the terahertz gap by developing new generation and detection techniques [17, 28–30]. Key innovations include photoconductive antennas (PCAs) that use ultrafast laser pulses to generate THz radiation [31–33], nonlinear optical techniques like optical rectification and difference-frequency generation [34–36], and quantum cascade lasers (QCLs) [37–40], which provide continuous-wave THz radiation through intersubband transitions.

Pulsed laser technologies offer a significant advantage through their capability to facilitate terahertz time-domain spectroscopy (THz-TDS) [21, 22]. The method enables the reconstruction of terahertz waveforms, which are challenging to detect using purely electronic or photonic methods. THz-TDS provides a significant advantage by capturing amplitude and phase information through Fourier transformation of the waveform. Figure 1.2 shows the Fourier-transformed transmitted signal through high-resistivity silicon, revealing comprehensive interference details in both amplitude and phase. This dual capability offers a substantial advantage over conventional spectroscopic or interferometric methods, which typically capture only intensity. The complex amplitude analysis provides a distinct advantage, enabling direct and comprehensive determination of the complex refractive index [41, 42].

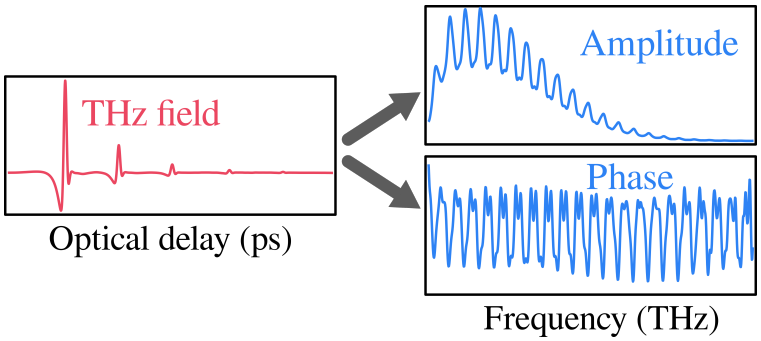


Figure 1.2: Time-Frequency demonstration of a THz field: The left panel shows the transmitted THz field through high-resistivity silicon, including several internal reflections. The right panels display the corresponding frequency-domain analysis, with interfered spectral amplitude and normalized phase.

1.1.3 Need for terahertz time-domain ellipsometry

It is essential to recognize that the terahertz range still presents significant challenges. Low-energy THz photons, pervasive background noise, and the pulsed nature of time-domain experiments necessitate extended averaging times [16–18]. Furthermore, the comparable scale between the wavelength (3 mm-30 μm) and layer thickness complicates measurements and significantly reduces sensitivity to thin films [43–46]. These challenges result in more significant errors when measuring the optical functions of materials compared to IR, VIS, and UV spectrophotometry and ellipsometry [47–50]. However, the sensitivity of terahertz spectroscopy can be enhanced by focusing on polarization responses.

Polarization-sensitive techniques, such as terahertz time-domain spectroscopic ellipsometry (THz-TDSE), address the limitations of conventional terahertz spectroscopy by leveraging the distinct interactions of s- and p-polarized light with materials [51–53]. Unlike intensity-based methods, THz-TDSE measures coherent changes in the polarization state, including phase and amplitude. Figure 1.3 illustrates the fundamental concept of THz-TDSE, where a linearly polarized THz pulse $\mathbf{E}_i$ interacts with the sample, causing changes in the azimuth Ψ and phase shift Δ of the reflected polarization state $\mathbf{E}_o$. These changes encode essential information about the sample's optical properties. The essence of ellipsometry lies in experimentally determining the sample's transformation matrix, which describes how the polarization state is altered. This is achieved using the Jones 2×2 matrix formalism to represent the polarization changes in a phase-resolved manner [54]. To determine this matrix, polarization measurements are performed by systematically varying the generated and detected polarization states. These measurements allow for the complete reconstruction of the transformation matrix, from which key material properties such as refractive index, thickness, and anisotropy can be extracted. Determining the full matrix significantly improves accuracy and sensitivity by enabling the simultaneous validation of all matrix elements, leading to a more comprehensive understanding of the material's optical behavior. The main advantages of THz-TDSE include:

- **Enhanced sensitivity**: Ellipsometry is susceptible to bulk and surface optical properties [53,55]. This advantage makes it particularly effective for analyzing thin films and multilayered systems, where traditional terahertz techniques struggle. THz-TDSE can detect even subtle variations in Fresnel coefficients using polarization-sensitive measurements [56–59]. Furthermore, the

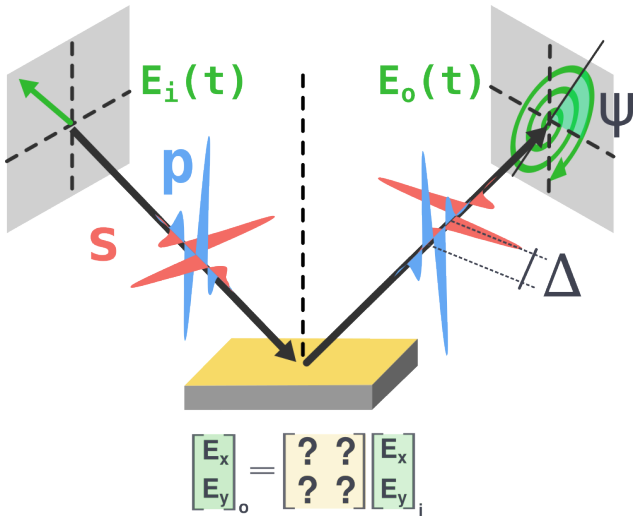


Figure 1.3: Illustration of the terahertz time-domain ellipsometry setup: The figure depicts a typical ellipsometry configuration where the incident electric field $\mathbf{E}_\mathrm{i}(t)$ interacts with the sample, resulting in a reflected electric field $\mathbf{E}_\mathrm{o}(t)$. Upon reflection, the electric field components are split into s- (red) and p-polarizations (blue). The angle Δ represents the phase difference between these components, and Ψ denotes the azimuth change. The unknown matrix equation relates the incident and reflected electric field components, representing the challenge of solving for the sample's optical properties.

coefficients become more sensitive in reflection at oblique angles of incidence. This increased sensitivity can be exploited by performing multiple measurements at different angles or samples' azimuths rotation, allowing for a more comprehensive and robust analysis through a broader data set from a single sample.

- **Characterization of anisotropic materials**: THz-TDSE provides a powerful approach for characterizing anisotropic materials, including liquid crystals, polymers, and crystalline solids, whose optical properties, such as refractive indices and absorption coefficients, vary with direction [60, 61]. These properties depend on terahertz radiation's polarization and propagation direction, making accurate analysis challenging. Many anisotropic crystals have optical axes that are tilted or misaligned relative to the sample orientation, and variations in crystallographic cuts add further complexity. Such characteristics can only be accurately analyzed using ellipsometry.

- **Analysis of optical activity and magneto-optical effects**: THz-TDSE is highly effective for studying optical activity [62–64], where the polarization of light rotates due to the chirality, and magneto-optical effects, where polarization changes in response to external magnetic fields [65, 66]. These phenomena are critical in understanding the behavior of chiral molecules in biology and materials with magnetic ordering in materials science. Accurately measuring these effects can be challenging due to the subtle polarization changes involved, which require high sensitivity and precise control of experimental conditions, especially at terahertz frequencies where interactions are typically weaker than at optical wavelengths.

Despite these advantages, implementing THz-TDSE presents several challenges, particularly regarding source efficiency, imperfect polarizing components, polarization control, and calibration,

which are crucial for accurate measurements.

1.2 Challenges in terahertz time-domain ellipsometry

Despite nearly three decades of intensive research in the terahertz domain [17, 28–30], developing robust polarimetric methods to capture accurate and comprehensive polarization data remains a formidable challenge, even with sophisticated coherent detection techniques. Polarization components, such as polarizers in the terahertz range, inherently suffer from limitations, particularly low extinction ratios (100-1000), compromising polarization purity and complicating accurate calibration and alignment [67, 68]. As a result, terahertz ellipsometry is often performed in the frequency domain using Mueller matrices [56, 59, 69], leveraging established methodologies from visible and infrared ellipsometry [70]. However, only incomplete 3×3 and 4×3 matrices can be obtained due to the challenges in generating and analyzing circular polarizations. This approach does not exploit the potential of time-domain measurements to obtain complete polarization and phase-sensitive information. The measurable range typically does not exceed 1.5 THz, offering high resolution, unless a synchrotron is used.

Currently, time-domain ellipsometry primarily focuses on determining the ratio between the reflection coefficients for p- and s-polarized light, expressed as $r_{pp}/r_{ss} = \tan\Psi \exp(-\mathrm{i}\Delta)$ [58, 71–73]. However, this standard ellipsometric approach primarily provides information about the diagonal elements of the Jones matrix, while the off-diagonal elements, which reveal cross-polarization coupling, remain undetermined. As a result, this method is most effective for isotropic or specifically oriented anisotropic samples, where the optical axes are aligned with the polarization directions. Many configurations determine the complete ellipsometric properties by rotating a polarization-sensitive detector [74, 75] to determine Mueller matrices even from time-domain measurements [76–78]. This approach typically loses information about absolute phases and focuses only on capturing polarized intensity differences.

Conversely, complete ellipsometry in the time domain offers the distinct advantage of directly measuring the electric field components of terahertz waves, utilizing complete coherence. This capability supports the application of Jones calculus, enabling a thorough and coherent polarization analysis. Despite its advantages, time-domain ellipsometry has seen limited realization, with only a single study demonstrating its application [79]. The limited adoption is mainly due to the technical complexity of the required instrumentation and the necessity for highly accurate calibration and alignment methods, which must correctly reconstruct the complex Jones matrix from a series of polarization measurements while eliminating systematic errors. The main challenges in THz-TDSE can be summarized as follows:

- **Sensitivity to environmental conditions**: Weak signals, pulsed regime, and scanning through the delay stage necessitate long acquisition times, which can be impractical and increase the susceptibility to environmental fluctuations. The THz measurements are sensitive to humidity and temperature fluctuations, which can introduce phase and amplitude instabilities, water absorption artifacts, and signal drift. This is especially problematic for ellipsometric measurements, which require high signal-to-noise ratios to detect small polarization changes across several measurements.

- **Polarization control**: Accurate polarization control is essential in ellipsometry to generate specific input polarization states and analyze the output polarization after interaction with

the sample. In the THz range, polarization components such as polarizers and waveplates often have intrinsic limitations. Low extinction ratios of polarizers compromise the analysis of linear polarization and polarization purity. The strong chromatic dependence of waveplates complicates analyzing circular polarizations, which is critical for intensity-based analysis. As a result, only an incomplete 3×3 Mueller matrix can be determined in the frequency-domain ellipsometry, omitting crucial information related to circular polarization. Generating various polarization states is often challenging by a terahertz source, primarily due to the reliance on nonlinear processes to achieve polarization-matching conditions or the need for specially engineered dipoles.

- **Robust calibration**: Precise calibration and alignment are required to reconstruct the sample's transformation matrix from polarization measurements accurately. Systematic errors due to imperfect components, misalignments of polarizers' azimuths, and environmental factors can significantly affect the reliability of the results. Developing robust calibration methods covering these factors is challenging, particularly when the THz components have inherent limitations. Most recent studies, including ellipsometry calibration, focus predominantly on alignment rather than developing methods to eliminate experimental errors effectively. Studies that experimentally determine complete Mueller matrices require 16 measurements to fully map the Poincaré sphere, whereas the Jones approach necessitates only four measurements, as it inherently includes phase information.

- **Complete ellipsometry framework**: Terahertz ellipsometry techniques are currently constrained to isotropic cases, incomplete Mueller matrix measurements, and complete Mueller matrix analyses excluding phase information. While valuable, these methods do not fully exploit the capabilities of time-domain measurements to capture the complete polarization state. However, determining the full Jones matrix—including amplitude and phase components—overcomes these limitations. The Jones matrix provides a more intrinsic description of optical systems and can be easily converted into the Mueller matrix. Jones's approach enables a more comprehensive polarization analysis, capturing cross-polarization effects and phase-sensitive information, making it a superior approach for general anisotropic media.

- **Interpreting complex ellipsometry data**: The interpretation of the Mueller matrix in ellipsometry is inherently complex, particularly for users with less experience. It consists of 16 interdependent elements that capture various polarization phenomena. These elements represent changes in intensity in the Stokes bases and are further complicated by transformations such as sample azimuth rotations, making it challenging to isolate and interpret specific phenomena. While the Jones matrix is more compact in its 2x2 format, this does not inherently simplify interpretation. Although it directly shows how the electric field components transform, all polarization effects are condensed into four elements, making it difficult to separate the different phenomena. The combination of amplitudes and phases makes it even more challenging to distinguish different polarization effects. The question remains: *how can we simplify the interpretation of complete ellipsometric data while preserving all essential information to make it more accessible for typical users?*

These challenges limit the practicality and accuracy of THz-TDSE, hindering its broader adoption in material characterization. Overcoming these obstacles requires the development of more efficient THz sources with dynamic polarization control, improved THz components, and robust calibration techniques.

1.3 Proposed solution: terahertz complete time-domain ellipsometry based on spintronic emitters

This research addresses these challenges by employing spintronic emitters and developing a new approach to applying terahertz ellipsometry in the time domain. While terahertz ellipsometry has been a research subject for over two decades [17, 28–30], it has predominantly been explored in its standard and incomplete forms, limiting its ability to analyze general anisotropic materials. In contrast, our terahertz complete time-domain spectroscopic ellipsometry (THz-cTDSE) method leverages inherent coherence to determine the Jones matrix experimentally. The Jones matrix provides a more fundamental representation of the polarization response, capturing both the amplitude and phase of the wave, which allows for a deeper understanding of the sample's optical properties. Additionally, the Jones matrix can be directly transformed into the Mueller matrix when the user prefers an intensity-based representation. By offering both the phase-resolved Jones matrix and the intensity-driven Mueller matrix, the method ensures flexibility for different experimental needs and user preferences.

However, interpreting the Jones and Mueller matrix can be challenging when multiple effects are present simultaneously. To address this, we shifted the interpretation of the Jones matrix to Pauli exponential coefficients [80–82], which directly correspond to diattenuation and retardation across all Stokes vector bases, covering both linear and circular polarization states. Diattenuation refers to the differential attenuation of light depending on its polarization, while retardation describes the phase shift between orthogonal polarization components as they pass through an anisotropic material. By expressing the Jones matrix in terms of these coefficients, we can isolate and directly analyze these polarization-dependent effects, leading to a clearer understanding of the sample's optical properties.

So far, the Pauli exponential approach has seen little attention and has only been explored theoretically [80, 81, 83], as it has not been applied in practical experiments due to the absence of coherent ellipsometry. By incorporating experimentally determined Jones matrices, we can now use Pauli exponential coefficients to observe field transformations and distinguish between optical phenomena such as linear and circular birefringence and dichroism. These effects involve phase shifts and polarization-dependent absorption and are challenging to separate using traditional intensity-based methods. This new approach allows for a more intuitive and precise polarization effects analysis, providing previously unavailable capabilities in conventional ellipsometry.

To ensure precise and reliable THz-cTDSE measurements, we proposed a calibration method that addresses systematic errors and polarizer misalignments. This procedure relies on polarization-sensitive reference measurements to correct system imperfections. The calibration method enables the optimized selection of generated and analyzed polarization states, facilitating the choice of a well-conditioned numerical solution for reconstructing the Jones matrix. Moreover, this method is generalized and can be applied to a broader range of ellipsometric systems.

Since we aimed to propose a versatile and broadly applicable ellipsometric methodology, we focused on applying spintronic terahertz emitters (STEs) [84–86]. They represent a new broadband and highly adaptable class of terahertz radiation sources. These emitters were selected for their unique ability to control polarization, high-extinction ratio, and compatibility with all pulsed laser systems, offering significant flexibility for various experimental setups. Their capacity to generate broadband terahertz radiation with precise polarization control makes them particularly suitable for advanced ellipsometric techniques, where accurate polarization manipulation is crucial for exploring

the optical properties of materials.

1.4 Principles of spintronic terahertz emitters

The spintronic emitter is composed of a metallic heterostructure, consisting of non-magnetic (NM) and ferromagnetic (FM) layers arranged in an NM/FM/NM configuration [84]. The operation of the STE relies on a pulsed optical excitation that induces spin injection from ferromagnetic to nonmagnetic layers, leading to terahertz generation [87]. This process is illustrated in Figure 1.4, where the fundamental mechanisms are outlined as follows:

Ultrafast optical excitation When a femtosecond laser pulse irradiates the FM layer, it excites electrons from occupied states below the Fermi level to unoccupied states above it. Due to the intrinsic magnetization ($\mathbf{M}$) of the FM material, these excited electrons are spin-polarized. This spin polarization arises because the density of states for spin-up and spin-down electrons is unequal in a ferromagnet—a consequence of exchange splitting. As a result, the optical excitation generates a non-equilibrium population of spin-polarized electrons.

Spin-polarized electron diffusion The spin-polarized electrons diffuse from the FM layer into the adjacent NM layer. This diffusion occurs on ultrafast timescales determined by the electron mean free path and spin diffusion length, typically a few nanometers. Efficient spin injection into the NM layer is crucial, as it determines the magnitude of the spin current ($\mathbf{j}_s$) that flows across the FM/NM interface.

Spin-to-charge conversion via the inverse spin Hall effect In the NM layer, which exhibits strong spin-orbit coupling (SOC), the spin current ($\mathbf{j}_s$) is converted into a transverse charge current ($\mathbf{j}_c$) through the inverse spin Hall effect (ISHE). The ISHE arises because the spin-orbit interaction causes electrons with opposite spins to scatter asymmetrically in opposite transverse directions. This results in a net charge current perpendicular to both the magnetization direction ($\mathbf{M}$) and the spin current direction, proportional to the cross product:

$$\mathbf{j}_c \propto \theta_{\text{ISHE}}\, \mathbf{j}_s \times \mathbf{M},$$

where θ_{ISHE} is the spin Hall angle, quantifying the efficiency of spin-to-charge conversion.

If a spintronic emitter consists of two non-magnetic layers with the same Spin Hall angle sign, the resulting spin directions will oppose each other, leading to currents that cancel out. Non-magnetic layers with opposite Spin Hall angles are required to prevent the cancellation and create constructive currents to double the emission, even if their efficiencies differ. The most effective materials for this application are platinum (Pt) and tungsten (W) [88–91].

Emission of terahertz radiation The transient charge current $\mathbf{j}_c(t)$ generated via ISHE acts as a source of electromagnetic radiation. According to Maxwell's equations, a time-varying current density radiates electromagnetic waves. The emitted THz electric field $\mathbf{E}_{\text{THz}}(t)$ is proportional to the time derivative of the charge current:

$$\mathbf{E}_{\text{THz}}(t) \propto \frac{\mathrm{d}\mathbf{j}_c(t)}{\mathrm{d}t}.$$

Since the charge current varies on femtosecond timescales, the resulting THz radiation is broadband, covering frequencies up to tens of terahertz.

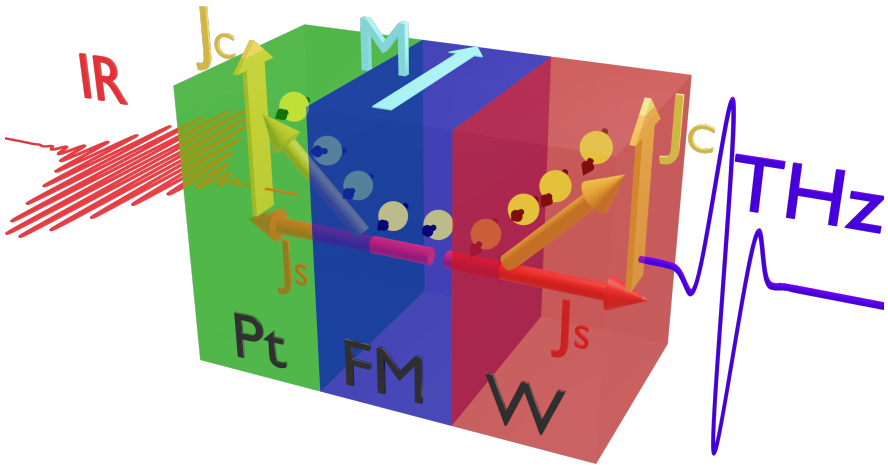


Figure 1.4: Operational principles of a spintronic terahertz emitter: (i) A femtosecond laser pulse excites the ferromagnetic (FM) layer, generating spin-polarized electrons due to its magnetization ($\mathbf{M}$). (ii) The spin-polarized electrons diffuse into the non-magnetic (NM) layer. (iii) Via the inverse spin Hall effect (ISHE), the spin current ($\mathbf{j}_s$) is converted into a transverse charge current ($\mathbf{j}_c$), leading to THz emission.

1.5 Potential of spintronic terahertz emitters

The spin-driven operational principles of spintronic terahertz emitters (STEs) confer several significant advantages over traditional THz sources [85, 92, 93]. They directly address limitations encountered in terahertz spectroscopy. Their ease of integration, fabrication, and compatibility with various excitation sources make them highly versatile for different experimental setups.

Since STEs are thin-film heterostructures composed of only a few nanometers thick layers, they can be fabricated using standard deposition techniques such as sputtering or molecular beam epitaxy [94, 95]. Their planar geometry and compact size facilitate straightforward integration into existing optical setups without complex alignment or phase-matching requirements. Additionally, the metallic layers in STEs absorb light uniformly across a broad wavelength range from visible to near-infrared, allowing flexibility in the choice of excitation laser systems. This compatibility enables researchers to utilize available laser sources, whether high-energy femtosecond amplifiers or low-energy oscillators, operating at various repetition rates from kilohertz to gigahertz [96, 97]. The fast recovery time of the spintronic emission process, typically on the order of 10–50 fs [98], ensures that the STEs remain efficient across a wide range of repetition rates, as the terahertz emission process is not limited by thermal accumulation or other slow dynamics.

1.5.1 Broadband and gapless THz emission

One of the most significant advantages of STEs is their ability to generate broadband and gapless THz radiation. The ultrafast spin and charge dynamics involved in their operation result in emitted THz

pulses with spectral content extending from below 1 THz up to 30 THz [99]. This broadband emission arises because the THz radiation is generated by transient charge currents varying on femtosecond timescales due to the inverse spin Hall effect (ISHE). The bandwidth is primarily limited by the duration of the excitation laser pulse and the intrinsic relaxation times of the spin-polarized carriers in the materials [87]. Figure 1.5 compares the spectral amplitude of STEs with that of conventional THz sources, highlighting STE emission's broad and gapless nature. In contrast, traditional THz sources, such as nonlinear optical crystals like ZnTe or GaP, suffer from phonon resonances that introduce absorption gaps in the THz spectrum [100], limiting their usable bandwidth. Photoconductive antennas are limited by the carrier lifetime in the semiconductor material, typically restricting the bandwidth to below 5 THz.

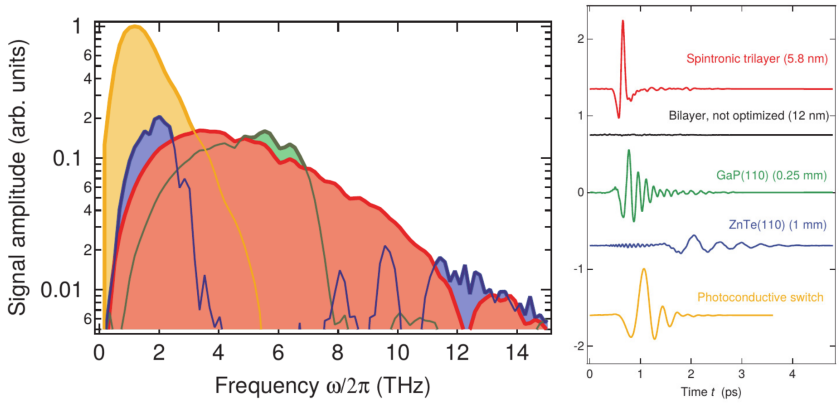


Figure 1.5: Frequency and time domain comparison of terahertz sources: The left panel shows the spectral amplitude for various sources, including a spintronic trilayer (red), an unoptimized bilayer (black), a GaP crystal (green), a ZnTe crystal (blue), and a photoconductive antenna (yellow). The spectra demonstrate each emitter's bandwidth and phonon absorption across the terahertz range. The right panel presents the corresponding time-domain waveforms for each emitter, indicating the pulse shape and duration corresponding with the spectrum observed on the left. Adapted from [99].

For the time-domain ellipsometry, the availability of a broadband and gapless THz source is crucial. It allows for continuous frequency coverage, enabling precise characterization of material properties over a wide spectral range. Materials often exhibit complex dielectric responses in the THz region, with features such as phonon resonances, vibrational modes, and electronic transitions occurring at different frequencies. A gapless broadband source like STEs ensures that none of these features are missed, enhancing the sensitivity and accuracy of THz-TDSE measurements.

1.5.2 Intrinsic polarization control

Another critical advantage of STEs is the intrinsic control over the generated polarization state. The THz polarization is directly linked to the direction of the transient charge current $\mathbf{j}_c$, which depends on the magnetization direction $\mathbf{M}$ of the ferromagnetic (F) layer. By manipulating $\mathbf{M}$, one can dynamically control the polarization state of the emitted THz waves. Several approaches have been recently demonstrated:

- **Rotating permanent magnets**: Hibberd et al. and Kong et al. [101, 102] demonstrated that by rotating a small permanent magnet around the STE, one can continuously adjust the

polarization state of the emitted THz radiation. This method allows for straightforward control without complex setups.

- **Metasurface integration**: Several studies [103–106] have shown that integrating STEs with metasurfaces allows for precise control of polarization states, including tunability between linear, elliptical, and circular polarization. The metasurfaces use nanoscale structures to control spin and charge behavior, enabling both polarization control and beam steering. This integration also allows for dynamic adjustment of the chirality and ellipticity of terahertz waves using external fields, enabling independent polarization tuning over a wide frequency range.

- **Cascade emitters**: Chen et al. [107] demonstrated the generation and manipulation of circularly polarized terahertz waves using cascade spintronic terahertz emitters. By precisely engineering magnetic field directions and phase differences between two-stage emitters, they achieved tunability of the chirality, azimuthal angle, and ellipticity of the emitted terahertz waves. This method provides fine control over polarization states without mechanical components, offering a flexible and highly tunable approach for terahertz applications.

These examples illustrate the versatility of STEs in achieving practical polarization control. Polarization control provided by spintronic emitters via external magnetic fields is highly advantageous for applications in polarimetry and ellipsometry, attributed to its straightforward implementation and potential for high polarization purity. A source with intrinsic polarization control simplifies the experimental setup by eliminating the need for external THz polarizers or mechanical rotation stages, which can introduce losses and complicate alignment.

1.5.3 Peak-power and optical-to-THz conversion efficiency

The ultrafast relaxation dynamics of spintronic terahertz emitters (STEs) produce Fourier-limited waveforms, resulting in sharp, single-cycle terahertz pulses. Figure 1.5 compares the time-domain signals between semiconductor-based and nonlinear crystal-based THz sources. Spintronic emitters demonstrate high peak electric fields, reaching 300 kV/cm and up to 1.5 MV/cm when large-area STEs are used in the millijoule pulsed regime [84, 108]. These field strengths are sufficient for applications in nonlinear terahertz spectroscopy.

Despite the high peak electric fields of the emitted THz radiation, the optical-to-THz conversion efficiency of STEs is relatively low compared to conventional THz sources. The typical conversion efficiency of STEs is on the order of 10^{-5} to 10^{-6} [99]. Several factors contribute to this low efficiency: (i) The limited optical absorption in the thin metallic layers of STEs; only 30–50% of the incident optical energy is absorbed, with the remainder reflected or transmitted [109]. The high reflectivity of metals at optical wavelengths leads to significant reflection losses. (ii) Another factor is the efficiency of spin-to-charge conversion via the inverse spin Hall effect (ISHE), which is constrained by the spin Hall angle (θ_{ISHE}) of the non-magnetic layer. For commonly used non-magnetic materials like platinum (Pt), the spin Hall angle ranges from 1.5% to 10% [88], meaning only a fraction of the spin current is converted into charge current that contributes to THz emission. (iii) Spin transport losses arise from imperfections at the ferromagnetic/non-magnetic (FM/NM) interface and the finite spin diffusion lengths of the materials. Spin scattering at the interface and within the layers reduces the spin current reaching the NM layer, thus lowering the overall efficiency. (iv) Additionally, some of the emitted THz radiation may be reabsorbed or reflected within the spintronic metallic layers or

the substrate, reducing the THz power emitted into free space. Impedance mismatch between the STE layers and free space can also contribute to attenuation.

Current research efforts aim to enhance the efficiency of STEs by addressing these challenges through various approaches:

- **Adjusting layer thicknesses**: Torosyan et al. [110] and Seifert et al. [84] showed that optimizing the thicknesses of the ferromagnetic (FM) and non-magnetic (NM) layers can balance optical absorption and terahertz (THz) emission. Thinner NM layers reduce absorption losses at THz frequencies, enhancing emission into free space.

- **Improving optical absorption**: Several studies [109, 111, 112] have integrated spintronic terahertz emitters with a Bragg mirror to form an optical cavity. This design enhances the optical field within the FM layer, increasing absorption by up to 1.9 times. More pump energy is absorbed due to constructive interference at the pump wavelength, leading to a larger population of spin-polarized electrons.

- **Using nano-plasmonic structures**: Liu et al. [113] and Bardolaza et al. [114] demonstrated that incorporating nano-plasmonic structures can significantly increase pump absorption. This strategy enhances efficiency by 70% for absorption improvement and achieves a threefold increase when combined with a silicon lens. However, metallic structures tens of nanometers thick may affect terahertz extraction due to impedance mismatching.

- **Enhancing interface quality**: Nenno et al. [115] showed that careful fabrication techniques, such as sputtering under ultra-high vacuum conditions and annealing, improve the FM/NM interface quality. This reduces scattering and spin memory loss, enhancing spin injection.

- **Combining Spin Hall and Orbital Hall effects**: Kumar et al. [116] proposed that combining the inverse Spin Hall Effect (ISHE) and the inverse Orbital Hall Effect (IOHE) can generate a charge current when either a spin or orbital current is injected into a non-magnetic material. Wang et al. [117] were the first to demonstrate experimentally that the synergistic application of these two effects could boost the emission capabilities of spintronic emitters.

- **Utilizing the inverse Rashba-Edelstein effect**: A promising mechanism is the inverse Rashba-Edelstein effect (IREE) [118, 119], where inversion symmetry breaking provides spin-orbital coupling at the interface of bismuth/silver (Bi/Ag) layers. However, IREE-based emitters have not yet outperformed ISHE trilayer emitters.

Improving the optical-to-THz conversion efficiency is crucial for THz-TDSE applications, where signal strength and signal-to-noise ratio are essential. Weak signals necessitate extended integration times, which are more time-consuming and susceptible to stability issues due to laboratory conditions such as temperature, humidity, and power fluctuations. These instabilities become particularly problematic when conducting a series of ellipsometric measurements, analyzing complete sample sets, performing sample rotations, or combining ellipsometry and optical pump analysis. Enhanced efficiency leads to stronger THz signals and better sensitivity, facilitating more accurate and faster ellipsometric measurements. It also reduces the required pump power, making the system more practical and cost-effective. By combining these strategies, ongoing research aims to bring the efficiency of STEs closer to that of conventional THz sources.

1.6 Development of spintronic emitters for ellipsometry: objectives and methodology

1.6.1 Research objectives

This thesis aims to advance the terahertz time-domain spectroscopic ellipsometry (THz-TDSE) by addressing its critical challenges by developing novel spintronic terahertz emitters (STEs) for high efficiency and advanced polarization control. The main objectives of the research are:

1. **Enhance optical-to-THz conversion efficiency**: Sources with low signal output and limited dynamic range are impractical for applications like spectroscopy and ellipsometry, which require a robust signal. Therefore, this research aimed to explore electromagnetic efficiency and maximize the pumping pulse and terahertz extraction utilization by integrating spintronic emitters with resonant cavities.

    - **Design and integration of photonic cavities**:
      We designed and fabricated one-dimensional photonic cavities composed of alternating layers of silicon dioxide (SiO_2) and silicon nitride (SiN_x). The purpose of the photonic cavity is to enhance the absorption of the pump laser within the STE's ferromagnetic (FM) layer. We achieved constructive interference by engineering the cavity to resonate at the pump laser wavelength (800 nm) and increased the optical field intensity inside the FM layer. The enhanced optical absorption leads to a higher generation rate of spin-polarized electrons, thereby increasing the spin current density and contributing to THz emission. We achieved one of the highest reported efficiencies by an amplitude factor of 2.45.
    - **Integration with terahertz cavities**:
      In addition to the photonic cavity, we integrated a terahertz resonant cavity by adding an ultra-thin sapphire layer and a metallic mirror on the substrate side of the STE. This configuration forms a Fabry-Pérot cavity for THz frequencies, enhancing the extraction of the emitted THz radiation through constructive interference, boosting the terahertz signal by a factor of 2. A method specifically targeting terahertz extraction in this way has not been previously reported, making this approach unique in the field.
    - **Damage threshold analysis**:
      To determine maximal pumping conditions, we systematically studied the damage thresholds of STEs across a wide range of laser repetition rates, from kilohertz to gigahertz regimes. By varying the pump fluence and monitoring the onset of damage, we identified two primary damage regimes: Field-dominated damage and Heat-dominated damage. The transition point between these regimes had been a significant question, as previous measurements focused primarily on the field-dominated regime [120].

2. **Develop advanced polarization control mechanisms**: Achieve precise control of the emitted THz polarization without relying on external magnetic fields or mechanical rotating components, thus simplifying the experimental setup and enhancing measurement stability. This approach aims to generate pure linear polarizations with significantly higher extinction ratios, far surpassing the limitations of conventional THz polarizers, ensuring superior polarization quality at the source of the ellipsometry system.

- **Engineering magnetic anisotropy**:

  We developed STEs with engineered uniaxial magnetic anisotropy by replacing the isotropic ferromagnetic layer with a ferromagnetic trilayer of FeCo/$TbCo_2$/FeCo. The magnetic anisotropy arises from the interfacial coupling between the layers, resulting in a preferred magnetization direction within the plane of the film. We tailored the magnetic properties to achieve a strong anisotropy that allows the magnetization direction to be manipulated with minimal external influence applied along the hard axis. This enables dynamic control of the THz polarization by simply varying a small in-plane magnetic field to achieve 360° coherent polarization control of the emitted THz radiation.

- **Voltage-controlled polarization using magnetostrictive materials**:

  To simplify the polarization control further, we explored voltage-induced magnetization rotation using magnetostrictive materials deposited on piezoelectric substrates, such as PMN-PT (lead magnesium niobate-lead titanate). Applying a voltage across the piezoelectric substrate induces mechanical strain, which is transferred to the magnetostrictive layer, causing a change in its magnetization direction due to the magnetoelastic effect. This approach allows for electrical control of the THz polarization without needing magnetic fields or mechanical motion, enabling rapid and precise modulation suitable for advanced THz-TDE applications.

3. **Demonstrate complete time-domain ellipsometry utilizing STEs**: Integrate the STEs into THz-cTDSE systems and develop advanced measurement and calibration techniques that comprehensively characterize complex materials, including anisotropic and optically active samples.

   We experimentally demonstrate the complete determination of Jones and Mueller matrices using spintronic emitters. We successfully characterized anisotropic materials, characterizing their retardation and diattenuation properties. We introduce a novel experimental approach using Pauli exponential coefficients for straightforward interpretation. To ensure accuracy and reliability in the THz-TDE measurements, we developed calibration methods that account for systematic errors and experimental imperfections.

4. **Explore ultra-broadband photomixing applications**:

   A significant aspect of our research involved exploring the capabilities of spintronic emitters in the frequency domain. We focused on developing a spintronic emitter capable of producing a uniform, gapless spectrum extending into the tens of terahertz, envisioning its application as a versatile photomixer. Unlike traditional photomixers, which suffer from limited tunability and reduced efficiency at higher frequencies due to resistance-capacitance roll-off, this spintronic photomixer would emit across the entire THz spectrum. Demonstrating such a device as a proof of concept could represent a significant advancement for terahertz frequency-comb ellipsometry, particularly in achieving exceptionally high spectral resolution, shown only in infrared region [121, 122].

   We successfully demonstrated ultra-broadband THz photomixing using STEs, achieving stable THz frequency comb generation up to 1.05 THz. This surpasses traditional photomixing methods and opens new possibilities for high-resolution spectroscopy, ellipsometry, and frequency comb generation.

1.7 Structure of the thesis

The presented dissertation is structured in an article-based format, with the results section composed of the author's published works. A total of eight articles are included, four of which are first-author publications. Significant contributions to the scientific development of all the articles were made, particularly in theoretical design, experimental implementation, and data interpretation. Of the eight articles, six have been published in peer-reviewed journals, one is currently under peer review, and one has been published as a conference proceeding. Although published as a proceeding, this article represents a crucial part of the research, and a peer-reviewed journal version is currently being prepared. Each article is preceded by a multi-page introduction that provides the necessary context and connects the individual findings to the broader scope of the research. The thesis is structured as follows.

The thesis begins with a fundamental overview of polarized light and ellipsometry principles in Chapter 2, offering essential background not thoroughly explored in the related publications. The primary objective of this chapter is to demonstrate the application and interpretation of Jones and Mueller's calculus in describing polarized light. The chapter further elaborates on how the elements of Jones and Mueller matrices correspond to fundamental optical effects like retardation, diattenuation, and depolarization. Finally, we introduce Pauli exponential coefficients as a crucial framework for conducting in-depth ellipsometric analysis and straightforward interpretation.

Chapter 3 outlines the experimental efforts involved in constructing the laser infrastructure required for developing time-domain terahertz ellipsometry. The discussion details the experimental setup developed as part of the doctoral research, which served as the foundation for advancing the time-domain terahertz ellipsometer. The experimental setup was specifically designed to fully leverage the capabilities of a 5 W amplifier and an optical parametric amplifier, spanning a wavelength range from 550 nm to 1.5 μm.

Chapter 4 provides the context and motivation for the published research papers, discussing their relevance to the thesis's core theme. These publications are explored in organized sections, focusing on the efficiency of spintronic emitters, polarization control, optical damage threshold, and their applications in time-domain ellipsometry and frequency-domain photomixing. One section presents the optical ellipsometry analysis of anisotropic materials with optical activity, providing a foundational understanding of traditional ellipsometry early in the research. Each publication is discussed for its objectives and key findings, with a summary of my contributions. The publications, in their complete form, including all supplementary materials, are included in Chapter 5. Chapter 6 comprehensively summarizes the dissertation's findings and explores potential potential applications and future directions of spintronic emitters.

2

INTRODUCTION TO POLARIZED LIGHT AND ELLIPSOMETRY

2.1 Polarization of light

Polarization of light refers to the direction of oscillation of the electric component of an electromagnetic wave. It is a fundamental property of light, crucial for understanding its interaction with materials. In many optical phenomena, such as reflection, refraction, and scattering, the behavior of polarized light differs significantly from that of unpolarized light [123–125]. The polarization state is particularly important when studying the optical properties of anisotropic materials, such as crystals, where the molecular structure plays a decisive role in determining how light propagates through the medium.

In anisotropic materials, the molecular arrangement, characterized by the material's permittivity tensor $\hat{\varepsilon}$, defines the electric displacement vector $\mathbf{D}$ in specific directions, given by

$$D_i = \varepsilon_{ij} E_j, \tag{2.1}$$

where $\mathbf{E}$ represents the electric field vector. As a result, the interaction between light and anisotropic materials depends critically on the orientation of the light's electric field vector relative to the material's optical axes. This orientation governs how the material influences the phase velocity and absorption of different polarization components, leading to birefringence, where the refractive index varies with polarization and propagation direction, and dichroism, where light absorption differs depending on its polarization state.

To mathematically describe the polarization state of light, we use the Jones vector formalism. The Jones vector is a two-dimensional complex vector that encapsulates the complex amplitudes of the electric field components perpendicular to the direction of propagation. It is expressed as follows

$$\mathbf{J} = \begin{bmatrix} \tilde{E}_{\mathrm{x}} \\ \tilde{E}_{\mathrm{y}} \end{bmatrix}, \tag{2.2}$$

where $\tilde{E}_{\mathrm{x}}$ and $\tilde{E}_{\mathrm{y}}$ represent the complex amplitudes of the electric field components along the x- and y-axes, respectively [54, 126]. The Jones vector formalism is only applicable to completely polarized light. It does not account for partially polarized or unpolarized light, which requires a more general framework such as the Stokes formalism.

The polarization vector generally describes an elliptical path when the $\tilde{E}_\mathrm{x}$ and $\tilde{E}_\mathrm{y}$ components are out of phase. The ratio of these complex amplitudes, $\tilde{\chi}$, offers an intuitive description of elliptically polarized light

$$\tilde{\chi} = \chi_\mathrm{r} + \mathrm{i}\chi_\mathrm{i} = \frac{\tilde{E}_\mathrm{x}}{\tilde{E}_\mathrm{y}} = \frac{\tan\vartheta + \mathrm{i}\tan\epsilon}{1 - \mathrm{i}\tan\vartheta\tan\epsilon}, \tag{2.3}$$

where χ_r and χ_i are the real and imaginary parts of the complex parameter $\tilde{\chi}$, and ϑ and ϵ are the azimuth and ellipticity angles, respectively [54, 127]. Ellipticity ϵ is a key parameter that describes the shape of the polarization ellipse, specifically characterizing the ratio of its major and minor axes. Physically, it quantifies how much the polarization deviates from purely linear, with $\epsilon = 0$ corresponding to linear polarization and $\epsilon = \pm\frac{\pi}{4}$ indicating circular polarization. Figure 2.1 illustrates the geometric significance of these angles in the polarization ellipse.

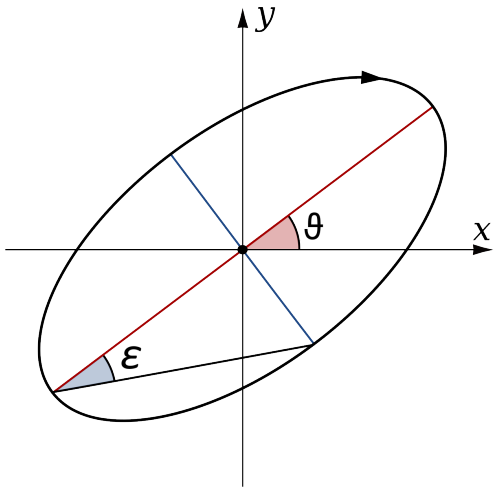


Figure 2.1: Graphical representation of the polarization ellipse formed by an oscillating electromagnetic field: This diagram illustrates the polarization ellipse traced by an oscillating electromagnetic field. The arrow indicates the direction of the electric field oscillation, while the angles ϑ and ϵ represent the azimuth and ellipticity of the ellipse, respectively.

The azimuth and ellipticity angles are related to the real and imaginary parts of the complex ratio $\tilde{\chi}$ through the following expressions

$$\tan 2\epsilon = \frac{2\chi_\mathrm{r}}{1 - |\tilde{\chi}|^2}, \tag{2.4}$$

$$\sin 2\vartheta = \frac{2\chi_\mathrm{i}}{1 + |\tilde{\chi}|^2}. \tag{2.5}$$

The Cartesian complex plane is often used to map the complex ratio $\tilde{\chi}$, with their real and imaginary components representing polarization states. The real axis χ_r corresponds to linear polarization states, ranging from horizontal to vertical, while the imaginary axis χ_i represents circular left- and right-handed polarizations. Off-axis positions indicate elliptical polarization, a combination of linear and circular states. This distribution is shown in Figure 2.2.

However, it can be challenging to represent all polarization states on the complex plane, as it extends infinitely. To address this, stereographic projection maps the polarization states onto the

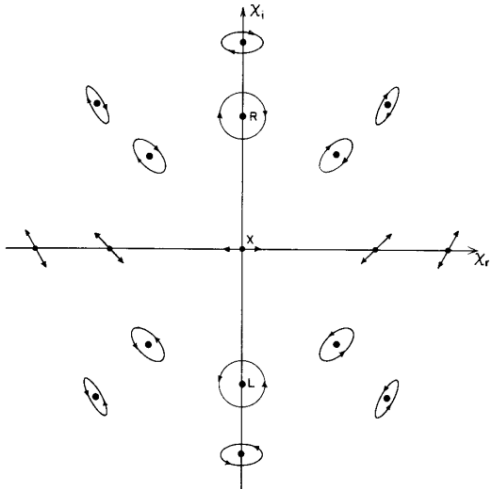


Figure 2.2: Schematic representation of polarization states in the infinite complex plane $\tilde{\chi}$: This diagram illustrates the distribution of polarization ellipses, with varying azimuth angles ϑ and ellipticity ϵ. The real axis corresponds to linear polarization, while the imaginary axis represents circular polarization. Adapted from [54].

surface of a finite sphere, known as the Poincaré sphere. This transformation enables the geometric representation of all possible polarization states on a finite surface. This transformation is illustrated in Figure 2.3 [54, 82]. In the end, the Poincaré sphere is rotated to display circular polarizations at the poles and linear polarization states along the equator, as demonstrated in Figure 2.4. Points in between correspond to elliptical polarization with varying degrees of ellipticity and azimuth [82], visualizing all possible polarization states.

The polarization state of light can also be described using the Stokes vector formalism. The Stokes vector provides an intensity-based description of polarization, particularly useful in experiments where phase information is not directly accessible. These Stokes elements can be expressed in various forms: through Jones vector elements, the polarization ellipse angles, or the corresponding intensity differences of polarized light, in the following form

$$\mathbf{S} = \begin{bmatrix} S_0 \\ S_1 \\ S_2 \\ S_3 \end{bmatrix} = \begin{bmatrix} |\tilde{E}_x|^2 + |\tilde{E}_y|^2 \\ |\tilde{E}_x|^2 - |\tilde{E}_y|^2 \\ 2\mathrm{Re}(\tilde{E}_x\,\tilde{E}_y^*) \\ -2\mathrm{Im}(\tilde{E}_x\,\tilde{E}_y^*) \end{bmatrix} = I_0 \begin{bmatrix} 1 \\ \cos 2\vartheta \cos 2\epsilon \\ \sin 2\vartheta \cos 2\epsilon \\ \sin 2\epsilon \end{bmatrix} = \begin{bmatrix} I_x + I_y \\ I_x - I_y \\ I_{+45^\circ} - I_{-45^\circ} \\ I_\mathrm{R} - I_\mathrm{L} \end{bmatrix}, \tag{2.6}$$

where S_0 represents the total intensity, and S_1, S_2, and S_3 correspond to different polarized intensities, with S_1 distinguishing between horizontal and vertical polarization, S_2 between diagonal polarization states (45° and -45°), and S_3 representing the difference between right- versus left-handed circular polarization [54, 82, 128]. The intensity satisfies the inequality $S_0^2 \geq S_1^2 + S_2^2 + S_3^2$, with the degree of polarization defined by the extent to which this inequality is satisfied.

2.1.1 Mueller and Jones calculus

The primary goal of ellipsometry is to determine the transformation matrix of a sample, which characterizes how the polarization state of light, given by the Jones vector $\mathbf{J}$ or the Stokes vector $\mathbf{S}$,

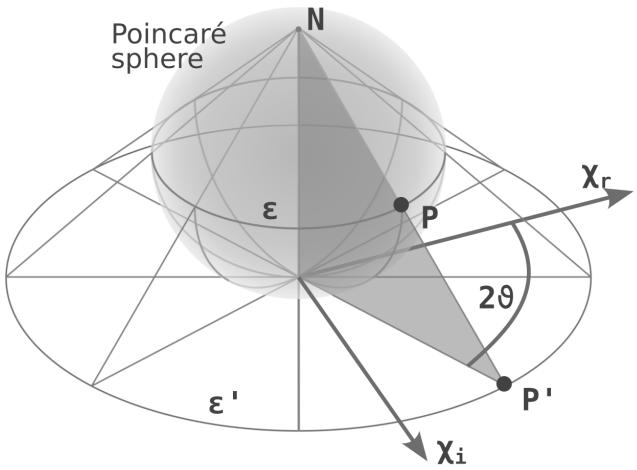


Figure 2.3: Creation of Poincaré sphere: This illustration depicts the transformation of polarization states from the infinite complex plane $\tilde{\chi}$ to the finite Poincaré sphere through stereographic projection. Each point on the plane is projected onto the sphere along a line extending from the north pole (N).

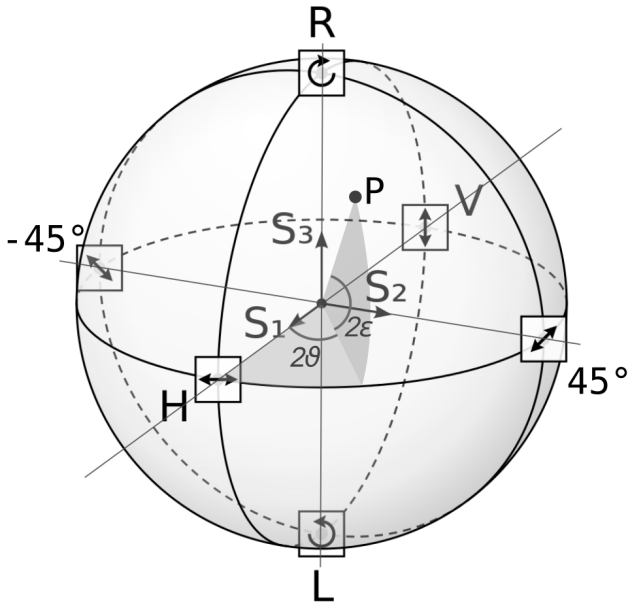


Figure 2.4: Poincaré sphere and Stokes vectors: The Poincaré sphere, with its Cartesian coordinate system (S_1, S_2, S_3), is shown, corresponding to the fundamental polarization states: horizontal (H), vertical (V), diagonal (+45° and -45°), and circular polarizations (right-handed and left-handed). The polarization state P is defined by the angles ϵ and ϑ.

changes from its input state to its output state after interacting with the material [49, 50, 129]. This transformation is crucial for extracting optical properties such as refractive index and thickness of thin films. The two main matrix frameworks used in ellipsometry to describe these transformations are the Jones calculus, which handles coherent light, and the Mueller calculus, which extends the analysis into intensity description, including depolarization effects.

In cases involving coherent light, these transformations are governed by the Jones matrix $\mathbb{J}$, which details how optical elements alter the complex amplitude components

$$\mathbf{J}_{\text{output}} = \underbrace{\begin{pmatrix} \tilde{j}_{11} & \tilde{j}_{12} \\ \tilde{j}_{21} & \tilde{j}_{22} \end{pmatrix}}_{\mathbb{J}} \mathbf{J}_{\text{input}}. \tag{2.7}$$

Comprising eight real parameters (four complex parameters), the Jones matrix $\mathbb{J}$ of a sample describes the amplitude and phase transformations between the orthogonal components of the complex field $\mathbf{J}$. For a series of n polarization components, the resulting polarization state is given by non-commutative multiplication, expressed as $\mathbf{J}_{\text{output}} = \mathbb{J}_n \ldots \mathbb{J}_2 \mathbb{J}_1 \mathbf{J}_{\text{input}}$. When an optical component is rotated by an angle θ, the Jones matrix must also be rotated to reflect the new orientation of the optical axis. This is achieved by applying a rotation matrix $\mathbb{T}_\theta$, which transforms the coordinate system to match the rotated element as

$$\mathbb{J}_\theta = \mathbb{T}_{-\theta} \mathbb{J} \, \mathbb{T}_\theta \tag{2.8}$$

where

$$\mathbb{T}_\theta = \begin{pmatrix} \cos\theta & \sin\theta \\ -\sin\theta & \cos\theta \end{pmatrix}. \tag{2.9}$$

While the Jones matrix offers a coherent description of polarization transformations, it does not address depolarization effects caused by multiple scattering processes or polarization inhomogeneities within the beam. Such limitations become particularly important when analyzing biological specimens, powdered substances, solutions, rough surfaces, and inhomogeneous materials [130–132]. Jones's calculus is limited to specific frequency ranges, such as radio, microwave, or terahertz, where the light remains coherent, and time-resolved techniques capture the entire waveform.

To account for the intensity-based properties of light, we employ Mueller calculus to transform Stokes vectors $\mathbf{S}$ [54, 133] by

$$\mathbf{S}_{\text{output}} = \underbrace{\begin{pmatrix} m_{11} & m_{12} & m_{13} & m_{14} \\ m_{21} & m_{22} & m_{23} & m_{24} \\ m_{31} & m_{32} & m_{33} & m_{34} \\ m_{41} & m_{42} & m_{43} & m_{44} \end{pmatrix}}_{\mathbb{M}} \mathbf{S}_{\text{input}}. \tag{2.10}$$

The Mueller matrix $\mathbb{M}$ comprises 16 real elements, twice as many as the Jones matrix [134]. The Mueller matrix is often normalized by its first element m_{11} to make relative intensity changes more apparent. Unlike the Jones matrix, which focuses solely on coherent field components, it captures depolarization effects and accommodates unpolarized and partially polarized light. This versatility makes it adaptable and robust for complex ellipsometric characterizations across the electromagnetic spectrum.

One can transform the Jones matrix into the Mueller matrix using a coherency theory approach through time-averaged quantities $<>$ [54], given by

$$\mathbb{M} = \mathbb{A} < \mathbb{J} \otimes \mathbb{J}^* > \mathbb{A}^{-1}. \tag{2.11}$$

The Kronecker product $\otimes$ is an operation that takes two matrices and produces a block matrix. This enables the transformation from a 2x2 Jones matrix to a 4x4 Mueller matrix. The matrix $\mathbb{A}$ represents the transformation $\mathbf{S} = \mathbb{A}\,\mathrm{vec}(\mathbb{C})$ between the vectorized coherency matrix

$$\mathbb{C} =< \mathbf{J} \times \mathbf{J}^* >= \begin{pmatrix} < \tilde{E}_\mathrm{x}\tilde{E}_\mathrm{x}^* > & < \tilde{E}_\mathrm{x}\tilde{E}_\mathrm{y}^* > \\ < \tilde{E}_\mathrm{y}\tilde{E}_\mathrm{x}^* > & < \tilde{E}_\mathrm{y}\tilde{E}_\mathrm{y}^* > \end{pmatrix} = \begin{pmatrix} \tilde{c}_{11} & \tilde{c}_{12} \\ \tilde{c}_{21} & \tilde{c}_{22} \end{pmatrix} \tag{2.12}$$

and the Stokes vector in the following form

$$\begin{bmatrix} S_0 \\ S_1 \\ S_2 \\ S_3 \end{bmatrix} = \underbrace{\begin{pmatrix} 1 & 0 & 0 & 1 \\ 1 & 0 & 0 & -1 \\ 0 & 1 & 1 & 0 \\ 0 & \mathrm{i} & -\mathrm{i} & 0 \end{pmatrix}}_{\mathbb{A}} \begin{bmatrix} \tilde{c}_{11} \\ \tilde{c}_{12} \\ \tilde{c}_{21} \\ \tilde{c}_{22} \end{bmatrix} \tag{2.13}$$

In the case of coherent fields, the resulting Mueller matrix sometimes referred to as the Mueller-Jones matrix, is non-depolarizing. However, the Mueller-Jones matrix describes the same polarization information as the Jones matrix; it excludes the total phase and amplitude information.

2.1.2 Interpreting Jones and Mueller Matrices

Interpreting experimentally obtained Jones and Mueller matrices is fundamental in ellipsometry [82, 135]. However, analyzing the elements of these matrices can be challenging, especially for those new to the field. The Jones matrix compactly describes polarization effects in a 2×2 complex matrix, while the Mueller matrix represents these effects in a 4×4 real matrix, comprising 16 elements (with 15 independent parameters due to normalization). Understanding how different polarization phenomena manifest within these matrices is crucial for accurately interpreting ellipsometric data. In this section, we illustrate how fundamental polarization components manifest in each matrix and discuss the key phenomena associated with individual elements. For simplicity, we will focus on non-rotated matrices, where each polarization effect is isolated in specific matrix elements. In practical situations, rotations and combinations of effects can distribute these influences across the entire matrix due to matrix multiplication. Nevertheless, even in these simplified examples, we can identify the elements where these phenomena most prominently manifest.

In the Jones matrix, the diagonal elements affect the original Jones vector components by introducing phase shifts and amplitude changes, while the off-diagonal elements couple one polarization component to the other. The general Jones matrix exhibits two main characteristics: diattenuation, responsible for amplitude changes due to absorption or reflection, and retardation, which causes phase shifts leading to wave delays and potential rotation of the polarization plane. To isolate these influences, we can decompose the Jones matrix into diattenuation and retardation matrices

$$\mathbb{J} = \mathbb{J}_\mathrm{diat}\mathbb{J}_\mathrm{ret}. \tag{2.14}$$

The Mueller matrix, in addition, accounts for depolarization effects, requiring the inclusion of an additional matrix in its decomposition to capture this phenomenon [135]

$$\mathbb{M} = \mathbb{M}_{\text{diat}}\mathbb{M}_{\text{ret}}\mathbb{M}_{\text{dep}}. \tag{2.15}$$

Diattenuation and retardation manifest differently depending on the polarization basis—whether the light is linearly or circularly polarized. Therefore, interpreting the elements of general Jones and Mueller matrices is essential for identifying phenomena such as linear and circular birefringence or dichroism. These effects can be analyzed using various polarization bases defined on the Poincaré sphere, including linear polarizations along the x and y axes, at $\pm 45°$, or circular polarizations.

Diattenuation

We begin our analysis with the diattenuation Jones matrix in the linear x,y basis [54]. This matrix represents linear dichroism or different ordinary and extraordinary transmission coefficients aligned with the coordinate system of the Jones vector

$$\mathbb{D}_{\text{linear}} = \begin{pmatrix} A_{\text{x}} & 0 \\ 0 & A_{\text{y}} \end{pmatrix}, \tag{2.16}$$

where A_{x} and A_{y} are the diattenuation coefficients (amplitude transmission factors) for the x and y components, respectively. When $A_{\text{x,y}} = 1$, there is no attenuation, and the matrix behaves like the identity matrix; conversely, when $A_{\text{x,y}} = 0$, the corresponding polarization component is completely attenuated.

In the x,y-basis, these diattenuation coefficients directly affect the main diagonal of the Jones matrix, corresponding to the amplitude changes of each polarization component. This section will highlight the matrix elements under discussion with a blue background.

When the Jones matrix $\mathbb{D}_{\text{linear}}$ is converted to the Mueller matrix $\mathbb{M}_{\text{D,linear}}$, it becomes

$$\mathbb{M}_{\text{D,linear}} = \frac{1}{2}\begin{pmatrix} A_{\text{x}}^2 + A_{\text{y}}^2 & A_{\text{x}}^2 - A_{\text{y}}^2 & 0 & 0 \\ A_{\text{x}}^2 - A_{\text{y}}^2 & A_{\text{x}}^2 + A_{\text{y}}^2 & 0 & 0 \\ 0 & 0 & 2\,A_{\text{x}}\,A_{\text{y}} & 0 \\ 0 & 0 & 0 & 2\,A_{\text{x}}\,A_{\text{y}} \end{pmatrix}. \tag{2.17}$$

In the Mueller matrix, linear diattenuation is primarily observed in the elements m_{12} and m_{21}, as well as in the main diagonal. Without diattenuation (when $A_{\text{x}} = A_{\text{y}}$), these off-diagonal elements m_{12} and m_{21} become zero, and the matrix simplifies to the identity matrix. Non-zero values in these off-diagonal elements indicate the presence of linear diattenuation within the system.

Next, we examine diattenuation in the diagonal linear basis ($45°/-45°$), particularly when the axes of the dichroic material do not align with the x,y basis. We define the diattenuation matrix $\mathbb{D}_{45}$ for the diagonal basis and transform it into the x,y basis using the transformation matrix $\mathbb{T}_{45}$

$$\mathbb{D}_{\text{diagonal}} = \mathbb{T}_{45}^{-1}\mathbb{D}_{45}\mathbb{T}_{45} = \frac{1}{2}\begin{pmatrix} A_{45}^2 + A_{-45}^2 & A_{45}^2 - A_{-45}^2 \\ A_{45}^2 - A_{-45}^2 & A_{45}^2 + A_{-45}^2 \end{pmatrix}, \tag{2.18}$$

where

$$\mathbb{T}_{45} = \frac{1}{\sqrt{2}}\begin{pmatrix} 1 & 1 \\ -1 & 1 \end{pmatrix}, \qquad \mathbb{D}_{45} = \begin{pmatrix} A_{45} & 0 \\ 0 & A_{-45} \end{pmatrix}, \tag{2.19}$$

and A_{45} and A_{-45} are the diattenuation coefficients in the $45°$ and $-45°$ basis, respectively. From the Jones matrix $\mathbb{D}_{\text{diagonal}}$, it is evident that the off-diagonal elements $\tilde{j}_{12}$ and $\tilde{j}_{21}$ now contain the diattenuation differences due to the rotated basis. Transforming this Jones matrix into the Mueller matrix, we obtain

$$\mathbb{M}_{\text{D,diagonal}} = \frac{1}{2}\begin{pmatrix} {A_{45}}^2 + {A_{-45}}^2 & 0 & {A_{45}}^2 - {A_{-45}}^2 & 0 \\ 0 & 2\,A_{45}\,A_{-45} & 0 & 0 \\ {A_{45}}^2 - {A_{-45}}^2 & 0 & {A_{45}}^2 + {A_{-45}}^2 & 0 \\ 0 & 0 & 0 & 2\,A_{45}\,A_{-45} \end{pmatrix}. \tag{2.20}$$

Here, diagonal diattenuation results in non-zero elements m_{13} and m_{31} in the Mueller matrix, indicating a difference in attenuation between the $45°$ and $-45°$ components.

Moving on to diattenuation in circular polarizations, we introduce the diattenuation matrix $\mathbb{D}_{\text{C}}$ in the circular basis. This matrix includes diattenuation coefficients for right-handed A_{R} and left-handed A_{L} circular polarizations. Converting it to the x,y linear basis using the transformation matrix $\mathbb{T}_{\text{C}}$, we get

$$\mathbb{D}_{\text{circular}} = {\mathbb{T}_{\text{C}}}^{-1}\mathbb{D}_{\text{C}}\mathbb{T}_{\text{C}} = \frac{1}{2}\begin{pmatrix} A_{\text{R}}^2 + A_{\text{L}}^2 & \text{i}(A_{\text{L}}^2 - A_{\text{R}}^2) \\ \text{i}(A_{\text{L}}^2 - A_{\text{R}}^2) & A_{\text{R}}^2 + A_{\text{L}}^2 \end{pmatrix}, \tag{2.21}$$

where

$$\mathbb{T}_{\text{C}} = \frac{1}{\sqrt{2}}\begin{pmatrix} 1 & \text{i} \\ 1 & -\text{i} \end{pmatrix}, \qquad \mathbb{D}_{\text{C}} = \begin{pmatrix} A_{\text{R}} & 0 \\ 0 & A_{\text{L}} \end{pmatrix}. \tag{2.22}$$

In this case, the off-diagonal elements of the Jones matrix are purely imaginary, reflecting the difference in attenuation between right-handed and left-handed circular polarizations. Distinguishing between diattenuation and retardation effects is crucial here, as diattenuation coefficients manifest as real or imaginary quantities depending on the basis.

Converting $\mathbb{D}_{\text{circular}}$ into the Mueller matrix yields

$$\mathbb{M}_{\text{D,circular}} = \frac{1}{2}\begin{pmatrix} {A_{\text{L}}}^2 + {A_{\text{R}}}^2 & 0 & 0 & {A_{\text{R}}}^2 - {A_{\text{L}}}^2 \\ 0 & 2\,A_{\text{L}}\,A_{\text{R}} & 0 & 0 \\ 0 & 0 & 2\,A_{\text{L}}\,A_{\text{R}} & 0 \\ {A_{\text{R}}}^2 - {A_{\text{L}}}^2 & 0 & 0 & {A_{\text{L}}}^2 + {A_{\text{R}}}^2 \end{pmatrix}, \tag{2.23}$$

where circular diattenuation appears in elements m_{14} and m_{41} of the Mueller matrix.

In summary, this analysis suggests that detecting diattenuation effects within the Mueller matrix involves identifying non-zero elements in the first row and column outside the main diagonal. Typically, when analyzing diattenuation effects and the compound effects of multiple matrix multiplications, these elements will show non-zero values only if diattenuation is present. Understanding these diattenuation effects is crucial in studying dichroism, where subtle differences in absorption between polarization states influence these elements. Relying solely on the main diagonal to detect these effects is not recommended, as it may also capture other phenomena like depolarization or retardation, potentially masking these finer variations.

An example of a diattenuator is a polarizer, which transmits one polarization state while attenuating others. To characterize a general polarizer's Jones matrix, we use a normalized Jones vector $\mathbf{p}$ to specify the transmitted polarization. The Jones matrix for such a polarizer is expressed as [133]:

$$\mathbb{J}_{\text{pol}} = \mathbf{p}\,\mathbf{p}^{\dagger} = \begin{pmatrix} p_1 p_1^* & p_1 p_2^* \\ p_1^* p_2 & p_2 p_2^* \end{pmatrix}, \tag{2.24}$$

where † denotes the Hermitian conjugate and

$$\mathbf{p} = \begin{bmatrix} p_1 \\ p_2 \end{bmatrix}. \tag{2.25}$$

This formulation allows for defining polarizers for any desired polarization state, including linear, circular, or elliptical.

Retardation

We now address the phenomenon of retardation as applied to modes on a specified basis [54]. We begin with linear retardation, commonly observed in uniaxial birefringent materials whose optical axes align with the x,y polarization basis. The Jones matrix for a linear retarder is

$$\mathbb{R}_{\text{linear}} = \begin{pmatrix} \mathrm{e}^{\mathrm{i}\phi_{\text{x}}} & 0 \\ 0 & \mathrm{e}^{\mathrm{i}\phi_{\text{y}}} \end{pmatrix}, \tag{2.26}$$

where ϕ_{x} and ϕ_{y} introduce phase shifts to each x,y polarization component. Transforming this Jones matrix into the Mueller matrix, we obtain

$$\mathbb{M}_{\text{R,linear}} = \begin{pmatrix} 1 & 0 & 0 & 0 \\ 0 & 1 & 0 & 0 \\ 0 & 0 & \cos\delta & -\sin\delta \\ 0 & 0 & \sin\delta & \cos\delta \end{pmatrix}, \tag{2.27}$$

where $\delta = \phi_{\text{x}} - \phi_{\text{y}}$ is the phase retardation between the two polarization components. The Mueller matrix measures the phase difference between the modes, emphasizing relative retardation rather than absolute phase values. Retardation primarily affects the elements m_{33}, m_{34}, m_{43}, and m_{44} of the Mueller matrix.

For example, consider a wave plate rotated to $45°$, which affects polarizations along the $45°$ and $-45°$ axes. The Jones matrix for this rotated retarder is derived by transforming the retardation matrix $\mathbb{R}_{45}$ using the transformation matrix $\mathbb{T}_{45}$

$$\mathbb{R}_{\text{diagonal}} = \mathbb{T}_{45}^{-1}\mathbb{R}_{45}\mathbb{T}_{45} = \frac{1}{2}\begin{pmatrix} \mathrm{e}^{\mathrm{i}\phi_{45}} + \mathrm{e}^{\mathrm{i}\phi_{-45}} & \mathrm{e}^{\mathrm{i}\phi_{45}} - \mathrm{e}^{\mathrm{i}\phi_{-45}} \\ \mathrm{e}^{\mathrm{i}\phi_{45}} - \mathrm{e}^{\mathrm{i}\phi_{-45}} & \mathrm{e}^{\mathrm{i}\phi_{45}} + \mathrm{e}^{\mathrm{i}\phi_{-45}} \end{pmatrix}, \tag{2.28}$$

where

$$\mathbb{R}_{45} = \begin{pmatrix} \mathrm{e}^{\mathrm{i}\phi_{45}} & 0 \\ 0 & \mathrm{e}^{\mathrm{i}\phi_{-45}} \end{pmatrix}. \tag{2.29}$$

Here, ϕ_{45} and ϕ_{-45} are the phase shifts along the $45°$ and $-45°$ axes, respectively. Linear retardation is evident in the off-diagonal elements of $\mathbb{R}_{\text{diagonal}}$, indicating coupling between the polarization components due to the rotated basis. The corresponding Mueller matrix is

$$\mathbb{M}_{\text{R,diagonal}} = \begin{pmatrix} 1 & 0 & 0 & 0 \\ 0 & \cos\delta' & 0 & \sin\delta' \\ 0 & 0 & 1 & 0 \\ 0 & -\sin\delta' & 0 & \cos\delta' \end{pmatrix}, \tag{2.30}$$

where $\delta' = \phi_{45} - \phi_{-45}$. Diagonal retardation affects elements m_{24} and m_{42} of the Mueller matrix.

Next, we consider a circular retarder, such as a quarter-wave plate, which introduces a phase difference between right-handed and left-handed circular polarizations. By transforming the circular retardation matrix $\mathbb{R}_{\text{C}}$ to the x,y basis using $\mathbb{T}_{\text{C}}$, we obtain

$$\mathbb{R}_{\text{circular}} = \mathbb{T}_{\text{C}}^{-1}\mathbb{R}_{\text{C}}\mathbb{T}_{\text{C}} = \frac{1}{2}\begin{pmatrix} e^{i\phi_{\text{L}}} + e^{i\phi_{\text{R}}} & i(e^{i\phi_{\text{L}}} - e^{i\phi_{\text{R}}}) \\ i(e^{i\phi_{\text{L}}} - e^{i\phi_{\text{R}}}) & e^{i\phi_{\text{L}}} + e^{i\phi_{\text{R}}} \end{pmatrix}, \tag{2.31}$$

where

$$\mathbb{R}_{\text{C}} = \begin{pmatrix} e^{i\phi_{\text{R}}} & 0 \\ 0 & e^{i\phi_{\text{L}}} \end{pmatrix}, \tag{2.32}$$

and ϕ_{R} and ϕ_{L} are the phase shifts for right-handed and left-handed circularly polarized modes, respectively. The off-diagonal elements are imaginary, reflecting the phase difference between circular polarizations. The Mueller matrix representation is

$$\mathbb{M}_{\text{R,circular}} = \begin{pmatrix} 1 & 0 & 0 & 0 \\ 0 & \cos\delta'' & \sin\delta'' & 0 \\ 0 & -\sin\delta'' & \cos\delta'' & 0 \\ 0 & 0 & 0 & 1 \end{pmatrix}, \tag{2.33}$$

where $\delta'' = \phi_{\text{L}} - \phi_{\text{R}}$. Circular retardation affects elements m_{23} and m_{32} of the Mueller matrix.

It's important to note that when optical components are rotated, or multiple effects are combined, the manifestations of retardation can spread across the entire submatrix $\mathbb{M}_{(2-4),(2-4)}$. Careful analysis is required to interpret these effects correctly, ensuring they are attributed to the appropriate retardation phenomena. However, the off-diagonal elements related to diattenuation (in the first row and column) remain zero when only retardation is present.

By understanding how diattenuation and retardation manifest in Jones and Mueller matrices, we can better interpret experimental ellipsometry data, accurately identify material properties, and advance the study of optical phenomena.

Depolarization

Depolarization reduces the polarization level of light due to factors such as multiple scattering, variable retardation throughout the beam, and sample inhomogeneities [82, 136]. We will explore this phenomenon using the Mueller matrix and define the anisotropic depolarization coefficient p_{ii}

with the following form

$$\mathbb{M}_{\text{dep}} = \begin{pmatrix} 1 & 0 & 0 & 0 \\ 0 & p_{22} & 0 & 0 \\ 0 & 0 & p_{33} & 0 \\ 0 & 0 & 0 & p_{44} \end{pmatrix}. \tag{2.34}$$

The first matrix element is set to one, preserving the original intensity of the Stokes component S_0. However, the depolarization coefficients on the main diagonal lead to information loss regarding the light's polarization state. This marks a significant distinction from a diattenuator, which fully absorbs the specific light states along with its total intensity. The degree of polarization (DoP) of light represented by the Stokes vector can be assessed through the depolarization index, derived from the vector as follows

$$\text{DoP} = \sqrt{\frac{S_1 + S_2 + S_3}{S_0}}. \tag{2.35}$$

A DoP value of 0 indicates no depolarization, values between 0 and 1 suggest partial depolarization and a DoP of 1 denotes complete depolarization. Figure 2.5 depicts the manifestation of depolarization on the Poincaré sphere, illustrating how the sphere is layered according to the Degree of Polarization (DoP). The sphere's outer surface represents states of complete polarization while decreasing S_0 values lead to progressively depolarized states within the sphere's inner layers. This representation clearly shows the transition of polarization states from fully polarized to various depolarization levels across the sphere.

The Jones matrix, which transforms the components of complex amplitude, cannot account for depolarization, as it only describes coherent and pure polarization states. In certain cases, depolarization may be understood as a randomization of light, where both the amplitude and phase become unpredictable. This is graphically depicted at the bottom of Figure 2.5, which shows that with increasing depolarization index, the polarization of light transitions from linear to chaotic. In such conditions, it becomes impossible to discern the polarization state of the waveform except for its measured intensity. A depolarized beam can also be thought of as spatially variably polarized. Upon intensity-based detection, this polarization information is lost by averaging because it is randomly distributed.

In coherent systems, depolarization cannot be directly measured. Polarization inhomogeneities across the beam may cause depolarization in a partially coherent regime, but in a fully coherent regime, they result in destructive interference and signal loss instead of measurable depolarization. When direct waveform measurements are available, enabling the Jones vector's determination, depolarization could only be resolved through detailed spatial mapping of the beam. Such coherent polarization-sensitive mapping would determine phase, amplitude, and polarization inhomogeneities across the beam profile.

Summary of matrix elements interpretation

Interpreting Mueller and Jones matrices that represent a single type of polarization effect and align with the previously discussed examples are generally the easiest to interpret. However, when matrices are multiplied or rotated, these effects can become coupled, complicating interpretation. Depolarization is most effectively observed in the main diagonal of the Mueller matrix; however, all retardation and diattenuation effects are also present there. Diattenuation effects are confined to the first row and column, while retardation effects are primarily observed within the Mueller submatrix

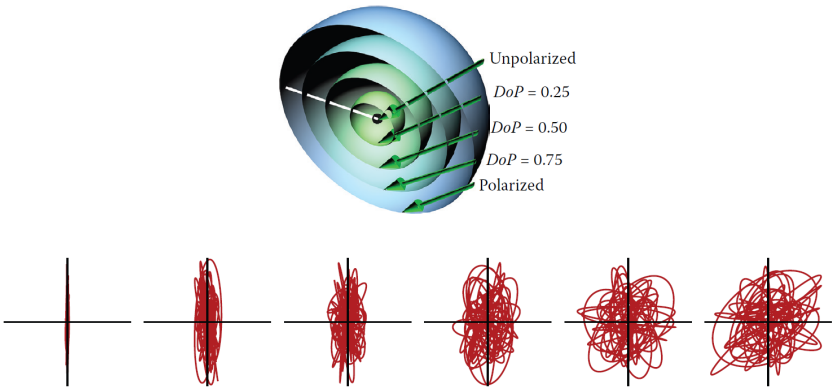


Figure 2.5: Illustration of depolarization: The diagram visually demonstrates depolarization effects within the Poincaré sphere. As one progresses into the sphere's inner layers, the Degree of Polarization (DoP) diminishes. Below the representation of the Poincaré sphere, an illustration depicts the transformation of a linear polarization state into a chaotic and undefined (depolarized) state as it moves deeper into the sphere. Points within the sphere, representing mixed polarization states, originate from integrating multiple surface states. Adapted from [82].

$m_{2-4,2-4}$. A simplified experimental geometry can significantly ease the analysis. For instance, when an optical component exhibits both linear and circular retardation, aligning the crystal to eliminate one of these effects allows for a clearer and more direct interpretation of the resulting matrix. If alignment is not feasible, developing a comprehensive model to simulate the data accurately becomes necessary. A thorough physical understanding of the sample's properties and parameters is crucial. If sample information is insufficient, methods like the Lu-Chipman decomposition [135] provide a viable solution. Decomposing matrices into diattenuation, retardation, and depolarization components effectively isolates these effects, especially in Mueller microscopy for interpreting images of optical or biological samples [137–139].

Figure 2.6 summarizes the observable effects within the Mueller matrix, highlighting specific effects in its elements. These effects are generally spread across all elements; however, their manifestation is primarily associated with these particular elements. In this context, A denotes diattenuation, R denotes retardation, and D denotes depolarization. The subscripts 'L', 'D', and 'C' correspond to linear, diagonal, and circular bases. A significant advantage of the Mueller matrix is its capacity to distribute these phenomena across various real-valued elements. In contrast, the Jones matrix, using the same graphical notation, shows these effects in identical elements but with differences in complex numbers. Superscripts 'r', 'i', 'c', and 'c" indicate purely real, purely imaginary, generally complex numbers, and complex numbers multiplied by the imaginary unit, respectively, aiding in detailed identification of the observed phenomena.

To achieve the same interpretation, one could analyze the differential Jones matrix and Mueller matrices [140, 141].

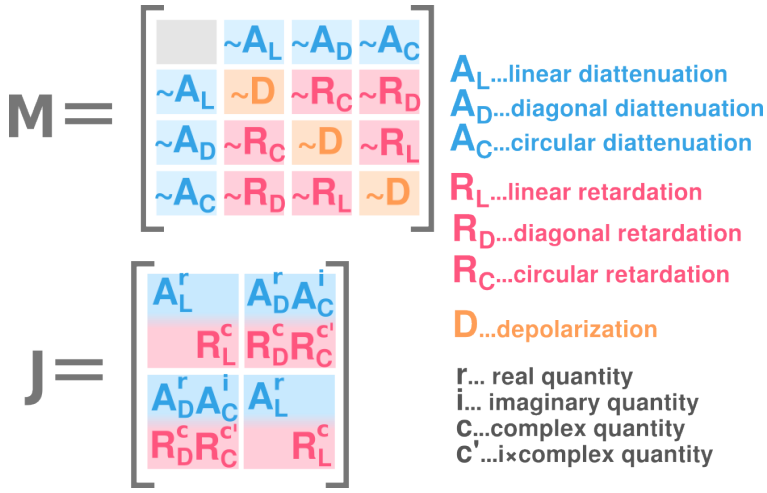


Figure 2.6: Graphical interpretation of Jones and Mueller matrices: The figure illustrates how fundamental changes in light polarization (retardation, diattenuation, and depolarization) are depicted within the bases of the Stokes vector across various elements of both the Mueller matrix $\mathbb{M}$ and the Jones matrix $\mathbb{J}$. It is crucial to assess whether each element of the Jones matrix is real, imaginary, or complex, as this distinction impacts the representation of multiple fundamental phenomena.

Interpreting Jones Matrices using Pauli matrices

A comprehensive understanding of the elements of the Jones and Mueller matrices can be challenging without an in-depth knowledge of ellipsometry. However, Pauli matrix decomposition provides an alternative method to interpret individual optical phenomena. With complete information on amplitude and phase in the coherent regime, the Jones matrix can be decomposed into a linear combination of several matrices, denoted as $\boldsymbol{\sigma}_\xi$, known as Pauli matrices [81, 82]

$$\mathbb{J} = \begin{pmatrix} \tilde{c}_0 + \tilde{c}_\mathrm{L} & \tilde{c}_\mathrm{D} - \mathrm{i}\tilde{c}_\mathrm{C} \\ \tilde{c}_\mathrm{D} + \mathrm{i}\tilde{c}_\mathrm{C} & \tilde{c}_0 - \tilde{c}_\mathrm{L} \end{pmatrix} = \tilde{c}_0 \underbrace{\begin{pmatrix} 1 & 0 \\ 0 & 1 \end{pmatrix}}_{\boldsymbol{\sigma}_0} + \tilde{c}_\mathrm{L} \underbrace{\begin{pmatrix} 0 & 1 \\ 1 & 0 \end{pmatrix}}_{\boldsymbol{\sigma}_\mathrm{L}} + \tilde{c}_\mathrm{D} \underbrace{\begin{pmatrix} 1 & 0 \\ 0 & -1 \end{pmatrix}}_{\boldsymbol{\sigma}_\mathrm{D}} + \tilde{c}_\mathrm{C} \underbrace{\begin{pmatrix} 0 & -\mathrm{i} \\ \mathrm{i} & 0 \end{pmatrix}}_{\boldsymbol{\sigma}_\mathrm{C}}. \tag{2.36}$$

The Pauli matrices are selected to correspond to fundamental operations that alter the polarization state of light. They represent complementary Jones matrices, each associated with a distinct physical interpretation. The matrix $\boldsymbol{\sigma}_0$ acts as the identity matrix, indicating an element that preserves the polarization state of light, thus functioning as a polarization-neutral component: $\boldsymbol{\sigma}_0\mathbf{E} = \mathbf{E}$. The matrix $\boldsymbol{\sigma}_\mathrm{L}$ corresponds to an optical element that interchanges the $\tilde{E}_\mathrm{x}$ and $\tilde{E}_\mathrm{y}$ linear components. This can be compared to a half-wave plate aligned to rotate the plane of polarization by $90°$, thus enabling a transition between x and y linear polarizations

$$\boldsymbol{\sigma}_\mathrm{L}\mathbf{E} = \begin{pmatrix} 0 & 1 \\ 1 & 0 \end{pmatrix} \begin{pmatrix} \tilde{E}_\mathrm{x} \\ \tilde{E}_\mathrm{y} \end{pmatrix} = \begin{pmatrix} \tilde{E}_\mathrm{y} \\ \tilde{E}_\mathrm{x} \end{pmatrix}. \tag{2.37}$$

The matrix $\boldsymbol{\sigma}_\mathrm{D}$ represents an element that inverts the phase of one polarization component. For instance, this can describe a half-wave plate designed to rotate the phase of one component by $180°$,

thereby switching between diagonal polarizations at $-45°$ and $+45°$:

$$\boldsymbol{\sigma}_{\mathrm{D}}\mathbf{E} = \begin{pmatrix} 1 & 0 \\ 0 & -1 \end{pmatrix} \begin{pmatrix} \tilde{E}_{\mathrm{x}} \\ \tilde{E}_{\mathrm{y}} \end{pmatrix} = \begin{pmatrix} \tilde{E}_{\mathrm{x}} \\ -\tilde{E}_{\mathrm{y}} \end{pmatrix}. \tag{2.38}$$

The matrix $\boldsymbol{\sigma}_{\mathrm{C}}$ represents a phase shift of $\pi/2$ between the components $\tilde{E}_{\mathrm{y}}$ and $\tilde{E}_{\mathrm{x}}$. This element can describe a quarter-wave plate, which converts linearly polarized light into circularly polarized light

$$\boldsymbol{\sigma}_{\mathrm{C}}\mathbf{E} = \begin{pmatrix} 0 & -i \\ i & 0 \end{pmatrix} \begin{pmatrix} \tilde{E}_{\mathrm{x}} \\ \tilde{E}_{\mathrm{y}} \end{pmatrix} = \begin{pmatrix} -i\tilde{E}_{\mathrm{y}} \\ i\tilde{E}_{\mathrm{x}} \end{pmatrix}. \tag{2.39}$$

In other words, it can change left-handed circular polarization into right-handed and vice versa, effectively facilitating switching between circular polarization bases. The circular polarization states are

$$\mathbf{E}_{\mathrm{R}} = \frac{1}{\sqrt{2}} \begin{pmatrix} 1 \\ -i \end{pmatrix}, \quad \mathbf{E}_{\mathrm{L}} = \frac{1}{\sqrt{2}} \begin{pmatrix} 1 \\ i \end{pmatrix}. \tag{2.40}$$

By applying σ_{C}, we transform the polarization as follows

$$\sigma_{\mathrm{C}}\mathbf{E}_{\mathrm{R}} = \frac{1}{\sqrt{2}} \begin{pmatrix} 0 & -i \\ i & 0 \end{pmatrix} \begin{pmatrix} 1 \\ -i \end{pmatrix} = \frac{1}{\sqrt{2}} \begin{pmatrix} -i(-i) \\ i(1) \end{pmatrix} = \mathbf{E}_{\mathrm{L}}, \tag{2.41}$$

$$\sigma_{\mathrm{C}}\mathbf{E}_{\mathrm{L}} = \frac{1}{\sqrt{2}} \begin{pmatrix} 0 & -i \\ i & 0 \end{pmatrix} \begin{pmatrix} 1 \\ i \end{pmatrix} = \frac{1}{\sqrt{2}} \begin{pmatrix} -i(i) \\ i(1) \end{pmatrix} = -\mathbf{E}_{\mathrm{R}}. \tag{2.42}$$

The four operations represented by the Pauli matrices correspond to transformations within identity, linear, diagonal, and circular bases.[1] These operations are intrinsically linked to the Stokes vector and Poincaré sphere, providing a comprehensive framework for describing the transformation of polarized light in a coherent regime. This method is particularly advantageous because it separates coupling effects within the Jones matrix. Additionally, the complex coefficients $\tilde{c}_\xi$ can represent both retardation and diattenuation in these Stokes ξ-bases. These coefficients can be readily calculated from the Jones matrix using the Pauli decomposition, as detailed in Equation (2.36), resulting in the following form

$$\tilde{c}_0 = \frac{\tilde{j}_{11} + \tilde{j}_{22}}{2}, \quad \tilde{c}_{\mathrm{L}} = \frac{\tilde{j}_{11} - \tilde{j}_{22}}{2}, \quad \tilde{c}_{\mathrm{D}} = \frac{\tilde{j}_{12} + \tilde{j}_{21}}{2}, \quad \tilde{c}_{\mathrm{C}} = \frac{\mathrm{i}(\tilde{j}_{12} - \tilde{j}_{21})}{2}. \tag{2.43}$$

However, instead of treating the Jones matrix as a direct sum of Pauli matrix components, it is more convenient to use an exponential representation. This approach naturally separates amplitude and phase effects within polarization transformations and provides a compact way to describe their combined influence. Since Pauli matrices satisfy the fundamental algebraic property

$$\sigma_\xi^2 = \mathbb{I}, \tag{2.44}$$

[1]The notation for the Pauli matrices used in this work differs from the standard convention ($\sigma_1, \sigma_2, \sigma_3$) in quantum mechanics. Here, the labeling is chosen based on optical considerations, specifically according to which type of polarization transformation each matrix influences: σ_L affects linear polarization (σ_1 in the standard convention), σ_D affects diagonal polarization (σ_3 in the standard convention), and σ_C affects circular polarization (σ_2 in the standard convention). This notation emphasizes the physical effects on polarization states in Stokes bases rather than their algebraic properties.

the exponential of any linear combination of them can be calculated explicitly. If we define

$$\mathbb{V} = \tilde{c}_{\mathrm{L}}\sigma_{\mathrm{L}} + \tilde{c}_{\mathrm{D}}\sigma_{\mathrm{D}} + \tilde{c}_{\mathrm{C}}\sigma_{\mathrm{C}}, \tag{2.45}$$

then it follows

$$\mathbb{V}^2 = (|\tilde{c}_{\mathrm{L}}|^2 + |\tilde{c}_{\mathrm{D}}|^2 + |\tilde{c}_{\mathrm{C}}|^2)\mathbb{I}. \tag{2.46}$$

The matrix exponential is defined by the Taylor series

$$\mathrm{e}^{\mathbb{V}} = \mathbb{I} + \mathbb{V} + \frac{\mathbb{V}^2}{2!} + \frac{\mathbb{V}^3}{3!} + \frac{\mathbb{V}^4}{4!} + \dots \tag{2.47}$$

Since $\mathbb{V}^2 = \|\mathbb{V}\|^2\mathbb{I}$, we substitute into the series

$$\sum_{k=0}^{\infty} \frac{(\mathbb{V})^{2k}}{(2k)!} = \sum_{k=0}^{\infty} \frac{\|\mathbb{V}\|^{2k}\mathbb{I}}{(2k)!} = \cos(\|\mathbb{V}\|)\mathbb{I}, \tag{2.48}$$

$$\sum_{k=0}^{\infty} \frac{(\mathbb{V})^{2k+1}}{(2k+1)!} = \sum_{k=0}^{\infty} \frac{\|\mathbb{V}\|^{2k+1}\mathbb{V}}{(2k+1)!\|\mathbb{V}\|} = \sin(\|\mathbb{V}\|)\frac{\mathbb{V}}{\|\mathbb{V}\|}. \tag{2.49}$$

As a result, the matrix exponential takes the form

$$e^{\mathbb{V}} = \cos(\|\mathbb{V}\|)\mathbb{I} + \sin(\|\mathbb{V}\|)\frac{\mathbb{V}}{\|\mathbb{V}\|}. \tag{2.50}$$

The exponential representation of a Jones matrix in the Pauli basis provides a natural way to separate diattenuation and retardance effects, clarifying their role in polarization transformations. Applying this identity, we obtain

$$\mathbb{J} = \tilde{c}_0\left(\boldsymbol{\sigma}_0 + \frac{\tilde{c}_{\mathrm{L}}\boldsymbol{\sigma}_{\mathrm{L}} + \tilde{c}_{\mathrm{D}}\boldsymbol{\sigma}_{\mathrm{D}} + \tilde{c}_{\mathrm{C}}\boldsymbol{\sigma}_{\mathrm{C}}}{\tilde{c}_0}\right) = \exp(\tilde{p}_0\boldsymbol{\sigma}_0)\exp\left[\frac{d_{\mathrm{L}} - \mathrm{i}\delta_{\mathrm{L}}}{2}\boldsymbol{\sigma}_{\mathrm{L}} + \frac{d_{\mathrm{D}} - \mathrm{i}\delta_{\mathrm{D}}}{2}\boldsymbol{\sigma}_{\mathrm{D}} + \frac{d_{\mathrm{C}} - \mathrm{i}\delta_{\mathrm{C}}}{2}\boldsymbol{\sigma}_{\mathrm{C}}\right], \tag{2.51}$$

where the exponentials contain coefficients $\tilde{p}_\xi = (d_\xi - \mathrm{i}\delta_\xi)/2$ for diattenuation d_ξ and retardation δ_ξ, except the exponential transforming the identity matrix, which contains total amplitude and phase change in the exponential coefficient $\tilde{p}_0$. This becomes evident when we convert the Jones matrix into its logarithmic form

$$\ln(\mathbb{J}) = \tilde{p}_0\boldsymbol{\sigma}_0 + \frac{d_{\mathrm{L}} - \mathrm{i}\delta_{\mathrm{L}}}{2}\boldsymbol{\sigma}_{\mathrm{L}} + \frac{d_{\mathrm{D}} - \mathrm{i}\delta_{\mathrm{D}}}{2}\boldsymbol{\sigma}_{\mathrm{D}} + \frac{d_{\mathrm{C}} - \mathrm{i}\delta_{\mathrm{C}}}{2}\boldsymbol{\sigma}_{\mathrm{C}} \tag{2.52}$$

The complex coefficients $(d_\xi - \mathrm{i}\delta_\xi)/2$ that scale the Pauli matrices correspond to manifestations of diattenuation and retardation across linear, diagonal, and circular bases. This offers a distinct advantage over traditional Mueller and Jones calculus, as all polarization phenomena are separated and easy to interpret for all Stokes bases.

3

DEVELOPMENT OF TERAHERTZ LABORATORY

3.1 Motivation behind constructing the laser infrastructure

This section details the development of the experimental infrastructure supporting terahertz time-domain ellipsometry. At the commencement of the PhD project, the laboratory lacked fundamental beam paths, necessitating the establishment of a new experimental setup. This endeavor was initiated with the implementation of time-domain terahertz spectroscopy. This foundational work was critical in advancing the ellipsometry setup and driving the progress of the research.

While the published papers focus on spintronic emitter development and the time-domain ellipsometry technique, this section emphasizes the parallel construction of a flexible experimental platform. The setup allows for advanced terahertz research, including studies of novel materials and sources, and extends its capabilities to pump-probe experiments for time-resolved investigations of material dynamics. It also integrates with terahertz ellipsometry to enable polarization-resolved measurements of dynamic changes.

Although the published work, which centers on the new ellipsometry developments, has not yet fully explored this infrastructure's full potential, it was designed to support a broad range of future research applications. This platform was intended to drive further advancements in terahertz studies and provide a robust foundation for future PhD students.

3.2 Development of STE-based THz-TDS ellipsometer

Figure 3.1 illustrates the experimental setup, which was developed for THz spectroscopy through the collaborative efforts of myself, Martin Mičica, and Iva Hlobílková. The setup features a beam path from Coherent's Vitara-T laser oscillator (orange line), operating at 80 MHz with pulse widths under 15 fs, a central wavelength of 800 nm, and approximately 250 mW output power. A dedicated beam pathway was also established for Coherent's Astrella laser amplifier (red line), delivering a 1 kHz repetition frequency, 5 W of average power, and pulse widths under 35 fs at 800 nm.

The output beam is divided between Coherent's OPerA optical parametric amplifier and the experimental setups, facilitating various spectroscopy techniques. Coherent's OPerA amplifier, tunable between 550 nm and 1.5 μm, provides dual outputs for visible and infrared light (green and blue lines), supporting optical pump-terahertz probe spectroscopy and tunable pump techniques.

Figure 3.2 depicts the terahertz time-domain ellipsometer, which employs the Astrella Ti:Sapphire 1 kHz amplifier. The entire setup is housed within a dry air-flushed box to prevent unstable absorption

from water vapor. This configuration incorporates an advanced, large-area spintronic emitter designed according to the specifications provided by Rougeriez et al. [112]. This emitter ensures precise polarization control and produces collimated emission with a 1 inch diameter. It operates at a maximum excitation power of 650 mW in the generation branch, guaranteeing optimal performance.

An external magnetic field generated by a Halbach array precisely controls the emitter's polarization. Mounted on a rotating stage, the emitter and magnet enable precise control of polarization and smooth transitions between vertical and horizontal modes. The resulting polarization is then analyzed using an additional polarizer. The setup employs a 500 μm thick ZnTe crystal plate for electro-optical sampling, capable of detecting signals up to 3.5 THz. The crystal thickness is selected to balance strong signal strength, considering birefringence, with the need for a broader spectral range. Using a thinner crystal offers a wider spectral range but reduces signal strength.

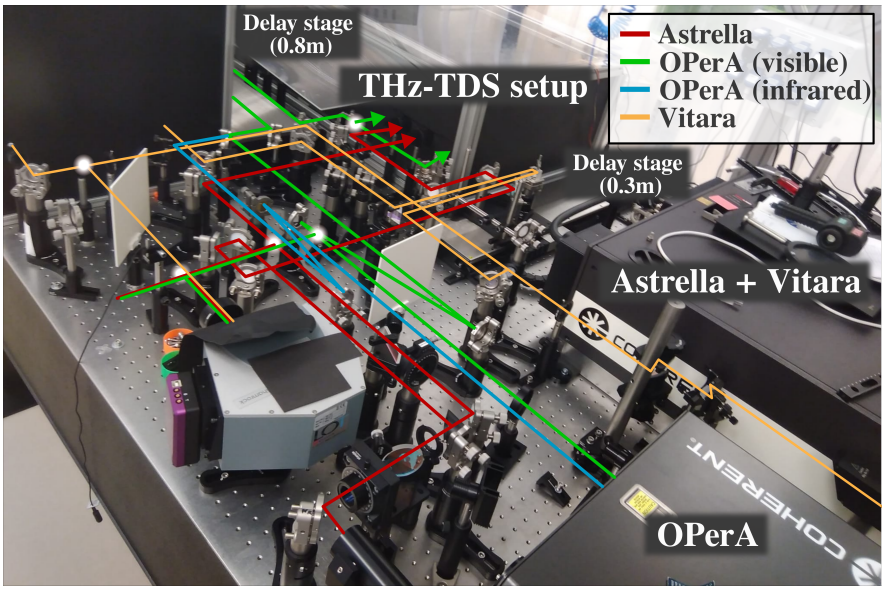


Figure 3.1: Developed ultrashort and high-power laser infrastructure: This image showcases the developed laser setup, marked by color-coded paths: red indicates the laser paths from the 1 kHz Astrella amplifier, orange traces the optical paths from the 80 MHz Vitara oscillator, green highlights the paths from the Optical Parametric Amplifier (OPerA) that translate radiation through the visible spectrum, and blue shows the paths from OPerA converting radiation into the infrared before converging into a unified path. Beams propagate through the optical table toward delay lines (800 mm and 300 mm) and proceed to the terahertz Time-Domain Spectroscopy (THz-TDS) experiment.

The detection process in electro-optic sampling proceeds as follows [142]. As the terahertz beam passes through the ZnTe crystal, a quarter-wave plate transforms the linear polarization into circular polarization. A Wollaston prism subsequently splits the beam into orthogonal polarizations, with the intensity difference detected by balanced diodes. The system is calibrated to zero the signal when terahertz radiation is absent. When exposed to terahertz radiation, the ZnTe crystal induces birefringence through the Pockels effect, altering the polarization of the probing infrared radiation. This polarization change is measured, yielding a relative measure of the terahertz radiation amplitude.

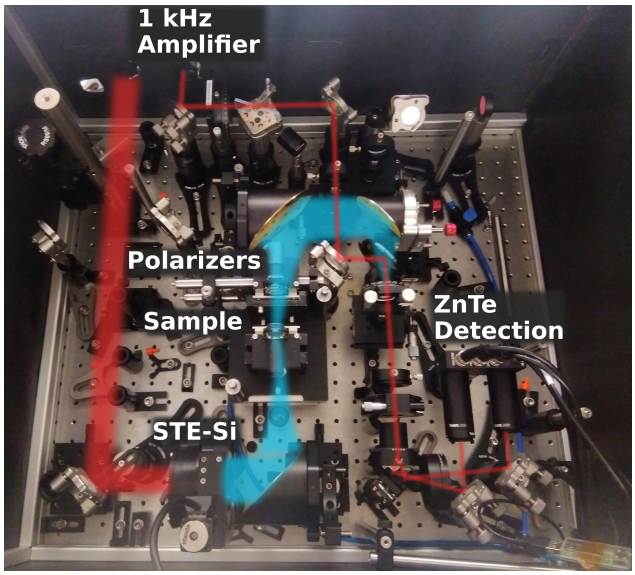


Figure 3.2: Photograph of the constructed terahertz time-domain ellipsometer: Image shows the developed time-domain terahertz ellipsometer, which utilizes the Astrella amplifier output for generation and detection. A large-area spintronic emitter (STE-Si) produces a collimated beam in the generation branch. This beam is focused onto the sample using a parabolic mirror, passes through polarizers, and is then re-focused onto a ZnTe electro-optic detector by additional parabolic mirrors.

3.3 Principle of acquisition with the amplifier

We have three configurations for signal acquisition at our disposal: 1) a lock-in amplifier, 2) a gated integrator, and 3) a combination of a gated integrator and a lock-in amplifier. The lock-in amplifier operates on the principle of frequency demodulation of the signal at the first harmonic of the modulation frequency. This technique enables measurements in continuous scan mode, where sampling is adjusted according to the time constant for averaging. The gated integrator averages the diode's signal within a time window (gate) matched to the duration of each pulse, ensuring comprehensive coverage of all harmonic components.

Focusing on the sampling provided by laser oscillators and amplifiers is essential for determining the appropriate system for signal acquisition. The primary distinction between an amplifier and an oscillator is the number of averaged samples and the adequate signal strength per pulse. The amplifier compensates the fewer samples with a significantly more robust signal. Figure 3.3 is an illustrative example to support understanding the diode signal's Fourier transform analysis with oscillators and amplifiers. It demonstrates how the frequency envelope is shaped by the diode's temporal response profile, which, in our setup, is approximately 100 ns, corresponding to a 10 MHz bandwidth. Operating in pulse mode, the spectrum comprises comb lines spaced by the laser's repetition frequency of 1 kHz versus 80 MHz. The 1 kHz system, therefore, produces a dense comb of harmonics, which are unsuitable for demodulation by a lock-in amplifier because only a minor fraction of the signal originates in the first harmonic. For oscillators, only a few spectral lines typically overlap with the diode's response bandwidth. This overlap results in a pronounced signal at the first harmonic, facilitating straightforward demodulation. Specifically, we observe a single spectral line in

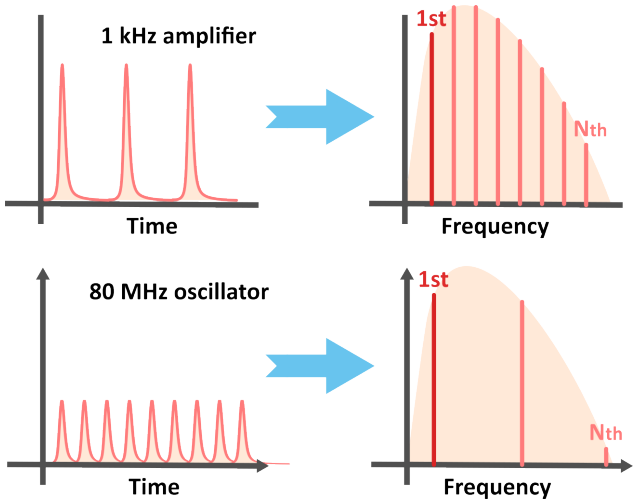


Figure 3.3: Comparison of repetition rate regimes of pulsed lasers: This figure illustrates the comparison of signal detection by a photodiode using a 1 kHz amplifier and an 80 MHz oscillator. The amplifier generates intense but infrequent pulses that are closely 1 kHz-spaced in the spectral domain. In contrast, the oscillator produces a dense trace of spectrally distant pulses. The resulting spectrum forms the diode's spectral envelope, with each harmonic dictated by the laser's repetition rate. Notably, the spectrum highlights the first harmonic, which is demodulated in lock-in detection, whereas other harmonics would be wasted.

our setup with an 80 MHz laser and a diode response bandwidth 10 MHz.

Therefore, we prefer using a gated integrator for experiments with the 1 kHz amplifier. However, the gated integrator cannot be synchronized with a delay line, as it only integrates the signal over a fixed time window. This restricts its use to step-scan mode, where measurements are taken at discrete positions of the delay line. For continuous scanning with the delay line, a lock-in amplifier and a gated integrator are required. In this setup, the lock-in amplifier manages the synchronization with the delay line, ensuring proper timing, while the gated integrator performs the signal integration. The lock-in amplifier then reads the averaged signal output from the gated integrator, allowing for continuous data acquisition during the scan.

3.4 Expansion of THz-TDS experimental capabilities

The modified experimental setup, designed to enhance versatility in terahertz research, is illustrated in Figure 3.4. This configuration allows the pump beam to be switched from the standard 800 nm to a tunable range of 550 nm to 1.5 μm using an optical parametric amplifier (OPA), providing greater flexibility for terahertz source pumping. These modifications build upon the setup introduced in Figure 3.2. This new capability facilitates terahertz emission spectroscopy and supports exploring diverse sources under tunable frequency excitation. It is particularly effective for researching 2D materials, topological insulators, and nonlinear crystals, where phase-matching conditions or exciton dynamics significantly influence emissions. The primary disadvantage is the required long optical paths to compensate for delays in the OPA unit, which can reduce beam stability and potentially

increase noise.

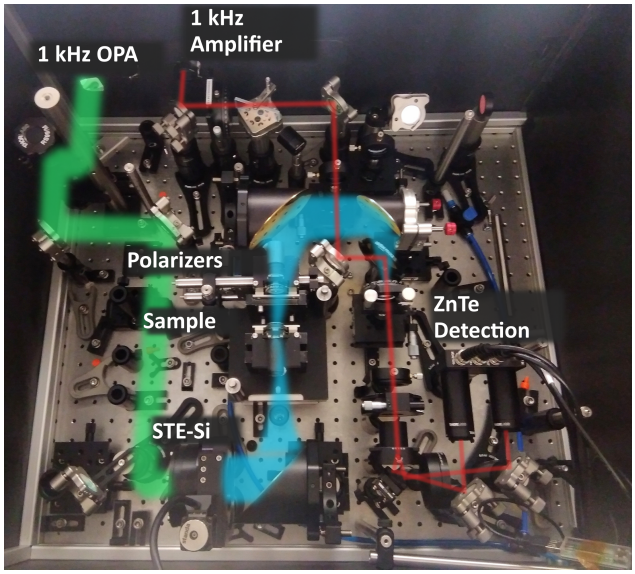


Figure 3.4: Constructed arrangement with tunable source pumping: The experimental setup shown in Figure 3.2 incorporates a modification in which the conventional pump laser for terahertz generation is replaced by the output from a parametric amplifier. This output is directed into a purge box, and a periscope is adjusted to align with the height of the experiment. The beam is subsequently directed through metallic mirrors to a spintronic emitter.

The primary advantage of using an amplifier, and the reason for its prevalent use, is its compatibility with optical-pump spectroscopy. This compatibility facilitates comprehensive THz time-domain ellipsometry for studying the dynamics of excited samples. This setup includes optical pumping from an optical parametric amplifier (OPA), as depicted in Figure 3.5. The Astrella laser serves as the pump for the spintronic emitter, ensuring efficient THz generation. The beam from the OPA passes through an 800 mm delay line, which is fixed for tunable excitation (Fig. 3.4), allowing for 2D scans in pump-probe experiments. This configuration enables ellipsometric measurements to capture temporal changes and the spectral evolution of the sample in response to the optical excitation delay.

Although the system primarily operates in a collimated source configuration, it is designed to integrate a parabolic mirror at the input, as depicted in Fig 3.6. This integration enables the pump beam to be focused on the terahertz source using either the Astrella amplifier or the OPA. This flexibility permits executing the same experiments as in the collimated configuration. A significant benefit of this setup is the ability to utilize emitters that do not require a large diameter for collimated excitation. Moreover, the polarization generated in this configuration is less affected by inhomogeneities in the magnetic field, thanks to spintronic emitters with induced magnetic anisotropy, enhancing polarization control.

The developed setup is designed for comprehensive ellipsometry in transmission, reflection, and attenuated total reflection (ATR) configurations. Flexibility is achieved through the interchangeable experimental modules, as depicted in Fig. 3.6. This modular approach facilitates the analysis of diverse sample types, including powders, transparent, and opaque materials, suited to specific experimental needs. The reflection and ATR configurations feature dedicated focusing optics,

requiring minimal adjustments on a short 300 mm delay line to match the effective optical paths between parabolic mirrors.

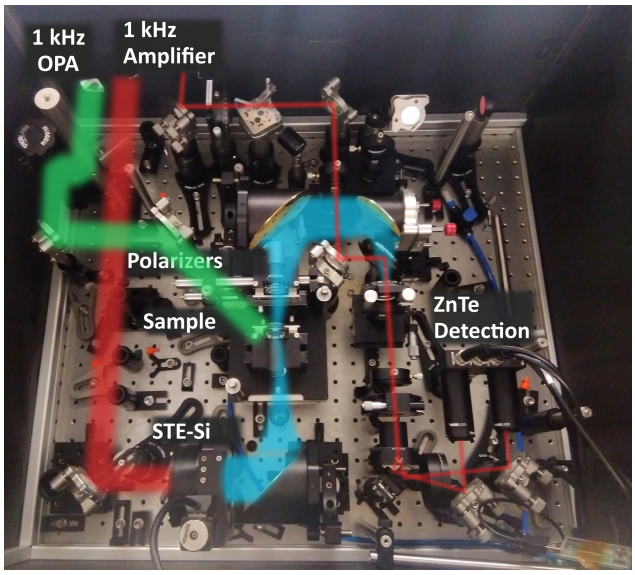


Figure 3.5: Constructed arrangement with tunable sample pumping: An alternative configuration of the experimental setup depicted in Figs 3.2,3.4 is presented. In this arrangement, the output from the Astrella amplifier is used as the pump beam to generate terahertz radiation. Simultaneously, the Optical Parametric Amplifier (OPerA) output excites the sample for optical pump-terahertz probe spectroscopy.

3.5 Concluding remarks on experimental design

This section introduced the experimental setup developed during the PhD research, specifically focusing on terahertz time-domain ellipsometry and using a spintronic terahertz emitter (STE). The current work has focused on establishing the beam paths and completing the complete ellipsometry system, providing the foundation for future studies in polarization-sensitive material characterization and terahertz source analysis.

In addition to sample characterization, the system supports ellipsometric analysis of terahertz sources, enabling measurements of the ellipticity and azimuth of the emitted polarization. These measurements are essential for characterizing the polarization behavior of the sources, further broadening the system's experimental capabilities.

Although typically not used in ellipsometry due to high precision and stability demands, we selected the 1 kHz amplifier and optical parametric amplifier (OPA) to enhance experimental flexibility. The amplifier introduces challenges, such as increased noise and longer optical paths required by OPA delay compensation. Despite these challenges, the advantages of broadband terahertz applications, particularly for experiments requiring tunable excitation sources, outweigh the drawbacks.

The system enables ellipsometric characterization of anisotropic samples under pump-probe conditions, which is essential for studying dynamic material responses. This capability allows

polarization-sensitive temporal and spectral evolution analysis during sample excitation, such as charge carrier dynamics in anisotropic semiconductors and solar heterostructures. Currently, pump-probe experiments are restricted to transmission geometry, as the reflection and ATR modules are not yet configured for this setup. Future efforts will focus on upgrading these modules to enable pump-probe experiments in non-transmission configurations, expanding the range of materials studied, including terahertz-opaque samples.

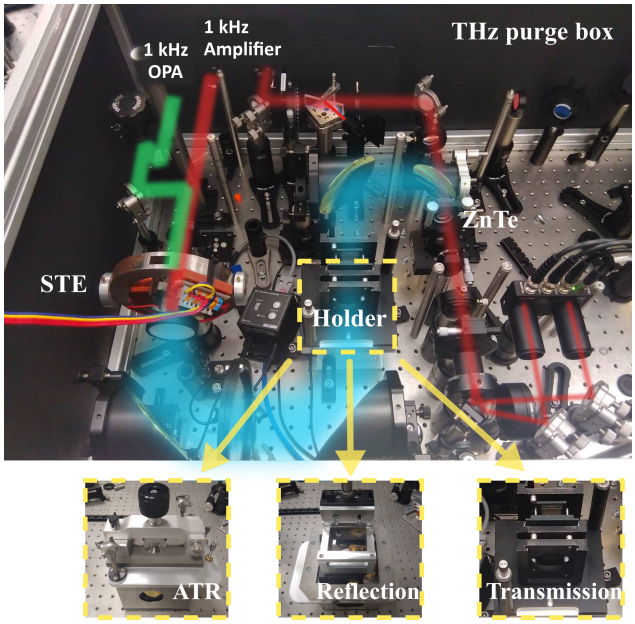


Figure 3.6: Alternative configuration in focused mode: The figure illustrates an alternative configuration to those shown in Figures 3.2, 3.4, 3.5. It introduces a parabolic mirror to switch the terahertz source from a collimated to a focused mode. The setup also employs the output from an optical parametric amplifier to generate terahertz radiation suitable for tunable-pump emission spectroscopy. Additionally, incorporating an external module enables examining samples in transmission, reflection, and attenuated total reflection (ATR) modes. Although not shown, the optical pump beam can be used as the optical pump as in Figure 3.5, specifically for a transmission configuration.

4

OVERVIEW OF PUBLICATIONS AND THEIR RELEVANCE TO THE THESIS

4.1 Enhancement of efficiency and performance of terahertz spintronic emitters

The relatively low optical-to-terahertz conversion efficiency of spintronic emitters presents a significant obstacle [84,85]. This reduced efficiency weakens the signal, creating difficulties for applications such as spectroscopy and ellipsometry, which rely on a wide dynamic range and a high signal-to-noise ratio. As a result, the impact of lower efficiency is particularly pronounced in these contexts. Overcoming this limitation would significantly improve the practicality and broader adoption of spintronic terahertz technology.

Fulop et al. compared current pulsed terahertz sources, emphasizing the maximum achievable terahertz pulse energy and peak electric field [143]. Figure 4.1 compares spintronic emitters with other nonlinear sources, including those utilizing optical rectification (OR) in lithium niobate (LN), semiconductors, and organic crystals, as well as difference frequency generation (DFG) in GaSe. The comparison also covers nonlinear generation via laser-induced plasma in gases, solids, and liquids, along with a high-power array of photoconductive antennas. When focusing on peak electric field strength, OR in organic crystals and DFG in GaSe emerge as the most robust sources. At the same time, spintronic emitters are positioned in the lower half, outperforming antennas and most semiconductors. In the comparison from the year 2020, the peak electric field of a spintronic emitter reached 30 MV/m [99]. However, when considering THz pulse energy, spintronic emitters are less competitive, with the demonstrated energy being only 5 nJ. This emitter, which utilized a 4.8 cm area in a collimated mode, was excited by a pulse with an energy of 5.5 mJ, a center wavelength of 800 nm, a duration of 40 fs, and a repetition rate of 1 kHz. However, the spectral bandwidth covers the entire terahertz gap from 1 to 10 THz. Rouzegar et al. later introduced further improvements to this large-area emitter, achieving a peak electric field of 150 MV/m, which would place spintronic emitters in the upper half of sources. However, with a total energy of 90 nJ, it still needs to catch up in the comparisons [108].

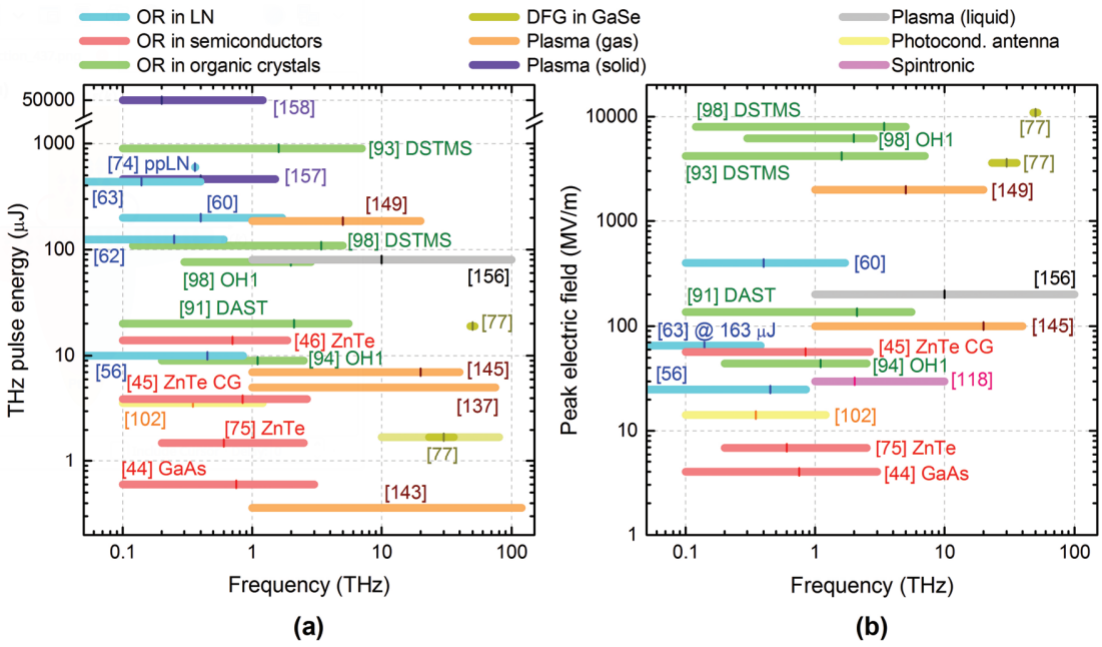


Figure 4.1: Comparison of terahertz sources based on different generation mechanisms, including optical rectification (OR), difference frequency generation (DFG), plasma sources, photoconductive antennas, and spintronic emitters: (a) THz pulse energy is a frequency function that highlights each emitter's energy output across its spectral bandwidth. (b) Peak electric field and spectral bandwidth show the electric field strength produced by each emitter across the same frequency range. The color coding in both graphs corresponds to the type of material or generation mechanism used. Adapted from [143]

Enhancing their overall performance and efficiency is essential for spintronic emitters to achieve widespread adoption. Boosting the efficiency of spintronic emitters necessitates advancements in fundamental mechanisms, including optical excitation, spin transport, and terahertz emission extraction. Torosyan et al. have developed a comprehensive model to better understand the efficiency of the Fe/Pt spintronic bilayer, building on optimization strategies proposed by Seifert et al. [84, 110, 144]

$$E_{\mathrm{THz}} \propto \underbrace{\frac{P_{\mathrm{abs}}}{d_{\mathrm{Fe}}+d_{\mathrm{Pt}}}}_{\text{pumping}} \cdot \underbrace{\tanh\left(\frac{d_{\mathrm{Fe}}-d_0}{2\lambda_{\mathrm{pol}}}\right)\cdot\tanh\left(\frac{d_{\mathrm{Pt}}}{2\lambda_{\mathrm{Pt}}}\right)}_{\text{spin-transport}} \cdot \underbrace{\exp\left(-\frac{d_{\mathrm{Fe}}+d_{\mathrm{Pt}}}{s_{\mathrm{THz}}}\right)}_{\text{THz absorption}} \cdot \underbrace{\frac{1}{n_{\mathrm{air}}+n_{\mathrm{MgO}}+Z_0\cdot(\sigma_{\mathrm{Fe}}d_{\mathrm{Fe}}+\sigma_{\mathrm{Pt}}d_{\mathrm{Pt}})}}_{\text{impedance matching}} \tag{4.1}$$

The model begins by addressing the absorbed power, P_{abs}, from the infrared beam, normalized by the combined thickness of the metal layers. The second term represents the interference caused by the ballistic diffusion of spin currents within the ferromagnetic and non-magnetic layers. It emphasizes the importance of ensuring that the layer thickness is comparable to the spin diffusion length to

maintain spin polarization. The third term represents the absorption of terahertz radiation emitted from the metal layers. Finally, the model includes the terahertz extraction process, emphasizing the challenges of impedance matching with surrounding layers. Here, the metal layers' high conductivity and the media's high refractive indices hinder terahertz radiation's emission.

Our approach for enhancing spintronic terahertz emission

Since standard spintronic emitters have already been optimized for spin transport and spin-orbit interaction efficiency [84], the potential for further improvement lies in enhancing the absorption efficiency of the pump beam and the terahertz extraction process. However, while the current model provides a rough estimate of overall performance, it cannot accurately determine absorption, emitted terahertz waveform, or the spectrum. Therefore, we decided to simulate electromagnetic efficiency, from optical excitation to terahertz extraction.

To calculate the dynamic evolution of a femtosecond electromagnetic field, we employ a Fourier series representation of the pulsed electric field vector

$$\mathbf{E} = \sum_{n=1}^{N} \mathbf{E}_n(\mathbf{r}) \exp\left(-\mathrm{j}\,\omega_n t\right) \tag{4.2}$$

where ω_n denotes the angular frequency of the electromagnetic wave, and $\mathbf{E}_n$ represents the complex amplitude vectors. The parameters t, $\mathbf{r}$, and j refer to time, the coordinate vector, and the imaginary unit, respectively. By summing a finite number N of harmonic plane waves $\mathbf{E}_n$, the Fourier series approach enables us to calculate the optical response for each frequency individually. We employ the scattering matrix formalism to calculate the transmission and reflection coefficients for the studied multilayered structure. Using Poynting's theorem, we determine the Joule heating to estimate the amount of pulse energy absorbed and converted into carrier motion within a lossy material. Additionally, we use a similar approach to optical excitation to simulate terahertz emission by combining the scattering matrix formalism with the Fourier series. The key difference lies in the emission's origin within the spintronic emitter.

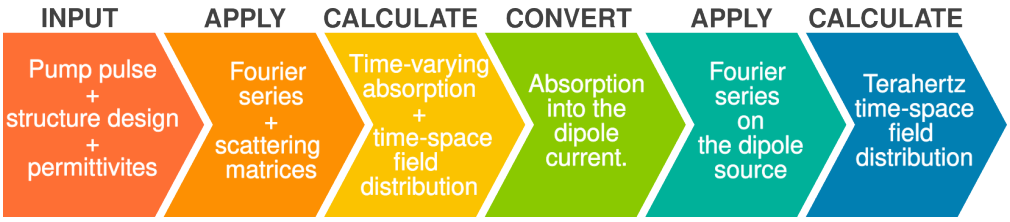


Figure 4.2: Process flow of our simulation framework: The diagram outlines the sequential steps in generating a terahertz field. The process begins with inputting the estimated pump pulse, required structure design, and material permittivities. Next, Fourier series and scattering matrices are applied, and non-stationary absorption and time-space field distribution are calculated. This is followed by converting the nonstationary absorption into dipole current and applying the Fourier series on the dipole source to calculate the terahertz time-space field distribution.

This approach enables both the investigation of spintronic emissions and their integration with photonic structures for improved performance. By improving infrared absorption within spintronic layers, we can increase the generation of spin-polarized electrons, thereby boosting the conversion

efficiency from optical to terahertz radiation. Additionally, optimizing terahertz emission can be done by choosing suitable substrates or integrating the emitter with terahertz cavities to enhance radiation extraction. Depending on the application and design, the simulation framework can maximize infrared absorption in arbitrary lossy layers, the terahertz peak electric field, or total energy. We use simplex methods and metaheuristic algorithms for global optimization, including swarm, genetic, and differential evolution [145]. In two publications, we showcased the enhancement of spintronic terahertz emitters through electromagnetic efficiency.

4.1.1 Maximizing the electromagnetic efficiency of spintronic terahertz emitters

Pierre Koleják, Geoffrey Lezier, Daniel Vala, Baptiste Mathmann, Lukáš Halagačka, Zuzana Gelnárová, Yannick Dusch, Jean-François Lampin, Nicolas Tiercelin, Kamil Postava, and Mathias Vanwolleghem

Advanced Photonics Research, 2024 (accepted, in print)

This research focuses on boosting the power output of spintronic emitters by increasing the number of spin-polarized electrons through more efficient absorption of the pumping beam. We explore integrating spintronic emitters with one-dimensional photonic structures that more effectively confine the pump pulse within the spintronic layers, thereby increasing the generation of spin-polarized electrons and enhancing terahertz emission. Typically, spintronic emitters absorb only 30-50% of the incident pump beam, with the rest being reflected or transmitted. This unutilized energy suggests the potential to increase absorption by a factor of 2-3$\times$, depending on the substrate orientation.

Motivation for field confinement using photonic cavities

The strategy is clear: a photonic structure could be integrated with a spintronic emitter to back-reflect unused radiation into the spintronic layers, allowing for re-excitation and increasing terahertz emission. Figure 4.3a illustrates the simulation of electric field intensity profiles $|E|^2$ for a spintronic emitter deposited on a sapphire substrate. The emitter is illuminated by a 100 fs pulse with a central wavelength of 800 nm, and the snapshot captures the moment when the field within the spintronic layers is at its maximum. While a significant amount of radiation transmits through the STE, a considerable fraction reflects, resulting in interference patterns. The spintronic layers absorb the remaining radiation. Figure 4.3c presents the time-dependent absorption profiles, with all curves normalized to this regular spintronic emitter.

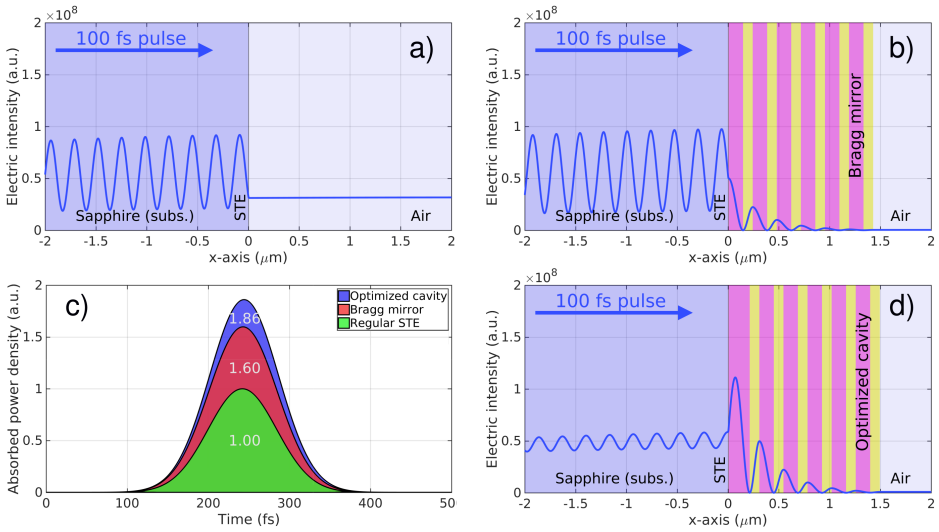


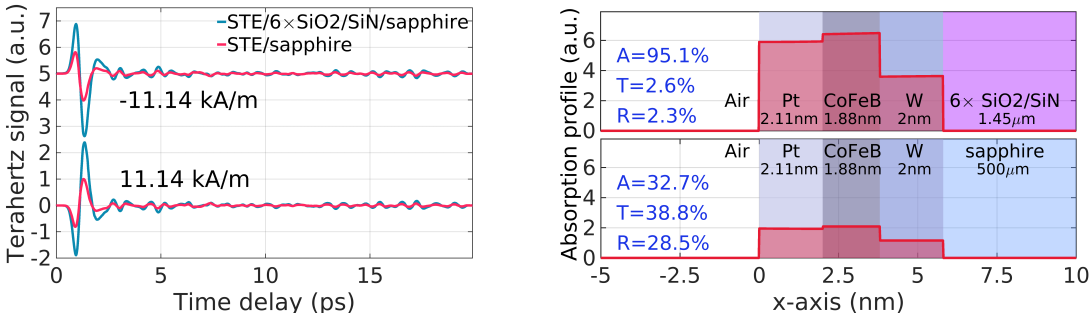
Figure 4.3: Simulation of THz emitter configurations: a) Electric field intensity distribution of a 100 fs pulse as it propagates through a sapphire substrate and standard terahertz emitter (STE) into the air. b) Electric field intensity distribution with the addition of a Bragg mirror structure behind the STE. c) Comparison of the absorbed power density over time for three configurations: regular STE (green), STE with Bragg mirror (red), and STE with an optimized cavity (blue), highlighting the enhancement in absorption. d) Electric field intensity distribution with an optimized cavity structure behind the STE, showing improved field confinement compared to the Bragg mirror configuration.

We use dielectric layers such as SiO_2, TiO_2, Ta_2O_5, and SiN to fabricate a dielectric cavity. This cavity is intended to back-reflect radiation through the spintronic layers to enhance absorption. The dielectric materials exhibit low refractive indices in the terahertz region, making them well-suited for impedance-matching and radiation extraction. Additionally, the total thickness of these dielectric cavities is on the order of several micrometers, which is sub-wavelength for terahertz frequencies, ensuring they do not interfere with terahertz wavelengths. Integrating an STE with six pairs of SiO_2/SiN cells creates a Bragg reflector, which has shown improved absorption in previous studies, up to a factor of 1.9 times [109, 111, 112]. We simulated this approach, as depicted in Figure 4.3b. However, while transmission is effectively suppressed, complete absorption is not achieved due to residual reflection. We aimed to develop a novel structure capable of entirely confining the back-reflected optical field, thereby maximizing absorption. To achieve this, we optimized the layer thicknesses through simulations to maximize absorption in the spintronic layers. The results in Figure 4.3d demonstrate that both transmitted and reflected waves are minimized, resulting in the highest absorption compared to other designs.

Experimental demonstration of spintronic emitters integrated with optimized photonic cavity

Our method achieved the most effective configuration with an optimized photonic structure comprising an STE/cavity/sapphire (0.5 mm). The designed cavity includes six pairs of SiO_2 (139 nm)/SiN_x (100 nm) layers optimized for 808 nm, with the first SiO_2 layer adjusted to 160 nm. The STE emitter consists of a finely tuned Pt (2.1 nm)/CoFeB (1.9 nm)/W (2 nm) trilayer. We fabricated this optimized design and conducted time-domain spectroscopy in a transmission arrangement to compare its emission with a regular spintronic emitter. Figure 4.4a shows the measured waveforms,

comparing them with the emission generated by a reference emitter fabricated on the same substrate. To confirm the spintronic origin of the emission, we measured the STE integrated with the cavity under reversed magnetic field polarity of ± 11.14 kA/m. The emission enhancement reaches a factor of 2.45, representing a significant improvement over current approaches [111, 113, 114, 146, 147]. Figure 4.4b illustrates the simulated increase in absorption within the spintronic metallic layers before and after integration with the optimized photonic cavity. Additionally, we calculate the relative absorbance (A), reflectance (R), and transmittance (T) of the pumping laser for both configurations. The simulation indicates that absorbance is expected to increase from 33% to 95%.



a) b)

Figure 4.4: Comparison of terahertz waveform and absorption profiles for the enhanced spintronic emitter: The left panel shows the terahertz signal as a function of time delay for two configurations: a standard STE/sapphire structure (red) and a STE/6×SiO2/SiN/sapphire structure (blue), under applied magnetic fields of ± 11.14 kA/m. The right panel presents the absorption profiles across the multilayer structures, highlighting the distribution of absorbed power among the metallic layers, including platinum (Pt), cobalt iron boron (CoFeB), and tungsten (W). The percentages indicate the overall absorption (A), transmission (T), and reflection (R) for each configuration.

Summary of findings and impact of the study

This study advances the performance of spintronic terahertz emitters, particularly those based on Pt/CoFeB/W trilayers, by integrating them with one-dimensional (1D) SiO_2/SiN_x photonic cavities. Through optimization, the optical-to-terahertz conversion efficiency was remarkably enhanced by 2.45 times, equivalent to an 8 dB increase in magnitude, effectively addressing a critical challenge in the field. The design strategy employed in this research is broadly applicable to other ultrafast spin-to-charge conversion systems, extending beyond the specific Pt/CoFeB/W system evaluated here. The optimized structure achieved a 95% absorption of the pump energy, significantly boosting spin current generation and subsequent THz emission. The experimental results closely aligned with theoretical predictions, underscoring the robustness of the design.

Furthermore, this work provides an in-depth analysis of spintronic emitters' performance and electromagnetic efficiency, focusing on optical pumping and terahertz field extraction. It examines various geometric configurations during emitter excitation, the direction of emission (whether in reflection or transmission), and the impact of substrate selection. This analysis is especially relevant given that existing literature primarily discusses the spintronic properties of these devices, often neglecting the effect of different excitation and emission geometries on efficiency.

These findings have far-reaching implications for spectroscopy, nonlinear optics, and THz communications, where efficient THz sources are vital. By addressing both the generation and extraction of THz radiation, this study offers a comprehensive solution to the efficiency challenges that have previously hindered the widespread adoption of spintronic THz technology.

My contributions

I conducted all calculations using custom codes that I developed, which were transformed into our simulation framework to estimate and optimize the terahertz performance of layered sources. I also designed the architecture and geometry of emitters to maximize efficiency. Additionally, I assisted in the experimental demonstration of these samples, led by Geoffrey Lezier and Nicolas Tiercelin, and was responsible for data processing. In collaboration with Mathias Vanwolleghem, I co-authored the article's main text and prepared the graphics.

4.1.2 Spintronic terahertz emitters with integrated metallic terahertz cavities

Martin Mičica, Adrien Wright, Pierre Koleják, Geoffrey Lezier, Kamil Postava, Jacques Hawecker, Anna De Vetter, Jerome Tignon, Juliette Mangeney, Henri Jaffres, Romain Lebrun, Nicolas Tiercelin, Mathias Vanwolleghem, and Sukhdeep Dhillon

Nanophotonics, 13(10), 1899-1907, 2024

Our study focused on optimizing terahertz field extraction to enhance emission efficiency. In conventional emitters, THz radiation is typically emitted in two opposite directions, with the portion directed away from the detector remaining undetected and, therefore, wasted. We engineered an emitter integrated with a spacing layer and 100 nm platinum layer behind the spintronic layers. This metallic mirror redirects the otherwise lost THz radiation toward the detector, thereby increasing the detected signal. The spacing layer ensures proper impedance matching and facilitates constructive interference between the back-reflected and direct emissions, forming a terahertz cavity.

This configuration can potentially increase the emitter's THz extraction efficiency by up to 70% if the primary and reflected pulses are precisely timed to create constructive interference. This configuration is exclusively suitable for reflection arrangements due to the opaque metallic layer, which completely blocks the pumping beam. Figure 4.5 illustrates our design, showing the direction of infrared excitation and subsequent THz emission.Terahertz radiation is emitted in both forward and backward directions by the emitter on a standard substrate. However, the back-reflection at the sapphire/air interface is too delayed and weak. In order to resolve this issue, the thick substrate is substituted with an ultrathin sapphire cavity measuring a few micrometers in thickness, which incorporates a deposited metal layer. This ultrathin sapphire cavity design minimizes delay and enhances constructive interference with the forward-emitted terahertz pulse. Notably, the spintronic layers do not contribute to reflections, acting as an ultra-broadband anti-reflection coating [148,149].

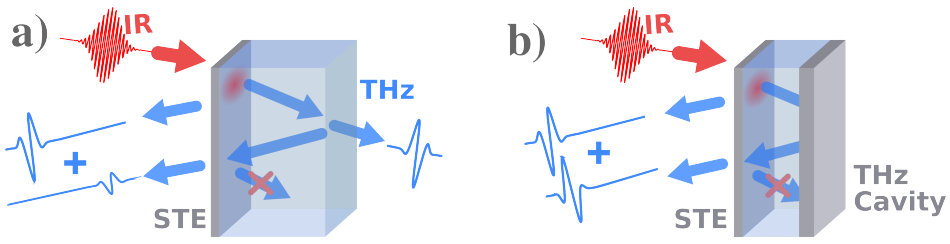


Figure 4.5: Scheme of spintronic terahertz emitter (STE) integrated with a terahertz cavity: An infrared (IR) pulse generates terahertz (THz) radiation in both forward and backward directions. The backward THz wave is then reflected in the forward direction, enhancing the efficiency of THz emission. The substrate acts as the medium through which the reflected THz waves delay compared to the direct emission, allowing them to superpose constructively.

Motivation for enhancing terahertz extraction using terahertz cavities

To demonstrate this concept, we simulate its terahertz response using our framework, which models the optical pumping process and subsequent terahertz emission, including all reflections. Our approach aimed to use a thin sapphire substrate as the spacing layer, but its thickness needed to be carefully determined. In Figure 4.6, we systematically varied the thickness of the sapphire between 5 and 80 μm. The simulations include a photoconductive antenna's response function, which affects the pulse shape and spectral range. All simulated terahertz emissions were compared to a reference sample of a standard spintronic emitter on a 500 μm sapphire substrate. Each curve in the graph illustrates the terahertz signal corresponding to a specific cavity thickness, plotted as a function of optical delay. The horizontal axis represents the varied cavity thickness, as indicated in the legend. The reflected pulse for the reference sample exhibits a significant delay and maintains its polarity. The reflection occurs at the sapphire/air interface, where the transition is from a denser to a less dense medium. Integrating a metallic mirror at the back of the substrate causes the polarity of the reflected pulse to invert due to reflection from the denser medium. However, waveforms only show one reflection because the spintronic emitter acts as a terahertz broadband anti-reflection coating and attenuates other reflections. [148–150]

As we can see, integrating the cavity increases the total energy of terahertz radiation. However, aligning the thickness to achieve the maximum electric field is crucial. With greater substrate thickness, the temporal offset between pulses leads to a chaotic waveform. As the sapphire thickness decreases, the resulting pulse peak increases by coherent interference between the direct and reflected emissions. The optimal electric field is achieved with a cavity thickness of approximately 25 μm, resulting in a twofold enhancement in terahertz peak. As the thickness is reduced further, the pulses become out of phase, leading to a marked decline in electric field intensity, reaching a minimum at a thickness of about 10 μm.

However, a 100 fs pulse spans approximately 30 μm in a vacuum. At low cavity thicknesses, the reflected infrared beam causes re-excitation of the spintronic emitter. This results in each excitation comprising both direct emission and reflected signals, which coherently sum in the time domain, affecting the overall terahertz waveform. The simulated temporal absorption profile is shown in Figure 4.7. We observe the absorption of the reference spintronic emitter without a cavity at around 0.2 ps. The infrared beam exhibits significant back-reflection from the metallic mirror. As the cavity thickness decreases, these reflections converge with the primary excitation, merging and enhancing the peak field, similar to the dielectric cavity described in the previous paper.

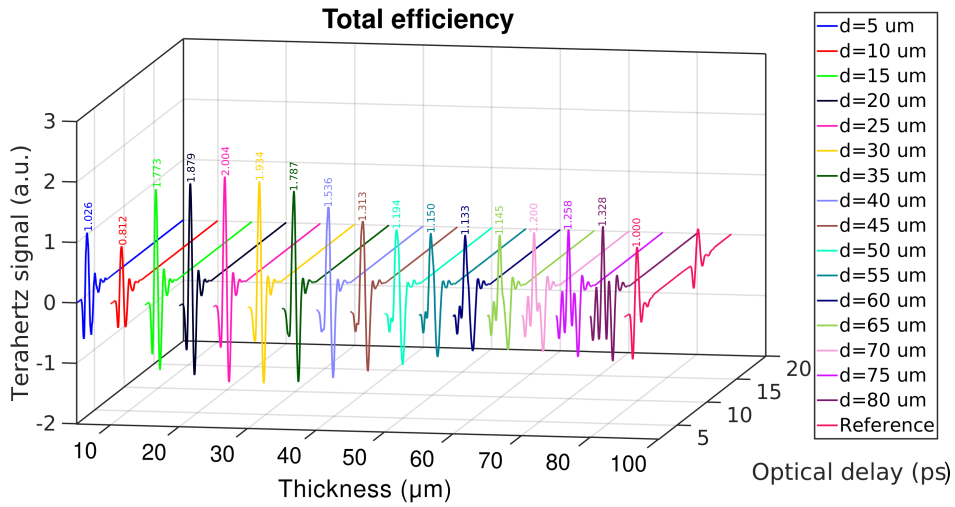


Figure 4.6: Simulated terahertz emission from a spintronic emitter integrated with a terahertz cavity: The 3D plot shows the terahertz signal. Each curve represents a different cavity thickness ranging from 5 μm to 80 μm, as the color-coded legend indicates. The plot illustrates how the thickness of the terahertz cavity influences the total efficiency and waveform of the emitted terahertz signal. The marks indicate the peak signal and are normalized by the reference for straightforward comparison. The reference represents the regular configuration STE/sapphire(500 μm).

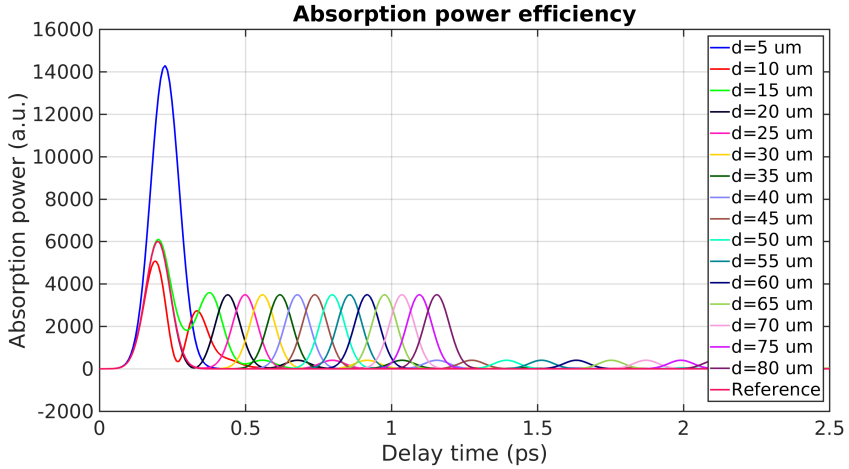


Figure 4.7: The simulated nonstationary absorption of a spintronic emitter integrated with the terahertz cavity: The plot shows the absorption profile as a function of delay time (ps). The cavity thickness d is varied from 5 μm to 80 μm, with each curve representing a different thickness as indicated by the color-coded legend. The results demonstrate how the thickness of the terahertz cavity affects the absorption power over time. The reference represents the regular configuration STE/sapphire(500 μm).

This suggests that the maximum electric field can be tuned for terahertz extraction and emission by optimizing cavity thickness to fulfill both conditions. Consequently, as seen in Figure 4.6, for cavity thicknesses up to 20 μm, the pulses overlap with multiple excitations, which increases efficiency without improving terahertz extraction. Figure 4.8 shows the normalized terahertz spectrum by the absorption, revealing terahertz extraction efficiency. The cavity enhances terahertz efficiency across the spectrum but introduces an interference dip, depending on whether the terahertz waves at specific frequencies constructively or destructively interfere. However, when the cavity thickness is low, the efficiency of terahertz decreases due to suboptimal impedance matching.

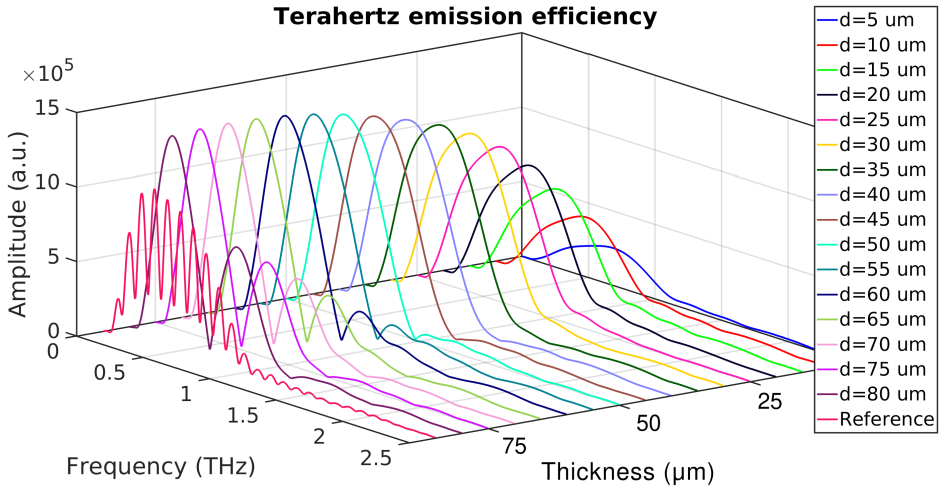


Figure 4.8: Simulated terahertz spectra of a spintronic emitter integrated with a terahertz cavity: The 3D plot displays the emitted spectral amplitude. The spectra have been normalized regarding their absorption to demonstrate terahertz efficiency. The thickness of the cavity d is varied from 5 μm to 80 μm, with each curve corresponding to a different cavity thickness, as indicated by the color-coded legend. The plot shows how cavity thickness influences the terahertz extraction and interferences in the spectrum. The reference represents the regular configuration STE/sapphire(500 μm).

Experimental demonstration of spintronic emitters integrated with terahertz cavity

In the publication, we present the experimental implementation of our terahertz cavity, constrained by the availability of sapphire substrates with discrete thicknesses of 25, 29, 39, and 111 μm. The measured terahertz emission using terahertz time-domain spectroscopy in a reflective configuration is shown in Figure 4.9a. The terahertz signal consists of four distinct pulses. The first pulse is the direct emission from the initial excitation, followed by the second pulse, which is the direct emission resulting from the secondary excitation. The third pulse, with inverted polarity, is generated by the reflection of the first excitation, while the fourth pulse corresponds to the emission from the second excitation. These four pulses constructively interfere as the substrate thickness decreases. Simulated emissions for the same configurations are presented in Figure 4.9b, demonstrating a strong correlation between our simulations and experimental results. The simulations also include the response function of the ZnTe crystal used in the experiment.

By employing the terahertz cavity, we increased terahertz extraction, thereby enhancing the energy of the emitted terahertz radiation. However, due to the substrates' discrete thicknesses, we

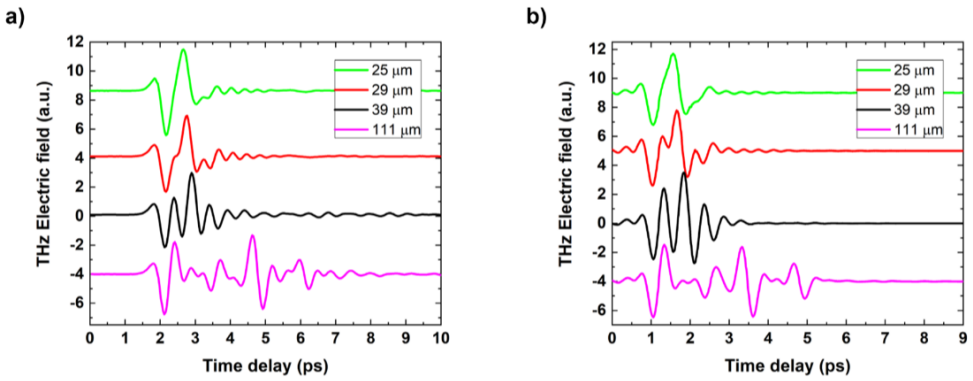


Figure 4.9: Comparison of experimental and simulated terahertz waveforms for a spintronic emitter integrated with a terahertz cavity: The figure presents the terahertz signals for fabricated cavities of 25 μm, 29 μm, 39 μm, and 111 μm thicknesses. (a) Experimental demonstration of the terahertz electric field of the fabricated emitters. (b) Simulated terahertz electric field for the same set of cavities.

needed to be able to precisely tune the constructive interference of the direct and reflected terahertz waves to achieve maximum efficiency. Given these limitations, we chose an A-cut sapphire spacing layer exhibiting linear birefringence. By rotating the spintronic emitter with the cavity, we can adjust the refractive index of sapphire to its ordinary and extraordinary values, thereby tuning the constructive interference between the direct and reflected beams. Additionally, the sapphire layer functions as a quarter-wavelength ($\lambda/4$) plate, allowing for manipulating the polarization of the emitted wave. This control of the phase delay of the reflected wave is experimentally demonstrated in Figure 4.10, where the spintronic emitter is rotated from 0° to 90° in 15° increments.

Summary of findings and impact of the study

The study demonstrates an enhancement in the performance of spintronic terahertz emitters by integrating them with ultra-thin sapphire layers and metallic terahertz cavities. We achieved a twofold increase in the emitted THz field intensity within targeted spectral ranges. By incorporating quarter-wavelength THz resonant cavities made from ultra-thin sapphire layers with metallic mirrors, we introduce a method for controlling the polarization state.

However, the potential of this work is greatly amplified when combining the approach of an optimized photonic cavity to maximize absorption, as demonstrated in the previous study, with the terahertz cavity technique to enhance terahertz extraction, as shown in this article. Figure 4.11 demonstrates preliminary results of the significant enhancement in terahertz emission efficiency achieved by integrating an optimized photonic cavity with the spintronic emitter and tuning the thickness of the terahertz cavity. With optimal tuning, the peak electric field amplification exceeds a factor of five (approximately 15dB). Additionally, constructive interference is achieved at a cavity thickness of around 35 μm, aligning with the available discrete sapphire substrate thicknesses. Furthermore, the simulated sweep now directly reflects terahertz efficiency, as the terahertz cavity no longer affects absorption or complicates the waveform with interference from four pulses but instead from two. The study opens up new possibilities for combining THz and optical cavities to further improve the performance of spintronic THz emitters, making them more competitive with

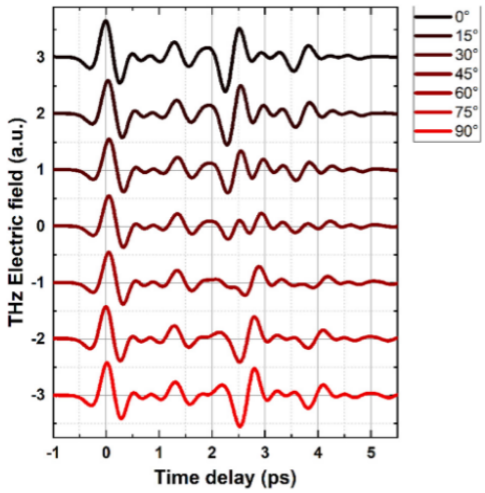


Figure 4.10: Demonstration of terahertz emitter integrated with an anisotropic A-cut sapphire substrate: The plot shows the measured terahertz waveforms for different rotation angles of the sample (0° to 90°). As the emitter is rotated, the reflected terahertz signal shifts in time and exhibits changes in emitted polarization.

traditional THz sources.

My contributions

In collaboration with École Normale Supérieure under Sukdeep Dhillon, my contributions to this research included conceptualizing and designing an innovative emitter to enhance efficiency through optimized terahertz extraction. My numerical calculations helped identify the optimal materials and their thicknesses, which led to an estimated efficiency improvement for the fabricated samples. The simulations addressed the efficiency of the terahertz cavity and the multi-excitation effects due to infrared radiation reflections within the cavity. Martin Mičica and Adrien Wright prepared the manuscript and experimentally demonstrated the fabricated structures.

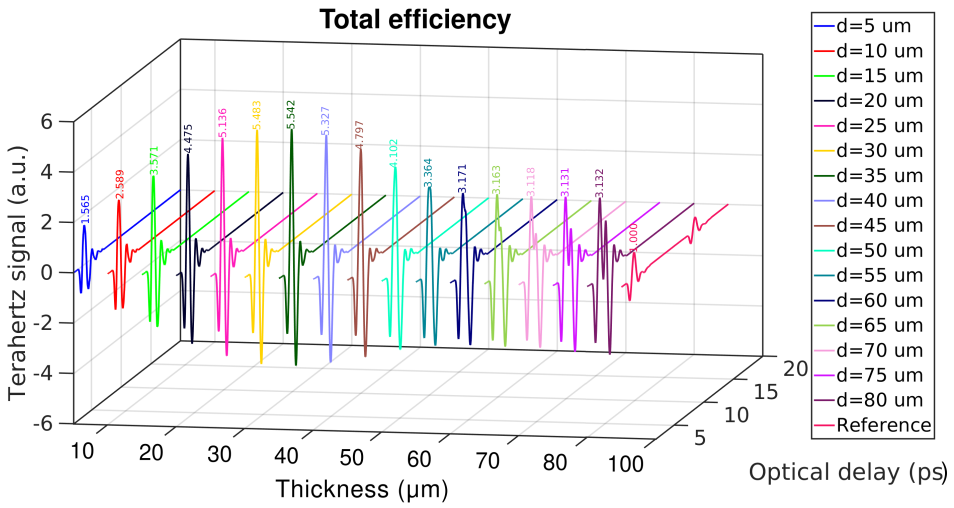


Figure 4.11: Simulated terahertz signal for a spintronic emitter integrated with an optimized photonic cavity and a terahertz cavity of varying thickness: The 3D plot illustrates the terahertz signal of the spintronic emitter with the optimized photonic cavity and the terahertz cavity. The thickness of the terahertz cavity d is varied from 5 μm to 80 μm, with each curve representing a different cavity thickness, as indicated by the color-coded legend. The optimized cavity increases absorption to its maximum, and the terahertz cavity varies in terahertz extraction efficiency. The reference represents the regular configuration STE/sapphire(500 μm).

4.1.3 Optical damage thresholds of single-mode fiber-tip spintronic terahertz emitters

Felix Paries, Felix Selz, Cristiane N. Santos, Jean-François Lampin, Pierre Koleják, Geoffrey Lezier, David Troadec, Nicolas Tiercelin, Mathias Vanwolleghem, Ahmed Adda, Tobias Kampfrath, Tom S. Seifert, Georg von Freymann, and Daniel Molter

Optics Express, 32(14), 24826-24838, 2024

The relatively low efficiency of spintronic emitters often necessitates using higher pump powers to increase the terahertz signal output proportionally. However, this raises the risk of exceeding the emitters' optical damage threshold. During my research, laser energies ranging from nanojoules to millijoules caused permanent damage to several spintronic terahertz emitter samples. The extent of this damage is directly related to the energy flux per unit area. Expanding the emitter's irradiated area becomes crucial to mitigate this risk while enhancing total power output. This strategy has led to the development of large-area spintronic emitters, operated in a collimated mode, which have demonstrated high power outputs using 1 kHz amplifiers with 5 mJ pulses [99, 108].

Motivation for exploring optical damage thresholds

Vogel et al. identified a critical pump fluence threshold of 5 mJ/cm^2 for saturation and thermal degradation in spintronic emitters [120]. Their experimental results, shown in Figure 4.12b, illustrate the emitted terahertz power as a function of fluence for a free-standing emitter (a). Furthermore, Figure 4.12c illustrates that the temperature of the emitter increases proportionally with the energy of the pump pulse. The emitted terahertz powers are demonstrated for repetition rates of 400, 200, and 133.3 kHz, indicating that at the same fluence, different average powers result in varying maximum temperatures. However, the damage threshold is reached at similar fluence levels across different repetition rates.

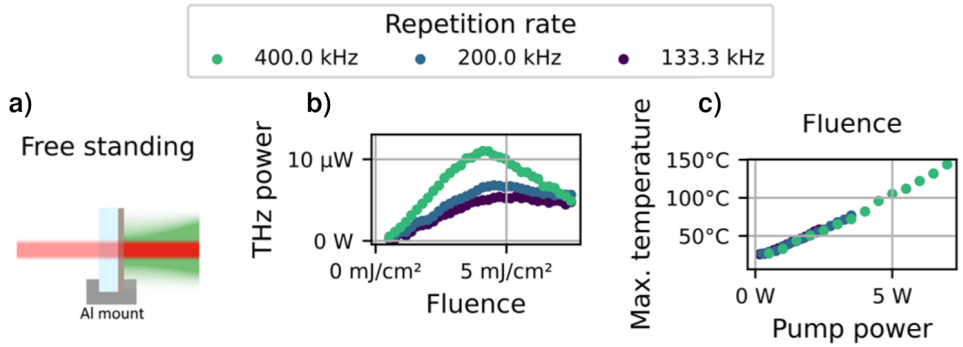


Figure 4.12: Fluent thresholds of the free-standing spintronic emitter at high power regime: (a) Schematic of the free-standing configuration of a terahertz emitter. (b) Emitted terahertz power as a function of fluence for different repetition rates (400 kHz, 200 kHz, and 133.3 kHz). (c) Maximum temperature of the emitter as a function of pump power for the same repetition rates, illustrating the thermal response of the system. Adapted from [120].

This result suggests that the electric field generated by each pulse is sufficiently strong to damage the internal structure of the spintronic emitter, even at different average power levels. However, Paries et al. observed that degradation shows a closer correlation to the repetition rate within fiber-integrated STEs. This observation suggests that at high repetition rates, the average pump irradiance, rather than fluence, emerges as the critical factor [151]. This discrepancy raises the question of when the dominant damage mechanism shifts from electric field effects to cumulative thermal effects in spintronic emitters.

Determining optical damage thresholds for field-dominated and heat-dominated regimes

For this analysis, it was necessary to confine the pump beam across different repetition rates to determine the boundary between the two damage regimes. Consequently, our research focused on integrating a spintronic terahertz emitter into a single-mode fiber. This configuration enables the use of MHz and GHz lasers at low pulse energies, in contrast to previous studies that primarily explored kHz regimes with amplifiers, where the electric field strength of individual pulses is a significant factor [116, 120]. The fiber-integrated spintronic emitter developed by Paries et al., shown in Figure 4.13, features spintronic layers deposited on the tip of the fiber. The primary advantage of the fiber-based configuration is that the beam is consistently concentrated to a radius of 5.75 μm, providing a well-defined interaction area. This consistency contrasts with free-standing



Figure 4.13: Close-up image of a fiber-tip spintronic terahertz emitter: The photograph shows a detailed view of a fiber-tip STE, with a fly resting on the emitter for scale. The image highlights the compact size of the emitter and its integration onto the fiber tip. Adapted from [151].

configurations, where the focus depends on the precise setup of focusing optics, beam properties, and the sample's position within the focal plane.

This study aims to determine the optical damage threshold for spintronic terahertz emitters using lasers with repetition rates ranging from 200 kHz to 1 GHz and continuous-wave irradiation. We employed a variety of lasers, including an in-house Erbium-doped fiber laser operating at 0.2-80 MHz, a 100 MHz Menlo ELMO, a 1 GHz Menhir 1550, and a continuous-wave Yenista Optics Tunics T100S-HP. The resulting damage thresholds, plotted against repetition frequency in Figure 4.14, clearly distinguish between regimes where damage is caused by the electric field (blue curve) and those where cumulative heat from average laser power is responsible (red curve). In the field-dominated regime, damage occurs at fluence levels around 1 mJ/cm^2, with cumulative heat playing no significant role, yet the pulse energy remains consistent. Terahertz output below this threshold decreases with lowering repetition frequency, indicating a limiting condition around 4 MHz.

In the heat-dominated regime, damage scales with the average laser power, corresponding to a power density of 4.8 kW/cm^2, consistent with damage observed under continuous wave conditions. This trend suggests that the material accumulates more energy at higher repetition rates, with insufficient time to dissipate heat between pulses, reducing threshold fluence. In this regime, the emitted terahertz power just below the threshold remains constant, but the pulse energy scales with repetition frequency. Effective heat dissipation through cooling can mitigate damage in this regime, making it preferable for increasing terahertz output compared to the field-dominated regime.

Summary of findings and impact of the study

Our study analyzes the optical damage thresholds for single-mode fiber-tip spintronic terahertz emitters across a wide range of repetition rates, from kilohertz to gigahertz, including continuous-wave irradiation. The research identifies two distinct damage regimes: a field-dominated regime and

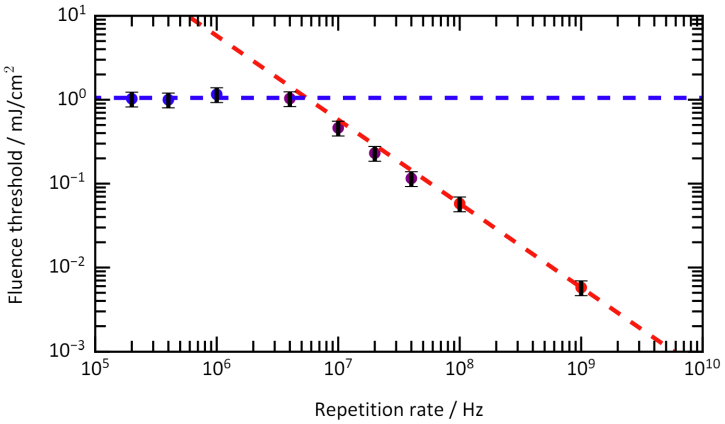


Figure 4.14: The optical damage threshold for a fiber-tip spintronic terahertz emitter: The plot shows the fluence threshold (in mJ/cm^2) as a function of the repetition rate (Hz). The data points represent experimental measurements, while the red dashed line indicates a constant averaged power model predicting a decrease in fluence threshold with increasing repetition rate. The blue dashed line represents a model predicting a constant fluence threshold across different repetition rates.

a heat-dominated regime, with the transition occurring around a repetition rate of 4 MHz.

By employing atomic force microscopy (AFM), infrared scattering-type scanning near-field optical microscopy (s-SNOM), and scanning transmission electron microscopy (STEM), the study identifies temperature-driven inter-layer diffusion, particularly between the FeCoB and Pt layers, as the primary failure mechanism for STEs in the high-repetition-rate regime. This diffusion leads to alloying between the layers, substantially impairs the optical-to-terahertz conversion efficiency.

These findings are crucial for designing and optimizing future spintronic terahertz emitters, particularly for applications that demand high repetition rates. A deeper understanding of these damage mechanisms enables the development of improved thermal management strategies, potentially extending the operational limits of STEs and enhancing their effectiveness in advanced THz technologies and applications.

My contributions

In this research project, led by Felix Paries from the Fraunhofer Institute, I worked closely with him to investigate the optical damage threshold of spintronic emitters and the associated mechanisms. We discussed these topics extensively in preparation for this publication. My responsibilities included experiment preparation, assisting with measurements to identify damage in the fibers through transmittance tests and microscopic analysis, and revising the manuscript.

4.2 Polarization control of spintronic emitters

Spintronic emitters present a significant advantage over conventional terahertz sources, particularly in their capacity to precisely control the polarization states via an external magnetic field [101, 102]. This polarization control originates from the fundamental principle of the inverse spin-Hall effect, which dictates the conversion of the spin current into charge current. Crucially, the resulting transverse charge current is intrinsically orthogonal to both the direction of spin injection and the magnetization of the ferromagnetic layer given by

$$\mathbf{j}_c \propto \gamma \mathbf{j}_s \times \mathbf{M}. \tag{4.3}$$

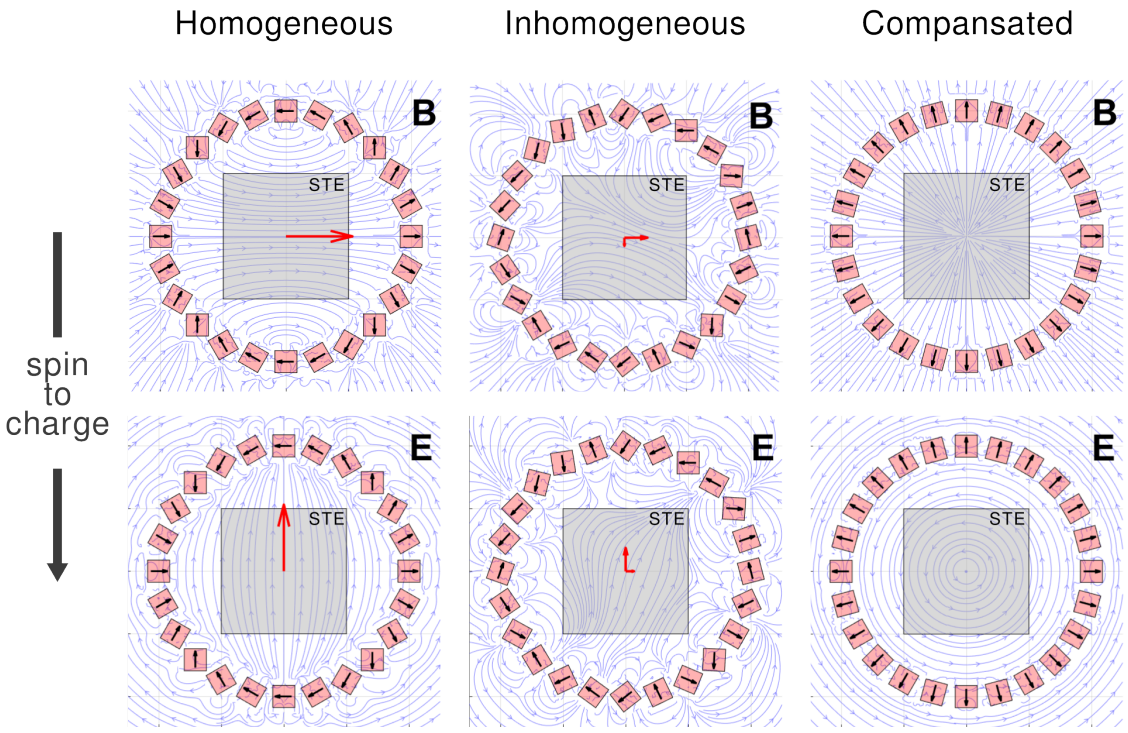


Figure 4.15: Simulated magnetic and terahertz polarization field distributions for spintronic emitter: The figure compares the magnetic (B) field and the influence of different magnetization configurations on the output terahertz polarization (E) through the spin-to-charge conversion process in the STE, including homogeneous, inhomogeneous, and compensated magnetization configurations. The red arrow indicates the averaged vector field across the emitter's surface. The left column illustrates the fields for a homogeneous magnetization, resulting in uniform field distributions and maximal emission. The middle column depicts inhomogeneous magnetization, leading to more complex field patterns that are partially compensated and an altered azimuth of the emitted field. The right column shows a compensated symmetric magnetization configuration, attenuating the output signal.

Figure 4.15 shows the calculated magnetic field distribution for polarization control using Halbach cylinder arrays composed of rotated permanent magnets. A spintronic emitter is positioned within the magnetic field shown in the upper images of the Halbach magnets (red squares). The lower images illustrate the normals of these magnetic field lines, which correspond to the spin-to-charge current vector field and, in turn, to the terahertz polarization. The red arrow indicates

the integrated vector field across the emitter's surface. Magnetic field uniformity is crucial for maintaining polarization purity; any deviations could lead to inhomogeneous beam polarization. Thus, we examine three distinct configurations. The homogeneous configuration generates a uniform and intense magnetic field, ideal for integrating a spintronic emitter. Minor opposing field components cancel out coherently, reducing the generated signal slightly. The cancellation of opposing components is mainly due to the symmetry of the magnetic field. An inhomogeneous configuration leads to a non-uniform magnetic field due to random magnet orientations. Any asymmetry induces a slight azimuthal shift as in-phase electric field vectors superpose. However, despite significant signal losses and azimuthal shifts, the output polarization remains predominantly linear and robust. The final example describes a configuration where complete field cancellation results in no detectable signal. However, phase differences caused by tilting the emitter or a curved emitting surface may alter the ellipticity of the emitted polarization. This out-of-phase generation implies that opposing polarizations do not cancel but shift relative to each other over time. Therefore, despite thin-film in-phase emissions, factors such as the size of the irradiated area, the emitter's centering within the field, field homogeneity, and phase-influencing factors remain crucial. While these factors warrant consideration for output polarization, they have a relatively minor impact on homogeneous configurations. Nonetheless, the polarization control method remains straightforward, providing precise linear polarization with a high-extinction ratio.

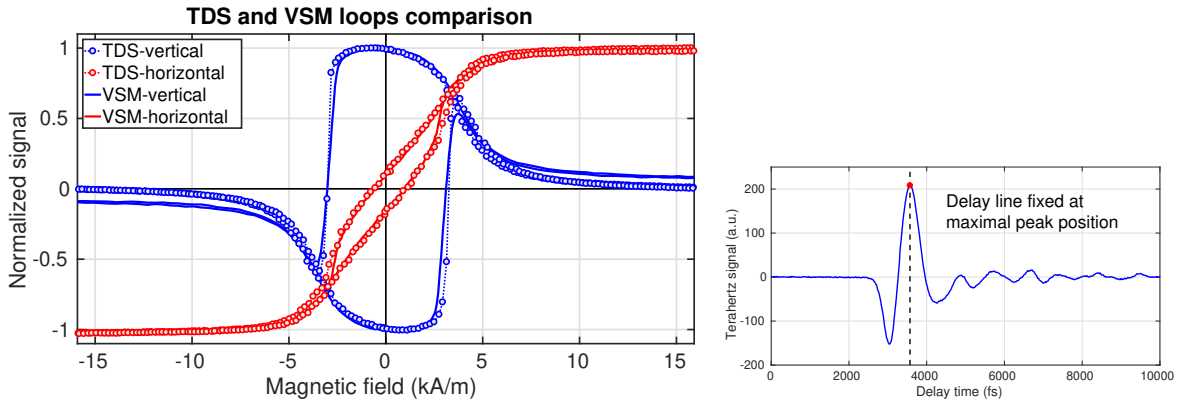


Figure 4.16: Comparison of magnetic hysteresis loops measured by terahertz time-domain spectroscopy and vibrating sample magnetometry: The left panel presents normalized magnetic hysteresis loops as a function of the magnetic field (kA/m) applied along the hard axis, displaying vertical and horizontal magnetization components measured by TDS (blue) and VSM (red). The right panel depicts the terahertz signal as a function of delay time (fs), with the delay line fixed at the maximum peak position.

In contrast, nonlinear terahertz generation methods like optical rectification necessitate precise control of the pumping electric field $\mathbf{E}$ and the nonlinear crystal's orientation [152]. This precise control is required because the nonlinear electric polarization $\mathbf{P}$ is governed by the susceptibility tensor $\chi^{(2)}$, expressed as $P_i = \chi^{(2)}_{ijk} E_j E_k$, which is quite restrictive.The crystal's rotation can change phase-matching conditions, requiring robust mechanical adjustment [74, 153]. In scenarios of four-wave mixing following polarization control through $P_i = \chi^{(3)}_{ijkl} E_j E_k E_l$ in laser-induced plasma, precise polarization control of input beams is crucial. This entails careful management of the polarizations of the first and second harmonics of the pumping beam, their separation, and the

accurate timing of their relative delays [154–157]. For photoconductive antennas, the orientation of the generated photocurrent and the specific antenna geometry are critical factors [158–160]. Such designs require two independent dipoles [161, 162], potentially limiting bandwidth and reducing efficiency compared to traditional single-dipole configurations. Hence, magnetic field-based control of spintronic emitters offers both efficiency and ease of implementation.

Spintronic terahertz emitters with induced magnetic anisotropy

In isotropic FeCoB, output polarization is primarily controlled by adjusting the external magnetic field. Magnetic anisotropy, however, provides a distinct mechanism for governing terahertz polarization through hysteresis. A direct correlation exists between spintronic-based terahertz polarization and the magnetic properties of spintronic emitters. Figure 4.16 compares vertical and horizontal terahertz polarizations, measured at the peak signal, with hysteresis loops obtained via a vibrating sample magnetometer (VSM). The comparison underscores a crucial correlation between spintronic terahertz polarization and the magnetization vectors.

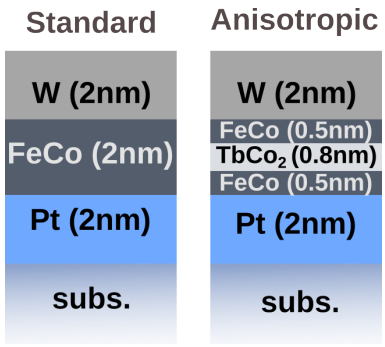


Figure 4.17: Comparison of standard and anisotropic spintronic terahertz emitter designs: The left diagram illustrates the layer structure of a standard spintronic terahertz emitter (STE), comprising a tungsten (W, 2 nm), iron-cobalt (FeCo, 2 nm), and platinum (Pt, 2 nm) stack on a substrate. The right diagram depicts an anisotropic STE structure, where the FeCo layer is divided to incorpora a terbium-cobalt ($TbCo_2$, 0.8 nm) layer sandwiched between two thinner FeCo layers (0.5 nm each).

Our recent research has focused on developing, testing, and modeling spintronic emitters with induced magnetic anisotropy. In contrast to conventional W/FeCoB/Pt samples, we replaced the isotropic FeCoB layer with a FeCo/$TbCo_2$/FeCo multilayer [163, 164]. Figure 4.17 compares these emitter designs. The ferromagnetic stack is engineered to introduce uniaxial magnetic anisotropy via interlayer coupling dynamics between FeCo and $TbCo_2$ layers. In Figure 4.18, the magnetic hysteresis of these designs is compared with that of the ferromagnetic heterostructure. The isotropic FeCo layer is magnetically soft, enabling the use of lower magnetic fields while still maintaining high magnetization. However, its isotropic nature requires altering the external magnetic field's orientation to change the magnetization direction. In contrast, $TbCo_2$ demonstrates pronounced anisotropy. Field variation along the hard axis alters magnetization vectors, leading to the magnetization rotation. However, its magnetic hardness requires a high saturation field. Another issue is its low magnetization, reducing the efficiency of a spintronic emitter based solely on the $TbCo_2$ layer. However, the optimal combination of these layers in a multilayer structure achieves a combination of their fundamental properties. The multilayer is both magnetically soft and strongly anisotropic.

Moreover, the overall magnetization is reduced by only a factor of two. This approach allows for the fabrication of spintronic emitters that are highly effective in polarization control.

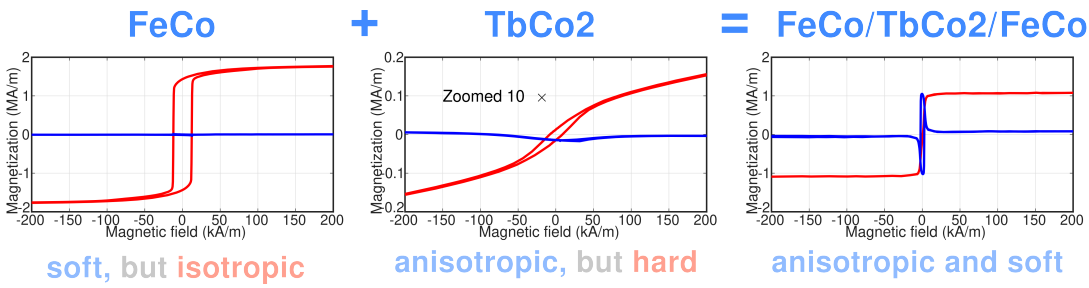


Figure 4.18: Magnetic properties of FeCo, $TbCo_2$, and FeCo/$TbCo_2$/FeCo Structures: The left plot shows the magnetization components for FeCo, illustrating its soft magnetic behavior but isotropic nature. The middle panel displays the magnetization of $TbCo_2$, which exhibits anisotropic behavior and hard magnetic properties (note the 10× zoomed-in view for clarity). The right panel combines these materials into a FeCo/$TbCo_2$/FeCo structure, resulting in a material that is both anisotropic and soft.

4.2.1 360° polarization control of terahertz spintronic emitters using uniaxial FeCo/$TbCo_2$/FeCo trilayers

Pierre Koleják, Geoffrey Lezier, Kamil Postava, Jean-François Lampin, Nicolas Tiercelin, and Mathias Vanwolleghem

ACS photonics, 9(4), 1274-1285, 2022

This research presents a novel approach to controlling terahertz spintronic polarization via magnetic uniaxial anisotropy, utilizing our FeCo/$TbCo_2$/FeCo emitter. In a uniaxial anisotropic sample, the magnetization aligns with the intrinsic easy axis (IEA) even without an external magnetic field [165], as illustrated in Figure 4.19a. As an external magnetic field $\mathbf{H}_{\text{Control}}$ is applied and increases along the intrinsic hard axis (IHA), the magnetization begins to rotate. This magnetization rotation, known as Stoner-Wohlfarth, is coherent and lossless in single-domain systems like the spintronic emitter. The rotation continues until it aligns with the intrinsic hard axis (IHA) as the field reaches the saturation field H_A. This alignment occurs because the magnetization of the sample follows the minimum energy balance E between the isotropic Zeeman energy and the anisotropic energy, expressed as follows:

$$E = -\mu_0 M_s H_{\text{Control}} \cos(\varphi - \varphi_{\text{Control}}) + K \cos^2 \varphi \tag{4.4}$$

where μ_0 represents the vacuum permeability, and the material constants M_s and K correspond to the saturation magnetization and the uniaxial anisotropy constant, respectively. The angles φ and φ_{Control} represent the orientation of the magnetization and the applied magnetic field $\mathbf{H}_{\text{Control}}$ relative to the intrinsic hard axis.

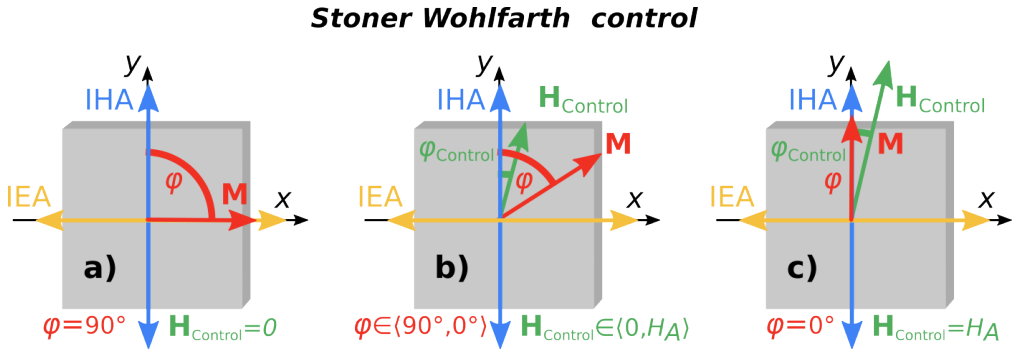


Figure 4.19: Magnetization control in spintronic terahertz emitters using the Stoner-Wohlfarth model: The diagrams depict the behavior of the magnetization vector $\mathbf{M}$ under various conditions of the control magnetic field $\mathbf{H}_{\text{Control}}$ relative to the intrinsic hard axis (IHA) and easy axis (IEA). When the control magnetic field is zero $\mathbf{H}_{\text{Control}} = 0$, the magnetization vector aligns with the intrinsic easy axis (IEA) at an angle of $\phi = 90°$. As the control magnetic field increases from zero to the anisotropic field $\mathbf{H}_{\text{Control}} \in (0, H_{\text{A}})$, the magnetization angle ϕ transitions smoothly from 90° to 0°. At saturation $\mathbf{H}_{\text{Control}} = H_{\text{A}}$, the magnetization aligns with the intrinsic hard axis (IHA) at an angle of $\phi = 0°$.

Figure 4.20 depicts the comprehensive strategy for polarization control, where an external magnetic field governs four distinct polarization states. The generated polarization is linear due to the generation from the ultra-thin metallic layers, and its azimuth is altered solely by adjusting the magnetic field strength. The method necessitates gradual changes in the magnetic field, permitting the magnetic domains to reorient progressively, with each state depending on the previous magnetization. As demonstrated in Figure 4.16, the generated polarization states follow the hysteresis behavior of the spintronic emitter. This hysteresis reflects the trajectory of the magnetization vector, as shown in the center of the schematic in Figure 4.20.

Figure 4.21 illustrates the 180° polarization rotation of terahertz waveforms, which is induced by applying a magnetic field along the hard axis of the spintronic terahertz emitter (STE). Projecting these waveforms onto a vertical-horizontal plane demonstrates linear polarization states' rotation. A modified terahertz time-domain spectroscopy setup adapted for polarimetry was used to measure terahertz signals and capture orthogonal polarizations.

Summary of findings and impact of the study

This study demonstrates that engineered magnetic anisotropy in uniaxial FeCo/$TbCo_2$/FeCo trilayers enables 360° coherent polarization control of terahertz radiation in spintronic emitters. This polarization control is accomplished without complex multipolar or rotating external magnetic fields. The ferromagnetic trilayer design facilitates THz polarization rotation by simply varying the applied magnetic field strength along the hard axis, following Stoner-Wohlfarth-like behavior. This study introduces a more straightforward and efficient method for controlling THz polarization, with significant potential for THz polarimetry and ellipsometry applications. The polarization response, governed by magneto-hysteresis, is highly repeatable, easily calibrated, and requires a low magnetic field. Direct control of polarization at the point of generation, without mechanical components, streamlines the design and integration of terahertz systems and eliminates the need for polarizers to control the input polarization.

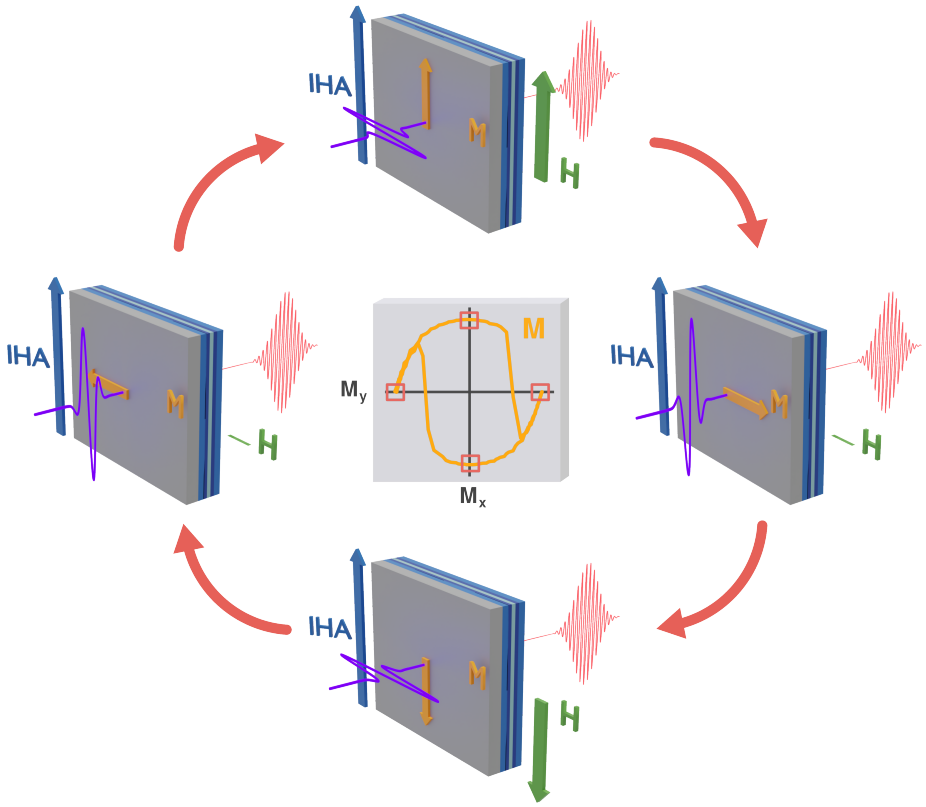


Figure 4.20: Stoner-Wohlfarth control of the polarization of uniaxial spintronic terahertz emitter: The figure illustrates the control of the magnetization vector (**M**) by the applied magnetic field **H** along the intrinsic hard axis (IHA) magnetic field. The central plot shows the hysteresis loop, indicating the trajectory of the magnetization vector as the magnetic field direction changes. The surrounding images depict the terahertz emission signal (in purple) after infrared pumping (in red), corresponding to different magnetization orientations relative to the applied magnetic field.

My contributions

With Nicolas Tiercelin and Mathias Vanwolleghem, I contributed to developing methods for controlling terahertz polarization through the coherent rotation of magnetization. Additionally, I developed the methodology for polarimetric measurements and their verification and assisted in setting up reflection and transmission experiments. My role also involved interpreting the data and supporting experiments led by Geoffrey Lezier and Nicolas Tiercelin. Furthermore, I participated in data processing and conducted simulations of magnetic response using the Stoner-Wohlfarth model, which I fitted to experimentally determined data. Alongside Mathias Vanwolleghem, I prepared the main text and created most of the graphics in the article.

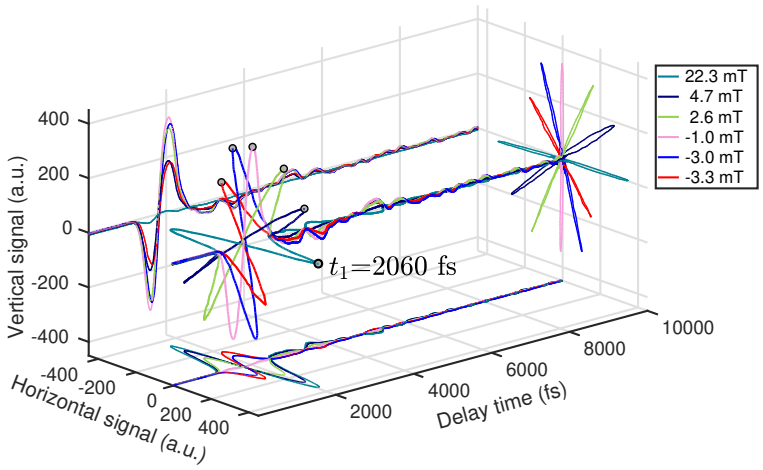


Figure 4.21: Experimental demonstration of time-resolved terahertz polarization control: The 3D plot illustrates the rotation of the terahertz electric field, reconstructed from both the horizontal and vertical polarization components under different applied magnetic fields, ranging from -3.3 mT to 22.3 mT. The distinct trajectories indicate how the polarization of the peak evolves under each magnetic field condition, with the specific time $t_1 = 2060$ fs highlighted to show the current polarization state.

4.2.2 Fully reversible magnetoelectric voltage controlled THz polarization rotation in magnetostrictive spintronic emitters on PMN-PT

Geoffrey Lezier, Pierre Koleják, Jean-Francois Lampin, Kamil Postava, Mathias Vanwolleghem, and Nicolas Tiercelin

Applied Physics Letters, 120(15), 2022

This research aims to develop a voltage-controlled mechanism for precise terahertz polarization rotation. The developed FeCo/$TbCo_2$/FeCo trilayers exhibit significant magnetostrictive properties in addition to magnetic anisotropy [166, 167]. Magnetostriction is a phenomenon in which the dimensions of a material change in response to variations in magnetization [168]. This effect is robust in rare-earth ions like terbium (Tb^{3+}), with an electronic configuration of $4f^8$. With unpaired spins and substantial orbital angular momentum, the eight f-orbital electrons collectively produce an intense magnetic moment [169]. This magnetostriction occurs due to the oval shape of the f-orbitals, which reorient in response to an external magnetic field, causing a change in the material's shape. Figure 4.22 illustrates three conditions: (a) In the absence of an external field (H = 0), the magnetic moments are randomly oriented, and the material retains its original shape. (b) When an upward-directed field (H) is applied, the magnetic moments align, resulting in material deformation. (c) Under an intense horizontal field (H), all magnetic moments fully align, resulting in maximum material deformation.

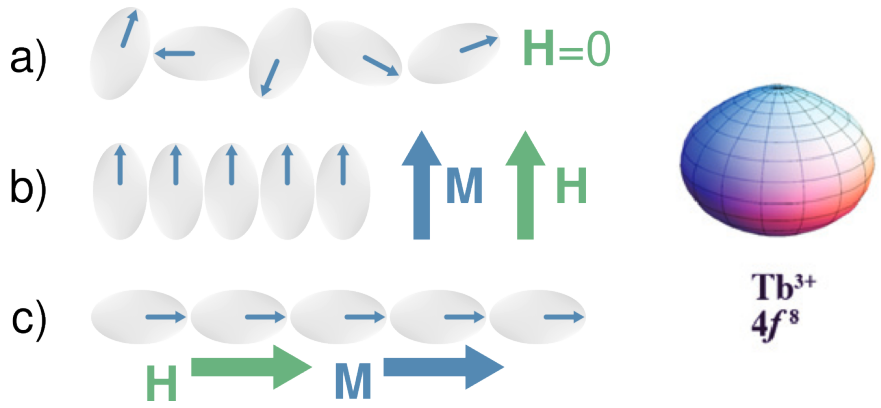


Figure 4.22: Demonstration of magnetostriction in a Tb^{3+} $4f^8$ system: The figure illustrates the effect of magnetostriction on the orbital configuration of a Tb^{3+} ion under varying magnetic field conditions. (a) In the absence of an external magnetic field ($\mathbf{H} = 0$), the orbitals are randomly oriented. (b) When a magnetic field ($\mathbf{H}$) is applied, the orbitals align along the direction of the magnetization ($\mathbf{M}$), showing the system's response to the magnetic field. (c) The application of the perpendicular magnetic field induces magnetostriction, causing strain that alters the spacing between orbitals and reorients the magnetization vector ($\mathbf{M}$). , The orbital adapted from [169]

The process is reversible: stretching the material alters its magnetization. Placing the spintronic emitter on an electro-active (1-x)[$Pb(Mg_{0.33}Nb_{0.66})O_3$]-x[$PbTiO_3$] (PMN-PT) substrate enables electrical control of the generated polarization [170, 171]. The schematic of this strategy is shown in Figure 4.23. The sample's magnetization is aligned along its intrinsic easy axis, generating linear terahertz polarization. Applying voltage to the piezoelectric material changes its dimensions, causing strain on the magnetostrictive FeCo/$TbCo_2$/FeCo layers. Strain along the hard axis induces rotation in the spintronic emitter's magnetization. In contrast to the Stoner-Wohlfarth model (4.4), the minimized energy balance now incorporates magnetoelastic energy

$$E = -\mu_0 M_s H_{\text{Control}} + K \cos^2 \varphi \cos(\varphi - \varphi_{\text{Control}}) + b^{\gamma,2} (\varepsilon_{xx} - \varepsilon_{yy}) \cos^2 \varphi, \tag{4.5}$$

where $\varepsilon_{xx} - \varepsilon_{yy}$ represents the applied mechanical stress along the intrinsic hard axis, and $b^{\gamma,2}$ denotes the magnetoelastic coefficient.

Figure 4.24 shows that time-domain spectroscopy measurements at fixed voltages demonstrate polarization control, with ellipticity slightly increasing as voltage rises to 6°. Maximum polarization rotation occurred at approximately 400 V during voltage cycling on the PMN-PT substrate. The polarization azimuth rotates by more than 65°, with horizontal polarization occurring without an applied field, while applied voltage induces tensile strain and horizontal magnetization. Reversibly lowering the voltage will restore the polarization to its original state.

Summary of findings and impact of the study

This study examines the fully reversible voltage control of terahertz polarization rotation in magnetostrictive spintronic emitters using a PMN-PT substrate. These findings significantly advance terahertz polarization control, aiming for voltage-controlled polarization control without external magnetic fields. This approach offers practical advantages, including more precise polarization

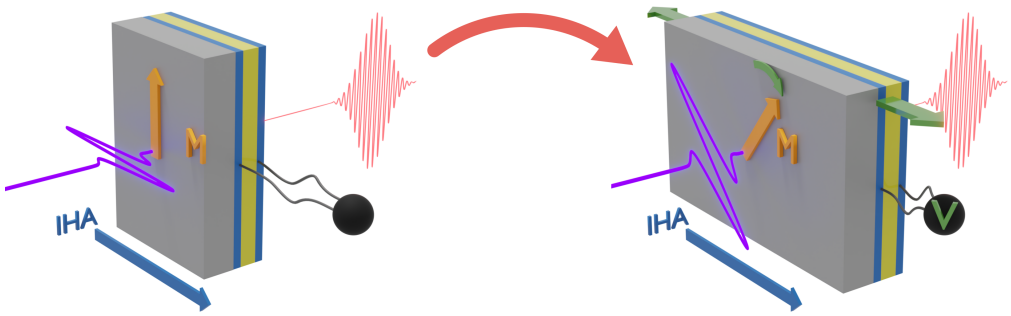


Figure 4.23: Control of terahertz polarization via the magnetoelastic effect: The figure illustrates the process of controlling terahertz polarization through the magnetoelastic effect. In the left panel, the initial state shows the magnetization (M) aligned with the intrinsic easy axis (IHA) under no external voltage. The right panel depicts the state after applying voltage to the PMN-PT substrate, which induces strain and causes the magnetization to rotate, thereby altering the polarization of the emitted terahertz wave.

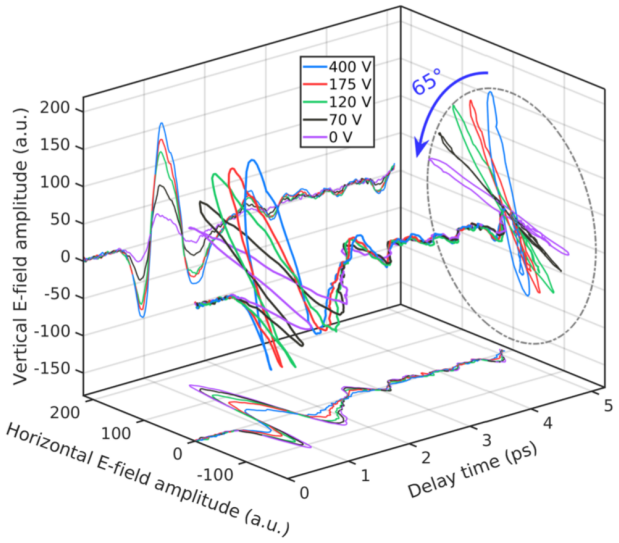


Figure 4.24: Experimental demonstration of polarization control via magnetostriction: The 3D plot shows the terahertz electric field amplitude's rotation in horizontal and vertical components under different applied voltages (0 V to 400 V). The application of voltage induces strain through magnetostriction, leading to a rotation of the polarization ellipse by up to 65°.

adjustments and fast polarization modulation. Applying an electric voltage to the magnetostrictive multilayer structure enables up to 70° of polarization rotation.

While the practical advantages of this method are evident for polarimetry and ellipsometry, the theoretical model suggests that achieving 90° rotation is possible. Further research could optimize the multilayer structure or piezoelectric substrate for full 360° rotation. The study identified slight ellipticity in the terahertz signal at higher voltages, likely due to the dielectric anisotropy of the substrate. Moreover, due to its high permittivity, integrating the PMN-PT substrate reduces terahertz field extraction. Furthermore, the thin metal layer on the back of the substrate to create electrodes further compromised the signal by lowering infrared transmission. Solving these challenges, such as using a spacing layer and reflective arrangements, could resolve these issues and enhance the efficiency of these emitters with electrical control.

My contributions

I was involved in polarimetric experiments led by Geoffrey Lezier and Nicolas Tiercelin, where I worked on aligning, interpreting, and processing the collected data. I also performed numerical verifications to assess the efficiency losses when integrating the spintronic emitter with PMN-PT. Additionally, I created graphics for the article and designed the cover art when our paper was selected for the journal's cover. Furthermore, I contributed to drafting and revising the article's main text.

4.3 Complete time-domain ellipsometry

Ellipsometry determines the response of a sample by measuring changes in the polarization state of light upon reflection or transmission [54, 126]. One widely used form is the standard ellipsometry in the time-domain [60, 172–174], which measures the ratio of Fresnel reflection coefficients, $\tilde{r}_{s,p}$, between two polarization states, expressed as

$$\tan(\Psi) = \left| \frac{\tilde{r}_p}{\tilde{r}_s} \right| \quad \text{and} \quad \Delta = \arg\left\{ \frac{\tilde{r}_p}{\tilde{r}_s} \right\},$$

where the ellipsometric angles Ψ and Δ characterize the amplitude and phase changes between orthogonal polarizations. Standard ellipsometry offers robustness by the polarization-sensitive response and by correcting phase errors caused by sample-reference displacement in reflective measurements [51–53], but it also has inherent limitations, such as:

- It primarily addresses phase and amplitude changes between two polarization components but does not fully capture the entire polarization state of light. As a result, phenomena responsible for s-to-p polarization transitions are indeterminable.
- This method is most effective for isotropic materials with uniform optical properties. Interpretation can become challenging or unattainable for anisotropic materials, where properties vary by direction, often requiring specific sample orientations or cuts.
- It cannot analyze materials with polarization responses in circular bases, such as optical activity, the Kerr effect, or dichroism.
- Ellipsometric equations may produce multiple combinations of refractive index n and absorption coefficient k corresponding to the same measured parameters Ψ and Δ, leading to ambiguities in interpretation. Since ellipsometry measures changes in the polarization of reflected light, which depends on n and k, these properties cannot be uniquely determined from Ψ and Δ alone.

In contrast, complete ellipsometry offers a much more detailed and comprehensive analysis of the optical properties of materials by employing Jones or Mueller matrices (discussed in Section 2.1.1). Instead of simply examining the ratio of reflection coefficients, it allows for fully characterizing the transformation of light's polarization states between the input and output. This method excels in analyzing materials with general anisotropy, where optical properties change with direction, and examining complex phenomena such as dichroism and optical activity. Standard ellipsometry can overlook or misinterpret these properties, while complete ellipsometry provides a deeper and more accurate insight.

Figure 4.25 compares the representation of optical phenomena in complete ellipsometry, illustrating the distribution of matrix elements in the time domain versus the frequency domain. In the time domain, coherent electric field waveforms are measured using time-resolved spectroscopy, enabling the reconstruction of the Jones matrix. The primary advantage of this method is its ability to provide complete information on the electric field's phase and amplitude changes. The Jones matrix characterizes fundamental polarization properties such as retardance and diattenuation for linear, diagonal, and circular polarization. However, these phenomena are often indirectly encoded within the matrix elements, making the information appear blended and challenging to interpret directly. This issue

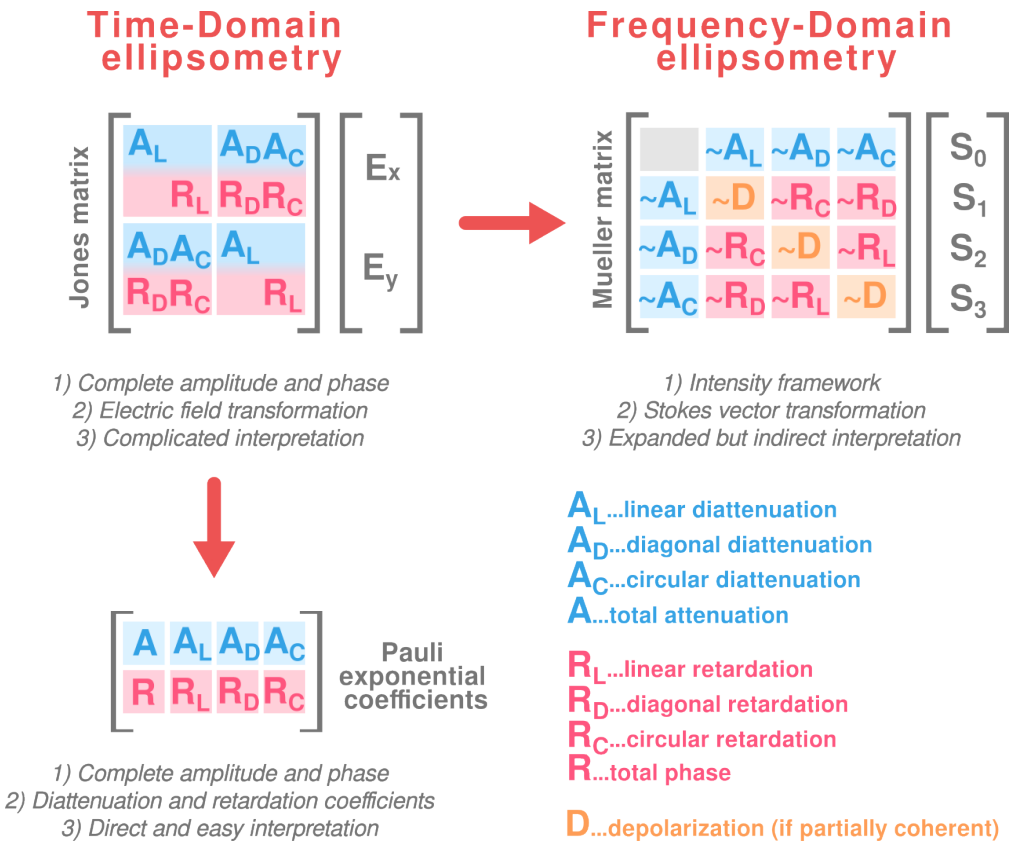


Figure 4.25: Comparison of complete time-domain versus frequency-domain ellipsometry: The diagram illustrates the relationships among the Jones matrix, Mueller matrix, and Pauli exponential coefficients used in time-domain and frequency-domain spectroscopy. The diagram highlights linear (L), diagonal (D), and circular (C) diattenuation effects (blue), retardation (red), and depolarization (orange), illustrating how these effects are distributed across each representation method. Time-domain ellipsometry provides the Jones matrix, offering complete amplitude and phase information and directly describing the transformation of the electric field components $E_{x,y}$. However, interpretation can be challenging due to overlapping phenomena. Frequency-domain ellipsometry utilizes the Mueller matrix, which operates within an intensity framework to transform the Stokes vector S_{0-3}. Jones matrix can be transformed into the Mueller matrix and Pauli exponential coefficients. Pauli's approach provides a unified framework that preserves complete amplitude and phase information. The coefficients correspond to diattenuation and retardation coefficients, leading to a more straightforward interpretation.

becomes particularly pronounced when the matrices are subjected to rotational transformations, which introduces additional complexity in distinguishing individual contributions. Understanding matrix elements in Jones and Mueller formalisms is extensively discussed in Section 2.1.2.

Frequency-domain ellipsometry characterizes light by its intensity, using Stokes vector transformation to describe the total intensity and changes in polarization across linear, diagonal, and circular bases. Depicted in Figure 4.25, the Mueller matrix organizes these effects into a 4×4 structure, where elements relate to specific Stokes bases. However, these elements often contain contributions from

multiple optical phenomena, complicating interpretation. Moreover, optical phenomena associated with other matrix elements can interfere with these effects, especially when the matrix is rotated. If the light is partially coherent, ellipsometry can also determine depolarization, quantifying the degree to which the polarization state of light is lost. In contrast, the inherently coherent Jones matrix can be converted into a Mueller-Jones matrix, which remains fully coherent and excludes depolarization effects, highlighting the flexibility of the Jones matrix for both ellipsometry frameworks.

Furthermore, our time-domain complete ellipsometry approach demonstrates a new experimental approach - Pauli exponential coefficients - transformed from the determined Jones matrix. Thus far, this method has been explored only theoretically [80–82], requiring complete coherent experimental ellipsometry provided in this research. These coefficients directly correspond to diattenuation and retardation coefficients in the Stokes bases, significantly simplifying the interpretation of ellipsometric data.

These matrix approaches enable the complete characterization of polarization responses in general anisotropic samples, which is impossible with standard ellipsometry. Complete ellipsometry is an invaluable tool for determining basic optical properties in the terahertz range and understanding the structure and orientation of complex characterized samples.

4.3.1 Terahertz time-domain ellipsometry with spintronic emitters: Pauli coefficients as a superior alternative to Jones and Mueller matrices

Pierre Koleják, Jiaming Liu, Robin Silber, Martin Mičica, Ondřej Ballada, Čestmír Barta, Romain Lebrun, Nicolas Tiercelin, Mathias Vanwolleghem, and Kamil Postava

2024 (submitted)

This study completes the primary objective of the thesis: developing terahertz ellipsometry in the time domain with spintronic terahertz emitters. It is the first practical application of spintronic terahertz emitters in ellipsometry for its exceptional polarization control. We employ a spintronic emitter with the highest demonstrated performance, achieved through its large-area design and integration with a 1D photonic crystal, provided by Rouzegar *et al.* [108].

Unlike conventional approaches that rely on standard ellipsometry calibrated through system alignment and component adjustment, our method introduces an experimental technique for reconstructing the complete Jones matrix (see Section 2.1.1). Only one other study has demonstrated complete Jones matrix ellipsometry [79], simplifying the reconstruction by leveraging symmetry assumptions with carefully aligned components. However, most existing research focuses on standard ellipsometry [58, 71–73] or on the Mueller matrix in both the time and frequency domains [56, 59, 69, 76–78], excluding the phase information provided by the time domain. A recent study on generalized standard time-domain ellipsometry using reflection coefficients [175] employs a pre-aligned system, thus eliminating the need for calibration based on ideal component settings. In contrast, we have developed a universal calibration approach that removes systematic measurement errors for any roughly aligned arrangement and facilitates the complete reconstruction of the Jones

matrix from multiple polarimetric measurements, making the method more accessible and reliable for broader applications.

Demonstration of Jones and Mueller matrix ellipsometry

The spintronic emitter directly controls incoming polarization, using orthogonal polarizations without polarizers that would otherwise reduce the signal by projecting the field horizontally or vertically. Our experimental setup employs ellipsometry in a transmission configuration to analyze anisotropic materials. We use specific configurations in our time-domain ellipsometry setup, schematized in Figure 4.26: A spintronic emitter generating polarization at 0° (horizontal) and 90° (vertical), a sample, an analyzer at 45° and -45°, and polarization detection at 90°. Vertical detection is achieved using a fixed polarizer in combination with ZnTe, which enhances the extinction ratio. We measure all four configurations to obtain the complete ellipsometric information.

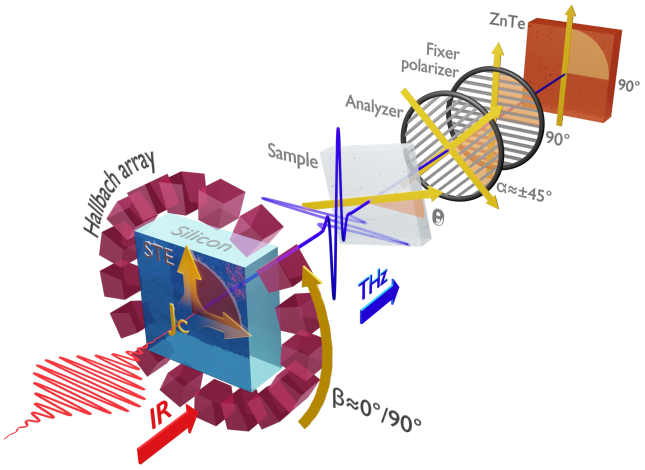


Figure 4.26: Schematic of the time-domain ellipsometry: The configuration includes a spintronic emitter generating polarization at 0° (horizontal) and 90° (vertical), followed by the sample, an analyzer set at 45° and -45°, and polarization detection at 90° by the fixed polarizer and ZnTe crystal.

To demonstrate our time-domain terahertz ellipsometry, we analyzed a c-cut quartz crystal with a thickness of 1.816 mm. Figure 4.27 presents the amplitude and normalized phase spectra of the experimentally obtained complex Jones matrix for optical axis rotations of 15°, 60°, 90°, and 135°. The measured data are compared with a theoretical model of quartz to validate the experimental results. The quartz plate is half-wave at approximately 1.7 THz. At 135° azimuth, the polarization rotates by 90° and s- and p- polarization interchange. This behavior results in maximum amplitudes in the off-diagonal components of the Jones matrix. When the crystal aligns with the input polarization, the amplitudes on the diagonal directly correspond to the ordinary and extraordinary wave responses, and off-diagonals are zero. In the phase spectrum, we observe the dispersion effects of the ordinary and extraordinary refractive indices as deviations from linear dependence. The phase shift of π indicates a change in wave polarity. This Jones matrix approach fully characterizes the sample's polarization response at any orientation of an anisotropic sample. Distinguishing between circular and linear birefringence can pose a significant challenge in the Mueller matrix form.

We transform the Jones matrix from Figure 4.27, as described in Section 2.1.1, into the normalized Mueller matrix shown in Figure 4.28. The main effects occur within the retardation submatrix

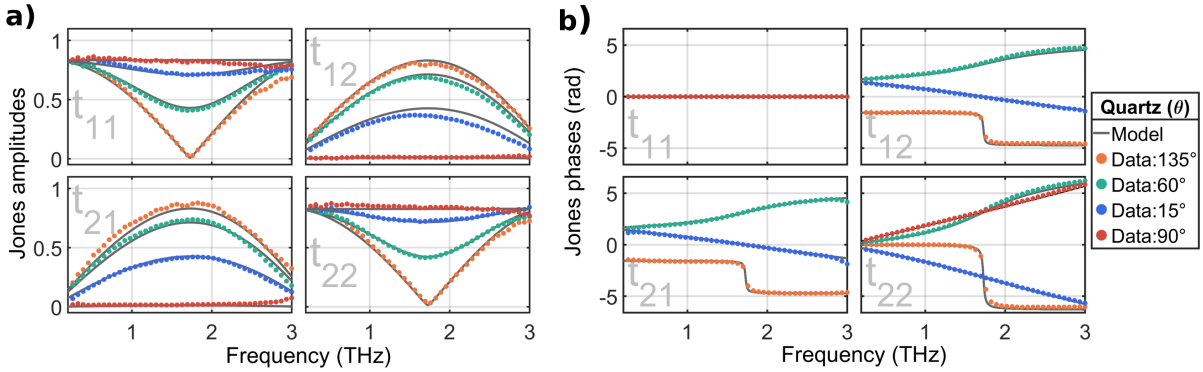


Figure 4.27: Demonstration of experimental Jones matrix: The figure shows the terahertz Jones matrix amplitudes (left) and normalized phases (right) for a quartz sample measured at different orientation angles (θ = 15°, 60°, 90°, 135°). The data illustrates the agreement between the experimental measurements and the theoretical model.

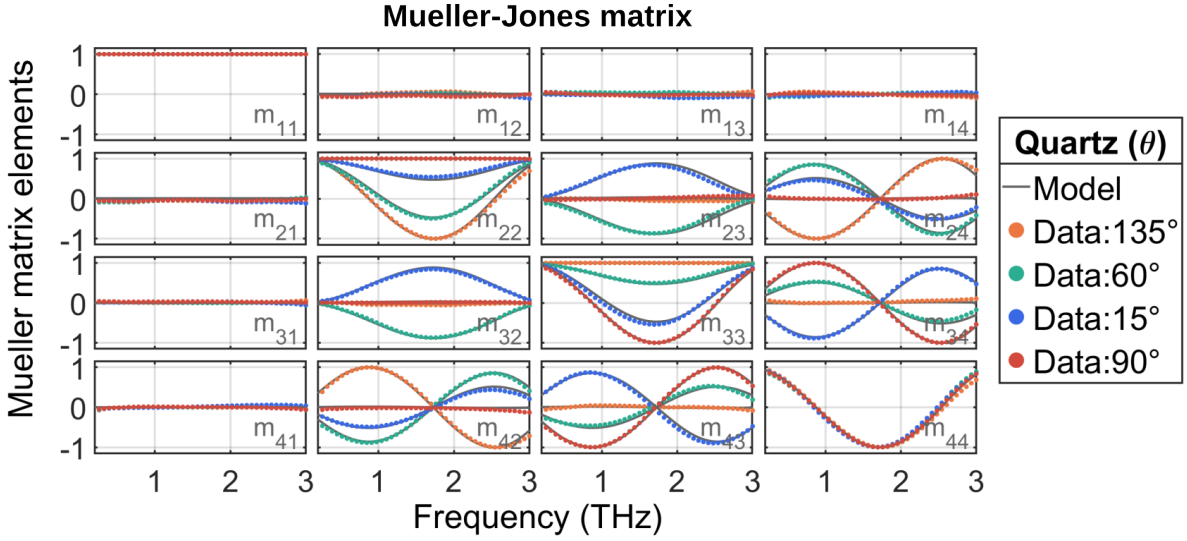


Figure 4.28: Demonstration of experimental Mueller matrix: The figure presents the terahertz Mueller matrix, illustrating polarization-dependent intensity changes for a quartz sample measured at azimuths (θ = 15°, 60°, 90°, and 135°). The experimental data are compared with a theoretical model (shown as a gray line).

$m_{2-4,2-4}$, while the first row and column, except for the normalization term m_{11}, are zero. This form indicates that the sample exhibits only retardance, with no evidence of diattenuation. The Mueller matrix for the unrotated sample at 90° azimuth exhibits a block-diagonal structure. This aligns with the analysis in Figure 4.25, where the off-diagonal elements m_{34} and m_{43} arise, representing linear retardance. Upon azimuthal rotation, the interpretation becomes more complex. Elements m_{24} and m_{42} become dominant, reflecting transitions into diagonal linear polarizations, which peak at 135° azimuth. Additionally, elements m_{32} and m_{23}, which represent circular retardance, are not zero. These elements reflect the intensity converted to circularly polarized light, generated by a linear

retarder at azimuths of 15° and 60°. This analysis of the quartz plate shows that although the Mueller matrix offers a complete polarization description, its interpretation can become complex even for linear and diagonal retardation.

Interpreting coherent ellipsometry through Pauli coefficients

Pauli coefficients are essential scalar values used in the linear combination of Pauli matrices to reconstruct the Jones matrix (see Section 2.1.2). Pauli exponential coefficients become crucial when dealing with the exponential of a matrix involving Pauli matrices, particularly in decomposing the Jones matrix $\mathbb{J}$ into linear (L), diagonal (D), and circular (C) bases. These coefficients also account for the total amplitude and phase changes (0). The Jones matrix decomposition is expressed as

$$\mathbb{J} = \mathbb{J}_0\,\mathbb{J}_\mathrm{L}\,\mathbb{J}_\mathrm{D}\,\mathbb{J}_\mathrm{C} = \exp\left\{p_0\boldsymbol{\sigma}_0 + \frac{d_\mathrm{L} - \mathrm{i}\delta_\mathrm{L}}{2}\boldsymbol{\sigma}_\mathrm{L} + \frac{d_\mathrm{D} - \mathrm{i}\delta_\mathrm{D}}{2}\boldsymbol{\sigma}_\mathrm{D} + \frac{d_\mathrm{C} - \mathrm{i}\delta_\mathrm{C}}{2}\boldsymbol{\sigma}_\mathrm{C}\right\}, \tag{4.6}$$

where $\boldsymbol{\sigma}_\xi$ are the Pauli matrices, and d_ξ and δ_ξ represent diattenuation and retardation for each basis. As detailed in Section 2.1.2 to obtain the Pauli exponential coefficients, the matrix logarithm of the Jones matrix must be calculated

$$\ln(\mathbb{J}) = p_0\boldsymbol{\sigma}_0 + \frac{d_\mathrm{L} - \mathrm{i}\delta_\mathrm{L}}{2}\boldsymbol{\sigma}_1 + \frac{d_\mathrm{D} - \mathrm{i}\delta_\mathrm{D}}{2}\boldsymbol{\sigma}_2 + \frac{d_\mathrm{C} - \mathrm{i}\delta_\mathrm{C}}{2}\boldsymbol{\sigma}_3. \tag{4.7}$$

Figure 4.29 shows the experimentally determined Pauli exponential coefficients for quartz, derived from the complex Jones matrix in Figure 4.27. The interpretation provides a clear and systematic insight into the specific optical phenomena of analyzing quartz, such as birefringence and diattenuation. The diattenuation coefficients are zero, indicating that dichroism is absent in all Stokes bases for quartz. The total amplitude change, represented by d_0, corresponds to the reflection losses at the quartz/air interface. For retardation, we observe a transition between linear and diagonal birefringence based on the sample's rotation, while circular birefringence remains zero. The coefficient δ_0 encompasses the total phase change experienced by the radiation as it passes through the sample. The phenomena in circular polarizations are zero, while the effects of linear and diagonal retardance are clearly visible, contrasting their less apparent manifestation in the Jones and Mueller matrices.

Summary of findings and impact of the study

This research demonstrates the first application of spintronic emitters to control polarization in terahertz time-domain ellipsometry (THz-TDSE). The spintronic emitter provides an elegant, robust, and straightforward solution for controlling input polarization, eliminating the need for a polarizer or a more complex mechanism. This capability significantly enhances the precision of material characterization, providing linear polarizations with a high extinction ratio.

Using Jones and Mueller-Jones matrices, we present a comprehensive ellipsometric method to describe general anisotropy, demonstrated with quartz and Hg_2C_2 crystals [176]. A significant advantage of this method is the access to both phase and amplitude information, which is not available in conventional complete ellipsometry. This approach enables using either Jones or Mueller matrices, depending on the specific sample or preference. In our method, only four independent polarization states are required to determine the polarization state, in contrast to the 16 states needed in traditional Mueller matrix ellipsometry, significantly reducing measurement time. Moreover, we demonstrate that employing linear polarizations is sufficient for complete coherent ellipsometry,

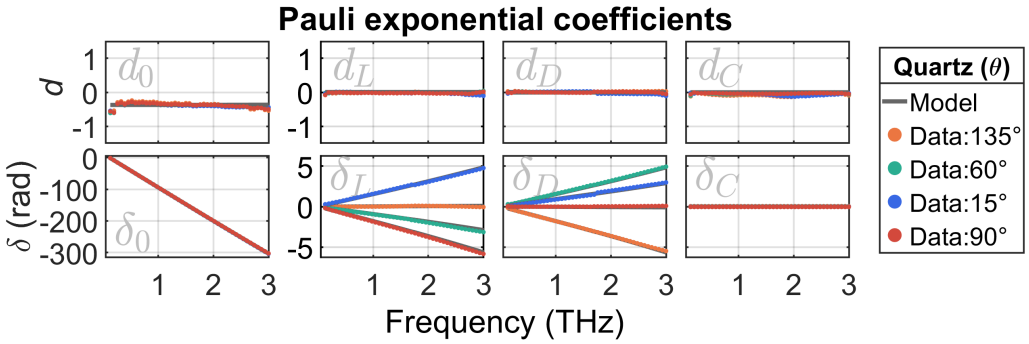


Figure 4.29: Experimental Pauli exponential coefficients for quartz: The top row of the figure displays the diattenuation coefficients ($d_0, d_\mathrm{L}, d_\mathrm{D}, d_\mathrm{C}$), while the bottom row displays the retardation coefficients ($\delta_0, \delta_\mathrm{L}, \delta_\mathrm{D}, \delta_\mathrm{C}$) for linear (L), diagonal (D) and circular (C) Stokes bases and the cumulative change (0). The quartz measurements were taken at various orientation angles (θ = 15°, 60°, 90°, 135°). Colored markers represent the experimental data, which closely align with the theoretical model, and are shown as solid black lines with minimal variation across the tested frequencies and angles.

removing the need to generate circular polarizations. This resolves a fundamental limitation of incomplete Mueller matrix ellipsometers in the terahertz frequency domain, excluding complete analysis of circular polarization effects.

This study introduces Pauli exponential coefficients, providing a more intuitive and direct interpretation of polarization transformations than Jones or Mueller matrices by explicitly quantifying retardation and diattenuation. This method offers immediate access to retardation and diattenuation coefficients, which quantify phase shifts and differential attenuation across all Stokes bases. Furthermore, this research introduces a novel and generalized calibration method that significantly enhances the accuracy of THz-TDSE by eliminating the dependence on precise polarizer alignment, improving the reliability of results, and being applicable across a wide range of polarization-sensitive configurations.

This generalized approach applies to ellipsometric configurations that require polarization control at both the input and output. The ability to fully characterize the polarization response of materials with greater accuracy may lead to the broader adoption of THz-TDSE in material science, including the analysis of complex materials such as biological samples, thin-film heterostructures, and metamaterials. This method also simplifies the interpretation of polarization data, making it more accessible and useful for various scientific and industrial applications.

My contributions

The research described in this paper stems from a custom-designed terahertz experiment that I developed during my PhD, in collaboration with Martin Mičica and Iva Hlobílková. I further improved this setup by adapting it for time-domain terahertz ellipsometry, laying the groundwork for all subsequent measurements. The development of measurement procedures and calibration methods was a collaborative effort involving Jiaming Liu, Robin Silber, and Kamil Postava, with me later taking the lead in generalizing these techniques. Jiaming Liu and I were responsible for conducting measurements and managing the data processing, interpretation, and fitting of Jones

and Mueller matrices. I extended the analysis using the coherent Pauli approach for simple and direct interpretation. Additionally, I conducted the error and robustness analysis for the ellipsometric measurements, drafted the paper's main text, and prepared the graphics.

4.3.2 Effects of optical activity to Mueller matrix ellipsometry of composed waveplates

Daniel Vala, Pierre Koleják, Kamil Postava, Morten Kildemo, Pavlína Provazníková, and Jaromír Pištora

Optics Express, 29(7), 10434-10450, 2021

The research started early in my PhD studies, extending my work presented by P. Koleják *et al.*, *J. Vac. Sci. Technol. B* 38.1 (2020) [177], which involved characterizing waveplates for polarimetric applications and identifying optical activity. This research was conducted before the development of the terahertz ellipsometer. The study had two primary objectives: (I) to develop theoretical and practical expertise with a commercial optical ellipsometry setup as an initial experience for constructing a terahertz ellipsometer. This included a comprehensive understanding of the experimental setup, the factors influencing measurements, and the interpretation and refinement of Mueller matrix data.

This research led to a collaboration with Meopta s.r.o., focusing on quartz waveplates, specifically bi-plates designed as zero-order retarders. The initial goal was to measure the retardation of these bi-plates and identify any misalignment between the individual waveplates. However, further investigation revealed that what was initially perceived as alignment errors was a combination of misalignment and optical activity. Despite the subtlety of these effects, they could be independently identified and accurately characterized. This discovery led to the second research objective: (II) to develop a comprehensive theoretical and numerical framework for accurately describing optical activity. Establishing and demonstrating this framework in the optical range was an essential step in preparing for its application in the terahertz range, where these phenomena were expected to be less pronounced but still critical to accurate measurements.

Characterization of single quartz waveplates

The research initially aimed to characterize individual waveplates by determining the retardation Γ by fitting a linear retarder model to the corresponding Mueller matrix, expressed as

$$\mathbf{M}_{\mathrm{R,LIN}}(\varphi,\Gamma)=\begin{pmatrix}1 & 0 & 0 & 0\\ 0 & \cos^2 2\varphi+\cos\Gamma\sin^2 2\varphi & (1-\cos\Gamma)\sin 2\varphi\cos 2\varphi & -\sin 2\varphi\sin\Gamma\\ 0 & (1-\cos\Gamma)\sin 2\varphi\cos 2\varphi & \sin^2 2\varphi+\cos\Gamma\cos^2 2\varphi & \cos 2\varphi\sin\Gamma\\ 0 & \sin 2\varphi\sin\Gamma & -\cos 2\varphi\sin\Gamma & \cos\Gamma\end{pmatrix}, \quad (4.8)$$

where φ indicates the azimuthal rotation of the waveplate. However, early measurements revealed that this model was insufficient for accurately determining the retardation, as additional effects

became evident in the experimental data. These unexpected phenomena indicated the presence of complexities beyond simple linear retardation, necessitating a more detailed analysis to characterize the waveplates' optical behavior.

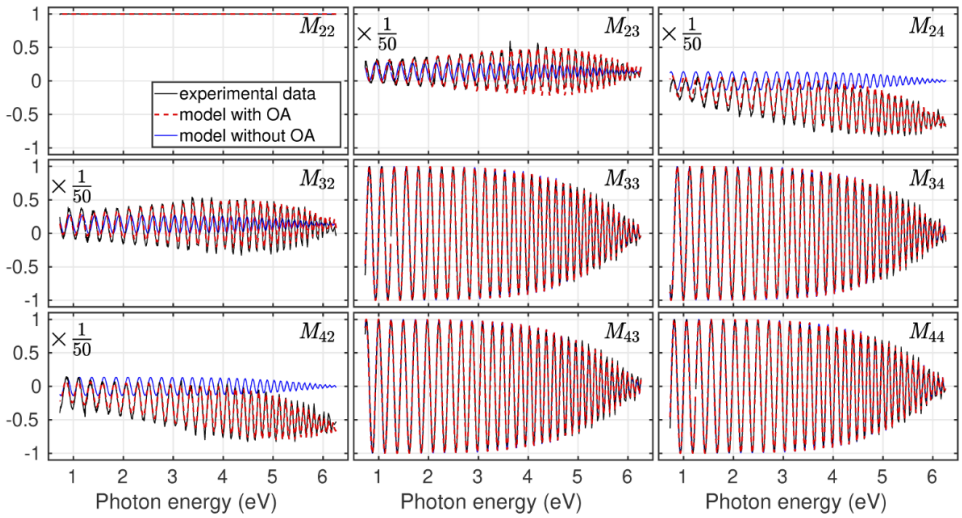


Figure 4.30: Comparison of experimental and theoretical Mueller Matrix elements of a quartz waveplate: The figure illustrates a comparison of experimental data (black solid lines) with two theoretical models: one including optical activity (OA, red dashed lines) and one without (blue solid lines). The plots show the Mueller retardation submatrix $m_{(2-4,2-4)}$ as functions of photon energy (eV). The comparison highlights the importance of including optical activity in accurately modeling the system's behavior.

Figure 4.30 displays the normalized Mueller submatrix $m_{(2-4,2-4)}$ obtained from measurements on a 536.63 μm thick quartz plate. The data indicated significant energy-dependent attenuation, which was not an intrinsic property of the sample. This attenuation was traced to an instrumental limitation of the spectrometer, specifically spectral averaging due to the finite bandwidth of the monochromator. The analysis incorporated Gaussian averaging with a defined width to model the data accurately. Additionally, a minor asymmetry in the data, attributed to the quartz's optical activity, was observed. This optical activity introduces a linearly independent contribution to the Mueller matrix, described as

$$\mathbf{M}_{\mathrm{R,EL}}(\varphi, \Gamma, \kappa) = \mathbf{M}_{\mathrm{R,LIN}}(\varphi, \Gamma) + \Delta\mathbf{M}_{\mathrm{OA}}(\varphi, \Gamma, \kappa), \tag{4.9}$$

where

$$\Delta\mathbf{M}_{\mathrm{OA}}(\varphi, \Gamma, \kappa) = \begin{pmatrix} 0 & 0 & 0 & 0 \\ 0 & 0 & 2\kappa \sin\Gamma & 4\kappa \cos 2\varphi \sin^2\frac{\Gamma}{2} \\ 0 & -2\kappa \sin\Gamma & 0 & 4\kappa \sin 2\varphi \sin^2\frac{\Gamma}{2} \\ 0 & 4\kappa \cos 2\varphi \sin^2\frac{\Gamma}{2} & 4\kappa \sin 2\varphi \sin^2\frac{\Gamma}{2} & 0 \end{pmatrix}, \tag{4.10}$$

where κ represents the chirality parameter. Figure 4.30 compares the experimentally derived Mueller submatrices with models that both include and exclude the effect of optical activity. The unexpected optical activity perpendicular to the optical axis required further analysis to understand its impact on the retardation determination.

Optical activity of quartz

Quartz exhibits optical activity due to its chiral crystal structure, a characteristic of its trigonal crystallization system [178]. In this system presented in Figure 4.31, the arrangement of silicon and oxygen atoms forms a helical structure that lacks inversion symmetry. This absence of inversion symmetry is crucial, as it means the crystal structure cannot be superimposed on its mirror image, making quartz inherently chiral. Quartz exists in two enantiomorphic forms, α-quartz and β-quartz, each capable of rotating polarized light to the left (levorotatory) or right (dextrorotatory). This enantiomorphism is a direct result of the screw axis along the crystallographic c-axis, which defines the direction of optical rotation.

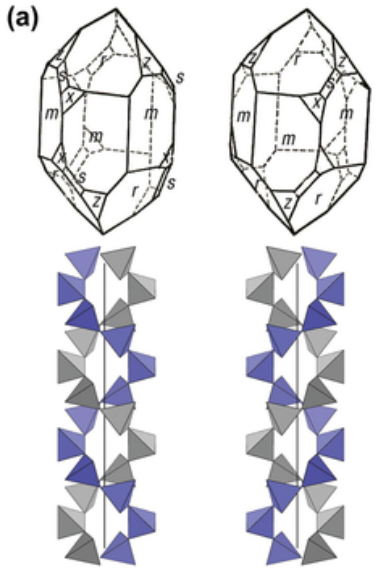


Figure 4.31: Quartz crystal faces and tetrahedral arrangement: The top part of the figure shows the crystal morphology of quartz with labeled crystallographic faces (m, r, s, z) for α and β-quartz enantiomers. The lower section illustrates the organization of SiO_4 tetrahedra along a c-axis within the quartz crystal, emphasizing the recurring units within the crystal lattice arranged in a spiral formation, significantly impacting its chiral properties. Adapted from [178]

However, quartz's optical activity is not uniform across all crystallographic axes. The crystal exhibits maximum optical rotation when light propagates along the c-axis, where the interaction between the helical crystal structure and the light is most pronounced. Conversely, the optical activity is significantly reduced when light travels perpendicular to the c-axis along any parallel axis. Therefore, detecting this initially weak effect through ellipsometry was unexpected.

We identified this manifestation as an optical activity through the Lu-Chipman decomposition [135]. The Lu-Chipman decomposition is a method used to break down a Mueller matrix M, which characterizes the polarization properties of an optical system, into three fundamental Mueller matrices: diattenuation (D), depolarization Δ, and retardation (R). The decomposition is expressed as:

$$\mathrm{M} = \mathrm{M_D} \cdot \mathrm{M_\Delta} \cdot \mathrm{M_R} \tag{4.11}$$

From the resulting retardation matrix, we were able to determine the presence of circular

birefringence. We extracted circular birefringence from the m_{32} and m_{23} matrix elements, as visible in (4.10). Figure 4.32 illustrates the slight rotating of the quartz plate's azimuth, as reported in [177]. This rotation alters the magnitude of the Mueller matrix element m_{32}, reflecting the interplay between birefringence and optical activity, while circular birefringence remains constant.

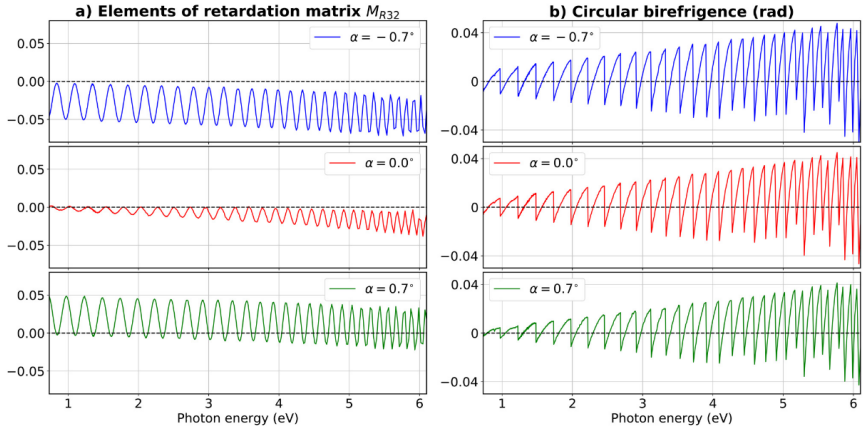


Figure 4.32: Comparison of retardation matrix elements and circular birefringence: a) Elements of the retardation matrix M_{R32} plotted as a function of photon energy for three different angles of incidence $\alpha = -0.7°$ (blue), $\alpha = 0.0°$ (red), and $\alpha = 0.7°$ (green). b) Circular birefringence (in radians) as a function of photon energy for the same set of incidence angles. The graph illustrates the variation of retardation about the angle while indicating that the birefringence remains constant. Adapted from [177]

Characterization of biplates

In the case of a single quartz plate, the effect of optical activity is measurable but relatively small. However, when characterizing quartz bi-plates, this effect significantly complicates the determination of misalignment between the optical axes of individual quartz plates. The Mueller matrix elements exhibit an interference-like pattern that increases with the misaligning plates' azimuths but does not decrease at small angles. This persistence is due to the coupling between misalignment and optical activity. Figure 4.33 demonstrates the Mueller matrix measurement with the systematic rotation of plates' azimuths. Optical activity prevents the oscillations from canceling out and provides an entirely different shape of oscillations than a model without optical activity. This refines the technique to determine both retardation and the misalignment between the plates by accurate modeling.

Summary of findings and impact of the study

The study demonstrates that neglecting the optical activity in the Mueller matrix model leads to inaccurate measurements of waveplate parameters, particularly the misalignment between waveplates in a biplate. The rigorous inclusion of optical activity is essential for precise waveplate analysis, especially for high-precision applications such as semiconductor manufacturing and polarimetry.

We demonstrated the exceptional sensitivity of visible-range ellipsometry by detecting optical activity in quartz waveplates, even when oriented perpendicular to the optical axis, where the effect

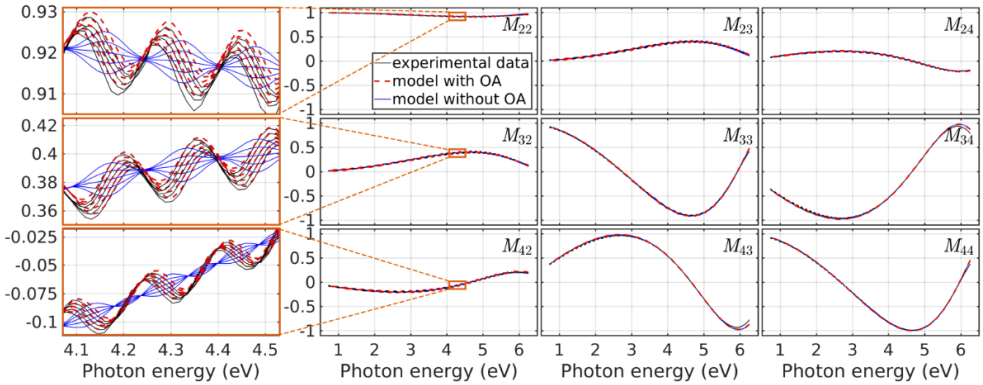


Figure 4.33: Comparison of experimental and theoretical Mueller matrix elements of quartz biplate: The figure shows a detailed comparison between experimental data (black solid lines), a theoretical model including optical activity (OA, red dashed lines), and a model excluding optical activity (blue solid lines) for various elements of the Mueller submatrix $m_{(2-4,2-4)}$ as functions of photon energy (eV). The left column highlights a zoomed-in view of the M_{22}, M_{32}, and M_{42} elements in the 4.1–4.5 eV range, providing a closer look at the fine interferences.

is considered negligible. We developed a rigorous theoretical model based on generalized Yeh's matrix algebra to account for optical activity in uniaxial chiral media. The proposed theoretical framework and model successfully quantify both controlled misalignment between waveplates and the influence of optical activity. This approach is particularly suited for studying general anisotropic materials and optical activity in the terahertz range. It represents a fast and noninvasive industrial tool for precisely managing waveplate misalignment during manufacturing.

My contributions

I actively contributed to the theoretical development of optical activity in bi-plates and validated this theory through numerical fitting with measured ellipsometric data. I conducted robustness checks to ensure the model's reliability. Additionally, I participated in the measurements, data processing, and interpretation. I collaborated closely with Daniel Vala on writing and revising the article and taking responsibility for preparing the graphics.

4.4 Ultra-broadband spin-driven photomixing

The thesis primarily focuses on applications of terahertz spintronic emitters in the time domain. However, they possess significant potential for high-resolution broadband frequency domain spectroscopy and ellipsometry [121]. Continuous terahertz waves are traditionally generated via photomixing [179, 180], a process based on optical heterodyne mixing of two coherent laser sources with a slight frequency offset corresponding to the desired terahertz frequency, as illustrated in Figure 4.34. When focused on a terahertz source, the laser beams induce photon absorption, which generates free charge carriers in a material. The interference pattern formed by the two laser waves leads to oscillations in the carrier density, producing an electric current at the difference frequency. This current is subsequently radiated as a terahertz continuous wave. The tunability of this method is achieved by adjusting the frequency difference between the laser beams, enabling precise control over the terahertz output frequency. Despite its versatility, photomixing has limitations such as low quantum yield, restricted device tunability, and relatively low terahertz output power.

At frequencies exceeding 1 THz, the efficiency of photomixing using photoconductive antennas declines sharply due to intrinsic physical limitations related to charge carrier dynamics and capacitive losses within the antenna [181, 182]. As the frequency increases, the material's recombination and transport rates become insufficient to match the high-frequency oscillations of the electromagnetic field, resulting in a reduction in the oscillating photocurrent and a corresponding decrease in terahertz radiation intensity. Additionally, increased capacitive impedance at higher frequencies restricts the antenna's ability to radiate efficiently. These combined factors lead to a marked reduction in terahertz output power, thereby driving ongoing research to enhance efficiency and explore novel materials to overcome these limitations [183, 184].

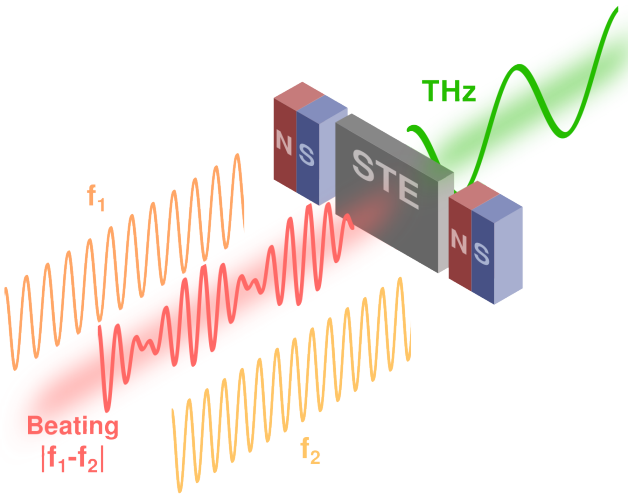


Figure 4.34: Generation of terahertz continuous wave using photomixing: Two input waves with frequencies f_1 and f_2 interfere, creating a beating pattern with a frequency difference $|f_1 - f_2|$. This beating envelope generates a modulated spin-current within a spintronic terahertz emitter (STE) in a magnetic field, generating THz radiation (green wave).

This thesis presents the proof of concept of terahertz spintronic photomixers, offering a broadband, gapless, and uniform spectrum. These photomixers enable tunable terahertz generation, effectively

addressing the limitations of traditional photoconductive antennas. The broadband response stems from ultrafast spin dynamics in metallic spintronic layers, driven by sub-picosecond (10–50 fs) demagnetization processes [98]. This ultrafast dynamic is facilitated by efficient coupling between spin currents and terahertz radiation through spin-orbit interactions in heavy-metal/ferromagnet heterostructures. As a result, the system generates a continuous and tunable terahertz spectrum across a wide frequency range, avoiding efficiency losses typically seen in conventional photomixing techniques at higher frequencies.

Moreover, spintronic materials enable room-temperature operation and scalability, positioning spintronic photomixers as a promising solution for next-generation terahertz sources. Although not yet published in a peer-reviewed journal, these findings were presented at the 48th International Conference on Infrared, Millimeter, and Terahertz Waves (IRMMW-THz), and a manuscript is currently under preparation.

4.4.1 Spintronic inverse spin hall photomixing beyond 1 THz

Pierre Koleják, Geoffrey Lezier, Guillaume Ducournau, Jean-François Lampin, Nicolas Tiercelin, Mathias Vanwolleghem

48th IRMMW-THz IEEE, (2023)

This study proposes a broadband spin-driven photomixing technique based on frequency comb spectroscopy. The method uses spintronic emitters' uniform spectral response and tunability, facilitating efficient terahertz generation driven by ultrafast spin dynamics across a broad frequency range. In our configurations, a mode-locked laser generates a sequence of pulses as illustrated in Figure 4.35, represented as a dense and equidistant series of comb lines in the frequency domain, driving the spintronic emitter. The repetition rate F_{rep} defines the spacing between the individual comb lines. Unlike continuous-wave, the pulsed operation enhances THz generation efficiency by focusing energy into concentrated bursts.

Subharmonic mixing is utilized for terahertz signal detection, with a local oscillator (LO) operating between 750 and 1050 GHz. This approach enables the down-conversion of high-frequency terahertz signals into intermediate frequencies (IF) within the detection range of conventional electronic systems. The difference frequency F_{Δ}, representing the offset between the LO and the comb lines, is defined as

$$F_{\Delta} = (n-1)F_{\mathrm{rep}} - F_{\mathrm{LO}}, \tag{4.12}$$

where n is the harmonic order. The IF signals are further given by

$$F_{\mathrm{IF}}^{\pm} = F_{\mathrm{rep}} \pm F_{\Delta}. \tag{4.13}$$

These frequencies correspond to the lower $(-)$ and upper $(+)$ sidebands of the intermediate frequency (IF). The down-conversion of high-frequency terahertz signals into GHz signals that is more easily

detectable. This method is essential for high-resolution terahertz spectroscopy, as it enables the detection and analysis of specific terahertz frequencies by tuning F_{LO}, efficiently accessing different parts of the spectrum.

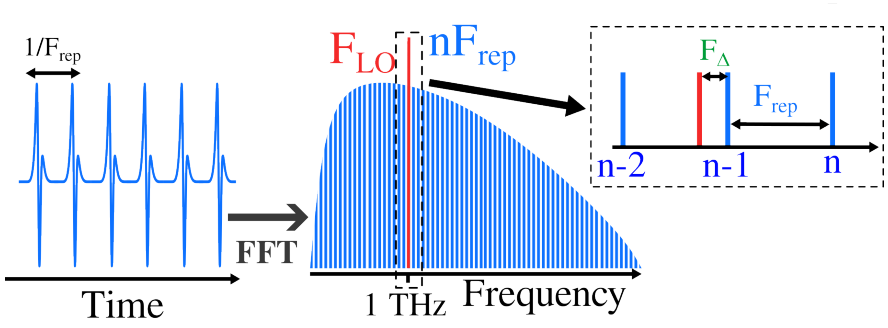


Figure 4.35: Schematic of terahertz frequency comb generation using a mode-locked laser: The temporal pulse train (left) with repetition rate F_{rep} is transformed into the frequency domain using a Fourier transform (FFT), resulting in a series of discrete frequency modes (blue). A local oscillator frequency F_{LO} (red) is mixed with the frequency comb to enable precise control over the comb lines across the terahertz range. The inset (right) shows the mode spacing, highlighting the repetition rate F_{rep} and the frequency offset F_{Δ} caused by the beating between the local oscillator and a specific comb line.

Instrumental challenges and stabilization techniques

The system measures the 750th to 1050th harmonics of frequency comb lines. Therefore, minor deviations in the repetition frequency result in errors in the detected intermediate frequency (IF) signals amplified by three orders of magnitude. Starting with the Menlo oscillator (1550 nm center wavelength, 1 GHz repetition rate, 245 mW excitation of STE), the repetition rate changed randomly by several kilohertz within a minute. This level of deviation is significant, as it causes the signal to shift out of the measurement window—typically on the order of kilohertz—making stable signal acquisition difficult without effective feedback control. Figure 4.36 shows the initial experimental results, which were highly unstable and drifting out of the span. The preliminary configuration made system adjustments challenging, as the signal frequently disappeared and was very low due to the lower efficiency of spintronic emitters with terahertz comb line energy on the order of -110 dBm.

To address this issue, a more stable Menhir solid-state laser amplified using an Erbium-Doped Fiber Amplifier (EDFA) was employed, generating pulses at a 1550 nm central wavelength, 1 GHz repetition rate, and 350 mW for spintronic terahertz emitter (STE) pumping. However, over a 10-minute interval, the observed repetition rate uniformly drifted by approximately 44 Hz, translating to a frequency drift of tens of kilohertz. Consequently, we constructed a feedback loop to stabilize the repetition frequency of the mode-locked laser, employing piezoelectric actuators to control the cavity length in real time. Figure 4.37 schematizes the feedback loop used to stabilize the repetition frequency of the mode-locked laser. The laser beam is directed into a photodiode to measure the repetition frequency (RF). The system utilizes a signal generator with a local oscillator signal (LO) frequency to reference the laser repetition rate and ensure stable operation. The RF and LO signals are then directed to an analogous photomixing unit, which detects the repetition rate deviations between the RF signal and the LO, denoted as $\Delta = \mathrm{RF} - \mathrm{LO}$.

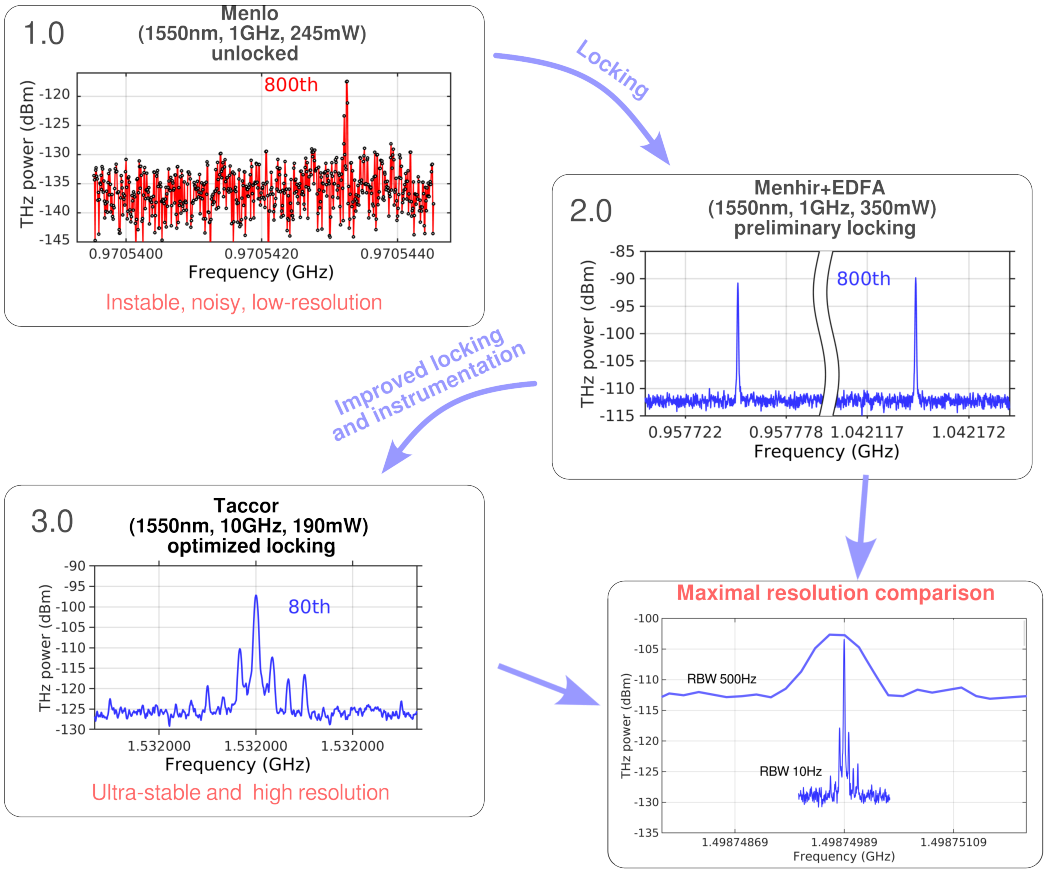


Figure 4.36: Evolution of frequency comb spectroscopy using spintronic terahertz emitters: The figure shows improved system performance regarding stability and spectral resolution. In (1.0), the unlocked Menlo system (1550 nm, 1 GHz, 245 mW) displays high noise, instability, and low resolution. In (2.0), preliminary locking of the Menhir+EDFA system (1550 nm, 1 GHz, 350 mW) significantly improves the signal stability and allows the observation of clear comb lines. In (3.0), the Taccor system (1550 nm, 10 GHz, 190 mW) with optimized locking achieves ultra-stable operation and high spectral resolution, resolving the 80th harmonic. The bottom-right panel compares the maximal frequency resolution, demonstrating a substantial improvement when reducing the resolution bandwidth (RBW) from 500 Hz to 10 Hz.

The fast piezoelectric transducer (PZT) actively adjusts the cavity length, enabling high-precision corrections to maintain the repetition frequency within the required stability range. The feedback control loop is closed by monitoring the output signal through the RF and error monitors, which provide real-time error signals. This configuration allows for highly precise and stable operation of the mode-locked laser, minimizing frequency drift and ensuring synchronization with external systems.

The introduction of this stabilization fundamentally improved measurement capabilities, as demonstrated in Figure 4.36. Previously, the system was constrained by rapid frequency drift, necessitating fast scans to capture meaningful data before the signal moved out of the detection window. As a result, performing multiple scans, long averaging, or high-resolution measurements was

impractical due to frequency instability, which led to inconsistent results. With stabilization in place, it became possible to conduct extended scans with higher resolution and to average across multiple measurements, significantly enhancing the terahertz spectral data's precision, reproducibility, and overall quality.

While this represented a significant improvement, the piezo actuators could maintain the feedback loop for approximately 20 minutes, with the custom-built locking system limiting the resolution bandwidth (RBW) to 500 Hz. Therefore, the system was upgraded by integrating a Taccor laser with a central wavelength 1550 nm and a repetition rate of 10 GHz. The commercially developed Taccor's feedback loop demonstrated significantly improved stability. The shift to the tenth harmonic resulting from the change in repetition rate led to a substantial reduction in frequency drift within the IF signal, amounting to an order-of-magnitude improvement. As illustrated in Figure 4.36, the final evolution step presents a high-resolution signal corresponding to an RBW of 10 Hz. The Taccor system demonstrates enhanced resolution in the lower-right corner, even detecting parasitic frequency lines from the repetition rate spectrum. It proves that the photomixed comb lines are ultra-narrow, which is the nature of the ultrafast response of spintronic emitters.

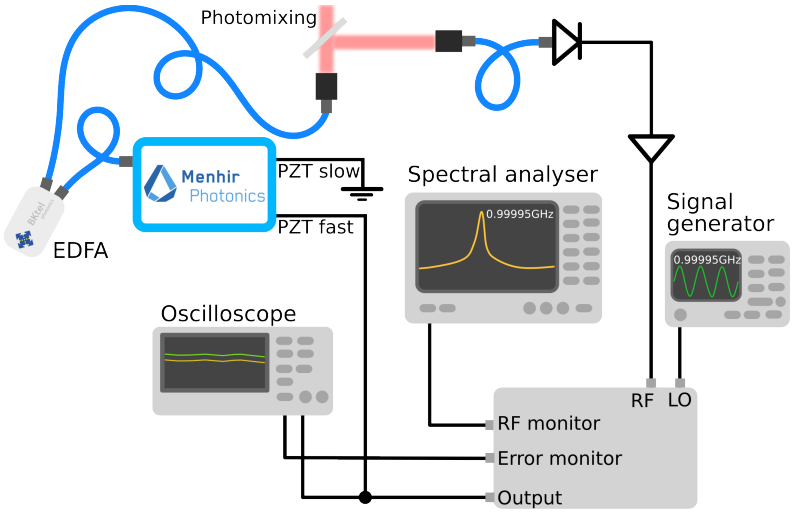


Figure 4.37: Scheme of a feedback loop to stabilize mode-locked repetition frequency: A mode-locked Menhir laser, amplified by an Erbium-Doped Fiber Amplifier (EDFA), is used for the frequency comb spectroscopy. The setup involves a signal generator that provides a local oscillator (LO) reference frequency. This frequency is then mixed with the measured repetition frequency using a photodiode. The spectral analyzer monitors the THz signal, while a piezoelectric transducer (PZT) with fast feedback loops stabilizes the system, ensuring precise repetition frequency control. An oscilloscope monitors the radio frequency (RF) signal - repetition rate- and the error signal, enabling real-time feedback.

Summary of findings and impact of the study

This study reports key terahertz generation advancements using spintronic Inverse Spin Hall Effect (ISHE) emitters. Through refinements in experimental setups, we demonstrate ultra-broadband THz photomixing at room temperature, with no frequency roll-off observed up to 1.05 THz, exceeding the performance of traditional methods. Integrating modelocked infrared lasers operating at a 1 GHz

repetition rate produced a stable, flat THz comb, with harmonics extending to the 1050th order. These findings demonstrate a significant improvement in photomixing technology.

Direct THz frequency comb generation from an infrared source presents a novel approach to THz comb spectroscopy, with potential applications in communication, sensing, and frequency comb terahertz ellipsometry. Room-temperature operation improves practical feasibility by eliminating the requirement for complex cooling systems. Theoretical models suggest that ISHE emitters could operate up to 10 THz, indicating considerable future potential. This study validates the performance of spintronic devices and establishes their critical role in advancing THz research and applications.

My contributions

In collaboration with Jean-François Lampin, I contributed to establishing the experimental setup that underpinned all subsequent experimental demonstrations. This research served as a proof of concept, with the initial conceptualization playing a pivotal role. I collaborated closely with Mathias Vanwolleghem and Jean-François Lampin during the initial phase. My primary responsibilities included constructing experiments, conducting measurements, and analyzing data. Our findings were presented in a conference proceeding at the 48th International Conference on Infrared, Millimeter, and Terahertz Waves (IRMMW-THz). Mathias Vanwolleghem and I co-authored the paper and created the accompanying graphics.

5

PUBLICATIONS

Paper I

Maximizing the electromagnetic efficiency of spintronic terahertz emitters

Pierre Koleják, Geoffrey Lezier, Daniel Vala, Baptist Mathmann, Lukáš Halagačka, Zuzana Gelnárová, Yannick Dusch, Jean-François Lampin, Nicolas Tiercelin, Kamil Postava, Mathias Vanwolleghem
Advanced Photonics Research, **2400064** (2024)

ADVANCED PHOTONICS RESEARCH
Open Access
www.adpr-journal.com

Maximizing the Electromagnetic Efficiency of Spintronic Terahertz Emitters

*Pierre Koleják, Geoffrey Lezier, Daniel Vala, Baptiste Mathmann, Lukáš Halagačka, Zuzana Gelnárová, Yannick Dusch, Jean-François Lampin, Nicolas Tiercelin, Kamil Postava, and Mathias Vanwolleghem**

Optically pumped spintronic terahertz emitters (STEs) have, in less than a decade, strongly impacted terahertz (THz) source technology, by the combination of their Fourier-limited ultrafast response, their phononless emission spectrum and their wavelength-independent operation. However, the intrinsic strength of the inverse spin Hall effect governing these devices introduces a challenge: the optical-to-terahertz conversion efficiency is considerably lower than traditional sources. It is therefore primordial to maximize at least their electromagnetic efficiency independently of the spin dynamics at play. Using a rigorous time-domain treatment of the electromagnetic generation and extraction processes, an optimized design is presented and experimentally confirmed. With respect to the strongest reported spintronic THz emitters it achieves a 250% enhancement of the emitted THz field and therefore an 8 dB increase of emitted power. This experimental achievement brings STE close to the symbolic barrier of mW levels. The design strategy is generically applicable to any kind of ultrafast spin-to-charge conversion (S2C) system. On a broader level, our work highlights how a rigorous handling of the purely electromagnetic aspects of THz spintronic devices can uncover overlooked aspects of their operation and lead to substantial improvements.

1. Introduction

Spintronic terahertz emitters (STEs) are currently attracting considerable research attention due to their versatility, ease of fabrication, and cost-effectiveness Seifert et al.[1] Bull et al.[2] Wu et al.[3] Seifert et al.[4] These emitters operate based on a femtosecond optical excitation of a nanometric stack of typically magnetic and non-magnetic metallic films, leading to ultrafast diffusion of spins from a ferromagnetic (FM) layer into adjacent heavy nonmagnetic (NM) layers with strong spin–orbit coupling (SOC). The inverse spin-hall effect (ISHE) deflection in the SOC NM layers is characterized by very fast relaxation times Kampfrath et al.[5] leading to a transient current dipole that is nearly Fourier-limited by the excitation pulse bandwidth. Femtosecond pump pulses thus generate near single cycle terahertz (THz) emission (**Figure 1**a). ISHE STE's offer many advantages over other traditional pulsed THz sources, being unhindered by phonon absorption, phase-matching requirements, and long relaxation times. The groundbreaking work by Seifert et al. demonstrated a broadband, gap-less spectrum spanning over 30 THz Seifert et al.[6]

ISHE THz pulses are independent of the pump wavelength and polarization, as they rely on an off-resonant generation of hot majority spin polarized carriers. This process depends only on the pump's fluence Papaioannou et al.[7] Herapath et al.[8] Moreover, these emitters are remarkably robust accommodating both collimated high-energy pulses on the order of millijoules at kHz repetition rates and tightly focussed low-energy pulses in the nanojoule range at sub-GHz repetition rates. At sub-MHz repetition rates, saturation and eventual thermal degradation sets in at a pump fluence of $\approx 5\,\mathrm{mJ\,cm^{-2}}$ Vogel et al.[9] while with increasing repetition rates the total average irradiance is the critical parameter. Highly confined fiber tip integrated STE's operate without degradation up to $1.5\,\mathrm{kW\,cm^{-2}}$ Paries et al.[10]

These observations underline that ISHE sources possess a highly scalable flexibility allowing to use any pump laser system for its specific characteristics (repetition rate, wavelength, power, frequency tunability, pulse duration, etc. Yamahara et al.[11] Takano et al.[12] This is nicely illustrated by the latest record

P. Koleják, D. Vala, L. Halagačka, Z. Gelnárová, K. Postava
Faculty of Materials Science and Technology
VSB – Technical University of Ostrava
17. listopadu 15, 708 00 Ostrava, Czech Republic

P. Koleják, G. Lezier, B. Mathmann, Y. Dusch, J.-F. Lampin, N. Tiercelin, M. Vanwolleghem
Université de Lille
CNRS
Centrale Lille
Université Polytechnique Hauts-de-France
UMR 8520 - IEMN
59000 Lille, France
E-mail: mathias.vanwolleghem@univ-lille.fr

The ORCID identification number(s) for the author(s) of this article can be found under https://doi.org/10.1002/adpr.202400064.

© 2024 The Author(s). Advanced Photonics Research published by Wiley-VCH GmbH. This is an open access article under the terms of the Creative Commons Attribution License, which permits use, distribution and reproduction in any medium, provided the original work is properly cited.

DOI: 10.1002/adpr.202400064

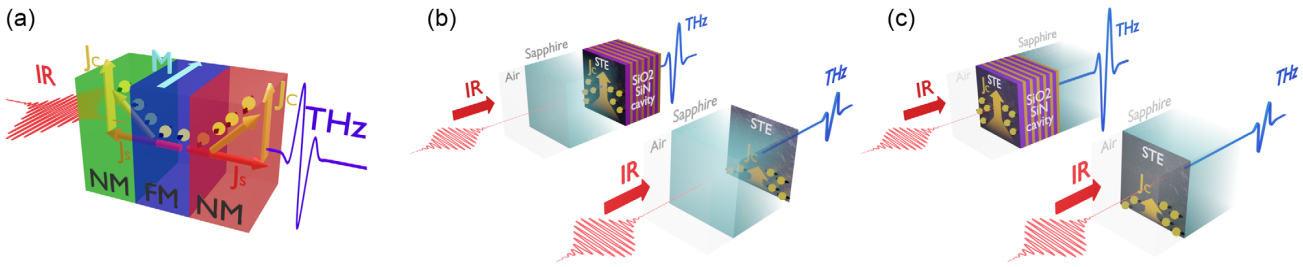


Figure 1. a) ISHE emitter principle: IR pulse activates a NM/FM/NM tri-layer under magnetization **M**, converting spin current j_s to charge current j_c and generating THz radiation. b) Sapphire/STE/cavity scheme: Details the excitation arrangement of the sapphire/STE/cavity sample in transmission geometry with its sapphire/STE reference. c) STE/cavity/sapphire scheme: Illustrates the meaning of STE/cavity/sapphire sample excitation configuration in transmission geometry and its STE/sapphire reference.

performance for W/CoFeB/Pt emitters. Exciting a large area emitter (5 cm diameter) with a collimated 2 cm wide beam of 5 mJ pulses (35 fs, 800 nm, 1 kHz) from an amplified Ti:sapphire laser generates record focal THz peak electric fields exceeding 1.5 MV cm^{-1} in sub-ps cycles with an integrated average THz power close to 100 μW Rouzegar et al.[13] Finally, with their easy lossless rotation of the emitted polarization plane by means of either a small rotating external magnet Hibberd et al.[14] Kong et al.[15] of a controlled Stoner–Wohlfarth rotation Koleják et al.[16] or even piezoelectrically controlled magnetoelastic rotation Lezier et al.[17] spintronic emitters have in a matter of just a few years taken an unique place as flexible, robust, and ultrabroadband THz sources. Their polarization control has even allowed modulation bandwidths up to 10 kHz and rates up to 10 MHz are within reach Gueckstock et al.[18] Lezier et al.[19]

The main drawback hindering a wider adoption of spintronic THz technology, is the low optical-to-terahertz efficiency, typically on the order of 10^{-5}–10^{-6} with respect to the total input energy Seifert et al.[6] This is at least one to two orders of magnitude lower compared to traditional optically pumped THz sources Fülöp et al.[20] STE's invariably require fs-lasers operating at multiwatt average power levels. Enhancing their conversion efficiency is a critical step toward achieving competitiveness with conventional THz sources.

In recent years, a lot of attention has been devoted to optimizing the pure spintronic aspects of the process: spin-current generation and S2C. Several excellent reviews give an overview of the different spin-generating and SOC materials that have been studied Seifert et al.[4] Bull et al.[2] Sinova et al.[21] Up till now, it proves hard to radically improve upon the performance of the sturdy Pt(2 nm)/CoFeB(1.8 nm)/W(2 nm)-system, though moderate increases have been reported by alloying the NM layers with Au to create spin sink effects and reduce spin reflection, and by replacing the FM spin injector by the semi-metal Heusler alloy Co_2MnGa for its very high degree of spin polarization Hawecker et al.[22] A promising new direction is to move toward strong interfacial S2C that occurs by spin momentum locking in inversion symmetry-broken systems. Such Inverse Rashba-Edelstein-Effect (IREE) systems are currently under heavy investigation with reports on Bi/Ag interfaces Jungfleisch et al.[23] on surface effects of several topological insulators ($SnBi_2Te_4$ Rongione et al.[24] Bi_xSb_{1-x} Rongione et al.[25] and Bi_2Se_3 Tong et al.[26] and recently monolayer Pt-based transition metal dichalcogenides Abdukayumov et al.[27]

With IREE emitters still undergoing further optimization and the mature ISHE emitters being led by the Pt/CoFe/W family, further improvements must come from extrinsic parameters in the generation, i.e., the electromagnetic design that determines the absorption of the pulse energy and the radiation of the current dipole into free space. A bare trilayer emitter absorbs only about 30–50% of the incident power in its spin-generation layer, and typical substrates are not impedance matched to free-space. Both factors combined reduce the generated charge current and the associated radiated THz E-field by nearly a factor ≈10, which amounts up to two orders of magnitude in radiated THz power. Increasing the extracted THz radiation has been achieved by integrating a hemispherical substrate-matched collimating lens Torosyan et al.[28] and by implementing antennas on the ISHE stack Nandi et al.[29] Talara et al.[30] albeit at the cost of redistributing the THz spectrum. Recycling unabsorbed IR pump photons more efficiently is a logical strategy for enhancing performance. By introducing a photonic layered structure, the confinement of the optical pump field in the FM layer can be maximized with minimal impact on the emitted THz field. The incorporation of a dielectric Bragg-like mirror has led to reports of an efficiency increase of a single STE by a factor of 1.9 Herapath et al.[8] Wagner et al.[31] Cascading multiple STEs is another way of recycling pump photons though this comes at the cost of increased THz losses Feng et al.[32] Jin et al.[33]

At present the research boom surrounding THz spintronics has led to a wealth of detailed insights concerning the intrinsic spintronic mechanisms, while the electromagnetic aspect of the devices' operation has remained less rigorously studied. Nevertheless, the optical perspective plays a crucial role in designing an optimal photonic geometry for the emitter. This applies both to the excitation and the emission processes at play. For instance, the pump absorption (and thus the efficiency) differs notably depending on whether the stack is excited from the substrate side or from the side of the metallic ISHE stack. Similarly, the emission is influenced by internal Fabry–Pérot reflections and scales differently toward either the substrate side or the air side.

It is the goal of this work to present a rigorous electromagnetic theoretical framework for metallic W/CoFeB/Pt-based ISHE

© 2024 The Author(s). Advanced Photonics Research published by Wiley-VCH GmbH

26999293, 0, Downloaded from https://onlinelibrary.wiley.com/doi/10.1002/adpr.202400064 by Technical University Ostrava, Wiley Online Library on [17/09/2024]. See the Terms and Conditions (https://onlinelibrary.wiley.com/terms-and-conditions) on Wiley Online Library for rules of use; OA articles are governed by the applicable Creative Commons License

26999293, 0, Downloaded from https://onlinelibrary.wiley.com/doi/10.1002/adpr.202400064 by Technical University Ostrava, Wiley Online Library on [17/09/2024]. See the Terms and Conditions (https://onlinelibrary.wiley.com/terms-and-conditions) on Wiley Online Library for rules of use; OA articles are governed by the applicable Creative Commons License

STE's and support this by experimental demonstrations of the predicted improvements. As the sub-picosecond dynamics of the emitter are a key aspect of its operation, we develop an original time-domain treatment correctly taking into account dispersion and non-stationary absorption. This theory is then applied for the design of an optimal structure that maximizes all aspects of the photonic processes at play. The experimental results confirm the numerical predictions by demonstrating THz peak field emissions enhanced by nearly 300% with respect to a bare reference emitter.

The article is organized as follows: The Results section begins with presentation of our optimization strategy focused on electromagnetic efficiency. We delve into key processes such as excitation and emission in STEs, reconstruction of Fourier responses, and the comprehensive optimization of our STE-SiO_2/SiN_x-cavity samples. Further, we demonstrate the enhancement of our cavity-integrated spintronic emitters, comparing them to traditional STEs using time-domain spectroscopy (TDS) and Fourier analysis. We also verify the linear correlation between THz emission and pump power in ISHE STE-cavity emitters, and explore how excitation wavelength affects THz enhancement. In the Discussion section, we demonstrate through simulation the critical role of the SiO_2 phase-matching layer in cavity design, which is essential for phase alignment and interference control. We show the optimal thickness is key to ensuring the absorption spectrum aligns correctly with the pump pulse. Thereafter, we delve into the efficiency of spintronic emitters, particularly in terms of THz extraction into free space and in the substrate direction. The performance and efficiency of STEs in various configurations, with and without photonic cavities, are thoroughly evaluated. The subsection Further improvement and outlook examines how substrate choice impacts the efficiency of STE, analyzing the effects of different substrates on absorption and THz emission. In conclusion, the article presents a cohesive overview of the advancements and potential further improvements in the field of STEs.

2. Results

2.1. Optimization Strategy

As has been noted, the traditional STEs do not exploit their full potential and exhibit a rather limited absorption of only 30–50% of the optical pump power. A significant portion of the incident power is wasted due to reflection and transmission losses. However, by effectively recycling the unused pump photons and optimizing the extraction of generated THz photons from the STE, we can achieve an extraordinary enhancement of the optical-to-terahertz efficiency. This electromagnetic perspective of STEs has never really been systematically studied. Their optimization has been primarily centered around spintronics, material engineering and magnetism Seifert et al.[4] Feng et al.[34] Papaioannou and Beigang,[35] Wu et al.[3]

Therefore, we have developed a theoretical electromagnetic framework (described in detail in Supporting information 1-4), that rigorously treats the pulsed excitation and emission processes to optimize STEs. It is based on the following numerical steps: 1) Discretization of the given excitation spectrum into individual monochromatic plane waves (Fourier series); 2) Calculation of optical response of each individual Fourier term, employing the scattering matrix formalism; 3) Reconstruction of the Fourier responses to estimate the time-dependent spatial absorption through Poynting's theorem, providing valuable insight into the absorption dynamics; 4) Utilization of this time-dependent absorption in the spin pumping layer as a source for temporal dipole emission by applying the scattering matrix formalism; and 5) Global optimization of a) the IR pump absorption within the desired temporal interval and specific layers or of b) the output THz signal. The goal function (a) is well-suited for resolving problems related to single THz pulse emission, especially when increased absorption plays a direct role in the THz generation process. However, the optimization of the IR pump absorption can introduce detrimental side-effects on the THz extraction part of the electromagnetic problem, by for instance introducing extra THz losses, Fabry–Pérot effects or even multiple pulse effects. Therefore approach (b) is the more robust choice for optimizing an arbitrary structure to achieve maximum THz total power or peak power. It is however considerably more time and memory consuming. Using our approach an optimized photonic cavity is designed that efficiently traps nearly the entire spectral power of the pump laser in the magnetic spin pumping layer. For this trapping, we have opted for 1D SiO_2/SiN_x distributed dielectric layer pairs (a DBR mirror) as the resulting photonic crystal structure becomes only a few microns thick, impacting minimally the phase of the generated THz wavelengths and therefore minimally hindering THz extraction. The thicknesses of the individual layers of this photonic cavity were optimized for maximal enhancement using a global optimization (combination of Simplex and Differential evolution algorithms Oldenhuis,[36] Lagarias et al.[37] Previous studies have primarily focused on augmenting absorption by placing a photonic trapping cavity on top of the STE and pumping the structure through the substrate. Such configurations have led to notable yet limited improvements of 60–80% of the STE electric peak-to-peak field strength Herapath et al.[8] Jin et al.[33] Wagner et al.[31] However, our innovative approach takes into consideration an alternative excitation geometry, namely the STE/cavity/substrate arrangement, implying a pump excitation from the metallic emitter side and a THz extraction through the substrate. Throughout the article, we apply this notation to outline the layer sequence of structures exposed to IR excitation. Figure 1b,c illustrate the difference between the STE/cavity/substrate design (c) and the common substrate/STE/cavity (b) arrangements, along with their corresponding references without cavities. It will be shown that The STE/cavity/substrate yields even higher levels of enhancement and superior overall performance. Notably, a recent study by Rouzegar et al. employed the STE/cavity/Si configuration, leading to twofold amplitude improvement Rouzegar et al.[13] We will show that our approach achieves further emission improvements and also sheds light on many mechanisms from an optical perspective. Specifically, we present a design that delivers an 2.45-fold THz field emission enhancement. This structure addresses the overlooked absorption disparity between STE/substrate (32%) and substrate/STE (50%). We also consider the enhanced extraction of the THz field toward the substrate direction as a significant factor. In the next

© 2024 The Author(s). Advanced Photonics Research published by Wiley-VCH GmbH

section, the experimental demonstration of this optimization strategy is presented.

2.2. THz Pulse Peak-to-Peak and Power Spectral Density Increase of PhC-Enhanced STE's

We performed thorough TDS measurements to evaluate the emission performance and improvement of the sapphire(0.5 mm)/STE/cavity and STE/cavity/sapphire (0.5 mm) configurations in transmission geometry. The cavity consists of 6 SiO_2(139 nm)/SiN_x(100 nm) cells for 808 nm, where the SiO_2 layer in the first cell is modified to 160 nm, and its optimization is explained in Section 3.1. We utilize an optimized Pt(2.1 nm)/CoFeB(1.9 nm)/W(2 nm) trilayer as the STE emitter. More details on the experimental setup and the sample fabrication process are provided in the Section S5, Supporting Information, where the used calibration technique is detailed. The estimated relative precision on the thickness of the STE layers is of the order of 10%. Simulations have shown that the optimization design is robust with respect to such subnanometric deviations. The agreement between the obtained experimental performance and the predicted simulated enhancement proves that the targeted thicknesses are reached with sufficient precision. **Figure 2**a,b plot the measured temporal traces for both geometries: 1) sapphire/STE/cavity; and 2) STE/cavity/sapphire, pumped with 73 mW of average power. For both configurations, the THz temporal pulses generated by the reference emitter (non-augmented by a cavity), fabricated in the same run on the same substrate, are plotted in red, $S_{ref}(t)$. The blue trace $S_{PC}(t)$ represents the STE integrated with the optimized photonic cavity measured under the same pump power. Note that in these figures, the traces are normalized with respect to the peak amplitude of the reference emitter. In both cases the trapping photonic cavity clearly amplifies the peak-to-peak amplitude of the generated THz pulses, by a factor 1.5 for configuration (I) and a remarkable 2.45 for configuration (II). Previous attempts in the literature did not achieve such a significant increase in emission Herapath et al.[8] Rouzegar et al.[13] Feng et al.[32] As the S2C depends in first instance on the energy delivered to the spin reservoir, the cost function for the design optimization is the electromagnetic absorption in the FM layer. The optimization predicts absorbance increases from 50% to 89% for (I) (i.e., by $\times 1.78$) and from 32% to 95% for (II) ($\times 2.97$), respectively. The measured peak-to-peak enhancement $S_{pp,PC} = A_{pp} \times S_{pp,ref}$ follows these predictions. Obviously, a full 100% absorbance in the FM layer can not be reached because of unavoidable reflection losses and the impossibility to perfectly confine the pump field. We also provide evidence of the spintronic origin of the emitted THz radiation by observing a reversal in polarity when the magnetic field is reversed from 11.14 to -11.14 kA m^{-1} (vertically shifted traces in Figure 2a,b). Apart from the slight influence by water absorption, leading to the presence of minor long Lorentz damped oscillations in the time domain, a striking feature in these measurements is the appearance of a strong echo in the sapphire/STE/cavity configuration (I). This reflected echo is suppressed in the STE/cavity/sapphire configuration thanks to a broadband anti-reflection phenomenon Kröll et al.[38] Ding et al.[39] Carli,[40] as schematically shown in Figure 2c. Forward-emitted THz pulses, when reflecting off the bottom of the substrate, produce weaker replicas that are delayed by twice the substrate's propagation time ($\Delta\tau = 2n_{Al_2O_3}d_{Al_2O_3}/c \approx 10$ ps). However, when pulses reflect

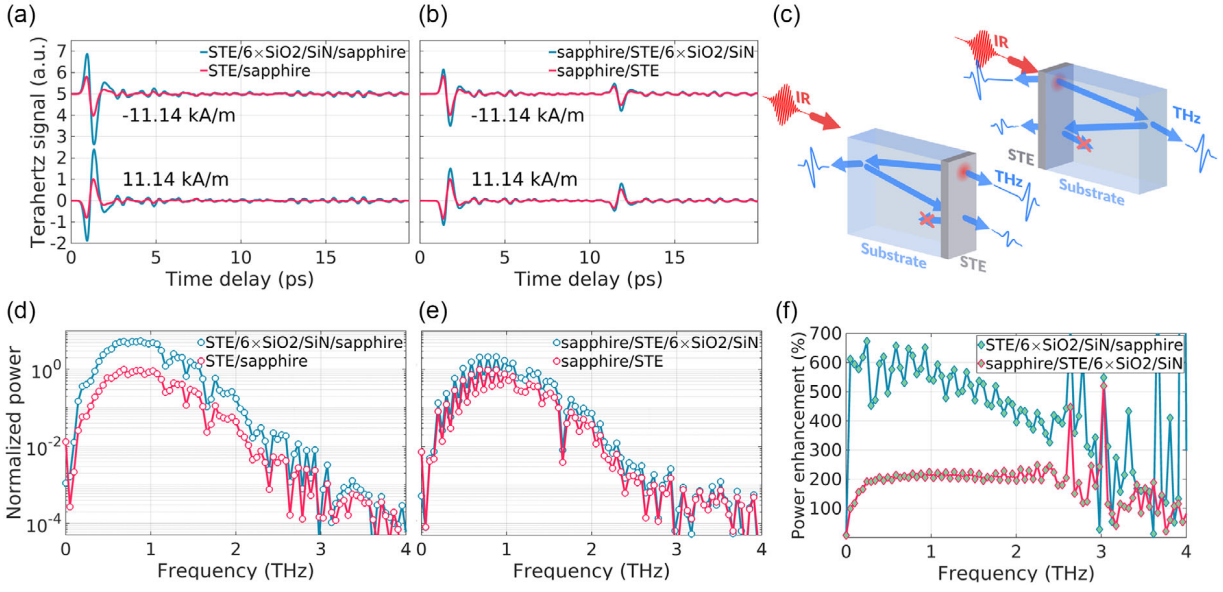


Figure 2. a) Comparison of measured THz emission for STE/cavity/sapphire sample and its STE/sapphire reference under magnetic fields of 11.14 and -11.14 kA m^{-1}. b) Measured THz emission comparison for sapphire/STE/cavity sample and sapphire/STE reference in magnetic fields of 11.14 and -11.14 kA m^{-1}. c) Diagram explaining the origin of THz echoes in measured signals for sapphire/STE and STE/sapphire geometries. Where the anti-reflective coating effect suppresses direct reflections from the STE. d) Spectral power of the STE/cavity/sapphire sample and comparison with its STE/sapphire reference. e) Spectral power comparison of the sapphire/STE/cavity sample against its sapphire/STE reference. f) Shows the enhancement spectrum of STEs integrated with photonic cavities, comparing the STE/cavity/sapphire and sapphire/STE/cavity configurations.

© 2024 The Author(s). Advanced Photonics Research published by Wiley-VCH GmbH

26999293, 0, Downloaded from https://onlinelibrary.wiley.com/doi/10.1002/adpr.202400064 by Technical University Ostrava, Wiley Online Library on [17/09/2024]. See the Terms and Conditions (https://onlinelibrary.wiley.com/terms-and-conditions) on Wiley Online Library for rules of use; OA articles are governed by the applicable Creative Commons License

off thin metallic layers, they result in almost perfect antiphase interference rather than a simple reflection. This effect is attributed to the nanometer thickness of these layers and the imaginary component of their Drude THz permittivity.

The squared modulus of the Fourier transforms of the TDS signals (of 20 ps window) presented in Figure 2d,e, reconfirm clear evidence of signal improvement across the entire spectrum of the STE signal, while the noise level remains unchanged. Not only is there a significant increase of the dynamic range in configuration (II), its spectrum is devoid from interference fringes due to the echo. Contrary to an electrooptic sampling, exact knowledge of the calibrated transfer function of the THz photoconductive receiver is not straightforward to determine Kampfrath et al.[41] As a result, absolute values for the transient electric field strength of the THz pulse are hard to extract out of our measurements. However, we can estimate the relative power increase of the PhC enhanced STE's by integrating the ratio of the TDS spectra $|\mathcal{S}_{\mathrm{PC}}(\omega)|^2/|\mathcal{S}_{\mathrm{ref}}(\omega)|^2$ (Figure 2d,e).

These integrated ratios yield values of 2.12 and 5.64, which closely match the increase predicted by merely considering the square of the peak-to-peak signal enhancement $A_{\mathrm{pp}}^2 = 1.5^2 = 2.25$ and $2.45^2 = 6$. The frequency-dependent ratios before integration illustrated in Figure 2f, suggest a consistent enhancement across the spectrum. This is attributed to the fact that the proportional change in absorption do not impact the dynamics of ISHE emission, and thus does not influence the THz spectrum. This phenomenon is observed in the Sapphire/STE/Cavity sample, but not in the STE/Cavity/Sapphire sample, for reasons that remain unclear to us. One possible explanation might be the different sequences in the fabrication of the STE and the cavity. In the STE/Cavity/sapphire configuration, the cavity is exposed to higher temperatures during STE deposition, potentially leading to changes in material properties. At low THz frequencies, the enhancement actually reaches predicted 600% compared to the integrated average of 564%, suggesting a decrease in efficiency at higher frequencies. However, at these higher frequencies, the signal is markedly weaker, which makes the inconsistent efficiency reduction almost unnoticeable in the time domain.

Configuration (II) increases the power conversion efficiency of Pt/CoFeB/W-emitters by almost 8 dB (implying an additional 2 dB enhancement with respect to Rouzegar et al. Rouzegar et al.[13]). Our operation at 80 mW (after the chopper) and 80 MHz results in pulses with a maximum energy of 2.0 nJ, limiting demonstration to TDS temporal trace analysis. Yet, extrapolating Rouzegar's findings suggests our configuration could potentially achieve >150 µW average THz power with high-energy pumping (5 mJ pulses). This would make spintronic THz emitters competitive with, and superior in pulse bandwidth to, conventional pulsed THz sources.

2.3. Pump Power and Wavelength Dependence

The transient current created in ISHE emitter is intrinsically proportional to the absorbed energy in the spin pumping layer. The THz field should thus be linearly dependent on the pump power. To validate this, we conducted an experimental power sweep using a tunable attenuator. This power adjustment was performed behind the chopper (see Section S6, Supporting Information). The power was swept from 0 to 80 mW. **Figure 3**a plots the variation of the peak-to-peak TDS signal of STE/Cavity/sapphire as a function of pump power (measured separately before each experiment). Over the entire range, a perfect linear dependence is observed, confirming the functional efficiency of cavities the structural integrity and non-saturating behaviour with increasing power. This is unsurprising as the pumping conditions (≈0.05 mJ cm^{-2} maximal fluence) are very conservative, compared to the reported damage thresholds Vogel et al.[9] Paries et al.[10]

An important advantage of the ISHE is its independence with respect to the center wavelength of the pump pulse Papaioannou et al.[7] This is a direct consequence of the superdiffusive spin transport models that have successfully described the THz transient dipole current in ISHE STE's Battiato et al.[42] The amplitude of the spin current at its origin is primarily determined by the energy dumped in the electron bath of the FM layer which has a broad largely wavelength independent absorption spectrum (see Section S7, Supporting Information). The wavelength dependence of the STE is therefore dominated by the electromagnetic response of the cavity system to the pump. This is again a clear argument in favour of devoting more attention to this aspect. We performed emission analysis while adjusting the excitation wavelength of the tunable Ti:sapphire oscillator Mai Tai-HP to investigate its impact on the predicted THz enhancement.

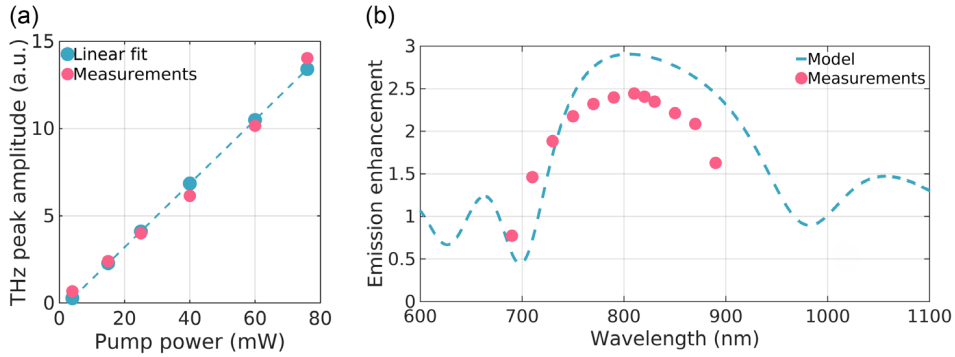


Figure 3. Demonstration of the robustness of STE/cavity/sapphire emitter: a) Generated electric field's linear response to varying average powers of an 808 nm, 100 fs IR pump pulse. b) Enhancement of THz amplitude with changing central wavelengths of the excitation pulse (under the same power) compared to model expectations.

© 2024 The Author(s). Advanced Photonics Research published by Wiley-VCH GmbH

26999293, 0, Downloaded from https://onlinelibrary.wiley.com/doi/10.1002/adpr.202400064 by Technical University Ostrava, Wiley Online Library on [17/09/2024]. See the Terms and Conditions (https://onlinelibrary.wiley.com/terms-and-conditions) on Wiley Online Library for rules of use; OA articles are governed by the applicable Creative Commons License

The oscillator's pulse duration is guaranteed to be sufficiently constant over its tuning range. It is therefore expected that the THz peak-to-peak enhancement will emulate the absorption spectrum of the designed photonic structure. This is presented in Figure 3b, plotting the ratio of the peak THz values for the STE/Cavity/sapphire configuration relative to the STE/sapphire sample, as a function of central wavelength. In doing so, we factor out the wavelength dependence of the average power of the laser oscillator. The measured enhancement follows qualitatively the modelled absorption spectrum of the designed photonic cavity and especially reproduces correctly the predicted spectral position of the gap of the DBR mirror. Even though the model predicts a 20% higher enhancement, the observation of maximum efficiency at 808 nm suggests accurate fabrication of the structure's bandgap and a reliable model used for the layers optimization strategy.

Thermal effects might explain the discrepancy between theoretical models and actual measurements. The ISHE's conversion efficiency is very low, around 10^{-5}–10^{-6}, meaning almost all pump power must be dissipated. Although sapphire substrates in traditional ISHE STEs serve as decent heat sinks, the thermal resistance significantly increases with the addition of a SiO_2/SiN_x DBR mirror Burghartz and Schulz,[43] Shan et al.[44] Talghader,[45] Sinha et al.[46] Kumar et al.[47] This, coupled with a threefold increase in power absorption, likely impacts the device's thermal management, an aspect not yet considered in our analysis but warrants further investigation.

3. Discussion

Having experimentally demonstrated the 245% THz field enhancement induced by the photonic cavity in the STE/cavity/substrate configuration, we delve a bit deeper into the design considerations having led to this optimised structure. This discussion will equally reveal why both pumping configurations (STE/cavity/substrate vs substrate/STE/cavity) behave drastically different despite nearly equal pump absorption. This section will conclude by an outlook on how to further improve STE emitters from an electromagnetic point of view.

3.1. Integrating PhC with STEs: Design and Optimization

Our cavity design features a SiO_2/SiN_x DBR mirror, enhanced by an additional SiO_2 layer acting as a phase-matching layer. This layer is crucial as it introduces an extra variable to counteract the phase shift from the Bragg mirror, thus fine-tuning the interference within the FM layer. Our experiments show that six pairs of SiO_2/SiN_x are adequate for effective trapping, with additional pairs not further improving FM layer absorption. The thickness of the SiO_2 phase-matching layer was optimized to 159 nm for the sapphire/STE/Cavity and 162 nm for the STE/Cavity/sapphire, resulting in configurations of (I): Sapphire/STE/SiO_2 (23 nm)/6× [SiO_2(139 nm)/SiN_x(100 nm)] and (II): STE/SiO_2 (20 nm)/6× [SiO_2(139 nm)/SiN_x(100 nm)]/Sapphire.

In both configurations (I) and (II), only the layers of the cavity structure were varied during the optimization procedure. The Bragg mirror converges to a 239 nm thick unit cell: SiO_2(139 nm)/SiN_x(100 nm). This is a logical consequence of optimizing a trapping structure centered around 808 nm. Each layer in the unit cell presents approximately a $\lambda/4$ of the material at 808 nm Malitson,[48] Luke et al.[49]

To demonstrate the impact of the phase-matching SiO_2 layer's thickness, we conducted simulations over a range of 100–250 nm. The results of this fine-tuning compensation are evident in the alteration of the infrared field distribution, as shown in **Figure 4**a,b, with varying the SiO_2 layer thickness. When the thickness is not optimally set, the interference maximum is positioned outside the spintronic layers (curves in blue shades), leading to significant field reflection and transmission through the cavity, and consequently, low overall absorption.

While the SiO_2/SiN_x cavity is engineered to produce a bandgap at 808 nm, the misalignment in phase across different STE/(phase-matching layer) configurations results in the absorption bandgap shifting to different wavelengths. This shift occurs when the standing wave at these wavelengths fulfills the criteria for enhancing the field in the spintronic emitter, but not necessarily for a pulse at 808 nm. Figure 4e,f illustrates the transformation of the absorption spectrum (shown in shades of blue) compared to the spectrum of a 100 fs pulse with a central wavelength of 808 nm. After optimizing the SiO_2 layer, ≈160 nm for both cases, including a 20 nm phase-matching layer, the absorption spectrum is aligned with the pulse spectrum. However, at the optimal thickness the interference maximum of the field is aligned within the spintronic layers in Figure 4a,b. This alignment effectively minimizes reflection and transmission from the structure. The cavity on the STE side is terminated with SiO_2, selected because the electric field in the distributed Bragg reflectors reaches an interference maximum in materials that are optically less dense. Consequently, at the interface with STE, the field strength is inherently high. This implies that the phase alignment is close to optimal with the current thickness of the basic cell, and only a small adjustment is required for additional phase correction. While the structure can alternatively be terminated with SiN_x, achieving phase reversal in the optically denser medium generally necessitates adjustments that approximate the thickness of the original layer. Technologically, extending the SiO_2 layer by 20 nm is more feasible than depositing a substantially thicker SiN_x layer.

In a more direct approach, we demonstrate the changes in total absorption and the corresponding alterations in the central wavelength of the absorption spectrum on the varying thickness of the SiO_2 layer. Figure 4c,d effectively illustrates these changes, where each marked point corresponds to an optimized solution for a 100 fs excitation pulse. The optimized solutions we obtained correspond to the peaks in the absorption curves. It is crucial to emphasize that the thickness dependency is not overly acute, thereby enabling fabrication within a few nanometers of precision. As anticipated, the solution's bandgap central wavelength is found to be around 800 nm.

The design and fabrication of structures for sub-100 fs pulses is inherently more challenging. Shorter pulses exhibit a broader spectrum to align with an equally broad bandgap. For pulses as short as about 10 fs (≈3 μm in the air), their dimensions become comparable to the cavity size itself. In these scenarios, the temporal evolution of interference patterns, especially during the reflection of the pulse from the cavity, emerges as a critical aspect. Consequently, the design of cavities should give primary

© 2024 The Author(s). Advanced Photonics Research published by Wiley-VCH GmbH

26999293, 0, Downloaded from https://onlinelibrary.wiley.com/doi/10.1002/adpr.202400064 by Technical University Ostrava, Wiley Online Library on [17/09/2024]. See the Terms and Conditions (https://onlinelibrary.wiley.com/terms-and-conditions) on Wiley Online Library for rules of use; OA articles are governed by the applicable Creative Commons License

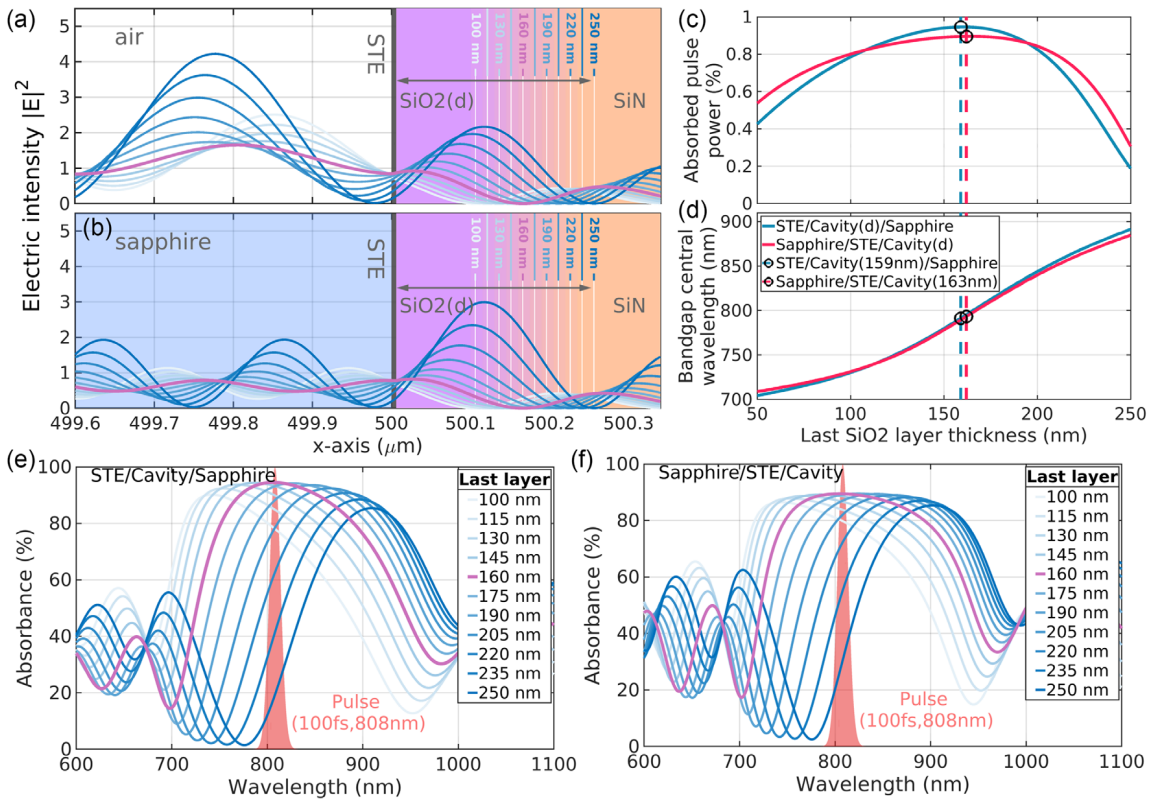


Figure 4. Sensitivity analysis of STE/cavity/sapphire and sapphire/STE/cavity to variation of the phase-matching SiO_2 layer thickness: a,b) Variation of the electric intensity of the infrared pump beam (curves in blue shades) near the spintronic layers as a function of varying thickness for the last phase matching SiO_2 layer in the DBR structure (100–250 nm). The variation of the SiO2 layer is depicted with a linear gradient and lines illustrating individual thicknesses. The optimal configuration (160 nm - magenta) achieves maximum field intensity within the spintronic layers for both configurations. c) Comparison of changes in the absorbed energy of an excitation pulse (100 fs, 808 nm) and d) the central absorption spectrum wavelength with different SiO_2 layer thicknesses. Optimized solutions are marked. e,f) Absorption spectrum transformation in STE/cavity/sapphire and sapphire/STE/cavity structures with varying SiO_2 thickness. The shaded blue curves illustrate the bandgap shift across wavelengths, while the magenta line approximates the 160 nm solution corresponding to a pulse (100 fs, 808 nm), whose spectrum is shown for comparison.

importance to femtosecond pulse considerations, rather than to the design based on infinite monochromatic waves at the central wavelength of the pulse.

Note that this distinguishes this design from a Tamm plasmon surface state between a metal and a DBR mirror Kaliteevski et al.[50] Jiang et al.[51] A Tamm plasmon resonance searches to create a surface eigenstate with a moderate quality factor confined near a metal but at in-plane wave vectors accessible by direct optical excitation. Here the goal is to maximize the absorption inside the metal of the incidence pulse rather than to achieve a resonant field buildup near the metal. It can be seen from Figure 4e,f that the pump absorption is not peaked at any wavelength but high over the entire pump pulse spectrum.

3.2. Generation Process

To provide further insights into the performance of both STE geometries, we present the estimated spectral absorbance, transmittance, and reflectance in **Figure 5**a, specifically comparing a conventional sapphire-based STE (dashed lines) with a cavity-enhanced STE (continuous lines). The optical characterization of CoFeB and the resulting material properties are detailed in Section S7, Supporting Information. For the other metallic and dielectric layers, the optical functions were found to be in good agreement with the tabulated values for Palik,[52] J.A. Woollam,[53] sapphire J.A. Woollam,[54] SiN_x Luke et al.[49] and and SiO_2 Malitson,[48] and are utilized in simulations throughout the entire article. In Figure 5a the red and blue curves refer to respectively pumping from the substrate or the spintronic stack. Due to reciprocity the transmittance of a bare emitter is independent of its excitation direction. One would therefore be tempted to conclude that the excitation sense with the lowest reflectance, i.e., sapphire/STE, will inevitably lead to the strongest THz emission. As will be seen in Section 3.3, this is not necessarily true. The integration of a cavity in both excitation geometries creates a bandgap that nearly perfectly recycles the pump photons: the transmittance through the DBR mirror is in both cases lower than 3% over the bandgap. For a comprehensive overview, we present the integrated total absorbance (A), transmittance (T), and reflectance (R) of the IR pulse (100 fs, 808 nm) in Figure 5b (the pair on the right), accounting for contributions from Fabry–Pérot reflections and the effects of all interfaces.

© 2024 The Author(s). Advanced Photonics Research published by Wiley-VCH GmbH

26999293, 0, Downloaded from https://onlinelibrary.wiley.com/doi/10.1002/adpr.202400064 by Technical University Ostrava, Wiley Online Library on [17/09/2024]. See the Terms and Conditions (https://onlinelibrary.wiley.com/terms-and-conditions) on Wiley Online Library for rules of use; OA articles are governed by the applicable Creative Commons License

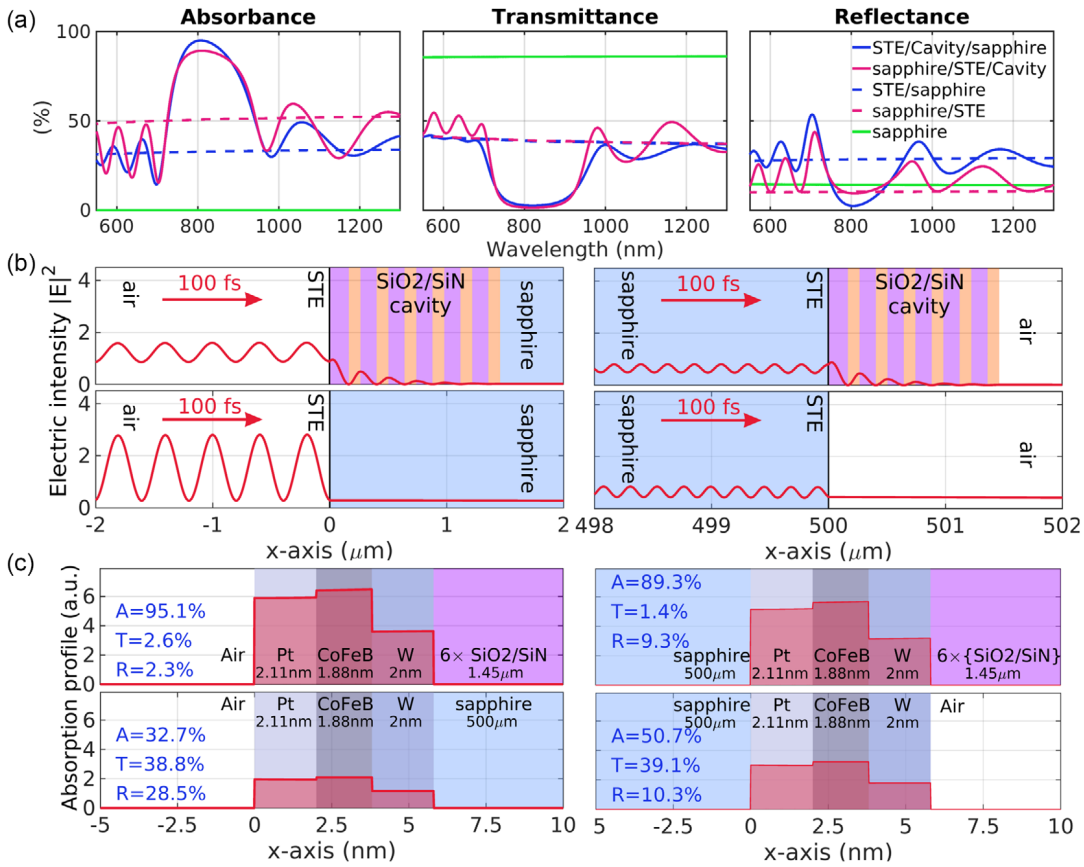


Figure 5. Analysis of absorption during IR excitation: a) Calculated absorbance, transmittance, and reflectance from extracted material properties for the studied sample configurations, shown in a non-coherent approximation (excluding coherent interference with substrate reflection). b) Distribution of the $|E|^2$ field during excitation with a 100-fs pulse (arrow indicates direction) in STE-cavity and their STE references, demonstrating changes in the reflected, absorbed, and transmitted intensities and field distribution within spintronic layers. c) Absorption distribution $Q(x,t)$ across Pt, CoFeB, W layers. Each subplot's left side summarizes the excitation pulse conversion into absorption, transmission, and reflection for each configuration.

In the substrate/STE/cavity configuration, the DBR cavity effectively reduces the transmission of pump photons and converts it to absorption, but it does not significantly reduce the internal reflection from the STE layers, which are inherently low. The total reflectance of the structure remains at least always at the same level as without the cavity (comparing the full and dashed red curves in Figure 5a). In this scenario, the main factor contributing to reflectance is the reflection at the air/sapphire interface, which accounts for losses of ≈7.6%. Given that the total reflection amounts to ≈10%,, the reflection from the sapphire/STE interface makes a minimal contribution, amounting to just a few percent, even in the absence of a cavity. This is fundamental consequence of the different phase of the first Fresnel reflection at the entrance interface of the STE stack. This is a first reason why exciting the STE through substrate is less optimal. From an electromagnetic point of view, even by adding a trapping cavity, the pump photons will always undergo a minimal entrance reflection. For the STE/cavity/substrate configuration on the contrary, the total reflectance is drastically reduced within the DBR gap, yet it still comprises a few percent. This fundamentally different behaviour limits the maximal achievable absorption when exciting a STE through an optically dense layer.

Time-domain simulations confirm the above frequency domain findings. Figure 5b plot snapshots of the intensity distribution $|E|^2$ (red line) halted at the instant of peak intensity inside the spin pumping layer upon excitation by a 100 fs pulse (30 μm long, centred at 808 nm). The red arrow denotes the direction of excitation. In the STE/cavity/sapphire configuration, the cavity creates an antireflection effect, resulting in decreased interference compared to the STE/sapphire reference. This portion of the electromagnetic energy is now absorbed by the spintronic layers. In the sapphire/STE/cavity configuration however, as explained above, the unavoidable entrance loss at the air/sapphire interface, limits a drastic further reduction of the reflection loss of the STE layers. The cavity can only minimally further reduce the reflection losses, hence the considerably lower intensity and minimal reduction of the interference ripple in this configuration. The interference of the exciting and back-reflected fields appears nicely, revealing for instance how in the substrate/STE/cavity configuration the interference ripple is minimally reduced. The cavity manages to recycle the pump photons that would otherwise be transmitted, but it can't do anything about the IR photons that are reflected by the STE/sapphire interface. Hence the absence of pump reflection reduction in this

© 2024 The Author(s). Advanced Photonics Research published by Wiley-VCH GmbH

26999293, 0, Downloaded from https://onlinelibrary.wiley.com/doi/10.1002/adpr.202400064 by Technical University Ostrava, Wiley Online Library on [17/09/2024]. See the Terms and Conditions (https://onlinelibrary.wiley.com/terms-and-conditions) on Wiley Online Library for rules of use; OA articles are governed by the applicable Creative Commons License

26999293, 0, Downloaded from https://onlinelibrary.wiley.com/doi/10.1002/adpr.202400064 by Technical University Ostrava, Wiley Online Library on [17/09/2024]. See the Terms and Conditions (https://onlinelibrary.wiley.com/terms-and-conditions) on Wiley Online Library for rules of use; OA articles are governed by the applicable Creative Commons License

configuration (as already shown in Figure 5a). Additionally, our time-domain framework allows to plot the spatial distribution of the energy absorption as a function of time. Figure 5c shows a zoom of the structure on the metallic stack, plotting on top of it the absorption distribution $Q(x,t)$, paused at the maximal field fluence in the FM layer (see Section S2, Supporting information, for the definition and the physical meaning of Q).

This simulated $Q(x,t)$ snapshot shows that even though our structure manages to radically improve the absorption in the spin pumping layer (see the twofold and threefold Q increase in the CoFeB layer in Figure 5c), the optimization strategy cannot avoid that an important part of the absorbed pump energy is lost in the non-magnetic non-spin polarized layers. In detail, the energy is distributed among the Pt/CoFeB/W layers in the following ratio: 37.0% for Pt, 40.3% for CoFeB, and 22.7% for W. This is a fundamental limitation due to the optical properties of Pt and W. Remember that a variation of the thicknesses of these layers might heavily impact the efficiency of the inverse Spin Hall effect itself. As Pt and W provide the SOC for the S2C their thickness is determined by their spin diffusion length Tao et al.[55] Yu et al.[56]

3.3. THz Extraction/Emission

So far, our focus has been primarily on optimizing pump absorption, specifically in terms of THz generation, without discussing the electromagnetic details related to the emission of THz into free space. Now, our investigation shifts to a detailed analysis of the true efficiency of spintronic emitters including the extraction. The conventional spintronic emitter demonstrates comparable peak-to-peak effectiveness, comparing principal pulses in both the STE/sapphire and sapphire/STE geometries, as experimentally demonstrated by the transmission measurements in Figure 2a,b. This observation might appear paradoxical, considering the significant discrepancies in pump absorption across the different geometries (32% vs 50%). Hence, we would logically expect the primary pulse to be stronger in the sapphire/STE configuration when a cavity is absent. However, a radiating dipole between two different media, oriented parallel to their interface, will have a continuous electric tangential field independent of the refractive index of the medium into which it radiates. To illustrate this concept, we conducted simulations of the dipole emission and field distribution throughout the radiation process emanating from spintronic layers situated between sapphire and air. The procedure for conducting the THz emission simulation will be explained in the subsequent section. **Figure 6**a plots the THz pulse fields at multiple intervals post-excitation by an infrared pulse. In both sapphire and air, the fields reach the expected similar magnitudes. It's illustratively evident that the field in sapphire is scaled due to its higher permittivity.

Therefore, even though the electric fields reach the same values in both the sapphire and air media, the electromagnetic intensity ε is scaled by the refractive index n

$$\mathscr{E} = \frac{1}{2} c\varepsilon_0 n \mathbf{E} \times \mathbf{E}^* \tag{1}$$

where c represents the velocity of light, ε_0 is the vacuum permittivity and $\mathbf{E}$ denotes the complex electric amplitude. In a simple approximation, a pumped STE emits an intensity into its surrounding media in proportion to the respective impedance of these media. If the substrate is semi-infinite, the ratio of the radiated intensities between substrate and air superstrate is thus $Z_{\mathrm{vac}}/Z_{\mathrm{sub}}$, or simply n_{sub}, where $Z = Z_0/n$ is the impedance Saleh and Teich.[57] However, terminating the substrate with an air interface reduces this emission by a Fresnel power transmission coefficient, given by $4Z_{\mathrm{vac}}Z_{\mathrm{sub}}/(Z_{\mathrm{vac}} + Z_{\mathrm{sub}})^2$ under normal incidence Button.[58] By combining these two relationships, we obtain the intensity ratio $r_{\mathrm{I}} = 4Z_{\mathrm{vac}}^2/(Z_{\mathrm{vac}} + Z_{\mathrm{sub}})^2$, roughly equal to 2.25 for a sapphire substrate. For conventional STE's, the absorption ratio is ≈0.31/0.5 between STE/sapphire and sapphire/STE, resulting in a radiated intensity ratio of $r_{\mathrm{R}} = \left(\frac{0.31}{0.5}\right)^2 = 0.39$. In this idealized scenario, this ratio r_{R} is almost compensated by the r_{I}, yielding $r_{\mathrm{R}} \times r_{\mathrm{I}} = 2.25 \times 0.39$.

3.4. STE Versus STE-Cavity: Efficiency in Different Geometries

In our effort to assess the performance of spintronic THz emitters both with and without cavities in transmission and reflection geometries, we focus on the dynamics of absorption under femtosecond excitation and its distribution over time to reconstruct the emission profile, leading to the efficiencies. This approach is detailed in Section S2.4, Supporting information. So far, our representation of absorption has primarily been through frequency-dependent spectra and visual snapshots of field distributions, as demonstrated in Figure 5a–c. Now, we calculated the time-dependent absorption power $P_{\mathrm{ab}}(t)$ for all studied configurations: STE/sapphire versus sapphire/STE, and STE/cavity/sapphire versus sapphire/STE/Cavity, demonstrated in Figure 6c (middle subplot). The percentage of absorbed energy is indicated by the marked areas under the curves, with the vertical axis scaled to approximate the percentage of absorbed power, correlating directly with amplitude. The absorption time profiles for spintronic emitters, with and without an integrated cavity, indicate that the excitation duration remains unchanged. This is despite a significant portion of the 100 fs pulse being delayed and returned as standing waves during reflection. This suggests that the recycling of photons, which are reflected back by the cavity, occurs almost instantaneously and does not influence the length of excitation.

The absorption profiles in the time-domain, along with the previous analysis of absorption spectra in Figure 5a, indicate that most absorption occurs within the principal excitation. Although we do observe Fabry–Pérot reflections, their contribution is typically less than 2%, as detailed upon in the logarithmic scale. This results in only a marginal fraction of energy reaching the STE for Fabry–Pérot absorption and secondary emission. The time delay in the principal excitations of the spintronic layers between the STE/sapphire and sapphire/STE configurations is a consequence of the excitation pulse propagating through the 500 μmthick sapphire substrate. Finally, the radiating dipole field of spintronic emitters is determined by taking the derivative of the dipole source, as $E_{\mathrm{dipole}} \propto \frac{\partial P_{\mathrm{ab}}}{\partial t}$.

Subsequently, the emitted field propagates through the specified structures using Scattering matrices, as detailed in the Section S4, Supporting Information. Furthermore, we can numerically predict emission for both reflection and

© 2024 The Author(s). Advanced Photonics Research published by Wiley-VCH GmbH

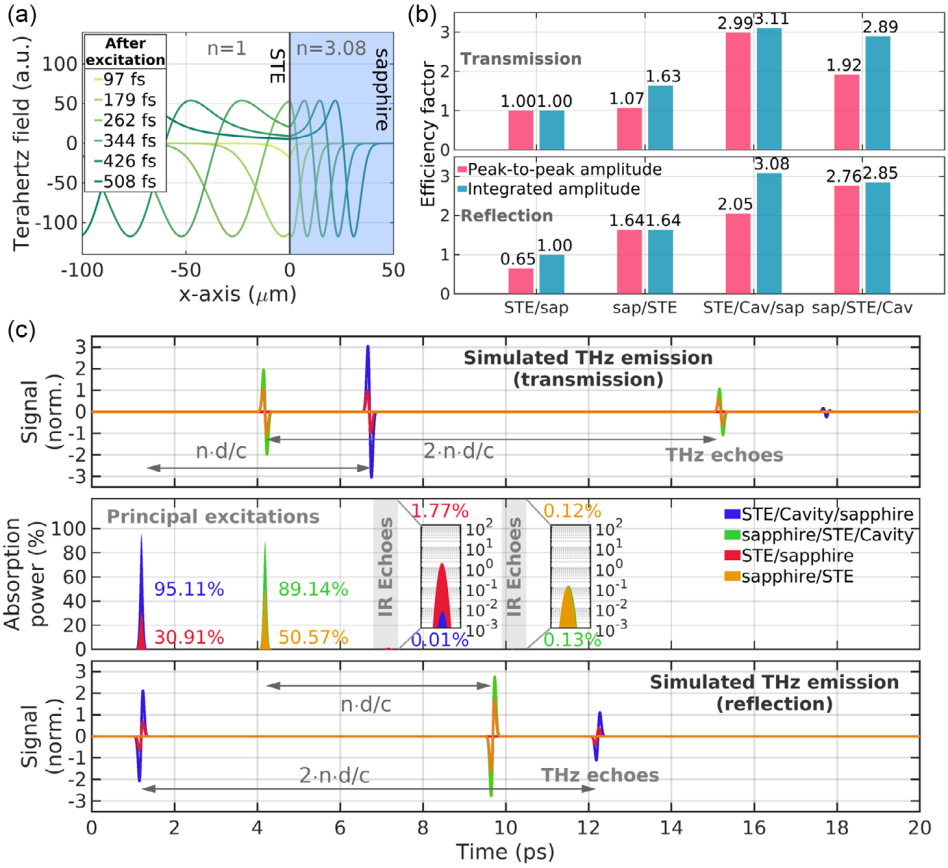


Figure 6. a) Simulation illustrates THz field development (shades of green) emitted from spintronic emitter layers into sapphire and air, displayed at various moments post-IR pump excitation (97–508 fs), showing consistent amplitude in both mediums and differing intensities based on $I = \frac{1}{2} cn\varepsilon_0 \mathbf{E} \times \mathbf{E}^*$. b) Comparison of efficiency for different samples in reflective and transmissive configurations, comparing peak-to-peak values in the time domain as well as integrated full wavefront area in the time domain. c) Middle subplot: shows dynamic absorption over time for all samples from Poynting's theorem, with the *Y*-axis scaled to reflect absorption percentage. The absorpted power is indicated by the area under each curve. IR echoes are marginal and detailed in logarithmic scale. Top and bottom subplots: depict calculated THz emissions from these absorptions, directed in transmission and reflection, respectively, all normalized against the STE/sapphire emission.

transmission, even though our experimental setup is limited to transmission measurements. All simulation results for reflection (displayed in the bottom subplot) and transmission (in the top subplot) are presented in Figure 6c, normalized concerning the highest observed peak-to-peak value in the STE/sapphire configuration for transmission. This normalization serves to enable a realistic comparison of which configurations are effective relative to each other, rather than merely discussing improvements over the configuration without a cavity. The adoption of time-dependent absorption guarantees the consideration of absorption scaling and the treatment of all THz and IR reflections (echoes, losses), leading to valuable estimations of simulated efficiencies. As an illustration, the simulations of the conventional STE/sapphire and sapphire/STE configurations in Figure 6c exhibit identical behaviour in the transmission arrangement as experimental results in Figure 2a,b. Their normalized peak-to-peak efficiency in the time domain are comparable and close to one.

Evaluating signals based on their maximal peak-to-peak in the time domain is crucial for generating intense pulses in spectroscopy to obtain a wide dynamic range, and equally important for nonlinear applications that require an intense pump. However, it becomes evident that the sapphire/STE configuration includes an echo, contributing to the overall energy and resulting in a larger energy yield in this configuration. The origin of this echo was explained in Section 2.2 and in the diagram Figure 2c. The contribution of the echo alters the efficiencies in all integrated pulses to 1.63 and extends the possibilities for applications in the spectral domain, particularly amplifying at resonant frequencies corresponding to the substrate thickness. Therefore, we will present a summary of both the normalized peak-to-peak and integrated waveform efficiency in Figure 6b.

When we redirect the emission of conventional emitters toward a reflective direction, it becomes evident that the balance between absorption and THz efficiency is disrupted. In such scenario, the STE/sapphire configuration exhibits relatively low absorption (31%) and decreased THz emission into the surrounding air (refer to Section 3.2), resulting in the lowest efficiency 0.65 (1.00 for all integrated pulses) when compared to other configurations. Conversely, the sapphire/STE arrangement

© 2024 The Author(s). Advanced Photonics Research published by Wiley-VCH GmbH

26999293, 0, Downloaded from https://onlinelibrary.wiley.com/doi/10.1002/adpr.202400064 by Technical University Ostrava, Wiley Online Library on [17/09/2024]. See the Terms and Conditions (https://onlinelibrary.wiley.com/terms-and-conditions) on Wiley Online Library for rules of use; OA articles are governed by the applicable Creative Commons License

26999293, 0, Downloaded from https://onlinelibrary.wiley.com/doi/10.1002/adpr.202400064 by Technical University Ostrava, Wiley Online Library on [17/09/2024]. See the Terms and Conditions (https://onlinelibrary.wiley.com/terms-and-conditions) on Wiley Online Library for rules of use; OA articles are governed by the applicable Creative Commons License

stands out as the most effective basic configuration of 1.64 efficiency due to its significant absorption (50%) and intense THz extraction toward the substrate, leading to the integrated efficiency of 1.64. These simulations indicate that for scenarios excluding a cavity, the sapphire/STE configuration in reflective geometry offers the most promise. Moreover, it provides echo-free time domains, which are particularly advantageous for data processing in THz-TDS spectroscopy or THz-pump experiments, where a secondary THz-pump could interfere with the ongoing process.

For STE configurations incorporating cavities, the STE/cavity/sapphire configuration in a transmission geometry emerges as the superior choice. It showcases the highest absorption at 95% and elevates emission toward the substrate, resulting in an efficiency of 2.99 (and 3.11 when considering integrated waveform). This is followed by sapphire/STE/cavity in reflection, where the cavity limits absorption to no more than 89%, but the radiation is directed into the sapphire, achieving an efficiency of 2.76 (2.85 in integrated waveforms). The efficiencies are the lowest and comparable in the configurations of sapphire/STE/cavity in transmission (1.92 and 2.89) and for STE/cavity/sapphire in reflection with efficiencies (2.05 and 3.08).

In closing this section, although our focus has primarily been on efficiently recycling pump power, it's important to note, as recently demonstrated by Mičica et al. Mičica et al.[59] that there is equally a considerable potential to apply a similar recycling strategy for the generated THz photons. By cladding the backside of the substrate with a metal mirror and optimizing the substrate's thickness, they have demonstrated that all generated THz photons can be constructively combined in a reflective configuration. In combination with the here presented IR trapping cavity this would lead to an ultimate maximal electromagnetic performance of a STE.

3.5. Further Improvements and Outlook

In the final section, we investigate how selecting the optimal substrate can further enhance the performance of spintronic emitters, leading to variations in both excitation and extraction efficiency. The selection of a substrate influences the pump's absorption in thin spintronic layers that are directly deposited onto it. **Figure 7**a illustrates the changes in simulated absorbance within the spintronic layers of a standard emitter as the refractive index of the substrate varies from 1 to 4 at 800 nm. While the STE/substrate configuration exhibits a decreasing trend in absorbance as the refractive index increases, due to greater reflection from the optically dense material of the metal films, the substrate/STE configuration reaches a peak absorption of 50% at a refractive index around 1.7. This maximum results from the combined effect of enhanced transmission through the optically denser substrate via STE and the reflection loss at the air/substrate interface. The simulation compares several commonly used substrate materials with optical parameters from Marple,[60] Stephens and Malitson,[61] Ghosh,[62] Li,[63] Phillip and Taft,[64] Malitson and Dodge,[65] Tsuda et al.[66] these materials are listed in the legend.

Sapphire is highly suitable for the Substrate/STE configuration, as are materials like quartz, MgO, MgF_2, and others. In the STE/Substrate configuration, materials with lower refractive indices, like MgF_2 or LiF, are associated with increased absorption. However, Substrate/STE consistently results in higher absorptions. In the substrate/STE configuration, efficiency is reduced as the IR pulse gets reflected at the air–substrate interface, which results in a loss described by $|(Z_{vac} - Z_{sub})/(Z_{vac} + Z_{sub})|^2$. To mitigate this effect, an anti-reflective coating can increase efficiency by an additional 3–20% for the mentioned substrates.

Subsequently, the choice of substrate also impacts the extraction of THz emission from spintronic layers in two significant ways. Firstly, (I) THz emission is scaled by a factor of $1/(n_{vac} + n_{sub} + Z_0 \int_0^d \sigma(z) \mathrm{d}z)$ Seifert et al.[1] This implies that an increase in the substrate's refractive index leads to a decrease in the emitter's overall efficiency. (II) As previously discussed in Section 3.3, the emission toward the substrate is n_{sub}-fold more intense compared to emission into the air. In the free-space direction, THz emission always decreases with an increasing refractive index. Conversely, toward the substrate, emission increases (point II) until the overall reduction in emission outweighs this benefit (point I). This trend is evident in the simulated peak-to-peak efficiency in the time domain, as demonstrated when varying the THz refractive index, as shown in Figure 7b.

To better assess relative enhancements, we normalize our results against the widely-used STE/sapphire transmission configuration (towards substrate), allowing for a clearer comparison. Geometry selection is key and both STE/substrate (reflection) and substrate/STE (transmission) geometries face notable limitations in achieving optimal THz efficiency. Yet the evident effect of substrate choice on THz efficiency cannot be overlooked.

In the simulation involving typical substrates with THz properties from Rogalin et al.[67] Sajadi et al.[68] Tcypkin et al.[69] Grischkowsky et al.[70] Palik,[71] Fan et al.[72] materials with low refractive indices like PMMA show the highest performance. Additionally, we have used material properties from Seifert et al. Seifert et al.[73] for our simulations. Quartz and MgF_2 are also promising as substrate materials. Conversely, sapphire, when evaluated for THz efficiency, proves to be a less suitable option. In addition, reflective losses at the interface between substrate and air are notably higher for the listed materials, in the range of 3–30%. This is linked to their increased refractive index in the THz range, which can be partially balanced by using an anti-reflection coating designed for THz frequencies.

To better understand the overall peak-to-peak efficiency of common spintronic emitters, which depends on both IR absorption and THz extraction, we present contour maps in Figure 7c–f illustrating STE efficiency based on THz-IR refractive indices. For comparative clarity, efficiencies across all geometries are normalized against the STE/sapphire configuration in transmission geometry. The map includes various common materials, enabling a comparison of the effects of different substrates. The Substrate/STE configuration in reflection emerges as the most efficient, showing up to a 1.7-fold enhancement. This peak efficiency, achieved through effective extraction and absorption, aligns with refractive indices near 1.5. Such indices are typical for materials like plastics, demonstrated by PMMA, and extend to others such as Teflon, TPX, Zeonex, and Topas Du et al.[74] Islam et al.[75] In this context, enhancing efficiency through THz extraction is more

© 2024 The Author(s). Advanced Photonics Research published by Wiley-VCH GmbH

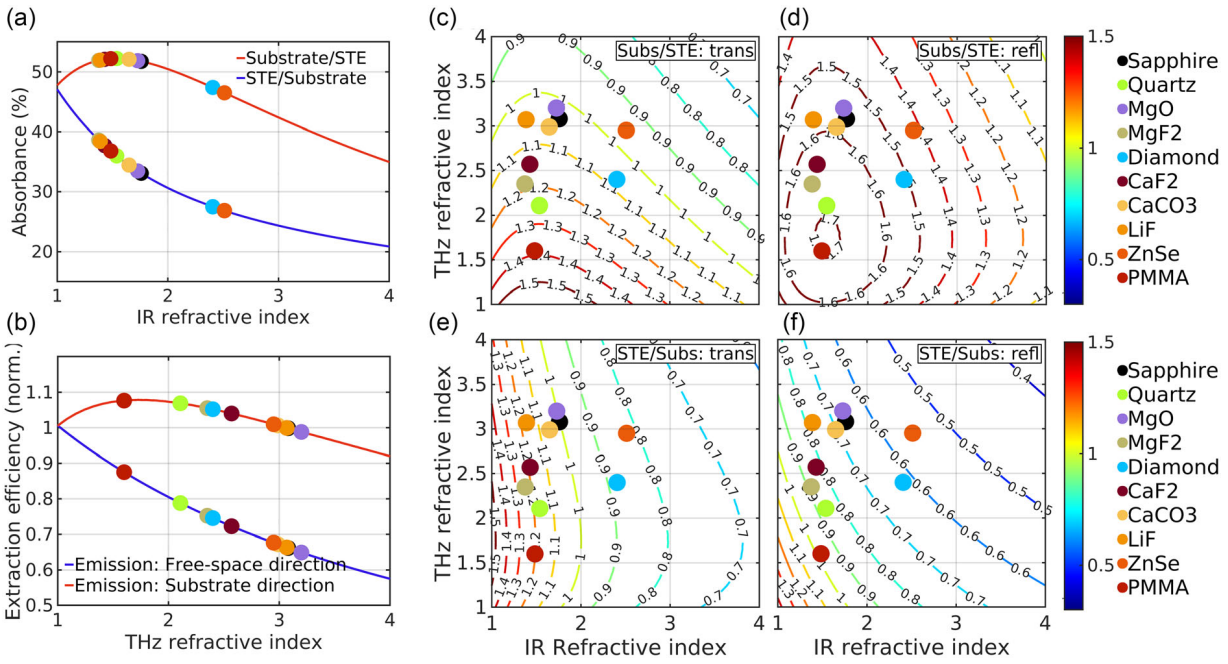


Figure 7. Simulated efficiency impact of substrate selection in Spintronic Emitters: The graphs illustrate efficiency's dependence on the refractive index within the THz/IR range. Each simulation compares typical substrate materials to illustrate their performance. Efficiencies are normalized against the STE/sapphire transmission configuration for straightforward comparison. a) Simulated change in absorbance of a 100 fs, 808 nm pulse due to varying IR refractive indices of a substrate in Substrate/STE and STE/Substrate configurations. b) Simulated dependence of the normalized emission efficiency of a constant dipole current on a varying substrate THz refractive index, directed either toward air (blue) or to the substrate (red). c–f) Efficiency maps of configurations: (c) Substrate/STE in transmission, (d) substrate/STE in reflection, (e) STE/substrate in transmission, and (f) STE/substrate in reflection. Labeled contours and color bars depict the normalized efficiency across the simulated map.

advantageous than focusing on absorption, which reaches its maximum potential with cavity integration. Nonetheless, the STE/Substrate configuration still significantly improves absorption. The least efficient is the STE/Substrate configuration in reflection, where both extraction and absorption are ineffective, requiring materials with very low refractive indices.

Clearly, the appropriate selection of materials is key to further enhancing efficiency. However, increasing the refractive index beyond 1.5–2 typically leads to a decrease in efficiency. Our simulations didn't account for the absorption coefficient, which can greatly affect efficiency, particularly at higher THz frequencies. Attention is needed for reflective losses at the substrate/air interface, which can be mitigate for both THz and IR spectra with the use of anti-reflective coatings. Apart from these materials' optical efficiency, factors like surface quality and adhesion properties are crucial, impacting the deposition and integrity of spintronic layers Nenno et al.[76] Moreover, the importance of thermal conductivity for passive cooling and the damage threshold cannot be overstated, with sapphire being a practical choice for these properties Shan et al.[44] Burghartz and Schulz.[43] The choice of substrate also dictates the fabrication process and, consequently, the cost.

4. Conclusion

This research was dedicated to the improvement in the performance of Pt/CoFeB/W spintronic emitters, with the objective of maximizing their efficiency to its fullest potential. These emitters are becoming more acknowledged within the THz community for their versatile applications, cost-effectiveness, and user-friendliness. A significant drawback of these emitters, compared to traditional sources, is their optical-to-terahertz conversion efficiency, which is lower by several orders of magnitude. However, the ultrafast demagnetization process enables these emitters to achieve extraordinarily high peak performances, producing broadband pulses of up to 30 THz. Despite high peak performance, the significant efficiency limitations of these spintronic emitters hinder their extensive use in spectroscopy, nonlinear applications, and communications, limiting the full utilization of their potential.

Therefore, our objective was to maximize the enhancement of spintronic emitters by integrating them with 1D SiO_2/SiN_x photonic cavities, aiming to enable these sources to rival conventional ones. We developed a robust and comprehensive methodology for optimizing these devices, thereby introducing a new perspective to address this technical challenge. The design of our cavities played a pivotal role in significantly enhancing the trapping of excitation photons. This enhancement was crucial in amplifying the generation of spin electrons, thereby intensifying the spintronic emission. Our fabricated samples demonstrated an exceptional absorption rate of ≈95% of the excitation pulse and a substantial enhancement of the emitter's THz amplitude, achieving 2.45 times the performance of traditional spintronic emitters, along with an 8 dB increase in energy output – a distinct achievement in this field. We provide a comprehensive guide

© 2024 The Author(s). Advanced Photonics Research published by Wiley-VCH GmbH

26999293, 0, Downloaded from https://onlinelibrary.wiley.com/doi/10.1002/adpr.202400064 by Technical University Ostrava, Wiley Online Library on [17/09/2024]. See the Terms and Conditions (https://onlinelibrary.wiley.com/terms-and-conditions) on Wiley Online Library for rules of use; OA articles are governed by the applicable Creative Commons License

detailing the design of these structures, alongside sharing our developed solutions of STE-Cavities, which are finely tuned for optimal performance. Additionally, through our analysis of the fabricated samples, which involved varying the pump power and adjusting the central wavelength of the excitation pulse, we demonstrated the robustness and operational effectiveness of these enhanced spintronic emitters.

This study is the first to provide a detailed comparison of the STE/sapphire/cavity with the sapphire/STE/cavity configuration. Our theoretical approach aids in explicating the key factors that influence emitter efficiency and electromagnetic functionality. We offer a thorough evaluation of emitter efficiencies in both reflective and transmission geometries, essential for researchers in selecting the most suitable emitter configuration, given the substantial differences in efficiency. Our findings reveal, for example, that the pure emitter's maximum efficiency, without a cavity, is significantly higher for substrate/STE configuration in reflection – showing nearly 60% more efficiency compared to its transmission geometry. Furthermore, our results establish that superior performance is exclusively attainable with the STE/cavity/sapphire configuration, which effectively combines maximal absorption and enhanced THz emission directed toward the substrate.

Despite the promising findings, it's crucial to acknowledge that our access was limited to an 80 MHz oscillator, restricting our ability to test the spintronic emitters under high-energy millijoule (mJ) excitation pulses. This limitation leaves potential high-energy impacts, like saturation and thermal damage, unexplored. Furthermore, we acknowledge that our simulations might overestimate the results compared to empirical data, possibly overlooking aspects such as heat generation, saturation effects, or the sensitivity to the materials used in the simulations. Therefore, a crucial point was characterizing the spintronic layers' properties, which we conducted through ellipsometry and transmission measurements. Despite these limitations, we are confident that our simulations provide a realistic representation of the spintronic emitters' behavior.

Finally, we analyzed the impact of substrates on spintronic emitters and propose ways to further enhance their efficiency. Our simulation strategy presents a promising perspective, not limited to just augmenting excitation via increased absorption, but also extends to the careful optimization of structures for optimal THz field extraction, incorporating techniques like anti-reflective coatings and THz cavities.

In closing, this study marks a substantial advancement in optimizing spintronic emitters for THz applications. Our results provide a generic approach to optimize spintronic emitters from the optical viewpoint. But the specific findings on cavity design, efficiency analysis, substrate influence, and pulse-based simulations can also be applied to optimize the electromagnetic design of an even wider variety of THz emitter configurations beyond purely spintronic ones such as plasmonic-based photoconductors.

Supporting Information

Supporting Information is available from the Wiley Online Library or from the author.

Acknowledgements

The authors acknowledge financial support from the Horizon 2020 Framework Programme of the European Commission under FET-Open grant no. 863155 (s-Nebula) and from the French ANR research agency under the grant TRAPIST (ANR-21-CE24-0011). The infrastructure used was made available through project No. CZ.02.01.01/00/22_008/0004631 "Materials and Technologies for Sustainable Development", funded by the European Union and the state budget of the Czech Republic within the framework of the Jan Amos Komensky Operational Program. The research was supported by Czech Science Foundation (grant no. 22-33060S). This work was supported by the Ministry of Education, Youth and Sports of the Czech Republic through the e-INFRA CZ (ID:90254) and SP2024/086. The authors thank the french RENATECH Network for the support in the realization of the devices. Authors would like to acknowledge and thank Felix Paries for his invaluable feedback and providing expert and practical advice.

Conflict of Interest

The authors declare no conflict of interest.

Author Contributions

The study was prepared with contributions from all authors. **Pierre Kolejak**: Conceptualized the idea and performed simulations (lead); Data curation (lead), and Visualization (lead). **Geoffrey Lezier** performed the experimental validation. **Daniel Vala** led the optical characterization of STEs. Mathias Vanwolleghem provided study supervision.

Data Availability Statement

The data that support the findings of this study are openly available in zenodo at https://doi.org/10.5281/zenodo.10650948, reference number 10650948.

Keywords

inverse spin Hall effect, photonic crystals, spintronics, terahertz generation, time-resolved spectroscopy

Received: April 29, 2024
Revised: July 21, 2024
Published online:

[1] T. Seifert, S. Jaiswal, U. Martens, J. Hannegan, L. Braun, P. Maldonado, F. Freimuth, A. Kronenberg, J. Henrizi, I. Radu, E. Beaurepaire, Y. Mokrousov, P. M. Oppeneer, M. Jourdan, G. Jakob, D. Turchinovich, L. M. Hayden, M. Wolf, M. Münzenberg, M. Kläui, T. Kampfrath, *Nat. Photonics* **2016**, *10*, 483.
[2] C. Bull, S. M. Hewett, R. Ji, C.-H. Lin, T. Thomson, D. M. Graham, P. W. Nutter, *APL Mater.* **2021**, *9*, 090701.
[3] W. Wu, C. Yaw Ameyaw, M. F. Doty, M. B. Jungfleisch, *J. Appl. Phys.* **2021**, *130*, 091101.
[4] T. S. Seifert, L. Cheng, Z. Wei, T. Kampfrath, J. Qi, *Appl. Phys. Lett.* **2022**, *120*, 180401.
[5] T. Kampfrath, K. Tanaka, K. A. Nelson, *Nat. Photonics* **2013**, *7*, 680.
[6] T. Seifert, S. Jaiswal, M. Sajadi, G. Jakob, S. Winnerl, M. Wolf, M. Kläui, T. Kampfrath, *Appl. Phys. Lett.* **2017**, *110*, 252402.

© 2024 The Author(s). Advanced Photonics Research published by Wiley-VCH GmbH

26999293, 0, Downloaded from https://onlinelibrary.wiley.com/doi/10.1002/adpr.202400064 by Technical University Ostrava, Wiley Online Library on [17/09/2024]. See the Terms and Conditions (https://onlinelibrary.wiley.com/terms-and-conditions) on Wiley Online Library for rules of use; OA articles are governed by the applicable Creative Commons License

[7] E. T. Papaioannou, G. Torosyan, S. Keller, L. Scheuer, M. Battiato, V. K. Mag-Usara, J. L'huillier, M. Tani, R. Beigang, *IEEE Trans. Magn.* **2018**, *54*, 9100205.
[8] R. I. Herapath, S. M. Hornett, T. S. Seifert, G. Jakob, M. Kläui, J. Bertolotti, T. Kampfrath, E. Hendry, *Appl. Phys. Lett.* **2019**, *114*, 041107.
[9] T. Vogel, A. Omar, S. Mansourzadeh, F. Wulf, N. M. Sabanés, M. Müller, T. S. Seifert, A. Weigel, G. Jakob, M. Kläui, I. Pupeza, T. Kampfrath, C. J. Saraceno, *Opt. Express* **2022**, *30*, 20451.
[10] F. Paries, N. Tiercelin, G. Lezier, M. Vanwolleghem, F. Selz, M.-A. Syskaki, F. Kammerbauer, G. Jakob, M. Jourdan, M. Kläui, Z. Kaspar, T. Kampfrath, T. S. Seifert, G. Von Freymann, D. Molter, *Opt. Express* **2023**, *31*, 30884.
[11] K. Yamahara, A. Mannan, I. Kawayama, H. Nakanishi, M. Tonouchi, *Sci. Rep.* **2020**, *10*, 14633.
[12] K. Takano, M. Asai, K. Kato, H. Komiyama, A. Yamaguchi, T. Iyoda, Y. Tadokoro, M. Nakajima, M. I. Bakunov, *Sci. Rep.* **2019**, *9*, 3280.
[13] R. Rouzegar, A. L. Chekhov, Y. Behovits, B. R. Serrano, M. A. Syskaki, C. H. Lambert, D. Engel, U. Martens, M. Münzenberg, M. Wolf, G. Jakob, M. Kläui, T. S. Seifert, T. Kampfrath, *Phys. Rev. Appl.* **2023**, *19*, 034018
[14] M. T. Hibberd, D. S. Lake, N. A. B. Johansson, T. Thomson, S. P. Jamison, D. M. Graham, *Appl. Phys. Lett.* **2019**, *114*, 031101.
[15] D. Kong, X. Wu, B. Wang, T. Nie, M. Xiao, C. Pandey, Y. Gao, L. Wen, W. Zhao, C. Ruan, J. Miao, Y. Li, L. Wang, *Adv. Opt. Mater.* **2019**, *7*, 1900487.
[16] P. Koleják, G. Lezier, K. Postava, J.-F. Lampin, N. Tiercelin, M. Vanwolleghem, *ACS Photonics* **2022**, *9*, 1274.
[17] G. Lezier, P. Koleják, J.-F. Lampin, K. Postava, M. Vanwolleghem, N. Tiercelin, *Appl. Phys. Lett.* **2022**, *120*, 152404.
[18] O. Gueckstock, L. Nádvorník, T. S. Seifert, M. Borchert, G. Jakob, G. Schmidt, G. Woltersdorf, M. Kläui, M. Wolf, T. Kampfrath, *Optica* **2021**, *8*, 1013.
[19] G. Lezier, P. Kolejaák, P. Koleják, J. F. Lampin, K. Postava, M. Vanwolleghem, N. Tiercelin, in *CLEO 2023, Technical Digest Series*, paper SF2I.4 Optica Publishing Group **2023**.
[20] J. A. Fülöp, S. Tzortzakis, T. Kampfrath, *Adv. Opt. Mater.* **2020**, *8*, 1900681.
[21] J. Sinova, S. O. Valenzuela, J. Wunderlich, C. H. Back, T. Jungwirth, *Rev. Mod. Phys.* **2015**, *87*, 1213.
[22] J. Hawecker, E. Rongione, A. Markou, S. Krishnia, F. Godel, S. Collin, R. Lebrun, J. Tignon, J. Mangeney, T. Boulier, J.-M. George, C. Felser, H. Jaffrès, S. Dhillon, *Appl. Phys. Lett.* **2022**, *120*, 122406.
[23] M. B. Jungfleisch, Q. Zhang, W. Zhang, J. E. Pearson, R. D. Schaller, H. Wen, A. Hoffmann, *Phys. Rev. Lett.* **2018**, *120*, 207207.
[24] E. Rongione, S. Fragkos, L. Baringthon, J. Hawecker, E. Xenogiannopoulou, P. Tsipas, C. Song, M. Mičica, J. Mangeney, J. Tignon, T. Boulier, N. Reyren, R. Lebrun, J-M. George, P. Le Fèvre, S. Dhillon, A. Dimoulas, H. Jaffrès, *Adv. Opt. Mater.* **2022**, *10*, 2102061
[25] E. Rongione, L. Baringthon, D. She, G. Patriarche, R. Lebrun, A. Lemaître, M. Morassi, N. Reyren, M. Mičica, J. Mangeney, J. Tignon, F. Bertran, S. Dhillon, P. Le Févre, H. Jaffrès, J-M. George, *Adv. Sci.* **2023**, *10*, 2301124.
[26] M. Tong, Y. Hu, Z. Wang, T. Zhou, X. Xie, X' Cheng, T. Jiang, *Nano Lett.* **2021**, *21*, 60.
[27] K. Abdukayumov, M. Mičica, F. Ibrahim, L. Vojáček, C. Vergnaud, A. Marty, J-Y. Veuillen, P. Mallet, I. G. De Moraes, D. Dosenovic, S. Gambarelli, V. Maurel, A. Wright, J. Tignon, J. Mangeney, A. Ouerghi, V. Renard, F. Mesple, J. Li, F. Bonell, H. Okuno, M. Chshiev, J-M. George, H. Jaffrès, S. Dhillon, M. Jamet, *Adv. Mater.* **2024**, *36*, 2304243.
[28] G. Torosyan, S. Keller, L. Scheuer, R. Beigang, E. T. Papaioannou, *Sci. Rep.* **2018**, *8*, 1311.
[29] U. Nandi, M. S. Abdelaziz, S. Jaiswal, G. Jakob, O. Gueckstock, S. M. Rouzegar, T. S. Seifert, M. Kläui, T. Kampfrath, S. Preu, *Appl. Phys. Lett.* **2019**, *115*, 022405.
[30] M. Talara, D. S. Bulgarevich, C. Tachioka, V. K. Mag-Usara, J. Muldera, T. Furuya, H. Kitahara, M. C. Escaño, Q. Guo, M. Nakajima, G. Torosyan, R. Beigang, M. Watanabe, M. Tani, *Appl. Phys. Express* **2021**, *14*, 042008.
[31] F. M. Wagner, S. Melnikas, J. Cramer, D. A. Damry, C. Q. Xia, K. Peng, G. Jakob, M. Kläui, S. Kičas, M. B. Johnston, *J. Infrared Millim. Terahertz Waves.* **2023**, *44*, 52.
[32] Z. Feng, R. Yu, Y. Zhou, H. Lu, W. Tan, H. Deng, Q. Liu, Z. Zhai, L. Zhu, J. Cai, B. Miao, H. Ding, *Adv. Opt. Mater.* **2018**, *6*, 1800965.
[33] Z. Jin, Y. Peng, Y. Ni, G. Wu, B. Ji, X. Wu, Z. Zhang, G. Ma, C. Zhang, L. Chen, A. V. Balakin, A. P. Shkurinov, Y. Zhu, S. Zhuang, *Laser Photonics Rev.* **2022**, *16*, 2100688.
[34] Z. Feng, H. Qiu, D. Wang, C. Zhang, S. Sun, B. Jin, W. Tan, *J. Appl. Phys.* **2021**, *129*, 010901.
[35] E. T. Papaioannou, R. Beigang, *Nanophotonics* **2021**, *10*, 1243.
[36] R. Oldenhuis, *GODLIKE - A Robust Single-& Multi-Objective Optimizer*, GitHub **2023**, https://github.com/rodyo/FEX-GODLIKE/releases/tag/v1.5.
[37] J. C. Lagarias, J. A. Reeds, M. H. Wright, P. E. Wright, *SIAM J. Optim.* **1998**, *9*, 112.
[38] J. Kröll, J. Darmo, K. Unterrainer, *Opt. Express* **2007**, *15*, 6552.
[39] L. Ding, X. Wang, N. S. S. Ang, C. Lu, V. Suresh, S.-J. Chua, J. Teng, *IEEE J. Sel. Top. Quantum Electron.* **2017**, *23*, 8500508.
[40] B. Carli, *JOSA* **1977**, *67*, 908.
[41] T. Kampfrath, J. Nötzold, M. Wolf, *Appl. Phys. Lett.* **2007**, *90*, 231113.
[42] M. Battiato, K. Carva, P. M. Oppeneer, *Phys. Rev. Lett.* **2010**, *105*, 027203.
[43] S. Burghartz, B. Schulz, *J. Nucl. Mater.* **1994**, *212–215*, 1065.
[44] J. Shan, F. Wang, E. Knoesel, M. Bonn, T. F. Heinz, *Phys. Rev. Lett.* **2003**, *90*, 247401.
[45] J. J. Talghader, *J. Phys. D: Appl. Phys.* **2004**, *37*, R109.
[46] A. K. Sinha, H. J. Levinstein, T. E. Smith, *J. Appl. Phys.* **1978**, *49*, 2423.
[47] S. Kumar, P. S. Maji, R. Das, *Sens. Actuators, A* **2017**, *260*, 10.
[48] I. H. Malitson, *J. Opt. Soc. Am.* **1965**, *55*, 1205.
[49] K. Luke, Y. Okawachi, M. R. E. Lamont, A. L. Gaeta, M. Lipson, *Opt. Lett.* **2015**, *40*, 4823.
[50] M. Kaliteevski, I. Iorsh, S. Brand, R. A. Abram, J. M. Chamberlain, A. V. Kavokin, I. A. Shelykh, *Phys. Rev. B* **2007**, *76*, 165415
[51] Y. Jiang, H. Li, X. Zhang, F. Zhang, Y. Xu, Y. Xiao, F. Liu, A. Wang, Q. Zhan, W. Zhao, *Photonics Res.* **2023**, *11*, 1057.
[52] E. D. Palik, *Handbook of Optical Constant of Solids*, Vol. *1*, Academic Press, Boston, MA **1991**.
[53] J.A. Woollam, Co., Inc., CompleteEASE Software v6.72, Platinum Optical Constants from KK Fit to Opaque film: 192–1700 nm **1999–2023**, https://www.jawoollam.com/ellipsometry-software/completeease.
[54] J.A. Woollam, Co., Inc., CompleteEASE Software v6.72, GenOsc Model for Saphire Substrate – Ordinary (extraordinary) Axis: 175–1700 nm, https://www.jawoollam.com/ellipsometry-software/completeease.
[55] X. Tao, Q. Liu, B. Miao, R. Yu, Z. Feng, L. Sun, B. You, J. Du, K. Chen, S. Zhang, L. Zhang, Z. Yuan, D. Wu, H. Ding, *Sci. Adv.* **2018**, *4*, eaat1670.
[56] R. Yu, B. F. Miao, L. Sun, Q. Liu, J. Du, P. Omelchenko, B. Heinrich, M. Wu, H. F. Ding, *Phys. Rev. Mater.* **2018**, *2*, 074406.
[57] B. E. A. Saleh, M. C. Teich, *Fundamentals of Photonics*, John Wiley & Sons, Inc, New York **1991**.

© 2024 The Author(s). Advanced Photonics Research published by Wiley-VCH GmbH

26999293, 0, Downloaded from https://onlinelibrary.wiley.com/doi/10.1002/adpr.202400064 by Technical University Ostrava, Wiley Online Library on [17/09/2024]. See the Terms and Conditions (https://onlinelibrary.wiley.com/terms-and-conditions) on Wiley Online Library for rules of use; OA articles are governed by the applicable Creative Commons License

[58] K. J. Button, *Infrared and Millimeter Waves*, Vol. *10*, Elsevier, Walthm, MA **1979**.
[59] M. Mičica, A. Wright, P. Koleják, G. Lezier, K. Postava, J. Hawecker, A. De Vetter, J. Tignon, J. Mangeney, H. Jaffres, R. Lebrun, N. Tiercelin, M. Vanwolleghem, S. Dhillon, *Nanophotonics* **2024**, *13*, https://doi.org/10.1515/nanoph-2023-0807.
[60] D. T. F. Marple, *J. Appl. Phys.* **1964**, *35*, 539.
[61] R. E. Stephens, I. H. Malitson, *J. Res. Natl. Bur. Stand.* **1952**, *49*, 249.
[62] G. Ghosh, *Opt. Commun.* **1999**, *163*, 95.
[63] H. H. Li, *J. Phys. Chem. Ref. Data* **1980**, *9*, 161.
[64] H. R. Phillip, E. A. Taft, *Phys. Rev.* **1964**, *136*, A1445.
[65] I. H. Malitson, M. J. Dodge, *J. Opt. Soc. Am* **1972**, *62*, 1405.
[66] S. Tsuda, S. Yamaguchi, Y. Kanamori, H. Yugami, *Opt. Express* **2018**, *26*, 6899.
[67] V. E. Rogalin, I. A. Kaplunov, G. I. Kropotov, *Opt. Spectrosc.* **2018**, *125*, 1053.
[68] M. Sajadi, M. Wolf, T. Kampfrath, *Opt. Express* **2015**, *23*, 28985.
[69] M. Zhukova, M. Melnik, I. Vorontsova, A. Tcypkin, S. Kozlov, *Photonics* **2020**, *7*, 98.
[70] D. Grischkowsky, S. Keiding, M. Van Exter, C. Fattinger, *J. Opt. Soc. Am. B* **1990**, *7*, 2006.
[71] E. D. Palik, *Handbook of Optical Constants of Solids*, Elsevier, Academic Press, Boston, MA **1997**, https://www.sciencedirect.com/book/9780125444156/handbook-of-optical-constants-of-solids.
[72] F. Fan, X. Zhang, S. Li, D. Deng, N. Wang, H. Zhang, S. Chang, *Opt. Express* **2015**, *23*, 27204.
[73] T. S. Seifert, N. M. Tran, O. Gueckstock, S. M. Rouzegar, L. Nadvornik, S. Jaiswal, G. Jakob, V. V. Temnov, M. Münzenberg, M. Wolf, M. Kläui, T. Kampfrath, *J. Phys. D* **2018**, *51*, 364003.
[74] L. Du, F. Roeder, Y. Li, M. Shalaby, B. Beleites, F. Ronneberger, A. Gopal, *Appl. Phys. A* **2021**, *127*, 846.
[75] M. S. Islam, C. M. B. Cordeiro, M. J. Nine, J. Sultana, A. L. S. Cruz, A. Dinovitser, B. W.-H. Ng, H. Ebendorff-Heidepriem, D. Losic, D. Abbott, *IEEE Access* **2020**, *8*, 97204.
[76] D. M. Nenno, L. Scheuer, D. Sokoluk, S. Keller, G. Torosyan, A. Brodyanski, J. Lösch, M. Battiato, M. Rahm, R. H. Binder, H. C. Schneider, R. Beigang, E. T. Papaioannou, *Sci. Rep.* **2019**, *9*, 13348.

© 2024 The Author(s). Advanced Photonics Research published by Wiley-VCH GmbH

26999293, 0, Downloaded from https://onlinelibrary.wiley.com/doi/10.1002/adpr.202400064 by Technical University Ostrava, Wiley Online Library on [17/09/2024]. See the Terms and Conditions (https://onlinelibrary.wiley.com/terms-and-conditions) on Wiley Online Library for rules of use; OA articles are governed by the applicable Creative Commons License

Supporting information: Maximizing the electromagnetic efficiency of spintronic terahertz emitters

Pierre Koleják[1,2], Geoffrey Lezier[2], Daniel Vala[1], Baptiste Mathmann[2], Lukáš Halagačka[1], Zuzana Gelnárová[1], Yannick Dusch[2], Jean-François Lampin[1], Nicolas Tiercelin[2], Kamil Postava[1], and Mathias Vanwolleghem[2]

[1]IT4Innovations National Supercomputing Center & Faculty of Materials Science and Technology, VSB – Technical University of Ostrava, 17. listopadu 15, 708 00 Ostrava, Czech Republic

[2] Université de Lille, CNRS, Centrale Lille, Université Polytechnique Hauts-de-France, UMR 8520 - IEMN, 59000 Lille, France

1 Simulation framework: Optical excitation

To compute the dynamic evolution of a femtosecond electromagnetic field, we utilize a Fourier series representation of the pulsed electric field vector [1, 2],

$$\mathbf{E} = \sum_{n=1}^{N} \mathbf{E}_n = \sum_{n=1}^{N} A_n \exp\left(\mathrm{j}\,\omega_n t\right) \Big[\mathbf{E}_{\mathrm{F},n} \exp\left(-\mathrm{j}\,\mathbf{k}_n \cdot \mathbf{r}\right) + \\ + \mathbf{E}_{\mathrm{B},n} \exp\left(\mathrm{j}\,\mathbf{k}_n \cdot \mathbf{r}\right) \Big], \tag{1}$$

where $\mathbf{k}_n$ represents the complex wave vector, while ω_n denotes the angular frequency. The electric amplitude vectors $\mathbf{E}_{\mathrm{F},n}$ and $\mathbf{E}_{\mathrm{B},n}$ correspond to the forward and backward amplitudes, respectively. The parameters t, $\mathbf{r}$, and j refer to time, the coordinate vector, and the imaginary unit, respectively. By combining a finite number (N) of harmonic plane waves $\mathbf{E}_n$, each characterized with the amplitude coefficient A_n following a Gaussian distribution, the Fourier series approach enables the individual calculation of the optical response for each frequency. This approach offers particular advantages for analyzing multilayered 1D structures, such as spintronic emitters. In such scenarios, the scattering matrix formalism proves to be an invaluable tool, providing numerical stability when dealing with materials that exhibit high absorption and layers that have significant differences in thickness (e.g., nanometer-scale metallic films versus micrometer-scale substrates) [3, 4].

By utilizing the scattering matrix formalism, we can determine transmission and reflection coefficients for the studied multilayered structure [2, 4]. Moreover, it enables us to calculate the forward and backward amplitudes at each layer for all frequencies independently. This allows for the superposition of these amplitudes to create the time-varying field distribution within the structure. We extend our analysis beyond the mere consideration of the spintronic emitter interface and a semi-infinite substrate. We include the entirety of the structure's layers, taking into account additional effects such as reflections at the vacuum/substrate interface and Fabry-Pérot reflections within the substrate itself.

It is crucial to acknowledge, however, that the Fourier series method has its limitations. Artifact signals, manifesting as periodically repeating time-domain signals and the Gibbs phenomenon may occur when the number of terms is insufficient [5, 6]. Nevertheless, this issue can be mitigated by carefully selecting the number of terms to ensure an accurate representation. Primarily, it is crucial to ensure that the simulated signal, encompassing all echoes, is sufficiently long before it begins to repeat. Otherwise, echoes from a previous period may appear

in the signal, or the signal may prematurely enter a repeating cycle. Significantly, the need for higher resolution becomes more acute with thicker layers and higher refractive indices. This requirement is not only due to the increased optical path length but also because of the more pronounced internal reflections associated with the latter.

2 Simulation framework: Nonstationary absorption

To accurately estimate the amount of pulse energy absorbed and converted into carrier motion within a lossy material, we examine the total mechanical energy E_{mech} of charged particles within a volume V [7, 8]. This mechanical energy is directly related to the Joule heating effect, represented by the right side of the equation, through the following relationship:

$$\frac{\mathrm{d}E_{\mathrm{mech}}}{\mathrm{d}t} = \mathrm{Re}\left\{\frac{1}{2}\int_V \mathbf{j}^* \cdot \mathbf{E}, \mathrm{d}x^3\right\}, \tag{2}$$

Here, $\mathbf{j}$ denotes the current density. To gain deeper insights, we further elaborate on the Joule heating expression by employing Poynting's theorem [7, 8, 9]:

$$\begin{aligned}\frac{1}{2}\int_V \mathbf{j}^* \cdot \mathbf{E}\,\mathrm{d}x^3 = -\frac{1}{2}\int_V \Big[&\nabla \cdot (\mathbf{E} \times \mathbf{H}^*) + \\ &+ \mathbf{E} \cdot \frac{\partial \mathbf{D}^*}{\partial t} + \mathbf{H}^* \cdot \frac{\partial \mathbf{B}}{\partial t}\Big]\mathrm{d}x^3,\end{aligned} \tag{3}$$

Within this equation, $\mathbf{H}$, $\mathbf{D}$, and $\mathbf{B}$ represent the Fourier series of the magnetic field, electric displacement, and magnetic induction, respectively. These components are associated with the $\mathbf{E}$ field as discribed in Equation (1). The Joule heating expression can be dissected into three distinct terms: (I) the divergence of the Poynting vector $\frac{1}{2}\nabla\cdot(\mathbf{E}\times\mathbf{H}^*)$, which represents the local energy flux in both incoming and outgoing directions; (II) the electric reactive power $\frac{1}{2}, \mathbf{E}\cdot\frac{\partial \mathbf{D}^*}{\partial t}$, which captures temporal changes in electric energy density; and (III) the magnetic reactive power $\frac{1}{2}, \mathbf{H}^*\cdot\frac{\partial \mathbf{B}}{\partial t}$, reflecting temporal variations in magnetic energy density.

Given that the interaction between the electromagnetic field and matter at optical frequencies predominantly occurs through charges, the electric reactive power term plays a pivotal role in absorption. We define a quantity, the absorptive heating density Q, to characterize the time-varying distribution of absorption power. By applying the Fourier series approach (as outlined in Section 1) to the electric reactive power term, we derive the following expression for the absorptive heating density Q:

$$\begin{aligned}\frac{1}{2}\,\mathbf{E}\cdot\frac{\partial \mathbf{D}^*}{\partial t} = \sum_{n=1}^{N}\sum_{m=1}^{M}\frac{1}{2}\,\mathrm{Re}\{\epsilon_m\}\,\frac{\partial \mathbf{E}_m^*}{\partial t}\cdot\mathbf{E}_n + \\ \underbrace{+\sum_{n=1}^{N}\sum_{m=1}^{M}\frac{1}{2}\,\mathrm{j}\,\mathrm{Im}\{\epsilon_m\}\,\frac{\partial \mathbf{E}_m^*}{\partial t}\cdot\mathbf{E}_n}_{Q},\end{aligned} \tag{4}$$

Here, ϵ denotes the complex permittivity. The spintronic emitter under consideration may comprise multiple ferromagnetic layers, totaling L layers. Each layer, indexed by l, possesses a thickness d_l. The total absorbed power P_{ab} within the spin-source layers is determined by integrating Q_l across the respective thicknesses and summing across all ferromagnetic layers:

$$P_{\mathrm{ab}}(t) = \sum_{l=1}^{L}\int_{d_l} Q_l(x,t)\;\mathrm{d}x. \tag{5}$$

Finally, the total absorbed energy, E_{ab}, is calculated by integrating the total absorbed power over time:

$$E_{\mathrm{ab}} = \int_t P_{\mathrm{ab}}(t)\,\mathrm{d}t. \tag{6}$$

3 Simulation framework: Optimization process

Our methodology is designed to optimize time-resolved absorption, with a particular focus on the initial excitation period. This approach is crucial in scenarios involving additional layers, thin substrates, short pulses, or spintronic cascades. In such cases, factors like backward reflection and multiple excitations play a significant role in shaping the time-dependent current source profile. Consequently, it becomes more relevant to analyze the evolution of absorption over time, rather than focusing solely on total absorbance. Notably, total absorbance encompasses all pulsed excitations, including those arising from Fabry-Pérot reflections within the substrate. Our strategy aims to synchronize all pulses within the spintronic layers temporally, moving away from the traditional use of infinite continuous waves to ensure a comprehensive solution. Additionally, it is essential to acknowledge that periodic structures may present multiple local solutions, particularly when a 2π phase condition is applied to the layers, potentially causing pulses to diverge. Our primary interest lies in the absorption at the ferromagnetic layers responsible for generating spin-electrons, rather than in the overall absorption which includes nonmagnetic layers, substrates, etc.

Furthermore, accounting for material dispersion becomes crucial, especially for ultrashort pulses with durations of 100 fs or less, characterized by their broad pulse spectrum. To meet these specific requirements, we utilize custom simulation codes that rely on Fourier series analysis (as discussed in Section 1). These models allow us to precisely track the dynamic evolution of pulse excitation and accurately capture the temporal absorption profile.

Accurately determining absorption is a critical component of our optimization process, as increased absorption contributes to the efficiency of spintronic emitters. For dielectric cavities, however, their influence on THz dipole emission is minimal. Our simulation codes further enable the optimization of either the peak-to-peak amplitude or the integrated power of the terahertz signals over time. This can be approached as either a single or a multi-objective global optimization problem. Such optimization is especially crucial for materials characterized by high permittivity or strong absorption. In these cases, the thickness of the layers becomes a key factor, and terahertz absorption significantly affects the overall efficiency of spintronic terahertz emitters (STE).

4 Simulation framework: Terahertz emission

To simulate terahertz emission, we employ a methodology analogous to that used for optical excitation, utilizing the scattering matrix formalism in tandem with Fourier series analysis, as discussed in [2, 4]. The primary difference, however, resides in the origin of emission within the interior of the spintronic emitter. To accurately model the emission source in our simulations, we suggest partitioning the scattering matrix $\boldsymbol{S}$ at a specific source coordinate into two parts: $\boldsymbol{S}1, p^-$ and $\boldsymbol{S}p^+, n$, subject to the following conditions:

$$\begin{bmatrix} F_p + F_{p+} \\ B_1 \end{bmatrix} = \underbrace{\begin{bmatrix} T_{1,p} & R_{p,1} \\ R_{1,p} & T_{p,1} \end{bmatrix}}_{\boldsymbol{S}_{1,p-}} \cdot \begin{bmatrix} F_1 \\ B_p + B_{p-} \end{bmatrix} + \begin{bmatrix} F_{p+} \\ 0 \end{bmatrix} \tag{7}$$

$$\begin{bmatrix} F_n \\ B_p + B_{p-} \end{bmatrix} = \underbrace{\begin{bmatrix} T_{p,n} & R_{n,p} \\ R_{p,n} & T_{n,p} \end{bmatrix}}_{\boldsymbol{S}_{p+,n}} \cdot \begin{bmatrix} F_p + F_{p+} \\ B_n \end{bmatrix} + \begin{bmatrix} 0 \\ B_{p-} \end{bmatrix}, \tag{8}$$

This division is schematically illustrated in Figure 1. The source terms F_{p+} (forward emission) and B_{p-} (backward emission) represent the distribution of forward (F_p) and backward (B_p) field amplitudes within the structure under study. These forward and backward amplitudes correspond to the components of the electric field, $\mathbf{E}\mathrm{F}, n$ and $\mathbf{E}\mathrm{B}, n$, as defined in Equation (1), respectively. Given that the structure is not externally illuminated by terahertz waves, the conditions $F_1 = B_n = 0$ apply. By solving the system of equations (8) and (7), we obtain the values

of B_1 and F_n. The inputs to the source terms F_{p+} and B_{p-} at the p-th layer are determined by the temporal derivative of the absorbed power $P_{ab} \approx \mathbf{j}_p$, which is indicative of the generated current.

$$F_{p+} = B_{p-} \propto \frac{\partial P_{ab}(x,t)}{\partial t} \tag{9}$$

The source can be positioned arbitrarily within the structure. Additionally, it is feasible to include multiple sources to simulate spintronic terahertz emitter (STE) cascades or volume emission throughout the entire layer. For this purpose, each source is computed separately, and their resulting fields are then coherently superimposed. The synchronization of the timing for multiple non-local sources is achieved by calculating the time-dependent absorption power, $Q(t)$, utilizing an approach that captures the temporal absorption profile. It should be noted that the plane-wave approximation might not perfectly align with the dipole emission characteristic of STEs. However, in the simulations presented here, this discrepancy has a minimal impact, as they are performed under conditions of normal incidence.

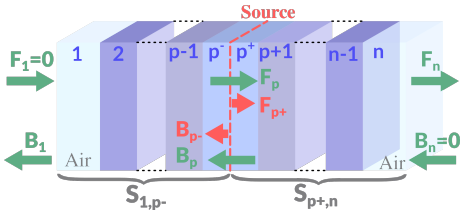


Figure 1: Implementation scheme for dipole source into S-matrix formalism: The sources F_{p^+} and B_p^- are placed between the S-matrix S_{1,p^-} of the first half and $S_{p^+,n}$ of the second half of the structure. The scheme also indicates that the input fields from an external source, F_1 and B_n, are not considered. The fields propagating through the structure are determined by the sources, aiming to identify the output fields F_n and B_1.

Similar approaches to introducing a source term in a matrix formalism are utilized in simulations involving dipoles, cavity-lasers, spin-transport, phonon-transport [10, 11, 12, 13, 14]. This approach has been extended to T-matrices for spintronic emitters as well [15]. However, our work facilitates a fully integrated simulation that links the excitation of spintronic terahertz emitters (STE) with their subsequent emission.

In the simulation's time domain (Section 3.4, Figure 6c), pulses are detected immediately outside the sample's edge. When STE is at the geometry's perimeter, it induces no delay; however, a delay of nd/c is produced when THz pulses pass through sapphire. Terahertz echoes, delayed by $2nd/c$, are significant only in cases where anti-reflective coatings are not applied. A minor reflection between 17 and 18 ps occurs as the anti-reflective coating counters an exceptionally broad 30 THz pulse for STE-Cavity. In the simulation, THz pulses represent the duration of excitation and are not influenced by the detector's response function, making them very short. Experimentally, these uncompensated echoes are not observable in Fig. 2a-b of Section 2.2. The presence of this small parasitic echo is noted in all simulations that incorporate a cavity. This occurrence may be attributed to the fact that the anti-reflective coating phenomenon is most effective at interfaces featuring a high refractive index [16, 17], specifically sapphire in contrast to SiO_2. Additionally, the optical characteristics of metals are critical and differ significantly for few-nanometer layers compared to bulk materials [18, 19, 20, 21]. We have used material properties from [22] for our simulations.

5 Fabrication Methods

The cavity consist of $6\times\{SiO_2/SiN_x\}$ layers (Section 1, Fig 1b-c) ended by an extra SiO_2 phase-matching layer. The choice for a DBR using silicon nitride and silica is the result of a compromise between realizing sufficient refractive index difference in the DBR and the available materials in our CVD system. Importantly, SiN_x and SiO_2 display similar dispersion over the wavelength range of the modelocked pumping laser, with an approximate refractive index difference of 0.54,

ensuring the creation of a robust photonic bandgap for the pump spectrum [23, 24]. The STE emitter itself is a conventional Pt/CoFeB/W trilayer, known for its record combination of strong and opposite spin Hall angles in Pt and W combining the contributions of opposite spin currents from CoFeB in a constructive manner [25, 22]. The Pt(2.1nm)/CoFeB(1.9nm)/W(2nm)-trilayer has been fabricated by RF-Diode sputtering in a LEYBOLD Z550 deposition equipment. The base vacuum in the deposition chamber is close to $3{\cdot}10^{-7}$mbar after filling the liquid nitrogen cold trap up. In order to induce a preferential magnetic direction in the emitters, the substrates are placed in an in-plane magnetic field with an approximate strength of 25 kA/m. The individual layers are sputtered from circular 4 inches targets. All three materials are deposited with a RF power P_{RF} of 216 W under a pure Argon atmosphere at $2{\cdot}10^{-3}$ mbar. The high precision of the nanometric thicknesses is ensured by a careful calibration of the deposition rate for each target in oscillation mode: for this method, the substrates are placed on a rotary susbtrate holder with a perfectly controllable rotation speed which allows a high repeatability. Each individual metal is calibrated by depositing a high number of passages under the sputtering target at a fixed rotation speed of 1rpm. Typically 150 "oscillations" (i.e. passages under the sputtering target) are performed. The resulting thickness is of the order of 100–150nm (at the chosen fixed rotation speed of 1rpm) and measured on a profilometer with a relative precision of a few %. This results in an extracted deposition rate expressed in nm/oscillation. This can then be further finetuned by slightly adjusting the rotation speed. If the extracted deposition rate would predict a fractional number of oscillations for the targeted thickness, this can be brought back to an integer number by modifying the rotation speed (tunable between 0.1 and 17rpm). In this way each metal layer of the STE is deposited with a precision up to 10%. The photonic crystal cavity was fabricated by Plasma Enhanced Chemical Vapor Deposition (PE-CVD) in an OXFORD Plasmalab80plus equipment. The SiN_x layers were fabricated in a base vacuum of 1000 mTorr ($\sim$1.3 mbar) under a flow of 360 sccm of 5% SiH_4/N_2, and 20 sccm of NH_3 precursor gas, at a temperature of 300°C and a RF power of 10 W. The deposition rate of the SiN layers is close to 14 nm/min, with a highly repeatable process and an expected 1% deviation of the thickness for a 200 nm layer. The SiO_2 layers were fabricated in the same 1000 mTorr base vacuum, under a flow of 150 sccm of 5% SiH_4/N_2, and 700 sccm of N_2O precursor gas, at a temperature of 300°C and a RF power of 20 W. The deposition rate of the SiO_2 layer is 77 nm/min, with a 0.5% deviation of the thickness for a 200 nm layer. All samples have been fabricated on z-cut double-side polished 500 µm thick sapphire substrates. Moreover, to reliably estimate the enhancement induced by the cavity, one quadrant of the substrates was masked during deposition of the crystal in order to keep an uncoated emitter zone as a reference.

6 Characterization of Materials through THz-TDS Analysis

The STE-Cavity samples were analysed on a home-made customised terahertz time-domain spectroscopy setup (THz-TDS), illustrated in Fig. 2. It is pumped by a Ti:sapphire oscillator MaiTai-HP from Spectra-Physics (< 100fs pulse duration, 80 MHz repetition rate), with a central wavelength tunability between 690-900 nm. The output beam is split into two separate beams: probe and pump. The probe beam is guided through a delay stage with a maximal delay of 2 ns in steps of 6.66 fs to control pump-probe delay and is subsequently focused on a LT-GaAs photoconductive (PC) dipole antenna (40 μm long), integrated with a hemispherical Si lens of 10 mm diameter to sample the generated THz signal. The pump beam is chopped at 1336 Hz and then tightly focused to a spotsize of approximately 50μm in diameter using a lens of 50 mm focal length to excite the investigated cavity-enhanced STE's. The excitation (average) pump power can reach up to 260 mW, but the presence of a tunable attenuator offers a flexible power control within the range of 0 to 80 mW. Placing the power meter probe beyond the attenuator and the chopper in the generation optical branch, we measure the adjusted modulated average power. This leads to pump pulse energies of maximally 2 nJ and maximum fluences of 0.05 mJ/cm^2, well below the reported destruction thresholds[26, 27].

To ensure proper magnetization, the STE is placed in an electromagnet and saturated at $\pm$11.14 kA/m. The generated emission is collimated by employing a TPX lens (25 mm) and directed onto the PC antenna. For reliable data acquisition, we implemented averaging through

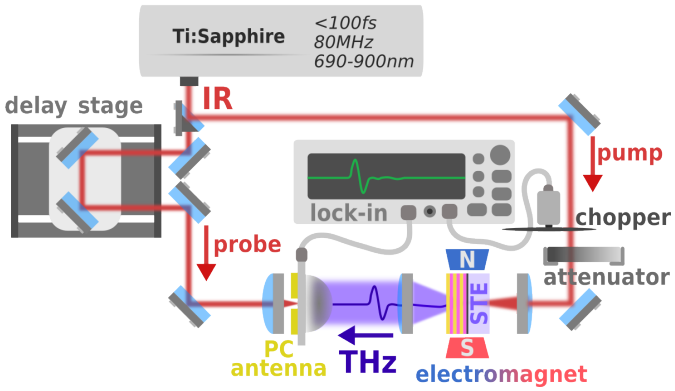


Figure 2: THz-TDS Setup: A Ti:Sapphire laser beam is divided into probe (directed through a delay line to a PC antenna) and pump paths (channeled through a chopper and adjustable attenuator onto an STE-cavity sample within a magnetic field, with detection by a lock-in amplifier).

a lock-in amplifier with a time constant of 100 ms, which was referenced with the chopping frequency.

7 Material characterization

We aimed to accurately assess the absorption characteristics of thin, highly absorptive spintronic materials - a crucial factor in optimizing enhancement cavities and achieving effective phase matching. The inherent sensitivity due to the thinness of these materials and their high absorption rates posed a challenge, as conventional tabulated values of CoFeB often resulted in underestimated absorption measurements. This underestimation significantly impacted the optimization process of our enhancement cavities. To overcome these limitations, we employed a combination of Mueller matrix ellipsometry and transmission measurements. This approach was necessary because regular multi-angle ellipsometry alone proved insufficient for determining the accurate absorption rates of these materials. The combined methodology allowed for a more precise characterization, essential for the effective design and optimization of our spintronic terahertz emitters.

Mueller matrix spectroscopic ellipsometry (MMSE) is a non-destructive optical technique widely renowned for its reliable performance characterizing multilayer systems [28, 29, 30, 31], including those as thin as a few tenths of a nanometer [32, 33, 34]. Even such minor changes in thickness cause easily measurable differences in the phase of polarization states, which ellipsometry detects. Such sensitivity makes MMSE an excellent tool for analyzing a spintronic emitter (STE) composed of three 2/1.8/2 nm thick Pt/CoFeB/W layers on a 0.5 mm sapphire substrate. A complete analysis (determining the optical functions and thicknesses of the individual STE layers) presents challenges due to the correlation of measured parameters and misinterpretation risks. The goal of the analysis is much easier here. We aim to obtain a correct multilayer model of the STE and check whether it satisfies the transmission intensity measured at a normal angle of incidence (measured using an Agilent Cary7000 double-beam spectrophotometer). This procedure requires two primary steps: determining the optical functions of CoFeB and correcting the substrate thickness. Given the well-defined layer thicknesses (sub-nm accuracy guaranteed by the fabrication process) and standard tabulated optical functions for W [35], Pt [36], and sapphire [37], the focus is on CoFeB layer material constants. This necessitates the determination of the CoFeB optical functions because of their expected variation due to possible different elemental abundances in the alloy.

We utilized a commercial Woollam RC2-DI Mueller matrix spectroscopic ellipsometer (MMSE), spanning the range 193–1700 nm, capable of tracking the complete polarization response of the sample, including anisotropy, depolarization, and multiple backside reflections. We analyzed the STE at reflection configuration at angles of incidence (AOIs) from 50 to 70

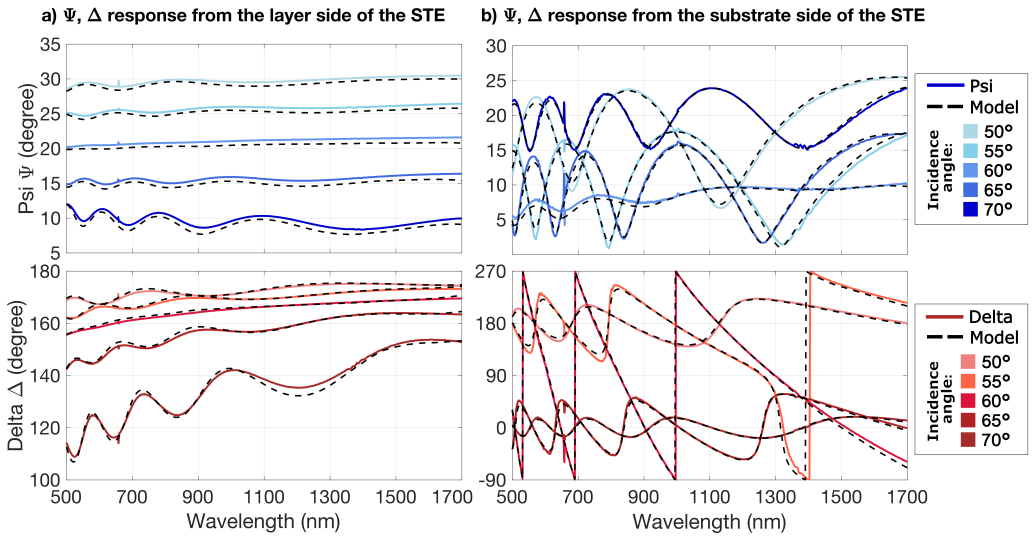


Figure 3: **a)** Ellipsometric angles ψ and Δ for the STE measured from the layer side across the 500—1700 nm spectral range. Solid and dashed lines represent respective model fits and experimental data for AOIs from 50 to 70 degrees. The sparse oscillations in ψ and Δ oscillations reflect the ultra-thin layer structure of the STE. **b)** Ellipsometric angles ψ and Δ from the substrate side of the STE. Much stronger changes in Δ confirm the sensitivity to the sapphire substrate. At the same time, concurrent spectral oscillations convey critical details about the multilayer structure in the back-reflection configuration.

degree, in 5-degree increments. Higher AOIs enhance sensitivity to polarization response, which is critical for accurately determining the STE's optical functions and thicknesses. We thus excluded AOI below 50 degrees and above 70 degrees, where the spot size exceeded the sample surface. The two-step procedure explained before requires two runs of measurements: from the layer and substrate sides.

Measurements from the STE layer side shown in Fig. 3a reveal the typical polarimetric response of ultra-thin metallic layers: a relatively flat ψ, Δ behavior with only sparse low-amplitude spectral oscillations reflecting the fine structure of the STE. These oscillations are extremely sensitive to small variations in the thicknesses of the layers. At fixed thicknesses, however, the oscillations take over the central role in identifying the material constants of the CoFeB. On the other hand, the significant Δ phase differences measured from the back side of the STE (Fig. 3b) indicate a sensitivity mainly to the substrate thickness. Furthermore, the presence of spectral oscillations in this configuration confirms the MMSE sensitivity to the STE multilayers even in this back-reflection arrangement. Combining these measurements provides a comprehensive understanding of the STE structure crucial for robust and accurate modeling.

Minimizing the parametric multilayer model requires two principal steps: obtaining a preliminary set of material constants for CoFeB and sapphire thickness based on ψ, Δ measurements. The optical constants of the CoFeB were parameterized using a B-Spline function, ensuring physical correctness by adhering to the Kramers-Kronig relations and using a resolution fine enough (node per 0.05 eV) to capture the complex spectral response of the CoFeB layer, but remaining far from the point-by-point fitting process that can lead to unphysical results. At this stage, the model imitated the ellipsometric data pretty well, providing the CoFeB optical functions quite similar to those depicted in Fig. 5. However, the optimization utterly fails to reproduce the measured transmittance of the STE. In other words, even negligible changes in the absorption spectrum of CoFeB make the model prefer different local minima, which causes drastic alterations in the modeled transmittance. Therefore, the next step is to correct the model for the measured transmission intensity depicted in Fig. 4, which involves further optimization against ψ, Δ, and intensity, assigning the intensity 20.000 times greater weight in the model. Such a weight appears to be excessive at first glance, however, this is where the model starts prioritizing intensity data over ellipsometry while managing previously obtained fitting results. The resulting model is compared with experiment in Fig. 3, Fig. 4, yields CoFeB optical

functions depicted in Fig. 5, and determines the sapphire substrate thickness to be 0.5023 mm.

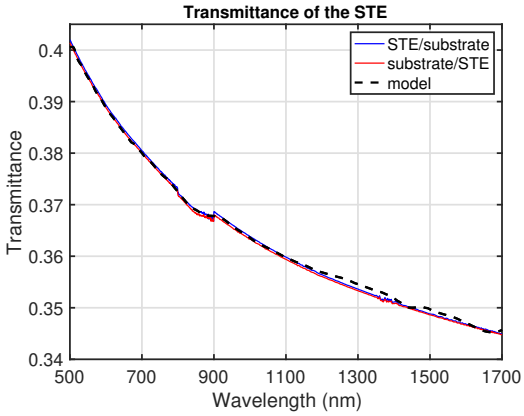


Figure 4: The transmittance of the STE measured from both side at a normal angle of incidence. The $\approx 0.2\,\%$ discrepancy between 800 nm and 900 nm is due to instrument systematic error and causes basically no inaccuracy in the model.

Indeed, the model inherits some limitations. It does not accurately represent experimental data below 500 nm, likely due to complex CoFeB absorption bands in this spectrum. Consequently, we excluded this region from our analysis, as it lies outside our area of interest. Attempts to incorporate surface roughness or intermixing layers (effective medium approximation, EMA) resulted in unphysical EMA layer thicknesses (50–100 % of actual STE layers) and failed to improve the model. Additionally, the instrument-induced change of grating and detector causes a systematic decrease in transmittance of about 0.2 % between 800–900 nm. However, this discrepancy has negligible influence on the overall fit quality and reliability since the fit-quality major determining factors are shape of the transmission curve and dominant sensitivity of the model to the ellipsometric response.

Concluding, a combined approach of MMSE and spectrophotometry is essential to assess the STE morphology and transmission performance. Relying on either method in isolation could lead to gross inaccuracies in determining the STE's optical functions or transmittance. Although we acknowledge that even with these constants, the model remains somewhat overestimated, whether due to the constants themselves or simplifications in the model. We highlight that there has been a substantial improvement, leading to effective optimization of the cavities.

It is also worth noting that these constants were also employed to demonstrate the responses of absorbance, reflectance, and transmittance observed in Figs. 3b, 4c-f and 5a. However, the simulation involves a thick substrate (500 µm of sapphire), leading to curves characterized by dense interference, which complicates their presentation. Considering the dense interference, we opted for a moving average (convolution filter) as the incoherent strategy because it is less computationally demanding than generating random phases [38]. This approach also eliminates the need for additional smoothing that would be necessary with random phase methods. For improved accuracy with incoherent methods, considering approaches that specifically address thick layers or rely on intensity-based formalisms is recommended [39, 40].

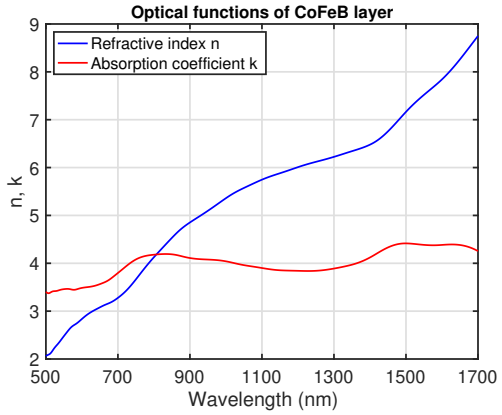


Figure 5: Derived refractive index and absorption coefficient for the CoFeB layer from the optimal model fit corrected to the transmission intensity.

References

[1] J.-C. Diels and W. Rudolph, *Ultrashort Laser Pulse Phenomena*. Elsevier, Academic Press, 2006.

[2] P. Bienstman, *Rigorous and efficient modelling of wavelenght scale photonic components*. PhD thesis, Gent University, 2001.

[3] L. Li, "Formulation and comparison of two recursive matrix algorithms for modeling layered diffraction gratings," *J. Opt. Soc. Am. A, JOSAA*, vol. 13, pp. 1024–1035, May 1996.

[4] A. Yariv and P. Yeh, *Optical Waves in Crystals: Propagation and Control of Laser Radiation*. Hoboken, NJ, USA: Wiley, Nov. 2002.

[5] A. J. Jerri, *The Gibbs Phenomenon in Fourier Analysis, Splines and Wavelet Approximations*. Springer US, 1998.

[6] D. Gottlieb and C.-W. Shu, "On the Gibbs Phenomenon and Its Resolution," *SIAM Rev.*, Aug. 2006.

[7] J. D. Jackson, *Classical Electrodynamics, 3rd Edition*. Hoboken, NJ, USA: Wiley, Aug. 1998.

[8] L. D. Landau and E. M. Lifshitz, *Electrodynamics of Continuous Media*. Oxford, England, UK: Pergamon, 1984.

[9] B. E. A. Saleh and M. C. Teich, *Fundamentals of Photonics*. John Wiley & Sons, Inc, Aug. 1991.

[10] K. Kurokawa, "Power Waves and the Scattering Matrix," *IEEE Trans. Microwave Theory Tech.*, vol. 13, pp. 194–202, Mar. 1965.

[11] V. Chiloyan, S. Huberman, Z. Ding, J. Mendoza, A. A. Maznev, K. A. Nelson, and G. Chen, "Green's functions of the Boltzmann transport equation with the full scattering matrix for phonon nanoscale transport beyond the relaxation-time approximation," *Phys. Rev. B*, vol. 104, p. 245424, Dec. 2021.

[12] V. P. Amin and M. D. Stiles, "Spin transport at interfaces with spin-orbit coupling: Formalism," *Phys. Rev. B*, vol. 94, p. 104419, Sept. 2016.

[13] H. Benisty, R. Stanley, and M. Mayer, "Method of source terms for dipole emission modification in modes of arbitrary planar structures," *J. Opt. Soc. Am. A, JOSAA*, vol. 15, pp. 1192–1201, May 1998.

[14] T. Fördös, H. Jaffrès, K. Postava, M. S. Seghilani, A. Garnache, J. Pištora, and H. J. Drouhin, "Eigenmodes of spin vertical-cavity surface-emitting lasers with local linear birefringence and gain dichroism," *Phys. Rev. A*, vol. 96, p. 043828, Oct. 2017.

[15] Y. Yang, S. Dal Forno, and M. Battiato, "Transfer-matrix description of heterostructured spintronics terahertz emitters," *Phys. Rev. B*, vol. 104, p. 155437, Oct. 2021.

[16] B. Carli, "Reflectivity of metallic films in the infrared," *JOSA*, vol. 67, no. 7, pp. 908–910, 1977.

[17] J. Kröll, J. Darmo, and K. Unterrainer, "Metallic wave-impedance matching layers for broadband terahertz optical systems," *Optics express*, vol. 15, no. 11, pp. 6552–6560, 2007.

[18] J. M. Camacho and A. Oliva, "Morphology and electrical resistivity of metallic nanostructures," *Microelectronics Journal*, vol. 36, no. 3-6, pp. 555–558, 2005.

[19] P. Fan, K. Yi, J.-D. Shao, and Z.-X. Fan, "Electrical transport in metallic films," *Journal of applied physics*, vol. 95, no. 5, pp. 2527–2531, 2004.

[20] N. Trivedi and N. Ashcroft, "Quantum size effects in transport properties of metallic films," *Physical Review B*, vol. 38, no. 17, p. 12298, 1988.

[21] D. K. C. Macdonald and K. Sarginson, "Size effect variation of the electrical conductivity of metals," *Proceedings of the Royal Society of London. Series A. Mathematical and Physical Sciences*, vol. 203, no. 1073, pp. 223–240, 1950.

[22] T. S. Seifert, N. M. Tran, O. Gueckstock, S. M. Rouzegar, L. Nadvornik, S. Jaiswal, G. Jakob, V. V. Temnov, M. Muenzenberg, M. Wolf, *et al.*, "Terahertz spectroscopy for all-optical spintronic characterization of the spin-Hall-effect metals Pt, W and $Cu_{80}Ir_{20}$," *Journal of Physics D: Applied Physics*, vol. 51, no. 36, p. 364003, 2018.

[23] K. Luke, Y. Okawachi, M. R. Lamont, A. L. Gaeta, and M. Lipson, "Broadband mid-infrared frequency comb generation in a Si_3N_4 microresonator," *Optics letters*, vol. 40, no. 21, pp. 4823–4826, 2015.

[24] I. H. Malitson, "Interspecimen comparison of the refractive index of fused silica," *Josa*, vol. 55, no. 10, pp. 1205–1209, 1965.

[25] T. Seifert, S. Jaiswal, U. Martens, J. Hannegan, L. Braun, P. Maldonado, F. Freimuth, A. Kronenberg, J. Henrizi, I. Radu, *et al.*, "Efficient metallic spintronic emitters of ultrabroadband terahertz radiation," *Nature photonics*, vol. 10, no. 7, pp. 483–488, 2016.

[26] T. Vogel, A. Omar, S. Mansourzadeh, F. Wulf, N. M. Sabanés, M. Müller, T. S. Seifert, A. Weigel, G. Jakob, M. Kläui, *et al.*, "Average power scaling of THz spintronic emitters efficiently cooled in reflection geometry," *Optics Express*, vol. 30, no. 12, pp. 20451–20468, 2022.

[27] F. Paries, N. Tiercelin, G. Lezier, M. Vanwolleghem, F. Selz, M.-A. Syskaki, F. Kammerbauer, G. Jakob, M. Jourdan, M. Kläui, Z. Kaspar, T. Kampfrath, T. S. Seifert, G. von Freymann, and D. Molter, "Fiber-tip spintronic terahertz emitters," *Opt. Express*, vol. 31, pp. 30884–30893, Sep 2023.

[28] X. Chen, H. Gu, L. Jiamin, C. Chen, and S. Liu, "Advanced Mueller matrix ellipsometry: Instrumentation and emerging applications," *Science China Technological Sciences*, vol. 65, 08 2022.

[29] E. Garcia-Caurel, A. D. Martino, J.-P. Gaston, and L. Yan, "Application of Spectroscopic Ellipsometry and Mueller Ellipsometry to Optical Characterization," *Applied Spectroscopy*, vol. 67, no. 1, pp. 1–21, 2013. PMID: 23317664.

[30] D. Aspnes, "Spectroscopic ellipsometry — Past, present, and future," *Thin Solid Films*, vol. 571, pp. 334–344, 2014. 6th International Conference on Spectroscopic Ellipsometry (ICSE-VI).

[31] M. Losurdo and K. Hingerl, *Ellipsometry at the Nanoscale*. Springer Berlin Heidelberg, 2013.

[32] J. N. Hilfiker, N. Hong, and S. Schoeche, "Mueller matrix spectroscopic ellipsometry," *Advanced Optical Technologies*, vol. 11, no. 3-4, pp. 59–91, 2022.

[33] A. Cumurcu, X. Feng, L. D. Ramos, M. A. Hempenius, P. Schön, and G. J. Vancso, "Sub-nanometer expansions of redox responsive polymer films monitored by imaging ellipsometry," *Nanoscale*, vol. 6, pp. 12089–12095, 2014.

[34] Y. Karmakov, A. Paskaleva, and D. Spassov, "Depth profiling of very thin HfO_2/Al_2O_3 stacks by ellipsometry," *Journal of Physics: Conference Series*, vol. 2240, no. 1, p. 012049, 2022.

[35] E. D. Palik, *Handbook of Optical Constant of Solids*, vol. 1. Boston: Academic Press, 1991.

[36] J.A. Woollam, Co., Inc., "CompleteEASE software v6.72," 1999-2023. Platinum optical constants from KK fit to opaque film: 192–1700 nm.

[37] J.A. Woollam, Co., Inc., "CompleteEASE software v6.72," 1999-2023. GenOsc model for saphire substrate – ordinary (extraordinary) axis: 175–1700 nm.

[38] M. C. Troparevsky, A. S. Sabau, A. R. Lupini, and Z. Zhang, "Transfer-matrix formalism for the calculation of optical response in multilayer systems: from coherent to incoherent interference," *Opt. Express*, vol. 18, pp. 24715–24721, Nov. 2010.

[39] B. Harbecke, "Coherent and incoherent reflection and transmission of multilayer structures," *Appl. Phys. B*, vol. 39, pp. 165–170, Mar. 1986.

[40] K. Postava, T. Yamaguchi, and R. Kantor, "Matrix description of coherent and incoherent light reflection and transmission by anisotropic multilayer structures," *Appl. Opt.*, vol. 41, pp. 2521–2531, May 2002.

II

Paper II

Spintronic terahertz emitters with integrated metallic terahertz cavities

Martin Mičica, Adrien Wright, Pierre Koleják, Geoffrey Lezier, Kamil Postava, Jacques Hawecker, Anna de Vetter, Jerome Tignon, Juliette Mangeney, Henri Jaffres, Romain Lebrun, Nicolas Tiercelin, Mathias Vanwolleghem, Sukhdeep Dhillon
Nanophotonics, **13** (2024)

Research Article

Martin Mičica*, Adrien Wright, Pierre Koleják, Geoffrey Lezier, Kamil Postava, Jacques Hawecker, Anna De Vetter, Jerome Tignon, Juliette Mangeney, Henri Jaffres, Romain Lebrun, Nicolas Tiercelin, Mathias Vanwolleghem and Sukhdeep Dhillon*

Spintronic terahertz emitters with integrated metallic terahertz cavities

https://doi.org/10.1515/nanoph-2023-0807
Received November 14, 2023; accepted February 12, 2024;
published online March 1, 2024

Abstract: Spintronic terahertz emitters (STEs), based on optical excitation of nanometer thick ferromagnetic/heavy metal (FM/HM) heterojunctions, have become important sources for the generation of terahertz (THz) pulses. However, the efficiency of the optical-to-THz conversion remains limited. Although optical techniques have been developed to enhance the optical absorption, no investigations have studied the application of THz cavities. Here, to enhance the THz efficiency of STEs in a selected THz spectral range, FM/HM structures are realized on ultra-thin sapphire layers with metallic mirrors to create $\lambda/4$ THz resonant cavities. THz emission time domain spectroscopy of these STE/sapphire/mirror heterostructures, with sapphire thicknesses ranging from 110 μm to 25 μm, shows enhancement of the emitted THz field that fits the $\lambda/4$ cavity resonance with up to a doubling of the field in the spectrum, and in agreement with temporal simulations of the emitted THz pulse. By taking advantage of birefringent materials, we further show the potential of control of the polarization state of the emitted THz pulse. This work shows the potential of enhancing and engineering THz emission from STEs using THz cavities that can be controlled over a broad spectral range, which can be easily combined with optical cavities.

Keywords: THz spintronic emitters; THz time domain spectroscopy; metallic resonator

***Corresponding authors: Martin Mičica and Sukhdeep Dhillon**, Laboratoire de physique de l'Ecole Normale Supérieure, ENS, Université PSL, CNRS, Sorbonne Université, Université Paris Cité, F-75005, Paris, France, E-mail: martin.micica@phys.ens.fr (M. Mičica), sukhdeep.dhillon@phys.ens.fr (S. Dhillon).
https://orcid.org/0000-0002-5487-9570 (S. Dhillon)
Adrien Wright, **Anna De Vetter**, **Jerome Tignon and Juliette Mangeney**, Laboratoire de Physique de l'Ecole Normale Supérieure, ENS, Université PSL, CNRS, Sorbonne Université, Université Paris Cité, F-75005, Paris, France, E-mail: adrien.wright@phys.ens.fr (A. Wright), anna.de-vetter@phys.ens.fr (A. De Vetter), jerome.tignon@phys.ens.fr (J. Tignon), juliette.mangeney@phys.ens.fr (J. Mangeney).
https://orcid.org/0000-0002-4354-4257 (J. Mangeney)
Pierre Koleják, Univ. Lille, CNRS, Centrale Lille, Univ. Polytechnique Hauts-de-France, UMR 8520-IEMN, F-59000, Lille, France; and IT4Innovations National Supercomputing Center & Faculty of Materials Science and Technology, VSB - Technical University of Ostrava, 17. listopadu 15, 708 00 Ostrava, Czech Republic, E-mail: pierre.kolejak@vsb.cz
Geoffrey Lezier, **Nicolas Tiercelin and Mathias Vanwolleghem**, Univ. Lille, CNRS, Centrale Lille, Univ. Polytechnique Hauts-de-France, UMR 8520-IEMN, F-59000, Lille, France, E-mail: geoffrey.lezier@centralelille.fr (G. Lezier), nicolas.tiercelin@iemn.fr (N. Tiercelin), mathias.vanwolleghem@univ-lille.fr (M. Vanwolleghem)
Kamil Postava, IT4Innovations National Supercomputing Center & Faculty of Materials Science and Technology, VSB - Technical University of Ostrava, 17. listopadu 15, 708 00 Ostrava, Czech Republic, E-mail: kamil.postava@vsb.cz
Jacques Hawecker, Femtosecond Spectroscopy Unit, Okinawa Institute of Science and Technology Graduate University, Onna-son, Okinawa, 904-0495, Japan, E-mail: jacques.Hawecker@oist.jp
Henri Jaffres and Romain Lebrun, Laboratoire Albert Fert, CNRS, Thales, Université Paris-Saclay, 1 Avenue Augustin Fresnel, 91767, Palaiseau, France, E-mail: henri.jaffres@cnrs-thales.fr (H. Jaffres), romain.lebrun@cnrs-thales.fr (R. Lebrun)

1 Introduction

Spintronic terahertz emitters (STEs) are promising sources for the generation of THz short pulses by near-infrared (NIR) femtosecond excitation for THz time domain spectroscopy (TDS). Over a short period of time, they can now compete with well-established THz sources such as optical rectification in nonlinear crystals. There are several advantages of STEs including their very broad spectral bandwidth, negligible dependence on optical pump wavelength, manipulation of the polarization of the emitted THz pulse by an applied magnetic field, and no requirements for electric bias or crystal orientation [1]–[5]. Further, the active material is only a few nanometers thick with easily manipulated materials, making it possible to deposit these STEs on any supporting substrate or support [6], [7]. These features make STEs a versatile and novel source for generating THz radiation for a wide range of applications, bringing new device

Open Access. © 2024 the author(s), published by De Gruyter. This work is licensed under the Creative Commons Attribution 4.0 International License.

concepts that would not be possible with other types of THz sources.

The operation of an STE is based on spin-to-charge conversion (SCC) via the inverse spin-Hall effect (ISHE) [8], [9]. A typical STE consist of ferromagnetic (FM) and heavy metal (HM) layers with thicknesses on the order of a few nanometers. When excited by a NIR femtosecond pulse, electrons (majority with spin-up) in the FM layer are excited above their Fermi level and a spin polarized current flows through the spin selective interface between the FM and HM. This spin current is converted to short charge current in the HM by the ISHE and results in the emission of a THz pulse. The polarization of emitted THz pulse is perpendicular to the magnetization of FM layer and the spin current. A range of studies have investigated different metallic systems to optimize the conversion efficiency and bringing insights into the SCC processes [10]–[12]. Beyond the inverse SHE, which is purely a bulk effect, extensive investigations have investigated STEs through the inverse Rashba–Edelstein effect that occurs at quantum interfaces such as in FM/topological insulator heterostructures [13]–[15].

Photonic-based techniques have become important to increase the THz efficiency of STEs and take advantage of the integration possibilities of STEs. For example, cavities based on photonic crystals or dielectric mirrors have been investigated to maximize the NIR pump absorption in the FM layers, permitting to increase the NIR to THz conversion by up to 2.5 times [16] and permitting peak fields greater than 1.5 MV/cm [17], [18] in large area STEs pumped by amplified laser systems. However, no photonic methods have been applied directly on the THz pulse generated. In this work, we demonstrate the realization of STEs with integrated THz quarter wavelength cavities, permitting to enhance and control the THz spectral emission from these structures. We exploit metallic-based THz cavities (quasi Fabry–Perót) [19] where STEs are deposited on ultra-thin sapphire substrates with a back metal mirror. The acquired data are supported by theoretical simulations in the time and frequency domains and provides an important tool for further improvements in the performance and engineering of THz cavities. Additionally, we take this THz cavity approach and demonstrate the concept of polarization control of the THz radiation utilizing a cavity constructed around a birefringent medium.

2 Concept of THz cavity

Figure 1 shows conceptually our approach where a THz pulse is generated in an STE using a femtosecond laser. The THz pulse generated in the FM/HM layer propagates in both left and right directions with similar amplitudes, as shown in Figure 1(a). Owing to the lower contrast of refractive indices between metal/substrate (usually glass or sapphire) compared to metal/air, more power can be emitted into the side with the substrate. In the reflection configuration, when the STE is optically pumped directly (not through the substrate) and the THz pulse is collected from the same side, the second pulse propagating via the substrate can be reflected in the same direction by incorporating a metallic mirror. This results in two THz pulses in the time domain, with a delay given by thickness of substrate and refractive index of the substrate, as depicted on Figure 1(b). The second pulse will exhibit an opposite phase owning to the reflection from the metal. Note that this can be observed only for substrates with low absorption in THz spectral range, such as sapphire or high resistivity silicon. By choosing the right thickness of the substrate, typically corresponding to a quarter wavelength condition, the delay between pulses can be decreased to the level that the pulses overlap and their electric field sum together (Figure 1(c)). Assuming that both pulses have similar amplitudes, the final amplitude can be potentially doubled or even further enhanced at resonant conditions (i.e., where thickness, $d = \lambda/4n$ where λ is the wavelength and n is refractive index) [19].

3 Samples and experimental setup

To realize the THz cavity, spintronic emitters were fabricated on double side polished sapphire substrates (A cut, $1\bar{1}02$) with varying thicknesses ranging from 111 µm to 25 µm (chosen to highlight the effect of cavity thicknesses – see simulations below). These substrate types were also chosen to highlight the possibility of adding an extra functionality in the control of the THz polarization (see below). An optimized spintronic trilayer was deposited by magnetron sputtering on the top side consisting of W(2 nm)/CoFeB(1.8 nm)/Pt(2 nm). On the opposite side of the substrates, a thick metal layer (Pt, approx. 200 nm) was deposited, acting as metallic mirror and thus creating the THz cavity. After this growth preparation, the thicknesses of the samples were verified by a calibrated gauge that confirmed thicknesses of 111 µm, 39 µm, 29 µm, and 25 µm.

A custom THz TDS system, shown in Figure 2, was employed to study THz pulse generation from the prepared STEs. A NIR pulse from a Ti:Sapphire oscillator (Coherent Mira, 100 fs, central wavelength 800 nm, 200 mW average power after optical chopper) was focused by a lens through the hole in the back of a parabolic mirror onto the sample under normal incidence. The emitted THz pulses from the STEs were collected by the same parabolic mirror and

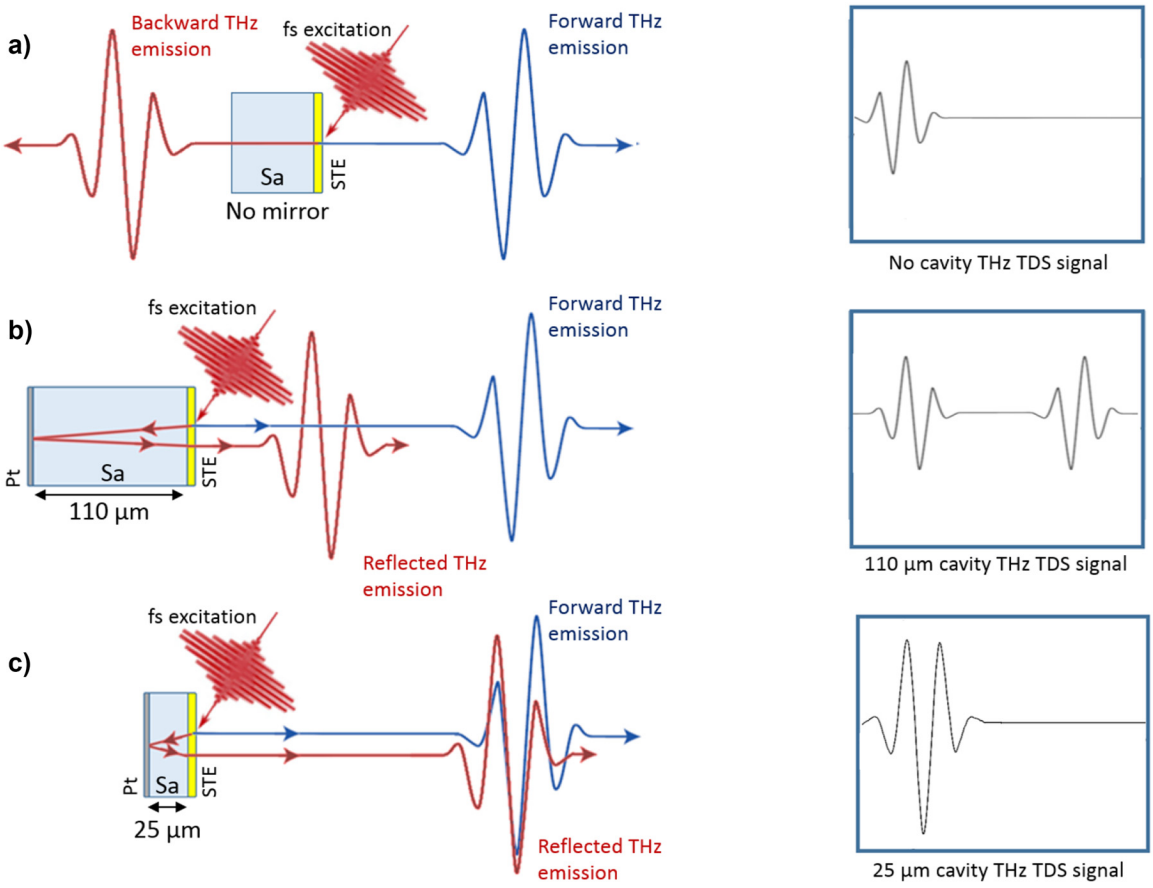


Figure 1: THz signal enhancement principle based on THz cavities optically excited with a femtosecond laser. (a) Standard STE emitting THz pulses in both left and right directions (reflection from substrate not shown), (b) collection of the second pulse with 110 µm thick substrate with back metal mirror, and (c) adjustment of the substrate thickness to 25 µm to realize a THz cavity and hence a single pulse for maximum THz field strength.

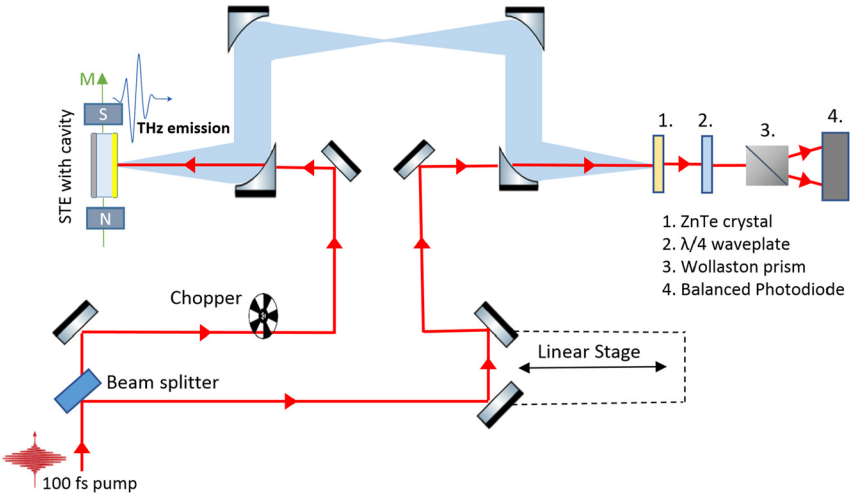


Figure 2: Scheme of terahertz time domain setup in reflection configuration where STE is excited with a femtosecond laser, generating a THz pulse that is detected using standard electro-optic sampling.

focused by a set of parabolic mirrors on to an electro-optic crystal (ZnTe, 1 mm) for coherent sampling using a probe NIR beam from the oscillator. The delay of the probe was controlled by a linear motor stage. The probe was focused through the hole in the last parabolic mirror to superpose with the THz pulse on the electro-optic crystal.

An electro-optic signal with sensitivity to the horizontal THz polarization with femtosecond resolution was then measured by a Wollaston prism, a balanced photodetector and the delay line. The STE samples were mounted in a rotation stage with permanent magnets (approx. 30 mT field) with independent rotation of the in-plane magnetic field and the sample. The THz beam path was purged by dry air to remove water vapor absorption. Teflon and polyethylene filters were used to remove residuals of the NIR pump pulse.

4 Results and discussion

The measured THz time domain signals of the different STEs are shown in Figure 3(a). The signal from the thickest 111 µm sample shows a temporal trace with a total of four pulses, the forward and the reflected, separated by 2.5 ps on their arrival time at the detection scheme.

The extra optical path length p that the THz pulse propagates can be approximated (by neglecting both interfaces Pt/sapphire and sapphire/STE) by the formula $p = 2 \times d \times n_{\mathrm{THz}}$, where n is the refractive index of the cavity medium (sapphire fast axis, 1.76 @ 800 nm [20], 3.07 @ 1 THz [21]) and d is thickness of the cavity. As the 111 µm cavity is thick, the overlap of the different generated THz pulses is effectively zero. The first detected pulse at ∼2 ps corresponds to the main pulse propagating toward the collecting parabolic mirror after excitation by the NIR pulse. Owing to the transparency of the sapphire substrate, the NIR pump pulse residue after excitation of the STE propagates inside the sapphire substrate and is reflected from the Pt mirror back toward the STE layer, which generates a second THz pulse at ∼3.5 ps about 0.5× of the first pulse amplitude. As the optical path length for NIR pulse is short, owing to the low refractive index, the detected THz signal is close to the first THz pulse. This is followed by the third THz pulse at ∼4.5 ps, which corresponds to the reflection of the first THz

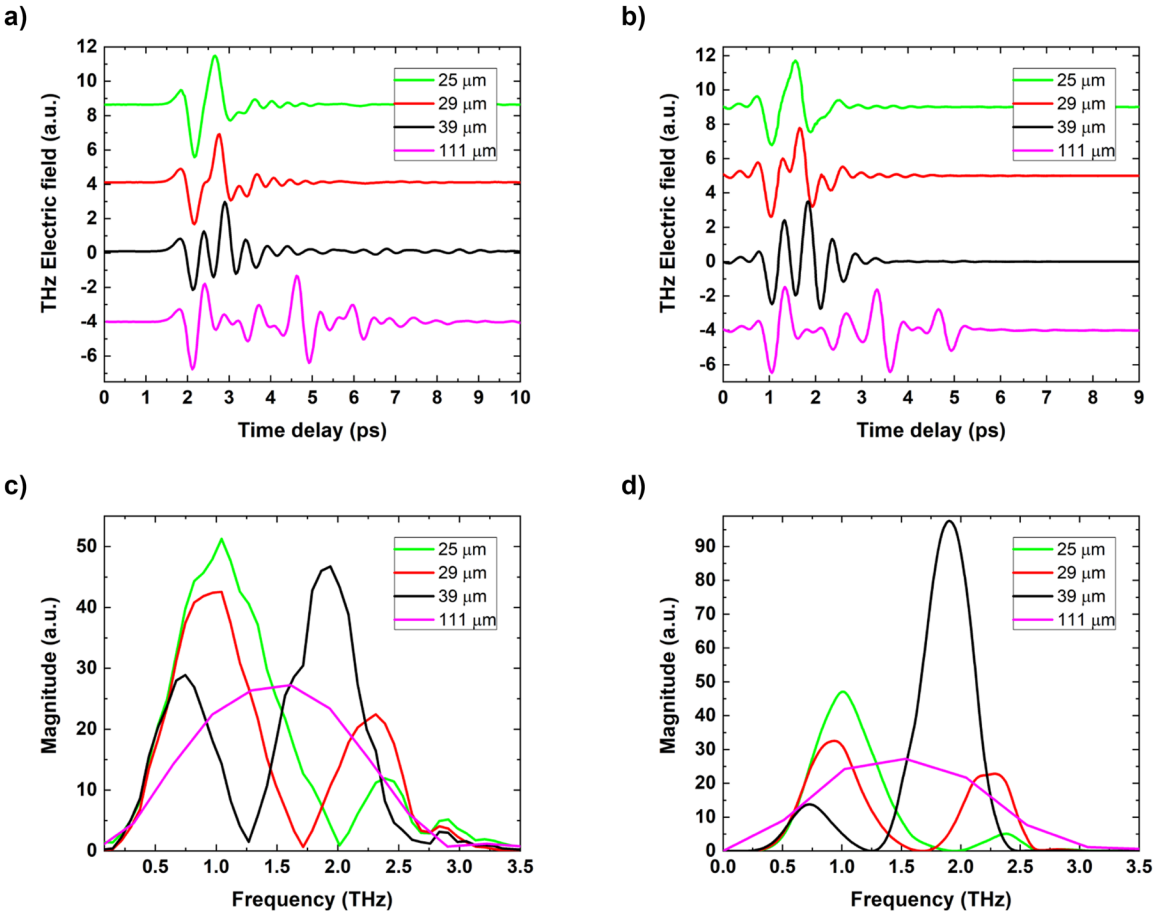


Figure 3: Comparison of experimental and simulated THz emission from spintronic THz cavities. (a) Experimental and (b) simulated THz TDS temporal signals, (c) experimental spectra and (d) simulated spectra of the signals for four different size sapphire cavities. Simulations of (b) and (d) were calculated by using the Scattering Matrix formalism. Spectra for the 111 µm sample is apodized only around the first pulse to remove the interference pattern.

pulse propagating in opposite direction (into the substrate) and then reflected by the back Pt mirror. The fourth THz pulse at ∼6 ps is the reflection of the second NIR excitation of STE that propagates back and forth from the substrate. As the STE layer behaves as antireflection coating in THz frequencies [22], further reflections between STE and Pt mirror are not observed, and further excitations by the propagating NIR pump are negligible owing to their reduced intensities. The reflection of THz pulses from Pt mirror causes a phase reversal for the third and fourth THz pulses. The phase of the second one is not reversed as it originates from the STE excitation, which is independent of the phase and polarization of the NIR pump and is dependent only on orientation of the magnetic field.

As the thickness of the substrate is decreased, the temporal form changes drastically. As noted above, for the 111 µm sample (Figure 3(a)), we can observe and identify individual pulses. However, for the 39 µm thick cavity, the pulses start to sufficiently overlap to create a complex and long oscillating profile of the THz signal. For the 29 µm cavity, one pulse is formed with slight deformations. For a cavity thickness of 25 µm, the pulses overlap enough to create one single cycle with a slight oscillating tail after the main pulse.

The THz emission spectra of the STE samples on 111 µm, 39 µm, 29 µm, and 25 µm sapphire substrates are shown in Figure 3(b). The spectra are obtained by applying a Fast Fourier Transform on the time domain signals.

The sum of the multiple time shifted pulses in the time domain creates a magnitude modulation of the signal in the frequency domain owning to the cavity resonances. The typical reference STE spectrum, i.e., without the effect of the substrate/cavity, is obtained by apodization of the time trace of the 111 µm sample around the first pulse. The spectrum is continuous, with a 2 THz bandwidth centered at a frequency of 1.5 THz. This also highlights the performance benchmark of our THz TDS system with a detection bandwidth of up to 3.5 THz. The spectral bandwidth is dominantly limited by the length of NIR probe pulse and properties of electro-optic crystal [23], [24] (e.g., thickness).

For the spectrum of the 39 µm thick cavity (without time domain apodization), we observe an interference pattern with two maxima (at 0.75 and 1.8 THz) and one minimum (at 1.25 THz). These represent constructive ($\lambda/4$ cavity conditions) and destructive ($\lambda/2$ cavity condition for the latter) interferences inside the cavity resonator. As the thickness decreases, these features shift toward higher frequencies with increasing magnitude in the first maximum as expected ($d \simeq \lambda/4n$). Figure 4 shows a summary of the improvements in peak-to-peak signal amplitude in the time domain (top) and magnitude of interference

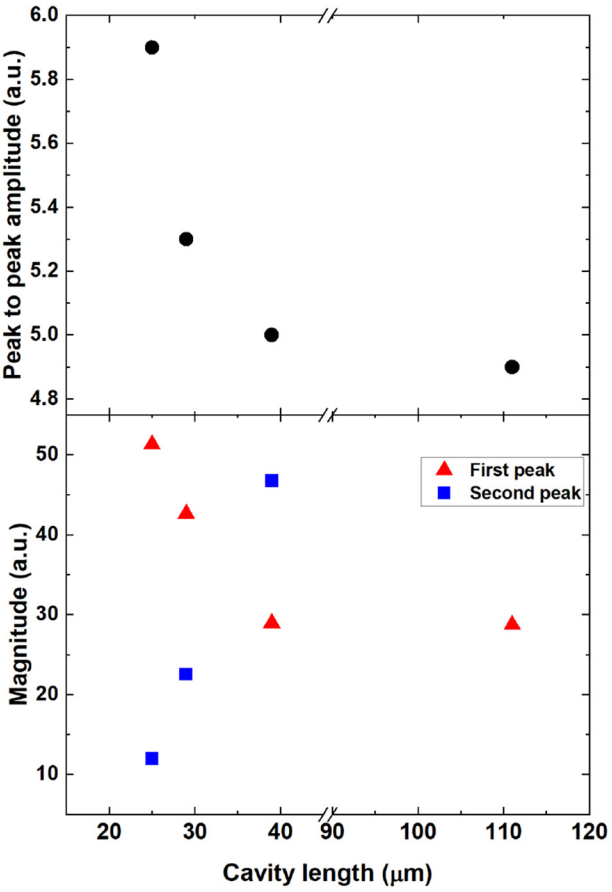


Figure 4: Peak-to-peak value of the temporal signals (top) and spectral magnitude of the two emission peaks (bottom) as a function of sapphire substrate thickness.

maxima position in the spectral domain (bottom). Continuous increase of the peak-to-peak amplitude is observed with decreasing thickness of the substrates with 1.2× increase in the time domain and 2× in the frequency domain for 25 µm cavity. From a frequency spectra point of view, it is possible to modify the emission bands of the STE by choosing the corresponding thickness of the substrate, with the enhancement in magnitude reaching double that of the STE without THz cavity.

To further investigate the influence of the cavity length on the frequency bandwidth of the STE, we performed several simulations by the finite element method (FEM) in commercially available software (COMSOL Multiphysics) and a custom frequency-domain nonstationary field dynamics code. The latter approach facilitates the simulation of time-dependent NIR excitation within STEs and the subsequent pulsed terahertz emission. This is accomplished through the application of the Scattering Matrix formalism (S-formalism) and Fourier series decomposition [25]–[27]. The method involves the coherent summation of the

calculated field at each frequency component, resulting in a nonstationary/pulsed response and Poynting's theorem for the time-evolution of the absorption, serving as the current source for dipole emission. The main advantage of S-formalism is its numerical stability, particularly in structures that combine thin metallic layers with thick multilayer structures. The results of simulated terahertz emission are corrected for the instrument function derived from measurements of a well-known reference sample (i.e., without cavity).

The electric field simulation results for the time domain (Figure 3(b)) and frequency domain (Figure 3(d)) show an excellent agreement with the measured data. The 39 μm cavity frequency components around 2 THz, however, overestimate the magnitude by a factor of 2, possibly a result of higher losses in type A sapphire. These simulations can also be used as a tool to investigate the optimal thickness to, for example, avoid the deconstructive interference in the measured spectral bandwidth. Figure 5 shows the peak-to-peak field in the time domain as a function of cavity thickness, predicting the highest field enhancement of 2.3 for a cavity with a thickness of 6 μm. Although this would be difficult to realize using sapphire materials, this would be relatively easily achievable using silicon-based membranes.

Regarding FEM simulations, Figure 6 shows the field collected in the far field from the emitter as a function of frequency and sapphire cavity thickness based on the simulations of the radiated field. This FEM approach is based on the terahertz emission being simulated with a transient current generated on the sample surface at the interface with air. Note that the optical pump generation mechanism

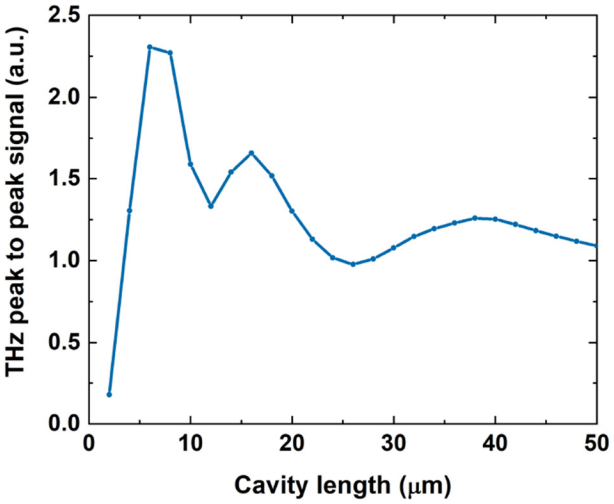


Figure 5: Simulated peak-to-peak THz signal by Scattering Matrix formalism showing maximum potential enhancement of the peak-to-peak field for thickness of 6 μm.

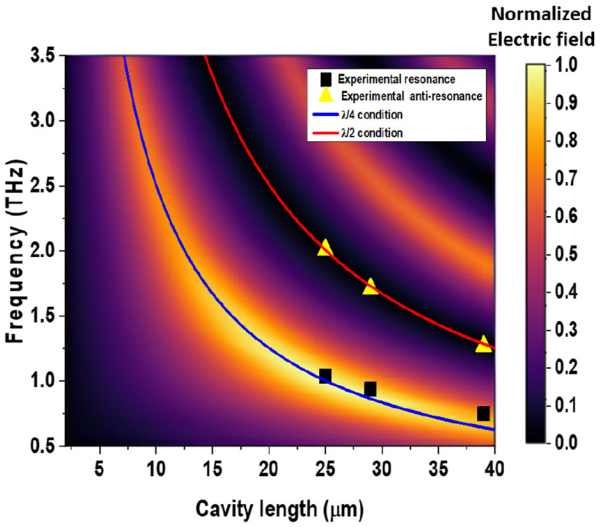


Figure 6: The FEM (COMSOL) simulated electric field as a function of frequency and cavity length (sapphire substrate thickness). The $\lambda/4$ and the $\lambda/2$ conditions are represented by a blue and a red line, with points showing experimental results for emission peak and emission gap.

is not included and, therefore, the second excitation owing to the transmission of part of the NIR pulse through the sapphire and its reflection back to the STE is not taken in account. Figure 7 shows an example of the simulated 2D radiated field at 1.0 THz emission, which is used to calculate the emitted field as a function of frequency of Figure 6. A resonant behavior is observed with a shift of the peak emission frequency toward higher THz values as the cavity thickness is reduced. The $\lambda/4$ and the $\lambda/2$ condition are represented by a blue line and a red line, respectively. The experimentally measured emission peak and emission gap of the 25 μm, 29 μm, and 39 μm cavity emitters are represented in the plot by squared black dots and triangular

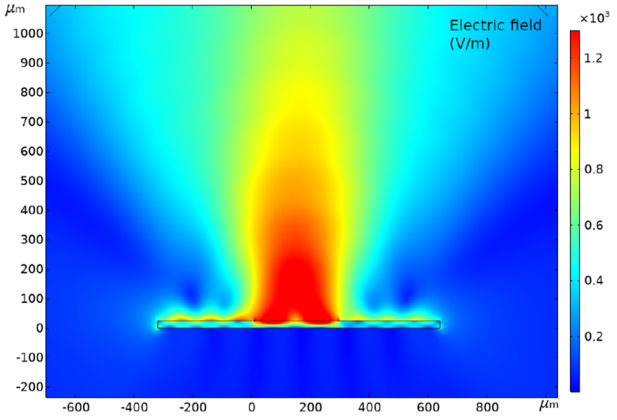


Figure 7: Example of electric field simulation by FEM (COMSOL) for 25 μm thick cavity at 1 THz resonance.

yellow dots, respectively. This plot shows that all three experimental gaps and peaks fit very well with the $\lambda/4$ condition and the $\lambda/2$ condition.

Figure 8 shows a comparison between experimental and FEM simulated spectra of the cavity STEs. Positions of maxima and minima fits well despite an overestimate of the first peak for the 29 and 39 µm cavities, which can be a result of the extra propagating NIR pulses owing to the optical transparency of sapphire (presence of total 4 THz pulses in experimental results – see above), while the FEM simulations include only the two THz pulses.

5 Toward THz polarization control

As a perspective of this work, we study the potential of integrated polarization control using the birefringent nature of the single crystal sapphire, where ordinary and extraordinary refractive indices at 1 THz are $n_o = 3.07$ and $n_e = 3.41$, respectively [21]. The sapphire substrates used in our samples are from A-cut sapphire, in which n_o and n_e are perpendicular to each other in the plane of the sample. Therefore, by rotating the sample, refractive index for THz pulse changes as the substrate behaves like waveplate. This can be used to change the polarization of the reflected THz pulse. Figure 9 shows change in horizontal polarization of emitted THz pulse during rotation of the 111 µm thick substrate crystal from fast (n_o) to slow (n_e) axis.

It can be seen that the time domain signal for the two last pulses (reflections from the back mirror) changes with the angle of rotation. Signals for 0° and 90° have the same shape but are shifted in time owning to higher optical path length for pulses traveling along the slow axis with higher refractive index n_e.

The situation is different for the thinnest cavity sample, where the change of polarization is not so high owning to the short path in the birefringent substrate. Figure 10 shows time domain signal from the 25 µm cavity for orientation 0° and 45° and where the horizontal and vertical THz electric field polarizations are measured. The former contains virtually only horizontally polarized THz pulses, but at 45°, the ellipticity of the THz pulse is noticeable. This ellipticity is created by the two THz pulses where the first is polarized horizontally and the second can have arbitrary polarization (depending on the thickness and rotation angle of the substrate). Note that here the substrate acts as monochromatic waveplate and the ellipticity of the second pulse varies for frequency components so would be on most interest for narrowband THz generation [28]. By designing the substrate not only for THz cavity but also for proper phase retardation over larger bandwidth of the THz pulses (i.e., achromatic waveplate), an STE source that can produce any desired linear, circular, or any arbitrary elliptical polarization can be potentially realized. This would be of particular interest for THz time domain ellipsometry.

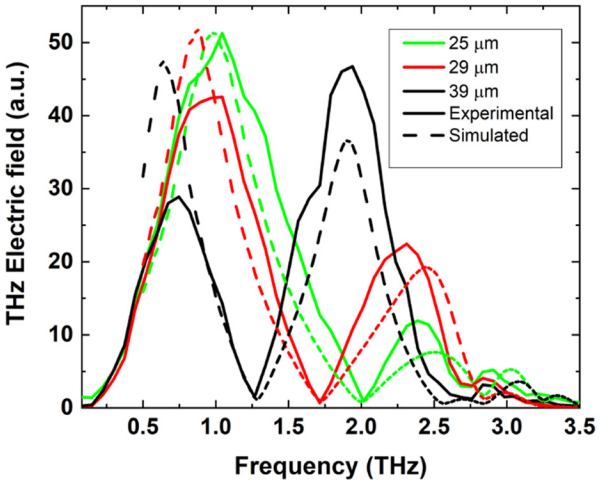


Figure 8: Comparison of experimental (continuous line) and spectra simulated by FEM (COMSOL, dashed line) as a function of frequency for the four different cavity thicknesses.

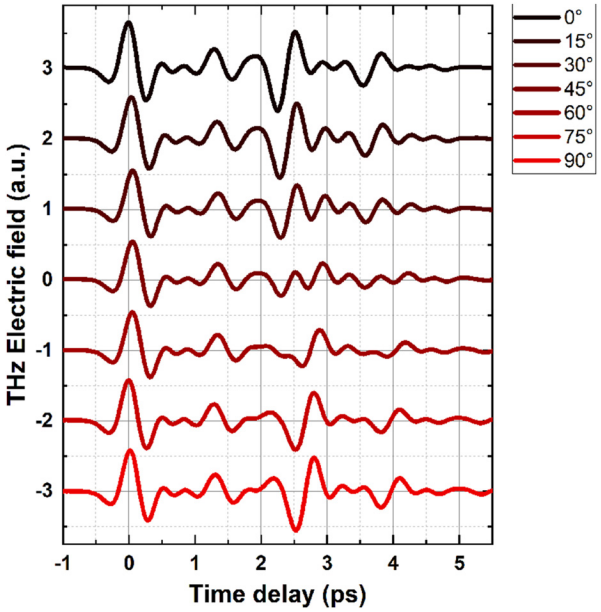


Figure 9: Change of THz time domain signal of STE sample on 111 µm thick substrate as a function of the rotation of the substrate crystal. Shift of time traces is a result of the birefringence in A-type sapphire. Only horizontal polarization is detected.

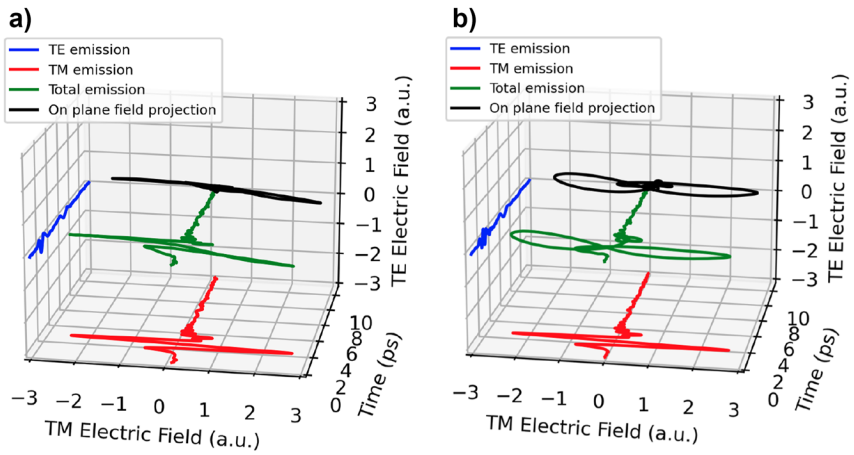


Figure 10: Transverse electric (red) and transverse magnetic (blue) experimental fields of the 25 µm thick cavity for azimuthal angle with (a) the smallest TE component (0°) and (b) with the highest TE component (45°). The green curve is the total emission to highlight the elliptical nature of the emitted pulse and the black curve is the 2D projection on the back plane.

6 Conclusions

The aim of our presented study was to show the incorporation of STEs with THz cavities, permitting to enhance and control the spectral field of the emitted THz pulse. All previous approaches have been based on enhancing the optical absorption using optical cavities with no photonic control of the THz emitted pulse. Here, this was achieved by incorporating a back metallic reflector on thin transparent sapphire substrates, effectively creating quarter wavelength THz cavities. Several STE samples on sapphire substrates were investigated with thickness 111 µm, 39 µm, 29 µm, and 25 µm, with a deposited back metallic mirror. THz emission time domain spectroscopy in reflection configuration revealed and improved maximum peak amplitudes of the THz signal in both time domain and frequency domain with the thinnest cavity showing the most important enhancements (twice the spectral amplitude at maximum emission), with single cycle emission. The frequency domain showed interference effects with maxima and minima in the spectra that shifted toward higher frequencies with decreasing thicknesses. Experimental results were compared with simulations by finite element method and a custom frequency-domain nonstationary field dynamics approach with a very good agreement. While our design is currently applicable only in reflection configuration, it would be possible to realize an emitter working in transmission configuration using a material with a cavity that is transparent for NIR pump and reflecting for the generated THz beam. These proof-of-principle of STE-based THz cavities can be further improved, where the developed simulations tools predicting improvements of doubling the temporal field for thinner cavities. This approach is scalable and could also be easily combined with optical dielectric mirrors or photonic cavities to further enhance the efficiency or the maximum THz emitted fields from STEs. As well as improving the STEs, this work of THz field enhancements could also open up perspectives of efficient even-order harmonic generation and THz down-conversion from spintronic heterojunctions [29].

Research funding: The authors acknowledge the support from the European Union's Horizon 2020 research and innovation Programme under grant agreement No 863155 (FET-OPEN sNebula) and No 964735 (FET-OPEN EXTREME-IR), and the French National Research Agency (ANR) under ANR-21-CE24-0011-02 TRAPIST. This work was supported by a government grant managed by the ANR as a part of the France 2030 investment plan from PEPR SPIN ANR-22-EXSP 0003. This work was supported by the Ministry of Education, Youth and Sports of the Czech Republic through the e-INFRA CZ (ID:90254) and SP2023/026.

Author contributions: All authors have accepted responsibility for the entire content of this manuscript and approved its submission.

Conflict of interest: Authors state no conflict of interest.

Data availability: The datasets generated during and/or analyzed during the current study are available from the corresponding author on reasonable request.

References

[1] T. Seifert, *et al*., "Efficient metallic spintronic emitters of ultrabroadband terahertz radiation," *Nat. Photonics*, vol. 10, no. 7, pp. 483—488, 2016.

[2] E. T. Papaioannou and R. Beigang, "THz spintronic emitters: a review on achievements and future challenges," *Nanophotonics*, vol. 10, no. 2, pp. 1243—1257, 2021.
[3] W. Wu, C. Yaw Ameyaw, M. F. Doty, and M. B. Jungfleisch, "Principles of spintronic thz emitters," *J. Appl. Phys.*, vol. 130, no. 9, p. 091101, 2021.
[4] Z. Feng, *et al*., "Spintronic terahertz emitter," *J. Appl. Phys.*, vol. 129, no. 1, p. 010901, 2021.
[5] P. Koleják, G. Lezier, K. Postava, J.-F. Lampin, N. Tiercelin, and M. Vanwolleghem, "360° polarization control of terahertz spintronic emitters using uniaxial FeCo/$TbCo_2$/FeCo trilayers," *ACS Photonics*, vol. 9, no. 4, pp. 1274—1285, 2022.
[6] F. Paries, *et al*., "Fiber-tip spintronic terahertz emitters," *Opt. Express*, vol. 31, no. 19, pp. 30884—30893, 2023.
[7] Z. Jin, *et al*., "Cascaded amplification and manipulation of terahertz emission by flexible spintronic heterostructures," *Laser Photonics Rev.*, vol. 16, no. 9, p. 2100688, 2022.
[8] B. Miao, S. Huang, D. Qu, and C. Chien, "Inverse spin hall effect in a ferromagnetic metal," *Phys. Rev. Lett.*, vol. 111, no. 6, p. 066602, 2013.
[9] J. Sinova, S. O. Valenzuela, J. Wunderlich, C. Back, and T. Jungwirth, "Spin hall effects," *Rev. Mod. Phys.*, vol. 87, no. 4, pp. 1213—1260, 2015.
[10] J. Hawecker, *et al*., "Spintronic THz emitters based on transition metals and semi-metals/Pt multilayers," *Appl. Phys. Lett.*, vol. 120, no. 12, p. 122406, 2022.
[11] C. Bull, *et al*., "Spintronic terahertz emitters: status and prospects from a materials perspective," *APL Mater.*, vol. 9, no. 9, p. 090701, 2021.
[12] J. Hawecker, *et al*., "Spin injection efficiency at metallic interfaces probed by THz emission spectroscopy," *Adv. Opt. Mater.*, vol. 9, no. 17, p. 2100412, 2021.
[13] M. B. Jungfleisch, *et al*., "Control of terahertz emission by ultrafast spin-charge current conversion at Rashba interfaces," *Phys. Rev. Lett.*, vol. 120, no. 20, p. 207207, 2018.
[14] E. Rongione, *et al*., "Ultrafast spin-charge conversion at $SnBi_2Te_4$/Co topological insulator interfaces probed by terahertz emission spectroscopy," *Adv. Opt. Mater.*, vol. 10, no. 7, p. 2102061, 2022.
[15] E. Rongione, *et al*., "Spin-momentum locking and ultrafast spin-charge conversion in ultrathin epitaxial $Bi_{1x}Sb_x$ topological insulator," *Adv. Sci.*, vol. 10, no. 19, p. 2301124, 2023.
[16] P. Kolejak, *et al*., "Highly efficient terahertz spintronic emitter integrated with optimized photonic crystal," in *Conference Paper*, vol. 2022-August, 2022 [Online]. Available at: https://www.scopus.com/inward/record.uri?eid=2-s2.0-85139843190&doi=10.1109%2fIRMMW-THz50927.2022.9895662&partnerID=40&md5=ea3a0f771e5737df73fda633a8908b0e.
[17] T. Seifert, *et al*., "Ultrabroadband single-cycle terahertz pulses with peak fields of 300 kV/cm^{-1} from a metallic spintronic emitter," *Appl. Phys. Lett.*, vol. 110, no. 25, p. 252402, 2017.
[18] R. Rouzegar, *et al*., "Broadband spintronic terahertz source with peak electric fields exceeding 1.5 MV/cm," *Phys. Rev. Appl.*, vol. 19, no. 3, p. 034018, 2023.
[19] J. Hawecker, *et al*., "Cavity-based photoconductive sources for real-time terahertz imaging," *Photonics Res.*, vol. 8, no. 6, pp. 858—863, 2020.
[20] M. J. Dodge, "Refractive index," in *Handbook of Laser Science and Technology*, vol. IV, CRC Press, 1986, p. 30.
[21] D. Grischkowsky, S. Keiding, M. Van Exter, and C. Fattinger, "Far-infrared time-domain spectroscopy with terahertz beams of dielectrics and semiconductors," *J. Opt. Soc. Am. B*, vol. 7, no. 10, pp. 2006—2015, 1990.
[22] J. Kröll, J. Darmo, and K. Unterrainer, "Metallic wave-impedance matching layers for broadband terahertz optical systems," *Opt. Express*, vol. 15, no. 11, pp. 6552—6560, 2007.
[23] T. Kampfrath, J. Nötzold, and M. Wolf, "Sampling of broadband terahertz pulses with thick electro-optic crystals," *Appl. Phys. Lett.*, vol. 90, no. 23, p. 231113, 2007.
[24] S. Casalbuoni, H. Schlarb, B. Schmidt, P. Schmüser, B. Steffen, and A. Winter, "Numerical studies on the electro-optic detection of femtosecond electron bunches," *Phys. Rev. Spec. Top. — Accel. Beams*, vol. 11, no. 7, p. 072802, 2008.
[25] P. Koleják, *et al*., "Maximizing the electromagnetic efficiency of spintronic terahertz emitters," 2024, Preprint. [Online]. Available at: https://arxiv.org/abs/2402.05833.
[26] P. Bienstman, "Rigorous and efficient modelling of wavelength scale photonic components," Ph.D. dissertation, Ghent University, 2001.
[27] K. Postava, T. Yamaguchi, and R. Kantor, "Matrix description of coherent and incoherent light reflection and transmission by anisotropic multilayer structures," *Appl. Opt.*, vol. 41, no. 13, pp. 2521—2531, 2002.
[28] P. Kolejak, *et al*., "Spintronic inverse spin hall photomixing: demonstration of THz CW and frequency comb generation," in *Conference Paper*, vol. 2022-August, 2022 [Online]. Available at: https://www.scopus.com/inward/record.uri?eid=2-s2.0-85139845793&doi=10.1109%2fIRMMW-THz50927.2022.9896051&partnerID=40&md5=d4b23b62a146d47ff5565ff7ed4196d1.
[29] I. Ilyakov, *et al*., "Efficient ultrafast field-driven spin current generation for spintronic terahertz frequency conversion," *Nat. Commun.*, vol. 14, no. 1, p. 7010, 2023. .

Paper III

III

Optical damage thresholds of single-mode fiber-tip spintronic terahertz emitters

Felix Paries, Felix Selz, Jean-François Lampin, Pierre Koleják, Geoffrey Lezier, Nicolas Tiercelin, Mathias Vanwolleghem, Tobias Kampfrath, Tom S. Seifert, Georg von Freymann, Daniel Molter
Optics Express, **32/14** (2024)

Research Article | Vol. 32, No. 14 / 1 Jul 2024 / Optics Express 24826
Optics EXPRESS

Optical damage thresholds of single-mode fiber-tip spintronic terahertz emitters

FELIX PARIES,[1,2,*] FELIX SELZ,[1,2] CRISTIANE N. SANTOS,[3] JEAN-FRANÇOIS LAMPIN,[3] PIERRE KOLEJÁK,[3,4] GEOFFREY LEZIER,[3] DAVID TROADEC,[3] NICOLAS TIERCELIN,[3] MATHIAS VANWOLLEGHEM,[3] AHMED ADDDA,[5] TOBIAS KAMPFRATH,[6] TOM S. SEIFERT,[6,7] GEORG VON FREYMANN,[1,2] AND DANIEL MOLTER[1]

[1] *Fraunhofer Institute for Industrial Mathematics ITWM, Department Materials Characterization and Testing, 67663 Kaiserslautern, Germany*
[2] *Department of Physics and Research Center OPTIMAS, RPTU Kaiserslautern-Landau, 67663 Kaiserslautern, Germany*
[3] *University of Lille, CNRS, Centrale Lille, Université Polytechnique Hauts-de-France, UMR 8520-IEMN, 59000 Lille, France*
[4] *Faculty of Materials Science and Technology, VSB-Technical University of Ostrava, 708 00 Ostrava, Czech Republic*
[5] *University of Lille, CNRS, INRAE, Centrale Lille, UMR 8207–UMET, 59000 Lille, France*
[6] *Department of Physics, Freie Universität Berlin, 14195 Berlin, Germany*
[7] *TeraSpinTec GmbH, Lüneburger Str. 26, 10557 Berlin, Germany*
[*] *felix.paries@itwm.fraunhofer.de*

Abstract: Spintronic terahertz emitters (STEs) are gapless, ultrabroadband terahertz sources that can be driven within a wide pump-wavelength and repetition-rate range. While STEs driven by strong pump lasers operating at kilohertz repetition rates excel in generating high electric field strengths for terahertz spectroscopy or ellipsometry, newly advancing technologies such as ultrafast modulation of terahertz polarization, scanning tunneling microscopy, laser terahertz emission nanoscopy, and fully fiber-coupled integrated systems demand an STE pumping at megahertz repetition rates. In all these applications the available terahertz power is ultimately limited by the STE's optical damage threshold. However, to date, only very few publications have targeted this crucial topic and investigations beyond the kilohertz repetition-rate regime are missing. Here, we present a complete study of our single-mode fiber-tip STEs' optical damage thresholds covering the kilohertz, megahertz, and gigahertz repetition-rate regimes as well as continuous-wave irradiation. As a very important finding, we introduce the necessity of classifying the optical damage threshold into two regimes: a low-repetition-rate regime characterized by a nearly constant fluence threshold, and a high-repetition-rate regime characterized by an antiproportional fluence dependence ("average-power threshold"). For our single-mode fiber-tip STEs, the transition between these regimes occurs around 4 MHz. Moreover, we present a cohesive theory of the damaging thermodynamical processes at play and identify temperature-driven inter-layer diffusion as the primary cause of the STE failure. These findings are substantiated by atomic force microscopy, infrared scattering-type scanning near-field optical microscopy, and scanning transmission electron microscopy measurements. This new level of understanding offers a clear optimization lever and provides valuable support for future advancements in the promising field of spintronic terahertz emission.

© 2024 Optica Publishing Group under the terms of the Optica Open Access Publishing Agreement

#525747 https://doi.org/10.1364/OE.525747
Journal © 2024 Received 4 Apr 2024; revised 2 May 2024; accepted 2 May 2024; published 24 Jun 2024

Optics EXPRESS

1. Introduction

Over the last decades, a variety of different terahertz emitters have been developed. A useful classification divides them into two main classes: (1) those based on off-resonant charge motion within nonlinear media of broken inversion symmetry ("optical rectification") [1,2] such as inorganic crystals [3] or suitable organic materials [4], and (2) those based on resonantly induced photocurrents such as photoconductive antennas [5–8], laser-ionized gases and liquids [9–13], or the recently developed spintronic terahertz emitters (STEs) [14–18].

STEs are based on the down conversion of an ultrashort laser pulse into an ultrabroadband terahertz pulse through a sequence of spin-current generation, spin-to-charge conversion, and current-to-field conversion. Due to their simple metallic thin-film-stack design, they can be sputtered onto various substrates and, thus, be fabricated and scaled at low cost. The metallic nature in combination with an excess-energy-induced terahertz spin voltage [19] enables the STEs to be pumped across a broad wavelength range encompassing terahertz [20], infrared [21], visible [22], and ultraviolet [23], which makes them a very versatile class of terahertz emitters. Moreover, their emission was shown to cover the full terahertz range without any spectral gaps outperforming all terahertz emitter classes except laser-ionized gases in terms of bandwidth [24]. However, in contrast to laser-ionized gases, STEs do not necessarily require pulse energies on the order of hundreds of microjoules to photo-ignite a plasma [17] but can be operated at pulse energies in the picojoule regime. To compete with the traditional emitter classes in terms of generated terahertz power and electric field strength, large-area STEs are used. Using a beam expander in combination with appropriate thermal management, terahertz pulses with peak electric fields above 1.5 MV/cm and fluences above 1 mJ/cm^2 were achieved offering a promising alternative to traditional $LiNbO_3$-crystals as a high-field source [25].

As all solid-state-terahertz emitters, STEs are subject to material destruction if a specific pump-fluence or average-pump-power-density threshold is exceeded. This property becomes a major challenge in applications where either a high electric field strength or a small beam diameter is required.

However, to date, only two studies have targeted this crucial challenge of optical damage threshold. Both of them, by Kumar et al. (1 kHz, 4-8 mJ/cm^2) [26] and Vogel et al. (100-400 kHz, 4-5 mJ/cm^2) [27], addressed repetition rates below 400 kHz. To the best of the authors' knowledge, the optical damage behavior at repetition rates above 400 kHz has not been investigated in detail yet, even though it is of crucial importance for many recently emerging STE applications such as ultrafast modulation of terahertz polarization [28,29], scanning tunneling microscopy (STM) [30], laser terahertz emission nanoscopy (LTEN) [31], inverse-spin-Hall photomixing [32], and fully fiber-coupled integrated systems [33].

Here, we reveal the necessity of classifying the optical damage threshold into two regimes: a high-peak-power, low-repetition-rate regime characterized by a nearly constant fluence threshold, and a low-peak-power, high-repetition-rate regime characterized by an antiproportional fluence dependence ("average-power threshold"). Taking advantage of our recently developed single-mode fiber-tip STEs, where the pump field is guaranteed to be nearly identical for every sample due to its waveguiding nature, we were able to characterize the optical damage threshold with high accuracy. Covering a repetition-rate range from 200 kHz to 1 GHz as well as continuous-wave irradiation, we could reveal a transition from the constant-fluence-threshold regime to the average-power-threshold regime at approximately 4 MHz.

Moreover, using atomic force microscopy (AFM), infrared scattering-type scanning near-field optical microscopy (s-SNOM), and scanning transmission electron microscopy (STEM) measurements, we found temperature-driven inter-layer diffusion to be the responsible damage mechanism restricting the optical-to-terahertz-conversion processes.

Optics EXPRESS

2. Methods

2.1. Fabrication

The spintronic W(2.0 nm) / FeCoB(1.8 nm) / Pt(2.0 nm) tri-layer structure was deposited on the fiber tips using a thin-film sputtering process. Prior to deposition, a cleaning procedure involved ultrasonication in successive baths of acetone (30 s), isopropyl alcohol (120 s), and de-ionized water (120 s). The W/FeCoB/Pt spintronic emitters were deposited by RF-diode sputtering in LEYBOLD Z550 equipment where the individual layers are sputtered from circular 4-inch targets. In particular, the $Fe_{60}Co_{20}B_{20}$ alloy is obtained from a target with this stoichiometry. To ensure high precision in the thicknesses, the deposition was carried on a rotatory turn-table substrate holder in an oscillation mode: each time the substrate passes under the target, which corresponds to one oscillation, a layer of the material is deposited with a thickness that depends on the angular speed of the turn-table. The deposition is carefully calibrated beforehand by depositing a film with 100 oscillations.

2.2. Method of inflicting damage

To precisely measure the optical damage threshold with statistical significance, we destroyed more than 30 single-mode fiber-tip STEs by intentionally exceeding the pump threshold. Due to the waveguiding nature of the single-mode glass fibers, the pump field is guaranteed to be nearly identical for every sample (5.75 μm mode field radius). This removes the mode field area as a free parameter and allows calculating the fluence accurately with only the irradiance to be measured. The irradiance has been controlled via a suitable combination of pump current and attenuation.

Figure 1(a) illustrates the damage setup consisting of an erbium-doped fiber laser (EDFL), an erbium-doped fiber amplifier (EDFA), and a fiber-tip STE sample. The fiber-tip STEs are butt-coupled to the pump fiber via a standard FC/PC fiber connection and an index-matching gel is used to minimize reflection losses at the interface. Additionally, the transmittance is carefully monitored to ensure identical initial conditions for each sample. The repetition-rate dependence of the optical damage threshold is investigated by employing four EDFL systems operating at around 1550 nm. These systems cover the repetition-rate range from 200 kHz to 1 GHz as well as continuous-wave irradiation (0.2-80 MHz: *in-house EDFL + APE pulseSelect*, 100 MHz: *Menlo ELMO*, 1 GHz: *Menhir 1550*, CW: *Yenista Optics Tunics T100S-HP*).

Figure 1(b) depicts the damage method: each fiber-tip STE sample is irradiated for 2 minutes at each pump stage (0 - 10 mW, 1 mW step size). The material damage is monitored between the pump stages at a reference level 1 mW below the threshold and during each pump stage. The decision for a pump period of 2 minutes was based on our experience that this duration is typically long enough to detect a damage onset. In previous measurements, e.g. near-field imaging [33], we did not observe any performance decrease while operating the single-mode fiber-tip STEs below the damage threshold for many hours. Nevertheless, due to the ramping and limited irradiation periods, the measured damage thresholds may be slightly biased towards higher pump powers.

2.3. Methods of detecting damage

To detect and investigate the optical damage thresholds of our single-mode fiber-tip STEs, we employed three different detection methods: (a) terahertz-amplitude detection, (b) optical-microscopy detection, and (c) infrared-transmittance detection. These are illustrated in Fig. 2.

2.3.1. Terahertz-amplitude detection

As will be seen in the results, the pump-induced material damage is accompanied by an irreversible drop in infrared-to-terahertz conversion efficiency. Thus, recording the temporal evolution of the terahertz peak-to-peak amplitude in the time domain for each pump stage provides the most

Optics EXPRESS

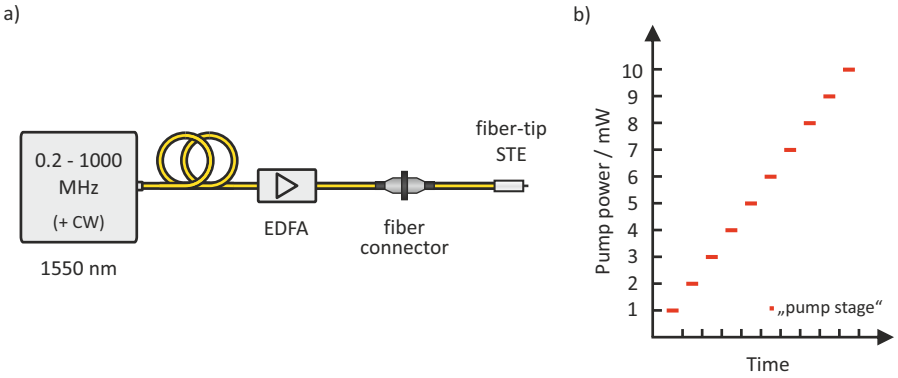


Fig. 1. Method of inflicting damage. a) The single-mode fiber-tip STE is damaged by intentionally exceeding the pump threshold. To cover a broad repetition-rate range from 0.2-1000 MHz (+CW), various erbium-doped fiber laser systems with a central wavelength around 1550 nm have been employed. More than 30 fiber-tip STEs have been destroyed to achieve statistical significance. b) Each of the samples underwent a ramp with 2 minutes of irradiation at each pump stage. Between and during each pump stage, damage-detection measurements have been conducted.

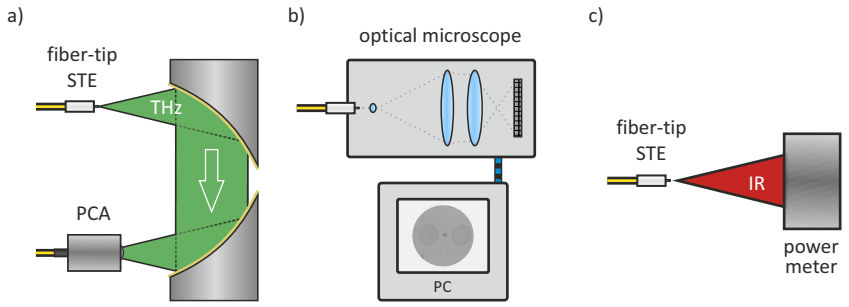


Fig. 2. Damage-detection methods. a) A conventional single-laser terahertz time-domain spectroscopy (TDS) setup with an interferometrically monitored mechanical delay line is used to measure the terahertz waveforms. The terahertz peak-to-peak amplitude serves as a damage measure. b) The fiber-tip STEs' end facets are imaged with a commercially available fiber-inspection microscope. The darkening is quantified by self-developed image analysis software within the region of the fiber core. c) The infrared transmittance is measured using a Germanium-based high-resolution photodiode.

Optics EXPRESS

direct damage measure. We acquired this measure for two identically fabricated fiber-tip STEs exemplary using a standard delay-line-based terahertz time-domain spectroscopy setup at 100 MHz repetition rate (Fig. 2(a)). However, these terahertz measurements are error-prone due to a relatively weak signal-to-noise ratio and the adaptation to the low repetition-rate regime is not straightforward especially as the damage threshold of the used photoconductive detector may be exceeded. Consequently, we switched to equivalent damage measures accessible in the visible and near-infrared where the high photon energy allows for robust and highly sensitive detection via the photo effect.

2.3.2. Optical-microscopy detection

Since the pump-induced material damage coincides with a visible darkening of the material, it is possible to monitor the damage with commercially available optical microscopes for fiber inspection. Consequently, we took a microscopy image after each 2-minute pump stage and quantified the darkening using a self-developed imaging analysis software that determines the degree of darkening based on the taken images. This turned out to be a highly sensitive method. However, it requires considerable analysis effort.

2.3.3. Infrared-transmittance detection

Since the pump-induced material damage is accompanied by an increase in infrared transmittance, very accurate commercially available infrared power meters can be used to observe the damage. We used a Germanium-based photodiode with a resolution of 2 nW (Thorlabs S122C) to monitor the transmittance between the pump stages at a chosen reference level as well as during each pump stage. This turned out to be an excellent method combining both high simplicity and high sensitivity.

3. Results

3.1. Terahertz-amplitude detection

Figure 3(a) shows the terahertz peak-to-peak amplitude measured for two single-mode fiber-tip STEs after each pump stage at a reference level of 4 mW. With increasing pump stages, the terahertz peak-to-peak amplitude decreases irreversibly. Figure 3(b) displays the amplitude's temporal evolution during a 4 mW and a 5 mW irradiation interval. At 5 mW, the terahertz peak-to-peak amplitude decreases irreversibly by 10 percent over an irradiation period of 2 minutes. At 4 mW, the decrease, if any, is found to be minor. Consequently, the derived damage threshold is 5 mW corresponding to an average-pump-power density of 4.8 kW/cm^2.

3.2. Optical-microscopy detection

Figure 4 shows three images of a continuous-wave-irradiated single-mode fiber-tip STE with different degrees of destruction. After two minutes of continuous-wave irradiation at 4 mW, the sample does not show any darkening within the fiber's core area. However, after consecutive two-minute irradiation periods at 4, 5, 6, and 7 mW, a subtle darkening becomes apparent. Continuing the destruction procedure, the darkening increases and the dark spot becomes highly pronounced. Using self-developed imaging analysis software, we quantified this darkening based on the mean change of the 8-bit grayscale value within the region of the fiber's core.

Figure 5 displays this quantified darkening after each pump stage averaged over three continuous-wave-irradiated samples. The error bars illustrate the standard deviation.

3.3. Infrared-transmittance detection

The blue markers in Fig. 5 illustrate the relative change of infrared transmittance at the end of each pump stage. The results are in excellent quantitative agreement with the darkening data

Optics EXPRESS

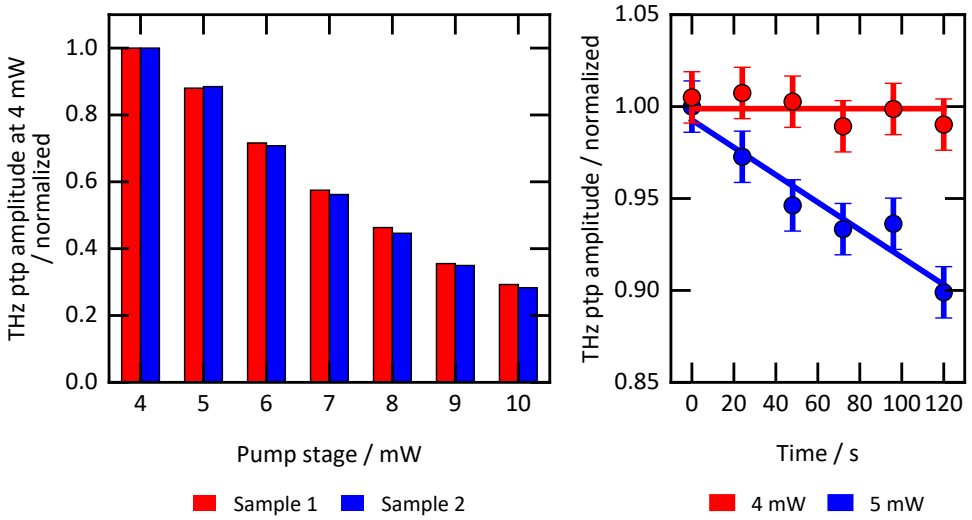


Fig. 3. Terahertz peak-to-peak (ptp) amplitude at a 4 mW reference level after each pump stage (left) and the temporal evolution at 4 and 5 mW (right). Beginning with the 5 mW pump stage, an irreversible decrease is evident.

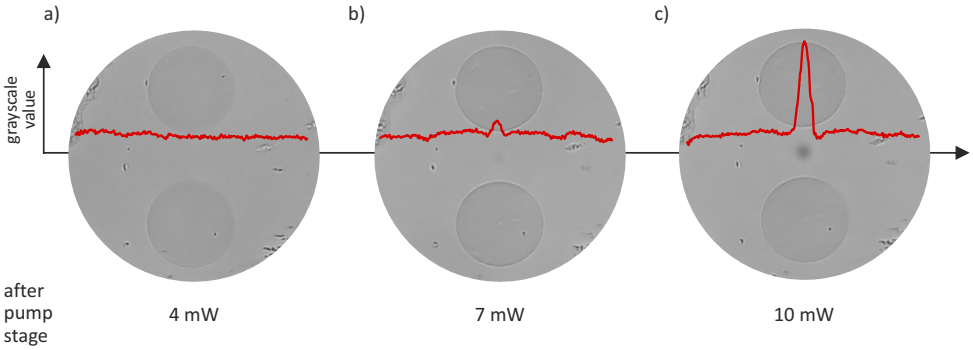


Fig. 4. Microscopy images of a fiber-tip STE's end facet after three continuous-wave pump stages. The grayscale values corresponding to central line scans are depicted in red at equal scale. While the fiber-tip STE exhibits no signs of destruction after the 4 mW pump stage (a), a faint darkening becomes noticeable within the region of the fiber's core after the 7 mW pump stage (b). After the 10 mW pump stage, the darkening is highly pronounced (c).

Optics EXPRESS

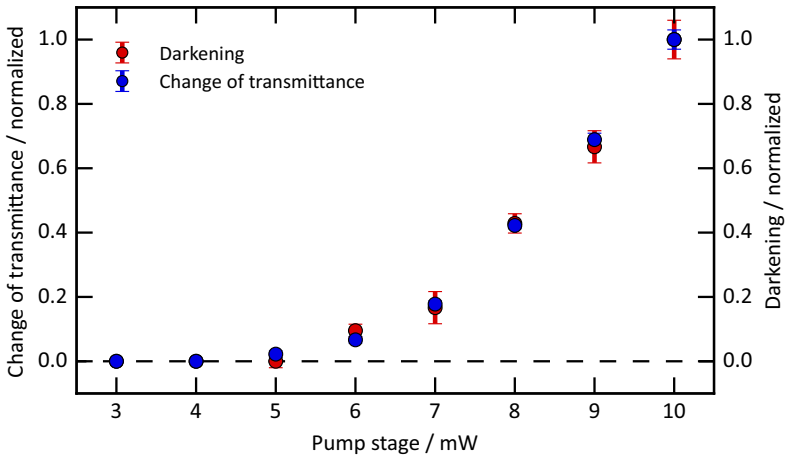


Fig. 5. Comparison of the optical-microscopy-detected darkening and the change of infrared transmittance averaged over three continuous-wave-irradiated samples. The change of transmittance and the quantified darkening evolve nearly identically. The damage onset (defined by a transmittance increase of 10 µW) is observed around 5 mW.

verifying the interchangeability of these two methods. Moreover, the damage thresholds were found to be identical to those derived from the terahertz-amplitude detection. Thus, for the subsequent measurements, we decided to detect solely in the infrared since it is the simplest and least error-prone method. The threshold value is determined by pinpointing the average optical power where the infrared transmittance increased by at least 10 µW.

Figure 6 displays the evolution of the relative change of transmittance for various repetition rates above 10 MHz. Interestingly, the measured damage threshold is nearly independent of the repetition rate in the studied high-repetition-rate regime. Moreover, the damage thresholds are very close, if not identical, to the measured continuous-wave threshold. This suggests that a heat-accumulation effect rather than a single-pulse phenomenon is causing the damage.

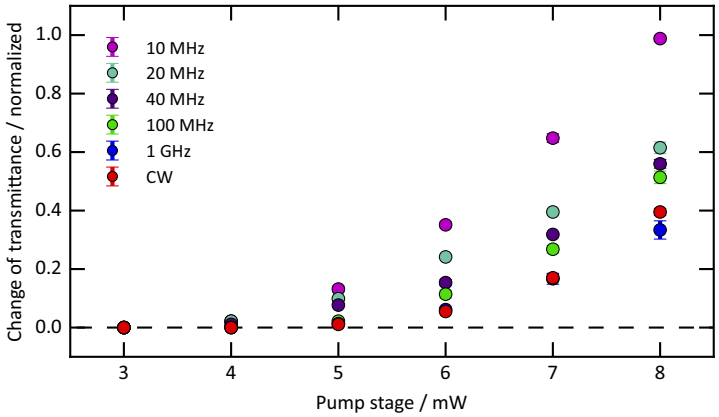


Fig. 6. Relative change of transmittance for various repetition rates. The damage onset (defined by a transmittance increase of 10 µW) remains nearly independent of the repetition rate. However, the damage rate increases with increasing repetition rate as the fluence rises.

Optics EXPRESS

However, even though the fluence ("single-pulse-energy density") has minimal to no impact on the damage threshold in this regime, it does have an impact on the damage rate with a clear tendency to increase with increasing fluence.

3.4. Fluence thresholds

Figure 7 shows the fluence threshold over the entire repetition-rate range. To calculate the fluence, we assumed a Gaussian beam profile with a $1/e^2$ mode field radius ω of 5.75 μm (as specified by Fujikura Ltd. for the used polarization-maintaining single-mode fiber "SM15-PS-U25D") which corresponds to an effective mode area $A_{\text{eff}} = \pi\omega^2 = 103.87\ \mu m^2$. The fluence is then defined as the ratio of pulse energy and A_{eff}. For each repetition rate, the pulse energy has been carefully determined by measuring the average optical power with a power meter and analyzing the amplified spontaneous emission (ASE) background noise using a calibrated fast photodiode.

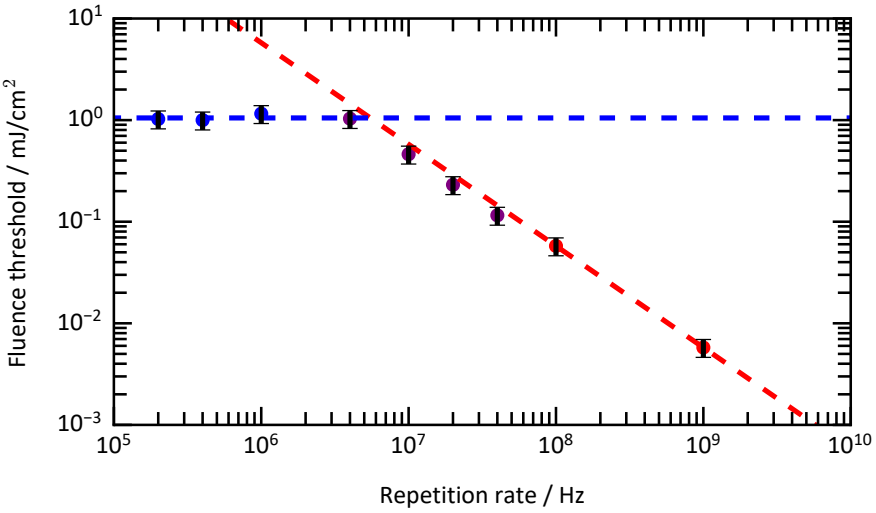


Fig. 7. Extracted fluence threshold in dependence on the repetition rate. Two clearly distinguishable regimes are apparent: a high-pulse-power low-repetition-rate regime characterized by a constant fluence threshold (blue), and a low-pulse-power high-repetition-rate regime characterized by an antiproportional fluence-dependence ("average-power threshold"). The red dashed line corresponds to the measured continuous-wave average-power threshold extrapolated to the entire repetition-rate range by applying an inverse proportionality.

Evidently, the repetition-rate range is split into two distinct regimes: a low-repetition-rate regime being governed by a constant fluence threshold (blue) and a high-repetition-rate regime being governed by an antiproportional fluence dependence (red). The red dashed line represents the measured continuous-wave average-power threshold extrapolated to the entire repetition-rate range. Most notably, the fluence thresholds remain strikingly consistent with the continuous-wave threshold down to a repetition rate of approximately 4 MHz. Below, the established regime with a constant fluence threshold is entered.

It is noteworthy that these measurements suggest an optimal operation point for electro-optic detection around 4 MHz as the generated terahertz field increases with increasing pump fluence. This results in a higher change of probe polarization and, thus, a better signal-to-noise ratio.

Optics EXPRESS

3.5. Thermodynamics and nanoscopy

3.5.1. Theory

The two regimes indicate two different damage processes being at play. In the low-repetition-rate regime, the period duration between two subsequent pulses is long enough for the material system to cool down to its initial state again. As a result, heat accumulation does not happen and only single-pulse interactions are responsible for the material damage. Hence, the damage threshold is directly linked to fluence and peak power.

On the contrary, in the high-repetition-rate regime, the period duration is too short for the material system to cool down to its initial state again. Consequently, heat accumulates and the temperature equilibrates at a new average-pump-power-dependent level. Once a specific temperature threshold is surpassed, the system's thermal energy is high enough to drive inter-layer diffusion of atoms, especially between the FeCoB- and the Pt-layer. In other words, the high temperature causes the FeCoB- and Pt-layer to alloy. As shown in a recent study that compares the terahertz emission of Fe/Pt bilayer STEs across various degrees of alloying [34], the electrical properties of the bilayer and alloyed heterostructure differ drastically with the result that the terahertz emission is almost entirely canceled for the fully alloyed phase. To test this theory of temperature-driven inter-layer diffusion, we performed AFM, infrared s-SNOM, and STEM measurements for a pristine and a cw-destroyed sample, respectively.

3.5.2. AFM and s-SNOM

Figure 8(a) shows the AFM images for a pristine and a cw-destroyed sample (comparable to the samples shown in Fig. 4(a) and (c)). The measured topography reveals an irreversible expansion of more than 3 nm with a spatial profile mapping the Gaussian pump-mode field. Anticipating the STEM measurements below, the expansion does not originate from an enlargement of the STE heterostructure, but from the glass substrate. This observation hints at a prior transient rise in temperature as the material properties of glass depend on its thermal history.

Moreover, in addition to the permanent substrate expansion, the optical properties have been altered indicating a change in chemical composition. The infrared s-SNOM measurements in Fig. 8(b) resolve this chemical transformation spatially and provide another clear mapping of the Gaussian pump-mode field.

Combining these two findings, the temperature-driven nature becomes evident.

3.5.3. STEM

To complete the picture and verify the inter-layer diffusion, STEM measurements have been performed. Figure 9 shows the resulting high-angle annular dark field (HAADF) and bright field images: In the pristine sample, the individual layers (W, FeCoB, and Pt) are distinguishable in both dark-field and bright-field measurements. However, in the destroyed sample, the heterostructure is altered and individual layers are barely, if at all, distinguishable. Figure 9(c) shows the spatial distribution of W, FeCoB, and Pt measured with energy-dispersive X-ray spectroscopy. It becomes apparent that the FWHMs of the FeCoB and Pt distributions along the out-of-plane direction are significantly increased for the destroyed sample compared to the pristine one. In other words, an inter-layer diffusion between the FeCoB- and the Pt-layer had taken place.

Optics EXPRESS

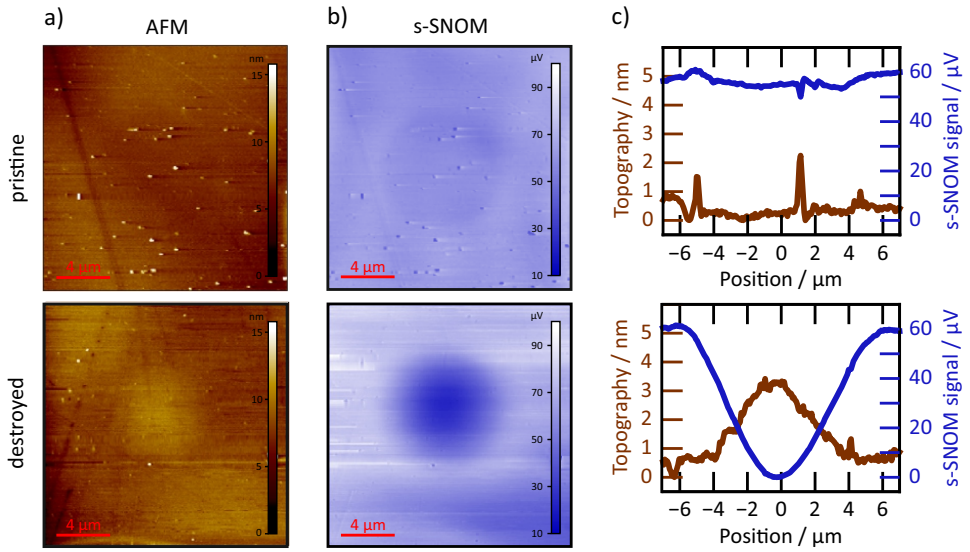


Fig. 8. AFM and infrared s-SNOM measurements for a pristine and a cw-destroyed single-mode fiber-tip STE. a) The AFM images of the pristine and destroyed samples show a similar surface roughness. However, for the destroyed sample, a substrate expansion within the fiber's core region becomes visible. b) A comparison of the infrared s-SNOM images provides an even higher contrast indicating a change in chemical composition. In the image of the pristine sample, the fiber's core is slightly visible as the difference in refractive index yields a difference in reflectance. c) The line scans through the center reveal that both the topography (brown) and the s-SNOM signal (blue) of the destroyed sample map the Gaussian pump-mode field.

Optics EXPRESS

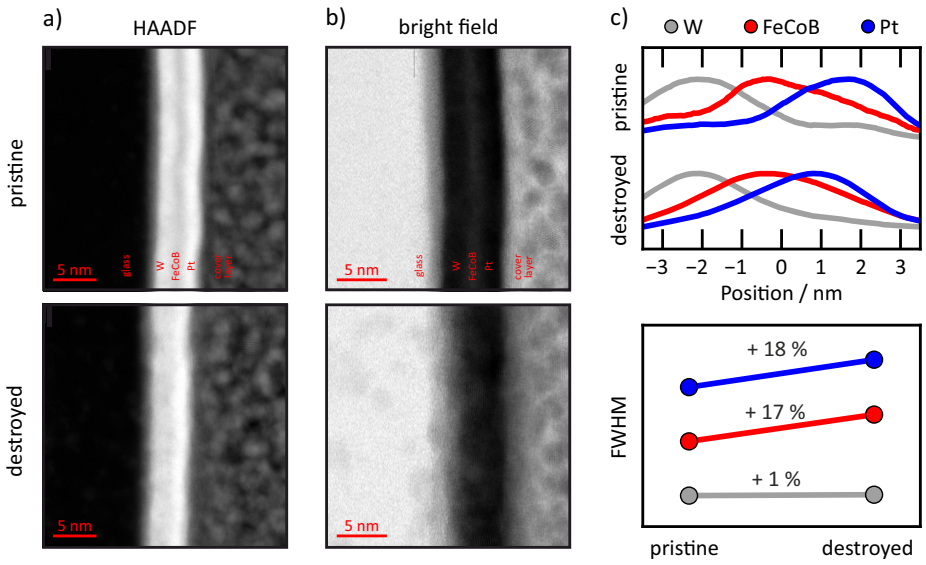


Fig. 9. Scanning transmission electron microscopy (STEM) measurements for a pristine and a destroyed single-mode fiber-tip STE. The pristine tri-layer heterostructure is visible in both dark-field (a)) and bright-field (b) imaging. In the destroyed sample, the tri-layer heterostructure is altered clearly and only barely, if at all, discernible in the dark field imaging. The individual layers' spatial distributions, measured with energy-dispersive X-ray spectroscopy, support the theory of an inter-layer diffusion between the FeCoB- and Pt-layer as the FWHMs are significantly increased for the destroyed sample.

Optics EXPRESS

4. Conclusions

In summary, we presented a complete study of our single-mode fiber-tip STEs' optical damage threshold covering the kilohertz, megahertz, and gigahertz repetition-rate regimes as well as continuous-wave irradiation. We show that the optical damage threshold of fiber-tip spintronic terahertz emitters can be classified into two regimes: a high-peak-power low-repetition-rate regime governed by a constant-fluence threshold, and a low-peak-power high-repetition-rate regime governed by an antiproportional fluence dependence ("average-power threshold"). In other words, we demonstrated continuous-wave-irradiation damage of STEs and could show that this cw-damage regime transitions to the known constant-fluence-damage regime only around 4 MHz for our single-mode fiber-tip STEs. Moreover, we provided a thermodynamic explanation of the processes at play and substantiated it with AFM, s-SNOM, and STEM measurements. While interpreting damage as a single-pulse phenomenon is applicable in the low-repetition-rate regime, a transition to a complex accumulated heat phenomenon occurs as the repetition rate enters the megahertz regime. Consequently, above a specific threshold, a temperature-driven inter-layer diffusion of atoms is driven which causes the FeCoB- and Pt-layer to alloy. The resulting drastic change in electrical properties shuts down the optical-to-terahertz conversion.

These findings contribute to a better understanding of the current limitations of spintronic terahertz emitters and, thus, may have a significant impact on the design of future STEs. Some strategies to circumvent damage in certain free-space applications have already been demonstrated, either by cooling the STE [27] or reducing the effective repetition rate through rotation of the STE [30].

Funding. Material and Technologies for Sustainable Development, Jan Amos Komensky Operational Program, and Czech Science Foundation (22-33060S, CZ.02.01.01/00/22_008/0004631); H2020 Marie Skłodowska-Curie Actions (860060 (MagnEfi)); Horizon 2020 Framework Programme (863155 (s-Nebula)); Deutsche Forschungsgemeinschaft (SPP 2314 - KA 3305/5-1 - ITISA, TRR 173 - 268565370 - B11, TRR 227 - 328545488 - A05, B02, B05).

Acknowledgement. The authors acknowledge funding from the Horizon 2020 European Union Research and Innovation program under FET-OPEN Grant agreement No. 863155 (S-Nebula) and Marie Skłodowska-Curie Grant agreement No. 860060 "Magnetism and the effect of Electric Field" (MagnEFi), as well as from the Deutsche Forschungsgemeinschaft (DFG, German Research Foundation) TRR 173 - 268565370 (SPIN+X, project B11), TRR 227 - 328545488 (Ultrafast spin dynamics, projects A05, B02, and B05), and SPP 2314 - KA 3305/5-1 (INTEREST, project ITISA). Furthermore, the authors acknowledge the project No. CZ.02.01.01/00/22_008/0004631 "Materials and Technologies for Sustainable Development," funded by the European Union and the state budget of the Czech Republic within the framework of the Jan Amos Komensky Operational Program and Czech Science Foundation 22-33060S. Moreover, the authors would like to thank the French RENATECH Network and the Nano Structuring Center at the RPTU Kaiserslautern-Landau for their technical support during the fabrication of the fiber-tip spintronic terahertz emitters.

Disclosures. The authors declare no conflicts of interest.

Data availability. The data that support the findings of this study are openly available at [35].

References

1. B. B. Hu, X.-C. Zhang, D. H. Auston, *et al.*, "Free-space radiation from electro-optic crystals," Appl. Phys. Lett. **56**(6), 506–508 (1990).
2. J. A. Fülöp, S. Tzortzakis, and T. Kampfrath, "Laser-Driven Strong-Field Terahertz Sources," Adv. Opt. Mater. **8**(3), 1900681 (2020).
3. H. Hirori, A. Doi, F. Blanchard, *et al.*, "Single cycle terahertz pulses with amplitudes exceeding 1 MV/cm generated by optical rectification in LiNbO3," Appl. Phys. Lett. **98**(9), 091106 (2011).
4. X.-C. Zhang, X. F. Ma, Y. Jin, *et al.*, "Terahertz optical rectification from a nonlinear organic crystal," Appl. Phys. Lett. **61**(26), 3080–3082 (1992).
5. D. H. Auston and C. V. Shank, "Picosecond Ellipsometry of Transient Electron-Hole Plasmas in Germanium," Phys. Rev. Lett. **32**(20), 1120–1123 (1974).
6. D. H. Auston, K. P. Cheung, and P. R. Smith, "Picosecond photoconducting Hertzian dipoles," Appl. Phys. Lett. **45**(3), 284–286 (1984).
7. M. B. Ketchen, D. Grischkowsky, T. C. Chen, *et al.*, "Generation of subpicosecond electrical pulses on coplanar transmission lines," Appl. Phys. Lett. **48**(12), 751–753 (1986).
8. A. Dohms, S. Breuer, S. Keyvaninia, *et al.*, "Fiber-coupled THz transceiver based on rhodium-doped InGaAs with 6.5 THz bandwidth and up to 106 μW emitted THz power," 48th IRMMW-THz (2023).

Optics EXPRESS

9. Y. Chen, Y. He, L. Liu, *et al.*, "Plasma-based terahertz wave photonics in gas and liquid phases," Photonics Insights **2**(3), R06 (2023).
10. H. Hamster, A. Sullivan, S. Gordon, *et al.*, "Subpicosecond, electromagnetic pulses from intense laser-plasma interaction," Phys. Rev. Lett. **71**(17), 2725–2728 (1993).
11. D. Kuk, Y. J. Yoo, E. W. Rosenthal, *et al.*, "Generation of scalable terahertz radiation from cylindrically focused two-color laser pulses in air," Appl. Phys. Lett. **108**(12), 121106 (2016).
12. I. Dey, K. Jana, V. Y. Fedorov, *et al.*, "Highly efficient broadband terahertz generation from ultrashort laser filamentation in liquids," Nat. Commun. **8**(1), 1184 (2017).
13. Z. Yu, N. Zhang, J. Wang, *et al.*, "0.35% THz pulse conversion efficiency achieved by Ti:sapphire femtosecond laser filamentation in argon at 1 kHz repetition rate," Opto-Electron. Adv. **5**(9), 210065 (2022).
14. T. Kampfrath, M. Battiato, P. Maldonado, *et al.*, "Terahertz spin current pulses controlled by magnetic heterostructures," Nat. Nanotechnol. **8**(4), 256–260 (2013).
15. E. T. Papaioannou and R. Beigang, "THz spintronic emitters: a review on achievements and future challenges," De Gruyter Nanophotonics **10**(4), 1243–1257 (2021).
16. Z. Feng, H. Qiu, D. Wang, *et al.*, "Spintronic terahertz emitter," J. Appl. Phys. **129**(1), 010901 (2021).
17. C. Bull, S. M. Hewett, R. Ji, *et al.*, "Spintronic terahertz emitters: Status and prospects from a material perspective," APL Mater. **9**(9), 090701 (2021).
18. T. Seifert, L. Cheng, Z. Wei, *et al.*, "Spintronic sources of ultrashort terahertz electromagnetic pulses," Appl. Phys. Lett. **120**(18), 180401 (2022).
19. R. Rouzegar, L. Brandt, L. Nádvorník, *et al.*, "Laser-induced terahertz spin transport in magnetic nanostructures arises from the same force as ultrafast demagnetization," Phys. Rev. B **106**(14), 144427 (2022).
20. I. Ilyakov, A. Brataas, T. V. A. G. de Oliveira, *et al.*, "Efficient ultrafast field-driven spin current generation for spintronic terahertz frequency conversion," Nat. Commun. **14**(1), 7010 (2023).
21. U. Nandi, M. S. Abdelaziz, S. Jaiswal, *et al.*, "Antenna-coupled spintronic terahertz emitters driven by a 1550 nm femtosecond laser oscillator," Appl. Phys. Lett. **115**(2), 022405 (2019).
22. E. Th. Papaioannou, G. Torosyan, S. Keller, *et al.*, "Efficient Terahertz Generation Using Fe/Pt Spintronic Emitters Pumped at Different Wavelengths," IEEE Trans. Magn. **54**(11), 1–5 (2018).
23. I. Ilyakov, N. Agarwal, J.-C. Deinert, *et al.*, "Terahertz-wave decoding of femtosecond extreme-ultraviolet light pulses," Optica **9**(5), 545 (2022).
24. T. Seifert, S. Jaiswal, U. Martens, *et al.*, "Efficient metallic spintronic emitters of ultrabroadband terahertz radiation," Nat. Photonics **10**(7), 483–488 (2016).
25. R. Rouzegar, A. L. Chekhov, Y. Behovits, *et al.*, "Broadband Spintronic Terahertz Source with Peak Electric Fields Exceeding 1.5 MV/cm," Phys. Rev. Applied **19**(3), 034018 (2023).
26. S. Kumar, A. Nivedan, A. Singh, *et al.*, "Optical damage limit of efficient spintronic THz emitters," iScience **24**(10), 103152 (2021).
27. T. Vogel, A. Omar, S. Mansourzadeh, *et al.*, "Average power scaling of THz spintronic emitters efficiently cooled in reflection geometry," Opt. Express **30**(12), 20451 (2022).
28. O. Gueckstock, L. Nádvorník, T. S. Seifert, *et al.*, "Modulating the polarization of broadband terahertz pulses from a spintronic emitter at rates up to 10 kHz," Optica **8**(7), 1013–1019 (2021).
29. G. Lezier, P. Koleják, J.-F. Lampin, *et al.*, "Ultrafast Modulation of Polarization in Spintronic THz Emitters Enhanced by Field Induced Spin Reorientation Transition.," *CLEO: Science and innovation*9 (2023).
30. A. Vaitsi, V. Sleziona, L. E. Parra Lopéz, *et al.*, "High-power operation of Spintronic Terahertz emitters for THz-field-driven scanning probe microscopy at MHz repetition rates," 48th IRMMW-THz (2023).
31. J. Cai, M. Dai, S. Chen, *et al.*, "Terahertz spin currents resolved with nanometer spatial resolution," Appl. Phys. Rev. **10**(4), 041414 (2023).
32. P. Kolejak, G. Lezier, G. Ducournau, *et al.*, "Spintronic inverse spin hall photomixing beyond 1 THz," 48th IRMMW-THz (2023).
33. F. Paries, N. Tiercelin, G. Lezier, *et al.*, "Fiber-tip spintronic terahertz emitters," Opt. Express **31**(19), 30884 (2023).
34. L. Scheuer, M. Ruhwedel, D. Karfaridis, *et al.*, "THz emission from Fe/Pt spintronic emitters with $L1_0$-FePt alloyed interface," iScience **25**(5), 104319 (2022).
35. Felix Paries, "Optical damage thresholds of single-mode fiber-tip spintronic terahertz emitters," Fraunhofer Institute for Industrial Mathematics (2024), https://zenodo.org/doi/10.5281/zenodo.10926628.

Paper IV

360° Polarization control of terahertz spintronic emitters using uniaxial FeCo/$TbCo_2$/FeCo trilayers

Pierre Koleják, Geoffrey Lezier, Kamil Postava, Jean-François Lampin, Nicolas Tiercelin, Mathias Vanwolleghem
ACS Photonics, **9** (2022)
Reprinted with permission, Copyright 2022 American Chemical Society.

IV

ACS Photonics

pubs.acs.org/journal/apchd5 Article

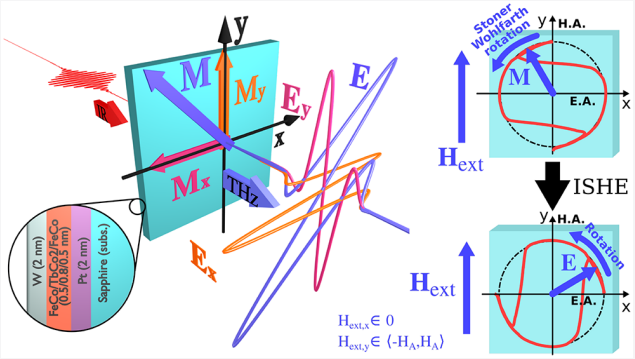
360° Polarization Control of Terahertz Spintronic Emitters Using Uniaxial FeCo/$TbCo_2$/FeCo Trilayers

Pierre Koleják,* Geoffrey Lezier, Kamil Postava, Jean-François Lampin, Nicolas Tiercelin, and Mathias Vanwolleghem*

Cite This: *ACS Photonics* 2022, 9, 1274−1285 Read Online

ACCESS | Metrics & More | Article Recommendations | Supporting Information

ABSTRACT: Polarization control of THz light is of paramount interest for the numerous applications offered in this frequency range. Recent developments in THz spintronic emitters allow for a very efficient broadband emission, and especially unique is their ability of THz polarization switching through magnetization control of the ferromagnetic layer. Here we present an improved scheme to achieve full 360° nearly coherent polarization rotation that does not require multipolar or rotating external magnetic bias nor complex cascaded emitters. By replacing the FM layer of the spintronic emitter with a carefully designed FeCo/$TbCo_2$/FeCo anisotropic heterostructure, we experimentally demonstrate Stoner−Wohlfarth-like coherent rotation of the THz polarization over a full 2π azimuth only by a bipolar variation of the strength of the hard axis field, and with only a negligible decrease in the emission efficiency as compared to standard Pt/CoFeB/W inverse spin Hall emitters. THz measurements are in agreement with our model of the nonperfect Stoner−Wohlfarth behavior. These emitters are well adapted for the implementation of polarimetric characterization not requiring any mechanically rotating polarizing elements. An example is given with the characterization of the birefringence in a quartz plate.



KEYWORDS: *terahertz spinorbitronics, exchange-coupled rare-earth multilayer, inverse spin hall effect, magnetic anisotropy, Stoner−Wohlfarth rotation, terahertz ellipsometry*

Downloaded via TECHL UNIV OF OSTRAVA on September 20, 2022 at 18:19:09 (UTC).
See https://pubs.acs.org/sharingguidelines for options on how to legitimately share published articles.

1. INTRODUCTION

THz technology has now entered many societally important applications with exciting demonstrations of nondestructive spectroscopy and chemical sensing.[1−5] Continuous improvements of the performance of the building blocks of a THz analysis chain (sources, modulators, receivers) are bringing many of these demonstrators close-to-market. Control and flexible manipulation of the polarization state of a THz beam is a functionality in the toolbox that is not straightforwardly realized. Such control would open applications for spectroscopic ellipsometry, coherent control, or even polarization multiplexed communications at THz frequencies.

THz polarization states can be controlled by Fresnel-rhomb wave plates, wire-grid polarizers, birefringent wave plates, or active metamaterial-based devices. While these approaches are robust and can sometimes be actively controlled, they are most often either bulky or narrowband and present important insertion losses.[6−9] Controlling the emitted polarization state directly upon generation is in this sense a more logical approach. THz polarization shaping has been demonstrated by optical rectification in nonlinear crystals of double or multiple optical pulses with different polarizations,[10−12] by optical polarization pulse shaping before rectification,[13] by spatial structuration of the shape of the electrical contacts in a photoconductive switch,[14] or even by tailoring two-color laser plasma filamentation.[15−17] While all these approaches achieve a high degree of polarization control upon THz generation, their implementation is cumbersome, necessitating subtle instrumentation, high power, or exhibiting limited tunability.

Ideally, polarization control should be achieved by an easily accessible degree of freedom of the THz generation mechanism itself. THz emission by the inverse spin Hall effect (ISHE) offers this possibility. Photoinduced ultrafast demagnetization of thin film magnetic heterostructures presenting interfaces between ferromagnetic (FM) transition metals and nonmagnetic (NM) 5d metals with strong spin−orbit coupling (SOC), has come to the forefront as a

Received: November 20, 2021
Published: March 31, 2022



ACS Publications © 2022 American Chemical Society

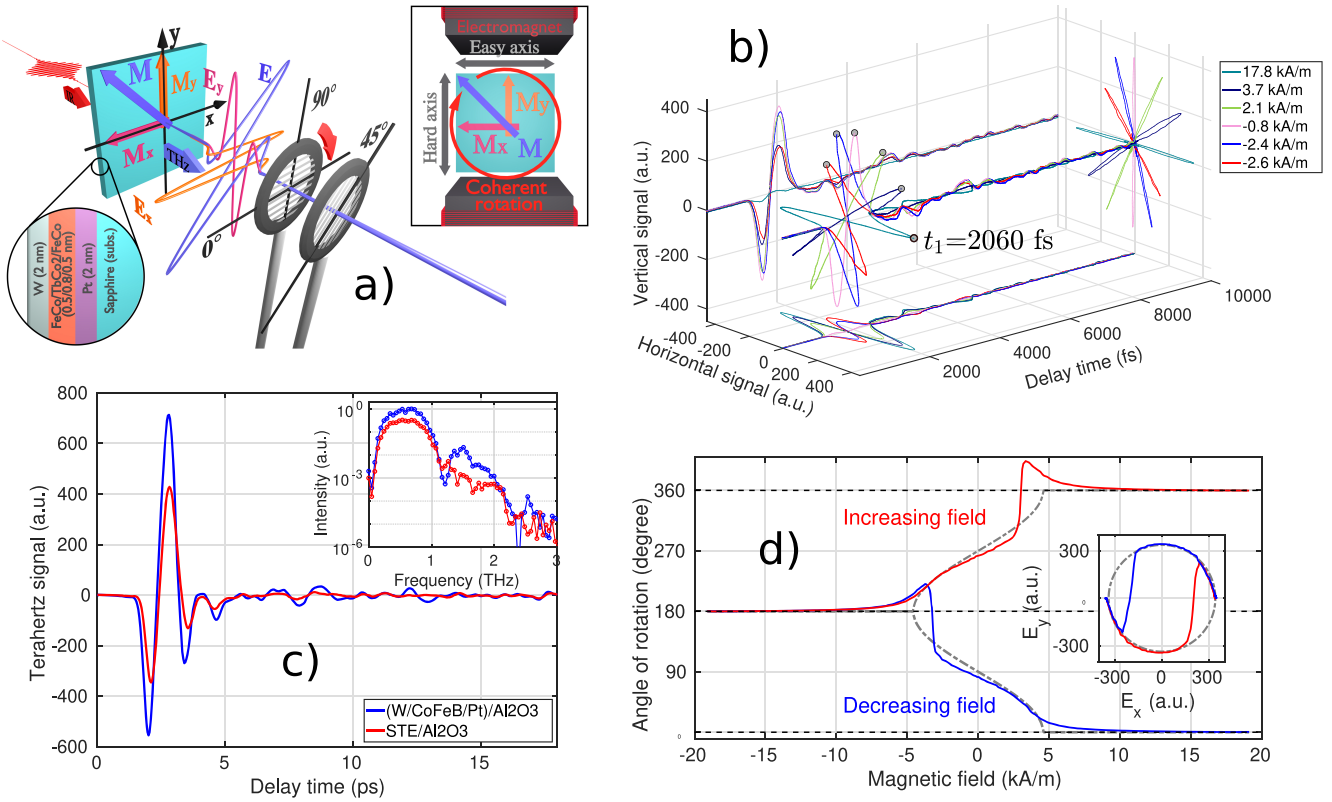


Figure 1. Spintronic terahertz polarization rotation. (a) Schematic representation of the spintronic emitter with magnetic uniaxial anisotropy. The STE emitter is excited by an IR pulse from the metallic heterostructure side. This trilayer has an engineered uniaxial anisotropy allowing to control its magnetization direction over a full 360° by only applying a hard axis field as represented in the inset. The polarization of the spin−orbitronic generated terahertz emission $\mathbf{E}(t)$ perpendicular to $\mathbf{M}$ therefore rotates accordingly with the applied hard axis field. The polarization components $E_x(t)$ and $E_y(t)$ are detected by 2 wire grid polarizers in series (0/90° switching and 45° fixed). (b) 3D representation of the measured time domain traces for the horizontal $E_x(t)$ and vertical components $E_y(t)$ of the transient electric field $\mathbf{E}(t)$ for different values of the externally applied field, showing the rotation of the polarization. (c) Comparison of the emitted THz signal between the CoFeB-based reference STE (blue) and the ECML-based emitter (red) in the temporal domain and frequency domain (inset). (d) Polarization angle measured as a function of the applied magnetic field. The inset shows the vectorial amplitude of the THz beam at the fixed delay of 2060 fs, illustrating the quasi-lossless full 360° rotation over a hard axis field cycle.

promising new type of THz emitters.[18,19] ISHE creates a picosecond spin-to-charge dipole current burst when majority spins are pumped by a femtosecond infrared pulse from the FM into the NM layer. Globally speaking the efficiency of ISHE spintronic THz emitters has a hard time competing with that of traditional semiconductor photoconductive switches,[20] optical rectification in nonlinear crystals[21] (such as $LiNbO_3$, GaP, ZnTe, ...), or even THz ponderomotive acceleration in two-color plasma filaments.[22,23] Such systems have commonly been demonstrated to reach easily average THz power levels close to or even beyond the mW level (with THz pulse energies approaching microJoules). Such levels are up until now not within reach for spintronic THz emission, though recent work has demonstrated that with proper cooling upscaling toward tens of μW average power levels is within reach.[24] Where ISHE STEs offer true leverage for pulsed THz generation as compared to the mentioned techniques is in the combination of the absence of phonon gaps in their output spectrum, their intrinsic Fourier-limited broadband character, and their linear response even at low excitation pump fluences. Moreover, being metallic emitters, their excellent heat dissipation causes them to have rather high pump fluence damage thresholds.

Moreover, ISHE spintronic terahertz emitters (STE) emit a linear polarization state that is perfectly orthogonal to the FM's magnetization, allowing for straightforward polarization shaping by local control of the magnetization of the FM layer. Rotating linear polarization by 90° degrees has been demonstrated by mechanically rotating the external magnetic saturation field.[19] An alternative to mechanical rotation of the external magnetic bias has been demonstrated by adding a crossed AC modulated magnetic field to a static magnetic bias.[25] Spintronic THz polarization modulation over 90° in isotropic CoFeB-based emitters at speeds of 10 kHz have been obtained, mainly limited by the reactance of the electromagnet providing the AC magnetic applied field and the need to overcome the coercivity of the CoFeB. There has been an observation of elliptically polarized THz beams from a CoFeB STE with locally "twisting" in-plane magnetization.[26] These could however not fully be predicted by a reproducible, verifiable magnetization distribution. Applying a quadripolar external magnetic field with opposing polarities on a $Ni_{80}Fe_{20}$/Pt bilayer STE induces a well controlled nonuniform magnetization profile with singular polarity points in the center. The measured resulting THz phase front reproduces this exotic polarization profile with very strong field values at the singularity in the center.[27] Control of the terahertz spin

https://doi.org/10.1021/acsphotonics.1c01782
ACS Photonics 2022, 9, 1274−1285

current by the photothermal effect, which was demonstrated by switching the polarity of the electric field, also has potential for polarization control. However, the control is performed by tuning the high pump fluence and accompanied by a varying external magnetic field, which imposes application limitations.[28] Fully reconfigurable control of circularly polarized THz has been obtained in a two-stage cascaded scheme with orthogonally magnetized STEs that are subtly positioned to obtain the correct phase difference and amplitude equality.[29] These demonstrations of magnetic field leveraged THz polarization control are notable but suffer from a complex implementation or lack of reconfigurability.

To overcome these limitations, we propose in this Article a STE with FM layer that has engineered uniaxial anisotropy. By inducing an in-plane easy axis in a ferromagnetic multilayer with a reasonably low anisotropy field H_A, the in-plane magnetization is expected to rotate in a Stoner−Wohlfarth (SW) fashion over a full 2π azimuth by applying only a varying external field perpendicular to the anisotropy axis.[30] Used as a spin pumping FM layer in a STE, such an anisotropic layer greatly eases THz polarization control. To this end, we have developed a Pt/W-based trilayer STE with an anisotropic spin pumping layer based on an intermetallic heterostructure combining rare-earth and transition metals. We will demonstrate that the azimuth of the emitted linear THz polarization can be coherently rotated over a full circle by simply setting the strength of the hard axis field to the appropriate value. Moreover, the rare-earth intermetallic heterostructure multilayer adds this functionality without sacrificing THz field strength as compared to the record CoFeB-based STE.[18] An accurate analysis of the magnetic free energy accounting for deviations of the perfect SW monodomain behavior, correctly fits the observed the polarization rotation cycles. This improved scheme for a STE with polarization control does not require any mechanical moving magnets nor special magnetic patterns but a low value simple uniaxial bias. As a result this THz polarization setting is easy to implement in a practical emitter and can extend greatly the potential of this type of emitters for THz spectroscopy and coherent control applications.[31−33]

2. THZ POLARIZATION CONTROL USING SPINTRONIC FERROMAGNETIC HETEROSTRUCTURE

Exchange-coupled multilayer (ECML) heterostructures based on repeated $TbCo_2$/FeCo bilayers grown under a polarizing magnetic field are known to imprint the strong uniaxial anisotropy of the rare-earth alloy on the magnetic multilayer but with a lowered value for the effective anisotropy field $H_{A,\mathrm{eff}}$ and an averaged effective saturation magnetization $M_{s,\mathrm{eff}}$.[34,35] Using such a uniaxial ferromagnetic multilayer as spin pumping layer in an ISHE STE is expected to lead to a linear THz polarization that will emulate the hysteresis of the multilayer. In particular, if perfect monodomain uniaxial anisotropy is achieved, it is known from magnetism that according to the Stoner−Wohlfarth model the magnetization of the ECML will uniformly rotate over 180° by varying the applied field only along the hard axis in the range of the anisotropy field strength $[-H_{A,\mathrm{eff}}, +H_{A,\mathrm{eff}}]$. Specifically we have grown a W(2 nm)/CoFe(5 Å)/$TbCo_2$(8 Å)/CoFe(5 Å)/Pt(2 nm) stack on a c-cut sapphire substrate. During the growth a magnetic induction $\mu_0 H_d \approx 0.1$ T is applied in the plane of the substrate to induce an easy axis direction in the anisotropic layer (see Supporting Information). The 5d metals Pt and W provide the ISHE with opposite signs for θ_{SH}.[36] Placed on opposite sides of the ferromagnetic spin pumping layer, they will therefore convert incoming spin currents into charge currents of the same sense, as follows directly from $\vec{J}_C = \theta_{\mathrm{SH}} \frac{2e}{\hbar} \vec{J}_S \cdot \vec{\sigma}$, where $\vec{J}_C$, $\vec{J}_S$, and $\vec{\sigma}$ are respectively the charge current density, the injected spin current density, and the spin polarization direction.[36] Figure 1a illustrates the proposed principle of the polarization controlled spintronic emitter. The sample is mounted between the pole shoes of an electromagnet providing a uniform external biasing magnetic field $H_{\mathrm{ext,max}} = 40 \frac{\mathrm{kA}}{\mathrm{m}}$ (i.e., $B_{\mathrm{ext,max}} = 50$ mT). Its operation is verified on a customized time-domain spectroscopy setup (see Supporting Information). The emitter was excited by femtosecond infrared pulses from a Ti:sapphire oscillator (100 fs pulses, center wavelength 820 nm, repetition rate 80 MHz, average power 185 mW) that are normally incident on the metallic ECML stack. The emitted THz pulses were observed from the substrate side in a transmission geometry. In this way, echoes in the time domain transients are strongly suppressed since the metallic stack behaves as a good antireflective coating for THz frequencies.[37,38] The transient electric field emitted by the magnetically anisotropic ECML was coherently sampled using a photoconductive low-temperature grown GaAs dipole antenna. A couple of wideband wiregrid polarizers allow to select between the orthogonal polarization components of the emitted THz wave (see Supporting Information). Throughout this work, the convention is used that the (horizontal) x-axis is aligned with the induced anisotropy of the ECML. The x- and y-axes in this work can thus also be read as easy-axis (EA) and hard-axis (HA) directions.

Figure 1b plots the measured horizontal (x) and vertical (y) components, $E_x(t)$ and $E_y(t)$, of the transient electric field $\mathbf{E}(t)$ for different values of the external applied field $H_{\mathrm{ext},y}$. When projecting these traces as vectorial parametric curves on a 2D plane as is done in this figure, the obtained polarization cycles illustrate the main points of the suggested operation principle. First, as expected from theory, the horizontal and vertical components are in phase. At all applied field strengths, $E_x(t)$ and $E_y(t)$ reach their zeroes and extrema at the same time delays. The generated charge current pulse acts as a dipole emitter exactly perpendicularly polarized to the polarity of the spin current without any phase difference. The emitted polarization is thus perfectly linear. We believe that the very small ellipticity observed at 3.8 $\frac{\mathrm{kA}}{\mathrm{m}}$ is a spurious instrumental effect. Long TDS cycles at high field values might lead to joule heating of the electromagnet coils and thus resistance variations. Since the electromagnet is voltage controlled, this leads to small current and hence magnetic field variations. This ellipticity was henceforth never again observed when switching to current source control of the electromagnet, which strengthens our assumptions. Note also that there is no possible optical THz anisotropy induced by the sapphire substrate since it is c-cut and the emitter is observed along the z-axis. Second, as the applied external magnetic field $H_{\mathrm{ext},y}$ is decreased, the polarization plane starts gradually rotating from being perfectly aligned with the x-axis toward the y-axis (as M_y rotates toward M_x). In order to visualize this rotation more clearly, we have plotted in Figure 1d as a function of $H_{\mathrm{ext},y}$ the THz polarization azimuth φ with respect to the x-axis obtained

https://doi.org/10.1021/acsphotonics.1c01782
ACS Photonics 2022, 9, 1274−1285

by $\varphi = \arctan\left(\frac{E_y}{E_x}\right)\Big|_{t=t_1}$, evaluated at a chosen fixed time delay (for convenience an extremum of the transient signal, t_1 = 2060 fs). In doing so, it is assumed that the dynamics of the spin-to-charge conversion are up to first order unaffected by the polarization of the spin current. In other words, there is no anisotropy in the generated dipole current burst in the heavy nonmagnetic metal layers, and the spin Hall angle is a scalar isotropic constant.[39,40] The temporal traces of Figure 1b indicate that indeed all $\mathbf{E}(t)$-traces reach their extrema at equal time delay, independent of the applied $H_{\mathrm{ext},y}$. The measured hysteresis exhibited by the polarization azimuth as a function of hard axis field proves that the proposed emitter allows to rotate the linear THz polarization over a full circle by only a modest variation of an uniaxially applied magnetic field within a range of just $\pm 10\ \frac{\mathrm{kA}}{\mathrm{m}}$ ($\mu_0 H \approx \pm 12$ mT). The inset polar plot of the vectorial **E**-field amplitude proves that this hysteretic rotation is quasi-perfect except near the switching field. Moreover inspecting the behavior in Figure 1d, φ seems to follow a $\cos\varphi \propto \frac{H_{\mathrm{ext},y}}{H_A}$ with $H_A \approx 5\ \frac{\mathrm{kA}}{\mathrm{m}}$, as indicated by the dashed-dotted cosine curve. Thus, $E_x = |\mathbf{E}|\cos\varphi$ depends linearly on the applied hard axis field. According to the physics of the ISHE, this implies that σ_y, the HA projection of the polarization of the injected majority spin current pulse, likewise depends linearly on the HA field $H_{\mathrm{ext},y}$. Such a behavior is reminiscent of a Stoner−Wohlfarth rotation of the magnetization of the FM stack. The measurements of Figure 1 suggest that this mechanism is transposed to the emitted THz radiation. We will show in the next section that the THz polarization is indeed an exact "carbon copy" of the magnetostatic behavior of the FM ECML stack. Polarization control in THz ISHE emitters can therefore be engineered by controlling the magnetic anisotropy of the spin pumping layer. The deviation of the perfect cosine-behavior close to field strengths of about $\pm 2.5\ \frac{\mathrm{kA}}{\mathrm{m}}$ is due to a combination of nonideal monodomain behavior and rapid switching of the ECML stack.[41] This will be further discussed in Section 4.

In any case, the measured one-to-one correspondence between polarization azimuth and applied field strength allows to set the polarization angle at will, not needing any mechanically rotating parts nor complex cascading of dephased THz emitters. Spurious crosspolarization is not observed or at least better than the 30 dB rejection rate of the wiregrid polarizers used.[42] The limited field strengths needed to cover 2π-rotations open possibilities to implement nonquasistatic rotations of the THz polarization. This finds applications in THz polarimetry and ellipsometry, or as a THz emitter with built-in fast polarization modulation using ferromagnetic resonance (FMR) techniques.[43] An example of its use in polarimetry will be given in Section 5.

3. UNIAXIAL ANISOTROPIC INVERSE SPIN HALL EMITTER: PERFORMANCE STUDIES

With the THz polarization rotation established, we turn our attention to the building blocks allowing this mechanism and assess their performance. The impact of the use of an exchange coupled anisotropic multilayer as spin pumping layer, instead of a single layer ferromagnetic isotropic transition metal alloy, needs to be evaluated. Within the family of intrinsic ISHE THz emitters those based on (W/FM/Pt)-trilayers are known to achieve the strongest spin-to-charge current conversion (and hence THz power).[44] In Figure 1c the anisotropic ECML-based emitter is compared to the reference record ISHE trilayer W(2 nm)/$Co_{20}Fe_{60}B_{20}$(1.8 nm)/Pt(2 nm) emitter by measuring its transient electric field on the TDS setup under identical experimental conditions. The reference CoFeB emitter was grown on the same type double-side polished c-cut sapphire substrate. This emitter was provided to us through a collaboration (see Funding Sources and Acknowledgments) with the group that did the seminal work on ISHE THz emitters. Its properties and performance are therefore well established.[45] The 5d nonmagnetic SOC layers are the same in both emitters. The total thickness of the FM stack in the rare-earth based emitter is the same as that of the optimized isotropic CoFeB emitter. Both emitters are magnetically saturated along their easy axis ($H_{\mathrm{ext}} = \frac{200}{4\pi}\frac{\mathrm{kA}}{\mathrm{m}}$). They were excited from the metal side in order to suppress THz echoes in the TDS measurements.[46] As the THz emission is governed by the spin-to-charge conversion in the 5d SOC metals and since both emitters use the same ones and in the same stacking order, both measured E-field transients present the same polarity and identical temporal dynamics (see Figure 1c).

Remarkably, the $TbCo_2$/FeCo-based emitter achieves a peak-to-peak THz signal that is as high as 60% of that of the reference CoFeB trilayer. The Fourier transform (plotted as inset in Figure 1c) confirms this observation. It is known that THz pulses generated by the ISHE in 5d metals are quasi Fourier-limited in view of the very short electron lifetimes in the metal layers.[44] The bandwidth of the spectra is therefore dominated by the response time of the Auston switch of the TDS setup (see Supporting Information) and not by the dynamics of the ISHE. Nevertheless, the observed bandwidth of about 3THz is close to the minimum time-bandwidth product of the 100 fs pulses in the custom TDS setup ($\Delta f \approx$ 4THz).

The measured spectral width of the ECML-based emitter is unchanged with respect to the reference CoFeB-based emitter, underlining again that dynamics is governed by the 5d metal layers. When assessing the observed THz efficiency of the ECML emitter, it was pointed out by Seifert in ref 18 that ISHE THz generation presents an optimum as a function of total metal thickness. The other parameters governing this optimum formula are all intrinsic material properties (spin Hall angle and THz refractive indices or conductivities). This was refined by Torosyan in ref 46 to take into account the individual FM and NM layer thicknesses and their conductivities. Making a reasonable assumption that the conductivity of the $TbCo_2$/FeCo multilayer is not radically different from that of the amorphous CoFeB alloy and also ignoring self-ISHE in the spin pumping layer, and all the rest being equal in both emitters, the difference in THz efficiency is thus entirely attributed to a less efficient spin current generation and injection for the ECML emitter. This can have multiple origins. An impact of the two extra interfaces in the ECML in the form of spin scattering losses in the superdiffusive spin current is likely to occur. But the dominant factor is believed to be the lower net saturation magnetization of the ECML, leading to a lower maximal absolute spin polarization injection in the 5d metals.

In order to corroborate this assumption we have studied the static magnetization properties of the stack using an ADE EV9 vectorial vibrating sample magnetometer (VSM) and com-

https://doi.org/10.1021/acsphotonics.1c01782
ACS Photonics 2022, 9, 1274−1285

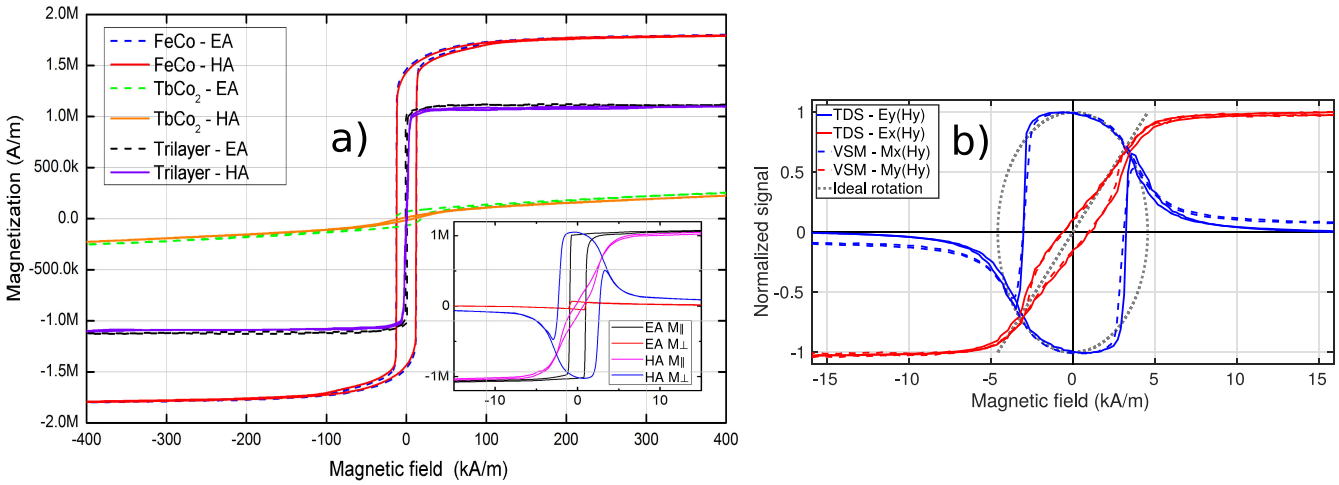


Figure 2. Terahertz magnetostatic hysteresis of the uniaxial FeCo/$TbCo_2$/FeCo heterostructure. (a) VSM measured magnetization characteristics for single layers of FeCo, $TbCo_2$, and a FeCo(5 Å)/$TbCo_2$(8 Å)/FeCo(5 Å), all sputter deposited under a polarizing magnetic field inducing an easy axis (EA). The main graph shows the $M_{\parallel}$-component along the applied field direction, oriented for all layers either along the induced EA or orthogonal to it (HA). Exchange coupling in the trilayer results in an engineered uniaxial anisotropy with averaged M_s and lowered H_A. The inset zooms in on the trilayer's vectorial hysteresis, evidencing its well-defined uniaxial anisotropy. For HA fields the $M_{\parallel}$ (pink) and $M_{\perp}$ (blue) hysteresis exhibit near perfect SW rotation with an anisotropy field of 5 kA/m. (b) Comparison between magnetization hysteresis loops measured using VSM (dashed lines) and E-field THz-TDS measurements (full lines) at the maximal peak position. The gray dotted line illustrates the ideal circular hysteresis. The magnetostatic properties of the spin pumping layer are perfectly recovered in the polarization behavior of the spintronic terahertz generation.

pared it to those of its constituents. For that purpose, separate samples of CoFe and $TbCo_2$ have been grown under the same polarizing field H_d using the same method as the ECML. Figure 2a plots the magnetization component for all three systems (FeCo, $TbCo_2$, and FeCo/$TbCo_2$/FeCo) measured along the direction of the magnetic field, when it is applied either along the induced easy axis (EA) or perpendicular to it (HA). These data demonstrate clearly how the coupling strongly lowers the effective anisotropy field of the rare earth alloy, and averages the M_s of the complete stack. The M_s of the ECML is indeed lowered to about 60% of that of the amorphous FeCo alloy explaining the lower spin polarization in the anisotropic emitter. This observation leads us to believe that the efficiency of ISHE THz generation using this new type of spin pumping layer is up to good approximation fully dominated by the difference in spin polarization due to the lower saturation magnetization. Future further optimization of the Tb-based emitter will clearly necessitate precise characterization of infrared absorption and THz conductivity of the individual FM layers. But the pragmatical comparison experiment of Figure 1c, combined with the VSM M_s measurement, leads us to believe that this will only be a second order effect.

The exchange coupling between thin films of intermetallic rare earth and transition metal alloys is thus a very efficient mechanism to introduce anisotropic control in ISHE emitters without sacrificing significantly the spin injection mechanism. The zoom on the ECML hysteresis in the inset of Figure 2a makes its uniaxial anisotropy more apparent. An anisotropy field reduced to approximately $5\,\frac{\mathrm{kA}}{\mathrm{m}}$ is observed while maintaining a saturation magnetization close to that of the isotropic CoFe system ($M_s \approx \frac{1\,\mathrm{MA}}{\mathrm{m}} \approx 0.6\,M_{s,\mathrm{CoFe}}$). By using vectorial VSM probes, this uniaxial anisotropy is also observed in the near perfect SW-like rotation of the magnetization in the plane of the ECML. Varying the applied magnetic field perpendicular to the induced easy axis, the magnetization component along this direction (M_y) varies almost perfectly linearly between $\pm H_A$, while the orthogonal component (M_x) simultaneously follows nearly a $M_x(H_{\mathrm{ext}}) = \sqrt{1 - M_y^2(H_{\mathrm{ext}})}$ law for $H_{\mathrm{ext}} \leq H_A$. This is signatory SW-behavior.[30] The observed deviations are the combined effect of a small (intentional) misalignment (see ref 41) between the applied field and the anisotropy axis and the appearance of multidomains during magnetization reversal, as will be seen in Section 4.

The physics of the ISHE imply that the emitted THz polarization should perfectly emulate this magnetostatic Stoner–Wohlfarth rotation. While it cannot be straightforwardly deduced from the temporal vectorial polarization traces as a function of applied hard axis field in Figure 1b, it was hinted at by the behavior of the azimuth of the polarization (see the inset in Figure 1d). To make this fully visible, we compare in Figure 2b normalized hard axis hysteresis cycles obtained by vectorial VSM magnetometry (dashed lines) of the in-plane M_x and M_y components (refer to the inset in Figure 2a) with the normalized $E_y(t_1)$ and $E_x(t_1)$ THz polarization components (full lines) measured via TDS (at the same time delay t_1 = 2060 fs in Figure 1b). Clearly the TDS vectorial polarization cycles reproduce exactly VSM magnetometry. The difference in asymptotic behavior between E_x (TDS) and M_y (VSM) are not related to ISHE physics but are an artifact of the VSM measurements. VSM is a volumetric method and therefore the slight paramagnetic contribution of the substrate is also picked up. This one-to-one correspondence between VSM magnetometry and TDS THz polarimetry in ISHE emitters is a striking result that reconfirms that the THz polarization rotation occurs without signal loss. Superposed on the TDS and VSM hysteresis cycles, the dotted curves illustrate ideal SW rotation with an anisotropy field close to $5\,\frac{\mathrm{kA}}{\mathrm{m}}$. As indicated previously, the magnetization flip

https://doi.org/10.1021/acsphotonics.1c01782
ACS Photonics 2022, 9, 1274–1285

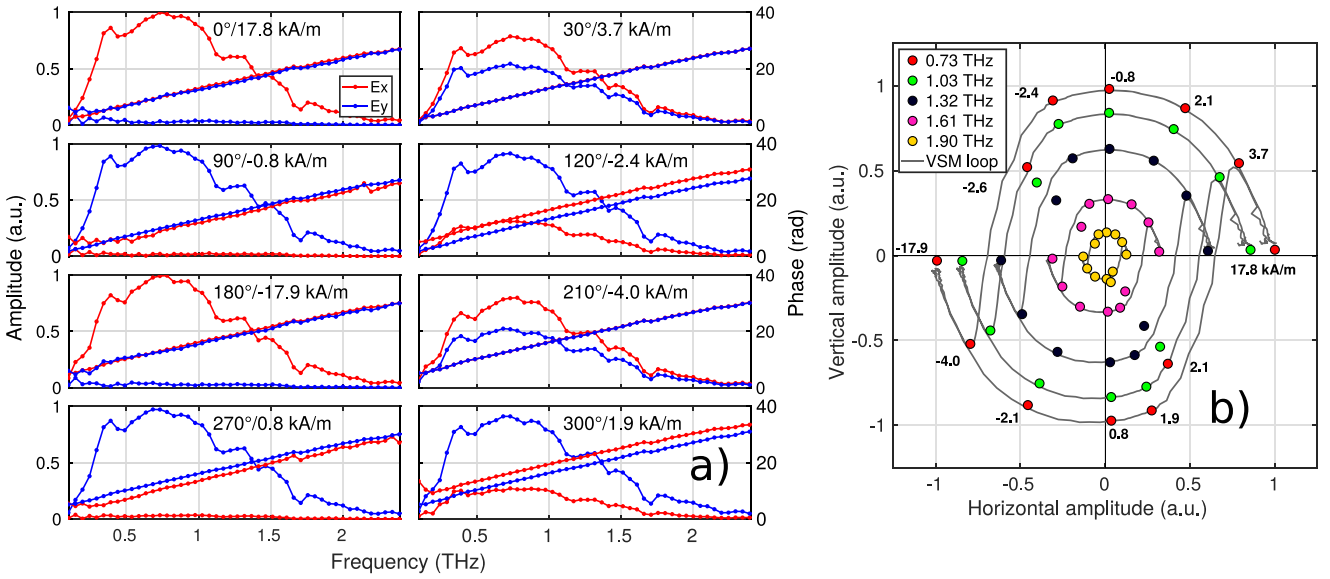


Figure 3. Analysis of the terahertz polarization rotation in Fourier space. (a) Evolution of normalized spectral amplitudes and extracted phases of E_x (red) and E_y (blue) components during a full hard axis cycle (for 8 rotation angles/magnetic fields distributed over a full circle). Note that the phase extraction for near-zero components is saddled by numerical noise. Still it is clear that both components are always perfectly in-phase or antiphase depending on the quadrant angle of the polarization, underlining the perfect linearity of the polarization. (b) Cartesian parametric plot of the vectorial Fourier amplitude $\mathbf{E}(\omega) = \mathbf{1}_x|E_x(\omega)| + \mathbf{1}_y|E_y(\omega)|e^{j\Delta\phi(\omega)}$ for selected frequencies up to 2 THz. As $\Delta\phi = 0,\pi$ there is no ellipticity and Im $\mathbf{E}(\omega) = 0$. The Stoner−Wohlfarth rotation is recovered throughout the spectral content of the pulse. Homothetically scaled VSM hysteresis curves are added as guide to the eye.

during the rotation prevents a perfect Stoner−Wohlfarth single domain rotation. Indeed, in the narrow window where the jump occurs, the polarization is extremely sensitive to the external field. Still, a 360° rotation is observed.

Up until now the discussion has been limited to the time domain, analyzing the polarization behavior at a fixed point in the transient signal. Even though the temporal traces in Figure 1b seem to suggest that both THz field components always remain in phase, this can only be correctly assessed by Fourier analysis. Moreover the spectral behavior of the polarization is crucial for spectroscopic and ellipsometric applications. Figure 3a plots the amplitude and the phase of the Fourier transform of the measured field components $e_{x,y}(t)$ at 8 different values of $H_{\mathrm{ext},y}$ leading to polarization angles distributed over the four quadrants and aligned along the Cartesian axes, as extracted from Figure 1d. The amplitudes have been normalized to the maximum of the spectrum when the sample is saturated along the hard axis. The spectra are plotted in a linear scale in order to make the linearity of E_x (red spectra) with $\frac{H_{\mathrm{ext},y}}{H_A}\left(H_A \approx 5\ \frac{\mathrm{kA}}{\mathrm{m}}\right)$ more evident. It is already qualitatively clear how the field spectra transform almost unperturbed over the (xy)-Cartesian plane as a function of HA field. In order to make this more obvious, Figure 3b plots a Cartesian projection of the evolution of the spectral amplitudes from Figure 3a in a Cartesian plane for frequencies every 0.3 THz between the spectrum peak (0.73 THz) and 2 THz. Note that this parametric plot takes into account the phase difference $\Delta\phi = \arg(E_y) - \arg(E_x)$ by plotting the real part of the vector $\mathbf{E}(\omega) = \mathbf{1}_x|E_x(\omega)| + \mathbf{1}_y|E_y(\omega)|e^{j\Delta\phi(\omega)}$. As expected, the observed Stoner−Wohlfarth rotation in the time domain (see Figure 1d) is recovered here in the spectral content of the pulses. While the measured vectorial spectral hysteresis is plotted at only a few selected field values, a homothetically scaled version of the vectorial VSM cycle acts as a guide to the eye proving the presence of SW rotation over the whole spectral content of the pulse. In order to make this argument even stronger, the Fourier spectra in Figure 3a also plot the phase of both components. First of all, the phase behavior is featureless (except for the natural linear increase due to the air propagation between emitter and detector), which correctly implies that the ISHE pulses are Fourier transform limited due to the extreme bandwidth of the ISHE in SOC metals. Second, both components exhibit a perfect in- or antiphase behavior over the entire spectrum. Except for the cases where the polarization is purely x- or y-oriented (when one of either components is close to the noise floor), the phase difference is flat and nearly perfectly 180° or 0°. This also proves the basic assumption of ISHE physics, namely that the spin-to-charge current burst behaves as a point-like dipole source without any feasible phase shift during the magnetization rotation. All of the above proves that the linearity of the polarization is stable over the entire spectrum of the pulse and during the full coherent 2π-rotation.

Before moving on to a precise model of the polarization hysteresis loop, it should be mentioned that in our work we have up until now not studied thermal effects. Our experiments have always been performed under the same pump fluence levels of the order of 1 mJ/cm^2. While metallic spintronic emitters are generally known to be efficient thermal conductors, the low spin-to-charge conversion efficiencies lead nevertheless to an important temperature increase in the emitter. It has recently been demonstrated by Agarwal et al. that photothermal effects can have an important impact on the anisotropy of the spin pumping layer.[28] Intense infrared control pulses can as such switch the polarity of the THz signal by a strong reduction of the coercivity. In our work, the emitter is operated in a thermal equilibrium. The fluence of the pump pulse train is never varied. Hence the anisotropy field (measured to be close to 60 Oe in our experimental conditions) remains constant. However, increasing or decreas-

https://doi.org/10.1021/acsphotonics.1c01782
ACS Photonics 2022, 9, 1274−1285

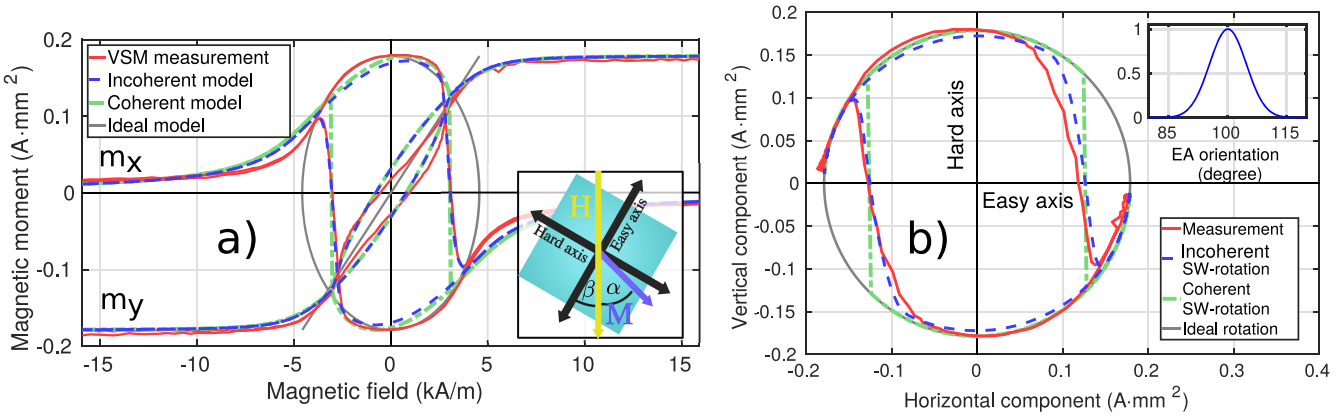


Figure 4. Hysteresis fitting. Comparison of incoherent (blue dashed) and coherent (green dot-dashed) fitted models with VSM measurement (red line) for (a) both m_x and m_y and (b) the magnetic moment rotation (gray line represents the ideal circular rotation). The geometrical meaning of the angles α and β is schematized as the inset of (a). To illustrate the phenomenological extended multidomain incoherent SW model, the inset of (b) shows the fitted Gaussian distribution of the easy axis orientation β_i of the domains.

ing the pump conditions might likely modify the anisotropy strength (and even collapse it). Given the rather strong uniaxial anisotropy that we observe under considerably strong pumping conditions, we do not expect a sudden anisotropy collapse and therefore expect the full polarization control to remain feasible even under stronger pumping. This merits further study in future work.

4. EXTENDED STONER–WOHLFARTH INCOHERENT ROTATION FITTING FOR ECML SPINTRONIC EMITTERS

Having established the uniaxial field control of the THz polarization over a full 360°, we now demonstrate how the hysteresis loop can be perfectly modeled. This is of practical importance. In view of the demonstrated perfect orthogonality between the emitted linear THz polarization and the magnetization of the multilayer, such a model would allow a one-to-one relationship between HA field and polarization azimuth, that can be used for instance in polarimetric applications. The starting point is the assumption that the ECML rotates according to the Stoner–Wohlfarth model as a single domain with an uniaxial in-plane magnetic anisotropy axis.[30] This is motivated by the observations above. In the following we will elaborate an extended multidomain SW model that correctly fits the observed slight deviations. The equilibrium position of the magnetization of a given domain is described by the minimization of the magnetic energy E_m,

$$E_m(\alpha, \beta, \mathbf{H}) = -\mu_0|\mathbf{H}|m_s \cos(\alpha) + K_u V \sin^2(\alpha - \beta) \quad (1)$$

where μ_0 is the vacuum permeability and the material domain parameters m_s, K_u, and V are the saturation magnetic moment, the uniaxial anisotropy constant, and the domain volume, respectively. The angles α and β denote respectively the orientation of the magnetization and of the induced easy axis with respect to the external magnetic field $\mathbf{H}$ as illustrated in the inset of Figure 4. The first term of eq 1 is the standard Zeeman field energy describing the potential energy in an external magnetic field. The second term describes the uniaxial anisotropic energy, assuming the coupled multilayers behave as an effective system with a magnetocrystalline energy having a 180-degree rotation symmetry. This symmetry originates in the induced magnetic anisotropy by interlayer coupling, which implies an analogy with the magnetic anisotropy of tetragonal lattice systems.[47]

If the coupled multilayers behave as a perfect single magnetic domain, this Stoner–Wohlfarth model predicts the saturation magnetization to uniformly rotate as a function of applied field with an abrupt switch when the Zeeman energy overcomes the anisotropy energy. This sudden switch depends on the angle between the anisotropy axis and the magnetic field. It becomes less pronounced as the anisotropy axis approaches orthogonality with the applied field. In the latter limiting case the magnetization perfectly coherently rotates over full 2π angle. In practice the magnetization reversal is the result of a complex interplay of domain nucleation, domain wall motion, curling or buckling, and other reversal processes that can only be correctly modeled by micromagnetic simulations.[48,49] It is beyond the scope of this work to account for these processes. Instead we propose in the following a pragmatic phenomenological modeling approach that allows to fit with reasonable accuracy the observed magnetization reversal. The VSM-measured magnetization switching presents a somewhat rounded and smoothed out behavior. Especially close to the critical field values the m_x hysteresis curves of Figure 4(a) (full red line) can be seen as the averaged switching of an ensemble of polycrystalline domains with distributed easy axes around $\beta = \pi/2$.

Taking this phenomenological approach to describe the magnetization reversal, the hysteresis loops are approached by an incoherent sum of magnetic moments m_i of multiple domains with a normal distribution of their easy axes β_i about an average axis β_c.

$$g_i(\beta_i) = \exp\left[-\frac{(\beta_i - \beta_c)^2}{G^2}\right] \quad (2)$$

where G and β_c are the Gaussian width and the central angle of easy axes of domains, respectively. Each domain is assumed to contribute the same saturation magnetic moment m_s, just as it is assumed that the domains extend over the thickness of the exchange coupled stack. The jump accompanying the magnetization rotation when $\beta \neq \pi/2$ is now smoothed out by the creation of multidomains and slightly different easy axis orientation of magnetic domains in the whole plane of the

https://doi.org/10.1021/acsphotonics.1c01782
ACS Photonics 2022, 9, 1274–1285

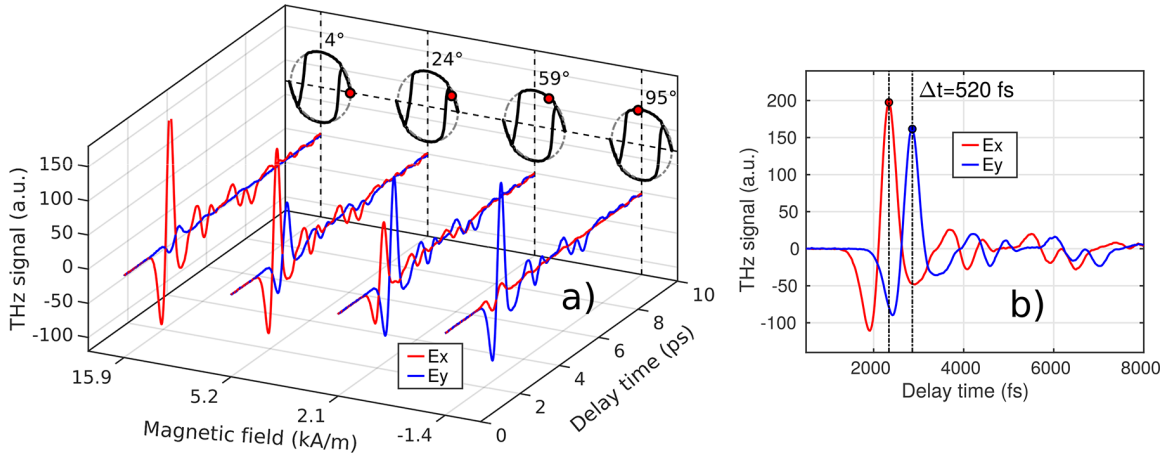


Figure 5. Terahertz birefringence characterization of quartz. The uniaxial magnetic field control of the polarization state of the spintronic emitter is exploited to probe the ordinary and extraordinary wave delay of quartz without any rotating polarizing elements. (a) Evolution of the detected transient trace (decomposed into its Cartesian components) as a function of hard axis field on the emitter. The corresponding polarization angle is obtained from the model in Section 4 and indicated by a red mark on the amplitude rotation profile (black line). The gradual transition of the character of the transient from ordinary to extraordinary delay is strikingly visible. (b) The extracted phase shift between the fast and slow axis of orthogonal polarizations obtained by simply switching the hard axis field between saturation and near-zero.

ferromagnetic stack. This results in the following fitting model for the *x*,*y*-component of the effective magnetic moment $\mathbf{m}_{\text{eff}}$ of the ferromagnetic heterostructure as a noncoherent summation of distributed magnetic moments $\mathbf{m}_i$.

$$m_{\text{eff}}^{x,y} = \frac{\sum_{i=1}^{N} g_i(\beta_i) m_i^{x,y}(\alpha_i, \beta_i)}{\sum_{i=1}^{N} g_i(\beta_i)} \tag{3}$$

where

$$m_i^x = m_s \cos(\alpha_i) \quad m_i^y = m_s \sin(\alpha_i) \tag{4}$$

for the external magnetic field **H** aligned vertically. The fitting consists of a two-step procedure where for a chosen normal distribution (with parameters (β_c, G)), N domains are uniformly sampled with easy axis angles β_i. The magnetization orientation of the i-th domain (α_i) is then obtained minimization of the magnetic energy $E(\alpha_i, \beta_i, \mathbf{H})$ described by the Stoner−Wohlfarth rotation (eq 1) for each domain separately and for all field values of the cycle. The noncoherent sum (eq 3) is then compared to the VSM data over the complete hysteresis cycle. This procedure is repeated until convergence (see Supporting Information).

The vectorial VSM hysteresis loops (solid red lines in Figure 4), measured along the hard axis, are fitted both to a single domain (eq 1) and the above multidomain SW model (eq 3), with M_s and K_u as fitting parameters for the multilayer treated as a single effective uniaxial anisotropic layer. In the MD model the phenomenological statistical parameters β_c and G are the two additional fitting parameters. Figure 4 plots the results of this coherent (green dot-dashed) and incoherent (blue dashed) Stoner−Wohlfarth rotation. The MD model clearly fits the magnetization reversal better. Combining the horizontal and vertical hysteresis loops and their fits in an in-plane parametric rotation plot in Figure 4(b) illustrates how the typical abrupt switching of monodomain SW rotation fails to correctly grasp the measured reversal. While there remain some residual differences between the incoherent model and the VSM data, the ease of implementation of a multidomain model with normally distributed anisotropy axes combined with its reasonable fitting proves that this is a powerful tool to obtain effective material parameters even without any knowledge about the interlayer coupling process.[50] Obviously only an advanced micromagnetic approach (domain walls, interlayer coupling, defects, temperature influence, etc.) would be needed to describe in detail the magnetic anisotropic rotation. This is both beyond the scope of this work and is of no practical importance for the targeted application.

The inset in Figure 4(b) shows the normalized easy axis distribution corresponding to the fitted magnetization rotation. The obtained central angle $\beta_c = 100.06°$ is off the ideal circular rotation (gray line) by 10°, which was arbitrarily chosen to demonstrate the magnetization switching and the effectiveness of the model.[41] The relatively important smoothing of the experimental hysteresis curves is confirmed by the fitted value for the Gaussian width of the normal distribution of $G = 6.598°$. Finally, an effective saturation magnetic moment $m_s = 0.179$ A·mm^2 and anisotropy energy of $K_uV = 514.2$ pJ are extracted. This implies a saturation magnetization $M_s = m_s/V \approx 994.5$ kA/m and an anisotropic constant $K_u \approx 2.857$ kJ/m^3 given the ferromagnetic ECML thickness of 1.8 nm and a sample surface of ≈10 × 10 mm^2. These values are in agreement with what was typically found in the literature for Co-based tetragonal systems.[47,51,52]

5. APPLICATION EXAMPLE AND PERSPECTIVES

The easy control of the linear THz polarization by a simple variation of an uniaxial external field finds several important applications in THz technology. One straightforward example is the characterization of the birefringent properties of a material without the need for rotating polarizing optical elements. Quartz is a well-known uniaxial birefringent material used in a very wide frequency range for waveplate applications. In the THz band quartz moreover presents excellent low absorption.[53,54] Typical THz characterization of quartz's birefringence consists of mechanically aligning its optic axis with respect to the polarization of the probing THz beam. This is prone to misalignments and related inaccuracies. The here presented spintronic emitter permits a polarimetric characterization of the birefringent properties by a simple sweep of the applied magnetic field bias on the THz emitter, given the near

https://doi.org/10.1021/acsphotonics.1c01782
ACS Photonics 2022, 9, 1274−1285

perfect 360° rotation of the linear THz polarization over this sweep. As such both the ordinary and extraordinary rays in a quartz plate can be probed without any mechanical rotation of either the sample or a polarizing optical element. Given moreover the broadband character of the spintronic emitter, this allows for a wideband THz characterization of the birefringence.

We have characterized a 3 mm thick quartz plate with its optical axis approximately aligned with the magnetic anisotropy axis of the spintronic emitter (throughout this paper chosen as the x-axis). Figure 5 illustrates as a function of applied magnetic field the evolution of the THz transients from the spintronic emitter when passing through the quartz plate. To facilitate the analysis and to better illustrate the potential of the emitter, the measured transient has been decomposed into its constituting vectorial components (using a switching ±90° and fixed 45° WGP before the Auston switch dipole as described in Supporting Information). This can also be achieved without two polarizer settings using electro-optical sampling.[55] Using the fitted model of Section 4 the polarization state of the THz pulse incident on the quartz plate is known for each field setting. This is indicated in Figure 5 by the point on the hysteresis curve per measured transient. As the HA field $H_{ext,y}$ is gradually reduced from near saturation (15.9 kA/m) toward near-zero (−1.4 kA/m) the magnetization evolves from near HA- to near EA-aligned, or the polarization from near x-oriented to near y-oriented. The linear THz polarization thus varies from being almost aligned with quartz's optic axis to being almost perpendicular to it. The measured transient pulse on the TDS setup therefore presents a group delay evolving from a pure ordinary fast wave to a pure extraordinary slow wave while passing through a regime where both delays are hybridly mixed. This is clearly visible in the four decomposed transients in Figure 5a. Near HA saturation of the emitter (i.e., polarization parallel to the optic axis of quartz), the transient measured on the Auston switch exhibits principally the delay characteristics of the ordinary (x-polarized) wave in quartz. The decomposition nicely shows that in agreement with the point on the hysteresis curve, a small contribution of the extraordinary wave is expected due to a small magnetization component along the EA (or thus a small y-polarized wave). This small e_y-transient (blue trace) at 15.9 kA/m appears as a temporally shifted pulse with the same phase as the principal e_x-transient. For the subsequent field values, Figure 5a illustrates the gradual increase of the e_x-transient in agreement with the evolution of the emitted THz polarization. It is striking to see how the pulse evolves nearly unaffected to a temporally shifted copy. One also notices how at the 95° polarization the x-transient pulse has taken on the opposite phase in accordance with the polarization entering the second quadrant!

Figure 5b focuses on this temporal delay for the limiting cases of nearly pure ordinary and extraordinary ray excitation. It can be seen that the emitted THz pulse is uniformly shifted as expected. The observed group delay shift Δt_g = 520 fs should correspond to a difference of group index of $\Delta(n_g) = \Delta t_g \times c/L$. With L = 3000 μm and $c \approx 300$ μm/ps this gives $\Delta(n_g) \approx 0.052 = \Delta n_{e,o} + \omega\Delta\left(\frac{\partial n_{e,o}}{\partial \omega}\right)$. As up to first order the dispersion of quartz's ordinary and extraordinary index is equal, the group index difference equals quartz's THz birefringence $\Delta n_{e,o}$. The obtained value of 0.052 reproduces the birefringence of quartz close to 0.75 THz (the pulse's central frequency) as reported in literature.[53,56]

The goal of this experiment was mainly to illustrate the potential of the emitter allowing fast and efficient characterization of anisotropic materials without needing any polarizing elements or rotation of the materials under study. A precise characterization of the anisotropy of quartz would require a more detailed modeling using matrix formalisms to account for the transmission through the quartz layer and Jones calculus. In any case, the magnetic anisotropy controlled spintronic emitter opens as such an effective way to implement time domain ellipsometry at THz frequencies. This technique has during the past decade established itself as a powerful THz spectroscopic tool allowing to bypass the need for a measurement against a standard reference sample, having a larger spectral coverage than frequency domain spectroscopy, and providing direct access to phase information.[57,58] Of the remaining challenges to be solved, the quality of the THz polarizing optical component needed to obtain the ellipsometric functions is an important one.[59] Using the here proposed emitter, a source with easily variable s- and p-polarization becomes available that is moreover intrinsically very broadband. As such the polarization analysis in a time-domain spintronic THz ellipsometer would not require a rotating analyzer anymore as all polarization states can easily be generated upon emission.

6. CONCLUSION

In this work we have improved, optimized, and added to the physical insights of a conceptually new approach for spintronic THz polarization control as preliminary demonstrated in ref 60. Our approach combines the intrinsic polarization versatility of inverse spin Hall terahertz emitters (i.e., emitted polarization strictly orthogonal to their magnetization state) with scalar field Stoner−Wohlfarth magnetization rotation offered by an uniaxially anisotropic ferromagnetic spin pumping layer. To achieve this, a rare-earth based intermetallic thin film heterostructure has been developed. Exchange coupling between a strongly anisotropic hard magnetic $TbCo_2$ thin film and soft magnetic isotropic CoFe layers leads to an effective ferromagnetic heterostructure with a lowered anisotropy field (down to 5kA/m) with an average saturation magnetization (close to 60% of the CoFe alloy). Sandwiched between W and Pt layers as spin−orbit coupling metals, this anisotropic spin pumping layer achieves THz strengths comparable to the strongest STEs reported with similar Fourier-limited bandwidths while simultaneously allowing polarization rotation over a full 2π radians with just a uniaxial field sweep of 5 kA/m (or $\mu_0 H$ = 6.5 mT). A practical extended model for the Stoner−Wohlfarth mediated polarization rotation allows to set on-demand any linear THz polarization by applying the appropriate hard axis field. As such this anisotropic spintronic terahertz emitter can act as a new versatile source for terahertz time domain broadband ellipsometry. This has been qualitatively demonstrated on a quartz sample. But the impact of the easy polarization control of this emitter type has several other far reaching applications. In this work the Stoner−Wohlfarth type magnetization control was mainly quasistatically exploited. Dynamic fast control of the reversible magnetization is imaginable by operating the uniaxial anisotropic emitter near the spin reorientation transition (SRT), where the magnetization along the easy axis moves unhindered by an energy barrier under small

https://doi.org/10.1021/acsphotonics.1c01782
ACS Photonics 2022, 9, 1274−1285

amplitude RF excitations. Modulation speeds well beyond 10 MHz are expected.[43,61] Such a wideband fast-modulated STE with near 100% modulation index is a missing component for wireless THz datacom but could also find use in low-noise modulation ellipsometric THz spectroscopy. Furthermore, by cascading such emitters and exploiting the full 360° polarization control, any chosen elliptical THz polarization state can be created at will if a precise phase control between both cascaded emitters is implemented. This might find interesting use in Terahertz circular dichroism spectroscopy. The needed phase control between both emitters does however limit somewhat the broadband character.

Besides implementing SRT modulation in these anisotropic rare-earth based intermetallic spintronic emitters, a further perspective is offered by the magnetoelastic properties of such systems. These structures have been demonstrated to exhibit giant magnetostriction.[62] As a result the anisotropic rotation of the THz polarization could be controlled by magnetoelectric coupling of the stress in the rare-earth based emitters with a piezoelectric substrate. As such, this would completely remove the need for magnetic biasing to rotate the polarization, which could now be achieved by proper voltage gating of a piezoelectric carrier. In any case, it is clear that within the research activity on terahertz spintronics, the use of engineered magnetic anisotropic emitters is a fertile playing ground with a perspective toward several improved terahertz functionalities.

■ ASSOCIATED CONTENT

Supporting Information

The Supporting Information is available free of charge at https://pubs.acs.org/doi/10.1021/acsphotonics.1c01782.

Details about the fabrication process of the spintronic emitters; Procedure for THz-TDS polarization measurements; Numerical details of the magnetic hysteresis fitting; Extended discussion about the spintronic emitter performance on different substrates (PDF)

■ AUTHOR INFORMATION

Corresponding Authors

Pierre Koleják − *Univ. Lille, CNRS, Centrale Lille, Univ. Polytechnique Hauts-de-France, UMR 8520 − IEMN − Institut d'Electronique de Microélectronique et de Nanotechnologie, F-59000 Lille, France; IT4Innovations & Faculty of Materials Science and Technology, Technical University of Ostrava, 708 00 Ostrava, Poruba, Czech Republic*; Email: pierre.kolejak@vsb.cz

Mathias Vanwolleghem − *Univ. Lille, CNRS, Centrale Lille, Univ. Polytechnique Hauts-de-France, UMR 8520 − IEMN − Institut d'Electronique de Microélectronique et de Nanotechnologie, F-59000 Lille, France;* orcid.org/0000-0003-1759-459X; Email: mathias.vanwolleghem@univ-lille.fr

Authors

Geoffrey Lezier − *Univ. Lille, CNRS, Centrale Lille, Univ. Polytechnique Hauts-de-France, UMR 8520 − IEMN − Institut d'Electronique de Microélectronique et de Nanotechnologie, F-59000 Lille, France*

Kamil Postava − *IT4Innovations & Faculty of Materials Science and Technology, Technical University of Ostrava, 708 00 Ostrava, Poruba, Czech Republic*

Jean-François Lampin − *Univ. Lille, CNRS, Centrale Lille, Univ. Polytechnique Hauts-de-France, UMR 8520 − IEMN − Institut d'Electronique de Microélectronique et de Nanotechnologie, F-59000 Lille, France*

Nicolas Tiercelin − *Univ. Lille, CNRS, Centrale Lille, Univ. Polytechnique Hauts-de-France, UMR 8520 − IEMN − Institut d'Electronique de Microélectronique et de Nanotechnologie, F-59000 Lille, France*

Complete contact information is available at: https://pubs.acs.org/10.1021/acsphotonics.1c01782

Funding

This research was funded by FET project s-NEBULA/Grant No. 863155, Doctoral grant competition CZ.02.2.69/0.0/0.0/19_073/0016945 under project DGS/TEAM/2020-027, and the IT4Innovations Path to Exascale project CZ.02.1.01/0.0/0.0/16_013/0001791.

Notes

The authors declare no competing financial interest.

The measurement data are publicly available through the ZENODO server under the reference 10.5281/zenodo.5705210.

■ ACKNOWLEDGMENTS

The authors thank the RENATECH Network for the support in the realization of the devices and the Barrande Fellowship Programme arranging Czech-French mobilities. Tobias Kampfrath of Department of Physics and the Frits Haber Institute at the Freie Universität Berlin (Germany), and Martin Jourdan of Institut of Physics, of the Johannes Gutenberg-Universität in Mainz (Germany), for providing us with a sample of the optimized Pt/CoFeB/W STE emitter.

■ REFERENCES

(1) Dhillon, S. S.; et al. The 2017 terahertz science and technology roadmap. *J. Phys. D: Appl. Phys.* **2017**, *50*, 043001.

(2) Hindle, F.; Kuuliala, L.; Mouelhi, M.; Cuisset, A.; Bray, C.; Vanwolleghem, M.; Devlieghere, F.; Mouret, G.; Bocquet, R. Monitoring of food spoilage by high resolution THz analysis. *Analyst* **2018**, *143*, 5536−5544.

(3) Jepsen, P. U.; Cooke, D. G.; Koch, M. Terahertz spectroscopy and imaging - Modern techniques and applications. *Laser Photonics Rev.* **2011**, *5*, 124−166.

(4) Ellrich, F.; Bauer, M.; Schreiner, N.; Keil, A.; Pfeiffer, T.; Klier, J.; Weber, S.; Jonuscheit, J.; Friederich, F.; Molter, D. Terahertz Quality Inspection for Automotive and Aviation Industries. *J. Infrared Millim. Terahertz Waves* **2020**, *41*, 470−489.

(5) Nagatsuma, T.; Ducournau, G.; Renaud, C. C. Advances in terahertz communications accelerated by photonics. *Nat. Photonics* **2016**, *10*, 371−379.

(6) Shan, J.; Dadap, J. I.; Heinz, T. F. Circularly polarized light in the single-cycle limit: The nature of highly polychromatic radiation of defined polarization. *Opt. Express* **2009**, *17*, 7431.

(7) Konishi, K.; Kan, T.; Kuwata-Gonokami, M. Tunable and nonlinear metamaterials for controlling circular polarization. *J. Appl. Phys.* **2020**, *127*, 230902.

(8) Grady, N. K.; Heyes, J. E.; Chowdhury, D. R.; Zeng, Y.; Reiten, M. T.; Azad, A. K.; Taylor, A. J.; Dalvit, D. A.; Chen, H. T. Terahertz metamaterials for linear polarization conversion and anomalous refraction. *Science* **2013**, *340*, 1304−1307.

(9) Markovich, D. L.; Andryieuski, A.; Zalkovskij, M.; Malureanu, R.; Lavrinenko, A. V. Metamaterial polarization converter analysis: Limits of performance. *Appl. Phys. B: Laser Opt.* **2013**, *112*, 143−152.

(10) Amer, N.; Hurlbut, W. C.; Norton, B. J.; Lee, Y. S.; Norris, T. B. Generation of terahertz pulses with arbitrary elliptical polarization. *Appl. Phys. Lett.* **2005**, *87*, 1−3.
(11) Shimano, R.; Nishimura, H.; Sato, T. Frequency tunable circular polarization control of Terahertz radiation. *Jpn. J. Appl. Phys.* **2005**, *44*, L676−L678.
(12) Lee, K.; Yi, M.; Song, J. D.; Ahn, J. Polarization shaping of few-cycle terahertz waves. *Opt. Express* **2012**, *20*, 12463.
(13) Sato, M.; Higuchi, T.; Kanda, N.; Konishi, K.; Yoshioka, K.; Suzuki, T.; Misawa, K.; Kuwata-Gonokami, M. Terahertz polarization pulse shaping with arbitrary field control. *Nat. Photonics* **2013**, *7*, 724−731.
(14) Hirota, Y.; Tani, M.; Hangyo, M. Polarization modulation of terahertz wave by multipole type photoconductive antenna. *IQEC Proc.* **2005**, *2005*, 1767−1768.
(15) Dai, J.; Karpowicz, N.; Zhang, X. C. Coherent polarization control of terahertz waves generated from two-color laser-induced gas plasma. *Phys. Rev. Lett.* **2009**, *103*, 1−4.
(16) Wen, H.; Lindenberg, A. M. Coherent Terahertz Polarization Control through Manipulation of Electron Trajectories. *Phys. Rev. Lett.* **2009**, *103*, 2−5.
(17) You, Y. S.; Oh, T. I.; Kim, K.-Y. Mechanism of elliptically polarized terahertz generation in two-color laser filamentation. *Opt. Lett.* **2013**, *38*, 1034−1036.
(18) Seifert, T.; Jaiswal, S.; Martens, U.; Hannegan, J.; Braun, L.; Maldonado, P.; Freimuth, F.; Kronenberg, A.; Henrizi, J.; Radu, I.; et al. Efficient metallic spintronic emitters of ultrabroadband terahertz radiation. *Nat. Photonics* **2016**, *10*, 483−488.
(19) Yang, D.; Liang, J.; Zhou, C.; Sun, L.; Zheng, R.; Luo, S.; Wu, Y.; Qi, J. Powerful and tunable THz emitters based on the Fe/Pt magnetic heterostructure. *Adv. Opt. Mater.* **2016**, *4*, 1944−1949.
(20) Kohlhaas, R.; Breuer, S.; Liebermeister, L.; Nellen, S.; Deumer, M.; Schell, M.; Semtsiv, M.; Masselink, W.; Globisch, B. 637 μ W emitted terahertz power from photoconductive antennas based on rhodium doped InGaAs. *Appl. Phys. Lett.* **2020**, *117*, 131105.
(21) Huang, S.-W.; Granados, E.; Huang, W. R.; Hong, K.-H.; Zapata, L. E.; Kärtner, F. X. High conversion efficiency, high energy terahertz pulses by optical rectification in cryogenically cooled lithium niobate. *Opt. Lett.* **2013**, *38*, 796.
(22) Roskos, H.; Thomson, M.; Kreß, M.; Löffler, T. Broadband THz emission from gas plasmas induced by femtosecond optical pulses: From fundamentals to applications. *Laser Photonics Rev.* **2007**, *1*, 349−368.
(23) Koulouklidis, A. D.; Gollner, C.; Shumakova, V.; Fedorov, V. Y.; Pugžlys, A.; Baltuška, A.; Tzortzakis, S. Observation of extremely efficient terahertz generation from mid-infrared two-color laser filaments. *Nat. Commun.* **2020**, *11*, 1−8.
(24) Vogel, T.; Omar, A.; Mansourzadeh, S.; Wulf, F.; Sabanés, N. M.; Müller, M.; Seifert, T. S.; Weigel, A.; Jakob, G.; Kläui, M.; Pupeza, I.; Kampfrath, T.; Saraceno, C. J. Average power scaling of THz spintronic emitters in reflection geometry. *arXiv*, December 17, 2021, arXiv:2112.09582.
(25) Gueckstock, O.; Nádvorník, L.; Seifert, T.; Borchert, M.; Jakob, G.; Schmidt, G.; Woltersdorf, G.; Kläui, M.; Wolf, M.; Kampfrath, T. Modulating the polarization of broadband terahertz pulses from a spintronic emitter at rates up to 10 kHz. *Optica* **2021**, *8*, 1013−1019.
(26) Kong, D.; Wu, X.; Wang, B. B.; Nie, T.; Xiao, M.; Pandey, C.; Gao, Y.; Wen, L.; Zhao, W.; Ruan, C.; Miao, J.; Li, Y.; Wang, L. Broadband Spintronic Terahertz Emitter with Magnetic-Field Manipulated Polarizations. *Adv. Opt. Mater.* **2019**, *7*, 1−9.
(27) Hibberd, M. T.; Lake, D. S.; Johansson, N. A.; Thomson, T.; Jamison, S. P.; Graham, D. M. Magnetic-field tailoring of the terahertz polarization emitted from a spintronic source. *Appl. Phys. Lett.* **2019**, *114*, 031101.
(28) Agarwal, P.; Medwal, R.; Kumar, A.; Asada, H.; Fukuma, Y.; Rawat, R. S.; Battiato, M.; Singh, R. Ultrafast Photo-Thermal Switching of Terahertz Spin Currents. *Adv. Funct. Mater.* **2021**, *31*, 2010453.
(29) Chen, X.; Wu, X.; Shan, S.; Guo, F.; Kong, D.; Wang, C.; Nie, T.; Pandey, C.; Wen, L.; Zhao, W.; Ruan, C.; Miao, J.; Li, Y.; Wang, L. Generation and manipulation of chiral broadband terahertz waves from cascade spintronic terahertz emitters. *Appl. Phys. Lett.* **2019**, *115*, 221104.
(30) Stoner, E. C.; Wohlfarth, E. P. A mechanism of magnetic hysteresis in heterogeneous alloys. *Philos. Trans. R. Soc. A* **1948**, *240*, 599−642.
(31) Kampfrath, T.; Tanaka, K.; Nelson, K. A. Resonant and nonresonant control over matter and light by intense terahertz transients. *Nat. Photonics* **2013**, *7*, 680−690.
(32) Cocker, T. L.; Huber, R. Ultrafast pulse shaping: A new twist on terahertz pulses. *Nat. Photonics* **2013**, *7*, 678−679.
(33) Mosley, C. D.; Failla, M.; Prabhakaran, D.; Lloyd-Hughes, J. Terahertz spectroscopy of anisotropic materials using beams with rotatable polarization. *Sci. Rep.* **2017**, *7*, 1−9.
(34) Le Gall, H.; Ben Youssef, J.; Socha, F.; Tiercelin, N.; Preobrazhensky, V.; Pernod, P. Low field anisotropic magneto-striction of single domain exchange-coupled (TbFe/Fe) multilayers. *J. Appl. Phys.* **2000**, *87*, 5783−5785.
(35) Ben Youssef, J.; Tiercelin, N.; Petit, F.; Le Gall, H.; Preobrazhensky, V.; Pernod, P. Statics and dynamics in giant magnetostrictive $Tb_xFe_{1-x}/Fe_{0.6}Co_{0.4}$ multilayers for MEMS. *IEEE Trans. Magn.* **2002**, *38*, 2817−2819.
(36) Hoffmann, A. Spin hall effects in metals. *IEEE Trans. Magn.* **2013**, *49*, 5172−5193.
(37) Carli, B. Reflectivity of metallic films in the infrared. *JOSA* **1977**, *67*, 908−910.
(38) Kröll, J.; Darmo, J.; Unterrainer, K. Metallic wave-impedance matching layers for broadband terahertz optical systems. *Opt. Express* **2007**, *15*, 6552−6560.
(39) Neumann, L.; Meier, D.; Schmalhorst, J.; Rott, K.; Reiss, G.; Meinert, M. Temperature dependence of the spin Hall angle and switching current in the nc-W (O)/CoFeB/MgO system with perpendicular magnetic anisotropy. *Appl. Phys. Lett.* **2016**, *109*, 142405.
(40) Hao, Q.; Xiao, G. Giant spin Hall effect and switching induced by spin-transfer torque in a W/Co 40 Fe 40 B 20/MgO structure with perpendicular magnetic anisotropy. *Phys. Rev. Appl.* **2015**, *3*, 034009.
(41) Perfect monodomain rotation is an idealized picture that is in principle only attained at perfect orthogonality between the applied field and the anisotropy axis. In practice, the anisotropy axis is intentionally slightly tilted to impose a rotation sense during a hysteresis cycle and avoid collapse of the latter. In our experiments the easy axis was intentionally tilted by $\approx 10°$. This causes an abrupt magnetization flip at a critical field H_c lower than the anisotropy field H_A. This flip is observed both in the behavior of the polarization azimuth and the field rotation.
(42) PureWavePolarizers, 5 μm wire grid polarizer, https://www.purewavepolarizers.com/wire-grid-polarizers/5-micron-wire-far-ir-thz-polarizer (accessed January 14, 2022).
(43) Klimov, A.; Ignatov, Y.; Tiercelin, N.; Preobrazhensky, V.; Pernod, P.; Nikitov, S. Ferromagnetic resonance and magnetoelastic demodulation in thin active films with an uniaxial anisotropy. *J. Appl. Phys.* **2010**, *107*, 093916−6.
(44) Dang, T. H.; et al. Ultrafast spin-currents and charge conversion at 3d-5d interfaces probed by time-domain terahertz spectroscopy. *Appl. Phys. Rev.* **2020**, *7*, 041409.
(45) Seifert, T.; Jaiswal, S.; Sajadi, M.; Jakob, G.; Winnerl, S.; Wolf, M.; Kläui, M.; Kampfrath, T. Ultrabroadband single-cycle terahertz pulses with peak fields of 300 kV cm-1 from a metallic spintronic emitter. *Appl. Phys. Lett.* **2017**, *110*, 252402.
(46) Torosyan, G.; Keller, S.; Scheuer, L.; Beigang, R.; Papaioannou, E. T. Optimized spintronic terahertz emitters based on epitaxial grown Fe/Pt layer structures. *Sci. Rep.* **2018**, *8*, 1311.
(47) Cullity, B. D.; Graham, C. D. *Introduction to Magnetic Materials*; John Wiley & Sons, 2011.
(48) Vaz, C.; Bland, J.; Lauhoff, G. Magnetism in ultrathin film structures. *Rep. Prog. Phys.* **2008**, *71*, 056501.

https://doi.org/10.1021/acsphotonics.1c01782
ACS Photonics 2022, 9, 1274−1285

(49) Arrott, A. S.; Heinrich, B. Phenomenology of anisotropy in the ferromagnetism of ultrathin films. *J. Magn. Magn. Mater.* **1991**, *93*, 571−586.
(50) Kools, J. Exchange-biased spin-valves for magnetic storage. *IEEE Trans. Magn.* **1996**, *32*, 3165−3184.
(51) Boyd, E. L. Magnetic anisotropy in single-crystal thin films. *IBM J. Res. Dev.* **1960**, *4*, 116−129.
(52) Heinrich, B.; Bland, J. A. C. *Ultrathin Magnetic Structures II: Measurement Techniques and Novel Magnetic Properties*; Springer Science & Business Media, 2006; Vol. *2*.
(53) Grischkowsky, D.; Keiding, S.; van Exter, M.; Fattinger, C. Far-infrared time-domain spectroscopy with terahertz beams of dielectrics and semiconductors. *J. Opt. Soc. Am. B* **1990**, *7*, 2006.
(54) Davies, C. L.; Patel, J. B.; Xia, C. Q.; Herz, L. M.; Johnston, M. B. Temperature-Dependent Refractive Index of Quartz at Terahertz Frequencies. *J. Infrared Millim. Terahertz Waves* **2018**, *39*, 1236−1248.
(55) Planken, P. C.; Nienhuys, H.-K.; Bakker, H. J.; Wenckebach, T. Measurement and calculation of the orientation dependence of terahertz pulse detection in ZnTe. *JOSA B* **2001**, *18*, 313−317.
(56) Castro-Camus, E.; Johnston, M. Extraction of the anisotropic dielectric properties of materials from polarization-resolved terahertz time-domain spectra. *J. Opt.* **2009**, *11*, 105206.
(57) Agulto, V. C.; Iwamoto, T.; Kitahara, H.; Toya, K.; Mag-usara, V. K.; Imanishi, M.; Mori, Y.; Yoshimura, M.; Nakajima, M. Terahertz time-domain ellipsometry with high precision for the evaluation of GaN crystals with carrier densities up to 10^{20}cm^{-3}. *Sci. Rep.* **2021**, *11*, 18129.
(58) Nagashima, T.; Tani, M.; Hangyo, M. Polarization-sensitive THz-TDS and its Application to Anisotropy Sensing. *J. Infrared Millim. Terahertz Waves* **2013**, *34*, 740−775.
(59) Neshat, M.; Armitage, N. P. Developments in THz range ellipsometry. *J. Infrared Millim. Terahertz Waves* **2013**, *34*, 682−708.
(60) Khusyainov, D.; Ovcharenko, S.; Gaponov, M.; Buryakov, A.; Klimov, A.; Tiercelin, N.; Pernod, P.; Nozdrin, V.; Mishina, E.; Sigov, A.; Preobrazhensky, V. Polarization control of THz emission using spin-reorientation transition in spintronic heterostructure. *Sci. Rep.* **2021**, *11*, 697.
(61) Tiercelin, N.; Preobrazhensky, V.; Mortet, V.; Talbi, A.; Soltani, A.; Haenen, K.; Pernod, P. Thin film magnetoelectric composites near spin reorientation transition. *J. Magn. Magn. Mater.* **2009**, *321*, 1803−1807.
(62) Debray, A.; Ludwig, A.; Bourouina, T.; Asaoka, A.; Tiercelin, N.; Reyne, G.; Oki, T.; Quandt, E.; Muro, H.; Fujita, H. Application of a multilayered magnetostrictive film to a micromachined 2-D optical scanner. *J. Microelectromech Syst* **2004**, *13*, 264−271.

Recommended by ACS

Nanoscale Optical Addressing of Valley Pseudospins through Transverse Optical Spin
Su-Hyun Gong, L. Kuipers, *et al.*
MAY 14, 2020
NANO LETTERS
READ

Tunable Damping in Magnetic Nanowires Induced by Chiral Pumping of Spin Waves
Hanchen Wang, Haiming Yu, *et al.*
MAY 12, 2021
ACS NANO
READ

Light-Driven Spintronic Heterostructures for Coded Terahertz Emission
Mingyu Tong, Tian Jiang, *et al.*
MAY 03, 2022
ACS NANO
READ

Room-Temperature Valley Polarization in Atomically Thin Semiconductors *via* Chalcogenide Alloying
Sheng Liu, Qihua Xiong, *et al.*
JULY 30, 2020
ACS NANO
READ

Get More Suggestions >

https://doi.org/10.1021/acsphotonics.1c01782
ACS Photonics 2022, 9, 1274−1285

Supporting Information: 360° polarization control of terahertz spintronic emitters using uniaxial FeCo/$TbCo_2$/FeCo trilayers

Pierre Koleják,*,†,‡ Geoffrey Lezier,† Kamil Postava,‡ Jean-François Lampin,† Nicolas Tiercelin,† and Mathias Vanwolleghem*,†

†*Univ. Lille, CNRS, Centrale Lille, Univ. Polytechnique Hauts-de-France, UMR 8520 - IEMN - Institut d'Electronique de Microélectronique et de Nanotechnologie, F-59000 Lille, France*

‡*Technical University of Ostrava, IT4Innovations & Faculty of Materials Science and Technology, 708 00 Ostrava - Poruba, Czech Republic*

E-mail: pierre.kolejak@vsb.cz; mathias.vanwolleghem@univ-lille.fr

1 Sample preparation

The W(2nm)/CoFe(5Å)/$TbCo_2$(8Å)/CoFe(5Å)/Pt(2nm) spintronic emitters were deposited by RF-Diode sputtering in a LEYBOLD Z550 equipment in a sputter down configuration. The emitters considered in the paper were grown on 10mm x 10mm x 0.5mm double side polished c-cut sapphire substrates with a surface roughness Ra $<$ 0.5nm as indicated by the provider. Extra measurements detailed below were performed on emitters deposited on 10mm x 10mm x 0.38mm Silicon and Oxidized Silicon (2μm thermal oxide) as well as 9mm

x 9mm x 0.160mm corning glass.

Prior to the sputtering, the substrates were cleaned by 5 minutes ultrasonication steps in successive baths of dichloromethane, acetone, iso-propylic alcool and deionized water. The typical base vacuum in the deposition chamber is $3 \cdot 10^{-7}$mbar. In order to imprint an in-plane magnetic anisotropy, the substrates are placed between two permanent magnets generating an in plane field with an approximate strength of 80 kA/m.

The individual layers are sputtered from circular 4 inches targets. The $TbCo_2$ and FeCo alloys are obtained from composite targets : the FeCo target is a Fe target with patches of Co glued with conductive epoxy, whereas the TbCo target is a Co target with patches of Tb. In both cases, the surface ratio is adjusted to obtain the correct stoechiometry in the given sputtering conditions. During this adjustment phase, the composition was obtained using standard EDX measurements in a Scanning Electron Microscope. W, Pt and FeCo are deposited with a RF power P_{RF} of 440W under a pure Argon atmosphere at $2{\cdot}10^{-3}$ mbar. $TbCo_2$ is deposited with a RF power P_{RF} of 250W at 10^{-3} mbar. Given the desired thicknesses, these rates are very low to ensure a good repeatability. This is achieved by using RF-Diode sputtering (no magnetron) under relatively low sputtering pressures of 10^{-3} mbar. To add increased repeatability, the deposition is made in an oscillation mode, where the sample is laid on a rotary turn table and passes under the target at a fixed speed for a given number of oscillations The sputtering technique is highly reproducible: most of the spintronic stacks in the world are realized with this technique and require the control of the layers with sub-nm precision. Therefore, we are confident in the fact that the deposited thickness is the aimed one. Although we have not done it on the presented structure, we have confirmed this assumption in the past : High resolution STEM imagery has confirmed the deposited thicknesses in previously studied FeCo/$TbCo_2$ multilayers (see Fig. S1).[S1] Fig. S1 shows that intermixing occurs at the interfaces, but as it is limited to a few angströms, the FeCo(5Å)/ $TbCo_2$(8Å) /FeCo(5Å) will retain a trilayer structure.

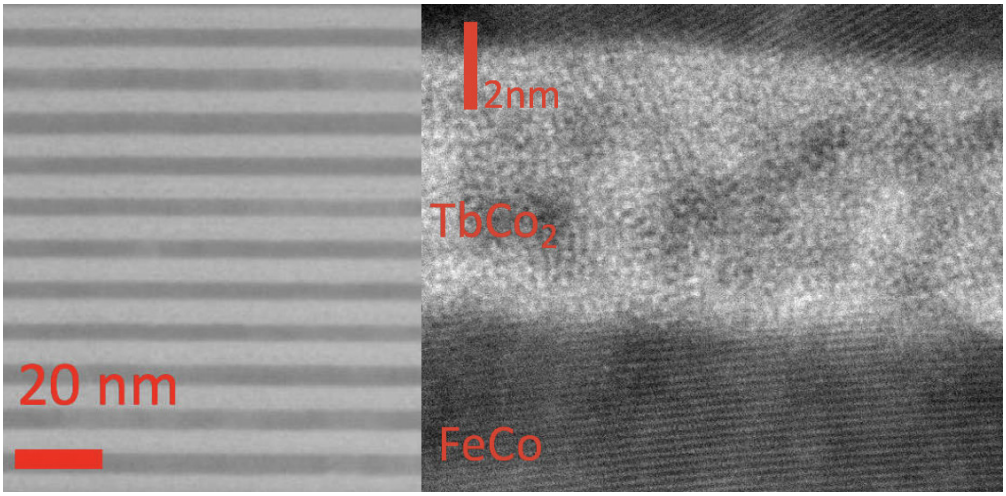


Figure S1: Scanning Transmission Electron Microscope imaging of a 25 x [$TbCo_2$(5nm) /FeCo(5nm)] multilayer. Albeit some intermixing is appearing at the interfaces, it shows that it is limited to a few angstroms.[S1]

2 Experimental methods

The terahertz emission from our ECML-based emitter was studied using a time-domain terahertz spectroscopy (THz-TDS) setup in a transmission arrangement, as schematized in Fig. S2. The Ti:sapphire laser emission (80 MHz repetition rate, centre wavelength 820 nm and 100 fs pulse duration) is split 50:50 into generation and detection branches. The generation branch includes in this order : A 50% attenuator to adjust the incident laser power, a mechanical chopper working at 1377 Hz, a lens with a 50mm focal length, a STE excited at the focal point, a 25mm focal length TPX lens to collimate the terahertz radiation, a polyethene and Teflon filter to block residual IR radiation, a set of wire grid polarizers from PureWavePolarizers company for polarization measurements and a lt-GaAs dipole antenna measuring the horizontal component of the electric field.[S2] A hemispherical silicon lens is placed in front of the latter to focalize the THz signal in its detection area.

The measured average power at the emitter in our experimental conditions was 185mW, hence an individual pulse energy of 2.3nJ to generate the THz emission mediated by ISHE. To control the emission, the spintronic emitter is placed between the poles of an electro-

magnet with the magnetic field applied in the vertical direction with a range of -40 to 40 kA/m. The detection branch includes a delay line with a 10fs resolution to generate the time domain spectra. For each position of the delay line, the chopped signal of the dipole antenna is processed by a Ametek 7265 DSP lock-in amplifier.

The use of two polarizers provides polarimetric analysis of both polarization components of the STE despite polarization sensitivity in the horizontal direction. The first 0/90° switching polarizer allows the selection of the polarization component to be detected, and the 45° fixed polarizer provides the projection to the horizontal plane. For an easy understanding of the used polarimetric method, we can perform the Jones matrix calculus to describe the transformation of the emitted electric field passing through a series of polarizers with given orientations.[S3] The Jones matrix $\mathbb{J}(\theta)$ of an arbitrarily rotated polarizer with an angle θ with respect to the horizontal direction is given by

$$\mathbb{J}(\theta) = \begin{bmatrix} \cos^2(\theta) & \cos(\theta)\sin(\theta) \\ \cos(\theta)\sin(\theta) & \sin^2(\theta) \end{bmatrix}_{\theta}. \tag{1}$$

The input electric field $\mathbb{E} = [E_x, E_y]^{\mathrm{T}}$ transforms using series of polarizers: $\mathbb{J}(45°)\mathbb{J}(0°)\mathbb{E}$ and $\mathbb{J}(45°)\mathbb{J}(90°)\mathbb{E}$; into the following forms

$$\frac{1}{2}\begin{bmatrix} 1 & 1 \\ 1 & 1 \end{bmatrix}_{45°} \cdot \begin{bmatrix} 1 & 0 \\ 0 & 0 \end{bmatrix}_{0°} \cdot \begin{bmatrix} E_x \\ E_y \end{bmatrix} = \frac{1}{2}\begin{bmatrix} E_x \\ E_x \end{bmatrix} \tag{2}$$

and

$$\frac{1}{2}\begin{bmatrix} 1 & 1 \\ 1 & 1 \end{bmatrix}_{45°} \cdot \begin{bmatrix} 0 & 0 \\ 0 & 1 \end{bmatrix}_{90°} \cdot \begin{bmatrix} E_x \\ E_y \end{bmatrix} = \frac{1}{2}\begin{bmatrix} E_y \\ E_y \end{bmatrix}, \tag{3}$$

where the horizontally oriented dipole antenna detects only the first coordinate of the output vector. Although the signal is reduced by factor two, this approach enables the measurement

of both components with a stable calibration due to the polarization separation by the switching polarizer.

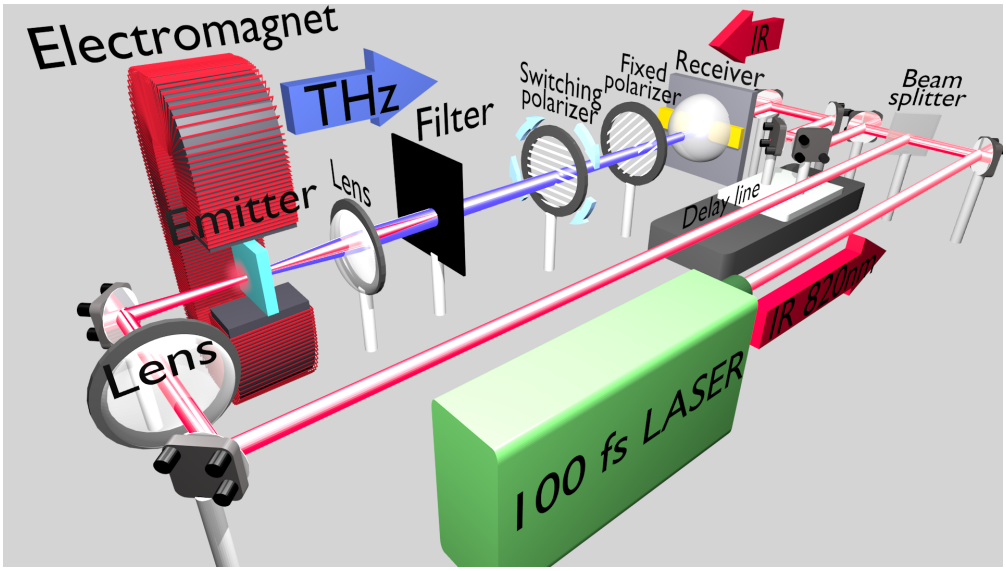


Figure S2: Schematic view of the customized terahertz time-domain spectroscopy (THz-TDS) setup for THz spin-orbitronic emission analysis. The terahertz detection is performed by the horizontal dipole receiver using field projections by two polarizers.

Precision on the TDS-THz amplitude measurements as a function of the magnetic field : The two polarization components were measured sequentially, and the control of the electromagnet did not allow to perform the measurement for identical magnetic field values. Therefore, a linear interpolation was performed on one of the measured components in order to display the orthogonal loop components on Figs 1d and 3b. This procedure was not necessary for VSM measurements as only one magnetic field cycle is needed with both components of magnetization simultaneously measured for each value of the field.

3 Extra measurements: reflective configuration

Besides c-cut sapphire substrates, we also prepared and characterized the W/CoFe/$TbCo_2$/CoFe/Pt STE on various substrates ($\langle 100 \rangle$ silicon, oxidized silicon, and corning glass). We consider it valuable to briefly discuss their comparison and the influence of the substrate in this section.

Even though transmission measurements are best suited to characterize the performance of the STE, it requires transparent substrates both for IR or THz waves. Furthermore, in a transmission configuration the measurements are influenced by factors unrelated to the ISHE emission (such as substrate absorption, Fabry-Pérot resonances, ...). Therefore, these measurements were made in 45°-reflection geometry. For this configuration, the dielectric mirror in front of the sample was replaced by the emitter together with the electromagnet (see Fig. S2). Then a new adjustment of the optical components is performed. It is important to note that the reflective arrangement in oblique incidence is not suitable for polarization analysis because the ISHE charge burst radiates in the form of a dipole (toroidal emission). Thus, the collected power is different when the polarization state changes due to the rotating dipole despite the fixed observation angle of the receiver. Therefore, emitters were equally magnetized along the vertical direction and the horizontal component of the electric field was measured under the same observation conditions.

Figure S3 compares the STEs on various substrates with a reference CoFeB-based STE. The differences in emissions show a direct influence of substrate impedance as predicted by Seifert.[S4] The high refractive indices of sapphire and silicon reduces the strength of the radiation, and even the silicon-based STE emits less due to the free electrons generated in the semiconductor. In contrast, the low optical density substrates glass and oxidized silicon show the most intense emission, and we assume that the visible difference is due to the simultaneous deterioration of the glass substrate due to the low thermal conductivity. We consider the usage of oxidized silicon as a proper substrate for reflective geometry due to high impedance and suitable thermal conductivity.

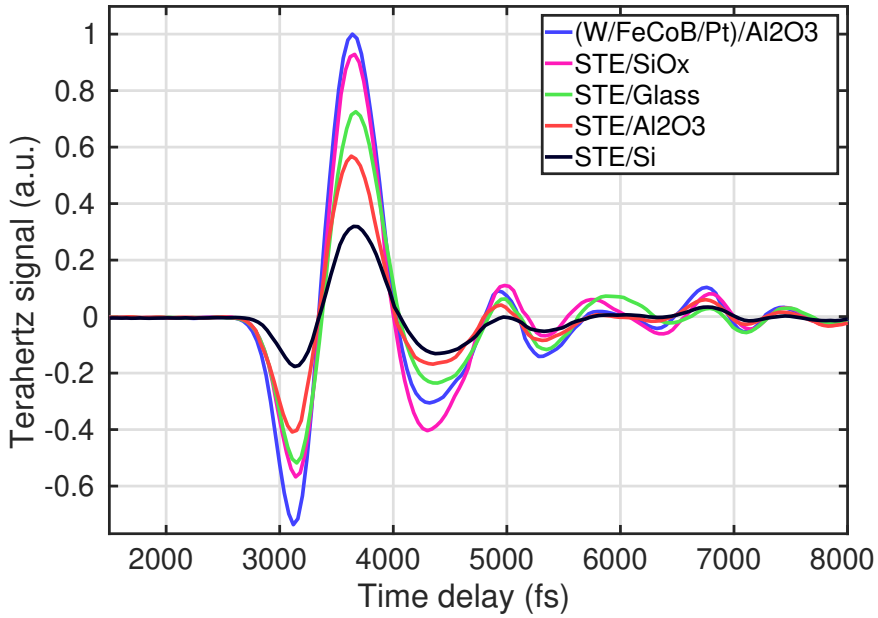


Figure S3: Time-domain spectra of the spintronic terahertz emission in reflection mode for the trilayer based emitters on various substrates, versus the reference CoFeB emitter on sapphire.

4 Numerical details on the fitting

The numerical procedure for fitting the hysteresis behaviour consists of three steps: (I) Minimization of the magnetic energy $E_i(\alpha_i)$ to determine the full magnetic cycle $\mathbf{m}_i(H)$: The algorithm optimizes the angle $\alpha_i(H_j)$ for a given domain and uses the optimized angle $\alpha_i(H_{j-1})$ from the previous step of the magnetic cycle as the initial value. (II) Incoherent summation of $\mathbf{m}_i(H)$ over the normal distribution to determine $\mathbf{m}_{\text{eff}}(H)$; (III) Least-square minimization between the VSM data and the incoherent model of both their hysteresis components together

$$\min\left\{\sum_{H_j}(m_{\text{eff}}-m_{\text{data}})_x^2+(m_{\text{eff}}-m_{\text{data}})_y^2\right\} \tag{4}$$

to properly fit the rotation process.

From one step to the next, the algorithm uses the previously calculated angle as an initial parameter for the following iteration. This way, it follows the local minimum of the magnetic energy, starting from magnetic saturation as an initial condition. If the starting magnetic field is positive : (i) At the magnetic saturation, the system lies in a global minimum of energy. (ii) while decreasing the magnetic field, the magnetization rotates following the new position of this minimum, which might not be the global minimum. (iii) At a critical point in the negative values of the applied magnetic field, the local minimum vanishes as the energy expressed as a function of α crosses its inflexion point, but the algorithm converges towards the global energy minimum, which results in an abrupt jump of magnetization across the hard axis. (iv) this new energy minimum is followed to the negative magnetic saturation. This behaviour corresponds to the physical reality where the system does not have enough energy to switch to the global minimum by crossing the local maximum of energy. A caveat is that a fine resolution of a magnetic field during the cycle has to be used. Overall, the algorithm proves itself robust enough to handle the little gradient and flat dependence during the jump. We have found the application of the Nelder-Mead simplex method[S5] to be appropriate. Of course, this model does not include the thermal energy fluctuations, nor the exchange and demagnetization energies and the presence of defects that could explain an earlier switch by magnetic domains, but it shows very close results to the experimental measurements which supports the fact that magnetization indeed rotates quasi-homogeneously in a Stoner-Wohlfarth fashion. Furthermore, the discretization of the distribution affects the smoothness of the magnetization curve during the switching, since it corresponds to the amount of already switched domains in the distribution. This numerical behaviour show some analogies with the Berkhausen effect when magnetic domains reshape.[S6]

References

(S1) Mazzamurro, A.; Dusch, Y.; Pernod, P.; Bou Matar, O.; Addad, A.; Talbi, A.; Tiercelin, N. Giant Magnetoelastic Coupling in a Love Acoustic Waveguide Based on TbCo2 / Fe Co Nanostructured Film on ST-Cut Quartz. *Physical Review Applied* **2020**, *13*, 1.

(S2) PureWavePolarizers, https://www.purewavepolarizers.com/wire-grid-polarizers/5-micron-wire-far-ir-thz-polarizer (accessed 2022-01-14), 5 micron wire grid polarizer.

(S3) Azzam, R. M.; Bashara, N. M.; Ballard, S. S. *Ellipsometry and polarized light*; 1978; Vol. 31; p 72.

(S4) Seifert, T.; Jaiswal, S.; Martens, U.; Hannegan, J.; Braun, L.; Maldonado, P.; Freimuth, F.; Kronenberg, A.; Henrizi, J.; Radu, I., et al. Efficient metallic spintronic emitters of ultrabroadband terahertz radiation. *Nat. Photonics* **2016**, *10*, 483–488.

(S5) Lagarias, J. C.; Reeds, J. A.; Wright, M. H.; Wright, P. E. Convergence properties of the Nelder–Mead simplex method in low dimensions. *SIAM J. Optim.* **1998**, *9*, 112–147.

(S6) Cullity, B. D.; Graham, C. D. *Introduction to magnetic materials*; John Wiley & Sons, 2011.

Paper V

Fully reversible magnetoelectric voltage controlled THz polarization rotation in magnetostrictive spintronic emitters on PMN-PT

Geoffrey Lezier, Pierre Koleják, Jean-François Lampin, Kamil Postava, Mathias Vanwolleghem, and Nicolas Tiercelin
Applied Physics Letters, **120** (2022)
Reprinted with the permission of AIP Publishing.

Applied Physics Letters ARTICLE scitation.org/journal/apl

Fully reversible magnetoelectric voltage controlled THz polarization rotation in magnetostrictive spintronic emitters on PMN-PT

Cite as: Appl. Phys. Lett. **120**, 152404 (2022); doi: 10.1063/5.0080372
Submitted: 30 November 2021 · Accepted: 27 February 2022 ·
Published Online: 15 April 2022

View Online Export Citation CrossMark

G. Lezier,[1] P. Koleják,[1,2] J.-F. Lampin,[1] K. Postava,[2] M. Vanwolleghem,[1] and N. Tiercelin[1,a)]

AFFILIATIONS

[1]Université de Lille, CNRS, Centrale Lille, Université Polytechnique des Hauts-de-France, UMR 8520-IEMN, F-59000 Lille, France
[2]IT4Innovations and Faculty of Materials Science and Technology, Technical University of Ostrava, 708 00 Ostrava-Poruba, Czech Republic

Note: This paper is part of the APL Special Collection on Ultrafast and Terahertz Spintronics.
[a)]**Author to whom correspondence should be addressed:** nicolas.tiercelin@iemn.fr

ABSTRACT

THz polarization control upon generation is a crucially missing functionality. THz spintronic emitters based on the inverse spin Hall effect (ISHE) allow for this by the strict implicit orthogonality between their magnetization state and the emitted polarization. This control was until now only demonstrated using cumbersome external magnetic field biasing to impose a polarization direction. We present here an efficient voltage control of the polarization state of terahertz spintronic emitters. Using a ferromagnetic spin pumping multilayer exhibiting simultaneously strong uniaxial magnetic anisotropy and magnetostriction in a crossed configuration, an emitter is achieved where, in principle, the stable magnetization direction can be fully and reversibly controlled over a 90° angle span only by an electric voltage. To achieve this, an engineered rare-earth based ferromagnetic multilayer is deposited on a piezoelectric $(1-x)[Pb(Mg_{0.33}Nb_{0.66})O_3]-x[PbTiO_3]$ (PMN-PT) substrate. We demonstrate experimentally a reversible 70° THz polarization rotation by sweeping the substrate voltage over 400 V. This demonstration allows for a fully THz polarization controlled ISHE spintronic terahertz emitter not needing any control of the magnetic bias.

Published under an exclusive license by AIP Publishing. https://doi.org/10.1063/5.0080372

Spintronic inverse spin Hall effect terahertz emitters (ISHE STEs) have in a matter of just a few years burst onto the scene as a promising and highly efficient paradigm for pulsed terahertz generation.[1–3] Even though their efficiency has a hard time competing with that of traditional semiconductor photoconductive switches[4] or optical rectification in nonlinear crystals,[5] the true leverage for pulsed THz generation lies in the combination of the absence of phonon gaps in their output spectrum, their intrinsic Fourier-limited broadband character, and their linear response even at low excitation pump fluences, while adding a unique direct access to the polarization direction of the emitted terahertz pulse by control of the magnetization direction of the spin pumping layer.[6] The physics of the ISHE inherently implies the emitted THz pulse to be strictly perpendicular to the magnetization of the spin pumping layer. This is a particularly interesting feature enabling, for instance, a compact and efficient source for time-domain terahertz ellipsometry.[7,8] Moreover, fast modulation of the magnetization direction opens the way for an efficient modulation format for THz wireless communications and could also find use in low-noise modulation ellipsometric THz spectroscopy.[9] While optimizations of the THz power[10–13] as well as THz emission control schemes[14,15] have been reported, the control of the THz polarization state has been limited to cumbersome implementations using perpendicularly crossed or mechanically rotating external magnetic fields.[16,17] Recently, we demonstrated an ISHE STE with a spin pumping layer with built-in uniaxial magnetic anisotropy.[18] This achieves full 2π-radians control of the polarization by setting only a single hard-axis external magnetic field. Although efficient, this method still requires an electromagnet and continuous currents to maintain the desired polarization. In the present work, we improve on this scheme. The intermetallic exchange coupled CoFe(5 Å)/TbCo2(8 Å)/CoFe(5 Å) multilayer (ECML) designed for the purpose of uniaxial magnetic anisotropy is also known for its strong magnetoelastic properties.[19,20] As such, the magnetic anisotropy can be fully controlled by applying an appropriate in-plane tensile strain. Using a piezoelectric substrate, the magnetization direction in the spin pumping layer can, therefore, be set solely by an electric voltage. Owing to this control of the magnetic anisotropy, one

Published under an exclusive license by AIP Publishing

can theoretically reach a 90° polarization rotation. Recently, Cheng *et al.* presented the study of a magnetoelectric effect in spintronic emitters using an iron–cobalt–boron alloy.[21] They could only obtain a 30° polarization rotation plagued, moreover, by an important loss of the THz signal, exhibiting very limited reversibility. We hereby experimentally demonstrate a scheme achieving a fully reversible voltage controlled coherent terahertz polarization rotation using a strain mediated magnetoelectric effect. With this aim, an exchange-coupled Pt/FeCo/$TbCo_2$/FeCo/W emitter is deposited onto an electro-active (1-x)[Pb($Mg_{0.33}Nb_{0.66}$) O_3]-x[$PbTiO_3$] (PMN-PT) substrate.[22]

We first demonstrate how by proper design the interplay of the magnetostriction and the uniaxial magnetic anisotropy of the ECML theoretically allows for a 90° rotation of the magnetization by a voltage control. The fabrication process of our emitters is then described. Their THz emission is characterized using an in-house customized terahertz time-domain spectroscopy setup, allowing a full vectorial measurement of the generated polarization. Finally, a phenomenological macrospin model that takes into account the Zeeman energy term, the uniaxial magnetic anisotropy energy, and the magneto-elastic energy correctly reproduces the experimentally measured THz polarization rotation sweep and helps us to understand the current limitations of the polarization angle span.

As stated earlier, we recently demonstrated the implementation of an ISHE STE based on a ferromagnetic layer possessing a uniaxial magnetic anisotropy.[18] As schematized in Fig. 1(a), the polarization control mechanism is based on the Stoner–Wohlfarth-like reorientation of the magnetization M in a uniaxial anisotropic layer submitted to a $H_{control}$ magnetic field along the magnetic intrinsic hard axis (IHA), which is the orthogonal direction to the intrinsic easy axis (IEA), both of these axes being in the plane of the film. The magnetization angle is determined by the competition between the Zeeman energy due to the applied field and the anisotropy energy. Varying $H_{control}$ between 0 and the value of the anisotropy field H_A allows for a rotation of almost 90° for the magnetization and, thus, polarization of the emitted THz signal. For symmetry reasons, a slight tilt of the magnetic field must be set to prevent the creation of magnetic domains[23] and ensure a coherent rotation of M. For the magnetoelectric control represented in Figs. 1(b) and 1(c), we can exploit the fact that a strong anisotropy can be induced by straining the ferromagnetic layer if it is also magnetostrictive. The added magnetoelastic anisotropy (MEA) energy competes with the two other terms and allows for a voltage control of M if the strain is generated by an electroactive substrate. Without strain, and in the configuration depicted in Fig. 1(b), M lies close to the vertical axis. A magnetic bias is also added to ensure no magnetic domains are created. Upon application of a tensile strain in the x direction (compressive in the y direction), the MEA is created along x, and M tends to align with it [Fig. 1(c)]. For a high enough strain, this anisotropy overcomes the uni-axial anisotropy and bias, and thus theoretically, the maximum angle span for the polarization rotation is 90°. For this principle to work properly, the deformation has to be strongly anisotropic, since the associated magnetoelastic energy is proportional to $b^{\gamma,2}(\varepsilon_{xx} - \varepsilon_{yy})$, where ε_{xx} and ε_{yy} are the relative displacements and $b^{\gamma,2}$ is the

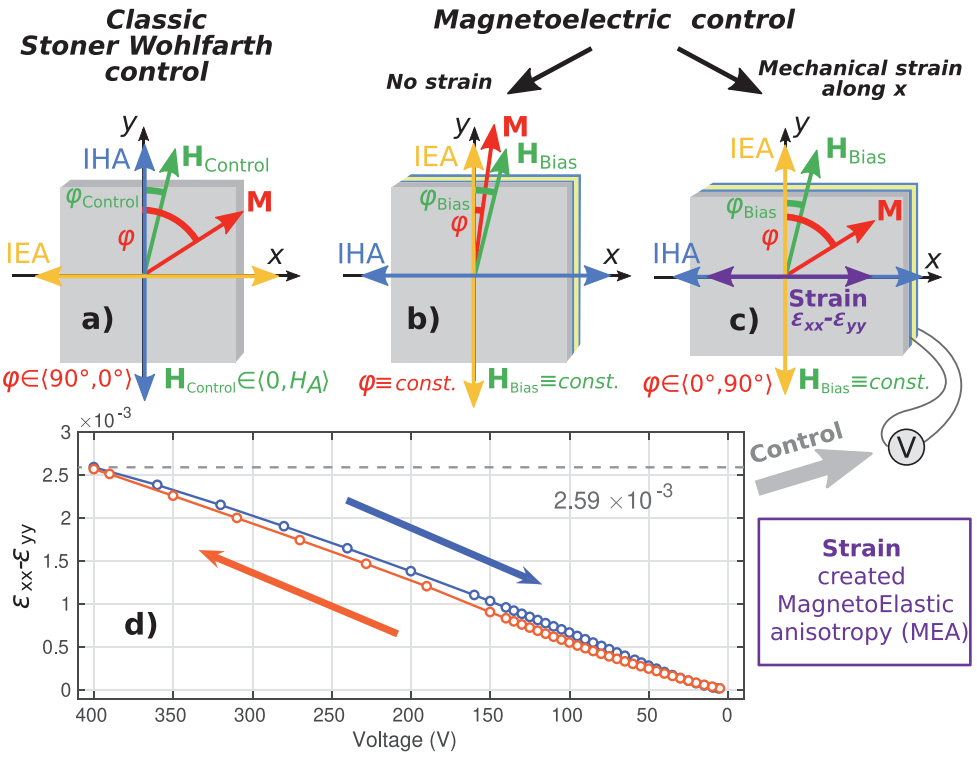


FIG. 1. (a) Stoner–Wohlfarth control of polarization; (b) and (c) magnetoelecric control; (d) $\varepsilon_{xx} - \varepsilon_{yy}$ PMN-PT anisotropic deformation as a function of the applied voltage while cycling from 400 to 0 V and back to 400 V.

Published under an exclusive license by AIP Publishing

magnetoelastic coefficient of the layer. Suitable substrates are single crystal PMN-PT in the ⟨011⟩ cut as they possess d_{31} and d_{32} piezoelectric coefficients with opposite signs.[20]

The chosen PMN-PT substrates were commercial ⟨011⟩-cut single crystal $10 \times 10 \times 0.5\,mm^3$ squares of the "X2A" reference provided by the TRS technologies company.[24] First, the anisotropic piezoelectric in-plane deformation of PMN-PT was measured as a function of the applied voltage with a standard double strain-gauge technique.[25] With this method, we were able to detect the sign of the in-plane deformations and make sure the extension of the substrate is in the horizontal direction x. The anisotropic deformation value $\varepsilon_{xx} - \varepsilon_{yy}$ is shown in Fig. 1(d) and is suitable for the magnetoelectric control.

The previously optimized W/FeCo/$TbCo_2$/FeCo/Pt ISHE emitters are grown on these substrates. Prior to deposition, both sides were mechanically polished down to a surface roughness of less 1 nm over a $2 \times 2\ \mu m^2$ area. The cleaning procedure involved 5 min ultrasonication steps in successive baths of dichloromethane, acetone, isopropyl alcohol, and de-ionized water. The W(2 nm)/CoFe(5 Å)/$TbCo_2$(8 Å)/CoFe(5 Å)/Pt(2 nm) spintronic emitters were deposited by RF-Diode sputtering in LEYBOLD Z550 equipment. The typical base vacuum in the deposition chamber is 3×10^{-7} mbar. During deposition, the substrates are placed in an in-plane field with an approximate strength of 80 kA/m to imprint an in-plane magnetic anisotropy along the Y direction. The individual layers are sputtered from circular 4 in. targets. The $TbCo_2$ and FeCo alloys are obtained from composite targets. W, Pt, and FeCo are deposited with a RF power P_{RF} of 440 W under a pure Argon atmosphere at 2×10^{-3} mbar. $TbCo_2$ is deposited with a RF power P_{RF} of 250 W at 10^{-3} mbar. To ensure a high precision in the thicknesses, the deposition was carried on a rotatory turn-table substrate holder in an oscillation mode: each time the substrate passes under the target, which corresponds to one oscillation, a layer of the material is deposited with a thickness that depends on the angular speed of the turn-table and is carefully calibrated beforehand by typically depositing a film with 100 oscillations. The CoFe/$TbCo_2$/CoFe tri-layer acts as an exchange-coupled multilayer, and the 5d metals Pt and W are known to provide strong spin–orbit coupling leading to record spin Hall angles.[2] On the backside of the substrate, an additional 2 nm platinum layer is sputtered to serve as an electrode to apply the driving voltage to PMN-PT.

The magnetization behavior is characterized with a vibrating sample magnetometer (VSM). With this kind of magnetic stack, an intrinsic magnetic easy axis (IEA) is usually created in the direction of the applied field during deposition. In the present case, while the uniaxial anisotropy is present, we found a slight offset of 7° with respect to the deposition field. While the origin of this effect is not clear, it is certainly due to the unusual nature of the PMN-PT substrate. The resulting anisotropy direction can be altered by the crystalline structure of the ⟨011⟩-cut PMN-PT or residual anisotropic stress. Figure 2 shows the magnetization loops along the IEA and IHA of the layer. They confirm the anisotropic nature of the layer, and the corresponding anisotropy field H_A is estimated to be approximately equal to 5 kA/m. The saturation magnetization is close to 900 kA/m. A schematic view of the emitter geometry is shown in Fig. 3.

THz emission was characterized on a customized terahertz time-domain spectroscopy (TDS) setup. ISHE-mediated terahertz emission is generated by pumping the sample with femtosecond pulses from a Ti:sapphire laser oscillator (80 MHz repetition rate, center wavelength

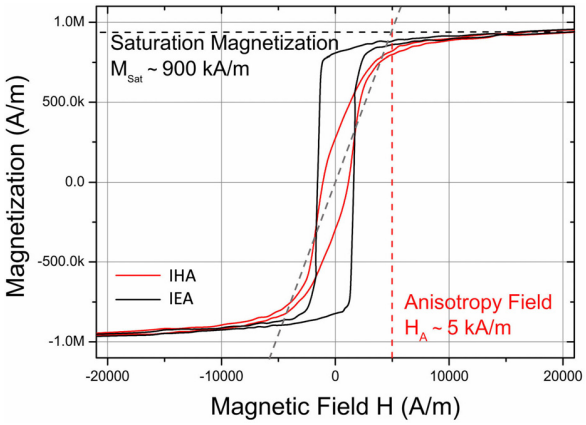


FIG. 2. VSM magnetization cycles for the spintronic emitter along the intrinsic easy and hard axes.

800 nm, and 100 fs pulse duration) and with an incident average power of $P_{pump} = 40$ mW. The E-field of the emitted terahertz pulse is measured by sampling the response of a photoconductive Auston switch that is probed by a split-off fraction of the femtosecond infrared pulse ($P_{probe} = 10$ mW) going through a delay line. The detector is composed of a 40 μm long dipole antenna with a 5 μm gap on a low temperature grown Ga–As substrate, onto which the THz beam is focalized with a hemispheric high resistivity silicon lens. In order to measure the horizontal and vertical components of the E-field and deduce the polarization angle, two wire-grid polarizers made of 5 μm diameter tungsten wires with a 12.5 μm pitch were inserted in the THz path. Since the receiving antenna is horizontal, a switching polarizer is used to select the horizontal or vertical projections of the electric field to be sampled, while a fixed polarizer ensures that a signal is detected with the same amplitude regardless of the projection as shown in Fig. 3. The emitter is maintained by a flexible adhesive on its holder, so that its free deformation is allowed. Wires are bonded to the front and

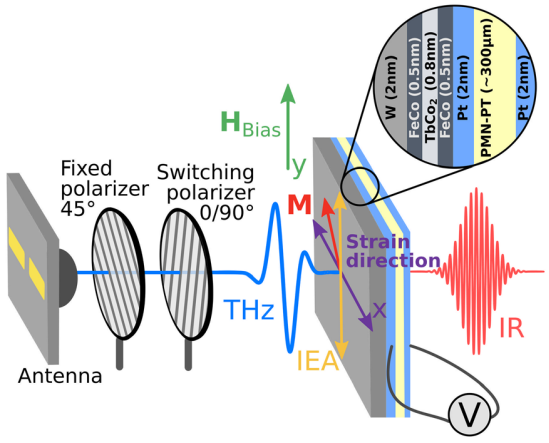


FIG. 3. Layer composition of the strain-mediated ISHE STE and polarimetric measurement scheme.

Published under an exclusive license by AIP Publishing

back electrodes with silver conductive epoxy and connected to a high voltage source. First, the TDS setup delay line was set to obtain the maximum signal amplitude. Preliminary voltage cycles showed a maximum polarization rotation toward the vertical direction for voltages of about 400 V. The E-field components were then measured while cycling the applied voltage on the PMN-PT substrate from the previously determined saturation of 400 to 0 V. The tilted magnetic bias H_{Bias} ensures that the formation of domains is minimal in the magnetic film. To that end, a 1.5 kA/m magnetic field is applied with an arbitrary chosen 10° tilt from the vertical direction to be superior to the 7° angle of anisotropy. The deducted polarization angle shown in Fig. 4 clearly shows the controlled rotation of the electric field polarization over a span of more than 65°. The emission behaves as expected: under no applied field, the emitted signal has a horizontal polarization since magnetization lies vertically along the IEA. Upon a voltage increase, the ⟨011⟩ PMN-PT generates a tensile strain, where it induces an anisotropy along the horizontal direction forcing magnetization to rotate to its new equilibrium position. A voltage decrease lowers the strain induced magnetic anisotropy, and the magnetization quasi-reversibly rotates back to its equilibrium position at 0 V. From that measurement, we can determine the polarization angle as a function of the applied voltage. The time domain spectroscopy measurements shown in Fig. 4 at fixed voltage values confirm the rotation of the polarization. Along with the rotation, a slight ellipticity appears for large values of the applied voltage. The main hypothesis that can be drawn to explain this is that part of the generated THz signal is received after reflection of the (lossy) PMN-PT substrate that itself possesses an important dielectric anisotropy as expected from its orthorhombic crystal structure. This will result in a phase lag between the reflection coefficients of the horizontal and vertical field components. Moreover, the anisotropy of PMN-PT is increasing with voltage in view of its strong piezoelectricity.[22,26] In any case, further detailed modeling and analysis is needed to elucidate this ellipticity, which seems to be limited to ≈6° in the worst case (at 400 V).

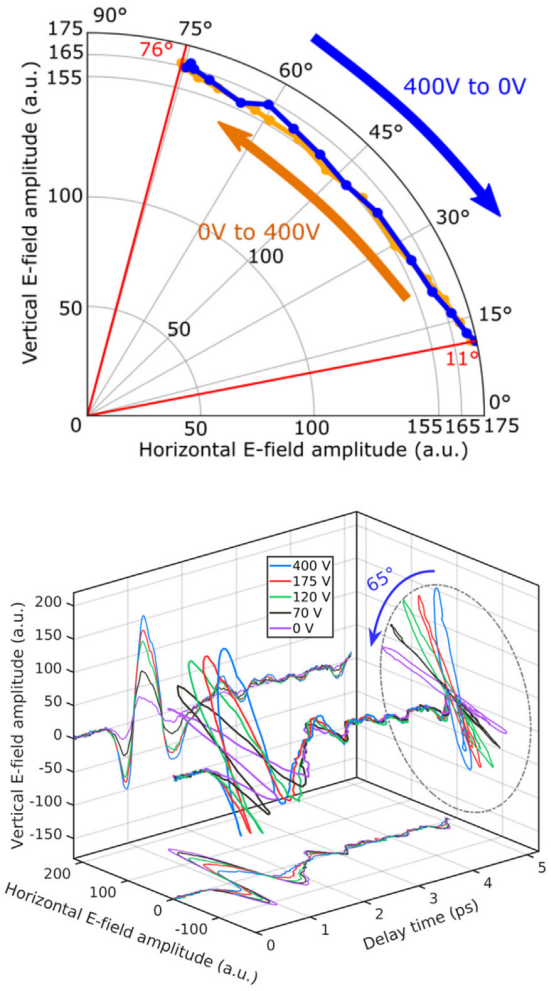


FIG. 4. Top: emitted electric field polarization and amplitude as a function of the applied driving voltage for an applied bias of 1.5 kA/m. Bottom: temporal TDS spectra for 400, 175, 120, 70, and 0 V.

As shown in Fig. 4, the polarization angle span we obtained is of about 65°, whereas the control via the magnetoelastic anisotropy can theoretically allow a 90° span. However, several geometrical factors have to be accounted for, and in particular, other contributions to the magnetic energy of the system, namely, the intrinsic uni-axial anisotropy of the layer and the bias that is applied to limit domain formation during the rotation process.

To understand the influence of these parameters, a macrospin model was used to calculate the angle of magnetization when the emitter is submitted to the anisotropic strain generated by PMN-PT when voltage is applied. We consider here that the magnetization coherently rotates in the plane of the film, which is a common assumption in Stoner–Wohlfarth-like anisotropic layers submitted to a magnetic bias. The anisotropic deformation value $\varepsilon_{xx} - \varepsilon_{yy}$ previously measured is introduced in the algorithm. For each voltage value, it will determine the angular position of the magnetization following the minimum of magnetic energy, which is the sum of the Zeeman interaction energy, the anisotropy energy due to the IEA of the film, and the magnetoelastic energy

$$\begin{aligned} E_m = &-\mu_0 M_{Sat} H_{Bias} \cos(\varphi - \varphi_{Bias}) \\ &-\frac{1}{2}\mu_0 M_{Sat} H_A \cos^2(\varphi - \varphi_{IEA}) \\ &+ b^{\gamma,2}(\varepsilon_{xx} - \varepsilon_{yy}) \cos^2(\varphi - \varphi_{ME}), \end{aligned} \quad (1)$$

where μ_0 is the vacuum permeability, M_{Sat} is the value of the saturation magnetization, H_{Bias} is the strength of the magnetic bias field, φ is the angular position of magnetization to be determined, φ_{Bias} is the angle of the applied magnetic field, H_A is the value of the anisotropy field, φ_{IEA} is the direction of the IEA, $b^{\gamma,2}$ is the magnetoelastic coefficient of the ferromagnetic film, and φ_{ME} is the angle of the anisotropy created by the PMN-PT deformation. For the calculations, all the considered angles are taken with respect to the vertical polarization component in the (X,Y) referential given by the polarizers, as shown in the inset of Fig. 5. Owing to that φ_{Bias}, φ_{IEA} and φ_{ME} can be determined using TDS polarimetric measurements, since the emitted polarization is perpendicular to magnetization: Cutting off the voltage and applying a large magnetic bias field of larger than 15 kA/m will force the magnetization along φ_{Bias}. Then it will align along φ_{IEA} when cutting off the

Published under an exclusive license by AIP Publishing

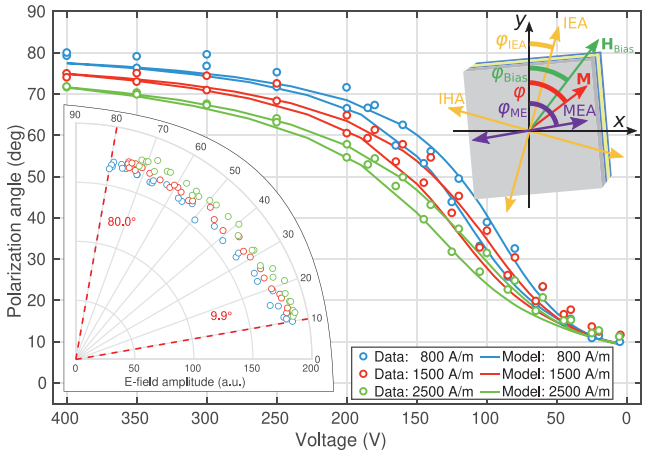


FIG. 5. Comparison between experimental data and model for the polarization angle as a function of the voltage while cycling from 400 to 0 V and back to 400 V for three values of the applied bias in the $\varphi_{Bias} = 10°$ direction. Top right inset: angle configuration. Bottom left inset: experimental measurements polar plot.

bias field. Finally, a 500 V voltage is applied to PMN-PT in order to create a large anisotropy in the φ_{ME} direction. In the chosen configuration, we find $\varphi_{Bias} = 10°$, $\varphi_{IEA} = 9°$, and $\varphi_{ME} = 85°$. From the VSM measurements, we find $M_{Sat} = 900\,kA/m$ and $H_A = 5\,kA/m$.

Figure 5 shows the results of the calculations and comparison with experimental measurements for three different values of the bias field. Both simulations and experiments agree very well, assuming a magnetoelastic coefficient $b^{7,2}$ equal to -2.6 MPa. Given the 2 nm thickness of the ferromagnetic layer, it was not possible to determine its magnetoelastic coefficient, but such a value is consistent with Terbium-transition metal based multilayer systems.[27,28] The hysteresis in the cycles is due to the hysteresis of the strain in PMN-PT shown in Fig. 1.

From Fig. 5, we can safely deduce that as expected, the magnetization M of the ferromagnetic layer, and thus the polarization of the emitted THz signal, is indeed governed by the deformation of the PMN-PT substrate upon application of the driving voltage: the strain induced anisotropy competes with the bias Zeeman energy and the original IEA anisotropy. For low voltages, the magnetization angle is set by the competition between the IEA and the bias, which is close to 10°. Upon increase in the voltage, M rotates toward the φ_{ME} direction. Here, we can see the influence of the bias field: as it increases, it makes it harder for M to rotate toward φ_{ME}, reducing the angle span. With $H_{Bias} = 1500\,A/m$, the angle span is 65°. Reducing H_{Bias} down to 800 A/m increases the span to 70°, while for $H_{Bias} = 2500\,A/m$, this span is only 60°. Nevertheless, there is a trade-off here since reducing the bias too much results in a decrease in the total strength of the THz strength (see Fig. 5, inset). This is likely an indication of magnetic domain formation preventing the rotation of M to be purely homogeneous. Finally, we can see that in order to increase the span, the IEA and the direction of H_{Bias} have to be as perpendicular as possible from the Magneto-Elastic Anisotropy (MEA) orientation. Since the MEA direction is linked to the PMN-PT substrate, the IEA has to be defined accordingly. As it was stated earlier, we noted that after the sputter deposition of our STE under a magnetic field, the IEA has a 7° offset compared to the desired direction, which is consistent with our polarization angle span. Further studies on the origin of this offset have to be led, but magnetic field annealing might also improve this characteristic and help one to reach a close to 90° polarization span.

Overall, we presented here the demonstration of a reversible magnetoelectric control of THz polarization rotation that paves the way to voltage-controlled THz devices. Thanks to the use of an anisotropic and magnetoelastic ferromagnetic layer in a spintronic emitter deposited on a PMN-PT substrate, our experimental device was able to show a reversible and repeatable control of the THz polarization with a 70° span for 400 V. Our macrospin model confirmed the control mechanism based on the creation of magnetoelastic anisotropy and gave insight on how to improve the device. This demonstration makes the intrinsic polarization control allowed by ISHE emitters more practical by removing the need for precise magnetic bias control. Only a constant external field is needed to prevent domain formation during rotation. In the present case, the modulation speed is limited by the electroactive substrate, which behaves essentially like a capacitor that cannot be charged instantly. However, in principle, the control of magnetization via the creation of magnetoelastic anisotropy is instantaneous and can, therefore, be used for high frequency modulation schemes, provided adequate strain can be generated.

This project has received funding from the European Union's Horizon 2020 research and innovation programme under Grant Agreement No. 863155 (s-Nebula). The authors would like to thank the RENATECH network and the Barrande Fellowship Programme and acknowledge the support from the Government of the Czech Republic (Doctoral Grant competition CZ.02.2.69/0.0/0.0/19_073/0016945 under Project No. DGS/TEAM/2020-027).

AUTHOR DECLARATIONS

Conflict of Interest

The authors have no conflicts to disclose.

DATA AVAILABILITY

The data that support the findings of this study are openly available on Zenodo at https://doi.org/10.5281/zenodo.5742851, Ref. 29.

REFERENCES

[1]T. Kampfrath, M. Battiato, P. Maldonado, G. Eilers, J. Nötzold, S. Mährlein, V. Zbarsky, F. Freimuth, Y. Mokrousov, S. Blügel, M. Wolf, I. Radu, P. M. Oppeneer, and M. Münzenberg, "Terahertz spin current pulses controlled by magnetic heterostructures," Nat. Nanotechnol. **8**, 256–260 (2013).

[2]T. Seifert, S. Jaiswal, U. Martens, J. Hannegan, L. Braun, P. Maldonado, F. Freimuth, A. Kronenberg, J. Henrizi, I. Radu, E. Beaurepaire, Y. Mokrousov, P. M. Oppeneer, M. Jourdan, G. Jakob, D. Turchinovich, L. M. Hayden, M. Wolf, M. Münzenberg, M. Kläui, and T. Kampfrath, "Efficient metallic spintronic emitters of ultrabroadband terahertz radiation," Nat. Photonics **10**, 483–488 (2016).

[3]E. T. Papaioannou, G. Torosyan, S. Keller, L. Scheuer, M. Battiato, V. K. Mag-Usara, J. L'Huillier, M. Tani, and R. Beigang, "Efficient terahertz generation using Fe/Pt spintronic emitters pumped at different wavelengths," IEEE Trans. Magn. **54**, 1–5 (2018).

[4]R. Kohlhaas, S. Breuer, L. Liebermeister, S. Nellen, M. Deumer, M. Schell, M. Semtsiv, W. Masselink, and B. Globisch, "637 μw emitted terahertz power from photoconductive antennas based on rhodium doped InGaAs," Appl. Phys. Lett. **117**, 131105 (2020).

[5]S.-W. Huang, E. Granados, W. R. Huang, K.-H. Hong, L. E. Zapata, and F. X. Kärtner, "High conversion efficiency, high energy terahertz pulses by optical

Published under an exclusive license by AIP Publishing

rectification in cryogenically cooled lithium niobate," Opt. Lett. **38**, 796 (2013).
[6]M. T. Hibberd, D. S. Lake, N. A. Johansson, T. Thomson, S. P. Jamison, and D. M. Graham, "Magnetic-field tailoring of the terahertz polarization emitted from a spintronic source," Appl. Phys. Lett. **114**, 031101 (2019).
[7]T. Nagashima and M. Hangyo, "Measurement of complex optical constants of a highly doped Si wafer using terahertz ellipsometry," Appl. Phys. Lett. **79**, 3917–3919 (2001).
[8]X. Chen, E. P. Parrott, Z. Huang, H.-P. Chan, and E. Pickwell-MacPherson, "Robust and accurate terahertz time-domain spectroscopic ellipsometry," Photonics Res. **6**, 768–775 (2018).
[9]O. Gueckstock, L. Nádvorník, T. S. Seifert, M. Borchert, G. Jakob, G. Schmidt, G. Woltersdorf, M. Kläui, M. Wolf, and T. Kampfrath, "Modulating the polarization of broadband terahertz pulses from a spintronic emitter at rates up to 10 kHz," Optica **8**, 1013 (2021).
[10]D. M. Nenno, L. Scheuer, D. Sokoluk, S. Keller, G. Torosyan, A. Brodyanski, J. Lösch, M. Battiato, M. Rahm, R. H. Binder, H. C. Schneider, R. Beigang, and E. T. Papaioannou, "Modification of spintronic terahertz emitter performance through defect engineering," Sci. Rep. **9**, 13348 (2019).
[11]G. Torosyan, S. Keller, L. Scheuer, R. Beigang, and E. T. Papaioannou, "Optimized spintronic terahertz emitters based on epitaxial grown Fe/Pt layer structures," Sci. Rep. **8**, 1311 (2018).
[12]Q. Zhang, Y. Yang, Z. Luo, Y. Xu, R. Nie, X. Zhang, and Y. Wu, "Terahertz emission from an exchange-coupled synthetic antiferromagnet," Phys. Rev. Appl. **13**, 054016 (2020).
[13]Y. Ogasawara, Y. Sasaki, S. Iihama, A. Kamimaki, K. Z. Suzuki, and S. Mizukami, "Laser-induced terahertz emission from layered synthetic magnets," Appl. Phys. Express **13**, 063001 (2020).
[14]M. Fix, R. Schneider, J. Bensmann, S. Michaelis De Vasconcellos, R. Bratschitsch, and M. Albrecht, "Thermomagnetic control of spintronic THz emission enabled by ferrimagnets," Appl. Phys. Lett. **116**, 012402 (2020).
[15]M. Fix, R. Schneider, S. Michaelis De Vasconcellos, R. Bratschitsch, and M. Albrecht, "Spin valves as magnetically switchable spintronic THz emitters," Appl. Phys. Lett. **117**, 132407 (2020).
[16]D. Kong, X. Wu, B. Wang, T. Nie, M. Xiao, C. Pandey, Y. Gao, L. Wen, W. Zhao, C. Ruan, Y. Li, and L. Wang, "Broadband spintronic terahertz emitter with magnetic-field manipulated polarizations," Adv. Opt. Mater. **7**, 1900487 (2019).
[17]D. Yang, J. Liang, C. Zhou, L. Sun, R. Zheng, S. Luo, Y. Wu, and J. Qi, "Powerful and tunable THz emitters based on the Fe/Pt magnetic heterostructure," Adv. Opt. Mater. **4**, 1944–1949 (2016).
[18]P. Koleják, G. Lezier, K. Postava, J.-F. Lampin, N. Tiercelin, and M. Vanwolleghem, "360° polarization control of terahertz spintronic emitters using uniaxial FeCo/$TbCo_2$/FeCo trilayers," arXiv:2111.07118 (2021).
[19]A. Debray, A. Ludwig, T. Bourouina, A. Asaoka, N. Tiercelin, G. Reyne, T. Oki, E. Quandt, H. Muro, and H. Fujita, "Application of a multilayered magnetostrictive film to a micromachined 2D optical scanner," Microelectromech. Syst., J. **13**, 264–271 (2004).
[20]Y. Dusch, N. Tiercelin, A. Klimov, S. Giordano, V. Preobrazhensky, and P. Pernod, "Stress-mediated magnetoelectric memory effect with uni-axial $TbCo_2$/FeCo multilayer on 011-cut PMN-PT ferroelectric relaxor," J. Appl. Phys. **113**, 17C719–17C714 (2013).
[21]H. Cheng, Q. Huang, H. He, Z. Zhao, H. Sun, Q. Wu, Z. Jiang, J. Wang, H. Huang, Z. Fu, and Y. Lu, "Giant electrical modulation of terahertz emission in $Pb(Mg_{1/3}Nb_{2/3})_{0.7}Ti_{0.3}O_3$/Co − Fe − B/Pt structure," Phys. Rev. Appl. **16**, 054011 (2021).
[22]F. Wang, L. Luo, D. Zhou, X. Zhao, and H. Luo, "Complete set of elastic, dielectric, and piezoelectric constants of orthorhombic $(0.71Pb(Mg_{1/3}Nb_{2/3})O_3 - 0.29PbTiO_3)$ single crystal," Appl. Phys. Lett. **90**, 212903 (2007).
[23]A. Klimov, N. Tiercelin, V. Preobrazhensky, and P. Pernod, "Inhomogeneous spin reorientation transition (SRT) in giant magnetostrictive $TbCo_2$/FeCo multilayers," IEEE Trans. Mag. **42**, 3090–3092 (2006).
[24]See http://www.trstechnologies.com/materials/high-performance-pmn-pt-piezoelectric-single-crystal for the substrates specifications.
[25]T. Wu, P. Zhao, M. Bao, A. Bur, J. L. Hockel, K. Wong, K. P. Mohanchandra, C. S. Lynch, and G. P. Carman, "Domain engineered switchable strain states in ferroelectric (011)$[Pb(Mg_{1/3}Nb_{2/3})O_3]_{(1-x)}$-$[PbTiO_3]_x$(PMN-PT, $x \approx 0.32$) single crystals," J. Appl. Phys. **109**, 124101 (2011).
[26]E. V. Colla, N. K. Yushin, and D. Viehland, "Dielectric properties of $(PMN)_{(1-x)}(PT)_x$ single crystals for various electrical and thermal histories," J. Appl. Phys. **83**, 3298–3304 (1998).
[27]J. Juraszek, A. Grenier, J. Teillet, N. Tiercelin, F. Petit, J. B. Youssef, and M. Toulemonde, "Swift ion irradiation of magnetostrictive multilayers," Nucl. Instrum. Methods Phys. Res., Sect. B **245**, 157–160 (2006).
[28]J. Ben Youssef, N. Tiercelin, F. Petit, H. Le Gall, V. Preobrazhensky, and P. Pernod, "Statics and dynamics in giant magnetostrictive $Tb_xFe_{1-x}/Fe_{0.6}Co_{0.4}$ multilayers for MEMS," IEEE Trans. Mag. **38**(5), 2817–2819 (2002).
[29]G. Lezier, P. Koleják, J.-F. Lampin, K. Postava, M. Vanwolleghem, and N. Tiercelin (2021), "Fully reversible magnetoelectric voltage controlled THz polarization rotation in magnetostrictive spintronic emitters on PMN-PT," Zenodo, Dataset https://doi.org/10.5281/zenodo.5742851

Published under an exclusive license by AIP Publishing

Paper VI

Terahertz time-domain ellipsometry with spintronic emitters: Pauli coefficients as a superior alternative to Jones and Mueller matrices

Pierre Koleják, Jiaming Liu, Robin Silber, Martin Mičica, Ondřej Ballada, Čestmír Barta, Romain Lebrun, Nicolas Tiercelin, Mathias Vanwolleghem, and Kamil Postava
submitted (2024)

Terahertz time-domain ellipsometry with spintronic emitters: Pauli coefficients as a superior alternative to Jones and Mueller matrices

PIERRE KOLEJÁK,[1,2,*] JIAMING LIU,[1] ROBIN SILBER,[1] MARTIN MIČICA,[3] ONDŘEJ BALLADA,[4] ČESTMÍR BARTA,[4] ROMAIN LEBRUN,[5] NICOLAS TIERCELIN,[2] MATHIAS VANWOLLEGHEM,[2] AND KAMIL POSTAVA[1,+]

[1] *Faculty of Materials Science and Technology, VSB-Technical University of Ostrava, 708 00 Ostrava, Czech Republic*
[2] *University of Lille, CNRS, UMR 8520-IEMN, 59000 Lille, France*
[3] *Laboratoire de Physique de l'Ecole Normale Supérieure, ENS, Université PSL, CNRS, Sorbonne Université, Université Paris Cité, F-75005, Paris, France*
[4] *BBT-Materials Processing, s.r.o., Doubická 790/11, 184 00 Praha, Czech Republic*
[5] *Laboratoire Albert Fert, CNRS, Thales, Université Paris-Saclay, 1 Avenue Augustin Fresnel, 91767, Palaiseau, France*
[*] *pierre.kolejak@vsb.cz,*[+] *kamil.postava@vsb.cz*

Abstract: We introduce terahertz complete time-domain spectroscopic ellipsometry (THz-cTDSE), extending traditional ellipsometry by determining full Jones and Mueller matrices for in-depth material characterization. This marks the first application of spintronic terahertz emitters in ellipsometry, achieving pure linear polarization for precise magnetization-based switching. Our complete phase-resolved ellipsometry transforms Jones matrices into an intuitive framework of diattenuations and retardations across all Stokes bases—Pauli exponential coefficients—previously unattainable with incomplete ellipsometry. A novel calibration technique ensures accurate Jones matrix reconstruction without requiring precise alignment of polarizing components, approaching the precision typical of visible-range ellipsometry. We demonstrate THz-cTDSE on quartz and Hg_2Cl_2 crystals, advancing the analysis of anisotropic materials.

1. Introduction

Over the past two decades, terahertz spectroscopic ellipsometry in both frequency-domain (THz-FDSE) and time-domain (THz-TDSE) has significantly advanced material characterization [1–4]. Applications include the characterization of thin films [5, 6], magneto-optical ellipsometry for determining carrier dynamics [7, 8], liquids in attenuated-total-reflection configurations [9], in vivo human tissue studies [10], and metasurface analysis [11].

Ellipsometry measures transformations in the polarization state of light [12, 13], where the 2x2 Jones matrix transforms the amplitude and phase of the electric field, while the 4x4 Mueller matrix converts Stokes vectors, capturing the total intensity and the degrees of linear and circular polarization. Due to challenges in generating broadband circular polarization in the terahertz range [14], THz-FDSE is limited to an incomplete 3×3 and 4×3 Mueller matrices that exclude circular polarization effects [15–17]. While offering high spectral resolution and stability, these systems face complex calibration procedures, limited spectral ranges up to 1.5 THz (10 THz with a synchrotron), high costs, and potential inaccuracies due to standing wave formations [18].

Standard ellipsometry, commonly used in time-domain ellipsometry, determines the ratio of complex amplitude coefficients for p- and s-polarized light. The ratio is given as $\tilde{\rho} = \tilde{r}_p/\tilde{r}_s = \tan\Psi \exp(-\mathrm{i}\Delta)$, where Ψ denotes the amplitude ratio and Δ represents the phase difference between p- and s-polarizations [13, 19]. Standard ellipsometry enhances precision

by correcting phase errors typically caused by sample-reference displacement in reflective measurements [6, 20, 21]. However, its application is primarily restricted to isotropic or ideally oriented birefringent materials. Polarization control in time-domain ellipsometry is typically achieved using photoconductive antennas with polarizers [22–25] or rotating nonlinear crystals [26–30]. Several studies have derived Mueller matrices from time-domain measurements to obtain comprehensive ellipsometric information. Nevertheless, these approaches are restricted to intensity-based descriptions that exclude absolute phase information [31–33].

Time-domain ellipsometry is a coherent method that captures both amplitude and phase information, enabling the use of the Jones calculus. However, only a single study has developed a method for determining the complete Jones matrix from time-domain measurements [34]. Zhao et al. employ dual-channel detection to measure both polarizations simultaneously. They reconstruct the Jones matrix elements by optimizing polarizer orientations and exploiting trigonometric symmetry. Recent work by Chen et al. extended standard ellipsometry using a multi-channel approach [35]. This method generalizes ellipsometric angles Ψ and Δ for all polarization conversions, including s-to-p transitions. With precisely aligned components, their system eliminates the need for additional calibration.

The challenge of obtaining complete ellipsometry primarily stems from the need to reconstruct the Jones matrix accurately, which requires advanced calibration techniques, as minor angular deviations can introduce systematic errors. To address this, we propose a novel calibration method that removes the need for precise polarizer alignment. By experimentally determining the actual configurations of polarizing components using reference measurements, our approach ensures accurate ellipsometric analysis and offers a more robust solution compared to methods focusing on precise alignment [21, 36, 37].

Achieving pure linear polarization with a high extinction ratio is often challenging to obtain using conventional terahertz polarizers but is crucial for accurate ellipsometric measurements. Equally important is maintaining stable control when switching between generated polarization states. We propose terahertz spintronic emitters (STEs) as a solution for ellipsometry applications. STEs consist of a nonmagnetic/ferromagnetic/nonmagnetic trilayer that emits terahertz radiation through spin-to-charge conversion, allowing for fine control of polarization via magnetic reorientation [38, 39]. They offer ultra-broadband emission up to 30 THz [40] and operate across excitation wavelengths from visible to infrared. While STEs have lower efficiency compared to conventional sources [40], recent advancements aim to enhance performance through efficient pumping [41–43], improved spin current generation [44–46] and terahertz extraction [47]. We employ a high-performance large-area STE integrated with a photonic crystal, capable of generating strong terahertz fields (1.5 MV/cm with 5 mJ pulses), provided by Rouzegar *et al.* [48]. This advancement drives progress in time-domain ellipsometry by enabling high-powered signal generation and robust polarization control.

This paper presents terahertz complete time-domain spectroscopic ellipsometry (THz-cTDSE), achieving experimental determination of 2×2 Jones matrices, 4×4 Mueller-Jones matrices, and primary Pauli exponential coefficients. Incorporating these coefficients introduces an innovative framework for data interpretation, simplifying analysis by converting the Jones matrix into diattenuation and retardation coefficients within various Stokes bases. This enables straightforward quantification of polarization phenomena. Although the Pauli linear combination has been theoretically explored [49–52], it has not been applied in experimental ellipsometry due to the need for a coherent and complete system. Our use of the exponential Pauli decomposition, derived from the matrix logarithm of the Jones matrix, is novel in ellipsometric practice.

This article is organized as follows. In Section 2, we present the instrumentation of our time-domain terahertz ellipsometer. Using a quartz crystal that exhibits only retardation, we demonstrate how the ellipsometer can precisely determine the amplitude and phase of the Jones matrix. Section 3 details extracting additional ellipsometric information by converting the Jones

matrix into an intensity-based Mueller-Jones matrix and performing a coherent decomposition into Pauli matrices. We discuss the choice of each approach based on sample properties and demonstrate the advantages of Pauli coefficients using the quartz crystal. Section 4 describes the calibration method, detailing how the Jones matrix of a sample is derived from a series of measurements. We estimate the accuracy of our method and present the experimentally determined errors for each element of the Jones matrix. Section 5 applies our ellipsometric technique to a more complex sample, a Hg_2Cl_2 crystal exhibiting both diattenuation and retardation. Finally, Section 6 discusses our method's limitations and potential improvements, comparing various terahertz ellipsometric techniques. The conclusion summarizes and reflects on the findings of our complete matrix approach.

2. Instrumentation and demonstration of THz-TDS complete ellipsometry

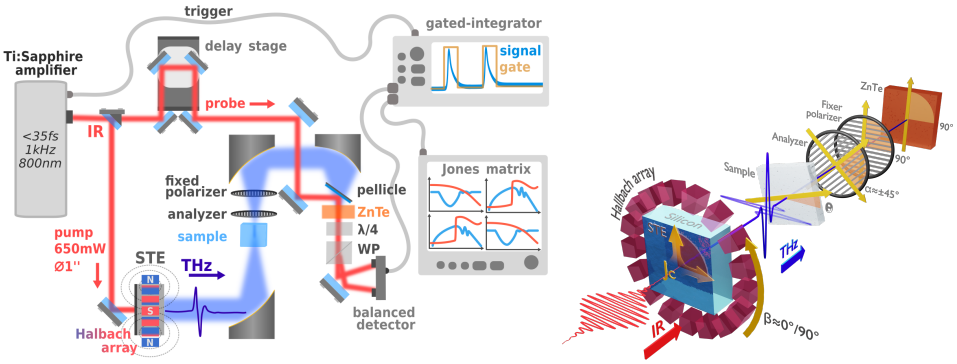


Fig. 1. THz-cTDSE scheme: a) Overview of the experimental setup and b) detail of the experimental terahertz ellipsometry section. The Ti:sapphire amplifier generates the initial beam, which splits into pump and probe beams. The pump beam excites a spintronic emitter (STE) within a Halbach array that controls the terahertz polarization; the emitted radiation is focused onto the sample; an analyzer selects the desired polarization; a fixed polarizer aligns it vertically for detection by the ZnTe crystal. The probe beam passes through a delay line, a pellicle beamsplitter, a ZnTe crystal, a quarter-wave plate ($\lambda/4$), and a Wollaston prism (WP) to balanced photodiodes. A gated integrator averages the signal, and the measurements are then converted into Jones matrices.

We introduce the THz complete time-domain spectroscopic ellipsometry (THz-cTDSE) in Figure 1a. The system uses a Ti:sapphire amplifier (Astrella from the company Coherent) to generate a 5 W average power infrared beam at a 1 kHz repetition rate, generating 5 mJ pulses. Pulses are shorter than 35 fs, with a central wavelength of 800 nm. The generated infrared beam is split into probing and pumping beamlines. The pumping beam excites the spintronic emitter, positioned within the magnetic field of a rotatable Halbach array. This configuration ensures a homogeneous and linear magnetic field of 10 mT, allowing precise control over the emitted polarization.

The emitter comprises a Pt/CoFeB/W trilayer stack, a one-dimensional SiO_2/TiO_2 photonic crystal, and a high-resistivity silicon substrate [48]. The photonic crystal increases pump beam absorption in the spintronic layers, thereby boosting terahertz emission [42, 43] The silicon substrate absorbs the residual pump beam, making additional filtering unnecessary. We use this broad-area emitter for collimated excitation with a 25.4 mm beam diameter and 650 mW laser power (0.65 mJ per pulse). In this configuration, the emitter operates well below its damage threshold [48, 53]. Furthermore, the signal can be further improved by increasing the pump

power, but the emitter isn't currently utilizing the amplifier's full power of 5 W due to other experiments.

Terahertz radiation is emitted in the form of a collimated beam and is subsequently focused onto a sample using an off-axis parabolic mirror with a focal length of 152.4 mm (6 in). Two wire-grid polarizers are placed after the sample: the analyzer and the fixed polarizer, both on motorized rotation stages. The analyzer selects the output polarization, while the fixed polarizer adjusts it vertically for stable detection by the ZnTe electro-optic crystal. The beam is recollimated and then focused onto the ZnTe detector using another parabolic mirror with a 101.6 mm (4 in) focal length, enhancing field intensity while minimizing defocusing and reducing the Gouy phase shift [54, 55]. The detail of the terahertz ellipsometry arrangement is illustrated in Figure 1b. The probing beam passes through a delay line and is directed onto the 500 µm thick ZnTe crystal using a pellicle beamsplitter. The beam then passes through a $\lambda/4$-waveplate and a Wollaston prism polarizer (WP), before being detected by balanced photodiodes. Operating at a 1 kHz repetition rate, we employ a gated integrator that captures all signal harmonics, offering a comprehensive alternative to traditional first harmonic demodulation via a lock-in amplifier.

2.1. Demonstration of complete Jones matrix ellipsometry

The primary goal of ellipsometry is to determine the transformation matrix that describes how a sample modifies the input polarization into the output polarization. In the time-domain approach, waveform measurements are inherently coherent, enabling the capture of complex field amplitudes.This coherence allows for reconstructing the vector electric field of the terahertz pulse, both with and without the sample, thus enabling the determination of the transformation matrix. The Jones matrix $\tilde{\mathbf{J}}$ characterizes the coherent polarization transformation by converting the input electric field vector $\tilde{\mathbf{E}}^{\mathrm{in}}$ into the output electric field vector $\tilde{\mathbf{E}}^{\mathrm{out}}$ as follows

$$\begin{pmatrix} \tilde{E}_{\mathrm{x}}^{\mathrm{out}} \\ \tilde{E}_{\mathrm{y}}^{\mathrm{out}} \end{pmatrix} = \underbrace{\begin{pmatrix} \tilde{j}_{11} & \tilde{j}_{12} \\ \tilde{j}_{21} & \tilde{j}_{22} \end{pmatrix}}_{\tilde{\mathbf{J}}} \begin{pmatrix} \tilde{E}_{\mathrm{x}}^{\mathrm{in}} \\ \tilde{E}_{\mathrm{y}}^{\mathrm{in}} \end{pmatrix}. \tag{1}$$

The Jones matrix provides complete and complex information about the polarization properties of the sample. The off-diagonal elements of the matrix indicate the coupling between orthogonal components of the electric field.

We aim to determine the complete Jones matrix, focusing on uniaxial anisotropic crystals as a representative example of the method's broader applicability. We start the demonstration with an A-cut 1.816 mm thick quartz crystal plate, which is non-absorbing and uniaxial, providing only retardation. We analyze it using time-domain spectroscopy in a transmission configuration, with the optical axis rotated by an angle θ. The polarization components are configured as follows: the spintronic emitter is vertically aligned, the analyzer is set at ±45 degrees to detect orthogonal modes, and the fixed polarizer is also vertically aligned, as shown in Figure 1b. Initially, we conduct time-domain measurements of the free-space reference without the sample, as shown in Figure 2a. In our case, the reference pulses overlap perfectly, exhibiting no amplitude differences between the polarization states and no time delay that would indicate a phase shift. The quartz sample was then measured under the same conditions, as shown in Figure 2a. The quartz is oriented at $\theta = 45$, so one polarization exhibits the ordinary refractive index while the other displays the extraordinary refractive index. Due to the ideal behavior of reference polarizations, the interpretation of quartz measurements is significantly simplified. The observed temporal delay between the orthogonal pulses highlights the retardation effect. The slight change in pulse shape results from the different dispersions in the ordinary and extraordinary directions. The observed amplitude losses, relative to the references, result from Fresnel reflection at the

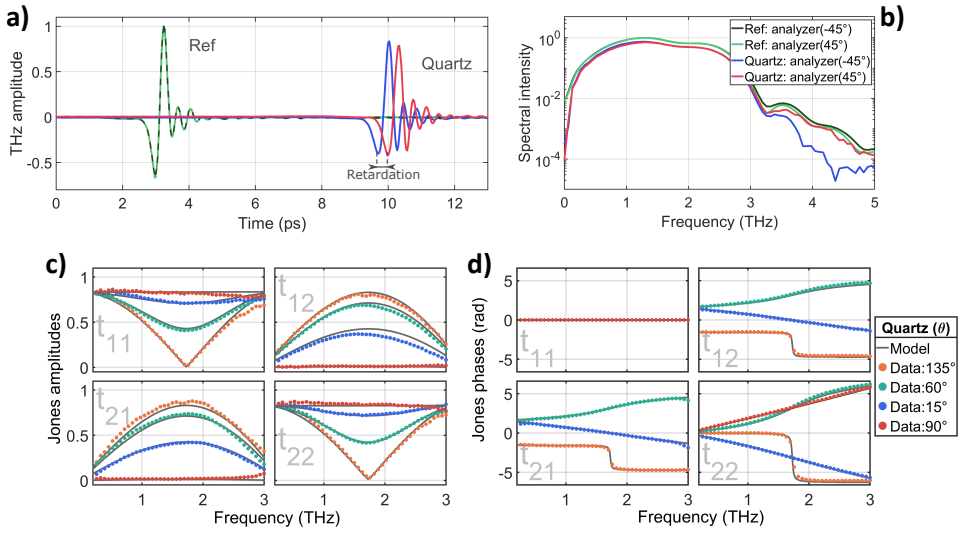


Fig. 2. Comparison of A-cut crystal quartz plate and free-space reference measurements: a) time-domain waveforms, and b) the corresponding spectral intensity at orthogonal polarizations. Polarization was selected by setting the analyzer at a ±45° azimuth. Demonstration of the complex Jones matrix for quartz at 15°, 60°, 90°, and 135° azimuths of optical axis: c) Jones amplitude spectra and d) normalized Jones phase spectra. The experimental results are compared to a theoretical model of quartz (gray lines). The quartz crystal functions as a linear retarder, exhibiting half-wave retardation at 1.7 THz. The off-diagonal phases at 90° azimuth were excluded from the plot, as they correspond to zero amplitudes, where the phase is inherently undefined.

quartz/air interfaces. Subsequently, we perform Fourier transformation on the time-domain signals to obtain the complex spectra, which include both phase and amplitude. The amplitude spectra are shown in Figure 2b.

Accurate characterization with this elementary polarimetric approach depends on a detailed understanding of the anisotropic sample's orientation and behavior. In contrast, complete ellipsometry provides deeper insights, enabling more precise and comprehensive polarimetric characterization. Figure 2c presents the amplitudes of experimentally determined complete Jones matrix for quartz, compared with the theoretical model (see Supplemental Material 1). Analysis of the amplitude spectrum shows that at 90° azimuth, the crystal axes align with the ellipsometer-generated polarizations, resulting in minimal off-diagonal elements. At 135° azimuth, the diagonal components drop to zero signal around 1.7 THz, indicating halfwave plate behavior. Here, the half-wave plate shifts the phase of one polarization component by 180°, effectively rotating the linear polarization direction by 90°. Therefore, the off-diagonal components are maximal at this frequency. Azimuths of 15° and 60° represent intermediate steps between Cartesian and diagonal bases. Half-waveplate behavior occurs at a specific frequency ν, where the retardation δ reaches π, as δ is frequency-dependent: $\delta = \frac{2\pi}{c}\,\nu\,(n_\mathrm{o} - n_\mathrm{e})$, with c being the speed of light. The difference between the ordinary n_o and extraordinary n_e indices is also frequency-dependent due to material dispersion. The analytical form of the Jones matrix for a uniaxial anisotropic crystal is presented in Supplementary Materials 1 for a more detailed understanding.

The complex Jones matrix offers crucial insights into absolute phases in polarization analysis.

To enhance clarity in the polarization phase spectra, we normalize the Jones phase matrix, $\arg\{\tilde{\mathbf{J}}\}$, by the phase element $\arg\{\tilde{j}_{11}\}$. This normalization highlights subtle polarization differences and removes the accumulated phase of hundreds of radians as the wave propagates through the crystal relative to a free-space reference. Figure 2d illustrates the normalized Jones phase matrix compared with the model, where the primary component is normalized to zero, and other components display phase differences relative to $\tilde{j}_{11}$. The normalized phases are linearly proportional to frequency, with slight curvatures in the phase response due to the dispersion between the ordinary and extraordinary refractive indices. A negative phase difference indicates a reduced propagation velocity relative to the $\tilde{j}_{11}$ element. In a half-wave plate rotated at a 135° azimuth, a phase shift of π indicates a reversal in polarization polarity. The figure does not show the phase response in the off-diagonal elements at the 90° azimuth, as these were computed from zero-amplitude signals. Furthermore, as the frequency approaches zero ($\nu \to 0$) for off-diagonal elements, phase offsets are mainly determined by interfaces, thus the phase differences in the complex Fresnel coefficients.

3. Comparison with Mueller and Pauli techniques in polarization analysis

Complete Jones matrices are highly effective in time-domain ellipsometry because they directly describe the transformation of complex electric field components. This method reveals amplitude and phase spectra changes, clearly outlining complex interactions within polarization states through diagonal and off-diagonal elements. However, extracting specific effects like retardation and diattenuation from the 2×2 Jones matrix may be challenging, particularly when both effects contribute to the same matrix elements. The Stokes bases offer an alternative interpretation approach. This system defines easily measurable polarization states: horizontal, vertical, diagonal, anti-diagonal, and left- and right-handed circular polarization. Traditionally, this approach is applied in intensity descriptions using Mueller matrices. However, we aim to demonstrate that this approach is highly robust in the coherent regime when applying Pauli exponential coefficients, ensuring both accuracy and efficiency in polarization analysis.

3.1. Mueller-Jones matrix approach

Mueller calculus provides a robust intensity-based framework for describing the polarization state of light. However, this approach results in the loss of total phase information accumulated during propagation through the sample. Although it does not directly capture phase, it reveals effects associated with phase differences. When absolute phase information is not required, an intensity-based description using the Stokes vector and 4×4 Mueller matrix offers an efficient polarization analysis. The transformation from the Jones matrix to the Mueller matrix proceeds as follows

$$\mathbf{M} = \mathbf{A}(\mathbf{J} \otimes \mathbf{J}^*)\mathbf{A}^{-1}, \text{ where } \quad \mathbf{A} = \begin{pmatrix} 1 & 0 & 0 & 1 \\ 1 & 0 & 0 & -1 \\ 0 & 1 & 1 & 0 \\ 0 & \mathrm{i} & -\mathrm{i} & 0 \end{pmatrix}, \tag{2}$$

enables the conversion of the vectorized coherency matrix into the Stokes bases [19, 56]. The Mueller matrix derived from the coherent Jones matrix is inherently non-depolarizing and commonly called the Mueller-Jones matrix. The Mueller matrix transforms the Stokes vector

components, which quantitatively describe polarized intensities as follows

$$\underbrace{\begin{pmatrix} I'_x + I'_y \\ I'_x - I'_y \\ I'_{+45^\circ} - I'_{-45^\circ} \\ I'_{\mathrm{R}} - I'_{\mathrm{L}} \end{pmatrix}}_{\mathbf{S}_{\mathrm{out}}} = \underbrace{\begin{pmatrix} m_{11} & m_{12} & m_{13} & m_{14} \\ m_{21} & m_{22} & m_{23} & m_{24} \\ m_{31} & m_{32} & m_{33} & m_{34} \\ m_{41} & m_{42} & m_{43} & m_{44} \end{pmatrix}}_{\mathbf{M}} \underbrace{\begin{pmatrix} I_x + I_y \\ I_x - I_y \\ I_{+45^\circ} - I_{-45^\circ} \\ I_{\mathrm{R}} - I_{\mathrm{L}} \end{pmatrix}}_{\mathbf{S}_{\mathrm{in}}} \tag{3}$$

where I_ξ represents the intensities corresponding to the ξ-polarization of the Stokes bases. Normalizing the Mueller matrix by the element m_{11} highlights relative changes in polarization properties. This matrix determines the intensity ratios for each base relative to the total intensity $I_x + I_y$. The first row $m_{1,1-4}$ and column $m_{1-4,1}$ are critical for transforming total intensity and demonstrating diattenuation. While the submatrix $m_{2-4,2-4}$ plays a crucial role in depicting retardation by affecting polarization states without altering total intensity [57].

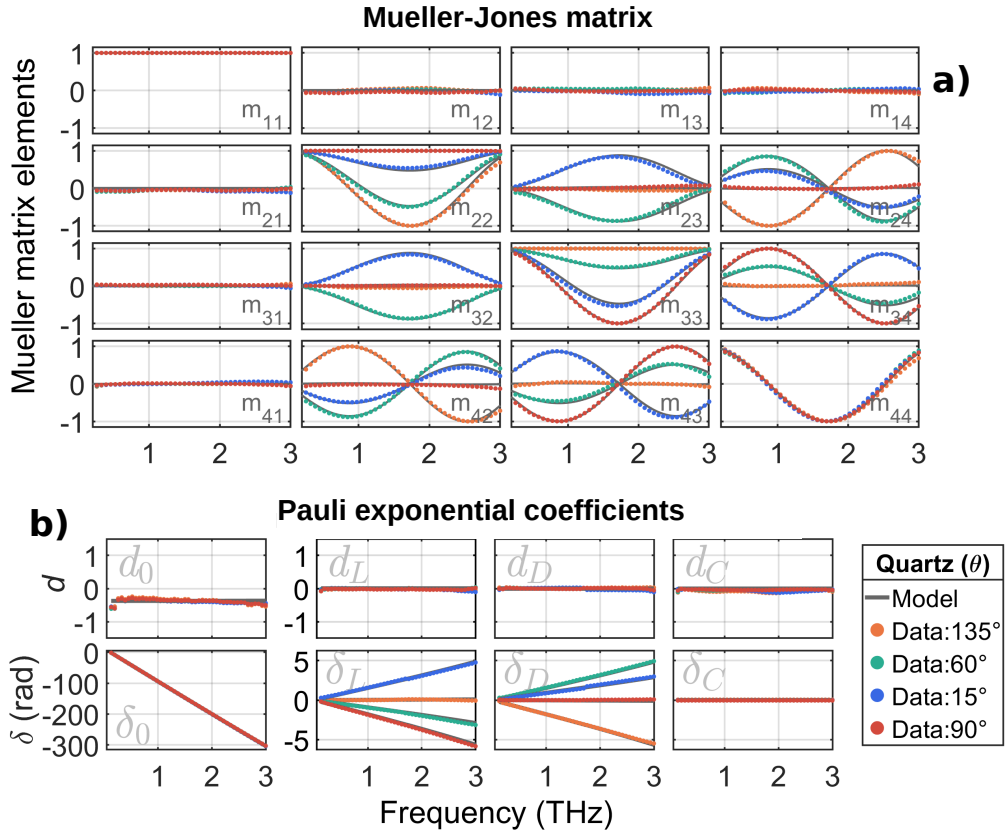


Fig. 3. Ellipsometric data of quartz for azimuth angles of 15°, 60°, 90°, and 135° presented as a) normalized Mueller-Jones matrix; b) exponential Pauli coefficients, where the real part corresponds to diattenuation d and the imaginary part to retardation δ. The subscript 0 denotes total absorption and phase; subscripts L, D, and C refer to linear polarizations in Cartesian coordinates, ±45° diagonal bases, and circular polarizations, respectively.

Figure 3a illustrates the conversion of the Jones matrix of quartz, shown in Figure 2c,d,

into the normalized Mueller-Jones matrix. The Mueller matrix exhibits the characteristic form of a linear retarder, in agreement with the analytical model provided in Supplementary Materials 2. Importantly, excluding m_{11}, the first row and column are zero, indicating no diattenuation in the transparent quartz crystal. The remaining submatrix aligns with the behavior expected of a linear retarder without diattenuation. At an azimuth of 135°, the Mueller matrix exhibits a block-diagonal structure. Significantly, the spectrum m_{44} corresponds to $\cos\delta$ and is independent of the waveplate's azimuth. The linear retarder behaves as a half-wave plate at the frequency corresponding to $m_{44} = -1$. The effects are distributed across the 4×4 matrix elements, simplifying data interpretation. Yet, this simplification comes at the cost of losing amplitude and phase information, which are more intuitive and easier to interpret. Interpreting experimental Mueller matrices can be challenging without an analytical model.

3.2. Pauli exponential coefficients

We utilize Stokes bases within a coherent framework, providing more detailed information than intensity-based methods, which is particularly advantageous for time-domain ellipsometry. A Jones matrix can be constructed by multiplying elementary Jones matrices $\mathbf{J}_\xi$ corresponding to all ξ-Stokes bases, as shown

$$\tilde{\mathbf{J}} = \tilde{\mathbf{J}}_0\tilde{\mathbf{J}}_\mathrm{L}\tilde{\mathbf{J}}_\mathrm{D}\tilde{\mathbf{J}}_\mathrm{C} = \exp(\tilde{p}_0\boldsymbol{\sigma}_0)\exp\left(\tilde{p}_\mathrm{L}\,\boldsymbol{\sigma}_\mathrm{L} + \tilde{p}_\mathrm{D}\,\boldsymbol{\sigma}_\mathrm{D} + \tilde{p}_\mathrm{C}\,\boldsymbol{\sigma}_\mathrm{C}\right), \tag{4}$$

where each elementary Jones matrix $\tilde{\mathbf{J}}_\xi = \exp(\tilde{p}_\xi\boldsymbol{\sigma}_\xi)$ is expressed as a matrix exponential, distinct from element-wise multiplication. The subscripts D, L, C refer to the vertical/horizontal linear, ±45° diagonal, and left/right-handed circular Stokes bases. The matrices $\boldsymbol{\sigma}_\xi$, known as the Pauli matrices, correspond to the fundamental Jones matrices used to interpret transformations within the Stokes vector bases. Specifically, $\boldsymbol{\sigma}_\mathrm{L}$ describes transitions from horizontal to vertical polarization, $\boldsymbol{\sigma}_\mathrm{D}$ describes changes from +45° to -45° diagonal polarization, and $\boldsymbol{\sigma}_\mathrm{C}$ describes transitions between left- and right-handed circular (or linear to circular) polarizations. The Pauli exponential coefficients are expressed as follows

$$\tilde{p}_\xi = \frac{d_\xi - \mathrm{i}\delta_\xi}{2} \tag{5}$$

and directly define the attenuation d_ξ and phase retardation δ_ξ for each specific Stokes basis. This formulation presents the Jones matrix as the product of individual optical effects, separated into interpretable complex coefficients $\tilde{p}_\xi$. Applying the matrix logarithm $\ln\tilde{\mathbf{J}}$ transforms the Jones matrix into a linear combination of Pauli matrices $\boldsymbol{\sigma}_\xi$, as follows

$$\tilde{\mathbf{K}} = \ln\tilde{\mathbf{J}} = \begin{pmatrix} \tilde{p}_0 + \tilde{p}_\mathrm{L} & \tilde{p}_\mathrm{D} - \mathrm{i}\tilde{p}_\mathrm{C} \\ \tilde{p}_\mathrm{D} + \mathrm{i}\tilde{p}_\mathrm{C} & \tilde{p}_0 - \tilde{p}_\mathrm{L} \end{pmatrix} = \tilde{p}_0\underbrace{\begin{pmatrix} 1 & 0 \\ 0 & 1 \end{pmatrix}}_{\boldsymbol{\sigma}_0} + \tilde{p}_\mathrm{L}\underbrace{\begin{pmatrix} 1 & 0 \\ 0 & -1 \end{pmatrix}}_{\boldsymbol{\sigma}_\mathrm{L}} + \tilde{p}_\mathrm{D}\underbrace{\begin{pmatrix} 0 & 1 \\ 1 & 0 \end{pmatrix}}_{\boldsymbol{\sigma}_\mathrm{D}} + \tilde{p}_\mathrm{C}\underbrace{\begin{pmatrix} 0 & -\mathrm{i} \\ \mathrm{i} & 0 \end{pmatrix}}_{\boldsymbol{\sigma}_\mathrm{C}}. \tag{6}$$

The exponential Pauli coefficients are derived from elements $\tilde{k}_{ij}$ of the complex matrix logarithm $\tilde{\mathbf{K}} = \ln\tilde{\mathbf{J}}$ as follows

$$\tilde{p}_0 = \frac{\tilde{k}_{11} + \tilde{k}_{22}}{2}, \quad \tilde{p}_\mathrm{L} = \frac{\tilde{k}_{11} - \tilde{k}_{22}}{2}, \quad \tilde{p}_\mathrm{D} = \frac{\tilde{k}_{12} + \tilde{k}_{21}}{2}, \quad \tilde{p}_\mathrm{C} = \frac{\mathrm{i}(\tilde{k}_{12} - \tilde{k}_{21})}{2}. \tag{7}$$

In the case of a waveplate, the coefficient $\tilde{p}_0$ takes the form of $\ln(\tilde{e}_\mathrm{o}\tilde{e}_\mathrm{e})$, representing the total changes in phase and amplitude of the ordinary and extraordinary polarizations $\tilde{e}_{\mathrm{o,e}}$. Conversely, the coefficients $\tilde{p}_\mathrm{L} = \cos 2\theta\ln(\tilde{e}_\mathrm{o}/\tilde{e}_\mathrm{e})$ and $\tilde{p}_\mathrm{D} = \sin 2\theta\ln(\tilde{e}_\mathrm{o}/\tilde{e}_\mathrm{e})$ correspond to the linear/diagonal effects of retardation and diattenuation and can readily reveal the presence of

linear birefringence and dichroism. To provide a detailed exploration of the polarization response in terms of Pauli exponential coefficients $\tilde{p}_\xi$, the Jones matrix $\tilde{\mathbf{J}}$ from (S1) is transformed into its matrix logarithm $\ln\tilde{\mathbf{J}}$ and subsequently mapped onto all Stokes bases through equation (7), leading to

$$\tilde{p}_0 = \frac{d_0 - \mathrm{i}\delta_0}{2} = \ln(\tilde{e}_\mathrm{o}\tilde{e}_\mathrm{e}) = \ln|\tilde{t}_\mathrm{o}||\tilde{t}_\mathrm{e}| + d_o + d_e - \mathrm{i}\,(\arg\tilde{t}_\mathrm{o}\tilde{t}_\mathrm{e} + \delta_o + \delta_e) \tag{8}$$

$$\tilde{p}_\mathrm{L} = \frac{d_\mathrm{L} - \mathrm{i}\delta_\mathrm{L}}{2} = \cos 2\theta\ \ln(\tilde{e}_\mathrm{o}/\tilde{e}_\mathrm{e}) = \cos 2\theta\left(\ln\frac{|\tilde{t}_\mathrm{o}|}{|\tilde{t}_\mathrm{e}|} + d - \mathrm{i}\left(\arg\frac{\tilde{t}_\mathrm{o}}{\tilde{t}_\mathrm{e}} + \delta\right)\right) \tag{9}$$

$$\tilde{p}_\mathrm{D} = \frac{d_\mathrm{D} - \mathrm{i}\delta_\mathrm{D}}{2} = \sin 2\theta\ \ln(\tilde{e}_\mathrm{o}/\tilde{e}_\mathrm{e}) = \sin 2\theta\left(\ln\frac{|\tilde{t}_\mathrm{o}|}{|\tilde{t}_\mathrm{e}|} + d - \mathrm{i}\left(\arg\frac{\tilde{t}_\mathrm{o}}{\tilde{t}_\mathrm{e}} + \delta\right)\right) \tag{10}$$

$$\tilde{p}_\mathrm{C} = \frac{d_\mathrm{C} - \mathrm{i}\delta_\mathrm{C}}{2} = 0, \tag{11}$$

where $d_{\mathrm{e,o}}$, $\delta_{\mathrm{e,o}}$, and $\tilde{t}_{\mathrm{e,o}}$ represent the ordinary and extraordinary attenuation coefficients, total phases, and cumulative Fresnel transmission coefficients, respectively. The quantity $d = d_\mathrm{o} - d_\mathrm{e}$ represents the diattenuation, while the retardation is given by $\delta = \delta_\mathrm{o} - \delta_\mathrm{e}$.

The Pauli exponential coefficient $\tilde{p}_0$ contains the cumulative phase $\arg\tilde{t}_\mathrm{o}\tilde{t}_\mathrm{e} + \delta_o + \delta_e$ and amplitude attenuation $\ln|\tilde{t}_\mathrm{o}||\tilde{t}_\mathrm{e}| + d_o + d_e$. The coefficient $\tilde{p}_0$ remains invariant to the sample's azimuth. In anisotropic materials with linear birefringence and dichroism, the coefficients $\tilde{p}_\mathrm{L}$ and $\tilde{p}_\mathrm{D}$ undergo a periodic transition between Cartesian and diagonal Stokes bases as a function of the angle θ. The real part, d_L and d_D, represents linear diattenuation and is proportional to $\ln(|\tilde{t}_\mathrm{o}|/|\tilde{t}_\mathrm{e}|) + d$. In contrast, the imaginary part determines retardation, with δ_D and δ_L based on $\arg(\tilde{t}_\mathrm{o}/\tilde{t}_\mathrm{e}) + \delta$. The parameter $\tilde{p}_\mathrm{C}$ remains zero because the circular polarization effects are not considered in the polarizations $\tilde{e}_{\mathrm{o,e}}$ (see Supplementary Material 1).

This behavior is evident in the experimentally determined Pauli exponential coefficients in Figure 3b compared with the analytical form. Results demonstrate that the diattenuation coefficients are zero, confirming that quartz exhibits no diattenuation d_ξ. Retardation is observed in both the linear and diagonal bases. In analyzing a uniaxial birefringent crystal oriented at azimuth θ, the linear retardation δ_L is found to be proportional to $\cos 2\theta$, while the diagonal polarization is proportional to $\sin 2\theta$. As expected, δ_C is zero, confirming the absence of optical activity and circular birefringence in quartz. The Pauli exponential coefficients facilitate a detailed polarization analysis in absolute terms, effectively separating amplitude and phase changes for each Stokes basis. This method eliminates the need for the complex modeling typically required in Jones or Mueller's approaches to interpret the individual matrix elements.

Notably, the imaginary part of the Pauli coefficients, expressed as $\sin(2\theta)\cdot\mathit{phase}$ and $\cos(2\theta)\cdot\mathit{phase}$, may lead to phase discontinuities if not correctly unwrapped. Therefore, we compute the matrix logarithm by normalizing it as $\ln(\tilde{\mathbf{J}}/\tilde{j}_{11}) + \boldsymbol{\sigma}_0\ln\tilde{j}_{11}$, which reduces the number of phase discontinuities. Then, we use the azimuth determined from $\tilde{p}_\mathrm{D}/\tilde{p}_\mathrm{L} = \tan 2\theta$ to scale the phase, unwrap it correctly, and rescale it to ensure continuity in the final result.

4. Calibration method

Calibration methods are designed to minimize errors from non-ideal settings or imperfections in optical components. Ellipsometry involves multiple measurements under different polarization conditions, requiring precise combinations to reconstruct the complete Jones matrix accurately. If not properly combined, these spectral matrices can contain systematic errors that may be mistaken for the material's polarization response, mainly when all systems' sensitivity depends on polarization. To overcome these challenges, we demonstrate a calibration method compensating for component misalignments and removing instrumental artifacts. As illustrated in the flowchart in Fig. 4a, the calibration technique involves several key steps: (i) rough alignment of the

experimental polarizing components; (ii) conducting free-space reference measurements under various configurations by adjusting the polarization of the STE-generated radiation and the analyzer's azimuth; (iii) calculating the true azimuths of the analyzer and spintronic emitter from the free-space references; (iv) measuring samples in identical configurations; (v) solving a system of linear equations from measurements; and (vi) reconstructing the Jones matrix to determine Pauli exponential coefficients.

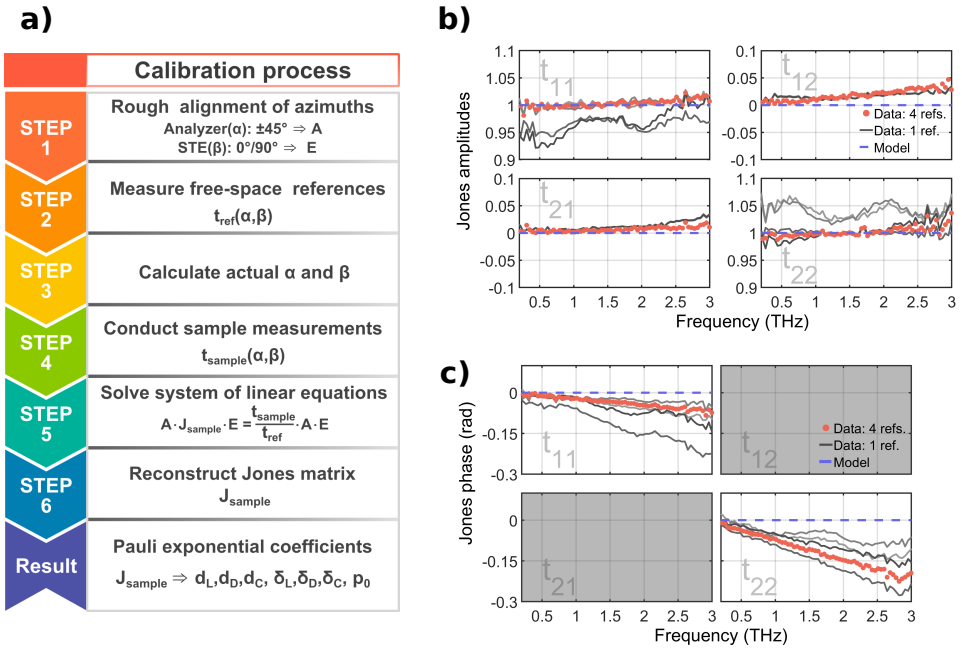


Fig. 4. Procedure and stability of the calibration: a)The calibration procedure for generalized time-domain ellipsometry: (1) A rough alignment of the analyzer to ±45° and the spintronic emitter to 0°/90°, corresponding to the vectors $\mathbb{A}_i$ and $\mathbb{E}_j$. (2) Measurement of the free-space reference in all four configurations. (3) Determination of the true azimuths of the analyzer and spintronic emitter. (4) Measurement of the sample in the same four configurations used for the free-space reference. (5) Construction and solution of the complex linear equations for each experimental configuration. (6) Reconstruction of the complex Jones matrix as the solution to the equation system. (7) In the final step, the Jones matrix is converted into Pauli exponential coefficients, directly corresponding to diattenuations and retardations in the linear, diagonal, and circular bases; b) Jones amplitude spectra, compared to a diagonal unit matrix in air, and c) Jones phase spectra, revealing absolute phase errors of free-space sample measurements, demonstrating the stability and accuracy of the generalized time-domain ellipsometer. The analysis compares the effectiveness of using four references versus a single reference in eliminating systematic errors during data reconstruction. The off-diagonal phase elements are excluded, as calculating them from zero signals would produce meaningless results.

4.1. Setting of polarizing components

Generating and detecting polarization states that provide sufficient information is crucial for determining the complete Jones matrix. We utilize vertical and horizontal polarization states generated by STE, combined with 45° diagonal and -45° anti-diagonal states at the analyzer, as shown in Figure 1b. Approximate azimuth settings are adequate since the calibration method

compensates for misaligned angles, removing the need for precise alignment. This STE and analyzer configuration ensures strong, non-zero signals in free-space measurements, simplifying the retrieval of phase and amplitude while enhancing sensitivity to subtle polarization effects. Conversely, using crossed polarizers or crossing the analyzer with the STE's polarization for reference measurements is not recommended, as it introduces significant noise from weak signals. Unlike traditional frequency domain ellipsometry, this strategy allows for the complete retrieval of amplitude and phase information using only linear polarizations. This approach removes the need for elliptically or circularly polarized states to detect circular birefringence and dichroism.

4.2. Reference and sample measurements

First, we perform four free-space reference measurements $\tilde{\boldsymbol{t}}_{\mathrm{ref}}(\alpha,\beta)$, followed by measurements of the investigated sample $\tilde{\boldsymbol{t}}_{\mathrm{sample}}(\alpha,\beta)$ under the same configurations. Assuming full time-domain coherence, the Jones formalism can be used to model the overall polarization response by multiplying the individual Jones matrices. The free-space reference model $\mathbb{t}_{\mathrm{ref}}$ is represented in matrix notation by sequentially multiplying the components as they appear in the experiment. The STE input field $\mathbb{STE}_j$ first passes through the analyzer $\mathbb{P}(\alpha)$, rotated by α_i, and then through the fixed polarizer $\mathbb{P}(90°)$, which is oriented vertically. Since only the vertical component is detected by the ZnTe crystal, the output is multiplied by vertical polarization selection $(0\ \ 1)$. For clarity, symbols in bold italic represent experimental variables, while double-struck font denotes theoretical models. Following this conditions, the measured complex amplitude $\tilde{\boldsymbol{t}}_{\mathrm{ref}}(\alpha,\beta)$ should be equal to

$$\tilde{\boldsymbol{t}}_{\mathrm{ref}}(\alpha_i,\beta_j) \stackrel{!}{=} \tilde{\mathbb{t}}_{\mathrm{ref}}(\alpha_i,\beta_j) = \underbrace{\begin{pmatrix}0 & 1\end{pmatrix}\mathbb{P}(90°)\,\mathbb{P}(\alpha_i)}_{\mathbb{A}_i}\ \mathbb{STE}_j, \tag{12}$$

where the relation $\stackrel{!}{=}$ indicates that the equality is expected between the experimental spectra and the theoretical model. Polarization detection is described by the analyzing vector $\mathbb{A}_i$, representing the coherent vertical-field detection after it passes through polarizers. The spintronic terahertz emission $\mathbb{STE}_j$ exhibits perfectly defined linear polarization, which we express using a rotated unit vector $\mathbb{E}_j$ in the following form

$$\mathbb{STE}_j = \tilde{\boldsymbol{E}}_\beta\,\mathbb{E}_j, \quad \mathbb{E}_j = \begin{pmatrix}\cos\beta_j\\ \sin\beta_j\end{pmatrix}, \tag{13}$$

where $\tilde{\boldsymbol{E}}_\beta$ refers to the complex amplitude of the emitted terahertz field. The emitted terahertz spectrum may vary with the azimuth β depending on the generation mechanism and polarization control. In our case, the spintronic emitter is mounted directly on the rotatable Halbach array, causing it to rotate with the polarization control. This rotation can potentially influence the spectrum.

Assuming an ideal polarizer, its Jones matrix for the azimuth α_i is given by

$$\mathbb{P}(\alpha_i) = \begin{pmatrix}\cos^2\alpha_i & \cos\alpha_i\sin\alpha_i\\ \cos\alpha_i\sin\alpha_i & \sin^2\alpha_i\end{pmatrix}. \tag{14}$$

However, polarizers in the terahertz range can exhibit non-ideal behavior, requiring representation through a Jones matrix of a linear diattenuator or a diattenuating retarder to accurately capture the extinction ratio or retardation. In our study, this adjustment had no significant impact and was therefore not applied. Finally, the sample is placed between the spintronic emitter and the analyzer for measurement. The expected complex spectrum $\tilde{\mathbb{t}}_{\mathrm{sample}}(\alpha_i,\beta_j)$ of the sample, corresponding to the measured response $\tilde{\boldsymbol{t}}_{\mathrm{sample}}(\alpha_i,\beta_j)$, is expressed as

$$\tilde{\boldsymbol{t}}_{\text{sample}}(\alpha_i,\beta_j) \stackrel{!}{=} \tilde{\mathbb{t}}_{\text{sample}}(\alpha_i,\beta_j) = \mathbb{A}_i\,\tilde{\boldsymbol{J}}_{\text{sample}}\,\mathbb{STE}_j, \tag{15}$$

where $\tilde{\boldsymbol{J}}_{sample}$ describes the Jones matrix of the sample, which we aim to determine experimentally.

4.3. Determining the actual orientation of STE and analyzer

The crucial step in the calibration method involves determining the actual azimuths α_i and β_j, initially set to detect ± 45° diagonal states for the analyzer, and to generate near-vertical and horizontal polarization states using the spintronic emitter. Four free-space reference measurements are used to calculate these azimuths by analyzing the reference ratios at identical azimuths of the spintronic emitter. We use a least squares method to determine the actual azimuths β_1 and α_1 relative to the fixed polarizer, formulated as

$$\underset{\alpha_1,\beta_1}{\arg\min}\left\{\sum_{\text{Frequency}}\sum_{j=1,2}\left(\frac{\mathbb{A}_1\,\mathbb{E}_j}{\mathbb{A}_2\,\mathbb{E}_j} - \left|\frac{\tilde{\boldsymbol{t}}_{\text{ref}}(\alpha_1,\beta_j)}{\tilde{\boldsymbol{t}}_{\text{ref}}(\alpha_2,\beta_j)}\right|\right)^2\right\}. \tag{16}$$

Since the azimuths α_2 and β_2 are orthogonal to α_1 and β_1, as ensured by the high precision motorized stages, it follows that $\alpha_2 = \alpha_1 + 90°$ and $\beta_2 = \beta_1 + 90°$. Additionally, using the same azimuth ratios for the spintronic emitter (β_j) eliminates the complex spectral amplitude $\tilde{\boldsymbol{E}}_\beta$, which would otherwise require experimental determination.

4.4. Reconstruction of complete Jones matrix

The Jones matrix of a sample, $\tilde{\boldsymbol{J}}_{\text{sample}}$, consists of four complex unknown spectra, requiring a robust and unique solution for each frequency. To determine these four complex unknown parameters, at least four distinct measurement configurations of the sample are necessary. Though a single reference could theoretically determine the delay relative to free-space, we define a reference in each sample configuration to eliminate $\tilde{\boldsymbol{E}}_\beta$'s influence and remove systematic artifacts. In each configuration, we establish the following equation to relate the models $\tilde{\mathbb{t}}$ and the measurements $\tilde{\boldsymbol{t}}$ for both references and samples as

$$\tilde{\mathbb{t}}_{\text{sample}}(\alpha_i,\beta_j) \stackrel{!}{=} \frac{\tilde{\boldsymbol{t}}_{\text{sample}}(\alpha_i,\beta_j)}{\tilde{\boldsymbol{t}}_{\text{ref}}(\alpha_i,\beta_j)}\,\tilde{\mathbb{t}}_{\text{ref}}(\alpha_i,\beta_j). \tag{17}$$

Applying equations (12) and (15) to each configuration, we obtain

$$\mathbb{A}_i\,\tilde{\boldsymbol{J}}_{\text{sample}}\,\mathbb{E}_j \stackrel{!}{=} \tilde{\boldsymbol{t}}_{ij}\mathbb{A}_i\mathbb{E}_j, \quad \tilde{\boldsymbol{t}}_{ij} = \frac{\tilde{\boldsymbol{t}}_{\text{sample}}(\alpha_i,\beta_j)}{\tilde{\boldsymbol{t}}_{\text{ref}}(\alpha_i,\beta_j)}, \tag{18}$$

where all experimental configurations are transformed into the complex matrix equation $\mathbb{W}\cdot\tilde{\boldsymbol{j}}_{\text{sample}} = \tilde{\boldsymbol{u}}$ in the following form

$$\begin{pmatrix} \mathbb{A}_1\otimes\mathbb{E}_1 & \mathbb{A}_1\otimes\mathbb{E}_2 \\ \mathbb{A}_2\otimes\mathbb{E}_1 & \mathbb{A}_2\otimes\mathbb{E}_2 \end{pmatrix}\begin{pmatrix} \tilde{\boldsymbol{j}}_{11} \\ \tilde{\boldsymbol{j}}_{12} \\ \tilde{\boldsymbol{j}}_{21} \\ \tilde{\boldsymbol{j}}_{22} \end{pmatrix} = \begin{pmatrix} \tilde{\boldsymbol{t}}_{11}\mathbb{A}_1\mathbb{E}_1 \\ \tilde{\boldsymbol{t}}_{12}\mathbb{A}_1\mathbb{E}_2 \\ \tilde{\boldsymbol{t}}_{21}\mathbb{A}_2\mathbb{E}_1 \\ \tilde{\boldsymbol{t}}_{22}\mathbb{A}_2\mathbb{E}_2 \end{pmatrix}. \tag{19}$$

Symbol ⊗ denotes the Kronecker product, and $\tilde{\boldsymbol{j}}_{\text{sample}}$ is the vectorized complex Jones matrix $\tilde{\boldsymbol{J}}_{\text{sample}}$. Solving this system of complex linear equations at each frequency yields the complete measured Jones matrix.

The experimental input data are entirely contained within the vector $\tilde{\boldsymbol{u}}$. Inaccuracies in these data directly impact the Jones matrix solution but do not affect the stability of the equation system. Inaccuracies in the models $\mathbb{A}_i$ and $\mathbb{E}_j$ within the matrix $\mathbb{W}$ will directly affect the resulting Jones matrix. Because the matrix $\mathbb{W}$ is theoretical, the system's stability depends on our choice of the vectors $\mathbb{A}_i$ and $\mathbb{E}_j$. These vectors must be linearly independent. The system's stability is evaluated by the condition number of the symmetric positive definite matrix $\mathbb{G} = \mathbb{W}^\dagger \cdot \mathbb{W}$, where $\dagger$ denotes the Hermitian transpose. The condition number $\kappa = \lambda_{\max}(\mathbb{G})/\lambda_{\min}(\mathbb{G})$ is defined by the maximum and minimum eigenvalues of $\mathbb{G}$, $\lambda_{\max}(\mathbb{G})$ and $\lambda_{\min}(\mathbb{G})$, respectively. The chosen Cartesian horizontal and vertical polarizations for $\mathbb{E}_j$ and diagonal and anti-diagonal polarizations for $\mathbb{A}_i$ result in a condition number κ of 1, ensuring ideal conditioning for stability, uniqueness, and robustness. In contrast, selecting horizontal and vertical states for both $\mathbb{A}_i$ and $\mathbb{E}_j$ leads to $\kappa \to \infty$, indicating a highly unstable solution. This outcome is expected experimentally, as measurements with crossed polarizations lead to zero signals. Thus, selecting $\mathbb{A}_i$ and $\mathbb{E}_j$ from independent basic polarization bases like Cartesian, diagonal, or circular is recommended for optimal conditioning.

4.5. Error analysis of the Jones matrix reconstruction

The precision in determining the Jones matrix relies on the quality of the theoretical descriptions of polarization components $\mathbb{A}_i$ and $\mathbb{E}_j$, as well as the accuracy of the measured data $\tilde{\boldsymbol{t}}_{ij}$. Errors in the Jones matrix can arise from both random and systematic artifacts in the data, as well as from inaccuracies in the component descriptions. To assess experimental errors, we follow these steps: (i) Taking four free-space reference measurements; (ii) Collecting an additional four free-space measurements after a one-hour delay, a standard timeframe between reference and sample measurements, this time treating the second set as the sample; (iii) Determining the Jones matrix, which is expected to be a unit diagonal matrix since both the sample and reference share the same configuration. We specifically selected free-space measurements for the sample because deviations in amplitude and phase from the diagonal matrix directly reflect instrumental errors and instabilities. We reconstructed the resulting Jones matrix in two ways: (a) Using four reference measurements in the corresponding sample configuration, as proposed in our method, to eliminate systematic errors; (b) Using only single reference to determine the Jones matrix, highlighting the advantage of employing four references.

In analyzing the amplitude Jones matrix shown in Figure 4b, the blue dashed line represents the theoretical diagonal unit matrix, while the red dots indicate the Jones matrix derived from four references. The grey lines illustrate the results obtained using only one reference. Relying on only one reference leads to substantial deviations from the theoretical model. These deviations may stem from idealized theoretical models, configuration-specific artifacts, or the azimuthal dependence of $\tilde{\boldsymbol{E}}_\beta$. Using four references significantly reduces the main diagonal errors to less than 2%. For the off-diagonal elements, the error is more pronounced, around 2-3%, possibly due to the unaccounted terahertz polarizer imperfections in the model.

We present the unnormalized absolute phases of the free-space Jones matrix in Figure 4c to demonstrate the absolute phase errors. Only the main diagonal elements are shown, as the off-diagonal elements have zero amplitude signals, making phase calculation irrelevant. The diagonal elements exhibit a phase shift of tenths of radians, likely caused by temperature or humidity fluctuations in the laboratory due to long beam paths. Using only one reference results in systematic errors that deviate significantly from the expected linear trend. In contrast, using four references forms a linear curve, indicating more accurate results. Notably, this represents the absolute phase error, which translates to a relative error of less than one per thousand when measuring a bulk sample with a total phase of hundreds of radians. This substantial reduction in amplitude and phase errors brings the precision of terahertz ellipsometry closer to that of the visible range.

5. Demonstration of complete ellipsometry with an advanced sample: Hg_2Cl_2

Up to now, we have demonstrated THz-cTDSE using the quartz plate, which exhibits only linear retardation. In this section, we explore the more advanced uniaxial anisotropic crystal Hg_2Cl_2 (Calomel) with a thickness of 2.15 mm and an in-plane optical axis. Due to its polarization-dependent phonon interactions in the terahertz spectrum, this crystal displays both linear retardation and dichroism. Figure 5a shows the time-domain signal that exhibits a significant delay and attenuation compared to the free-space reference signals. In one polarization, where strong absorption occurs, the signal follows the behavior of a damped harmonic oscillator. Driven by polarization-dependent phonon interactions, the retardation here is significantly greater than that observed in quartz (see Figure 2a). Figure 5b reveals a corresponding spectrum where phonon-induced cutoff begins at 1 THz, highlighting the diattenuating behavior of the crystal.

5.1. Jones analysis

Using our complete ellipsometry, we now investigate linear birefringence and diattenuation using the Jones matrix formalism. The predicted behavior of a birefringent diattenuating sample is detailed in Supplementary Material 1 for the Jones matrix, while optical constants derived from the Lorentz model. To illustrate its complex behavior, we analyze a Calomel crystal at 90° and 135° azimuths of its optical axis, corresponding to Cartesian linear and diagonal Stokes bases. We slightly rotated the azimuth in both orientations to ensure detectable signals in all components and avoid zero off-diagonal elements.

Figure 5c presents the experimentally determined amplitude Jones matrix, compared with the theoretical model. At a 90° azimuth, the generated polarizations travel through the crystal along the ordinary and extraordinary axes, corresponding to the diagonal elements. Consequently, the off-diagonal elements are nearly zero due to the absence of polarization conversion, except for a minor signal caused by the slight rotation in setting the crystal's azimuth. The diagonal amplitudes differ due to reflective losses influenced by different Fresnel coefficients and primarily by distinct phonon absorption. For the element $|\tilde{t}_{22}|$, the signal is fully absorbed by phonons starting at 1.4 THz. This notable difference in absorbed amplitude complicates data interpretation compared to quartz, where the amplitude was uniform and dependent on retardation. Nevertheless, the normalized amplitude form is unsuitable, leading to zero dividing at multiple points in the terahertz spectrum.

Setting the azimuth to 135° results in non-zero off-diagonal elements of the Jones matrix, which introduces oscillations in all its elements. As observed in quartz, these oscillations manifest as retardation caused by the difference between the ordinary and extraordinary refractive indices. The Calomel crystal functions as a half-wave plate, rotating the input polarization by 90° at frequencies where the diagonal elements approach zeros. Similarly, this behavior is evident in the amplitude maxima of the off-diagonal elements. The elements exhibit combined signals with ordinary and extraordinary absorption, and the oscillations cease when one polarization component is fully absorbed. It is crucial to recognize that combining these effects in a 2×2 matrix can become complex due to their coupling. Moreover, this sample does not consider more complex mixing, such as those involving circular polarization effects. However, amplitude changes due to the retardation can easily be mistaken for those related to absorption, underscoring the importance of analyzing the phase.

Figure 5d depicts the Jones phase matrix, normalized by the element t_{11}. Interpreting the phases is easier because they reflect minimal amplitude effects. The diagonal element t_{22} at 90° azimuth exhibits total retardation reaching hundreds of radians, which is an order of magnitude higher than in quartz. Retardation at a 135° azimuth is largely compensated but not completely nullified due to a slight azimuth deviation. Oscillations in the off-diagonal elements arise from phase jumps of π at frequencies corresponding to a half-wave plate caused by polarity changes in the waveform. Although noisy at a 90° azimuth due to minimal diagonal elements,

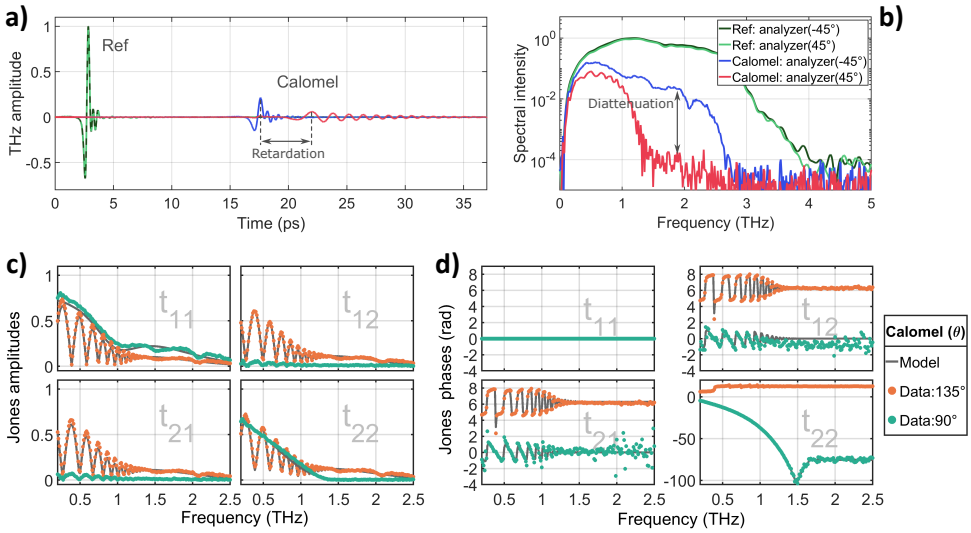


Fig. 5. Ellipsometric characterization of the Hg_2Cl_2 (Calomel) crystal at 90° and 135° azimuths, demonstrating significant diattenuation and retardation due to polarization-anisotropic phonons. a) Waveforms obtained via standard time-domain spectroscopy in orthogonal polarizations, compared with a free-space reference using the analyzer at ±45°; and b) the corresponding spectral intensity. c) Generalized time-domain ellipsometry: amplitude spectra of the Jones matrix and d) normalized phase spectra of the Jones matrix, compared with a model.

the phase still closely matches the theoretical model. Beyond 1.4 THz, the oscillations cease entirely as one polarization is fully attenuated, thus eliminating retardation.

5.2. Mueller matrix analysis

Figure 6a presents the experimentally determined normalized Mueller matrix for the Calomel crystal plate. The spectra of the Mueller matrix elements are in close agreement with the diattenuating retarder model described in Supplementary Material 2. The Mueller matrix highlights the retardation submatrix $m_{2-4,2-4}$, characterized by spectra that appear as damped trigonometric functions. Its off-diagonal elements are described by $J \cos 2\theta \sin \delta$ and $J \sin 2\theta \sin \delta$, where θ is the crystal's azimuth and δ represents the retardation introduced by the crystal. The coefficient J is a parameter associated with diattenuation. The oscillations in the spectra indicate retardation, whereas the presence of damping reveals diattenuation effects. At the 90° azimuth, the matrix elements m_{22}, m_{34}, and m_{43} reach their maxima, corresponding to linear retardation in Cartesian coordinates.

At the 135° azimuth, the matrix elements m_{33}, m_{24}, and m_{42} reach their maxima, corresponding to retardation in diagonal polarizations. The first row ($m_{1,2-4}$) and column ($m_{2-4,1}$), excluding m_{11}, directly indicate diattenuation without retardation effects, expressed as $K \cos 2\theta$ and $K \sin 2\theta$, with K associated with diattenuation. Minor diattenuation is observed at low terahertz frequencies. As diattenuation reaches its maximum at 1.4 THz, it indicates complete signal absorption, providing no further information. Similarly, elements m_{12} and m_{21} are associated with diattenuation in Cartesian coordinates, while m_{13} and m_{31} primarily correspond to diattenuation in diagonal coordinates. All retardation phenomena are coupled, complicating the interpretation. The Mueller matrix, comprising 15 elements, is often more comprehensible for complex samples

than the Jones matrix. However, it remains less straightforward than analysis based on Pauli exponential coefficients. In contrast to the Jones matrix and Pauli's exponential coefficients, the Mueller matrix does not include total phase information.

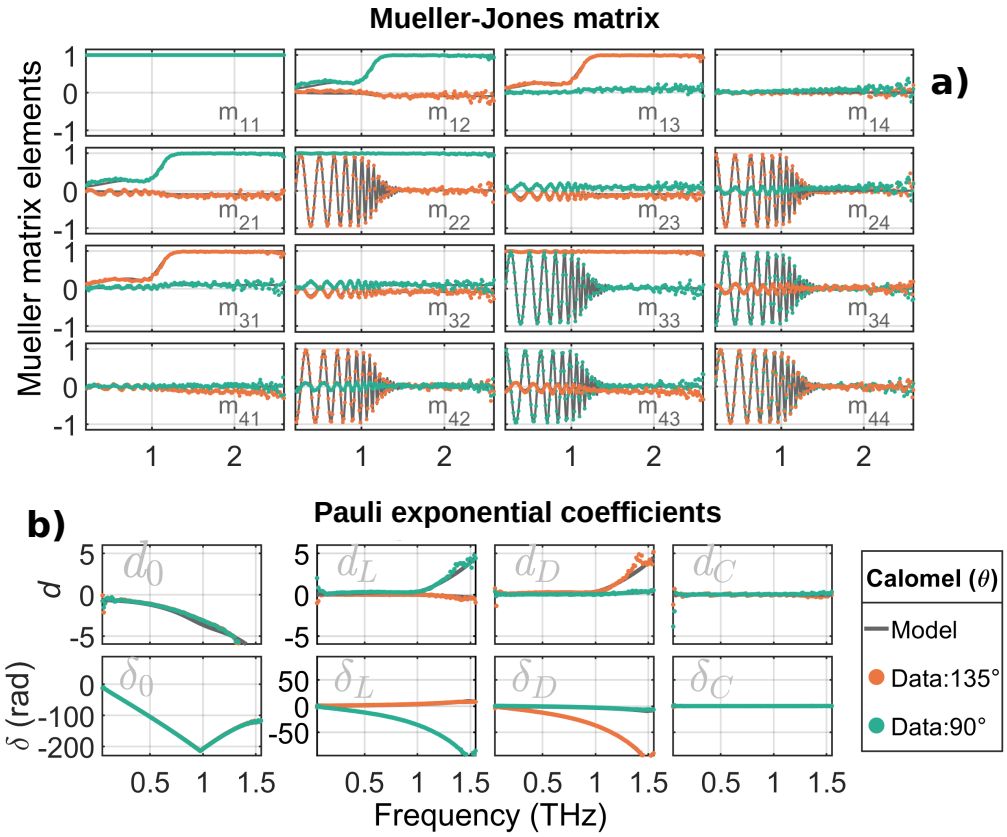


Fig. 6. The ellipsometric analysis of the Calomel crystal at 90° and 135° azimuths presented as a) normalized Mueller-Jones matrix calculated from the corresponding Jones matrix in Figure 5c,d. The first row and column, excluding the first element, correspond to diattenuation effects. The remaining submatrix represents a diattenuating retarder, with oscillations indicating retardation and damping signifying diattenuation. b) Exponential Pauli coefficients are associated with diattenuation represented by d and retardation represented by δ. The subscript 0 indicates total attenuation and phase, while subscripts L, D, and C correspond to linear polarizations in Cartesian coordinates, ±45° diagonal bases, and circular polarizations, respectively.

5.3. Pauli analysis

Interpreting the Jones matrix remains challenging despite the sample exhibiting only linear retardation and diattenuation. By converting to the logarithmic Jones matrix $\ln \tilde{\mathbf{J}}$, we decompose it into Pauli exponential coefficients $\tilde{p}_\xi$ for $\xi = 0, \mathrm{L}, \mathrm{D}, \mathrm{C}$, dividing all effects into retardation δ_ξ and diattenuation d_ξ across the Stokes ξ-bases. Supplementary Materials 3 provides the analytical expression for diattenuating birefringent materials regarding Pauli exponential coefficients. The Calomel crystal's experimentally determined Pauli exponential coefficients are plotted in Figure 6b. The coefficients' spectra are shown up to 1.5 THz since the absorption of one polarization makes determining diattenuation and retardation unattainable. The total

absorption coefficient $d_0 = \ln(|\tilde{t}_o||\tilde{t}_e|) + d_o + d_e$ is independent of polarization and sample rotation. It includes the sum of the ordinary and extraordinary attenuation coefficients $d_{o,e}$ and Fresnel transmission coefficients $\tilde{t}_{o,e}$. The total retardation $\delta_0 = \arg(\tilde{t}_o\tilde{t}_e) + \delta_o + \delta_e$ is primarily determined by the sum of the ordinary and extraordinary phases accumulated during propagation in the crystal. The coefficients $d_L = \cos 2\theta\ (\ln|\tilde{t}_o/\tilde{t}_e| + d_o - d_e)$ and $d_D = \sin 2\theta\ (\ln|\tilde{t}_o/\tilde{t}_e| + d_o - d_e)$ describe diattenuation effects in the vertical/horizontal and ±45° diagonal polarization bases for an uniaxial dichroic crystal. The diattenuation varies between $\tilde{p}_L$ and $\tilde{p}_D$ due to the crystal's azimuthal rotation θ. The primary onset of diattenuation is observed at 1 THz, although it slightly diattenuates before this frequency. The retardation coefficients $\delta_L = \cos 2\theta\ (\arg(\tilde{t}_o/\tilde{t}_e) + \delta_o - \delta_e)$ and $\delta_D = \sin 2\theta\ (\arg(\tilde{t}_o/\tilde{t}_e) + \delta_o - \delta_e)$ take an analogous form with diattenuation coefficients. In contrast, the retardation $\delta_{L,D}$ is observable across the entire THz spectrum. Finally, the effects δ_C and d_C are zero, corresponding to polarization phenomena in circular bases, which are absent in achiral uniaxial crystals.

6. Perspectives of THz-cTDSE

This study demonstrates complete ellipsometry in the time domain, offering significant advantages for analyzing anisotropic materials. The THz-cTDSE can be particularly advantageous in the terahertz and even mid-infrared regions, as it utilizes waveform measurements that provide both amplitude and phase information [58,59]. A key advantage of this approach is that all polarization states are determined exclusively from linear polarizations, obviating the requirement for circular polarization-based methods typically needed in Mueller matrix ellipsometry or circular dichroism measurements [15,60]. While many scientific advancements have employed polarimetry [61–63] or Stokes vector analysis [64–66], these techniques provide only limited information about the output polarization state. In contrast, complete ellipsometry offers a more comprehensive and intuitive understanding by capturing retardation and diattenuation of all coherent polarization states.

Although this study focuses on transmission measurements, straightforward adaptation to reflection configurations are more prevalent in ellipsometry due to the enhanced polarization sensitivity of reflective Fresnel coefficients at oblique angles. Furthermore, our method could be adapted to reflection by applying similar calibration procedures, such as using an isotropic reference material in reflection to determine the actual azimuth of the generated and analyzed polarization states. The Jones matrix reconstruction will utilize the reflection coefficient ratio $\tilde{\boldsymbol{r}}_{ij}$ in the same equation system $\mathbb{A}_i\, \tilde{\boldsymbol{J}}_{\text{sample}}\, \mathbb{E}_j \stackrel{!}{=} \tilde{\boldsymbol{r}}_{ij} \mathbb{A}_i \mathbb{E}_j$, as demonstrated for the transmission. We recommend normalizing the matrix by its first element or calculating the displacement error from the data to avoid phase errors caused by differently positioned references and samples in reflection [67–69], as this parameter remains constant across all frequencies and polarization measurements.

Spintronic emitters, demonstrated here as a universal polarization source, offer an additional avenue for enhancement. In our setup, the emitter facilitates straightforward polarization control, eliminating the need for polarizers at the ellipsometer input. Furthermore, by modulating the spintronic emitter's polarization with an oscillating magnetic field, the sensitivity of the ellipsometer could be improved through polarization demodulation [70,71]. Integrating spintronic detection via Zeeman torque sampling involves utilizing an external magnetic field to achieve a uniform and extensive polarization-sensitive waveform detection [72]. This breakthrough can potentially create a polarization-sensitive spintronic source and detector within the terahertz region, eliminating the need for polarizers.

Lastly, another potential improvement pertains to the calibration procedure. The calibration method demonstrated in this paper is critical for accurately determining the Jones matrix and compensates for systematic errors, ensuring reliable results. However, experimentally characterizing the vectors $\mathbb{A}_i$ and $\mathbb{E}_j$, which are assumed to exhibit ideal behavior, could further

enhance accuracy and performance. This approach, known as the eigenvalue calibration method, requires multiple known samples to determine the experimental vectors $\boldsymbol{A}_i$ and $\boldsymbol{E}_j$ [73, 74]. This technique is commonly used in Mueller matrix ellipsometry to determine the behavior of all included components. This strategy could prove highly effective in the terahertz region, where accurately describing polarizing components is challenging.

7. Backmatter

Funding. The authors acknowledge the partial support of the following projects: Czech Science Foundation 22-33060S; project No. CZ.02.01.01/00/22 008/0004631- "Materials and Technologies for Sustainable Development", funded by the European Union and the state budget of the Czech Republic within the framework of the Jan Amos Komensky Operational Program; project REFRESH – Research Excellence For Region Sustainability and High-tech Industries project number CZ.10.03.01/00/22 003/0000048 via the Operational Programme Just Transition; Student Grant System SP2024/086. This work was funded by FET project s-NEBULA/Grant No. 863155.

Acknowledgments. We thank Tobias Kampfrath, Tom S. Seifert, and Alexander Chekhov for providing the large-area spintronic terahertz emitter, which was essential for the experiments performed in this study.

Disclosures. The authors declare no conflicts of interest.

Data Availability Statement. Data underlying the results presented in this paper are available in *RepositoryIDxxx*.

Supplemental document. The Supplemental Material provides an analytical model, with Part 1 focusing on the Jones matrix formulation and Part 2 extending the analysis to the Mueller matrix.

8. Conclusion

In this work, we have introduced terahertz time-domain spectroscopic complete ellipsometry (THz-cTDSE), advancing beyond the limitations of standard and Mueller ellipsometry methods. Traditional standard ellipsometry is limited to isotropic samples and lacks comprehensive polarization information, while Mueller matrix ellipsometry, although providing complete intensity-based data, omits phase and amplitude information, making interpretation challenging. Our time-domain approach leverages the complex information inherent in terahertz signals, significantly enhancing ellipsometric capabilities by providing a detailed and intuitive description using Pauli exponential coefficients.

We have successfully determined the complete Jones and Mueller matrices, with the Jones matrix approach being unique in capturing the entire complex polarization response. The incorporation of Pauli exponential coefficients, seldom applied in experimental ellipsometry, provides direct and clear insights into diattenuation and retardation across all Stokes vector bases, extractable directly from the Jones matrix logarithm. The Pauli approach significantly streamlines ellipsometry analysis compared to the Jones and Mueller matrices, where distinguishing individual polarization phenomena is often complex due to their coupling.

Furthermore, we have developed the calibration method, which is crucial for accurately reconstructing the Jones matrix. Unlike previous terahertz ellipsometry techniques that relied on meticulous alignment, our method not only determines the actual settings of optical components but also compensates for systematic artifacts, enhancing robustness and reliability.

We demonstrated the practical application of spintronic terahertz emitters (STEs) in ellipsometry, taking advantage of their exceptional polarization properties. The STE allows straightforward polarization control of the terahertz source by simply adjusting an external magnetic field, a level of simplicity and precision not attainable with other methods for pulsed mJ-systems.

In conclusion, the THz-cTDSE method substantially advances terahertz ellipsometry, providing complete polarization characterization with improved accuracy and interpretability. This work

opens new avenues for investigating complex materials and phenomena in the terahertz regime, with potential applications across complex anisotropic samples, heterostructures, metamaterials, biological specimens, and materials exhibiting magneto-optical effects.

References

1. J. Kircher, R. Henn, M. Cardona, *et al.*, "Far-infrared ellipsometry using synchrotron radiation," J. Opt. Soc. Am. B, JOSAB **14**, 705–712 (1997).
2. M. Li, J. Fortin, J. Y. Kim, *et al.*, "Dielectric constant measurement of thin films using goniometric terahertz time-domain spectroscopy," IEEE J. Sel. Top. Quantum Electron. **7**, 624–629 (2001).
3. T. Nagashima and M. Hangyo, "Measurement of complex optical constants of a highly doped Si wafer using terahertz ellipsometry," Appl. Phys. Lett. **79**, 3917–3919 (2001).
4. T. Hofmann, C. M. Herzinger, A. Boosalis, *et al.*, "Variable-wavelength frequency-domain terahertz ellipsometry," Rev. Sci. Instrum. **81** (2010).
5. P. Marsik, K. Sen, J. Khmaladze, *et al.*, "Terahertz ellipsometry study of the soft mode behavior in ultrathin SrTiO3 films," Appl. Phys. Lett. **108** (2016).
6. N. Matsumoto, T. Hosokura, T. Nagashima, and M. Hangyo, "Measurement of the dielectric constant of thin films by terahertz time-domain spectroscopic ellipsometry," Opt. Lett. **36**, 265–267 (2011).
7. Y. Ino, R. Shimano, Y. Svirko, and M. Kuwata-Gonokami, "Terahertz time domain magneto-optical ellipsometry in reflection geometry," Phys. Rev. B **70**, 155101 (2004).
8. K. Yatsugi, N. Matsumoto, T. Nagashima, and M. Hangyo, "Transport properties of free carriers in semiconductors studied by terahertz time-domain magneto-optical ellipsometry," Appl. Phys. Lett. **98** (2011).
9. I. A. Azarov, Y. Yu. Choporova, V. A. Shvets, and B. A. Knyazev, "An Ellipsometric Technique with an ATR Module and a Monochromatic Source of Radiation for Measurement of Optical Constants of Liquids in the Terahertz Range," J. Infrared Milli. Terahz. Waves **40**, 200–209 (2019).
10. X. Chen, Q. Sun, J. Wang, *et al.*, "Exploiting Complementary Terahertz Ellipsometry Configurations to Probe the Hydration and Cellular Structure of Skin In Vivo," Adv. Photonics Res. **2**, 2000024 (2021).
11. N. Karl, M. S. Heimbeck, H. O. Everitt, *et al.*, "Characterization of an active metasurface using terahertz ellipsometry," Appl. Phys. Lett. **111** (2017).
12. R. M. A. Azzam and N. M. Bashara, *Ellipsometry and Polarized Light* (North-Holland Publishing Company, 1977).
13. H. Fujiwara, *Spectroscopic ellipsometry: principles and applications* (John Wiley & Sons, 2007).
14. S.-X. Huang, G. Wu, K. Chan, *et al.*, "Demonstration of a terahertz multi-spectral 3×3 Mueller matrix polarimetry system for 2D and 3D imaging." Opt. Express (2021).
15. T. Hofmann, C. M. Herzinger, J. L. Tedesco, *et al.*, "Terahertz ellipsometry and terahertz optical-Hall effect," Thin Solid Films **519**, 2593–2600 (2011).
16. T. Hofmann, U. Schade, C. M. Herzinger, *et al.*, "Terahertz magneto-optic generalized ellipsometry using synchrotron and blackbody radiation," Rev. Sci. Instrum. **77**, 063902 (2006).
17. M. K. Mainali, P. Uprety, Z. Song, *et al.*, "Terahertz optical Hall effect determination of carrier concentrations in component layers within low bandgap tin–lead halide perovskite photovoltaics and device simulation," Mater. Sci. Semicond. Process. **170**, 107936 (2024).
18. P. Kühne, N. Armakavicius, V. Stanishev, *et al.*, "Advanced Terahertz Frequency-Domain Ellipsometry Instrumentation for In Situ and Ex Situ Applications," IEEE Trans. Terahertz Sci. Technol. **8**, 257–270 (2018).
19. J. N. Hilfiker, N. Hong, and S. Schoeche, "Mueller matrix spectroscopic ellipsometry," Adv. Opt. Technol. **11**, 59–91 (2022).
20. A. Pashkin, M. Kempa, H. Němec, *et al.*, "Phase-sensitive time-domain terahertz reflection spectroscopy," Rev. Sci. Instrum. **74**, 4711–4717 (2003).
21. Z. Mazaheri, C. Koral, and A. Andreone, "Accurate THz ellipsometry using calibration in time domain," Sci. Rep. **12**, 1–10 (2022).
22. V. C. Agulto, T. Iwamoto, H. Kitahara, *et al.*, "Terahertz time-domain ellipsometry with high precision for the evaluation of GaN crystals with carrier densities up to 1020 cm-3," Sci. Rep. **11**, 1–10 (2021).
23. N. Matsumoto, T. Nagashima, T. Fujii, *et al.*, "Development of THz ellipsometer with variable incident angle," in *2009 34th International Conference on Infrared, Millimeter, and Terahertz Waves,* (IEEE), pp. 21–25.
24. K. Morino, S. Arakawa, T. Fujii, *et al.*, "Characterization of the electrical properties of an InN epilayer using terahertz time-domain spectroscopic ellipsometry," Jpn. J. Appl. Phys. **58**, SCCB22 (2019).
25. C. D. W. Mosley, M. Failla, D. Prabhakaran, and J. Lloyd-Hughes, "Terahertz spectroscopy of anisotropic materials using beams with rotatable polarization," Sci. Rep. **7**, 1–9 (2017).
26. C. M. Morris, R. V. Aguilar, A. V. Stier, and N. P. Armitage, "Polarization modulation time-domain terahertz polarimetry," Opt. Express **20**, 12303–12317 (2012).
27. K. Xu, E. Bayati, K. Oguchi, *et al.*, "Terahertz time-domain polarimetry (THz-TDP) based on the spinning E-O sampling technique: determination of precision and calibration," Opt. Express **28**, 13482–13496 (2020).
28. K. Xu, M. Liu, and M. H. Arbab, "Broadband terahertz time-domain polarimetry based on air plasma filament emissions and spinning electro-optic sampling in GaP," Appl. Phys. Lett. **120** (2022).

29. P. C. M. Planken, H.-K. Nienhuys, H. J. Bakker, and T. Wenckebach, "Measurement and calculation of the orientation dependence of terahertz pulse detection in ZnTe," J. Opt. Soc. Am. B, JOSAB **18**, 313–317 (2001).
30. A. Rice, Y. Jin, X. F. Ma, *et al.*, "Terahertz optical rectification from xn–110-wz3bi zinc-blende crystals," Appl. Phys. Lett. **64**, 1324–1326 (1994).
31. H. Dong, Y. Gong, V. Paulose, and M. Hong, "Polarization state and Mueller matrix measurements in terahertz-time domain spectroscopy," Opt. Commun. **282**, 3671–3675 (2009).
32. H. Dong, Y. Gong, and M. Olivo, "Measurement of Stokes parameters of terahertz radiation in terahertz time-domain spectroscopy," Microw. Opt. Technol. Lett. **52**, 2319–2324 (2010).
33. J.-B. Masson and G. Gallot, "Terahertz achromatic quarter-wave plate," Opt. Lett. **31**, 265–267 (2006).
34. G. Zhao, G. Savini, Y. Yu, *et al.*, "A dual-port THz Time Domain Spectroscopy System optimized for recovery of a sample's Jones matrix," Sci. Rep. **9**, 1–9 (2019).
35. H. Chen, K. Wang, X. Chen, and G. Fang, "Real-time and calibration-free generalized terahertz time-domain spectroscopic ellipsometry," Appl. Phys. Lett. **124** (2024).
36. X. Chen, E. P. J. Parrott, Z. Huang, *et al.*, "Robust and accurate terahertz time-domain spectroscopic ellipsometry," Photonics Res. **6**, 768–775 (2018).
37. Z. Mazaheri, C. Koral, A. Andreone, *et al.*, "Terahertz time-domain ellipsometry: tutorial," J. Opt. Soc. Am. A, JOSAA **39**, 1420–1433 (2022).
38. T. Seifert, S. Jaiswal, U. Martens *et al.*, "Efficient metallic spintronic emitters of ultrabroadb and terahertz radiation," Nat. Photonics **10** (2016).
39. T. Seifert, S. Jaiswal, M. Sajadi, *et al.*, "Ultrabroadband single-cycle terahertz pulses with peak fields of 300 kv cm- 1 from a metallic spintronic emitter," Appl. Phys. Lett. **110**, 252402 (2017).
40. J. A. Fülöp, S. Tzortzakis, and T. Kampfrath, "Laser-Driven Strong-Field Terahertz Sources," Adv. Opt. Mater. **8**, 1900681 (2020).
41. Z. Feng, R. Yu, Y. Zhou, *et al.*, "Highly Efficient Spintronic Terahertz Emitter Enabled by Metal–Dielectric Photonic Crystal," Adv. Opt. Mater. **6**, 1800965 (2018).
42. R. I. Herapath, S. M. Hornett, T. S. Seifert, *et al.*, "Impact of pump wavelength on terahertz emission of a cavity-enhanced spintronic trilayer," Appl. Phys. Lett. **114** (2019).
43. P. Koleják, G. Lezier, D. Vala, *et al.*, "Maximizing the Electromagnetic Efficiency of Spintronic Terahertz Emitters," Adv. Photonics Res. **n/a**, 2400064 (2024).
44. M. Tong, Y. Hu, Z. Wang, *et al.*, "Enhanced Terahertz Radiation by Efficient Spin-to-Charge Conversion in Rashba-Mediated Dirac Surface States," Nano Lett. **21**, 60–67 (2021).
45. J. Hawecker, E. Rongione, A. Markou, *et al.*, "Spintronic THz emitters based on transition metals and semi-metals/Pt multilayers," Appl. Phys. Lett. **120** (2022).
46. P. Yadav, C. Xinhou, S. Bhatt, *et al.*, "Highly Efficient Spintronic Terahertz Emitter Utilizing a Large Spin Hall Conductivity of Type-II Dirac Semimetal PtTe2," Nano Lett. **24**, 2376–2383 (2024).
47. M. Mičica, A. Wright, P. Koleják, *et al.*, "Spintronic terahertz emitters with integrated metallic terahertz cavities," Nanophotonics (2024).
48. R. Rouzegar, A. L. Chekhov, Y. Behovits, *et al.*, "Broadband Spintronic Terahertz Source with Peak Electric Fields Exceeding 1.5 MV/cm," Phys. Rev. Appl. **19**, 034018 (2023).
49. S. Li, "Jones-matrix analysis with pauli matrices: application to ellipsometry," JOSA A **17**, 920–926 (2000).
50. C. Russell, L. Wai Sze Tiffany, and Y. Garam, *Polarized Light and Optical Systems* (CRC Press, Boca Raton, FL, USA, 2018).
51. O. Arteaga and A. Canillas, "Pseudopolar decomposition of the Jones and Mueller-Jones exponential polarization matrices," J. Opt. Soc. Am. A, JOSAA **26**, 783–793 (2009).
52. S. R. Cloude, "Uniqueness of Target Decomposition Theorems in Radar Polarimetry," in *Direct and Inverse Methods in Radar Polarimetry,* (Springer, Dordrecht, The Netherlands, 1992), pp. 267–296.
53. T. Vogel, A. Omar, S. Mansourzadeh, *et al.*, "Average power scaling of THz spintronic emitters efficiently cooled in reflection geometry," Opt. Express **30**, 20451–20468 (2022).
54. P. Kužel, H. Němec, F. Kadlec, and C. Kadlec, "Gouy shift correction for highly accurate refractive index retrieval in time-domain terahertz spectroscopy," Opt. Express **18**, 15338–15348 (2010).
55. P. Koleják, K. Postava, M. Mičica, *et al.*, "Experimental Gouy phase shift compensation in Terahertz time-domain spectroscopy," Photonics Nanostruct. Fundam. Appl. **31**, 129–133 (2018).
56. K. Postava, T. Yamaguchi, and R. Kantor, "Matrix description of coherent and incoherent light reflection and transmission by anisotropic multilayer structures," Appl. Opt. **41**, 2521–2531 (2002).
57. P. Koleják, D. Vala, K. Postava, *et al.*, "Mueller matrix ellipsometry of waveplates for control of their properties and alignment," J. Vac. Sci. Technol., B **38**, 014006 (2019).
58. I. Pupeza, M. Huber, M. Trubetskov, *et al.*, "Field-resolved infrared spectroscopy of biological systems," Nature **577**, 52–59 (2020).
59. D. Molter, J. Klier, S. Weber, *et al.*, "Two decades of terahertz cross-correlation spectroscopy," Appl. Phys. Rev. **8** (2021).
60. J. Kwon, K. H. Park, W. J. Choi, *et al.*, "Chiral Spectroscopy of Nanostructures," Acc. Chem. Res. **56**, 1359–1372 (2023).
61. E. Castro-Camus, "Polarization-Resolved Terahertz Time-Domain Spectroscopy," J. Infrared Milli. Terahz. Waves

33, 418–430 (2012).
62. D. K. George, A. V. Stier, C. T. Ellis, *et al.*, "Terahertz magneto-optical polarization modulation spectroscopy," J. Opt. Soc. Am. B, JOSAB **29**, 1406–1412 (2012).
63. M. Okano and S. Watanabe, "Anisotropic optical response of optically opaque elastomers with conductive fillers as revealed by terahertz polarization spectroscopy," Sci. Rep. **6**, 1–11 (2016).
64. D. J. Aschaffenburg, M. R. C. Williams, D. Talbayev, *et al.*, "Efficient measurement of broadband terahertz optical activity," Appl. Phys. Lett. **100** (2012).
65. W. J. Choi, G. Cheng, Z. Huang, *et al.*, "Terahertz circular dichroism spectroscopy of biomaterials enabled by kirigami polarization modulators," Nat. Mater. **18**, 820–826 (2019).
66. W. J. Choi, K. Yano, M. Cha, *et al.*, "Chiral phonons in microcrystals and nanofibrils of biomolecules," Nat. Photonics **16**, 366–373 (2022).
67. V. Lucarini, Y. Ino, K. Peiponen, and M. Kuwata-Gonokami, "Detection and correction of the misplacement error in terahertz spectroscopy by application of singly subtractive Kramers-Kronig relations," Phys. Rev. B (2005).
68. E. Vartiainen, Y. Ino, R. Shimano, *et al.*, "Numerical phase correction method for terahertz time-domain reflection spectroscopy," J. Appl. Phys. (2004).
69. S. Saito, N. Sekine, I. Hosako, and K. Sakai, "Phase shift measurement of the THz wave with laser displacement sensor," Int. Conf. on Infrared, Millimeter, Terahertz Waves (2008).
70. G. Lezier, P. Koleják, J.-F. Lampin, *et al.*, "Fully reversible magnetoelectric voltage controlled THz polarization rotation in magnetostrictive spintronic emitters on PMN-PT," Appl. Phys. Lett. **120** (2022).
71. O. Gueckstock, O. Gueckstock, L. Nádvorník, *et al.*, "Modulating the polarization of broadband terahertz pulses from a spintronic emitter at rates up to 10 kHz," Optica **8**, 1013–1019 (2021).
72. A. L. Chekhov, Y. Behovits, U. Martens, *et al.*, "Broadband Spintronic Detection of the Absolute Field Strength of Terahertz Electromagnetic Pulses," Phys. Rev. Appl. **20**, 034037 (2023).
73. E. Compain, S. Poirier, and B. Drevillon, "General and self-consistent method for the calibration of polarization modulators, polarimeters, and Mueller-matrix ellipsometers," Appl. Opt. **38**, 3490–3502 (1999).
74. E. Garcia-Caurel, A. D. Martino, J.-P. Gaston, and L. Yan, "Application of Spectroscopic Ellipsometry and Mueller Ellipsometry to Optical Characterization," Appl. Spectrosc. **67**, 1–21 (2013). PMID: 23317664.

Terahertz time-domain ellipsometry with spintronic emitters: Pauli coefficients as a superior alternative to Jones and Mueller matrices: supplemental document

1. COHERENT DESCRIPTION OF AN A-CUT UNIAXIAL ANISOTROPIC MATERIAL USING THE JONES MATRIX

In this section, we describe the transmission model for a polarimetric response of an A-cut uniaxial achiral anisotropic material using the Jones matrix $\tilde{\mathbf{J}}$[1]. The transmitted polarizations $\tilde{e}_{o,e}$ propagate along the ordinary and extraordinary directions in such material. We used the rotated Jones matrix for the material's optical axis rotation by an angle θ as follows

$$\tilde{\mathbf{J}} = \begin{pmatrix} \tilde{e}_o \cos^2\theta + \tilde{e}_e \sin^2\theta & (\tilde{e}_o - \tilde{e}_e)\cos\theta\sin\theta \\ (\tilde{e}_o - \tilde{e}_e)\cos\theta\sin\theta & \tilde{e}_o \sin^2\theta + \tilde{e}_e \cos^2\theta \end{pmatrix}, \tag{S1}$$

We further assume that the material has distinct ordinary and extraordinary complex refractive indices $\tilde{n}_o \neq \tilde{n}_e$, exhibiting both linear birefringence and dichroism in the form

$$\tilde{e}_o = \frac{4\tilde{n}_o}{(1+\tilde{n}_o)^2} \exp\left[-i\frac{2\pi\nu}{c}(\tilde{n}_o - 1)\tau\right] = \tilde{t}_o \exp\left(-d_o\right) \exp\left(-i\delta_o\right), \tag{S2}$$

$$\tilde{e}_e = \frac{4\tilde{n}_e}{(1+\tilde{n}_e)^2} \exp\left[-i\frac{2\pi\nu}{c}(\tilde{n}_e - 1)\tau\right] = \tilde{t}_e \exp\left(-d_e\right) \exp\left(-i\delta_e\right), \tag{S3}$$

where the amplitude factors $\tilde{t}_{o,e}$ represent the cumulative Fresnel transmission coefficients for a single pass through the air-to-crystal and crystal-to-air interfaces. The exponential term describes the propagation of terahertz radiation through the crystal's thickness τ. Parameter ν represents the terahertz frequency, and c denotes the speed of light in vacuum. Importantly, this formulation presupposes only direct transmission, excluding subsequent echoes. In this form, the measured waveform should contain only the initial pulse, as time-domain spectroscopy enables the separation of Fabry-Pérot reflections due to their distinct time delays.

Our main interest lies in the differences in phase and absorption between the polarization eigenmodes of the anisotropic crystal, specifically the retardation $\delta = \mathrm{Re}(2\pi\nu/c(\tilde{n}_e - \tilde{n}_o)\tau) = \delta_o - \delta_e$ and the diattenuation $d = \mathrm{Im}(2\pi\nu/c(\tilde{n}_e - \tilde{n}_o)\tau) = d_o - d_e$. We describe the ordinary and extraordinary refractive indices $\tilde{n}_{o,e}$ of quartz crystal using the Sellmeier model

$$\tilde{n}^2_{o,e}(\lambda) = \varepsilon_{o,e} + \sum_{j=1}^{N} \frac{B_j^{o,e}\lambda^2}{\lambda^2 - C_j^{o,e}} \tag{S4}$$

with $\varepsilon_{o,e}$ being the static permittivity, and $B_j^{o,e}$, $C_j^{o,e}$ corresponding to the oscillator strengths and the resonant wavelengths, respectively.

For Hg_2Cl_2 (calomel) crystal plate, we model the refractive indices $\tilde{n}_{o,e}$ using the Lorentz oscillator model

$$\tilde{n}^2_{o,e}(\omega) = \varepsilon_{o,e} + \sum_{j=1}^{N} \frac{A_j^{o,e}}{\omega_j^{o,e2} - \omega^2 - i\gamma_j^{o,e}\omega} \tag{S5}$$

where $A_j^{o,e}$, $\omega_j^{o,e}$, and $\gamma_j^{o,e}$ represent the amplitude, resonance frequencies, and damping factors, respectively.

2. MUELLER MATRIX OF A-CUT UNIAXIAL CRYSTAL

By transforming the Jones matrix $\tilde{\mathbf{J}}$ from (S1) into the Mueller matrix using the conversion (equation (2)), we derive the following analytical expression [2, 3].

$$\mathbf{M}_{\text{rotated}} = \begin{pmatrix} 1 & D\cos 2\alpha & D\sin 2\alpha & 0 \\ D\cos 2\alpha & \cos^2 2\alpha + A\sin^2 2\alpha\cos\delta & A\sin 2\alpha\,\cos 2\alpha\,(1-\cos\delta) & A\sin 2\alpha\,\sin\delta \\ D\sin 2\alpha & A\sin 2\alpha\,\cos 2\alpha\,(1-\cos\delta) & \sin^2 2\alpha + A\cos^2 2\alpha\,\cos\delta & -A\cos 2\alpha\,\sin\delta \\ 0 & -A\sin 2\alpha\,\sin\delta & A\cos 2\alpha\,\sin\delta & A\cos\delta \end{pmatrix}, \tag{S6}$$

where the coefficients D and A represent the differences between the ordinary and extraordinary attenuations

$$A = \frac{2|\tilde{t}_\text{o}|\,|\tilde{t}_\text{e}|\,\exp(-d)}{|\tilde{t}_\text{o}|^2 + |\tilde{t}_\text{e}|^2\,\exp(2d)}, \quad D = \frac{|\tilde{t}_\text{o}|^2 - |\tilde{t}_\text{e}|^2\,\exp(2d)}{|\tilde{t}_\text{o}|^2 + |\tilde{t}_\text{e}|^2\,\exp(2d)}. \tag{S7}$$

The first row and column of the Mueller matrix are scaled by the coefficient D, which corresponds directly to diattenuation. The submatrix $m_{2-4,2-4}$ includes trigonometric functions of retardation δ, while also being influenced by diattenuation through the parameter A, which diminishes as diattenuation d becomes more pronounced.

In the case of quartz, where attenuation is negligible ($d_\text{o} = d_\text{e} \to 0$) and the transmission coefficients are nearly identical ($\tilde{t}_\text{o} \approx \tilde{t}_\text{e}$), the values $D \to 0$ and $A \to 1$ yield a Mueller matrix of a wave plate. However, as diattenuation increases ($d \to \infty$), the coefficient $D = -1$, indicating maximal absorption of one polarization, while $A = 0$ signifies the complete attenuation of retardation, as one polarization is fully absorbed.

REFERENCES

1. H. Fujiwara, *Spectroscopic ellipsometry: principles and applications* (John Wiley & Sons, 2007).
2. J. N. Hilfiker, N. Hong, and S. Schoeche, "Mueller matrix spectroscopic ellipsometry," Adv. Opt. Technol. **11**, 59–91 (2022).
3. E. Garcia-Caurel, A. D. Martino, J.-P. Gaston, and L. Yan, "Application of Spectroscopic Ellipsometry and Mueller Ellipsometry to Optical Characterization," Appl. Spectrosc. **67**, 1–21 (2013). PMID: 23317664.

Paper VII

Effects of optical activity to Mueller matrix ellipsometry of composed waveplates

Daniel Vala, Pierre Koleják, Kamil Postava, Morten Kildemo, Pavlína Provazníková, Jaromír Pištora
Optics Express, **29/7** (2021)

VII

Research Article | Vol. 29, No. 7 / 29 March 2021 / Optics Express 10434
Optics EXPRESS

Effects of optical activity to Mueller matrix ellipsometry of composed waveplates

DANIEL VALA,[1,2,3,6] PIERRE KOLEJÁK,[1,2,4] KAMIL POSTAVA,[1,2,7] MORTEN KILDEMO,[3] PAVLÍNA PROVAZNÍKOVÁ,[5] AND JAROMÍR PIŠTORA[1]

[1]*IT4Innovations, National Supercomputing Center, VšB – Technical University of Ostrava, 17. listopadu 15, 708 00 Ostrava-Poruba, Czech Republic*
[2]*Faculty of Materials Science and Technology, VšB – Technical University of Ostrava, 17. listopadu 15, 708 33 Ostrava-Poruba, Czech Republic*
[3]*Department of Physics, NTNU Norwegian University of Science and Technology, NO-7491 Trondheim, Norway*
[4]*Institute of Electronics, Microelectronics and Nanotechnology, UMR 8520 CNRS, Cité Scientifique, Avenue Henri Poincaré CS 60069, 59 652 Villeneuve d'Ascq Cedex, France*
[5]*Meopta - Optika, s.r.o., Kabelíkova 1, 750 02 Přerov, Czech Republic*
[6]*daniel.vala@vsb.cz*
[7]*kamil.postava@vsb.cz*

Abstract: Mueller matrix ellipsometry has been used to precisely characterize quartz waveplates for demanding applications in the semiconductor industry and high precision polarimetry. We have found this experimental technique to be beneficial to use because it enables us to obtain absolute and precise measurement of retardation in a wide spectral range, waveplate orientation, and compound waveplate adjustment. In this paper, the necessity of including the optical activity in the Mueller matrix model and data treatment is demonstrated. Particularly, the optical activity of the quartz influences the adjustment of misalignment between the perpendicularly oriented waveplates of the compound biplate. We demonstrate that omitting the optical activity from the model leads to inaccurate values of the misalignment. In addition, the depolarization effects caused by a finite monochromator bandwidth is included in the model. Incorporation of the optical activity to the Mueller matrix model has required a development of rigorous theory based on appropriate constitutive equations. The generalized Yeh's matrix algebra to bianisotropic media has been used for the calculation of the eigenmodes propagation in chiral materials with reduced symmetry. Based on the applied method, the authors have proposed approximated analytical form of the Mueller matrix representing optically active waveplate and biplate and provided discussion on the analytical and numerical limits of the method.

© 2021 Optical Society of America under the terms of the OSA Open Access Publishing Agreement

1. Introduction

Waveplates are polarization optical components with a broad field of applicability across the semiconductor industry [1,2], quality inspection in manufacturing processes [3,4], THz spectroscopy [5,6], analytical chemistry [7–9] and polarimetry [10–13]. From a polarimetric point of view, the waveplates are commonly used in optical spectrometers as compensators [14]. It is no exception to use the waveplates during high-precision-demanding procedures like calibration of various custom experimental setups [15–18]. Then, the quality of the used waveplates directly affects the quality of acquired data [19–24] and above mentioned industrial technological properties.

Typically, industrial inspection of manufactured waveplates is based on a configuration with two crossed polarizers and the waveplate being placed between them [25]. The method determines the orientation of the waveplate fast-axis and its single-wavelength relative retardation. The

#418186 https://doi.org/10.1364/OE.418186
Journal © 2021 Received 22 Dec 2020; revised 14 Feb 2021; accepted 23 Feb 2021; published 18 Mar 2021

Optics EXPRESS

waveplate retardation is given as the difference between phases of two orthogonal linearly polarized eigenmodes propagating through the plate [26,27]. Waveplates of higher order exhibit high chromatic dispersion, however, broadly used zero-order waveplate would be undesirably thin. To overcome this inconvenience, the waveplates are composed by two thicker higher order plates with crossed optical axes [28], so called biplates. However, this method may be insufficient nowadays, as the users demands on the waveplates precision fabrication raises significantly. Therefore, precise characterization of the composed waveplates in order to obtain the parameters of each of the constituting waveplate can be challenging, and proper treatment has to be established as various non-trivial effects may come to raise.

In our previous paper [29] we have shown the advantage of complete Mueller matrix inspection and we have demonstrated that spectral characterization and industrial inspection of waveplates requires the inclusion of the depolarization effects [30–32]. The Mueller calculus and Mueller matrix spectroscopic ellipsometry is a particularly advantageous [10] method for proper waveplate analysis as it is spectroscopic, non-destructive, and capable of incorporating all the mentioned phenomena due to high experimental precision [33,34]. In Ref. [29] we have also shown the presence of the nonzero circular birefringence related to optical activity (OA) using the Lu-Chipman decomposition [35] of the quartz waveplates experimental data.

In this article, the Mueller matrix spectroscopic ellipsometry in transmission configuration is used for precise quartz single waveplate and quartz waveplate biplates characterization. We exclusively measure the waveplates aligned with the optical axis perpendicular to the propagation direction and we demonstrate, that the effect of the OA can not be neglected to process the experimental data correctly. In studies [36,37], Mueller matrix ellipsometry was applied to study waveplate multiplets. Its model simplicity has an advantage in the calibration procedures involving the waveplates including their misalignment error. As long as the method doesn't account for the OA dispersion in the waveplates, the net elliptical properties of the waveplate effectively project into other waveplate characteristics causing their quasi-oscillatory behaviour. Therefore, we derived a rigorous model of the Mueller matrix including the gyration effects from the theory based on Fedorov's [38,39] and Yeh's [40] work and the Condon-Fedorov's constitution relations [38,41]. The rigorous model including the OA is compared to the experimental data for single waveplates and biplates. We further show, that the OA effect is separable and independent of other waveplate (biplates) characteristics like plates misalignment. All those parameters are obtained with very high numerical precision and great fit stability.

The paper is structured as follows: In Sec. 2, the rigorous Mueller matrix models for optically active single waveplates and waveplate biplates are derived. Section 3 describes the biplate samples and experimental configuration. Measurement analysis is divided into two steps. First of all, we model the parameters of single waveplates to use them during the biplate analysis afterwards in order to obtain precise biplate parameters including their misalignment. To demonstrate the necessity of using a Mueller matrix model with OA, we compare the experimental data with the models with and without OA. To understand the OA contribution in the Mueller matrix, in Appendix A., we generalize the standard Yeh's matrix algebra to bianisotropic and optically active media using various constitutive relation formalism, and in particular, eigenmodes for uniaxial chiral media are calculated in Appendix B.. Detailed derivation of the proposed Mueller matrix form is given in Appendix C.. In Appendix D., we offer an algebraic analysis on the manifestation difference between the misalignment and the OA in the proposed Mueller matrices.

2. Mueller matrices of waveplates including optical activity

Mueller matrix represents the complete polarimetric information, which can be acquired from the interaction between the sample and the polarized light, including depolarizations.

Optics EXPRESS

2.1. Mueller matrix of a standard linear retarder

The reduced 4×4 Mueller matrix (all elements are divided by M_{11}) describing a single waveplate consisting of a uniaxial anisotropic material with the optical axis parallel to the waveplate surface at the normal incidence (linear retarder) is given [14] as

$$\mathbf{M}_{\mathrm{R,LIN}}(\varphi,\,\Gamma) = \begin{bmatrix} 1 & 0 & 0 & 0 \\ 0 & \cos^2 2\varphi + \cos\Gamma \sin^2 2\varphi & (1-\cos\Gamma)\sin 2\varphi \cos 2\varphi & -\sin 2\varphi \sin\Gamma \\ 0 & (1-\cos\Gamma)\sin 2\varphi \cos 2\varphi & \sin^2 2\varphi + \cos\Gamma \cos^2 2\varphi & \cos 2\varphi \sin\Gamma \\ 0 & \sin 2\varphi \sin\Gamma & -\cos 2\varphi \sin\Gamma & \cos\Gamma \end{bmatrix}, \tag{1}$$

where φ is the azimuthal angle between the waveplate fast-axis and the vertical laboratory coordinate, and

$$\Gamma(\lambda) = \frac{2\pi}{\lambda}\left[n_{\mathrm{f}}(\lambda) - n_{\mathrm{s}}(\lambda)\right] d, \tag{2}$$

is the retardation angle between the fast and slow eigenmodes propagating in the waveplate with the refractive indices $n_{\mathrm{f,s}}$, which is dependent on the wavelength λ and the waveplate thickness d. Normally, the fast and slow eigenmodes correspond to linearly polarized eigenmodes propagating with ordinary and extraordinary refractive indices $n_{\mathrm{e,o}}$, respectively.

2.2. Mueller matrix of a single waveplate with optical activity

Natural or synthetic quartz monocrystal is very common material for the waveplate manufacturing. It belongs to uniaxial trigonal crystal symmetry [42,43] (Hermann-Maugin 32 point group) and is therefore optically active [44–46]. Across the literature, the effect of the OA in quartz (or quartz waveplates) has been studied in the configuration with the quartz optical axis being parallel (z-cut) to the direction of propagation [47] so far. Usually, the effect of the OA with optical axis perpendicular to the propagation direction is said to be experimentally negligible [48], which is inadequate for waveplate precise quality and properties control.

In our preceding work [29], the presence of non-zero circular birefringence was discovered using Lu-Chipman decomposition of experimental Mueller matrix, which we interpreted as the presence of the OA. Rigorous incorporation of the OA in waveplates requires (i) a solution of Maxwell equations based on a proper set of material equations introducing the gyration tensors $\hat{\alpha}$ and $\hat{g}$ with respect to the 32 point group which leads to the wave equation of the problem. Definition of the constitutive equations and a detailed discussion of suitability of various approaches is given in Appendix A., (ii) calculation of generally elliptical eigenmodes propagating in the waveplate based on the wave equation evaluation (see Appendix B.), (iii) derivation of Mueller matrix including the OA as a function of the chirality parameter

$$\kappa = \frac{1}{2G}\left[\left(n_{\mathrm{e}}^2 - n_{\mathrm{o}}^2\right) - \sqrt{\left(n_{\mathrm{e}}^2 - n_{\mathrm{o}}^2\right)^2 + 4G^2}\right], \tag{3}$$

where the spectrally dependent scalar gyration parameter G for our configuration is given by the gyration tensor component g_{11} derived in [47],

$$G = g_{11} = \frac{A_1 \lambda^3}{\left(\lambda^2 - B_1^2\right)^2}. \tag{4}$$

In this Section, we show the model of the Mueller matrix including the OA effect from the Jones matrix of an elliptical retarder, see Appendix C., Eq. (33). Eigenmodes propagating through a medium described by Eq. (33) are ellipticaly polarized and are propagating with corresponding

Optics EXPRESS

refractive indices. Since the effect of the OA is very small, the elliptical eigenmodes can be approximated as linear-like eigenmodes. Therefore, it is justifiable to linearly approximate κ, as long as it is a function of eigenmodes ellipticity, see Appendix C., Eq. (34). Moreover, the indices of refraction of the linear-like eigenmodes become equal with high precision to ordinary and extraordinary indices of refraction, respectively, see Appendix C., Eq. (31). The Mueller matrix of an elliptic retarder $\mathbf{M}_{\mathrm{R,EL}}(\varphi,\,\Gamma,\,\kappa)$ is in the linear approximation in the form

$$\mathbf{M}_{\mathrm{R,EL}}(\varphi,\,\Gamma,\,\kappa) = \mathbf{M}_{\mathrm{R,LIN}}(\varphi,\,\Gamma) + \mathbf{\Delta M}_{\mathrm{OA}}(\varphi,\,\Gamma,\,\kappa)\,, \tag{5}$$

where

$$\mathbf{\Delta M}_{\mathrm{OA}}(\varphi,\,\Gamma,\,\kappa) = \begin{bmatrix} 0 & 0 & 0 & 0 \\ 0 & 0 & 2\kappa\sin\Gamma & 4\kappa\cos 2\varphi\sin^2\frac{\Gamma}{2} \\ 0 & -2\kappa\sin\Gamma & 0 & 4\kappa\sin 2\varphi\sin^2\frac{\Gamma}{2} \\ 0 & 4\kappa\cos 2\varphi\sin^2\frac{\Gamma}{2} & 4\kappa\sin 2\varphi\sin^2\frac{\Gamma}{2} & 0 \end{bmatrix}, \tag{6}$$

is the matrix describing the effect of the OA by introducing linearly approximated chirality parameter κ.

In our approximation, we treat the quantity κ as a real parameter. This is in a conformity with the usual quartz waveplates application range over its transparent region. The Jones matrix (33) is valid generally for any of the parameter being complex, in contrast with the Mueller matrix (5). This is due to the form (Kronecker product) of the transformation Eq. (36). Therefore, in the vicinity of absorption bands, the Eq. (5) must be calculated assuming complex κ. The measurements over this spectral region is out of the scope of the paper and will not be further elaborated.

The experimental validity condition of the linear approximation is obtained by analyzing the quadratic (erroneous) terms in the Taylor series of $\mathbf{\Delta M}_{\mathrm{OA}}$ focused on the maximal possible error. The criterion is then set to $8\kappa^2<\sigma$, where σ stands for an error of the experimental Mueller matrix elements. Note, that in our experimental configuration, $\sigma = 0.001$ implies the condition for $\kappa<0.0112$. This criterion is fulfilled for the quartz waveplates [47] in the spectral range of further shown experiments.

The non-approximated matrix $\mathbf{M}_{\mathrm{R,EL}}$ stands for an equivalent solution with Mueller matrices of an elliptical retarder presented in [49] [Eq. (22)], in Ref. [50] [Eq. (14)] or on page 289 in Ref. [51]. Our proposed solution applied to the subject discussed in this paper provides the opportunity to have deeper physical insight into the problematic and to get more intuitive way of the result interpretation and discussion, as we show later. Also, in contrast with Eq. (22) in Ref. [49], we reduce the number of needed fitting parameters.

2.3. Mueller matrix of a biplate

The Mueller matrix for a biplate given by the product of Mueller matrices $\mathbf{M}_{\mathrm{R,EL1}}$, $\mathbf{M}_{\mathrm{R,EL2}}$ each representing a standalone waveplate with its own retardation Γ_1, Γ_2, respectively, and azimuthal angle φ_1, φ_2, respectively, is in the form

$$\mathbf{M}_{\mathrm{R,WB}} = \mathbf{M}_{\mathrm{R,EL2}}(\varphi_2,\,\Gamma_2,\,\kappa)\,\mathbf{M}_{\mathrm{R,EL1}}(\varphi_1,\,\Gamma_1,\,\kappa)\,. \tag{7}$$

Each waveplate is manufactured from the same material, therefore we assume the same optical activity dispersion, $\kappa_1 = \kappa_2 = \kappa$.

Note, that from now on, we will focus on the 3×3 Mueller submatrix $M_{22}\ldots M_{44}$ only, due to the structure of (1) and above discussed Mueller matrices.

Optics EXPRESS

3. Measurements and data processing

We applied spectral ellipsometric measurements using the dual rotating compensator Mueller matrix ellipsometer RC2-DI from Woollam company, which measures a full Mueller matrix in the spectral range from 0.74 to 6.42 eV (wavelength ranging from 193 to 1700 nm). The waveplates are measured in the normal-incidence transmission geometry.

We have investigated biplates consisting of a stack of two c-cut right-handed synthetic α-quartz high-order waveplates belonging to the 32 point group. The biplate constituting waveplates are attached to each other, having its fast axes mutually perpendicular, by perfectly polished surfaces, and therefore hold together only by the presence of Van der Waals forces. This fact allows us to split the biplate without causing damage, and measure each waveplate of the biplate separately to obtain its accurate parameters (thicknesses, retardation angles).

3.1. Single waveplate measurements

The measurements of both single waveplates constituting the biplate were performed in the normal incident transmission configuration for all azimuthal angles from 0° to 360° by the angle step of 5°. Figure 1 shows typical spectra (black curves) of the Mueller 3×3 submatrix for the high-order single waveplate. The oscillations correspond to the spectrally dependent wavelength retardation. The waveplate order m (e.g. $m = 9$ for $\lambda = 500$ nm) determines the oscillations density, which gets denser with increasing photon energy, while the oscillations amplitude decreases. The decreasing amplitude modulation for high photon energy is due to the dense oscillations spectral averaging caused by a finite monochromator bandwidth [52,53]. In our case, this corresponds to the spectral resolution of dispersion grating and finite pixel size of the CCD detector. The attenuation compensation is based on the incoherent summation of Mueller matrix model, which is commented in our preceding work (Eqs. (3) and (4) in [29]) in the detail. The spectral step we use in the averaging function is $\delta\lambda = 1.075$ nm.

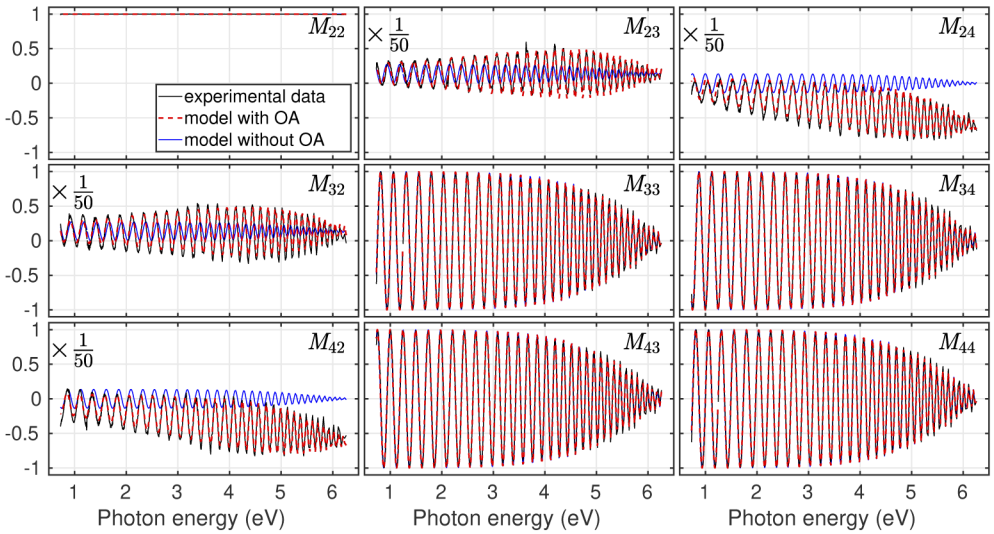


Fig. 1. Mueller 3×3 submatrix of the single waveplate of thickness $d_1 = 536.63\,\mu$m at the azimuthal angle $\varphi_1 = 180.078°$. The data are compared to the model of standard linear retarder (without the effect of OA) and to the model including the OA effect. Model with the OA effect disregarded is not capable to properly describe both the dispersion and the attenuation exhibiting in the first row and the first column of the Mueller submatrix off-diagonal elements. Note, that the axes of those Mueller matrix elements are scaled by the factor of $1/50$.

Optics EXPRESS

The data are compared to the model (1) including spectral averaging (blue curve) over high energy spectral range and shows a relatively good fit of the Mueller matrix elements M_{33}, M_{34}, M_{43}, M_{44}. For azimuthal rotations, for which the waveplate has its axes nearly perfectly aligned with the laboratory coordinate system, the oscillation amplitude within the measured elements M_{23}, M_{24}, M_{32}, M_{42} decreases with decreasing photon energy over low energy spectral ranges. Together with the modulation of the oscillations dispersion within these elements, it corresponds to the effect of the optical activity dispersion in the quartz waveplate. To properly fit all the elements of the Mueller submatrix, we model the influence of OA (red curve) using (5) with the spectral averaging included. The parameters $A_1 = 0.0277$ nm, $B_1 = 105.6$ nm of (4) are taken from Ref. [47]. The fitted thicknesses for each waveplate are $d_1 = 536.63$ μm, $d_2 = 549.03$ μm, and absolute retardations were obtained. The dispersion of n_o, n_e are taken from Ref. [54,55]. Note, the OA effects are very small in comparison with the linear retardation, therefore M_{23}, M_{24}, M_{32}, M_{42} Mueller matrix elements are expanded 50 times. Despite the fine effect of the OA, the response in the measured Mueller matrix is well detectable and shows high sensitivity of the proposed method.

3.2. *Fine control of waveplate biplate misalignment*

Biplate consists of two high-order waveplates with crossed optical axes to produce an effective low-order waveplate. Possible imperfections during the biplates manufacturing can introduce a misalignment between the waveplates, as they may not be aligned to each other with their optical axes being perfectly perpendicular, see Fig. 2. The misalignment between the waveplates is then defined as

$$\Phi = \varphi_1 - \varphi_2 - 90^\circ. \tag{8}$$

We have shown [29], that Mueller matrix approach is significantly sensitive to the waveplate misalignment. In this Section, we propose a robust and sensitive inspection method for the biplate misalignment determination based on a rigorous Mueller matrix model including OA.

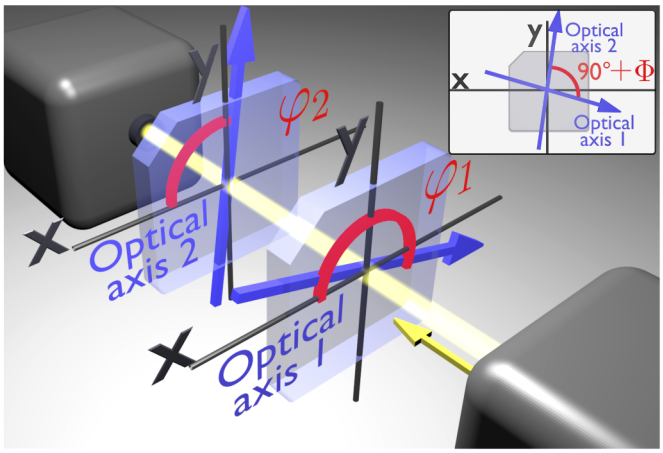


Fig. 2. Schematic configuration of the waveplates constituting the biplate. Their optical axes are ideally perpendicular, $\varphi_1 - \varphi_2 = 90^\circ$. The manufacture inaccuracy causes the deviation from this perpendicularity, and introduces the missalignment Φ, as shows the inset figure.

To simulate the misalignment between the waveplates of the biplate, one waveplate was placed fixed to the ellipsometer sample holder, while the second waveplate was rotated around the relative angle of 90° between the waveplates.

Optics EXPRESS

Figure 3 shows the Mueller submatrix spectra of the biplate with controlled φ_1 (and therefore controlled Φ) ranging from 185.7° to 186.1° with step 0.1° (Φ is ranging from −0.2° to 0.2° with step 0.1°). The Mueller 3 × 3 submatrix (right part of the Fig. 3) shows the dominant effect of the linear retardation dispersion without the dense spectral oscillations, which are typical for high-order waveplates. The presence of minor oscillations corresponds to combination of the misalignment between waveplates of the biplate and its optical activity. Left part of Fig. 3 shows the detail of the Mueller submatrix first column. Each curve of the same color corresponds to different φ_1, and therefore to different misalignment. First, the data are compared to the Mueller matrix model of the cascade of two standard linear retarders (7) without including the OA (blue lines), $\kappa = 0$, which is insufficient for the proper analysis of the misalignment between two waveplates. In contrast, the model (7) including the OA (red lines), $\kappa \neq 0$, shows very good fit of the measured data. The slight mismatch from the data is just above experimental error of the Mueller matrix elements (0.001). At this scale, the errors are inevitable. They could origin in the calibration quality, systematic errors, non-ideal plates parallelity, waveplate miscut or precision of used material dispersion parameters. The parameters $A_1 = 0.0277$ nm, $B_1 = 105.6$ nm of (4) are taken from Ref. [47], and the waveplate thicknesses ($d_1 = 536.63\,\mu$m, $d_2 = 549.03\,\mu$m), and retardation dispersions were determined from the measurements of each of the separated waveplates. The fitted parameters φ_1 and φ_2 were obtained from the fit of each biplate measurement independently. The Fig. 4 shows the waveplate misalignment obtained for the data fitted to Eq. (8) point by point. The fitted values of φ_1, φ_2 and Φ corresponding to each curve in Fig. 3 are shown in Table 1.

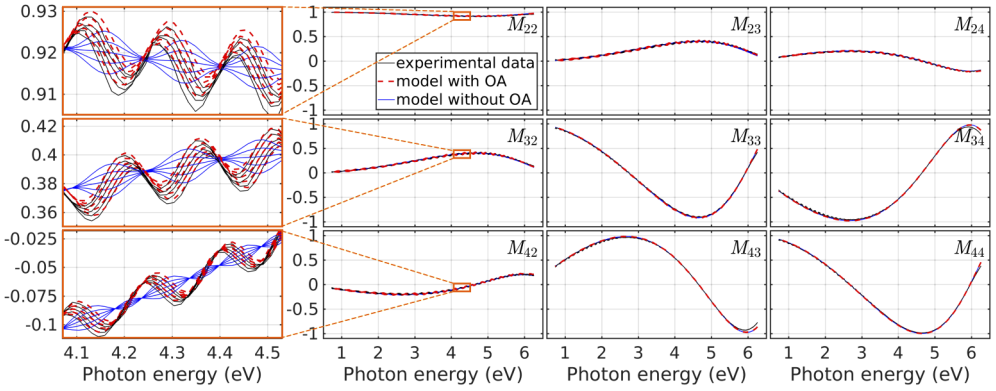


Fig. 3. Experimental Mueller submatrix for biplate. Each curve of the same color represents different value of φ_1 ranging from 185.7° to 186.1° with step 0.1°. Comparison between data and models with and without the effect of the OA shows the significance of the the OA phenomenon in proper determination of the misalignment, which is exhibited by the presence of the minor oscillation shown in the detail of the submatrix first column. Note, that the energy range from 4.1 eV to 4.5 eV corresponds to the wavelength range from 302.4 nm to 275.5 nm.

Table 1. Fitted values of φ_1, φ_2 and Φ for representative Mueller submatrix spectra shown in Fig. 3.

φ_1 (degree)	185.711	185.812	185.912	186.015	186.116
φ_2 (degree)	95.930	95.931	95.932	95.934	95.936
Φ (degree)	−0.218	−0.119	0.019	0.080	0.179

Figure 4(b) demonstrates the misalignment fit stability. Each point was calculated as a subtraction of the misalignment from consequent values during one waveplate azimuthal rotation.

Optics EXPRESS

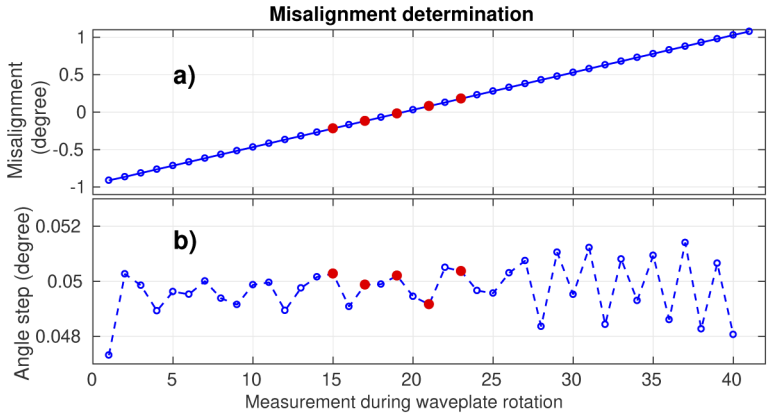


Fig. 4. a) Fitted values of the misalignment for each measurement with various azimuthal rotations of the waveplates. b) Fit stability of the misalignment determination is demonstrated comparing the calculated angle steps to the nominal value of 0.05°. Red points correspond to selected measurements presented in Fig. 3.

The mean value of the angle step corresponds well with the actual experimental angle step of 0.05°, which shows high stability of the misalignment determination without any correlation to the optical activity. Red points demonstrate selected measurements presented in Fig. 3.

Ultimately, it is important to mention, that excluding the presence of the OA from the model is leading to the misinterpretation of the OA with incorrect misalignment values. We show the linear expansion of the Mueller matrix of biplate (7) for both the misalignment (Φ) and the OA (κ) in Appendix D. to understand the significant difference between oscillations induced by κ and Φ. Both misalignment (45) and OA (46) dispersions have similar behavior in the form of minor oscillations shown in Fig. 3. These oscillations origin in the high-density trigonometric terms including only the retardation Γ_1 or Γ_2. If one tries to fit the data using the model without the OA (demonstrated for our case), the misalignment of around 0.5° will tend to compensate the OA with its amplitude. Nonetheless, such model does not match the data over the whole spectral range, because κ has spectral dependence given by Eq. (4), and thus, the amplitude of the oscillations changes. Such model without the OA also results in erroneous waveplate thicknesses, because the terms of $\mathbf{m}_\kappa$ and $\mathbf{m}_\Phi$ matrices are defined by terms in cosines or sines of the waveplates retardation. It is curious, that sine terms of one matrix correspond to appropriate cosine terms of second matrix and vice versa. Therefore, the fit without the OA will result in thicknesses imperfections for both waveplates by 6.4 μm to compensate the phase shift. However, their thickness difference remains the same due to the major influence of the linear retarder (1). It results in the fact, that low-density trigonometric terms of the retardation difference $\Gamma_1 - \Gamma_2$ are not able to be compensated and thus make significant difference in the spectrum. Nevertheless, the sine and cosine terms are not only shifted one from another, but they also represent different functions which do not match the data, especially if both misalignment and the OA influence are present.

4. Conclusion

In this article, biplates represented by a couple of high-order waveplates with crossed optical axes have been measured by means of Mueller matrix ellipsometry in the spectral range from 193 to 1700 nm. In order to obtain accurate values of biplate parameters including the biplate misalignment, we theoretically revealed and experimentally confirmed, that it is necessary to include the effects of the optical activity into the derived model of Mueller matrix. To obtain the

Optics EXPRESS

exact solution of the Mueller matrix, it is needed to find the eigenmodes and propagation constants of the optically active medium represented by the quartz waveplate in this case. We emphasize, that omitting the optical activity from the model would lead to the incorrect interpretation of the optical activity phenomenon with the inaccurate values of the waveplate misalignment.

We believe, that the proposed method, which has an advantage in its great experimental sensitivity, fit stability and repeatability, could stand as a fast non-destructive industrial analysis for the accurate in-situ control of the biplates misalignment during the manufacturing process. Moreover, the concept based on the rigorous model can be extended for the analysis of the waveplate multiplets. In addition, waveplates parameters obtained from precise Mueller matrix characterization can be further used for the accuracy improvement of calibration procedures of various experimental setups involving waveplates and Mueller calculus based calibration procedures.

A. Wave equation in chiral media

A.1. Covariant form of Maxwell equations

In the following, the plane monochromatic wave is described by the electric field in the form

$$\mathbf{E} = \mathbf{E}_0\, e^{i(\omega t - \mathbf{k}\cdot\mathbf{r})}, \tag{9}$$

where ω is the angular frequency and $\mathbf{k}$ is the wave vector related to the refraction vector $\mathbf{N}$ using the wave number in a vacuum $k_0 = \omega/c$, where c is the light speed in a vacuum, as

$$\mathbf{k} = k_0\mathbf{N}. \tag{10}$$

The curl Maxwell equations for the monochromatic plane waves (9) relating the electric and magnetic fields $\mathbf{E}_0$, $\mathbf{H}_0$ to its displacements $\mathbf{D}_0$, $\mathbf{B}_0$, respectively, can be written in the covariant form

$$\mathbf{N}^{\times}\mathbf{E}_0 = c\mathbf{B}_0, \tag{11a}$$

$$\mathbf{N}^{\times}\mathbf{H}_0 = -c\mathbf{D}_0, \tag{11b}$$

$$c = \frac{1}{\sqrt{\varepsilon_0\mu_0}}, \tag{11c}$$

where ε_0 and μ_0 are the permittivity and permeability in a vacuum, respectively, and

$$\mathbf{N}^{\times} = \begin{bmatrix} N_x \\ N_y \\ N_z \end{bmatrix}^{\times} \equiv \begin{bmatrix} 0 & -N_z & N_y \\ N_z & 0 & -N_x \\ -N_y & N_x & 0 \end{bmatrix} = \frac{1}{k_0}\begin{bmatrix} 0 & -k_z & k_y \\ k_z & 0 & -k_x \\ -k_y & k_x & 0 \end{bmatrix}. \tag{12}$$

The direction of wave propagation is given by the wave vector $\mathbf{k} = k_0 \left[N_x\ N_y\ N_z\right]^{\mathrm{T}}$, and a set of constitutive relations must be chosen.

For a general anisotropic gyrotropic (bianisotropic) and magnetic media, various forms of constitutive equations have been developed [56] and compared to each other [57,58]. Nowdays, Tellegen [59] and Condon-Fedorov [38,41] material equations seem to be the most convenient and acceptable form of constitutive relations.

Optics EXPRESS

A.2. Tellegen constitutive relations

Tellegen relations take the form

$$\mathbf{D}_0 = \hat{\varepsilon}\mathbf{E}_0 + \hat{\xi}\mathbf{H}_0, \tag{13a}$$

$$\mathbf{B}_0 = \hat{\mu}\mathbf{H}_0 + \hat{\zeta}\mathbf{E}_0\,. \tag{13b}$$

The material tensors are in the form

$$\hat{\varepsilon} = \varepsilon_0\hat{\varepsilon}_\mathrm{r}, \tag{14a}$$

$$\hat{\mu} = \mu_0\hat{\mu}_\mathrm{r}, \tag{14b}$$

where $\hat{\varepsilon}_\mathrm{r}$, $\hat{\mu}_\mathrm{r}$ are the relative permittivity and the relative permeability tensors, respectively, and $\hat{\xi}$, $\hat{\zeta}$ are general second-rank coupling tensors, where we use the convention [60]

$$\hat{\xi} = (\hat{\nu} + i\hat{\eta})\sqrt{\varepsilon_0\mu_0}, \tag{15a}$$

$$\hat{\zeta} = \left(\hat{\nu} - i\hat{\eta}^\mathrm{T}\right)\sqrt{\varepsilon_0\mu_0}. \tag{15b}$$

Parameter $\hat{\nu}$ is related with the reciprocity of the medium, while $\hat{\eta}$ describes the optical activity. Substituting (13) into (11) and eliminating $\mathbf{H}_0$, the wave equation for $\mathbf{E}_0$ in the most general form is obtained:

$$\left[c^2\hat{\varepsilon} + \mathbf{N}^\times\hat{\mu}^{-1}\,\mathbf{N}^\times + c\left(\hat{\xi}\hat{\mu}^{-1}\mathbf{N}^\times - \mathbf{N}^\times\hat{\mu}^{-1}\hat{\zeta}\right) - c^2\hat{\xi}\mu^{-1}\hat{\zeta}\right]\mathbf{E}_0 = 0, \tag{16}$$

which represents a matrix form of the wave equation and can be implemented in the standard Yeh's matrix formalism to calculate reflection, transmission and wave-guided phenomena of multilayered structure.

A.3. Condon-Fedorov constitutive relations

For reciprocal chiral media ($\hat{\nu} = 0$, $\hat{\eta} \neq 0$) a set of Condon-Fedorov constitutive relations is commonly used:

$$\mathbf{D}_0 = \hat{\varepsilon}\mathbf{E}_0 + \frac{1}{c}i\hat{\alpha}\mathbf{H}_0, \tag{17a}$$

$$\mathbf{B}_0 = \hat{\mu}\mathbf{H}_0 + \frac{1}{c}i\hat{\beta}\mathbf{E}_0, \tag{17b}$$

where the tensors $\hat{\alpha}$ and $\hat{\beta}$ are the second-rank tensors describing the effect of optical activity. Applying the Onsager-Casimir principle [61–63] on Eq. (17) [64], the Condon-Fedorov equations can be rewritten [65] in the commonly used form as

$$\mathbf{D}_0 = \hat{\varepsilon}\mathbf{E}_0 + \frac{1}{c}i\hat{\alpha}\mathbf{H}_0, \tag{18a}$$

$$\mathbf{B}_0 = \hat{\mu}\mathbf{H}_0 - \frac{1}{c}i\hat{\alpha}^\mathrm{T}\mathbf{E}_0, \tag{18b}$$

where $\hat{\alpha}$ is the optical activity pseudotensor [48,57]. Using the same procedure as previously and using (11c), the equivalent wave equation is derived [48,66]:

$$\left[\hat{\varepsilon}_\mathrm{r} + \mathbf{N}^\times\hat{\mu}_\mathrm{r}^{-1}\,\mathbf{N}^\times + i\left(\hat{\alpha}\hat{\mu}_\mathrm{r}^{-1}\mathbf{N}^\times + \mathbf{N}^\times\hat{\mu}_\mathrm{r}^{-1}\hat{\alpha}^\mathrm{T}\right) - \hat{\alpha}\hat{\mu}_\mathrm{r}^{-1}\hat{\alpha}^\mathrm{T}\right]\mathbf{E}_0 = 0, \tag{19}$$

and following tensor identity is valid [38]:

$$\hat{\alpha}\hat{\mu}_\mathrm{r}^{-1}\mathbf{N}^\times + \mathbf{N}^\times\hat{\mu}_\mathrm{r}^{-1}\hat{\alpha}^\mathrm{T} \equiv (\hat{g}\,\mathbf{N})^\times\,. \tag{20}$$

The wave equation is then in the form

$$\left[\hat{\varepsilon}_\mathrm{r} + \mathbf{N}^\times\hat{\mu}_\mathrm{r}^{-1}\,\mathbf{N}^\times + i\,(\hat{g}\,\mathbf{N})^\times\right]\mathbf{E}_0 = 0. \tag{21}$$

Special case for bi-gyrotropic media was described in Ref. [67].

Optics EXPRESS

A.4. Born-Landau constitutive equations

Equation (20) stands for a definition of the gyration tensor $\hat{g} = g_{ij}$, which describes the optical activity effect in Born-Landau [68] constitutive relations

$$\mathbf{D}_0 = \hat{\varepsilon}\mathbf{E}_0 + i\varepsilon_0\mathbf{G}\times\mathbf{E}_0 = \left(\hat{\varepsilon} + i\varepsilon_0\mathbf{G}^{\times}\right)\mathbf{E}_0, \tag{22a}$$

$$\mathbf{B}_0 = \hat{\mu}\,\mathbf{H}_0\,, \tag{22b}$$

where $\mathbf{G} = \hat{g}\mathbf{N}$ is the gyration vector related with scalar gyration parameters

$$G = g_{ij}l_il_j = g_{11}l_1^2 + g_{22}l_2^2 + g_{33}l_3^2 + (g_{12}+g_{21})\,l_1l_2 + (g_{13}+g_{31})\,l_1l_3 + (g_{23}+g_{32})\,l_2l_3, \tag{23}$$

and l_i, l_j are directional cosines of the wave normal with respect to the coordinate system given by a triad of unit vectors c_i,

$$l_i \equiv \cos\left(\measuredangle N_i\, c_i\right). \tag{24}$$

A.5. Relation between the constitutive equations for optically active media

By the comparison of (15) with (18) we can see, that Condon-Fedorov equations are a special case of Tellegen material relations for *reciprocal chiral* media:

$$\hat{\xi} = \frac{1}{c}i\hat{\eta} \leftrightarrow \frac{1}{c}i\hat{\alpha}, \tag{25a}$$

$$\hat{\zeta} = -\frac{1}{c}i\hat{\eta}^{\mathrm{T}} \leftrightarrow -\frac{1}{c}i\hat{\alpha}^{\mathrm{T}}. \tag{25b}$$

Here, we justly state, that Condon-Fedorov and Born-Landau approaches are not fully equivalent. We strongly recommend the kind reader to see the detailed discussion in Ref. [69]. However, for our particular case of transparent waveplates, both constitutive equations can be applied. Moreover, within our (and generally achievable) experimental precision, the difference is negligible and these two approaches can be used in the equivalent way providing the same results for any, even absorbing material [69].

B. Eigenmodes propagating in chiral uniaxial media of point group 32

The manifestation of the OA for light propagation along the optical axis of nonmagnetic uniaxial gyrotropic media of 32 point group (i.e. quartz) is well-known fact. We emphasize, that the OA effect in quartz is given intrinsically because of its non-centrosymmetricity. Also, the OA has similar size along the principal axes of $\hat{\alpha}$ (or $\hat{g}$) [47], and is therefore non-negligible within the precision of contemporary Mueller matrix ellipsometry. Concluding, the OA is present in all possible experimental configurations (or cuts) of the quartz plate including light propagation perpendicular to the optical axis. In the following, we will discuss two important special orientations of the crystal optical axis.

For the propagation along the optical axis, the material tensors in (19) reduce to $\hat{\varepsilon}_{\mathrm{r}} = \mathrm{diag}\,[\varepsilon_{11}\ \varepsilon_{11}\ \varepsilon_{33}]$, $\hat{\mu}_{\mathrm{r}} = \mathrm{diag}\,[1\ 1\ 1]$, and $\hat{\alpha} = \mathrm{diag}\,[\alpha_{11}\ \alpha_{11}\ \alpha_{33}]$. Assuming normal incidence only, $\mathbf{N} = [0\ 0\ N_z]^{\mathrm{T}}$. The refractive indices of corresponding circularly polarized eigenmodes $N_{z,\,\alpha,\,k=\{1,2,3,4\},\,\|}$ have been published several times [48,57,66], and take the form

$$N_{z,\,\alpha,\,k,\,\|} = \pm\sqrt{\varepsilon}_{11} \pm \alpha_{11}\,. \tag{26}$$

Propagation perpendicular to the optical axis is carried out introducing the rotation tensor of the Cartesian coordinate system $\mathbf{R}$, which is defined by a triad of Euler angles defined same as in [70]. In Eq. (19), any material tensor $\mathbf{a}$ is replaced by tensor $\left(\mathbf{R}\,\mathbf{a}\,\mathbf{R}^{\mathrm{T}}\right)$ then. In particular, for

Optics EXPRESS

normal incidence and propagation perpendicular to optical axis, material tensors are transformed to $\hat{\varepsilon}_{\mathrm{r}} = \mathrm{diag}\,[\varepsilon_{11}\ \varepsilon_{33}\ \varepsilon_{11}]$, $\hat{\alpha} = \mathrm{diag}\,[\alpha_{11}\ \alpha_{33}\ \alpha_{11}]$, and $\mathbf{N} = [0\ 0\ N_z]^{\mathrm{T}}$.

Substituting the particular forms of material tensors into (19), a following set of equations is obtained:

$$\begin{bmatrix} \varepsilon_{11} - N_z^2 - \alpha_{11}^2 & -i\,(\alpha_{11}+\alpha_{33})\,N_z & 0 \\ i\,(\alpha_{11}+\alpha_{33})\,N_z & \varepsilon_{33} - N_z^2 - \alpha_{33}^2 & 0 \\ 0 & 0 & \varepsilon_{11} - \alpha_{11}^2 \end{bmatrix} \begin{bmatrix} E_x \\ E_y \\ E_z \end{bmatrix} = 0. \tag{27}$$

Because the effect of $\hat{\alpha}$ is small [48,66], it is justifiable to set the term $(\hat{\alpha}\hat{\alpha}^{\mathrm{T}})$ in (19) to zero. Using (20), following set of equations is derived:

$$\begin{bmatrix} \varepsilon_{11} - N_z^2 & -ig_{11}N_z & 0 \\ ig_{11}N_z & \varepsilon_{33} - N_z^2 & 0 \\ 0 & 0 & \varepsilon_{11} \end{bmatrix} \begin{bmatrix} E_x \\ E_y \\ E_z \end{bmatrix} = 0. \tag{28}$$

By solving the equations that the determinants of (27) and (28) are equal to zero, normal eigenmodes $N_{z,k=\{1,2,3,4\}}$ propagating in bianisotropic nonmagnetic media of 32 point group perpendicular to optical axis are calculated, respectively, as follows:

$$N_{z,\alpha,k}^2 = \frac{\varepsilon_{11}+\varepsilon_{33}}{2} + \alpha_{11}\alpha_{33} \pm \sqrt{\left(\frac{\varepsilon_{11}-\varepsilon_{33}}{2}\right)^2 + (\alpha_{11}+\alpha_{33})\,(\varepsilon_{33}\alpha_{11}+\varepsilon_{11}\alpha_{33})}, \tag{29}$$

and

$$N_{z,g,k}^2 = \frac{\varepsilon_{11}+\varepsilon_{33}+g_{11}^2}{2} \pm \frac{\sqrt{g_{11}^4 + 2g_{11}^2 + (\varepsilon_{11}+\varepsilon_{33}) + (\varepsilon_{11}-\varepsilon_{33})^2}}{2}. \tag{30}$$

Both of the solutions stand for an elliptically polarized eigenmodes. For the case of small effect of the optical activity with respect to birefrigence, the eigenmodes with propagation constants (29) and (30) become linearly-like polarized and represent ordinary and extraordinary refractive indices of linear retarder $n_{\mathrm{o,e}}$,

$$N_{z,\alpha,(1,3)} \approx N_{z,g,(1,3)} \approx n_{\mathrm{o}}, \tag{31a}$$

$$N_{z,\alpha,(2,4)} \approx N_{z,g,(2,4)} \approx n_{\mathrm{e}}, \tag{31b}$$

and the optical activity influence comes from the ellipticity of the eigenmodes as the result of the intrinsicality of the OA. Moreover, by comparison of the wave Eq. (27) with (28) we find the symmetry between the formalism for this case [47,48],

$$g_{11} = \alpha_{11} + \alpha_{33}. \tag{32}$$

C. Mueller matrix of the chiral waveplate

Jones matrix describing a general elliptical retarder in the transmission configuration with retardation angle Γ is given as [26,71]

$$\mathbf{T} = \frac{1}{1+\chi\chi^*} \begin{bmatrix} \mathrm{e}^{i\frac{\Gamma}{2}} + \chi\chi^*\mathrm{e}^{-i\frac{\Gamma}{2}} & 2i\chi^* \sin\frac{\Gamma}{2} \\ 2i\chi \sin\frac{\Gamma}{2} & \chi\chi^*\mathrm{e}^{i\frac{\Gamma}{2}} + \mathrm{e}^{-i\frac{\Gamma}{2}} \end{bmatrix}, \tag{33}$$

where the complex ellipsometric parameter χ is related to the ellipticity ϵ of the polarization ellipse with its principal axes parallel to Cartesian coordinate system by

$$\chi = i\tan\epsilon \equiv i\kappa. \tag{34}$$

Optics EXPRESS

With this setting, Eq. (33) becomes [48,72]

$$\mathbf{T}_{\mathrm{R,EL}} = \frac{1}{1+\kappa^2}\begin{bmatrix} \mathrm{e}^{i\frac{\Gamma}{2}} + \kappa^2 \mathrm{e}^{-i\frac{\Gamma}{2}} & 2\kappa \sin\frac{\Gamma}{2} \\ -2\kappa \sin\frac{\Gamma}{2} & \kappa^2 \mathrm{e}^{i\frac{\Gamma}{2}} + \mathrm{e}^{-i\frac{\Gamma}{2}} \end{bmatrix}. \tag{35}$$

Corresponding transmission Mueller matrix of the elliptic retarder in a general azimuthal rotation φ is derived using

$$\mathbf{M}_{\mathrm{R,EL}}(\varphi,\,\Gamma,\,\kappa) = \mathbf{M}_{\varphi}^{\mathrm{T}} \underbrace{\mathbf{A}\left(\mathbf{T}_{\mathrm{R,EL}} \otimes \mathbf{T}_{\mathrm{R,EL}}^{*}\right)\mathbf{A}^{\mathrm{T}}}_{\mathbf{M}_{\mathrm{R,EL}}(\varphi=0,\,\Gamma,\,\kappa)} \mathbf{M}_{\varphi}, \tag{36}$$

where $\mathbf{M}_{\varphi}$ is the Mueller matrix of azimuthal rotation about the angle φ, the matrix $\mathbf{A}$ is the matrix relating the statistical properties of incident electric field to corresponding Stokes parameters [14], and the symbol $\otimes$ stands for the Kronecker product. Because the effect of the real parameter κ is small [48,66], it is justifiable to use Mueller matrix (36) linearly approximated in κ.

The resulting expression of the approximated matrix $\mathbf{M}_{\mathrm{R,EL}}(\varphi,\,\Gamma,\,\kappa)$ can be separated into two parts as

$$\mathbf{M}_{\mathrm{R,EL}}(\varphi,\,\Gamma,\,\kappa) = \mathbf{M}_{\mathrm{R,LIN}}(\varphi,\,\Gamma) + \mathbf{\Delta M}_{\mathrm{OA}}(\varphi,\,\Gamma,\,\kappa), \tag{37}$$

where

$$\mathbf{M}_{\mathrm{R,LIN}}(\varphi,\,\Gamma) = \begin{bmatrix} 1 & 0 & 0 & 0 \\ 0 & \cos^2 2\varphi + \cos\Gamma \sin^2 2\varphi & (1-\cos\Gamma)\sin 2\varphi \cos 2\varphi & -\sin 2\varphi \sin\Gamma \\ 0 & (1-\cos\Gamma)\sin 2\varphi \cos 2\varphi & \sin^2 2\varphi + \cos\Gamma \cos^2 2\varphi & \cos 2\varphi \sin\Gamma \\ 0 & \sin 2\varphi \sin\Gamma & -\cos 2\varphi \sin\Gamma & \cos\Gamma \end{bmatrix} \tag{38}$$

is the Mueller matrix for a non-gyrotropic linear retarder, and

$$\mathbf{\Delta M}_{\mathrm{OA}}(\varphi,\,\Gamma,\,\kappa) = \begin{bmatrix} 0 & 0 & 0 & 0 \\ 0 & 0 & 2\kappa \sin\Gamma & 4\kappa \cos 2\varphi \sin^2\frac{\Gamma}{2} \\ 0 & -2\kappa \sin\Gamma & 0 & 4\kappa \sin 2\varphi \sin^2\frac{\Gamma}{2} \\ 0 & 4\kappa \cos 2\varphi \sin^2\frac{\Gamma}{2} & 4\kappa \sin 2\varphi \sin^2\frac{\Gamma}{2} & 0 \end{bmatrix} \tag{39}$$

is the matrix (*not* a Mueller matrix [73]) describing the linear effect of the optical activity. Note, that the limit case of $\kappa = 0$ will turn the matrix $\mathbf{M}_{\mathrm{R,EL}}(\varphi,\,\Gamma,\,\kappa = 0)$ into the limit of standard linear retarder $\mathbf{M}_{\mathrm{R,LIN}}(\varphi,\,\Gamma)$. To show, that for $\kappa = 1$, Mueller matrix $\mathbf{M}_{\mathrm{R,EL}}(\varphi,\,\Gamma,\,\kappa = 1)$ corresponds to the Mueller matrix of circular retarder, a non-approximated matrix $\mathbf{M}_{\mathrm{R,EL}}(\varphi,\,\Gamma,\,\kappa)$ in the form of 36 regarding strong effects of κ must be used.

The gyration parameter κ is usually derived [45,47,48,57] from the eigenvalue problem of the wave equation based on the Born-Landau constitution relations. The resultant expression with respect to the linear approximation of κ is given as

$$\kappa = \frac{1}{2G}\left[\left(n_{\mathrm{e}}^2 - n_{\mathrm{o}}^2\right) - \sqrt{\left(n_{\mathrm{e}}^2 - n_{\mathrm{o}}^2\right)^2 + 4G^2}\right], \tag{40}$$

where $n_{\mathrm{o}} = \sqrt{\varepsilon_{11}}$, $n_{\mathrm{e}} = \sqrt{\varepsilon_{33}}$ are ordinary and extraordinary refractive indices (without the effect of optical activity) of the uniaxial medium, respectively.

Optics EXPRESS

For point group 32, scalar gyration parameter G [Eq. (23)] is given by the non-zero components of $\hat{g}$ and the angle θ given by (24),

$$G = g_{11}\sin^2\theta + g_{33}\cos^2\theta. \tag{41}$$

The dispersion characteristics of the components of gyration tensor $\hat{g}$ were derived in [47] and are given by the dispersion equation

$$g_{ii} = \frac{A_i\lambda^3}{\left(\lambda^2 - B_i^2\right)^2}, \quad i = \{1, 3\}, \tag{42}$$

where λ is the wavelength and A_i, B_i are phenomenological constants. This dispersion model is based on the sum rule consistent model of coupled anisotropic oscillators, and was originally developed for the description of specific rotatory power dispersion [74].

D. Algebraic analysis of the optical activity and misalignment effects in the Mueller matrix of biplates

Let us consider the Mueller matrix of biplate in the form of (7), which differs from an ideal biplate by the presence of the waveplate misalignment $\Phi = \varphi_1 - \varphi_2 - \pi/2$ and the OA $\mathbf{M}_{\mathrm{R,EL}}(\varphi,\ \Gamma_1 - \Gamma_2, \kappa)$ given by (5), introduced as follows:

$$\mathbf{M}_{\mathrm{R,WB}} = \mathbf{M}_{\mathrm{R,EL2}}\left(\varphi + \frac{\Phi}{2} + \frac{\pi}{2},\ \Gamma_2,\ \kappa\right)\mathbf{M}_{\mathrm{R,EL1}}\left(\varphi - \frac{\Phi}{2},\ \Gamma_1,\ \kappa\right). \tag{43}$$

Considering only small effects in both misalignment and OA (κ, $\Phi \ll 1$), we express Mueller matrix (43) as its first order Taylor expansions. The resulting form of the matrix $\mathbf{M}_{\mathrm{R,WB}}$ is then represented as a sum of the Mueller matrix of an ideal biplate without the OA and perturbation matrices, each representing separate contribution of the OA and the misalignment in the form of fine spectral oscillations:

$$\mathbf{M}_{\mathrm{R,WB}} \approx \mathbf{M}_{\mathrm{R,LIN}}(\varphi,\ \Delta\Gamma) + \begin{bmatrix} 1 & \mathbf{0}^{\mathrm{T}} \\ \mathbf{0} & \mathbf{m}_\kappa \end{bmatrix} + \begin{bmatrix} 1 & \mathbf{0}^{\mathrm{T}} \\ \mathbf{0} & \mathbf{m}_\Phi \end{bmatrix}, \tag{44}$$

where

$$\mathbf{m}_\Phi = \Phi\begin{bmatrix} -\mathrm{S}_{4\varphi}(\mathrm{C}_{\Gamma_1} - \mathrm{C}_{\Gamma_2}) & \mathrm{C}_{4\varphi}(\mathrm{C}_{\Gamma_1} - \mathrm{C}_{\Gamma_2}) + W & \mathrm{C}_{2\varphi}(2\mathrm{S}_{\Gamma_1} - \mathrm{S}_{\Delta\Gamma}) \\ \mathrm{C}_{4\varphi}(\mathrm{C}_{\Gamma_1} - \mathrm{C}_{\Gamma_2}) - W & \mathrm{S}_{4\varphi}(\mathrm{C}_{\Gamma_1} - \mathrm{C}_{\Gamma_2}) & \mathrm{S}_{2\varphi}(2\mathrm{S}_{\Gamma_1} - \mathrm{S}_{\Delta\Gamma}) \\ -\mathrm{C}_{2\varphi}(2\mathrm{S}_{\Gamma_2} + \mathrm{S}_{\Delta\Gamma}) & -\mathrm{S}_{2\varphi}(2\mathrm{S}_{\Gamma_2} + \mathrm{S}_{\Delta\Gamma}) & 0 \end{bmatrix}, \tag{45}$$

$$\mathbf{m}_\kappa = \kappa\begin{bmatrix} 2\mathrm{S}_{4\varphi}V & 2\mathrm{S}_{\Gamma_1} + 2\mathrm{S}_{\Gamma_2} - 2\mathrm{C}_{4\varphi}V & 2\mathrm{C}_{2\varphi}(\mathrm{C}_{\Delta\Gamma} - 2\mathrm{C}_{\Gamma_1} + 1) \\ -2\mathrm{S}_{\Gamma_1} - 2\mathrm{S}_{\Gamma_2} - 2\mathrm{C}_{4\varphi}V & -2\mathrm{S}_{4\varphi}V & 2\mathrm{S}_{2\varphi}(\mathrm{C}_{\Delta\Gamma} - 2\mathrm{C}_{\Gamma_1} + 1) \\ -2\mathrm{C}_{2\varphi}(\mathrm{C}_{\Delta\Gamma} - 2\mathrm{C}_{\Gamma_2} + 1) & -2\mathrm{S}_{2\varphi}(\mathrm{C}_{\Delta\Gamma} - 2\mathrm{C}_{\Gamma_2} + 1) & 0 \end{bmatrix}, \tag{46}$$

and

$$\Delta\Gamma = \Gamma_1 - \Gamma_2, \tag{47a}$$

$$\mathrm{S}_{\mathrm{arg}} = \sin(\mathrm{arg}), \qquad \mathrm{C}_{\mathrm{arg}} = \cos(\mathrm{arg}), \tag{47b}$$

$$V = \mathrm{S}_{\Gamma_2} - \mathrm{S}_{\Gamma_1} + \mathrm{S}_{\Delta\Gamma}, \qquad W = \mathrm{C}_{\Gamma_1} + \mathrm{C}_{\Gamma_2} - \mathrm{C}_{\Delta\Gamma} - 1. \tag{47c}$$

Optics EXPRESS

Funding. Grantová Agentura České Republiky (18-22102S); European Regional Development Fund (CZ.02.1.01/0.0/0.0/16_013/0001791); EEA and Norway grants (EMP-CZ-MOP-2-013); Technology Agency of the Czech Republic (FV20020); DGS - Doctoral Grant System (CZ.02.2.69/0.0./0.0/19_073/0016945, Project DGS/TEAM/2020-030); SGS - Student Grant System (SP2020/71).

Acknowledgment. Partial support from the Czech Science Foundation (Project 18-22102S), the IT4Innovations Path to Exascale project CZ02.1.01/0.0/0.0/16013/0001791, EEA grant (EMP-CZ-MOP-2-013), the Project FV20020, doctoral grant system (CZ.02.2.69/0.0./0.0/19_073/0016945, Project DGS/TEAM/2020-030), and student grant system (SP2020/71) are acknowledged.

Disclosures. The authors declare no conflicts of interest.

References

1. M. Haiml, R. Grange, and U. Keller, "Optical characterization of semiconductor saturable absorbers," Appl. Phys. B **79**(3), 331–339 (2004).
2. D. J. Dixit, S. O'Mullane, S. Sunkoju, A. Gottipati, E. R. Hosler, V. K. Kamineni, M. E. Preil, N. Keller, J. Race, G. R. Muthinti, and A. C. Diebold, "Sensitivity analysis and line edge roughness determination of 28-nm pitch silicon fins using Mueller matrix spectroscopic ellipsometry-based optical critical dimension metrology," J. Micro/Nanolith. MEMS MOEMS **14**(3), 031208 (2015).
3. H.-T. Huang and F. L. Terry Jr., "Spectroscopic ellipsometry and reflectometry from gratings (Scatterometry) for critical dimension measurement and in situ, real-time process monitoring," Thin Solid Films **455-456**, 828–836 (2004).
4. M. Foldyna, T. Germer, and B. Bergner, "Mueller matrix ellipsometry of artificial non-periodic line edge roughness in presence of finite numerical aperture," Proc. SPIE **7971**, 79710N (2011).
5. J.-B. Masson and G. Gallot, "Terahertz achromatic quarter-wave plate," Opt. Lett. **31**(2), 265–267 (2006).
6. D. Wang, L. Zhang, Y. Gu, M. Q. Mehmood, Y. Gong, A. Srivastava, L. Jian, T. Venkatesan, C.-W. Qiu, and M. Hong, "Switchable Ultrathin Quarter-wave Plate in Terahertz Using Active Phase-change Metasurface," Sci. Rep. **5**(1), 15020 (2015).
7. D. Vala, M. Mčica, K. Postava, and J. Pištora, "Optical activity temperature-dependent measurements of chiral solutions using Mueller matrix spectroscopic ellipsometry," Proc. SPIE **10976**, 109760A (2018).
8. H. Lundén, A. Liotta, D. Chateau, F. Lerouge, F. Chaput, S. Parola, C. Brännlund, Z. Ghadyani, M. Kildemo, M. Lindgren, and C. Lopes, "Dispersion and self-orientation of gold nanoparticles in sol-gel hybrid silica – optical transmission properties," J. Mater. Chem. C **3**(5), 1026–1034 (2015).
9. Q.-H. Phan and Y.-L. Lo, "Stokes-Mueller matrix polarimetry system for glucose sensing," Opt. Lasers Eng. **92**, 120–128 (2017).
10. R. M. A. Azzam, "Mueller-matrix ellipsometry: A review," in *Polarization: Measurement, Analysis, and Remote Sensing*, vol. 3121 (International Society for Optics and Photonics, 1997), pp. 396–405.
11. K. Postava, R. Sýkora, D. Legut, and J. Pištora, "Determination of Anisotropic Crystal Optical Properties Using Mueller Matrix Spectroscopic Ellipsometry," Procedia Mater. Sci. **12**, 118–123 (2016).
12. M. Kildemo, J.-P. Banon, A. Baron, B. B. Svendsen, T. Brakstad, and I. Simonsen, "Optical response of gold hemispheroidal lattices on transparent substrates," Appl. Surf. Sci. **421**, 593–600 (2017).
13. K. Postava, A. Maziewski, T. Yamaguchi, R. Ossikovski, Š. Višňovský, and J. Pištora, "Null ellipsometer with phase modulation," Opt. Express **12**(24), 6040–6045 (2004).
14. E. Garcia-Caurel, R. Ossikovski, M. Foldyna, A. Pierangelo, B. Drévillon, and A. De Martino, "Advanced Mueller Ellipsometry Instrumentation and Data Analysis," in *Ellipsometry at the Nanoscale*, (Springer, 2013), pp. 31–143.
15. V. Andreev, C. Panda, P. Hess, B. Spaun, and G. Gabrielse, "A self-calibrating polarimeter to measure Stokes parameters.," ResearchGate (2017).
16. F. Stabo-Eeg, "Development of instrumentation for Mueller matrix ellipsometry," Ph.D. thesis, Norwegian University of Science and Technology (2009).
17. A. Pierangelo, A. Benali, M.-R. Antonelli, T. Novikova, P. Validire, B. Gayet, and A. De Martino, "Ex-vivo characterization of human colon cancer by Mueller polarimetric imaging," Opt. Express **19**(2), 1582–1593 (2011).
18. P. A. Letnes, I. S. Nerbø, L. M. S. Aas, P. G. Ellingsen, and M. Kildemo, "Fast and optimal broad-band Stokes/Mueller polarimeter design by the use of a genetic algorithm," Opt. Express **18**(22), 23095–23103 (2010).
19. T. Golovina, A. Konstantinova, B. Nabatov, and E. Evdishchenko, "Determination of the Optical Parameters of Uniaxial Optically Active Crystals Taking into Account the Imperfection of Spectrophotometric Complex Elements," Crystallogr. Rep. **63**(6), 964–968 (2018).
20. A. F. Konstantinova, T. G. Golovina, E. A. Evdishchenko, B. V. Nabatov, and G. I. Utkin, "Determination of the Optical Parameters of Uniaxial Crystals with Allowance for the Imperfection of the Spectrophotometric Complex Elements," Crystallogr. Rep. **63**(4), 606–613 (2018).
21. J. S. Jackson, J. L. Archibald, and D. S. Durfee, "Light splitting with imperfect wave plates," Appl. Opt. **56**(4), 1062–1068 (2017).
22. B. Boulbry, B. Bousquet, B. L. Jeune, Y. Guern, and J. Lotrian, "Polarization errors associated with zero-order achromatic quarter-wave plates in the whole visible spectral range," Opt. Express **9**(5), 225–235 (2001).

Optics EXPRESS

23. L. Broch, A. E. Naciri, and L. Johann, "Systematic errors for a Mueller matrix dual rotating compensator ellipsometer," Opt. Express **16**(12), 8814–8824 (2008).
24. E. A. West and M. H. Smith, "Polarization errors associated with birefringent waveplates," Opt. Eng. **34**(6), 1574–1580 (1995).
25. D. Bergman, "Analysis of elliptically polarized light," J. Opt. Soc. Am. **52**(9), 1080 (1962).
26. R. M. A. Azzam and N. M. Bashara, *Ellipsometry and Polarized Light* (North-Holland Publishing Company, 1977).
27. H. Fujiwara, *Spectroscopic Ellipsometry: Principles and Applications* (Wiley, 2007).
28. J. M. Beckers, "Achromatic linear retarders," Appl. Opt. **10**(4), 973–975 (1971).
29. P. Koleják, D. Vala, K. Postava, P. Provazníková, and J. Pištora, "Mueller matrix ellipsometry of waveplates for control of their properties and alignment," J. Vac. Sci. Technol., B: Nanotechnol. Microelectron.: Mater., Process., Meas., Phenom. **38**(1), 014006 (2020).
30. T. Novikova, J. Rehbinder, S. Deby, H. Haddad, J. Vizet, A. Pierangelo, P. Validire, A. Benali, B. Gayet, B. Teig, A. Nazac, B. Drévillon, F. Moreau, and A. D. Martino, "Multi-spectral mueller matrix imaging polarimetry for studies of human tissues," in *Biomedical Optics 2016*, (Optical Society of America, 2016), p. TTh3B.2.
31. L. Halagačka, K. Postava, and J. Pištora, "Analysis and Modeling of Depolarization Effects in Mueller Matrix Spectroscopic Ellipsometry Data," Procedia Mater. Sci. **12**, 112–117 (2016).
32. M. Foldyna, A. De Martino, R. Ossikovski, E. Garcia-Caurel, and C. Licitra, "Characterization of grating structures by Mueller polarimetry in presence of strong depolarization due to finite spot size," Opt. Commun. **282**(5), 735–741 (2009).
33. D. E. Aspnes, "Expanding horizons: New developments in ellipsometry and polarimetry," Thin Solid Films **455-456**, 3–13 (2004).
34. B. Johs and C. M. Herzinger, "Quantifying the accuracy of ellipsometer systems," Phys. Status Solidi C **5**(5), 1031–1035 (2008).
35. S.-Y. Lu and R. A. Chipman, "Interpretation of Mueller matrices based on polar decomposition," J. Opt. Soc. Am. A **13**(5), 1106–1113 (1996).
36. H. Gu, S. Liu, X. Chen, and C. Zhang, "Calibration of misalignment errors in composite waveplates using Mueller matrix ellipsometry," Appl. Opt. **54**(4), 684–693 (2015).
37. H. Gu, X. Chen, Y. Shi, H. Jiang, C. Zhang, P. Gong, and S. Liu, "Comprehensive characterization of a general composite waveplate by spectroscopic Mueller matrix polarimetry," Opt. Express **26**(19), 25408–25425 (2018).
38. F. I. Fedorov, *Theory of gyrotropy [in russian]* (Nauka i Technika, 1964).
39. F. I. Fedorov, *Optics of anisotropic media [in russian]* (Izdatělstvo Naučnoj i Učebnoj Literatury, 2004).
40. A. Yariv and P. Yeh, *Optical Waves in Crystals: Propagation and Control of Laser Radiation* (Wiley, 2002).
41. E. U. Condon, "Theories of Optical Rotatory Power," Rev. Mod. Phys. **9**(4), 432–457 (1937).
42. M. De Graef and M. E. McHenry, *Structure of Materials: An Introduction to Crystallography, Diffraction and Symmetry* (Cambridge University Press, 2012), 2nd ed.
43. D. E. Sands, *Introduction to Crystallography* (Courier Corporation, 1993).
44. D. Franta, "Symmetry of linear dielectric response tensors: Dispersion models fulfilling three fundamental conditions," J. Appl. Phys. **127**(22), 223101 (2020).
45. J. F. Nye, *Physical Properties of Crystals: Their Representation by Tensors and Matrices* (Clarendon, 1985).
46. F. G. Fumi, "Physical properties of crystals: The direct-inspection method," Acta Crystallogr. **5**(1), 44–48 (1952).
47. O. Arteaga, A. Canillas, and G. Jellison, "Determination of the components of the gyration tensor of quartz by oblique incidence transmission two-modulator generalized ellipsometry," Appl. Opt. **48**(28), 5307–5317 (2009).
48. A. F. Konstantinova, B. N. Grečušnikov, B. V. Bokut', and E. G. Valjaško, *Optical properties of crystals [in russian]* (Nauka i Technika, 1995).
49. O. Arteaga and A. Canillas, "Pseudopolar decomposition of the jones and mueller-jones exponential polarization matrices," J. Opt. Soc. Am. A **26**(4), 783–793 (2009).
50. J. Cervantes-L, D. I. Serrano-Garcia, Y. Otani, and B. Cense, "Mueller-matrix modeling and characterization of a dual-crystal electro-optic modulator," Opt. Express **24**(21), 24213–24224 (2016).
51. D. Kliger and J. Lewis, *Polarized Light in Optics and Spectroscopy* (Academic, 2012).
52. S.-M. F. Nee, "Depolarization and retardation of a birefringent slab," J. Opt. Soc. Am. A **17**(11), 2067–2073 (2000).
53. T. A. Germer and H. J. Patrick, "Effect of bandwidth and numerical aperture in optical scatterometry," in *Metrology, Inspection, and Process Control for Microlithography XXIV*, vol. 7638 (International Society for Optics and Photonics, 2010), p. 76381F.
54. T. Radhakrishnan, "Further studies on the temperature variation of the refractive index of crystals," Proc. - Indian Acad. Sci., Sect. A **33**(1), 22–34 (1951).
55. T. Radhakrishnan, "The dispersion, briefringence and optical activity of quartz," Proc. - Indian Acad. Sci., Sect. A **25**(3), 260–265 (1947).
56. I. V. Lindell, A. H. Sihvola, A. J. Viitanen, and S. A. Tretyakov, *Electromagnetic Waves in Chiral and Bi-isotropic Media* (Artech House, 1994).
57. A. F. Konstantinova, B. V. Nabatov, E. A. Evdishchenko, and K. K. Konstantinov, "Modern application packages for rigorous solution of problems of light propagation in anisotropic layered media: II. Optically active crystals," Crystallogr. Rep. **47**(5), 815–823 (2002).

Optics EXPRESS

58. A. H. Sihvola and I. V. Lindell, "Bi-isotropic constitutive relations," Microw. Opt. Technol. Lett. **4**(8), 295–297 (1991).
59. B. D. H. Tellegen, "The Gyrator: A New Electric Network Element," Philips Res. Rept. **3**, 81–101 (1985).
60. S. A. Tretyakov, A. H. Sihvola, A. A. Sochava, and C. R. Simovski, "Magnetoelectric Interactions in Bi-Anisotropic Media," J. Electromagn. Waves Appl. **12**(4), 481–497 (1998).
61. L. Onsager, "Reciprocal Relations in Irreversible Processes. I.," Phys. Rev. **37**(4), 405–426 (1931).
62. L. Onsager, "Reciprocal Relations in Irreversible Processes. II.," Phys. Rev. **38**(12), 2265–2279 (1931).
63. H. Casimir, "On Onsager's Principle of Microscopic Reversibility," Rev. Mod. Phys. **17**(2-3), 343–350 (1945).
64. S. Tretyakov, A. Sihvola, and B. Jancewicz, "Onsager-Casimir Principle and the Constitutive Relations of Bi-Anisotropic Media," J. Electromagn. Waves Appl. **16**(4), 573–587 (2002).
65. L. M. Barkovsky and G. N. Borzdov, "V.A. Shamburov's validity criteria for the gyrotropy theory," Opt. Spectrosc. **95**(1), 124–130 (2003).
66. R. Ossikovski and O. Arteaga, "Extended Yeh's method for optically active anisotropic layered media," Opt. Lett. **42**(18), 3690–3693 (2017).
67. K. Postava, J. Pištora, and P. Hlubina, "Effect of permeability on guided modes in planar structures," Proc. SPIE **3573**, 524–527 (1998).
68. L. D. Landau, L. P. Pitaevskii, and E. M. Lifshitz, *Electrodynamics of Continuous Media: Volume 8 (Course of Theoretical Physics S)* (Butterworth-Heinemann, 1984).
69. D. Franta and J. Vohánka, "Constitutive equations describing optical activity in theory of dispersion," J. Opt. Soc. Am. B **38**(2), 553–561 (2021).
70. H. Goldstein, C. P. Poole Jr., and J. L. Safko, *Classical Mechanics* (3rd Edition) (Pearson, 2001).
71. J. J. Gil Perez and R. Ossikovski, *Polarized Light and the Mueller Matrix Approach* (Taylor & Francis, 2017).
72. E. A. Evdischenko and A. F. Konstantinova, *Jones Transmission and Reflection Matrices for Low-Symmetric Absorbing Gyrotropic Crystals* (Springer, 1997), pp. 67–70.
73. D. G. M. Anderson and R. Barakat, "Necessary and sufficient conditions for a Mueller matrix to be derivable from a Jones matrix," J. Opt. Soc. Am. A **11**(8), 2305–2319 (1994).
74. C. Sivaramakrishna and B. W. Lawrence, "Optical rotatory dispersion of crystals," Proc. R. Soc. London A – Math. Phys. Sci. **259**, 531–553 (1961).

46.135.99.92 (ts '2021-03-19 15:23:29')

Paper VIII

Spintronic inverse spin hall photomixing beyond 1THz

Pierre Koleják, Geoffrey Lezier, Guillaume Ducournau, Jean-François Lampin, Nicolas Tiercelin, Mathias Vanwolleghem
48th IRMMW-THz IEEE, (2023)

Spintronic inverse spin hall photomixing beyond 1THz

Pierre Kolejak, Geoffrey Lezier, Guillaume Ducournau, Jean-François Lampin, Nicolas Tiercelin, Mathias Vanwolleghem

IEMN-CNRS, Université de LILLE, Villeneuve d'Ascq, France

***Abstract*— We have demonstrated experimentally how ultrabroadband inverse spin Hall emitters present an unprecedented new scheme for room temperature THz CW and frequency comb generation. Building on previous proof-of-principle demonstrations, we demonstrate here by improved experimental developments how this photomixing effectively does not present any frequency rolloff at least up to 1,05THz, contrary to standard photoswitches. A theoretical and numerical model implementing spin Hall dynamics in nanometric FM/HM stacks predict photomixing bandwidths up to 10THz.**

I. Introduction

SPINTRONIC Inverse Spin Hall Effect terahertz emitters (ISHE STE) have in a matter of just a few years burst onto the scene as a novel promising and highly efficient paradigm for pulsed terahertz generation. They compete with standard schemes based on nonlinear optical rectification or ultrafast semiconductor-based photoswitches, both in terms of emitted power and especially bandwidth. The ultrafast spin-to-charge conversion mechanisms in ferromagnetic/non-magnetic 3d/5d metallic heterostructures, have led to demonstrations of phonon-gapless pulsed emitters with near uniform bandwidth close to the theoretical time-bandwidth product of the IR pumping pulses (up to 30 THz) [1].

We have previously proven experimentally that as a direct consequence of this near instantaneous response of the spinorbitronic effect, an ISHE emitter can perform as a novel type of room-temperature THz photomixer. This proof-of-principle demonstration had been limited to low mm-wave frequencies at 300GHz and required a subtle heterodyne detection scheme to guarantee sufficient dynamic range to detect the limited THz power levels [2]. This is mainly due to the fact that CW THz generation (or a comb of stable narrow THz lines) is not a straightforwardly scaled version of the pulsed operation. There is easily 5-6 orders of magnitude difference in peak power for the same average pumping power. Therefore THz spintronic photomixing power levels are close to pW levels. By improving the stability of the measurements the dynamic range of the used heterodyne detection scheme can be greatly increased allowing us to extend the demonstration of spintronic photomixing over nearly two octaves (from 300GHz up to 1050GHz) and thereby confirming the absence of any rolloff (at least up to the receiving bandwidth of the used harmonic mixer receivers).

II. Method & Results

The key element in this demonstration is the stability of the mixing IR lines generating the THz beatnote. Indeed, the heterodyne measurements (in which the narrowband generated THz line is harmonically mixed with a multiplied electronic local oscillator and subsequently spectrally analysed at IF frequencies), require a minimal resolution bandwidth (RBW) to minimize the Johnson noise and allow sufficient dynamic range to detect THz pW levels or lower. While previously we concentrated our efforts on mixing two sub-Hz linewidth stabilized 1.5µm-DFB lasers [3], we now turned our attention towards spintronic THz downconversion of a 1GHz repetition rate 1.5 µm modelocked laser (Menhir Photonics) emitting Fourier-limited 250fs IR pulses of 50 pJ. After amplification using an EDFA fiber amplifier that is properly dispersion compensated, 120fs pulses are achieved with an average power close to 1W. The 1 GHz spaced infrared lines of this amplified modelocked laser cover approximately a 4THz bandwidth. Using these IR modelocked pulses to pump a record W(2nm)/CoFe(1.8nm)/Pt(2nm) ISHE emitter sputter-deposited on sapphire substrates generates a 1GHz train of THz pulses. The spectral analysis of this downconverted THz frequency comb will reveal the photomixing efficiency of the ISHE emitter as each THz line in this spectrum is the result of the mixing product of all beating IR modelocked lines sitting at the THz beat note. This experimental demonstration is thus nothing else than a precise characterization of the high order harmonics of the 1GHz repetition frequency in the THz pulse train. Fig.1 illustrates the measurement principle and also explains how the downconverted THz comb will create doublet lines in the IF spectrum in this heterodyne receiving scheme.

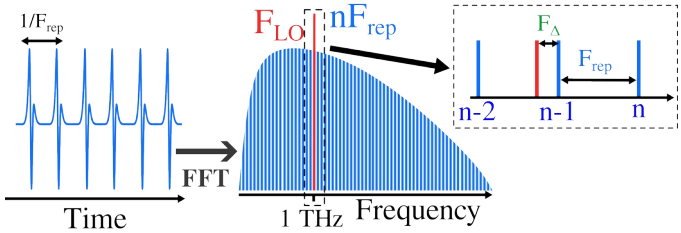


Fig.1: Principle of the heterodyne analysis of the THz pulse train. The THz blue comb lines are spaced by the repetition rate of the pulses. An electronically multiplied local oscillator (red – here close to 1THz) mixes with the THz comb lines in the subharmonic receiver to create a heterodyne IF signal. This IF signal contains obviously also the mirror of all the THz lines on the other side of the local oscillator. As a result doublets in the IF domain spaced by F_{rep} will be observed.

The THz beatnote generated by the ISHE STE was maximally collected by a hemispherical sapphire lens in contact with the substrate and focussed through a Zeonex lens on the horn antenna of a dedicated VDI 750-1050 GHz heterodyne subharmonic Schottky receiver. An electronically multiplied ultralow phase noise 8-12GHz synthesizer as local oscillator produced the IF mixing product that was analysed after on a Rohde & Schwarz electrical spectrum analyzer (ESA). In other words, this setup allows to measure all 1GHz harmonics in the THz comb up to the 1050th harmonic product! Key in this experiment is the stability of the 1GHz

repetition rate of the modelocked Menhir. Any fast drift of this repetition rate would be detrimentally multiplied in the IF spectrum of the heterodyne receiver, creating a jitter of the THz comb lines. For example, near the 1000th harmonic a repetition rate stability better than 10^{-9} is needed to allow a RBW below 1kHz (and thus a theoretical low Johnson noise floor of -144dBm) . This has been achieved by a feedback loop to error correct any fast drift of the Menhir laser. A tiny part of the IR pump beam was split off using a glass plate to generate an error signal for the repetition rate on a 1GHz InGaAs diode. Sharing the same clock reference between the laser, the spectrum analyser and the feedback loop allowed to stabilize the rep rate to Hz levels over several minutes. This scheme is depicted in Fig. 2

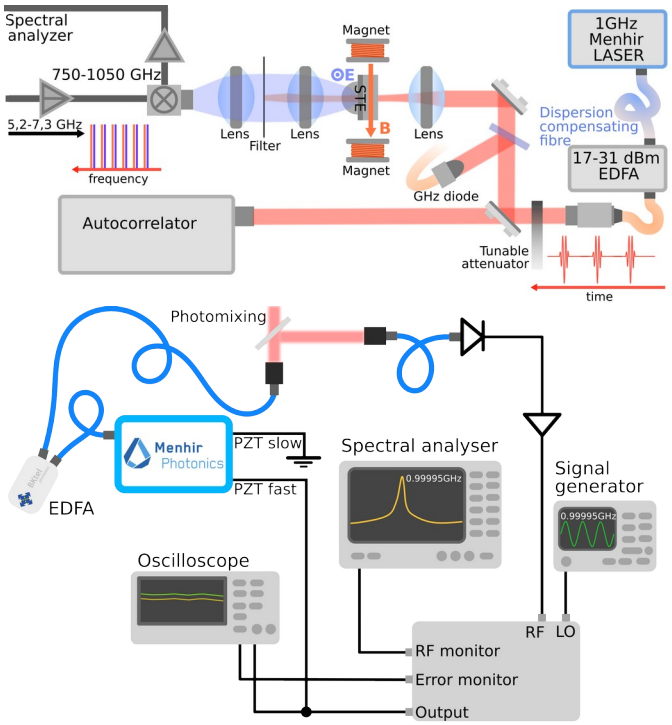


Fig.2: Schematic representation of the heterodyne spintronic photomixing setup. In the top panel the heterodyne mixing itself is shown. Besides the analysis of the spintronically generated THz pulse train using the VDI 1THz subharmonic receiver, one notices the extra instrumental elements added to the pumping beam: a fast GHz diode for locking the rep rate and a split off part to analyse by autocorrelation the temporal duration of the IR pulses. The bottom panel illustrates the locking mechanism for the rep rate of the Menhir using the 1GHz signal of the monitoring IR diode.

Using this setup, all harmonics within the bandwidth of the subharmonic receiver have been characterised. Fig. 3 shows the results for several selected higher harmonics (up to 1050th). For typical modelocked average pumping powers of 400mW a dynamic range exceeding the noise floor by almost 20dB at a RBW of 100Hz was obtained. This not only illustrates how the heterodyne receiver correctly detects both the nth and n-2th harmonic as mirror doublets (illustrated for the 750th harmonic) but most importantly that the IR comb is efficiently downconverted by spintronic photomixing to a THz comb. Further measurements with a VDI receiver covering the 300-350GHz band (not shown here) show that this spin-Hall photomixing downconverts the comb lines by a quasi-flat transfer function without any noticeable roll-off. While the spintronic conversion efficiency still limits the power of these comb lines to pW levels, the demonstration of a nearly 3 octave wide room temperature THz comb is a premier result that opens another rich application domain of THz spintronics. Especially the easy generation of a THz comb directly generated from a commercial IR comb is a completely novel avenue towards THz comb spectroscopy.

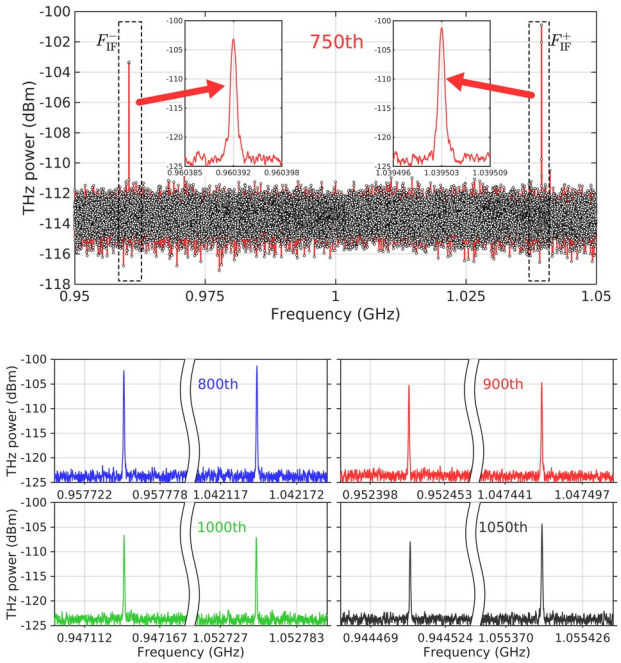


Fig.3: Successful demonstration of spintronic THz comb generation. An average pump power of 400mW was used leading to nearly flat comb lines close to pW levels over the full bandwidth of the heterodyne receiver. All harmonics up to 1050th have been observed with near constant mixing power. It is also noticed that the linewidth of the comb lines is only limited by the RBW of the spectral analyser. Spintronic mixing has a quasi Dirac response so that the THz lines replicate the linewidth of the lines of the modelocked laser.

As an outlook, based on FDTD simulations of the transport equations for spin-dependent diffusion in magnetic multilayers[4], taking typical values for the different spin dependent relaxation mechanisms in Co/Pt systems, it is expected that frequency cutoff of the mixing efficiency will only set in close to the spin-flip relaxation time constant (of the order of 100fs). ISHE emitters thus have the potential to generate very wide and nearly flat THz combs up to 10 THz (albeit at limited powers). Work is underway to investigate these very high THz regimes by using THz gas lasers[5] as local oscillators in a heterodyne scheme with a fast bolometer as a harmonic mixer.

REFERENCES

[1] Seifert et al.: Nature Photonics, 10(7): 483–488, https://doi.org/10.1038/nphoton.2016.91, (2016).

[2] P. Kolejak et al., 2022 47th International Conference on Infrared, Millimeter and Terahertz Waves (IRMMW-THz), Delft, Netherlands, 2022, pp. 1-2, doi: 10.1109/IRMMW-THz50927.2022.9896051.

[3] Burkart et al.: Optics Letters, 38(12):2062-2064, https://doi.org/10.1364/OL.38.002062, (2013).

[4] Dang, T. H. et al. (2020), Applied Physics Reviews, 7(4), p.041409. doi: 10.1063/5.0022369.

[5] A. Pagies, G. Ducournau, and J.-F. Lampin , APL Photonics 1, 031302 (2016) https://doi.org/10.1063/1.4945355

6

CONCLUSION

In this research, we addressed the critical challenge of developing a terahertz complete time-domain spectroscopic ellipsometry (THz-cTDSE) suitable for comprehensive material characterization. Despite the significant potential of THz time-domain ellipsometry in fields such as material science, biology, and optics, its practical implementation has been hindered by several key limitations: inadequate polarization control, incomplete or isotropic ellipsometry framework, and complexity of interpreting ellipsometry data. Furthermore, conventional terahertz sources do not offer the necessary bandwidth, high-quality generated polarization, and easily controlled polarization switching required for advanced ellipsometric techniques.

The primary objective of this research was to develop an enhanced ellipsometry method that overcomes these limitations by leveraging spintronic terahertz emitters (STEs). STEs offer intrinsic advantages, including broadband, gapless emission and inherent polarization control through magnetic reorientation. By integrating STEs into the time-domain ellipsometry, we achieved precise polarization manipulation with high-extinction ratio linear polarization. Furthermore, we aimed to develop spintronic emitters suitable for terahertz ellipsometry with advanced polarization control and robust generated signals. Therefore, we developed a numerical framework for integrating spintronic emitters with infrared and terahertz cavities for maximal performance and infrared-to-terahertz conversion efficiency. To simplify the polarization control, we developed a new architecture of spintronic layers to keep high spin-to-charge efficiency but exhibit magnetic anisotropy for a novel concept of polarization switching. The key results pertain to four fields:

1. Enhancing optical-to-THz conversion efficiency of STEs

Low terahertz signal and limited dynamic range significantly hinder the practical application of spintronic emitters, primarily due to low optical-to-terahertz conversion efficiency. Nevertheless, electromagnetic efficiency can be enhanced by maximizing pump energy absorption and optimizing terahertz extraction. Since THz-cTDSE involves multi-angle and azimuthal rotations of various samples, fast and stable time-domain measurements are required to ensure accurate results. Improving the efficiency of terahertz emitters is crucial for obtaining high-quality ellipsometric measurements and expanding the applicability of spintronic terahertz emitters.

- **STEs integration with photonic cavities**: We conducted a detailed study on maximizing the emission from spintronic emitters by enhancing absorption and optimizing the geometry to achieve optimal terahertz extraction. By integrating STEs with one-dimensional photonic

cavities composed of SiO_2/SiN_x layers, we enhanced the optical absorption within the ferromagnetic layer to 95%. This resulted in a 2.45-fold increase in conversion efficiency, effectively boosting the THz emission.

- **STEs integration with terahertz cavities**: We replaced the traditional substrate of the spintronic emitter with ultra-thin sapphire layers and metallic mirrors, forming a terahertz resonant cavity. This design reflects the backward-emitted terahertz wave back into the structure, enabling constructive interference that can amplify the forward terahertz emission by up to a factor of two.

- **Damage threshold analysis**: To achieve maximum performance from STEs under high-power conditions, we investigated the optical damage thresholds across a wide range of laser repetition rates, from kilohertz to gigahertz. This allowed us to determine whether systems driven by amplifiers or oscillators are more suitable. By identifying the transition between field-dominated and heat-dominated damage regimes, we gained critical insights into the thermal management of STEs. This knowledge enables the optimization of operational conditions to maximize efficiency without compromising STE's integrity.

The enhanced efficiency of STEs has significant implications for terahertz spectroscopy and ellipsometry, enabling shorter acquisition times and improved signal-to-noise ratios. Combining photonic and terahertz cavities presents a promising approach to amplify further terahertz emission, which is critical for applications such as terahertz nonlinear optics. Future work should focus on integrating anti-reflection coatings, exploring advanced materials, and targeting combined amplification in reflection and transmission geometries to improve efficiency and scalability.

2. Advanced Polarization Control Mechanisms

Precise polarization control is essential for accurate ellipsometric measurements, particularly when characterizing anisotropic and optically active materials. Traditional terahertz polarizers have low extinction ratios, and waveplates are limited in bandwidth, making precise polarization control challenging. Moreover, switching between generated polarization states utilizing polarizers is problematic because it often requires projection-based measurements at $\pm 45°$, reducing the signal. Spintronic emitters offer a more efficient solution, allowing polarization control by rotating an external magnet. To enhance stability and eliminate the need for an external magnet, we developed advanced methods for stable polarization switching without moving components, significantly improving system reliability and measurement accuracy.

- **Stoner-Wohlfarth polarization control**: We developed a new spintronic terahertz emitter with engineered uniaxial magnetic anisotropy in $FeCo/TbCo_2/FeCo$ ferromagnetic trilayers. The magnetic anisotropy enables the precise control of magnetization through Stoner-Wohlfarth rotation, requiring only minimal external magnetic fields applied along the hard axis. This design allows full 360° coherent polarization rotation of the emitted terahertz radiation. The method offers dynamic, repeatable, and precise polarization control without the need for mechanical rotation or complex external field configurations, significantly enhancing the capabilities and practicality of THz-TDSE.

- **Voltage-tunable polarization control**: To further simplify polarization control and enable rapid modulation, we explored voltage-induced magnetization rotation in magnetostrictive

FeCo/$TbCo_2$/FeCo-STEs deposited on piezoelectric substrates PMN-PT. Applying an electric voltage-induced mechanical strain in the substrate, resulting in up to 70° of terahertz polarization rotation. This approach enables electrical control of the terahertz polarization state without needing external magnetic fields or mechanical components, allowing for rapid and precise modulation, which is crucial for advanced ellipsometric techniques and potential applications in terahertz communication systems.

The advanced polarization control mechanisms simplify the experimental setup and improve measurement stability, which is vital for accurate THz-TDSE. By enabling precise electronic control of polarization, this system allows for fast and continuous modulation of the polarization state, similar to how visible PEM ellipsometers operate. This capability introduces broadband polarization switching and rotation, a feature not currently available for terahertz ellipsometry, making this a significant advancement for time-resolved and real-time Jones matrix determination. However, limitations such as the incomplete 90° rotation in voltage-controlled systems and potential signal attenuation due to impedance-matching with PMN-PT substrate still need to be addressed.

3. Development of a complete time-domain ellipsometry

Traditional terahertz ellipsometry captures only a limited subset of the Mueller matrix elements, neglects essential phase information, or focuses solely on isotropic ellipsometry ratios, making it inadequate for fully characterizing general anisotropic samples. As a result, these methods fail to exploit the full potential of time-domain ellipsometry for determining the complete Jones matrix. Ellipsometry is an inherently sensitive technique, placing high demands on precision in both instrumentation and data processing, requiring accurate calibration methods and robust polarization control. In the terahertz range, these requirements become even more challenging. Additionally, simplifying the interpretation for non-ellipsometry specialists is essential in expanding the technique's accessibility, which is a significant challenge in the terahertz domain.

The main results and their significance are:

- **Comprehensive polarization analysis**: Leveraging the inherent coherence of terahertz time-domain measurements, we experimentally determined the complete Jones matrix of anisotropic samples. This method captures amplitude and phase information, making it highly effective for analyzing a wide range of anisotropic and optically active materials. The Jones matrix enables a detailed characterization of the polarization behavior, including any coupling between orthogonal polarization components. Additionally, the complete Mueller matrix can be readily derived from the Jones matrix through a straightforward transformation.

- **Introduction of Pauli exponential coefficients**: To provide an intuitive interpretation of complex polarization responses, we transformed the Jones matrix using Pauli exponential coefficients. This method precisely captures retardation and diattenuation across all Stokes bases, facilitating the analysis of polarization effects such as linear and circular birefringence and dichroism. Our work represents the first experimental demonstration of this approach in terahertz ellipsometry, offering a significant advancement in the detailed characterization of anisotropic materials.

- **Spintronic terahertz emitters in ellipsometry**: This work introduces spintronic terahertz emitters (STEs) as the core polarization element of a complete ellipsometric system. By

harnessing their ultra-broadband properties, high extinction ratio, and precise polarization control, STEs enable a new level of performance in terahertz ellipsometry. Their integration represents a major step forward, with promising implications for the development of advanced terahertz technologies

- **Robust calibration method**: We developed a calibration procedure that addresses systematic errors and misalignments in the ellipsometry system. Using polarization-sensitive reference measurements, we accounted for these misalignments during the reconstruction of the Jones matrix, ensuring precise and reliable THz-TDSE measurements. This method is generalized and applicable to a wide range of ellipsometric systems, significantly improving the accuracy and reliability of the results.

The next crucial step in our research involves the demonstration of large-area STEs with induced magnetic anisotropy. This is a significant challenge, as maintaining uniform anisotropy across the entire surface is critical. However, achieving this would provide stable polarization control and high performance, making it well-suited for wide terahertz applications.

The current work focuses on complete ellipsometry in the transmission configuration, which limits its applicability primarily to transparent anisotropic samples. The method must be extended to reflection geometry to characterize more complex materials. The current experimental setup includes a reflection configuration tested with time-domain spectroscopy. However, applying this to ellipsometry introduces specific challenges. In the terahertz range, the Gaussian nature of the beam profile poses challenges in accurately defining the angle of incidence for broadband pulses, given the significant variations in beam properties across wavelengths. This step will require modifications to the calibration procedure, specifically to address phase differences between the calibration and studied samples in reflection mode.

Further calibration refinement could improve accuracy, such as the experimental characterization of polarizers. Implementing eigenvalue calibration methods, [185], which use multiple known samples to derive the cumulative response of polarization-generating and -analyzing elements, could be especially beneficial in the terahertz range, where accurately modeling polarizing components remains challenging.

Future research should also focus on testing the THz-cTDSE system with oscillators operating at higher repetition rates and greater stability. These systems would complement current ellipsometry measurements, as the current use of a 1 kHz amplifier, while flexible, introduces challenges such as increased noise and longer acquisition times.

The last key challenge is implementing pump-probe ellipsometry experimentally to study the dynamic properties of anisotropic samples and complex heterostructures. Accurately determining the conductivities of anisotropic semiconductors is crucial, as is improving sensitivity in reflection measurements for multi-layered structures like fuel cells. However, the stability of measurements, especially given the extended time required for time-delay scanning in pump-probe techniques, remains a difficult factor.

4. Exploration of ultra-broadband photomixing

Photomixing is a crucial technique for generating continuous-wave terahertz (THz) radiation, essential for high-resolution spectroscopy and frequency-domain applications. Traditional photomixers are limited by carrier transit times and parasitic capacitances, reducing efficiency at higher terahertz

frequencies. Overcoming these limitations is crucial for developing efficient, room-temperature THz sources that operate over ultra-broadband frequencies.

- **Demonstration of ultra-broadband THz photomixing**: We successfully demonstrated stable THz frequency comb generation from 750 GHz up to 1.05 THz using spintronic terahertz emitters (STEs), surpassing traditional photomixing performance. By integrating STEs with mode-locked infrared lasers operating at a 1 GHz repetition rate, we achieved a flat, gapless THz comb with harmonics extending to the 1050th order. Achieving stable signals at power levels in the femtowatt range required significant instrumental improvements. By employing advanced heterodyne detection techniques, we achieved a dynamic range exceeding 120 dB.

This proof-of-concept study demonstrates the potential of STEs for applications requiring ultra-broadband terahertz sources. STEs could potentially access frequency ranges currently achievable only with cryogenically cooled quantum cascade lasers or bulky molecular gas lasers but in a room-temperature and widely tunable manner. Despite these advancements, challenges remain due to the low terahertz-to-optical conversion efficiency and power levels of STE-based photomixers. We have already tested our enhanced spintronic emitters with cavities, achieving an 8dB improvement. Future research should focus on further improving efficiency, possibly by integrating photonic and terahertz cavities. Additionally, it is essential to demonstrate STE's effectiveness at higher terahertz frequencies. However, our measurements were limited to 1.05 THz by the upper bandwidth of our VDI 750-1050 GHz heterodyne subharmonic Schottky receiver, despite STE's potential to operate up to tens of THz.

Concluding remarks

Throughout this work, we have significantly contributed to advancing terahertz time-domain spectroscopic ellipsometry by overcoming critical limitations in polarization control, complete ellipsometry framework, calibration, and data interpretation. We believe this new and innovative approach could transform the current methodology, inspired mainly by visible range ellipsometry, into an unrivaled characterization technique. By developing optimized spintronic terahertz emitters with enhanced efficiency and advanced polarization control mechanisms, we have provided a solid foundation for precise and comprehensive material characterization in the terahertz range.

A crucial aspect of this research was the construction of the entire laser infrastructure required for developing the time-domain terahertz ellipsometer. This involved establishing complex beam paths and integrating a 5 W amplifier, and an optical parametric amplifier, spanning a wavelength range from 550 nm to 1.5 μm. The experimental setup developed during this Ph.D. project is the backbone for the advanced THz-TDSE system, enabling polarization-sensitive material characterization, pump-probe measurements, and terahertz source analysis.

This work results in successfully constructing a complete ellipsometry setup, developing advanced spintronic sources, and a new ellipsometric methodology. Beyond building the system, we also explored and expanded the use of spintronic emitters in the frequency domain, addressing significant instrumental challenges. This work demonstrates not only the versatility of the setup but also its potential for further developments in both time- and frequency-domain terahertz ellipsometry.

Bibliography

[1] D. Pavlidis, *Fundamentals of Terahertz Devices and Applications*. Hoboken, NJ, USA: Wiley, Aug. 2021.

[2] P. Gun-Sik, T. Masahiko, R. Jae-Sung, and P. Sang Yoon, *Advances in Terahertz Source Technologies*. Stanford, CA, USA: Jenny Stanford Publishing, Apr. 2024.

[3] S. Ho-Jin and N. Tadao, *Handbook of Terahertz Technologies*. Stanford, CA, USA: Jenny Stanford Publishing, Apr. 2015.

[4] K.-E. Peiponen, A. Zeitler, and M. Kuwata-Gonokami, *Terahertz Spectroscopy and Imaging (Springer Series in Optical Sciences, 171)*. Berlin, Germany: Springer, Oct. 2012.

[5] P. U. Jepsen, D. G. Cooke, and M. Koch, "Terahertz spectroscopy and imaging – Modern techniques and applications," *Laser Photonics Rev.*, vol. 5, pp. 124–166, Jan. 2011.

[6] X. Yin, B. W.-H. Ng, and D. Abbott, *Terahertz imaging for biomedical applications*. New York: Springer, c2012.

[7] Z. Yan, L.-G. Zhu, K. Meng, W. Huang, and Q. Shi, "THz medical imaging: from in vitro to in vivo," *Trends Biotechnol.*, vol. 40, pp. 816–830, July 2022.

[8] H. Kasban, "A comparative study of medical imaging techniques," *Int J Latest Trends Eng Technol*, vol. 4, p. 37, 2015.

[9] D. Samanta, M. P. Karthikeyan, D. Agarwal, A. Biswas, A. Acharyya, and A. Banerjee, "Trends in Terahertz Biomedical Applications," in *Generation, Detection and Processing of Terahertz Signals*, pp. 285–299, Singapore: Springer, Sept. 2021.

[10] N. Laman, S. S. Harsha, D. Grischkowsky, and J. S. Melinger, "High-Resolution Waveguide THz Spectroscopy of Biological Molecules," *Biophys. J.*, vol. 94, pp. 1010–1020, Feb. 2008.

[11] D. Mittleman, *Sensing with terahertz radiation*. Berlin: Springer, 2011.

[12] R. Miles, *Terahertz frequency detection and identification of materials and objects*. Dordrecht, The Netherlands: Springer, 1. ed. ed., 2007.

[13] A. Rostami, H. Rasooli, and H. Baghban, *Terahertz technology*. New York: Springer Verlag, c2011.

[14] C. Sirtori, "Bridge for the terahertz gap," *Nature*, vol. 417, pp. 132–133, May 2002.

[15] A. Y. Pawar, D. D. Sonawane, K. B. Erande, and D. V. Derle, "Terahertz technology and its applications," *Drug Inven. Today*, vol. 5, pp. 157–163, June 2013.

[16] V. Skoromets, H. Němec, V. Goian, S. Kamba, and P. Kužel, "Performance Comparison of Time-Domain Terahertz, Multi-terahertz, and Fourier Transform Infrared Spectroscopies," *J. Infrared Milli. Terahz. Waves*, vol. 39, pp. 1249–1263, Dec. 2018.

[17] A. Leitenstorfer, A. S. Moskalenko, T. Kampfrath, J. Kono, E. Castro-Camus, K. Peng, N. Qureshi, D. Turchinovich, K. Tanaka, A. G. Markelz, M. Havenith, C. Hough, H. J. Joyce, W. J. Padilla, B. Zhou, K.-Y. Kim, X.-C. Zhang, P. U. Jepsen, S. Dhillon, M. Vitiello, E. Linfield, A. G. Davies, M. C. Hoffmann, R. Lewis, M. Tonouchi, P. Klarskov, T. S. Seifert, Y. A. Gerasimenko, D. Mihailovic, R. Huber, J. L. Boland, O. Mitrofanov, P. Dean, B. N. Ellison, P. G. Huggard, S. P. Rea, C. Walker, D. T. Leisawitz, J. R. Gao, C. Li, Q. Chen, G. Valušis, V. P. Wallace, E. Pickwell-MacPherson, X. Shang, J. Hesler, N. Ridler, C. C. Renaud, I. Kallfass, T. Nagatsuma, J. A. Zeitler, D. Arnone, M. B. Johnston, and J. Cunningham, "The 2023 terahertz science and technology roadmap," *J. Phys. D: Appl. Phys.*, vol. 56, p. 223001, Apr. 2023.

[18] L. Duvillaret, F. Garet, and J.-L. Coutaz, "Influence of noise on the characterization of materials by terahertz time-domain spectroscopy," *J. Opt. Soc. Am. B, JOSAB*, vol. 17, pp. 452–461, Mar. 2000.

[19] R. A. Lewis, "A review of terahertz sources," *J. Phys. D: Appl. Phys.*, vol. 47, p. 374001, Aug. 2014.

[20] R. A. Lewis, "A review of terahertz detectors," *J. Phys. D: Appl. Phys.*, vol. 52, p. 433001, Aug. 2019.

[21] X.-C. Zhang and J. Xu, *Introduction to THz wave photonics*. New York: Springer, c2010.

[22] Y.-S. Lee, *Principles of Terahertz Science and Technology*. Springer US.

[23] B. D. Pham, "Satellite remote sensing of the variability of the continental hydrology cycle in the lower Mekong basin over the last two decades," *ResearchGate*, Feb. 2018.

[24] R. Singh, "Harmonic and Anharmonic Oscillator Models for Pure Vibrational Infrared Spectroscopy of Diatomic Molecules," *IJASE*, vol. 8, Aug. 2021.

[25] K. O. Douglass, J. C. Keske, F. S. Rees, K. Welch, H. S. Yoo, B. H. Pate, I. Leonov, and R. D. Suenram, "Rotational spectroscopy of vibrationally excited states by infrared-Fourier transform microwave–microwave triple-resonance spectroscopy," *Chem. Phys. Lett.*, vol. 376, pp. 548–556, July 2003.

[26] V. W. Laurie, "Microwave Spectrum and Internal Rotation of Ethyl Cyanide," *J. Chem. Phys.*, vol. 31, pp. 1500–1505, Dec. 1959.

[27] N. A. W. C. W. Division, *Electronic Warfare & Radar Systems Engineering Handbook*. July 2013.

[28] J. Neu and C. A. Schmuttenmaer, "Tutorial: An introduction to terahertz time domain spectroscopy (thz-tds)," *J. Appl. Phys.*, vol. 124, no. 23, 2018.

[29] J. El Haddad, B. Bousquet, L. Canioni, and P. Mounaix, "Review in terahertz spectral analysis," *TrAC, Trends Anal. Chem.*, vol. 44, pp. 98–105, 2013.

[30] S. Dhillon, M. Vitiello, E. Linfield, A. Davies, M. C. Hoffmann, J. Booske, C. Paoloni, M. Gensch, P. Weightman, G. Williams, *et al.*, "The 2017 terahertz science and technology roadmap," *J. Phys. D: Appl. Phys.*, vol. 50, no. 4, p. 043001, 2017.

[31] D. H. Auston, "Picosecond optoelectronic switching and gating in silicon," *Appl. Phys. Lett.*, vol. 26, no. 3, pp. 101–103, 1975.

[32] M. Tani, K. Yamamoto, E. S. Estacio, C. T. Que, H. Nakajima, M. Hibi, F. Miyamaru, S. Nishizawa, and M. Hangyo, "Photoconductive Emission and Detection of Terahertz Pulsed Radiation Using Semiconductors and Semiconductor Devices," *J. Infrared Milli. Terahz. Waves*, vol. 33, pp. 393–404, Apr. 2012.

[33] T. Sasaki, T. Tanabe, T. Sakamoto, and J. Nishizawa, "Continuous Wave Terahertz Signal Generator based on Difference Frequency Generation in Gallium Phosphide crystal and its applications for spectroscopy," *IEEE International Conference on Nano/Micro Engineered and Molecular Systems*, 2016.

[34] G. K. Kitaeva, "Terahertz generation by means of optical lasers," *Laser Phys. Lett.*, vol. 5, p. 559, May 2008.

[35] H. A. Hafez, X. Chai, A. Ibrahim, S. Mondal, D. Férachou, X. Ropagnol, and T. Ozaki, "Intense terahertz radiation and their applications," *J. Opt.*, vol. 18, p. 093004, Aug. 2016.

[36] R. Emadi, N. Barani, R. Safian, and A. Z. Nezhad, "Hybrid Computational Simulation and Study of Terahertz Pulsed Photoconductive Antennas," *J. Infrared Millim. Terahertz Waves*, vol. 37, Nov. 2016.

[37] R. Pecharromán-Gallego and R. Pecharromán-Gallego, "An Overview on Quantum Cascade Lasers: Origins and Development," in *Quantum Cascade Lasers*, Croatia: IntechOpen, Apr. 2017.

[38] M. S. Vitiello and A. Tredicucci, "Physics and technology of Terahertz quantum cascade lasers," *Adv. Phys.*, Jan. 2021.

[39] M. Razeghi, Q. Y. Lu, N. Bandyopadhyay, W. Zhou, D. Heydari, Y. Bai, and S. Slivken, "Quantum cascade lasers: from tool to product," *Opt. Express*, vol. 23, pp. 8462–8475, Apr. 2015.

[40] N. Opačak, *The origin of frequency combs in free-running quantum cascade lasers*. PhD thesis, Technische Universität, Wien, Austria.

[41] W. Withayachumnankul and M. Naftaly, "Fundamentals of Measurement in Terahertz Time-Domain Spectroscopy," *J. Infrared Milli. Terahz. Waves*, vol. 35, pp. 610–637, Aug. 2014.

[42] J. Neu and C. A. Schmuttenmaer, "Tutorial: An introduction to terahertz time domain spectroscopy (THz-TDS)," *J. Appl. Phys.*, vol. 124, Dec. 2018.

[43] P. Kužel, H. Němec, F. Kadlec, and C. Kadlec, "Gouy shift correction for highly accurate refractive index retrieval in time-domain terahertz spectroscopy," *Opt. Express*, vol. 18, pp. 15338–15348, July 2010.

[44] P. Koleják, K. Postava, M. Mičica, P. Kužel, F. Kadlec, and J. Pištora, "Experimental Gouy phase shift compensation in Terahertz time-domain spectroscopy," *Photonics Nanostruct. Fundam. Appl.*, vol. 31, pp. 129–133, Sept. 2018.

[45] J. F. O'Hara, W. Withayachumnankul, and I. Al-Naib, "A Review on Thin-film Sensing with Terahertz Waves," *J. Infrared Milli. Terahz. Waves*, vol. 33, pp. 245–291, Mar. 2012.

[46] W. Withayachumnankul, J. F. O'Hara, W. Cao, I. Al-Naib, and W. Zhang, "Limitation in thin-film sensing with transmission-mode terahertz time-domain spectroscopy," *Opt. Express*, vol. 22, pp. 972–986, Jan. 2014.

[47] Z. Yang, T. Albrow-Owen, W. Cai, and T. Hasan, "Miniaturization of optical spectrometers," *Science*, vol. 371, no. 6528, p. eabe0722, 2021.

[48] R. R. Jones, D. C. Hooper, L. Zhang, D. Wolverson, and V. K. Valev, "Raman techniques: fundamentals and frontiers," *Nanoscale Res. Lett.*, vol. 14, pp. 1–34, 2019.

[49] D. Aspnes, "Spectroscopic ellipsometry—past, present, and future," *Thin Solid Films*, vol. 571, pp. 334–344, 2014.

[50] M. Schubert, "Another century of ellipsometry," *Annalen der Physik*, vol. 518, no. 7-8, pp. 480–497, 2006.

[51] A. Pashkin, M. Kempa, H. Němec, F. Kadlec, and P. Kužel, "Phase-sensitive time-domain terahertz reflection spectroscopy," *Rev. Sci. Instrum.*, vol. 74, pp. 4711–4717, Nov. 2003.

[52] Z. Mazaheri, C. Koral, and A. Andreone, "Accurate THz ellipsometry using calibration in time domain," *Sci. Rep.*, vol. 12, pp. 1–10, May 2022.

[53] N. Matsumoto, T. Hosokura, T. Nagashima, and M. Hangyo, "Measurement of the dielectric constant of thin films by terahertz time-domain spectroscopic ellipsometry," *Opt. Lett.*, vol. 36, pp. 265–267, Jan. 2011.

[54] R. Azzam and N. Bashara, "Ellipsometry and polarized light north-holland personal library," *Elsevier, Amsterdam*, vol. 19872, pp. 417–486, 1977.

[55] P. Marsik, K. Sen, J. Khmaladze, M. Yazdi-Rizi, B. P. P. Mallett, and C. Bernhard, "Terahertz ellipsometry study of the soft mode behavior in ultrathin SrTiO3 films," *Appl. Phys. Lett.*, vol. 108, Feb. 2016.

[56] J. Kircher, R. Henn, M. Cardona, P. L. Richards, and G. P. Williams, "Far-infrared ellipsometry using synchrotron radiation," *J. Opt. Soc. Am. B, JOSAB*, vol. 14, pp. 705–712, Apr. 1997.

[57] M. Li, J. Fortin, J. Y. Kim, G. Fox, F. Chu, T. Davenport, T.-M. Lu, and X.-C. Zhang, "Dielectric constant measurement of thin films using goniometric terahertz time-domain spectroscopy," *IEEE J. Sel. Top. Quantum Electron.*, vol. 7, pp. 624–629, July 2001.

[58] T. Nagashima and M. Hangyo, "Measurement of complex optical constants of a highly doped Si wafer using terahertz ellipsometry," *Appl. Phys. Lett.*, vol. 79, pp. 3917–3919, Dec. 2001.

[59] T. Hofmann, C. M. Herzinger, A. Boosalis, T. E. Tiwald, J. A. Woollam, and M. Schubert, "Variable-wavelength frequency-domain terahertz ellipsometry," *Rev. Sci. Instrum.*, vol. 81, Feb. 2010.

[60] C. D. W. Mosley, M. Failla, D. Prabhakaran, and J. Lloyd-Hughes, "Terahertz spectroscopy of anisotropic materials using beams with rotatable polarization," *Sci. Rep.*, vol. 7, pp. 1–9, Sept. 2017.

[61] T. Nagashima, M. Tani, and M. Hangyo, "Polarization-sensitive THz-TDS and its Application to Anisotropy Sensing," *J. Infrared Milli. Terahz. Waves*, vol. 34, pp. 740–775, Nov. 2013.

[62] W. J. Choi, K. Yano, M. Cha, F. M. Colombari, J.-Y. Kim, Y. Wang, S. H. Lee, K. Sun, J. M. Kruger, A. F. de Moura, and N. A. Kotov, "Chiral phonons in microcrystals and nanofibrils of biomolecules," *Nat. Photonics*, vol. 16, pp. 366–373, May 2022.

[63] W. J. Choi, G. Cheng, Z. Huang, S. Zhang, T. B. Norris, and N. A. Kotov, "Terahertz circular dichroism spectroscopy of biomaterials enabled by kirigami polarization modulators," *Nat. Mater.*, vol. 18, pp. 820–826, Aug. 2019.

[64] D. J. Aschaffenburg, M. R. C. Williams, D. Talbayev, D. F. Santavicca, D. E. Prober, and C. A. Schmuttenmaer, "Efficient measurement of broadband terahertz optical activity," *Appl. Phys. Lett.*, vol. 100, June 2012.

[65] Y. Ino, R. Shimano, Y. Svirko, and M. Kuwata-Gonokami, "Terahertz time domain magneto-optical ellipsometry in reflection geometry," *Phys. Rev. B*, vol. 70, p. 155101, Oct. 2004.

[66] K. Yatsugi, N. Matsumoto, T. Nagashima, and M. Hangyo, "Transport properties of free carriers in semiconductors studied by terahertz time-domain magneto-optical ellipsometry," *Appl. Phys. Lett.*, vol. 98, May 2011.

[67] A. Partanen, J. Väyrynen, S. Hassinen, H. Tuovinen, J. Mutanen, T. Itkonen, P. Silfsten, P. Pääkkönen, M. Kuittinen, K. Mönkkönen, *et al.*, "Fabrication of terahertz wire-grid polarizers," *Appl. Opt.*, vol. 51, no. 35, pp. 8360–8365, 2012.

[68] F. Yan, C. Yu, H. Park, E. P. Parrott, and E. Pickwell-MacPherson, "Advances in polarizer technology for terahertz frequency applications," *J. Infrared Millim. Terahertz Waves*, vol. 34, pp. 489–499, 2013.

[69] P. Kühne, N. Armakavicius, V. Stanishev, C. M. Herzinger, M. Schubert, and V. Darakchieva, "Advanced Terahertz Frequency-Domain Ellipsometry Instrumentation for In Situ and Ex Situ Applications," *IEEE Trans. Terahertz Sci. Technol.*, vol. 8, pp. 257–270, Apr. 2018.

[70] J. A. Hillier, S. Camelio, W. Cranton, A. V. Nabok, C. J. Mellor, D. C. Koutsogeorgis, and N. Kalfagiannis, "When ellipsometry works best: A case study with transparent conductive oxides," *ACS photonics*, vol. 7, no. 10, pp. 2692–2702, 2020.

[71] X. Chen, H. Gu, L. Jiamin, C. Chen, and S. Liu, "Advanced Mueller matrix ellipsometry: Instrumentation and emerging applications," *Sci. China Technol. Sci.*, vol. 65, 08 2022.

[72] M. Neshat and N. P. Armitage, "Terahertz time-domain spectroscopic ellipsometry: instrumentation and calibration," *Opt. Express*, vol. 20, pp. 29063–29075, Dec. 2012.

[73] Q. Guo, Y. Zhang, Z. Lyu, D. Zhang, Y. Huang, C. Meng, Z. Zhao, and J. Yuan, "THz Time-Domain Spectroscopic Ellipsometry With Simultaneous Measurements of Orthogonal Polarizations," *IEEE Trans. Terahertz Sci. Technol.*, vol. 9, pp. 422–429, June 2019.

[74] P. C. M. Planken, H.-K. Nienhuys, H. J. Bakker, and T. Wenckebach, "Measurement and calculation of the orientation dependence of terahertz pulse detection in ZnTe," *J. Opt. Soc. Am. B, JOSAB*, vol. 18, pp. 313–317, Mar. 2001.

[75] A. Rice, Y. Jin, X. F. Ma, X.-C. Zhang, D. Bliss, J. Larkin, and M. Alexander, "Terahertz optical rectification from xn–110-wz3bi zinc-blende crystals," *Appl. Phys. Lett.*, vol. 64, pp. 1324–1326, Mar. 1994.

[76] C. M. Morris, R. V. Aguilar, A. V. Stier, and N. P. Armitage, "Polarization modulation time-domain terahertz polarimetry," *Opt. Express*, vol. 20, pp. 12303–12317, May 2012.

[77] K. Xu, E. Bayati, K. Oguchi, S. Watanabe, D. P. Winebrenner, and M. H. Arbab, "Terahertz time-domain polarimetry (THz-TDP) based on the spinning E-O sampling technique: determination of precision and calibration," *Opt. Express*, vol. 28, pp. 13482–13496, Apr. 2020.

[78] K. Xu, M. Liu, and M. H. Arbab, "Broadband terahertz time-domain polarimetry based on air plasma filament emissions and spinning electro-optic sampling in GaP," *Appl. Phys. Lett.*, vol. 120, May 2022.

[79] G. Zhao, G. Savini, Y. Yu, S. Li, J. Zhang, and P. Ade, "A dual-port THz Time Domain Spectroscopy System optimized for recovery of a sample's Jones matrix," *Sci. Rep.*, vol. 9, pp. 1–9, Feb. 2019.

[80] O. Arteaga and A. Canillas, "Pseudopolar decomposition of the Jones and Mueller-Jones exponential polarization matrices," *J. Opt. Soc. Am. A, JOSAA*, vol. 26, pp. 783–793, Apr. 2009.

[81] S. Li, "Jones-matrix analysis with pauli matrices: application to ellipsometry," *JOSA A*, vol. 17, no. 5, pp. 920–926, 2000.

[82] R. Chipman, W. S. T. Lam, and G. Young, *Polarized light and optical systems*. CRC press, 2018.

[83] S. R. Cloude, "Uniqueness of Target Decomposition Theorems in Radar Polarimetry," in *Direct and Inverse Methods in Radar Polarimetry*, pp. 267–296, Dordrecht, The Netherlands: Springer, 1992.

[84] T. Seifert, S. Jaiswal, U. Martens, J. Hannegan, L. Braun, P. Maldonado, F. Freimuth, A. Kronenberg, J. Henrizi, I. Radu, *et al.*, "Efficient metallic spintronic emitters of ultrabroadband terahertz radiation," *Nat. Photonics*, vol. 10, no. 7, pp. 483–488, 2016.

[85] C. Bull, S. M. Hewett, R. Ji, C.-H. Lin, T. Thomson, D. M. Graham, and P. W. Nutter, "Spintronic terahertz emitters: Status and prospects from a materials perspective," *APL Materials*, vol. 9, no. 9, p. 090701, 2021.

[86] W. Wu, C. Yaw Ameyaw, M. F. Doty, and M. B. Jungfleisch, "Principles of spintronic THz emitters," *J. Appl. Phys.*, vol. 130, no. 9, p. 091101, 2021.

[87] M. Battiato, K. Carva, and P. M. Oppeneer, "Superdiffusive Spin Transport as a Mechanism of Ultrafast Demagnetization," *Phys. Rev. Lett.*, vol. 105, p. 027203, July 2010.

[88] J. Sinova, S. O. Valenzuela, J. Wunderlich, C. H. Back, and T. Jungwirth, "Spin Hall effects," *Rev. Mod. Phys.*, vol. 87, pp. 1213–1260, Oct. 2015.

[89] O. Mosendz, J. E. Pearson, F. Y. Fradin, G. E. W. Bauer, S. D. Bader, and A. Hoffmann, "Quantifying Spin Hall Angles from Spin Pumping: Experiments and Theory," *Phys. Rev. Lett.*, vol. 104, p. 046601, Jan. 2010.

[90] S. O. Valenzuela and M. Tinkham, "Direct electronic measurement of the spin Hall effect," *Nature*, vol. 442, pp. 176–179, July 2006.

[91] X. Wang and A. Manchon, "Diffusive Spin Dynamics in Ferromagnetic Thin Films with a Rashba Interaction," *Phys. Rev. Lett.*, vol. 108, p. 117201, Mar. 2012.

[92] T. S. Seifert, L. Cheng, Z. Wei, T. Kampfrath, and J. Qi, "Spintronic sources of ultrashort terahertz electromagnetic pulses," *Appl. Phys. Lett.*, vol. 120, no. 18, p. 180401, 2022.

[93] E. Th. Papaioannou and R. Beigang, "THz spintronic emitters: a review on achievements and future challenges," *Nanophotonics*, vol. 10, pp. 1243–1257, Jan. 2021.

[94] M. B. Panish, "Molecular Beam Epitaxy," *Science*, vol. 208, pp. 916–922, May 1980.

[95] H. C. Theuerer and J. J. Hauser, "Getter Sputtering for the Preparation of Thin Films of Superconducting Elements and Compounds," *J. Appl. Phys.*, vol. 35, pp. 554–555, Mar. 1964.

[96] K. Yamahara, A. Mannan, I. Kawayama, H. Nakanishi, and M. Tonouchi, "Ultrafast spatiotemporal photocarrier dynamics near gan surfaces studied by terahertz emission spectroscopy," *Sci. Rep.*, vol. 10, no. 1, p. 14633, 2020.

[97] K. Takano, M. Asai, K. Kato, H. Komiyama, A. Yamaguchi, T. Iyoda, Y. Tadokoro, M. Nakajima, and M. I. Bakunov, "Terahertz emission from gold nanorods irradiated by ultrashort laser pulses of different wavelengths," *Sci. Rep.*, vol. 9, no. 1, p. 3280, 2019.

[98] T. Kampfrath, K. Tanaka, and K. A. Nelson, "Resonant and nonresonant control over matter and light by intense terahertz transients," *Nat. Photonics*, vol. 7, pp. 680–690, Sept. 2013.

[99] T. Seifert, S. Jaiswal, M. Sajadi, G. Jakob, S. Winnerl, M. Wolf, M. Kläui, and T. Kampfrath, "Ultrabroadband single-cycle terahertz pulses with peak fields of 300 kV cm^{-1} from a metallic spintronic emitter," *Appl. Phys. Lett.*, vol. 110, no. 25, p. 252402, 2017.

[100] R. A. Red'kin, S. A. Bereznaya, Z. V. Korotchenko, and S. Yu. Sarkisov, "A comparison of terahertz electro-optic sampling in ZnTe, ZnSe, GaP and GaSe1-xSx crystals," in *2015 International Siberian Conference on Control and Communications (SIBCON)*, pp. 21–23, IEEE.

[101] M. Hibberd, D. Lake, N. Johansson, T. Thomson, S. Jamison, and D. Graham, "Magnetic-field tailoring of the terahertz polarization emitted from a spintronic source," *Appl. Phys. Lett.*, vol. 114, no. 3, p. 031101, 2019.

[102] D. Kong, X. Wu, B. Wang, T. Nie, M. Xiao, C. Pandey, Y. Gao, L. Wen, W. Zhao, C. Ruan, *et al.*, "Broadband spintronic terahertz emitter with magnetic-field manipulated polarizations," *Adv. Opt. Mater.*, vol. 7, no. 20, p. 1900487, 2019.

[103] S. Wang, W. Qin, S. Zhang, Y. Lou, C. Liu, T. Wu, Q. He, C. Tian, L. Zhou, Y. Wu, and Z. Tao, "Nanoengineered Spintronic-Metasurface Terahertz Emitters Enable Beam Steering and Full Polarization Control," *Nano Lett.*, vol. 22, pp. 10111–10119, Dec. 2022.

[104] D. Schulz, B. Schwager, and J. Berakdar, "Nanostructured Spintronic Emitters for Polarization-Textured and Chiral Broadband THz Fields," *ACS Photonics*, vol. 9, pp. 1248–1255, Apr. 2022.

[105] C. Liu, S. Wang, S. Zhang, Q. Cai, P. Wang, C. Tian, L. Zhou, Y. Wu, and Z. Tao, "Active spintronic-metasurface terahertz emitters with tunable chirality," *Adv. Photonics*, vol. 3, p. 056002, Oct. 2021.

[106] W. Wu, S. Lendinez, M. T. Kaffash, R. D. Schaller, H. Wen, and M. B. Jungfleisch, "Controlling polarization of spintronic THz emitter by remanent magnetization texture," *Appl. Phys. Lett.*, vol. 121, Aug. 2022.

[107] X. Chen, X. Wu, S. Shan, F. Guo, D. Kong, C. Wang, T. Nie, C. Pandey, L. Wen, W. Zhao, C. Ruan, J. Miao, Y. Li, and L. Wang, "Generation and manipulation of chiral broadband terahertz waves from cascade spintronic terahertz emitters," *Appl. Phys. Lett.*, vol. 115, Nov. 2019.

[108] R. Rouzegar, A. L. Chekhov, Y. Behovits, B. R. Serrano, M. A. Syskaki, C. H. Lambert, D. Engel, U. Martens, M. Münzenberg, M. Wolf, *et al.*, "Broadband Spintronic Terahertz Source with Peak Electric Fields Exceeding 1.5 MV/cm," *Phys. Rev. Appl.*, vol. 19, no. 3, p. 034018, 2023.

[109] R. I. Herapath, S. M. Hornett, T. Seifert, G. Jakob, M. Kläui, J. Bertolotti, T. Kampfrath, and E. Hendry, "Impact of pump wavelength on terahertz emission of a cavity-enhanced spintronic trilayer," *Appl. Phys. Lett.*, vol. 114, no. 4, p. 041107, 2019.

[110] G. Torosyan, S. Keller, L. Scheuer, R. Beigang, and E. T. Papaioannou, "Optimized spintronic terahertz emitters based on epitaxial grown Fe/Pt layer structures," *Sci. Rep.*, vol. 8, no. 1, pp. 1–9, 2018.

[111] F. M. Wagner, S. Melnikas, J. Cramer, D. A. Damry, C. Q. Xia, K. Peng, G. Jakob, M. Kläui, S. Kičas, and M. B. Johnston, "Optimised Spintronic Emitters of Terahertz Radiation for Time-Domain Spectroscopy," *J. Infrared Millim. Terahertz Waves.*, pp. 1–14, 2023.

[112] R. Rouzegar, A. Chekhov, Y. Behovits, B. Serrano, M. Syskaki, C. Lambert, D. Engel, U. Martens, M. Münzenberg, M. Wolf, G. Jakob, M. Kläui, T. Seifert, and T. Kampfrath, "Broadband Spintronic Terahertz Source with Peak Electric Fields Exceeding 1.5 MV/cm," *Phys. Rev. Appl.*, vol. 19, p. 034018, 3 2023.

[113] S. Liu, F. Guo, P. Li, G. Wei, C. Wang, X. Chen, B. Wang, W. Zhao, J. Miao, L. Wang, *et al.*, "Nanoplasmonic-Enhanced Spintronic Terahertz Emission," *Adv. Mater. Interfaces*, vol. 9, no. 2, p. 2101296, 2022.

[114] H. R. Bardolaza, J. P. R. Ferrolino, I. C. M. Verona, V. P. P. Juguilon, L. N. F. Dela Rosa, M. L. Talara, H. Kitahara, A. S. Somintac, A. A. Salvador, N. I. F. Cabello, A. E. De Los Reyes, M. Tani, and E. S. Estacio, "Terahertz emission characteristics of a metasurface-enhanced spintronic terahertz emitter," *J. Mater. Sci. - Mater. Electron.*, vol. 35, pp. 1–8, Mar. 2024.

[115] D. M. Nenno, L. Scheuer, D. Sokoluk, S. Keller, G. Torosyan, A. Brodyanski, J. Lösch, M. Battiato, M. Rahm, R. H. Binder, *et al.*, "Modification of spintronic terahertz emitter performance through defect engineering," *Sci. Rep.*, vol. 9, no. 1, pp. 1–16, 2019.

[116] S. Kumar, A. Nivedan, A. Singh, Y. Kumar, P. Malhotra, M. Tondusson, E. Freysz, and S. Kumar, "Optical damage limit of efficient spintronic THz emitters," *IScience*, vol. 24, no. 10, p. 103152, 2021.

[117] P. Wang, Z. Feng, Y. Yang, D. Zhang, Q. Liu, Z. Xu, Z. Jia, Y. Wu, G. Yu, X. Xu, and Y. Jiang, "Inverse orbital Hall effect and orbitronic terahertz emission observed in the materials with weak spin-orbit coupling," *npj Quantum Mater.*, vol. 8, pp. 1–6, May 2023.

[118] M. B. Jungfleisch, Q. Zhang, W. Zhang, J. E. Pearson, R. D. Schaller, H. Wen, and A. Hoffmann, "Control of terahertz emission by ultrafast spin-charge current conversion at Rashba interfaces," *Phys. Rev. Lett.*, vol. 120, no. 20, p. 207207, 2018.

[119] M. Tong, Y. Hu, Z. Wang, T. Zhou, X. Xie, X. Cheng, and T. Jiang, "Enhanced terahertz radiation by efficient spin-to-charge conversion in Rashba-mediated Dirac surface states," *Nano Lett.*, vol. 21, no. 1, pp. 60–67, 2020.

[120] T. Vogel, A. Omar, S. Mansourzadeh, F. Wulf, N. M. Sabanés, M. Müller, T. S. Seifert, A. Weigel, G. Jakob, M. Kläui, *et al.*, "Average power scaling of THz spintronic emitters efficiently cooled in reflection geometry," *Opt. Express*, vol. 30, no. 12, pp. 20451–20468, 2022.

[121] T. Minamikawa, Y.-D. Hsieh, K. Shibuya, E. Hase, Y. Kaneoka, S. Okubo, H. Inaba, Y. Mizutani, H. Yamamoto, T. Iwata, *et al.*, "Dual-comb spectroscopic ellipsometry," *Nat. Commun.*, vol. 8, no. 1, p. 610, 2017.

[122] A. S. Kowligy, H. Timmers, A. J. Lind, U. Elu, F. C. Cruz, P. G. Schunemann, J. Biegert, and S. A. Diddams, "Infrared electric field sampled frequency comb spectroscopy," *Sci. Adv.*, vol. 5, no. 6, p. eaaw8794, 2019.

[123] D. H. Goldstein, *Polarized light*. CRC press, 2017.

[124] G. Konnen, *Polarized light in nature*. CUP Archive, 1985.

[125] D. S. Kliger and J. W. Lewis, *Polarized light in optics and spectroscopy*. Elsevier, 2012.

[126] H. Fujiwara, *Spectroscopic ellipsometry: principles and applications*. John Wiley & Sons, 2007.

[127] H. Tompkins and E. A. Irene, *Handbook of ellipsometry*. William Andrew, 2005.

[128] J. N. Hilfiker, N. Hong, and S. Schoeche, "Mueller matrix spectroscopic ellipsometry," *Adv. Opt. Technol.*, vol. 11, no. 3-4, pp. 59–91, 2022.

[129] D. E. Aspnes, "Spectroscopic ellipsometry—A perspective," *J. Vac. Sci. Technol., A*, vol. 31, Sept. 2013.

[130] G. J. Wilhelmi, J. W. Rouse, and A. J. Blanchard, "Depolarization of light back scattered from rough dielectrics∗," *JOSA*, vol. 65, pp. 1036–1042, Sept. 1975.

[131] Y. Yang, K.-S. Chen, X. Yang, Z.-L. Li, and J. Zeng, "Depolarized Scattering of Rough Surface With Dielectric Inhomogeneity and Spatial Anisotropy," *IEEE Trans. Geosci. Remote Sens.*, vol. 59, pp. 47–59, June 2020.

[132] M. Moscoso, J. B. Keller, and G. Papanicolaou, "Depolarization and blurring of optical images by biological tissue," *J. Opt. Soc. Am. A, JOSAA*, vol. 18, pp. 948–960, Apr. 2001.

[133] J. J. Gil and R. Ossikovski, *Polarized light and the Mueller matrix approach*. CRC press, 2022.

[134] R. M. A. Azzam, "Stokes-vector and Mueller-matrix polarimetry [Invited]," *J. Opt. Soc. Am. A, JOSAA*, vol. 33, pp. 1396–1408, July 2016.

[135] S.-Y. Lu and R. A. Chipman, "Interpretation of mueller matrices based on polar decomposition," *JOSA A*, vol. 13, no. 5, pp. 1106–1113, 1996.

[136] R. A. Chipman, "Depolarization," in *Proceedings Volume 3754, Polarization: Measurement, Analysis, and Remote Sensing II*, vol. 3754, pp. 14–20, SPIE, Oct. 1999.

[137] S. Alali and I. A. Vitkin, "Polarized light imaging in biomedicine: emerging Mueller matrix methodologies for bulk tissue assessment," in *Journal of Biomedical Optics, Vol. 20, Issue 6*, vol. 20, p. 061104, SPIE, Mar. 2015.

[138] D. Lara and C. Dainty, "Axially resolved complete Mueller matrix confocal microscopy," *Appl. Opt.*, vol. 45, pp. 1917–1930, Mar. 2006.

[139] Y. Wang, H. He, J. Chang, C. He, S. Liu, M. Li, N. Zeng, J. Wu, and H. Ma, "Mueller matrix microscope: a quantitative tool to facilitate detections and fibrosis scorings of liver cirrhosis and cancer tissues," in *Journal of Biomedical Optics, Vol. 21, Issue 7*, vol. 21, p. 071112, SPIE, Apr. 2016.

[140] R. M. A. Azzam, "Simple general analysis of the polarization-dependent insertion loss of a linear optical system," *Pure Appl. Opt.*, vol. 3, p. 731, Sept. 1994.

[141] R. Ossikovski, "Differential matrix formalism for depolarizing anisotropic media," *Opt. Lett.*, vol. 36, pp. 2330–2332, June 2011.

[142] Q. Wu, M. Litz, and X.-C. Zhang, "Broadband detection capability of znte electro-optic field detectors," *Appl. Phys. Lett.*, vol. 68, no. 21, pp. 2924–2926, 1996.

[143] J. A. Fülöp, S. Tzortzakis, and T. Kampfrath, "Laser-driven strong-field terahertz sources," *Adv. Opt. Mater.*, vol. 8, no. 3, p. 1900681, 2020.

[144] E. T. Papaioannou and R. Beigang, "Thz spintronic emitters: a review on achievements and future challenges," *Nanophotonics*, vol. 10, no. 4, pp. 1243–1257, 2020.

[145] rodyo, "FEX-GODLIKE," Aug. 2024. [Online; accessed 21. Aug. 2024].

[146] Z. Feng, R. Yu, Y. Zhou, H. Lu, W. Tan, H. Deng, Q. Liu, Z. Zhai, L. Zhu, J. Cai, *et al.*, "Highly efficient spintronic terahertz emitter enabled by metal–dielectric photonic crystal," *Adv. Opt. Mater.*, vol. 6, no. 23, p. 1800965, 2018.

[147] Z. Jin, Y. Peng, Y. Ni, G. Wu, B. Ji, X. Wu, Z. Zhang, G. Ma, C. Zhang, L. Chen, A. V. Balakin, A. P. Shkurinov, Y. Zhu, and S. Zhuang, "Cascaded Amplification and Manipulation of Terahertz Emission by Flexible Spintronic Heterostructures," *Laser Photonics Rev.*, vol. 16, p. 2100688, Sept. 2022.

[148] J. Kröll, J. Darmo, and K. Unterrainer, "Metallic wave-impedance matching layers for broadband terahertz optical systems," *Opt. Express*, vol. 15, no. 11, pp. 6552–6560, 2007.

[149] B. Carli, "Reflectivity of metallic films in the infrared," *JOSA*, vol. 67, no. 7, pp. 908–910, 1977.

[150] L. Ding, X. Wang, N. S. S. Ang, C. Lu, V. Suresh, S.-J. Chua, and J. Teng, "Ultrathin film broadband terahertz antireflection coating based on impedance matching method," *IEEE J. Sel. Top. Quantum Electron.*, vol. 23, no. 4, pp. 1–8, 2016.

[151] F. Paries, N. Tiercelin, G. Lezier, M. Vanwolleghem, F. Selz, M.-A. Syskaki, F. Kammerbauer, G. Jakob, M. Jourdan, M. Kläui, Z. Kaspar, T. Kampfrath, T. S. Seifert, G. von Freymann, and D. Molter, "Fiber-tip spintronic terahertz emitters," *Opt. Express*, vol. 31, pp. 30884–30893, Sep 2023.

[152] R. W. Boyd, *Nonlinear Optics*. Elsevier, Academic Press, 2008.

[153] N. Amer, W. C. Hurlbut, B. J. Norton, Y.-S. Lee, and T. B. Norris, "Generation of terahertz pulses with arbitrary elliptical polarization," *Appl. Phys. Lett.*, vol. 87, Nov. 2005.

[154] Q. Song, Q. Song, X. Yuan, X. Yuan, S. Hu, J. Huang, H. Zhong, H. Zhong, Q. Lin, Q. Lin, H. Wang, H. Wang, X. Lu, X. Lu, M. Zheng, M. Zheng, Y. Cai, Y. Cai, Y. Cai, X. Zeng, X. Zeng, S. Xu, S. Xu, and S. Xu, "Enhance terahertz radiation and its polarization- control with two paralleled filaments pumped by two-color femtosecond laser fields," *Opt. Express*, vol. 29, pp. 22659–22666, July 2021.

[155] J. Dai, N. Karpowicz, and X.-C. Zhang, "Coherent Polarization Control of Terahertz Waves Generated from Two-Color Laser-Induced Gas Plasma," *Phys. Rev. Lett.*, vol. 103, p. 023001, July 2009.

[156] H. Wen and A. M. Lindenberg, "Coherent Terahertz Polarization Control through Manipulation of Electron Trajectories," *Phys. Rev. Lett.*, vol. 103, p. 023902, July 2009.

[157] O. Kosareva, M. Esaulkov, N. Panov, V. Andreeva, D. Shipilo, P. Solyankin, A. Demircan, I. Babushkin, V. Makarov, U. Morgner, A. Shkurinov, and A. Savel'ev, "Polarization control of terahertz radiation from two-color femtosecond gas breakdown plasma," *Opt. Lett.*, vol. 43, pp. 90–93, Jan. 2018.

[158] S. Winnerl, B. Zimmermann, F. Peter, H. Schneider, and M. Helm, "Terahertz Bessel-Gauss beams of radial and azimuthal polarization from microstructured photoconductive antennas," *Opt. Express*, vol. 17, pp. 1571–1576, Feb. 2009.

[159] S. Bowers, A. Safaripour, and A. Hajimiri, "Dynamic Polarization Control," *IEEE J. Solid-State Circuits*, 2015.

[160] S. Dash, C. Psomas, A. Patnaik, and I. Krikidis, "An ultra-wideband orthogonal-beam directional graphene-based antenna for THz wireless systems," *Sci. Rep.*, vol. 12, pp. 1–10, Dec. 2022.

[161] Y. Hirota, R. Hattori, M. Tani, and M. Hangyo, "Polarization modulation of terahertz electromagnetic radiation by four-contact photoconductive antenna," *Opt. Express*, vol. 14, no. 10, pp. 4486–4493, 2006.

[162] K. Peng, D. Jevtics, F. Zhang, S. Sterzl, D. A. Damry, M. U. Rothmann, B. Guilhabert, M. J. Strain, H. H. Tan, L. M. Herz, *et al.*, "Three-dimensional cross-nanowire networks recover full terahertz state," *Science*, vol. 368, no. 6490, pp. 510–513, 2020.

[163] H. Le Gall, J. Ben Youssef, N. Tiercelin, V. Preobrazhensky, and P. Pernod, "Low field anisotropic magnetostriction single domain exchange-coupled (tbfe/fe) multilayers: Static and dynamical properties," *J. Magn. Soc. Jpn.*, vol. 25, no. 3_2, pp. 258–262, 2001.

[164] J. B. Youssef, N. Tiercelin, F. Petit, H. Le Gall, V. Preobrazhensky, and P. Pernod, "Statics and dynamics in giant magnetostrictive Tb/sub x/Fe/sub 1-x/-Fe/sub 0.6/Co/sub 0.4/ multilayers for MEMS," *IEEE Trans. Magn.*, vol. 38, pp. 2817–2819, Dec. 2002.

[165] S. E. Clifton and P. Wohlfarth E., "A mechanism of magnetic hysteresis in heterogeneous alloys," *Philosophical Transactions of the Royal Society of London. Series A, Mathematical and Physical Sciences*, vol. 240, pp. 599–642, May 1948.

[166] A. Debray, A. Ludwig, T. Bourouina, A. Asaoka, N. Tiercelin, and G. Reyne, "Application of a multilayered magnetostrictive film to a micromachined 2-D optical scanner," *J. Microelectromech. Syst.*, vol. 13, pp. 264–271, Apr. 2004.

[167] Y. Dusch, N. Tiercelin, A. Klimov, S. Giordano, V. Preobrazhensky, and P. Pernod, "Stress-mediated magnetoelectric memory effect with uni-axial TbCo2/FeCo multilayer on 011-cut PMN-PT ferroelectric relaxor," *J. Appl. Phys.*, vol. 113, p. 17C719, Mar. 2013.

[168] E. W. Lee, "Magnetostriction and Magnetomechanical Effects," *Rep. Prog. Phys.*, vol. 18, p. 184, Jan. 1955.

[169] S.-D. Jiang and S.-X. Qin, "Prediction of the quantized axis of rare-earth ions: the electrostatic model with displaced point charges," *Inorg. Chem. Front.*, vol. 2, pp. 613–619, June 2015.

[170] H. Cheng, Q. Huang, H. He, Z. Zhao, H. Sun, Q. Wu, Z. Jiang, J. Wang, H. Huang, Z. Fu, and Y. Lu, "Giant Electrical Modulation of Terahertz Emission in $\mathrm{Pb}(\mathrm{Mg}_{1/3}\mathrm{Nb}_{2/3})_{0.7}\mathrm{Ti}_{0.3}\mathrm{O}_3/\mathrm{Co}{-}\mathrm{Fe}{-}\mathrm{B}/\mathrm{Pt}$ Structure," *Phys. Rev. Appl.*, vol. 16, p. 054011, Nov. 2021.

[171] F. Wang, L. Luo, D. Zhou, X. Zhao, and H. Luo, "Complete set of elastic, dielectric, and piezoelectric constants of orthorhombic 0.71Pb(xn–Mg13Nb23-0f7de)O3–0.29PbTiO3 single crystal," *Appl. Phys. Lett.*, vol. 90, p. 212903, May 2007.

[172] V. C. Agulto, T. Iwamoto, H. Kitahara, K. Toya, V. K. Mag-usara, M. Imanishi, Y. Mori, M. Yoshimura, and M. Nakajima, "Terahertz time-domain ellipsometry with high precision for the evaluation of GaN crystals with carrier densities up to 1020 cm-3," *Sci. Rep.*, vol. 11, pp. 1–10, Sept. 2021.

[173] N. Matsumoto, T. Nagashima, T. Fujii, H. Takagi, and M. Hangyo, "Development of THz ellipsometer with variable incident angle," in *2009 34th International Conference on Infrared, Millimeter, and Terahertz Waves*, pp. 21–25, IEEE.

[174] K. Morino, S. Arakawa, T. Fujii, S. Mouri, T. Araki, and Y. Nanishi, "Characterization of the electrical properties of an InN epilayer using terahertz time-domain spectroscopic ellipsometry," *Jpn. J. Appl. Phys.*, vol. 58, p. SCCB22, May 2019.

[175] H. Chen, K. Wang, X. Chen, and G. Fang, "Real-time and calibration-free generalized terahertz time-domain spectroscopic ellipsometry," *Appl. Phys. Lett.*, vol. 124, Mar. 2024.

[176] J. Petzelt, I. Mayerová, Č. Bárta, and L. D. Kislovskii, "Polar optic phonons in Hg2Cl2 and Hg2Br2," *Czech. J. Phys.*, vol. 23, pp. 845–854, Aug. 1973.

[177] P. Koleják, D. Vala, K. Postava, P. Provazníková, and J. Pištora, "Mueller matrix ellipsometry of waveplates for control of their properties and alignment," *J. Vac. Sci. Technol., B*, vol. 38, p. 014006, Dec. 2019.

[178] S. W. Im, H.-Y. Ahn, R. M. Kim, N. H. Cho, and K. T. Nam, "Chiral Surface and Geometry of Metal Nanocrystals," *Adv. Mater.*, vol. 32, Dec. 2019.

[179] M. Tani, O. Morikawa, S. Matsuura, and M. Hangyo, "Generation of terahertz radiation by photomixing with dual- and multiple-mode lasers," *Semicond. Sci. Technol.*, vol. 20, p. S151, June 2005.

[180] S. Matsuura and H. Ito, "Generation of CW Terahertz Radiation with Photomixing," in *Terahertz Optoelectronics*, pp. 157–202, Berlin, Germany: Springer, May 2005.

[181] S. Preu, G. H. Döhler, S. Malzer, L. J. Wang, and A. C. Gossard, "Tunable, continuous-wave Terahertz photomixer sources and applications," *J. Appl. Phys.*, vol. 109, p. 061301, Mar. 2011.

[182] E. R. Brown, K. A. McIntosh, K. B. Nichols, and C. L. Dennis, "Photomixing up to 3.8 THz in low-temperature-grown GaAs," *Appl. Phys. Lett.*, vol. 66, pp. 285–287, Jan. 1995.

[183] R. Safian, G. Ghazi, and N. Mohammadian, "Review of photomixing continuous-wave terahertz systems and current application trends in terahertz domain," in *Optical Engineering, Vol. 58, Issue 11*, vol. 58, p. 110901, SPIE, Nov. 2019.

[184] J. Xie, W. Ye, L. Zhou, X. Guo, X. Zang, L. Chen, and Y. Zhu, "A Review on Terahertz Technologies Accelerated by Silicon Photonics," *Nanomaterials*, vol. 11, p. 1646, June 2021.

[185] E. Compain, S. Poirier, and B. Drevillon, "General and self-consistent method for the calibration of polarization modulators, polarimeters, and Mueller-matrix ellipsometers," *Appl. Opt.*, vol. 38, pp. 3490–3502, June 1999.